

Dynamic soil-pile interaction by random vibration methods

by

Mohammad Fotouhi

A dissertation submitted to the graduate faculty
in partial fulfillment of the requirements for the degree of
DOCTOR OF PHILOSOPHY

Major: Civil Engineering (Geotechnical Engineering)

Program of Study Committee:
Jeremy C. Ashlock, Major Professor
Thomas Rudolphi
Vernon R. Schaefer
Sri Sritharan
R. Christopher Williams

Iowa State University

Ames, Iowa

2014

Copyright © Mohammad Fotouhi, 2014. All rights reserved

DEDICATION

To my parents, who are playing the melody of love and kindness in my life.

TABLE OF CONTENTS

ACKNOWLEDGEMENTS	vi
ABSTRACT	vii
1. CHAPTER I: INTRODUCTION	1
1.1 Overview of Soil-Foundation Interaction	1
1.2 Overview of the Research	3
2. CHAPTER II: EXPERIMENTAL PHASE	6
2.1 Overview	6
2.2 Soil and Pile Properties	9
2.3 Pile-Cap	11
2.4 Excitation	12
2.5 Instrumentation and Data Acquisition Systems	16
2.6 Measurement Approach:	18
2.7 Centroidal Accelerances	30
2.8 Test Results and Interpretation	39
2.8.1 Representative Test	48
2.9 APPENDIX	69
2.9.1 CPT Profile	69
2.9.2 Modulus and Damping Profile from Formulas of Hardin & Drnevich	85
2.9.2.1 Strain range	89
2.9.2.2 Number of cycles	89
2.9.2.3 Plasticity index (PI)	91
2.9.2.4 Void ratio (e)	91
2.9.2.5 Stress history (OCR)	92
2.9.2.6 Effective strength parameters	92

	2.9.2.7 Summary of soil parameters	94
	2.9.2.8 Sensitivity analyses	95
3	CHAPTER III: THEORETICAL MODELING AND VERIFICATION	106
	3.1 Overview	106
	3.2 Theoretical Accelerance Formulation	110
	3.2.1 HC test configuration	110
	3.2.2 VE test configuration	119
	3.3 Soil-Pile Impedance Functions by Approximate Methods	122
	3.3.1 Overview of relevant previous studies	122
	3.3.2 Novak and Aboul-Ella method	130
	3.3.2.1 Verification of approximate method of Novak and Aboul-Ella	133
	3.4 Soil-Pile Impedance Functions by Boundary Element Method (BEM)	146
	3.4.1 Overview	146
	3.4.2 BEM program verification	155
	3.4.2.1 Two-domain model	156
	3.4.2.2 Three-domain models	170
	3.5 Parametric Studies and Sensitivity Analyses	189
	3.6 APPENDIX	198
	3.6.1 Inertial properties of system components	198
	3.6.1.1 Rigid pile-cap block with embedded pile segment	198
	3.6.1.2 Inertial properties of shaker	200
	3.6.2 Composite pile-cap-shaker properties for the three test configurations	204
	3.6.2.1 VC test configuration	205
	3.6.2.2 HC test configuration	205
	3.6.2.3 VE test configuration	206
	3.6.3 Summary	206

4	CHAPTER IV: COMPUTATIONAL MODELING AND OPTIMIZATION	207
4.1	Overview	207
4.2	Approximate Method versus BEM Analysis	207
4.3	Optimization of Soil Profiles	217
4.3.1	G_{\max} and $D_{S_{\max}}$ profiles	218
4.3.2	Incorporation of soil shear strain profile	223
4.3.2.1	Step 1	223
4.3.2.2	Step 2	224
4.3.2.3	Step 3	232
4.3.2.4	Step 4	235
4.3.2.5	Step 5	240
4.3.3	Modification factor, MF (z)	242
4.3.3.1	Special case $b=0$	245
4.3.3.2	Modification proposed in previous centrifuge study	275
4.4	Impedance Modification Factor (IMF) Approach	280
4.4.1	Overview	280
4.4.2	IMF results for tests in unimproved and improved soils	286
4.4.3	Insights from IMF method	294
4.5	Three-Domain Disturbed-Zone Computational Models	307
	CHAPTER V: SUMMARY AND CONCLUSIONS	313
	REFERENCES	318

ACKNOWLEDGEMENTS

I would like to express the deepest appreciation to my advisor, Dr Jeramy Ashlock, who went far beyond the ordinary duties of an advisor, by being a tremendous mentor, supportive friend, and thoughtful leader. Without his inspirational and philosophical guidance accomplishing this thesis would not have been possible.

I would especially like to thank my dear friends, Dr Mostafa Zamanian and Dr Mirzad Mohandespour who provided a constructive scientific environment outside the campus. Many thought provoking discussions we shared on related topics kept me motivated along the journey. I also appreciate their help on editing and writing style.

Without the unconditional support of my family and many helps from my lovely friends in Iowa, who perfectly played the role of my second family during these five years, this work would not have been accomplished.

I am grateful to Professors Thomas Rudolphi, Vernon R. Schaefer, Sri Sritharan and R. Christopher Wiliams for serving on my dissertation committee.

This material is based upon work supported by the National Science Foundation through grant number CMMI-0936627, and used the Extreme Science and Engineering Discovery Environment (XSEDE), which is supported by NSF grant number ACI-1053575. This support is gratefully acknowledged. Any opinions, findings, and conclusions or recommendations expressed in this material are those of the author and do not necessarily reflect the views of the National Science Foundation.

This project was a payload to the NEESR-SG project 0830328. The assistance of the NEESR-SG project teams and the nees@UCLA team is appreciated.

ABSTRACT

Dynamic soil-foundation interaction is an important consideration in the design of structures subjected to dynamic loads such as earthquakes, wind, machine vibration, vehicle loading, and impacts. One reason for this importance is that soil-structure interaction (SSI) can have detrimental effects on the dynamic response of soil-foundation-structure systems. However, present theories and solutions for dynamic soil-pile interaction can be quite complex and contain several parameters that are not known with a high degree of certainty. Additionally, several aspects of dynamic soil-pile interaction problems are difficult to characterize accurately, such as the highly-nonhomogeneous spatial distribution of soil properties, the nonlinear and stress-dependent mechanical response of soil, variable soil-pile contact conditions, and complexities of 3D wave propagation in nonhomogeneous media. Despite significant advancements in theoretical and experimental research on dynamic soil-pile interaction, many of the available simplified approaches as well as sophisticated numerical models fail to accurately capture the observed responses from realistic multi-modal experiments.

To help bridge the knowledge-gap between existing theories and experimental observations for dynamic soil-pile interaction problems, a program of full-scale dynamic field tests were performed in this study using two identical H-piles at the same site containing soft clay. One pile was installed in the natural soil profile, and the other was partially embedded in an improved soil-cement zone. A new servo-hydraulic inertial shaker testing system and modular pile-cap were developed, then used to perform forced-vibration tests on the piles using random vibration techniques. Three different types and intensities of broadband excitation were applied to the system using the shaker installed on the pile cap in three different testing configurations. For the

first time, the multi-modal vertical-eccentric (VE) dynamic test, first developed for scaled-model geotechnical centrifuge experiments, was performed on full-scale pile foundations in natural soil conditions, and verified to simultaneously capture the important aspects of the vertical, horizontal, and coupled horizontal-rocking modes of vibration. A new set of theoretical centroidal acceleration solutions was developed for the dynamic response of soil-pile systems for which an inertial shaker moving in rigid body motion with the pile-cap provides the excitation.

On the theoretical side, an existing approximate method was evaluated against the experiments as well a rigorous 3D boundary element program. It was shown that the approximate method lacks accuracy in the low frequency region and also in characterizing the vertical mode of vibration for the actual soil and pile conditions encountered. Two sets of shear modulus and damping profiles were introduced based on cone penetration tests and widely-used empirical design equations, and the effect of the dynamic shear strain level in the soil surrounding the pile was investigated. The numerical models were then calibrated to minimize the mismatch between theory and experiment by introducing a multi-modal error function which accounts for the three centroidal modes of vibration, while employing relative weighing factors developed through parametric studies and engineering judgment. The method of impedance modification factors (IMF) and the advanced three-domain computational disturbed-zone model developed from centrifuge experimentation were extended for the first time to the full-scale pile tests and natural soil conditions. The results verified that the IMF method can capture the experimental response for the pile in unimproved soil very well. The three-domain disturbed-zone computational continuum model showed promise for simultaneously capturing the experimental centroidal horizontal and rotational peak frequencies using modulus and damping profiles in the disturbed zone that were generated through reasonable modifications of the far-field profiles.

CHAPTER I: INTRODUCTION

1.1 Overview of Soil-Foundation Interaction

Deep foundations are commonly used to support important structures in problematic soils. Relative to shallow foundations, deep foundations have a greater contact area with the soil, and thus exhibit a greater dependence on the depth-wise variation of the soil properties. The load-bearing capacity and dynamic behavior of pile foundations is critically important to the design of structures subjected to dynamic loads such as earthquakes, wind, machine and vehicle vibration, and impacts. One of the major steps in pile design should therefore be devoted to investigation of the dynamic behavior of the soil-pile-foundation system and resulting dynamic load transfer between the soil, pile, and superstructure.

Dynamic soil-structure interaction (SFSI) remains an active and challenging area of research in civil engineering, since the dynamic response of soil-foundation-structure systems will differ depending on whether soil-structure interaction is included in the analysis. This difference in the structure's natural period is not always on the safe side and can cause higher demand based on the earthquake demand curve for the region (Mylonakis & Gazetas, 2000), and hence relates to the safety and serviceability of many important structures under dynamic loading. Dynamic SSI is also an important consideration for avoiding resonance in structures housing vibrating machinery (e.g., Wolf, 1985; Clough & Penzien, 1993; Beskos, 1994; Kramer, 1996; Hall & Oliveto, 2003; Andersen, 2006; Orense, et al., 2010). Theories and solutions for dynamic soil-pile interaction are

usually quite complex due to the often random nature of the dynamic loads, highly nonhomogeneous nature and nonlinear stress-dependent mechanical response of soil deposits, and complexities of 3D wave propagation and resulting geometrical damping. Additionally, the influence of soil-pile separation, pile installation effects, and dependence of the soil's response on the in-situ and load-induced spatial variation of shear modulus and damping can also complicate the pile response. As a result, many SSI theories contain several material parameters that are not known with a high degree of certainty.

To validate and calibrate theoretical solutions which may contain many unknowns and simplifying assumptions, intermediate-scale pile-soil interaction experiments (e.g., Boominathan & Ayothiraman, 2005; 2007) or model-scale centrifuge studies (Scott, 1981; Meymand, 1984; Coe, et al., 1985; Finn & Gohl, 1987; Ko, 1988; Lenke, et al., 1991; Wilson, et al., 1997; Ashlock & Pak, 2009; Liu, et al., 2011; Mason, et al., 2013) and relatively fewer full-scale soil-pile interaction studies (Alpan, 1973; Gle, 1981; Blaney & O'Neill, 1986; Dunnivant, 1986; Boominathan & Ayothiraman, 2006; Manna & Baidya, 2009; Ayothiraman, et al., 2014) have been performed to date. Although intermediate and centrifuge-scale tests may offer good control of soil properties and efficient parametric variation, they cannot fully replicate the full-scale stress-dependent behavior of soil and resulting soil-structure interaction phenomena. On the other hand, the high cost and logistical difficulties of full-scale dynamic pile testing have resulted in a limited number of such experiments.

To date, many analytical and numerical approaches to dynamic pile-soil interaction with different levels of complexity ranging from simplified 2D approximations (e.g., Novak, 1974; Kausel, 1975; Blaney G. W., 1976; Novak, 1978; Novak & Aboul-Ella, 1978; Gazetas, 1984; Dobry, 1985; Dobry & Gazetas, 1988; Gazetas, 1991; Kaynia & Kausel, 1991) to 3D numerical

models (e.g., Beskos, 1997; Pak & Guzina, 1999; Hall & Oliveto, 2003; Maheshwari, et al., 2004; Guzina, et al., 2006; Ashlock, 2006; Elgamal, et al., 2010; Kouroussis, et al., 2013) have been developed and described in the literature. However, validation of the various methods against full-scale field tests is essential for an understanding of their relative capabilities and limitations. Due to the many assumptions made and material properties used in their formulation, calibration of such theories against full-scale tests with realistic soil and loading conditions is also essential.

1.2 Overview of the Research

To help bridge the knowledge gaps between theory and experimental observation in soil-pile interaction problems, a program of full-scale dynamic field tests and complementary development of new computational models are performed in this study. The experimental results are used to assess the performance of some approximate solutions commonly used in practice. A rigorous 3D boundary element program is used to develop computational models, and the model parameters including soil shear modulus and material damping ratio profiles are calibrated through inverse signal-matching optimization procedures. To address the scopes of the experimental and computational phases of the research, the thesis is divided into 4 chapters.

Chapter 2 is devoted to the experimental phase of the study. Details of field tests of two identical steel H-piles installed to a depth of 6 m in soft clay are presented. A new portable servo-hydraulic inertial shaker system is developed, and its performance for dynamic testing of piles using random vibration techniques is explored. The new inertial shaker system is shown to successfully enable multi-modal dynamic testing of pile foundations without the requirements of costly reaction frames and hydraulic actuators. Experimental results are presented on the influence

of local soil improvement on the dynamic pile response. The outcome of separate tests of vertical and coupled horizontal-rocking modes as well as hybrid multi-mode tests are discussed. Centroidal accelerance functions are defined in this chapter and the experimental results are converted to this format. The various experiments on piles in improved and un-improved soils are then compared to provide further insight to the dynamic behavior of the soil-pile-shaker system. Two alternative approaches are presented in the appendix to characterize the profiles of shear modulus and damping based on in-situ cone penetration tests and empirical relations for modulus and damping developed from dynamic laboratory tests. Finally, sensitivity analyses of the parameters in the empirical modulus and damping equations are presented.

In Chapter 3, the theoretical framework of the study which contains a sub-structuring approach is presented. Two computational methods; one approximate and the other based on rigorous 3D boundary element analyses, are employed to solve the soil-pile interaction problem. The reliability of the approximate method is discussed and the related software programs are validated through a verification study. A parametric study at the end of this chapter brings better insight into the dynamic behavior of the system and helps to understand the sensitivity of the critical parameters in the model.

The results of the computational modeling and comparisons between the experimental data and theoretical results are presented in Chapter 4. An error function is defined to characterize the degree of fit between the theoretical and experimental results, and is then used to minimize the existing mismatch through a system-identification calibration process to determine the optimum model parameters, including soil modulus and damping profiles. The simplified Impedance Modification Factor method for use in engineering practice is examined and validated for the problem under study. Three-domain boundary element computational continuum models, which

incorporate a disturbed-zone around the pile and enable vertical and horizontal heterogeneity, are developed to improve the modeling capabilities. The disturbed-zone around the pile can enable the models to capture pile installation effects and nonlinear soil behavior in the near-field zone, while enabling the wave propagation in the far-field to be captured as well.

Finally, a summary of the experimental and theoretical findings along with some recommendations and suggestions for future studies are presented in Chapter 5.

CHAPTER II: EXPERIMENTAL PHASE

2.1 Overview

Full-scale elastodynamic vibration tests were performed on two steel HP piles installed to an approximate depth of 6 m in a soil profile containing soft clay in Miami, Oklahoma in September 2010. The present payload project uses a soil site and reaction piles from the NEESR-SG project entitled “Understanding and Improving the Seismic Behavior of Pile Foundations in Soft Clays” (NSF Award #0830328), which involves dynamic and cyclic lateral tests of open-ended pipe piles in soft clays similar to soils commonly found in seismically active areas. Current seismic design codes impose limits on lateral displacements of pile foundations in order to mitigate the development of plastic hinges below grade. Weak or liquefiable soils, however, may not be able to provide the required magnitudes of lateral resistance, in which case admixtures may be used to improve the soil’s stiffness and strength. The dynamic behavior of piles in such improved soft soils is not well understood, and the aforementioned project seeks to address this research need through analysis and testing of piles in both virgin and improved soils (Ashlock & Fotouhi, 2011).

Due to the nondestructive nature of the small-scale wave propagation tests described herein, the payload project was executed with minimal disturbance to the NEESR-SG project. However, as an added precaution against the high-frequency pile vibrations elevating the pore pressures in the surrounding soil which could alter the pile-soil contact conditions, the payload

tests were performed on the reaction H-piles instead of the pipe test piles of the NEESR-SG project. The two reaction piles tested in unimproved and improved soil profiles will be referred to as piles U and I, respectively. Figure 2-1 shows the configuration of the piles at the test site.



Figure 2-1. Test site and pile layout.

To address the problem, experimental capabilities were developed in this investigation to provide realistic multi-modal dynamic excitation of pile foundations over a wide range of frequencies. In particular, techniques developed through centrifuge testing of both shallow and deep foundations (Ashlock, 2006; Pak & Ashlock, 2000; Pak, et al., 2006; Pak, et al., 2008; Pak, et al., 2011; Ashlock & Pak, 2009) were extended for the first time to full-scale pile foundations. These techniques include the use of the hybrid-mode vertical eccentric (VE) test, in which simultaneous vertical and coupled lateral-rocking motions of the foundation are stimulated using a vertical excitation that is offset horizontally from the centroid of the pile cap. The result is a combination of a vertical force and net moment at the foundation centroid, activating the vertical and coupled lateral-rocking modes of vibration simultaneously. To examine the equivalence of a single VE test to the traditionally separate combination of tests having vertical and horizontal forcing, two other test types were performed in this study. These

are the vertical centric (VC) test, in which a vertical load is applied above the foundation centroid, and the horizontal centric (HC) test, in which a horizontal force is applied at an arbitrary elevation in the vertical plane of the centroid. These test set-ups are depicted in Figure 2-2.

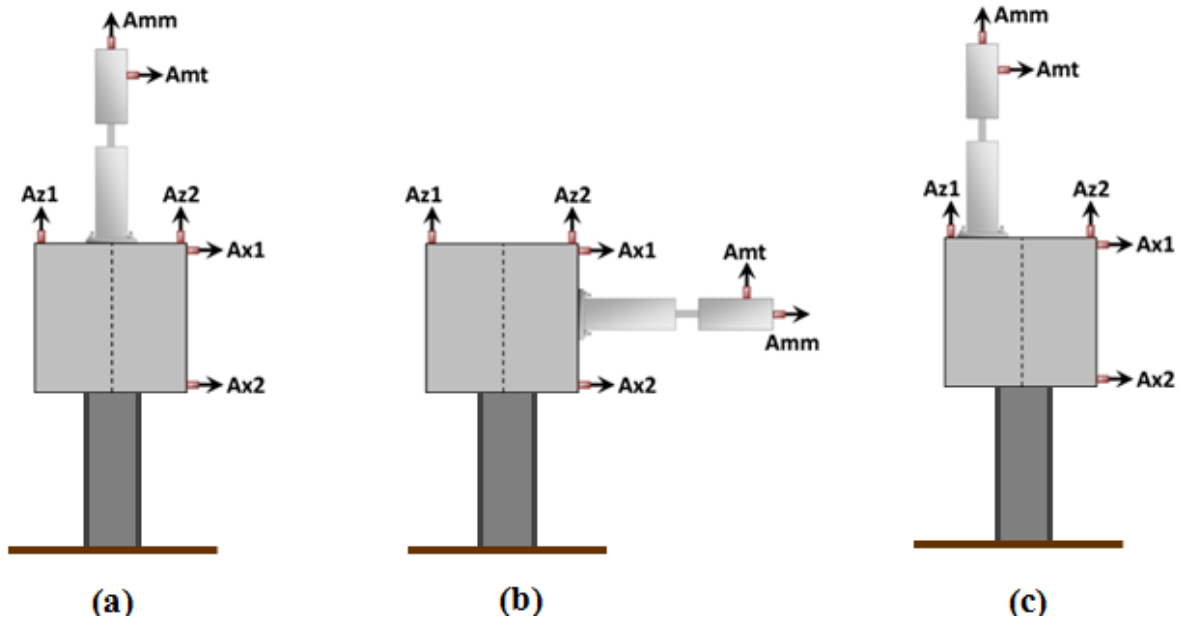


Figure 2-2. Three different test configurations used in this study;
(a) VC test, (b) HC test, (c) VE test.

For a symmetric pile cap, the VC test will invoke a purely vertical response, while the HC test will invoke a planar response consisting of coupled horizontal and rocking modes. Increased testing efficiency will be gained by demonstrating the equivalence of a single VE test to the combination of traditionally separate VC and HC tests. Furthermore, the VE test minimizes stress-history effects that arise when VC and HC tests are performed sequentially on the same pile, and alleviates concerns over the equivalence of soil properties when VC and HC tests are performed on separate piles and their response combined to obtain the general

behavior for multi-directional excitations. In addition to the benefits outlined above, the present study provides a valuable opportunity for the first full-scale verification of numerous experimental findings from centrifuge studies of pile vibration tests performed at the University of Colorado at Boulder (Pak, et al., 2006; Ashlock, 2006; Ashlock & Pak, 2009) and further refinement of advanced computational continuum boundary element models developed to simulate the observed dynamic behavior of the soil-pile system (Ashlock, 2006). Additionally, the first full-scale calibrations will be obtained for simplified engineering procedures (Pak, et al., 2006) for rectifying the poor performance of basic continuum theories for pile-soil interaction.

2.2 Soil and Pile Properties

Testing was performed next to the Neosho River in Miami, Oklahoma on September 27th through 29th, 2010. The test site consists of a 3.6 ft thick layer of lean clay with gravel and occasional construction debris, followed by 9.2 ft of silty clay to clayey silt, underlain by 8.2 ft of sandy gravel and limestone bedrock at a depth of 21 ft. Site investigation and in-situ testing performed for the NEESR-SG project included SPT tests, CPT and DMT soundings, and piston samples. Laboratory tests such as triaxial test, cyclic triaxial test, oedometer test, grain-size analysis, Atterberg limits test, and unconfined compressive strength test are then performed on the samples (Quiroga, 2013).

Both of the HP 10x42 piles tested in this study have a total length of approximately 25 feet and were installed by a vibratory hammer to embedment depths of 245 inches for Pile I

and 242 inches for Pile U. The above-ground unembedded lengths are 55.75 inches for Pile I and 57.75 inches for Pile U.

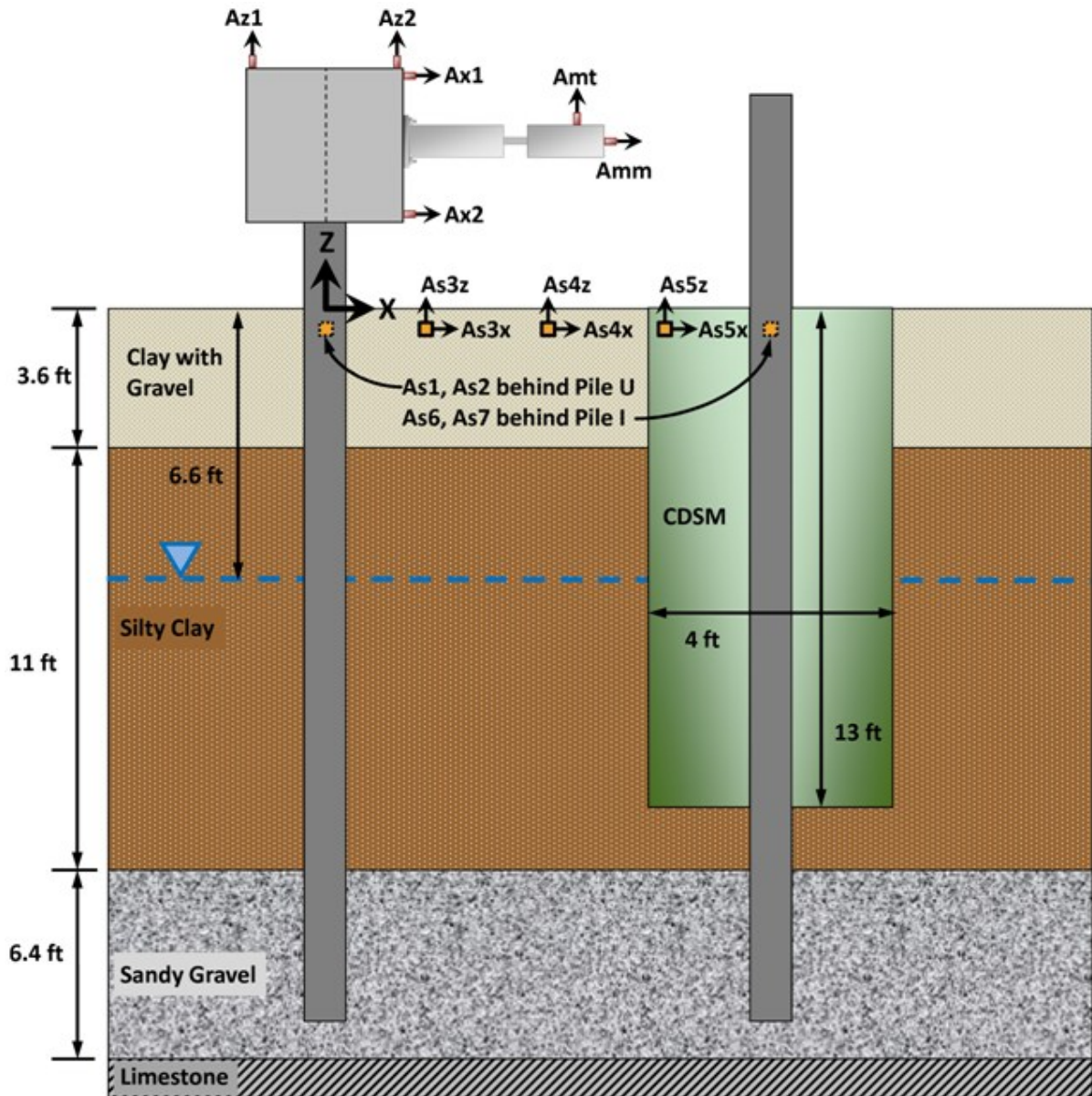


Figure 2-3. Site profile and sensor layout. Shaker shown in HC position on Pile U (Fotouhi & Ashlock, 2012).

The cylindrical CDSM improved zone around Pile I has a diameter of 48 inches and a depth of 13 ft. The estimated capacity of the pile in unimproved soil is 168 kips in compression

and 35 kips in tension, which increases to 374 kips in compression and 240 kips in tension for the pile in improved soil. The schematic in Figure 2-3 shows a section of the soil profile and CDSM zone, as well as the accelerometers mounted on the pile-cap, on the shaker, and in the soil.

2.3 Pile-Cap

To test the piles under dynamic loading, a two-piece modular pile cap was constructed. The pile cap was 3x3x3 ft in size and had a recess on each half forming a cavity such that the two pieces fit around the H-pile and are bolted together with six $\frac{3}{4}$ inch diameter threaded rods. The cavity extends to 8 inches below the top of the pile cap, so that the H-pile is embedded 28 inches into the cap. To ensure that tight contact would be achieved with various piles having slightly different tolerances, four steel shims were fabricated for insertion between the flanges of the H-pile and the inside of the pile cap. To ensure rigid body motion of the pile cap, a dense frame of reinforcing steel was designed using #5 bars, with #3 bars used for J-hooks (Figure 2-4).

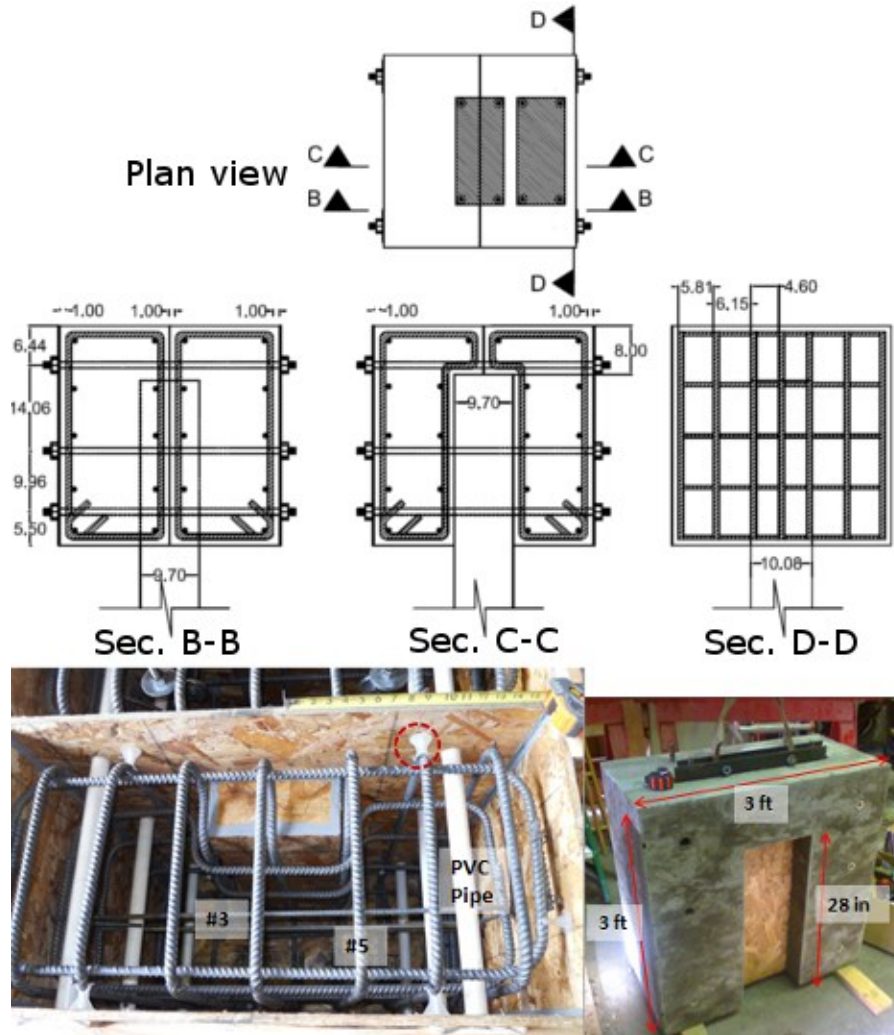


Figure 2-4. Pile-cap design drawings and photos of formwork, rebar, and one-half of finished cap. All dimensions in inches.

2.4 Excitation

As mentioned earlier, this study is focused on random vibration techniques applied to dynamic pile-soil interaction problems. Such techniques typically involve the excitation of a physical or electrical system over a wide range of frequencies, and complementary measurement techniques which efficiently characterize the system response in terms of Fast-Fourier Transforms (FFTs), correlation functions, spectral densities, transfer functions, coherence functions, and impulse response functions. Compatible excitation types are those

that can deliver energy over the measurement bandwidth of interest; typically random (white noise or pink noise), impulse or swept-sine signals. One of the experimental goals of this study is to evaluate the relative effectiveness of these three excitation types over a range of amplitudes.

Although a linear hydraulic actuator could be used to deliver the forcing, such an excitation source would require construction of a massive, costly and time-consuming reaction frame each time a test was performed. Additionally, linking the test structure to a reaction frame by an actuator can cause kinematic constraints leading to unwanted transverse forces applied to the structure. In this study, an efficient, portable testing system was desired which could be used at a variety of sites in the future without the need for reaction frames or a large generator to run an electric hydraulic pump. To meet these criteria, a servo-hydraulic inertial shaker system was designed and built by Anco Engineers to the specifications of the project. The key requirements were the capability to deliver user-specified broadband dynamic forcing with up to 2,000 lb of force over a bandwidth of 1-200 Hz, selectable force or displacement feedback control, and a modular design such that inertial reaction masses could be added by hand without the need for a crane. Table 2-1 lists the specifications of the shaker.

Table 2-1. Specifications of servo-hydraulic inertial shaker.

Peak dynamic force	2,000 lb (8,900 N)
Stroke	1.1 inch (28 mm) peak to peak
Valve size	Dual 5 GPM = 10 GPM (36 LPM) total
Operating pressure	3000-3400 psi
High frequency roll-off	~200 Hz
Moving Mass	115 lb (51 kg) min, 787 lb max
Weight	~300 lb (135 kg) + added weights

The shaker has a weight of 300 lb, of which 115 lb is a moving carriage. For variable control over the shaker's spectral performance curve, up to 14 extra masses weighing 48 lb each can be mounted on the carriage in pairs, giving a maximum moving mass of 787 lb. Adding extra masses provides greater force at low frequencies but decreases the maximum usable frequency. Because the schedule in this study was limited to a few days for payload tests, it was not possible to perform a parametric study to determine the optimum number of reaction masses for the given pile-cap-soil configuration. However, it was determined that four pairs of extra masses comprising a total reaction mass of 499 lb provided a good balance between low and high-frequency performance. The shaker is shown with different reaction masses in Figure 2-5.

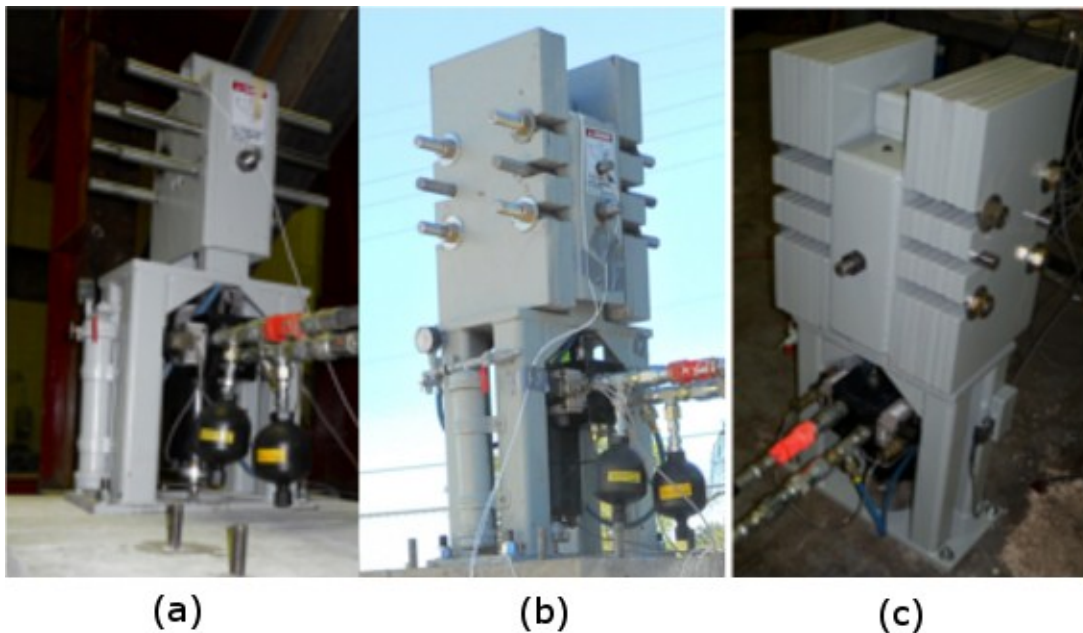


Figure 2-5. Servo-hydraulic inertial shaker with (a) zero masses, (b) 8 masses, and (c) 14 masses attached to moving carriage.

The shaker control system features a proportional-integral (PI) feedback control loop that allows a user-generated command voltage signal, and requires a hydraulic power supply with 3,000 psi pressure at a flow rate of 10 gallons per minute (GPM). To provide this capability in a portable package without the need for a large pump or generators, a Riemann & Georger Corporation model HV2310 Hydrapak gas-powered hydraulic pump with a 6-gallon hydraulic oil tank was used. The Hydrapak was modified to use 5 micron filtration as required for use with the shaker's servo-valve, and the pressure was adjusted down from the stock 3400 psi to the required 3000 psi.

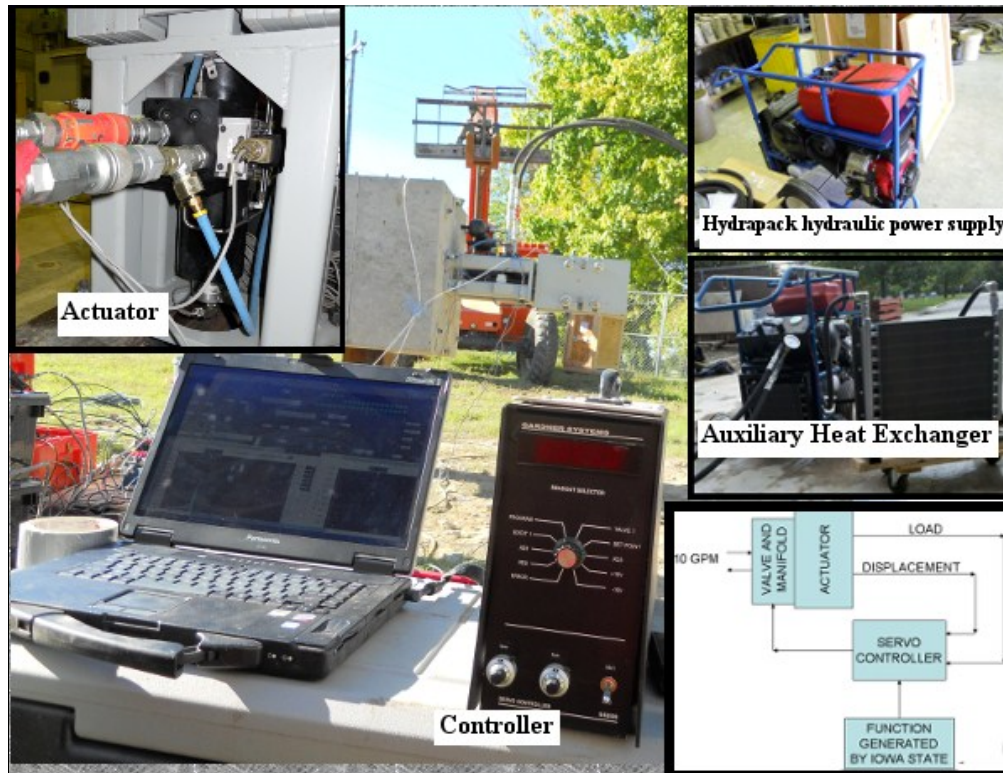


Figure 2-6. Control block diagram of shaking system and photos of its components.

During preliminary testing, it was found that the hydraulic oil was overheating due to the closed-center configuration of the servovalve, whereas the Hydrapak is typically used with

open-center servos. If allowed to overheat, the oil would damage the servovalve, requiring a costly repair. To eliminate overheating, the cooling capacity of the system was tripled by inserting a large auxiliary heat exchanger (Hayden Industrial model TTEC 20924) in the loop between the existing heat exchanger and the oil reservoir (Figure 2-6).

2.5 Instrumentation and Data Acquisition Systems

For data acquisition and real-time analysis in the time and frequency domains, a dynamic signal analyzer was programmed in LabVIEW. The analyzer features recording and display of time-histories, FFTs, spectral densities, transfer functions and coherence functions, and allows for a variety of excitation types including random, swept-sine and user-defined signals, with standard windowing and averaging capabilities built in. A screen-shot of the program is shown in Figure 2-7.

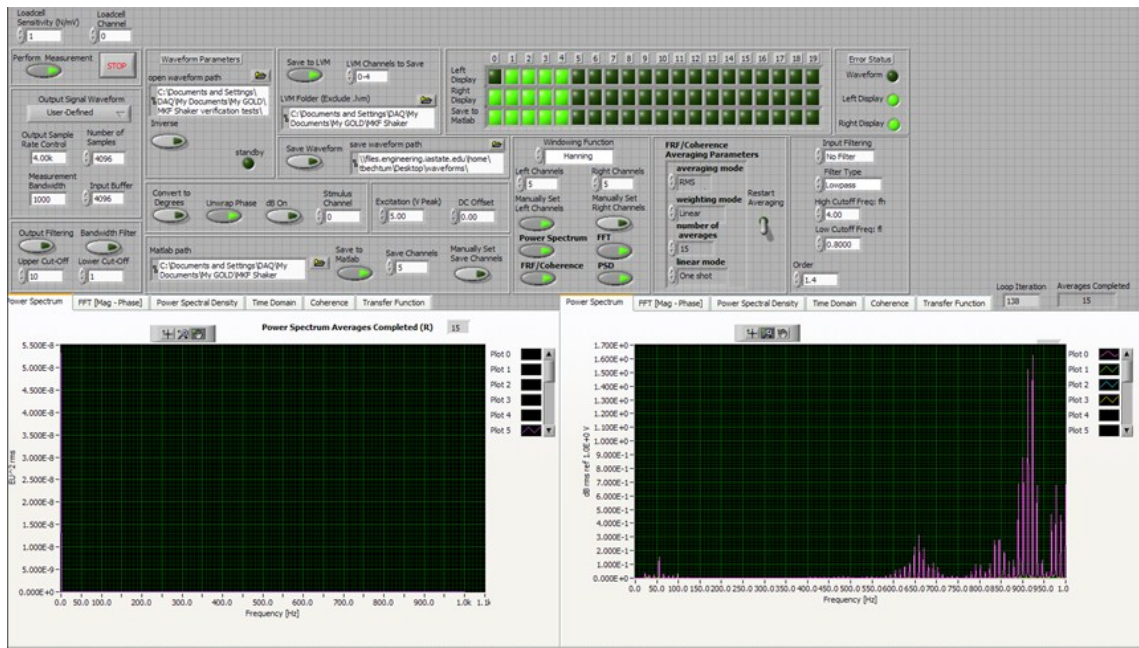


Figure 2-7. Screen-shot of the data acquisition program developed using LabVIEW.

The hardware components of the network analyzer consist of a National Instruments (NI) cDAQ 9172 USB chassis, five NI model 9234 4-channel analog input modules with 24-bit resolution and 51.2 kHz maximum sampling rate, and an NI 9263 analog output module for generating the command signal for the shaker. When performing frequency domain measurements, the sampling rate is either chosen directly or is typically calculated based on the requested measurement bandwidth and number of data points (frequency lines). The LabVIEW analyzer program follows the standard practice of setting the sampling rate (f_s) to 2.56 times the requested measurement bandwidth (B). Choosing the number of data points (N) to acquire then fixes the frequency resolution $\Delta f = f_s/N$, resulting in $B/\Delta f = N/2.56$ usable alias-free frequency lines. Additionally, most analyzers typically store only the final of a number of time-histories when performing spectral averaging, and this convention was followed in the LabVIEW program to maintain throughput performance. Since the acts of sampling the data at a chosen sample rate and saving only the last of a number of time-histories both represent some loss of information, the complete time-histories of the test data were also recorded for all signals so that users of NEEShub could evaluate the data using their own chosen techniques and sampling parameters. The complete time-histories also allow the frequency-domain measurements to be reconstructed in the event of lost data. All data signals were therefore split and the complete time-histories were recorded on the nees@UCLA Kinematics Granite seismic monitoring systems (Figure 2-8) at the maximum possible sampling rate of 1,000 Hz.

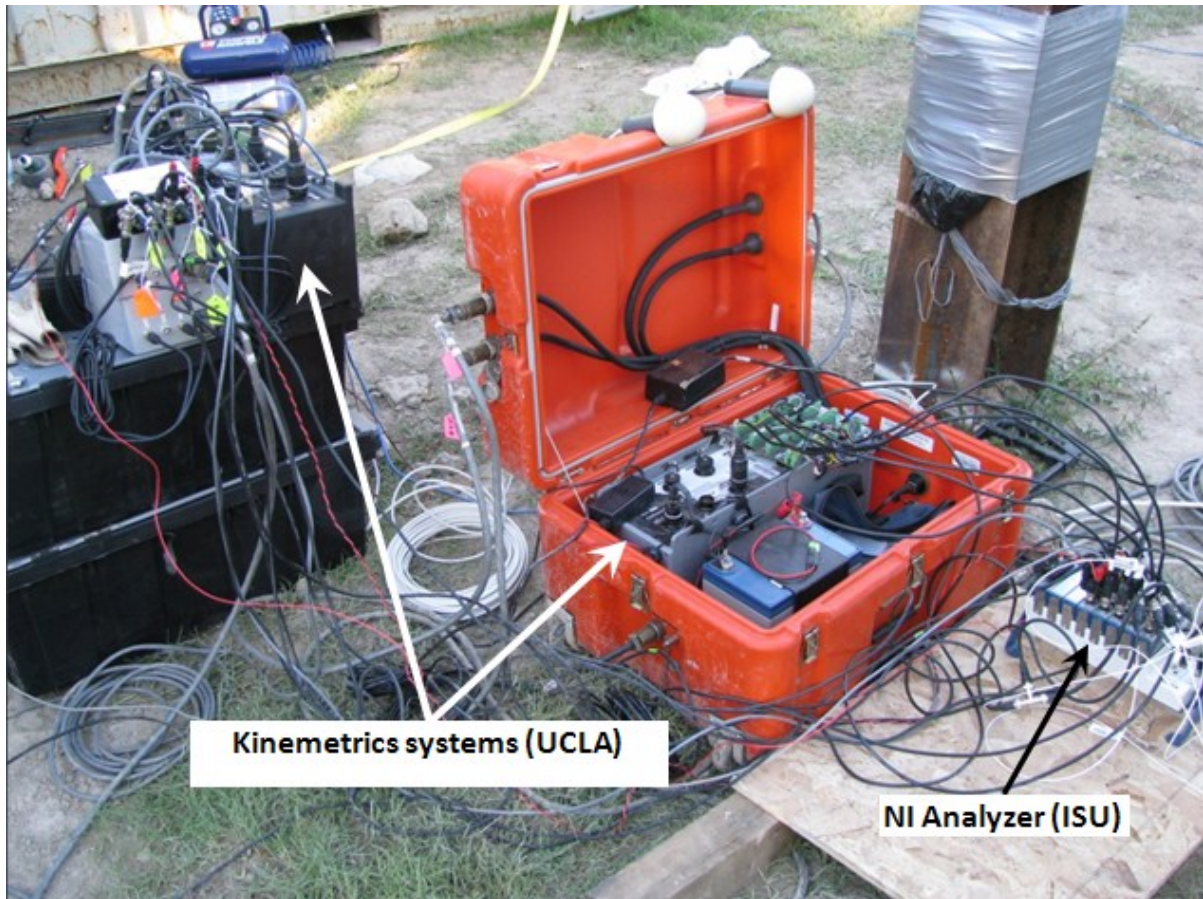


Figure 2-8. National Instruments dynamic signal analyzer and Kinematics Granite data acquisition systems.

2.6 Measurement Approach

In all tests, accelerations of the shaker's moving mass and the pile cap were recorded in the x (horizontal) and z (vertical) directions in the plane of motion of the pile cap using PCB Model 353B33 accelerometers, labeled as shown in Figure 2-3. The acceleration of the shaker's moving mass in the direction of shaking is denoted A_{mm} and is proportional to the dynamic force delivered to the pile cap. For use with careful analytical evaluation of higher-order loading effects, the acceleration of the shaker's moving mass transverse to the excitation direction was also measured, denoted A_{mt} . Vertical acceleration of the pile cap was measured

at the two edges, denoted A_{z1} and A_{z2} , the average of which gives the acceleration of the top-center point of the pile cap. Similarly, horizontal pile-cap accelerations were measured, denoted A_{x1} and A_{x2} , respectively in Figure 2-3. Accelerations in x and z directions were also recorded in the soil using 7 nees@UCLA Episensor triaxial accelerometers buried 6 inches below the soil surface as shown in Figure 2-9 and 2-10. Additional NEES resources from UCLA used in this study include the Mobile Command Center (MCC), telepresence cameras and the wireless network.

During testing, the acceleration signals were recorded by the NI analyzer in the time-domain and processed in the form of power spectral densities (PSD), coherence functions (COH) and transfer functions (XFER). In general, the transfer function between a system input $x(t)$ and output $y(t)$ can be defined as

$$H_{xy}(f) = \frac{\bar{G}_{xy}(f)}{\bar{G}_{xx}(f)} \quad (2.1)$$

in which f is frequency and $\bar{G}_{xy}(f)$ denotes the cross-spectral density of input and output and $\bar{G}_{xx}(f)$ is the auto-spectral density of the input (see Bendat & Piersol, 1986). In Equation (2.1), bars over the spectral densities denote ensemble averages, which are performed to minimize measurement errors due to random sources of noise. In the tests, the shaker moving mass A_{mm} was taken as the system input, and all other accelerations were taken as system outputs.

The resulting acceleration transfer functions can be divided by the shaker's moving mass of $499 \text{ lb}/32.2 \text{ ft/s}^2 = 15.5 \text{ lb-s}^2/\text{ft}$, to give acceleration-to-force transfer functions, commonly referred to as accelerance functions. This modification makes the transfer function independent of the moving mass of the shaker (M_{mm}) and converts the measured transfer

functions to the more general acceleration-to-force format of Equation 2.2, which can be more readily compared to other studies, and more easily interpreted and used by other analysts. Throughout this study, the accelerance, denoted A , will be used to present the experimental data as well as the results of theoretical analyses and computational simulations;

$$A_{xy}(f) = \frac{\bar{G}_{xy}(f)}{M_{mm}\bar{G}_{xx}(f)} \quad (2.2)$$

For example, the $A(\text{VC}/\text{VE})$ transfer function is defined as the vertical centric (VC) acceleration of the pile cap normalized by the vertical eccentric (VE) force $M_{mm}A_{mm}$ of the shaker moving mass in the VE test configuration. For a more global approach, the vertical and horizontal accelerations measured at three non-collinear points on the pile-cap can be reduced to three centroidal accelerances. The procedure is described in detail in section 2.7. These centroidal accelerances correspond to horizontal, vertical and rotational acceleration at the centroid, and will be denoted A_{xC} , A_{zC} and $A_{\theta C}$, respectively. The coherence function,

$$\gamma_{xy}^2(f) = \frac{|\bar{G}_{xy}(f)|^2}{\bar{G}_{xx}(f)\bar{G}_{yy}(f)} \quad (2.3)$$

is an indicator of measurement quality that takes a value of unity for a perfectly linear, time invariant system with no added noise. Deviations from any of these conditions cause the coherence to decrease towards zero. The coherence was observed in real-time during tests to obtain the best quality transfer functions by adjusting the intensities and frequency ranges of the various excitation waveforms.

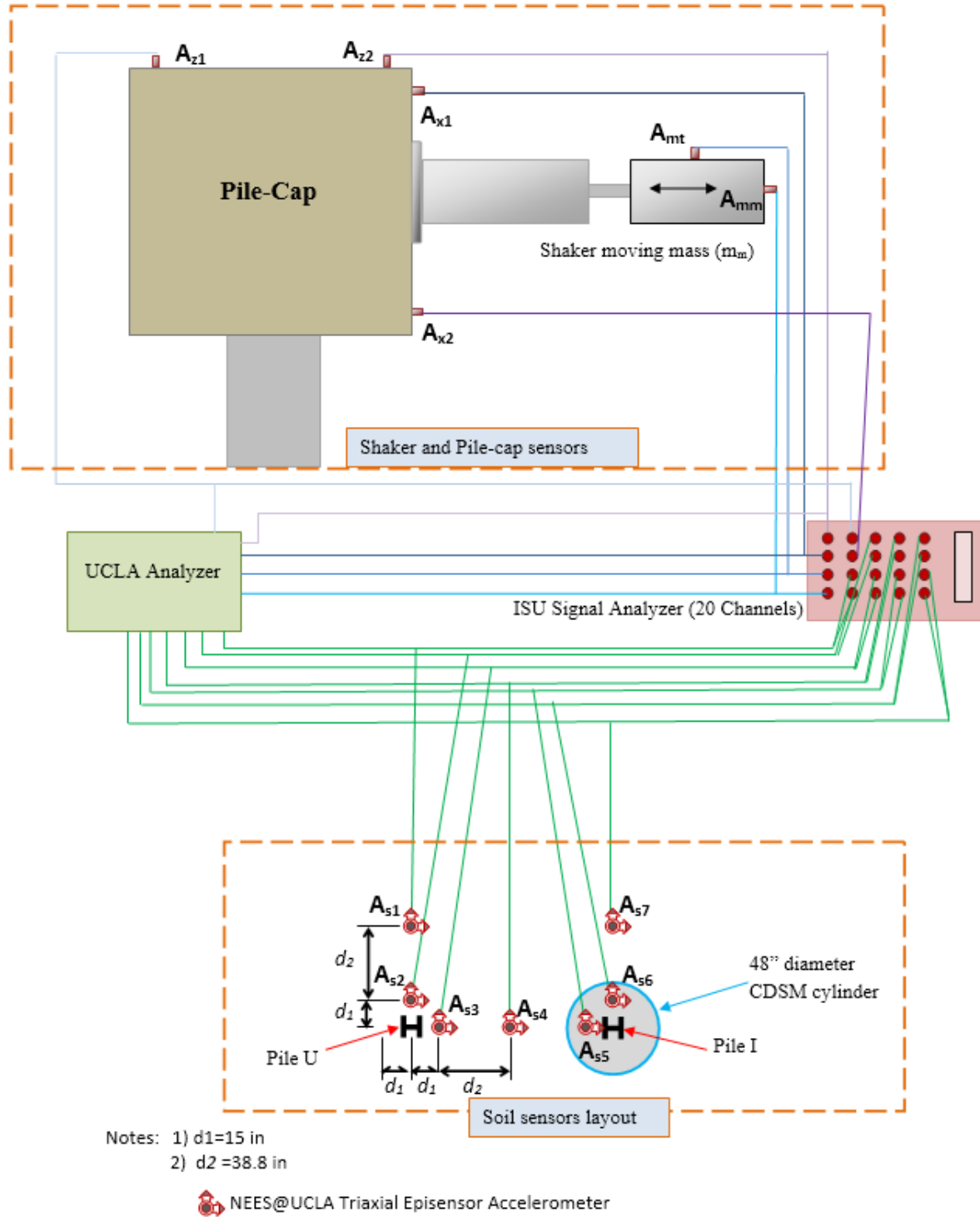


Figure 2-9. Top: Orientation and notation for accelerometers on shaker and pile cap (shaker in HC test position) Bottom: Soil accelerometers layout around the test piles.

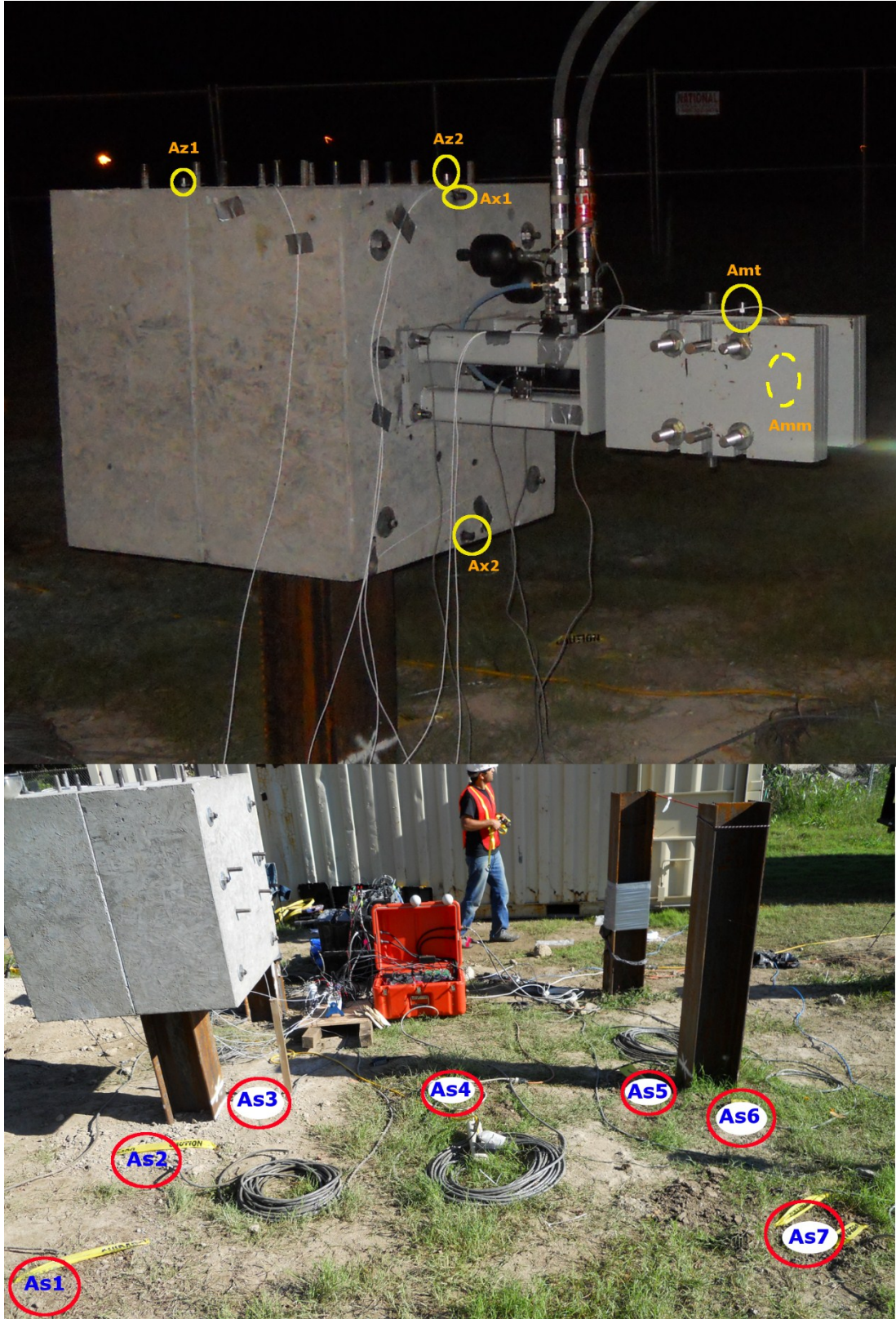


Figure 2-10. Locations of accelerometers mounted on pile-cap and embedded in soil.

To ascertain the level of ambient vibration caused by background sources such as generators and engines, nearby traffic and trains, and micro-seismic activity, accelerations were recorded before and after starting the portable hydraulic power supply without excitation from the shaker. Such ambient tests are useful for determining the signal-to-noise ratio in subsequent forced vibration tests. However, if the ambient sources are of sufficient magnitude, they can also be useful for characterizing the properties of the dynamic system, examples of which include centrifuge testing (Bendat & Piersol, 1986) or Refraction Micro-tremor studies. Following the ambient tests, three different types of forcing signals, referred to as random (R), chaotic impulse (C), and swept sine (S) were used to excite the pile.

Theoretically, the broadband random signal (R) contains energy at all frequencies in the selected bandwidth uniformly, i.e. the spectral density is constant. Due to physical limitations of the system, however, the spectral density of the force applied by the shaker is not perfectly uniform, but is of sufficient amplitude across the frequency band of interest to excite the response of the soil-structure system above the ambient levels.

The chaotic impulse signal (C) can be defined as a series of randomly-timed impulses with randomly distributed amplitudes. This type of excitation was found to be useful in centrifuge and field-scale studies of pile and footing vibration (Ashlock, 2006; Ashlock & Phipps, 2011). For testing configurations in which an electromagnetic exciter is used to deliver random forcing to a footing or pile through a load cell mounted on the structure, chaotic impulses can be generated by sending the exciter a random signal while moving its center of motion away from the load cell. The nature of the random excitation signal then creates a succession of randomly timed impulses, between which the structure undergoes temporary free-vibration. To avoid excessive periods of free vibration which would lead to decreased

coherence between the force and response, the durations between impacts are then adjusted by altering the exciter's center of motion to maximize the observed coherence. In aforementioned test setups using a load cell, the chaotic impulse technique has the effect of minimizing unwanted frictional effects, thus improving coherence and therefore quality of transfer functions. Because of its demonstrated usefulness in creating alternating forced- and free-vibration periods for effective stimuli in dynamic foundation testing, the chaotic impulse excitation technique was also examined in this study to evaluate its effectiveness when used with an inertial shaker system. Because the electromagnetic exciter was attached to a rigid reaction frame, it could deliver impacts to the test structure. However, since the inertial shaker was attached to the pile cap, it could not deliver impacts, but could instead apply short-duration impulses.

Chaotic impulse excitation was simulated in this study by sending the shaker a control signal consisting of the force time-history recorded by a load cell in a previous good-quality chaotic impulse test of a field-scale surface foundation (see Ashlock & Phipps, 2011). During the pile tests, however, it became evident that the time scale of the user-defined input signal became compressed, resulting in impulses occurring more rapidly than in the footing test from which the force signal was taken. Although the larger mass and lower fundamental period of the pile cap relative to the footing should logically be accounted for by a scaling of the time axis, the unintended scaling applied by the LabVIEW program was counter to the desired result. Due to the short time allotted for preparation and payload testing, the issue could not be corrected in the field, and thus chaotic impulse tests were performed using the time-compressed signal. The chaotic impulse tests should be further studied with careful

consideration of the input (load cell measurement) and output (control voltage signal) sample rates for the footing and pile tests, respectively.

The third type of excitation used was swept-sine (S), for which the frequency of a sinusoidal signal was continuously swept over the measurement bandwidth at a chosen sweep rate. While random excitation signals partition the energy across the frequency spectrum, swept-sine signals concentrate the signal's energy at a single frequency at any given time. Consequently, for the voltage output capabilities of a given measurement system, swept sine signals can be used to deliver larger excitation levels than those obtainable with random excitation, as will be demonstrated in the following experimental results.

Because the excitation types described above can deliver energy across the frequency spectrum of interest, they are useful for rapid measurement of the system's response in terms of spectral densities or transfer functions. In contrast to traditional stepped-sine tests in which the response is measured for a single excitation frequency at a time (e.g., when using eccentric mass shakers), random vibration techniques enable measurement of the system response at thousands of frequency points in a matter of seconds, providing much greater efficiency.

The testing program in this study consisted of 1,000 Hz bandwidth VC tests on the pile in improved soil (Pile I) using random (R), chaotic impulse (C) and swept-sine (S) excitation, performed initially at a low forcing intensity (denoted as excitation level 1). In the order performed, these tests were named I-VC-R1, I-VC-C1 and I-VC-S1. The loading intensity was then increased to an intermediate value (level 2), and the tests were repeated, named I-VC-R2, I-VC-C2 and I-VC-S2. Loading intensity was increased to level 3, and tests I-VC-R3, I-VC-C3 and I-VC-S3 were performed, followed by various additional tests in which the

forcing intensity was increased and other experimental parameters were varied. For example, the bandwidth was decreased to 250 Hz to examine the low-frequency behavior in more detail, the loading intensity was further increased to examine nonlinear behavior, and sweep rates of 1, 2 and 3 seconds were used. After the VC tests, the shaker was moved to the HC position and the suite of tests was repeated (i.e. tests I-HC-R1, I-HC-C1, etc.), followed by hybrid-mode VE tests (I-VE-R1, I-VE-C1, etc.). The pile cap was then moved from Pile I to Pile U and the program of tests was repeated, with the prefix I changed to U in the test names. Examples of the three excitation types and intensity levels are shown in the time and frequency domains in Figure 2-11 for VE tests on Pile I.

For organization and dissemination of test data on the Network for Earthquake Engineering Simulation hub (NEEShub), the entire test program was categorized into a hierarchy of experiments, trials, and repetitions. The tests were sorted into six different experiments corresponding to the different test configurations (Piles I and U with test types VC, HC and VE), where each experiment contains several trials corresponding to the different excitation parameters. This model of archiving data was required by the NEEShub and used to organize all the 109 tests performed during the project as shown in Figure 2-12.

As mentioned above, the acceleration of the shaker's moving mass was treated as the stimulus signal and all other accelerations of the pile cap and soil were treated as response quantities. In addition to the spectral measurements stored by the NI signal analyzer, the complete time-histories of all signals were recorded by the nees@UCLA Granite data acquisition systems for the geotechnical community to analyze using their own preferred methods and bandwidths. For example, using the raw data, one may compute transfer functions between the pile-cap and soil, or between different points in the soil for calibration

of analytical and computational models of the dynamic pile-soil interaction problem. Data and detailed documentation for the more than 100 tests can be downloaded by the public from the NEEShub at <http://nees.org/warehouse/project/940>. Test data may also be plotted online using the inDEED data exploration tool. To plot the frequency domain data using inDEED, the template builder command should be used to create a new template with frequency as the x-axis.

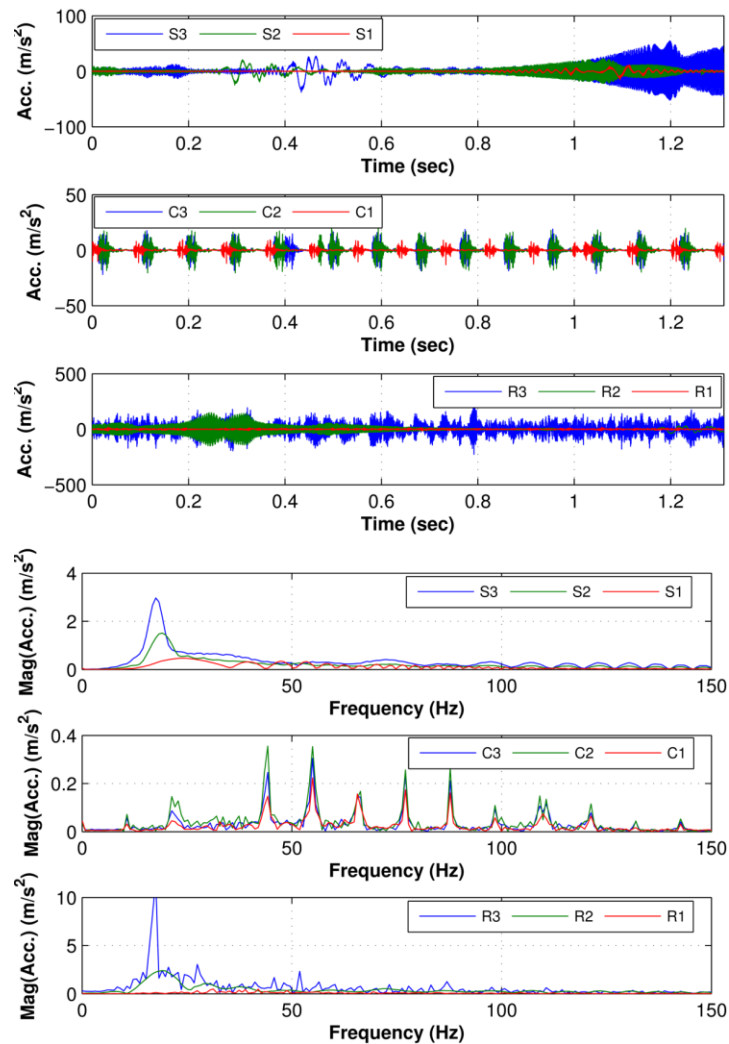


Figure 2-11. Acceleration time-histories A_{mm} of moving mass (top) and corresponding magnitude in frequency domain (bottom) for the three excitation types and intensity levels in VE tests of Pile I.

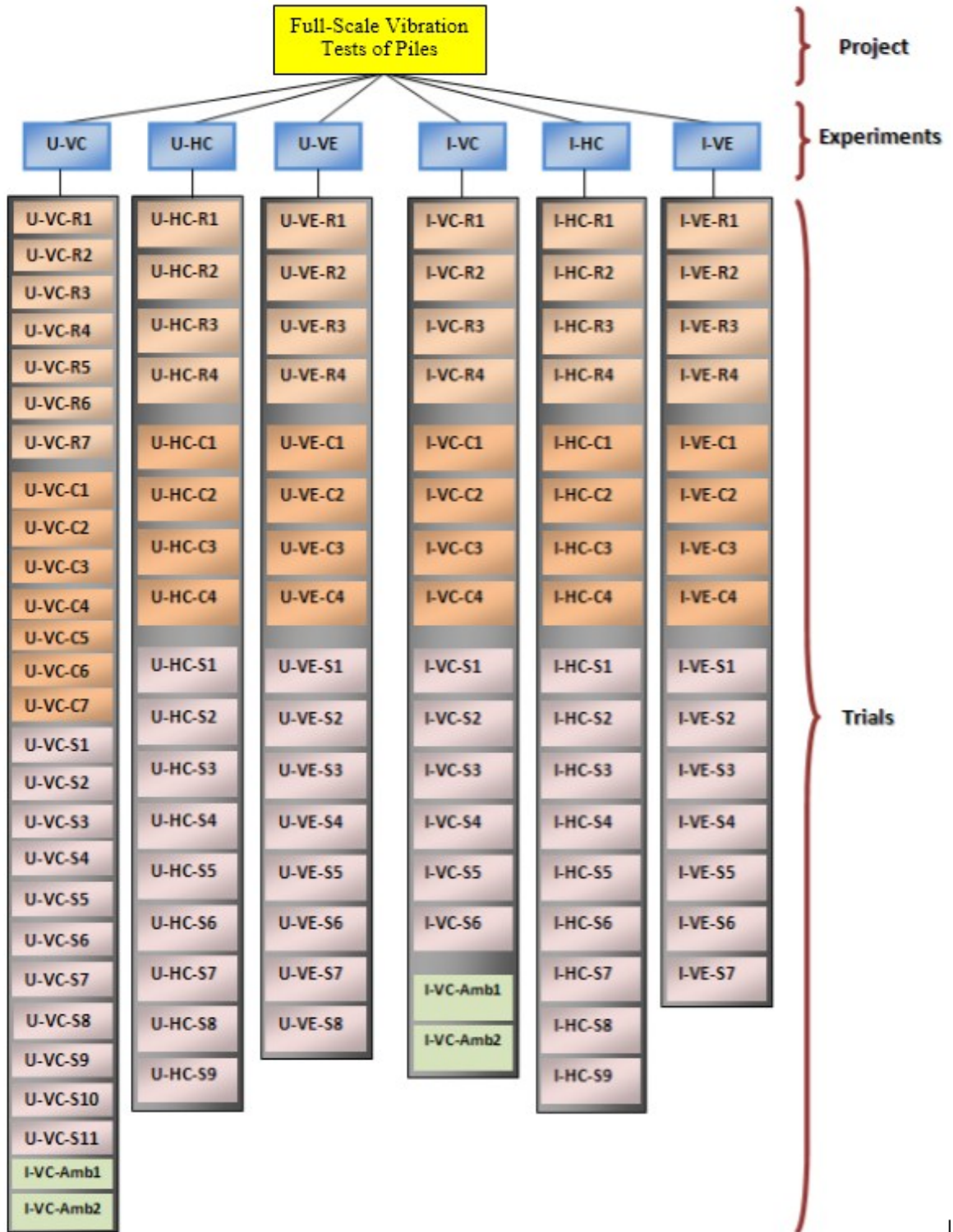


Figure 2-12. Organization of tests compatible with NEES User Data Model (Ashlock & Fotouhi, 2011).

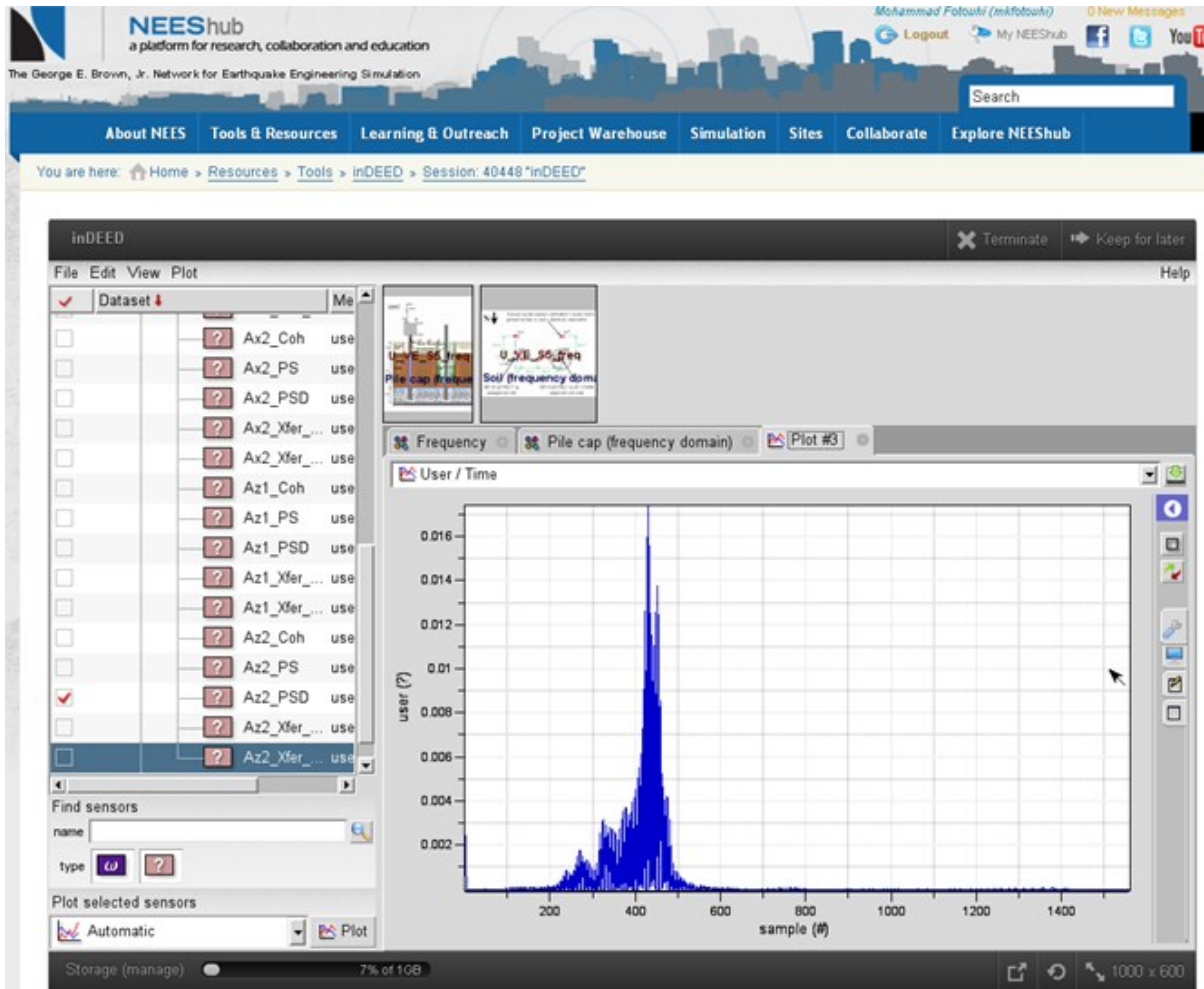


Figure 2-13. Example of experimental data plotted using inDEED data exploration tool on the NEEShub.

2.7 Centroidal Accelerances

As discussed above, the experimental data can be presented in the form of accelerance functions (ratios of directional acceleration to force) for each sensor location on the pile-cap. However, the pile-cap and stationary part of the shaker will be assumed to experience rigid body motion in the analyses, so it is more logical to represent the measured pile-cap motion by a set of centroidal accelerances corresponding to vertical, horizontal and rotational accelerations at the centroid of the composite pile-cap shaker system. Given the pile-cap properties and accelerance measurements at three non-collinear points on the pile-cap, one can easily calculate the centroidal accelerances using rigid body dynamics, as explained below.

For planar motion in the x - z plane, let point $P=(x_p, z_p)$ denote an accelerometer measurement point on the surface of the rigid pile-cap and point $C=(x_c, z_c)$ denote the centroid of the pile-cap-shaker system (Figure 2-14). Then a kinematic transformation matrix, \mathbf{T}_{PC} , can be used to relate the centroidal displacements \mathbf{U}_C at point C to the displacements \mathbf{U}_P as

$$\mathbf{U}_P = \mathbf{T}_{PC} \mathbf{U}_C \quad (2.4)$$

where

$$\mathbf{U}_P = \begin{bmatrix} U_{xp} \\ U_{zp} \\ \Theta_p \end{bmatrix} \quad \text{and} \quad \mathbf{U}_C = \begin{bmatrix} U_{xc} \\ U_{zc} \\ \Theta_c \end{bmatrix}$$

Defining the eccentricities $e_x = x_p - x_c$ and $e_z = z_p - z_c$ one may write for small rotations

$$\mathbf{T}_{PC} = \begin{bmatrix} 1 & 0 & -e_z \\ 0 & 1 & e_x \\ 0 & 0 & 1 \end{bmatrix} \quad (2.5)$$

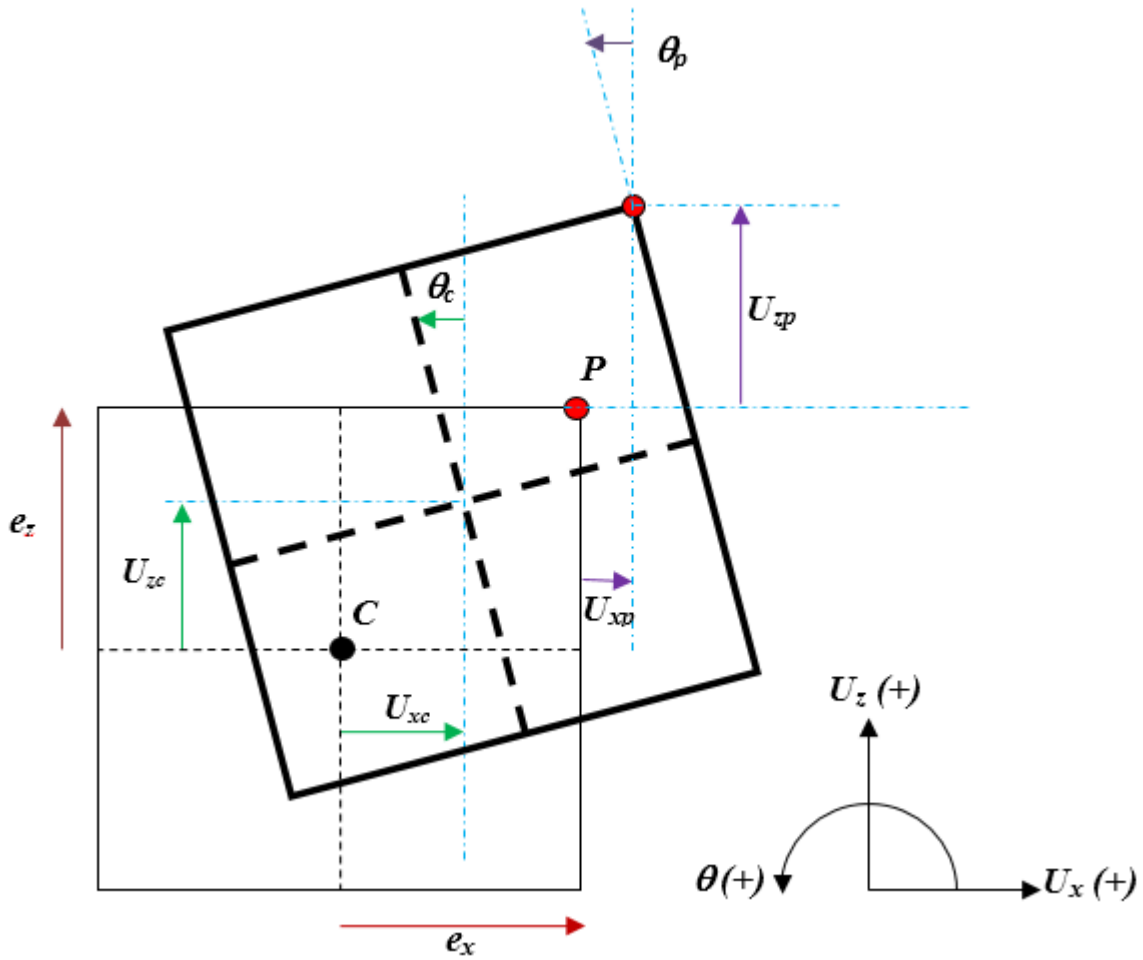


Figure 2-14. Geometrical parameters of pile cap and sign conventions used in the formulations.

For the layout of accelerometers on the pile-cap shown in Figure 2-3 and 2-9, the rigid body rotation can be calculated from either the vertical accelerometers as

$$\theta_y = \frac{U_{z2} - U_{z1}}{e_{x2} - e_{x1}} \quad (2.6)$$

or from the horizontal accelerometers as

$$\theta_y = -\frac{U_{x2} - U_{x1}}{e_{z2} - e_{z1}} \quad (2.7)$$

where the displacement U_{ij} at given frequency $\omega = 2\pi f$ is related to the acceleration \ddot{l}_j

through

$$U_{ij} = -\frac{\ddot{l}_j}{\omega^2} = -\frac{\ddot{l}_j}{4\pi^2 f^2} \quad i = x, z, \quad j = 1, 2$$

Strictly speaking, the rotations, displacements, and accelerations in the above equations are functions of frequency ω , and represent the Fourier transforms of their time-domain counterparts. For brevity, the dependence on ω has been omitted from the notation.

If the pile-cap were undergoing perfect rigid-body motion, the calculated centroid coordinates were exact, and errors due to the transverse sensitivity of the accelerometers were negligible, then the rotation values resulting from Equations (2.6) and (2.7) would be identical. Comparing the rotation angles from both equations therefore provides a good check of the pile-cap-shaker rigidity assumption and the centroid calculation accuracy. This comparison is presented in the form of rotational acceleration functions in Figure 2-17, where the pile-cap accelerometers are numbered as shown in Figure 2-15. As can be seen in the comparison, the accelerances are nearly identical over the frequency range of interest.

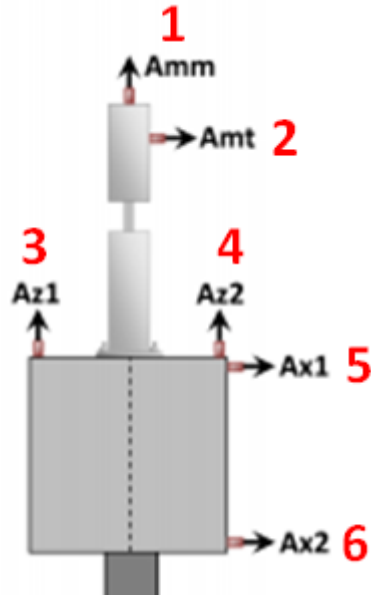


Figure 2-15. Accelerometer labeling convention used in the centroidal acceleration calculations (shaker shown in VC position).

The acceleration at a sensor located at point P can be expressed in terms of the displacements as

$$A_p = \frac{\ddot{U}_p}{M_{mm} \ddot{U}_{mm}} = \frac{-\omega^2 \times U_p}{M_{mm} \omega^2 \times U_{mm}} = \frac{U_p}{M_{mm} U_{mm}} \quad (2.8)$$

For sensors 4, 5 and 6 in Figure 2-15 where the shaker is in the VC position, one can write the following relationships using equation (2.8) and the parameters and sign conventions shown in Figure 2-14 (these sensors were selected because they are mounted on the same half of the pile-cap and move rigidly together):

$$A_4 = \frac{U_{z4}}{M_{mm} U_{mm}} = \frac{U_{zC} + e_{x4} \Theta_C}{M_{mm} U_{mm}} = A_{zC} + e_{x4} A_{\theta C} \quad (2.9)$$

$$A_5 = \frac{U_{x5}}{M_{mm}U_{mm}} = \frac{U_{xC} - e_{z5}\Theta_C}{M_{mm}U_{mm}} = A_{xC} - e_{z5}A_{\theta C} \quad (2.10)$$

$$A_6 = \frac{U_{x6}}{M_{mm}U_{mm}} = \frac{U_{xC} - e_{z6}\Theta_C}{M_{mm}U_{mm}} = A_{xC} - e_{z6}A_{\theta C} \quad (2.11)$$

The above three equations can be written in matrix form as

$$\begin{Bmatrix} A_4 \\ A_5 \\ A_6 \end{Bmatrix} = \mathbf{T}_{CP} \begin{Bmatrix} A_{xC} \\ A_{zC} \\ A_{\theta C} \end{Bmatrix} \quad (2.12)$$

or

$$\begin{Bmatrix} A_{xC} \\ A_{zC} \\ A_{\theta C} \end{Bmatrix} = \mathbf{T}_{PC} \begin{Bmatrix} A_4 \\ A_5 \\ A_6 \end{Bmatrix} \quad (2.13)$$

where

$$\mathbf{T}_{CP} = \begin{bmatrix} 0 & 1 & e_{x4} \\ 1 & 0 & -e_{z5} \\ 1 & 0 & -e_{z6} \end{bmatrix} \text{ and } \mathbf{T}_{PC} = \mathbf{T}_{CP}^{-1} = \frac{1}{(e_{z5} - e_{z6})} \begin{bmatrix} 0 & -e_{z6} & e_{z5} \\ e_{z5} - e_{z6} & e_{x4} & -e_{x4} \\ 0 & -1 & 1 \end{bmatrix} \quad (2.14)$$

The same procedure can be applied to obtain the centroidal accelerances for VE and HC test configurations. Table 2-2 lists all the necessary parameters in Equation (2.14) for the various test set-ups used. Calculation of the centroid coordinates is discussed in detail in Chapter 3. Since the experimental transfer functions are recorded in complex Cartesian form (i.e., real and imaginary components), one must first construct the complex numbers before performing the calculations.

Table 2-2. Coordinates of sensor locations and centroid of the rigid pile-cap-shaker assembly for the different test configurations (all dimensions in inches from bottom center of pile cap).

Test type	(A _{z2}) _x	(A _{z2}) _z	(A _{x1}) _x	(A _{x1}) _z	(A _{x2}) _x	(A _{x2}) _z	<i>x_C</i>	<i>z_C</i>	<i>e_{x4}</i>	<i>e_{z5}</i>	<i>e_{z6}</i>
VC	17	36	18	35	18	1	0	19.29	17	15.71	-18.29
VE	17	36	18	35	18	1	-0.55	19.29	17.55	15.71	-18.29
HC	17	36	18	35	18	1	1.57	17.72	15.45	17.28	-16.72

Equation (2.14) along with the data in Table 2-2 gives the following transformation matrices which are used in this study to calculate the experimental centroidal accelerances from the directional accelerances measured on the surface of the pile cap.

$$(\mathbf{T}_{PC})_{VC} = \begin{bmatrix} 0 & 0.5379 & 0.4621 \\ 1 & 0.5000 & -0.5000 \\ 0 & -0.0294 & 0.0294 \end{bmatrix} \quad (2.15)$$

$$(\mathbf{T}_{PC})_{VE} = \begin{bmatrix} 0 & 0.5379 & 0.4621 \\ 1 & 0.5165 & -0.5165 \\ 0 & -0.0294 & 0.0294 \end{bmatrix} \quad (2.16)$$

$$(\mathbf{T}_{PC})_{HC} = \begin{bmatrix} 0 & 0.4917 & 0.5082 \\ 1 & 0.4544 & -0.4544 \\ 0 & -0.0294 & 0.0294 \end{bmatrix} \quad (2.17)$$

As discussed above, Figure 2-17 validates the assumption of rigid-body motion for the pile cap and the precision of the calculated centroid location of the rigid portion of the pile-cap-shaker system in Test U-VE-S2. Furthermore, it reveals that errors incurred due to transverse sensitivity of the accelerometers was minimal. When the accelerometers were ordered from PCB, the technicians were asked to hand-selected units with exceptionally low

transverse sensitivities (below 1%, compared to the average of 5 to 10%), which took a few extra months. Similar verifications from the other tests confirmed that the centroid coordinates were accurate and rigidity assumption justified. The verification was performed by comparing the centroidal accelerances calculated using accelerometers 3, 4 and 5 in Figure 2-15 (with rotation calculated from two vertical accelerometers), to those from accelerometers 4, 5 and 6 (with rotation from two horizontal accelerometers). Both sensor combinations are seen to result in nearly the same centroidal accelerances.

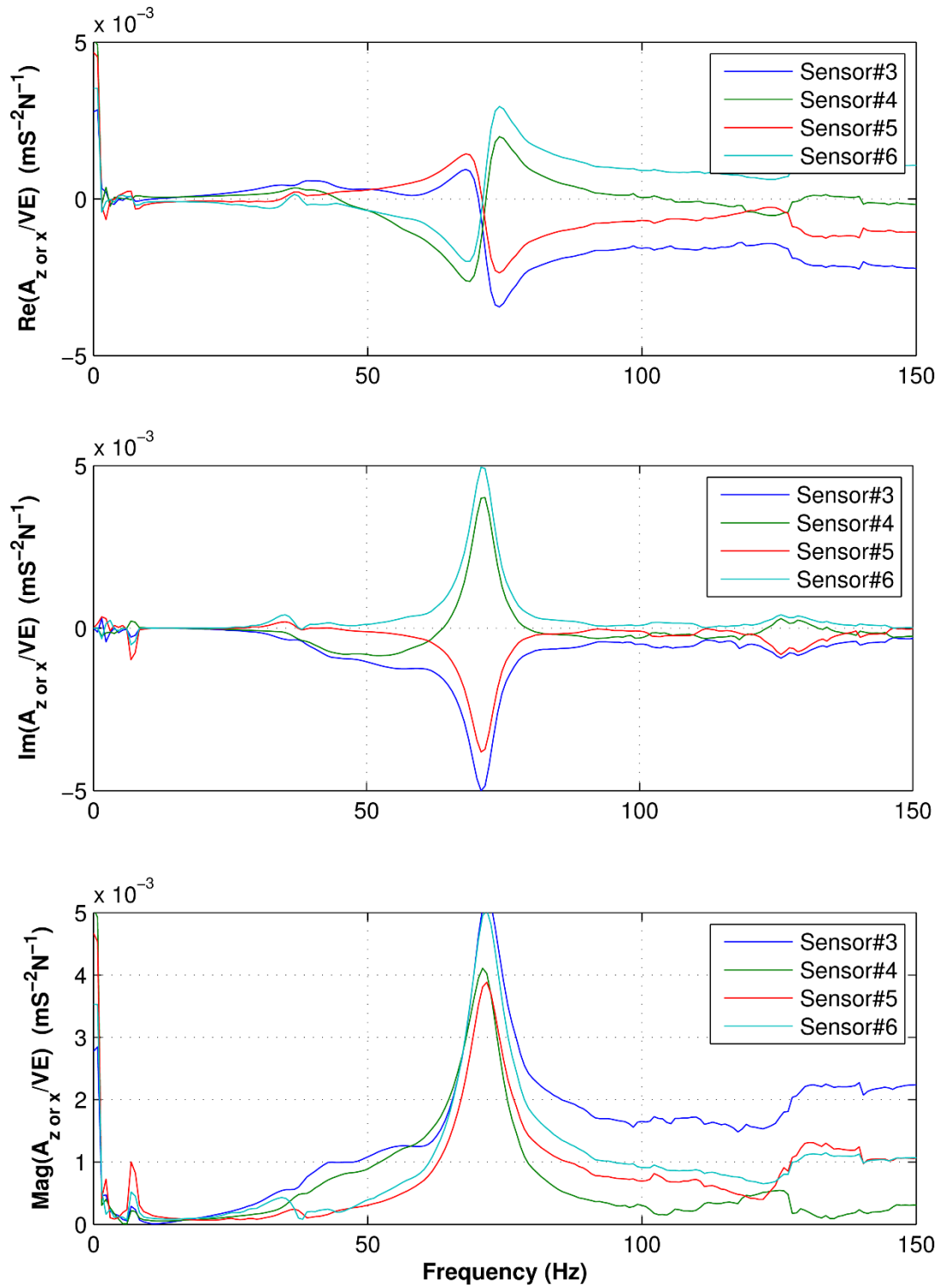


Figure 2-16. Comparison of centroidal accelerances from Test U-VE-S2 at the location of accelerometer 3 to 6.

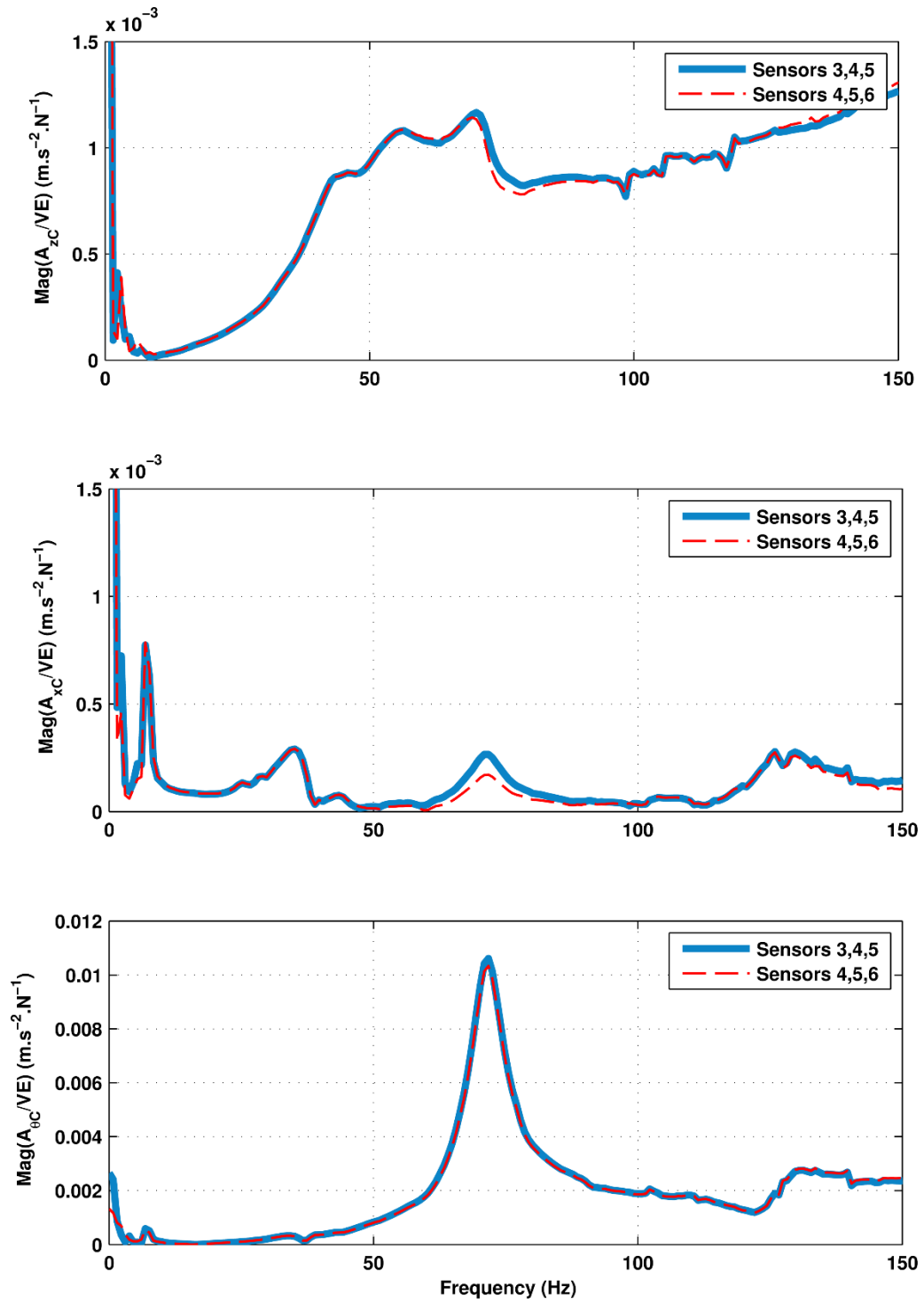


Figure 2-17. Comparison of centroidal accelerances from Test U-VE-S2 with rotation calculated from vertical versus horizontal accelerometers.

2.8 Test Results and Interpretation

In this section, the process experimental data will be presented to provide insight into the quality of the tests and the pile-soil system performance. Numerical simulations of the dynamic tests will be presented in Chapter 3 and 4. Several interesting conclusions can be drawn just by comparing experimental responses from the different test types and soil types. Figure 2-18 to 2-21 show the power spectral densities and corresponding coherence functions for VC, HC, and VE tests in both improved and unimproved soils. The vertical-centric response is calculated by averaging the PSD functions from the vertical accelerometers (sensors 3 and 4 in Figure 2-15). Similarly, the horizontal-centric PSD is the average from the two horizontal accelerometers (sensors 5 and 6). From this data, it can be seen that random and swept-sine excitations generally provide the most uniform power spectral densities, while chaotic impulse delivers the least uniform PSD. Additionally, the VE test successfully generated significant coupled horizontal-rotational motion as intended. In general, the relative amplitudes of the vertical and horizontal-rotational modes may be adjusted in VE tests by prescribing a different eccentricity of the vertical load, but a good balance of the three modes was achieved in this study. The coherence functions shown are those for the medium level of forcing at sensors 3 and 5, and as demonstrated in the figures, good coherence was obtained over a wide frequency range for random and swept-sine excitations. As evidenced in Figure 2-19 and 2-21 the measured coherence was generally more uniform for tests in unimproved soil than for tests in improved soil.

As mentioned previously, it was discovered during testing that the chaotic impulse excitation signal was scaled incorrectly in the LabVIEW program, with the result that the timing of impulses was more regularly spaced than desired. This resulted in impulses being

applied at a rate of roughly 11 Hz with secondary impulses in between. The power spectral density of this signal therefore appears similar to what would be seen for an 11 Hz periodic impulse, with higher harmonics spread out at 11 Hz intervals. The implementation of the chaotic impulse technique is currently being refined in LabVIEW, with the expected result that the frequency spectrum will become smoother and resemble that of random loading once the nearly periodic impulses are corrected to have a more random temporal distribution.

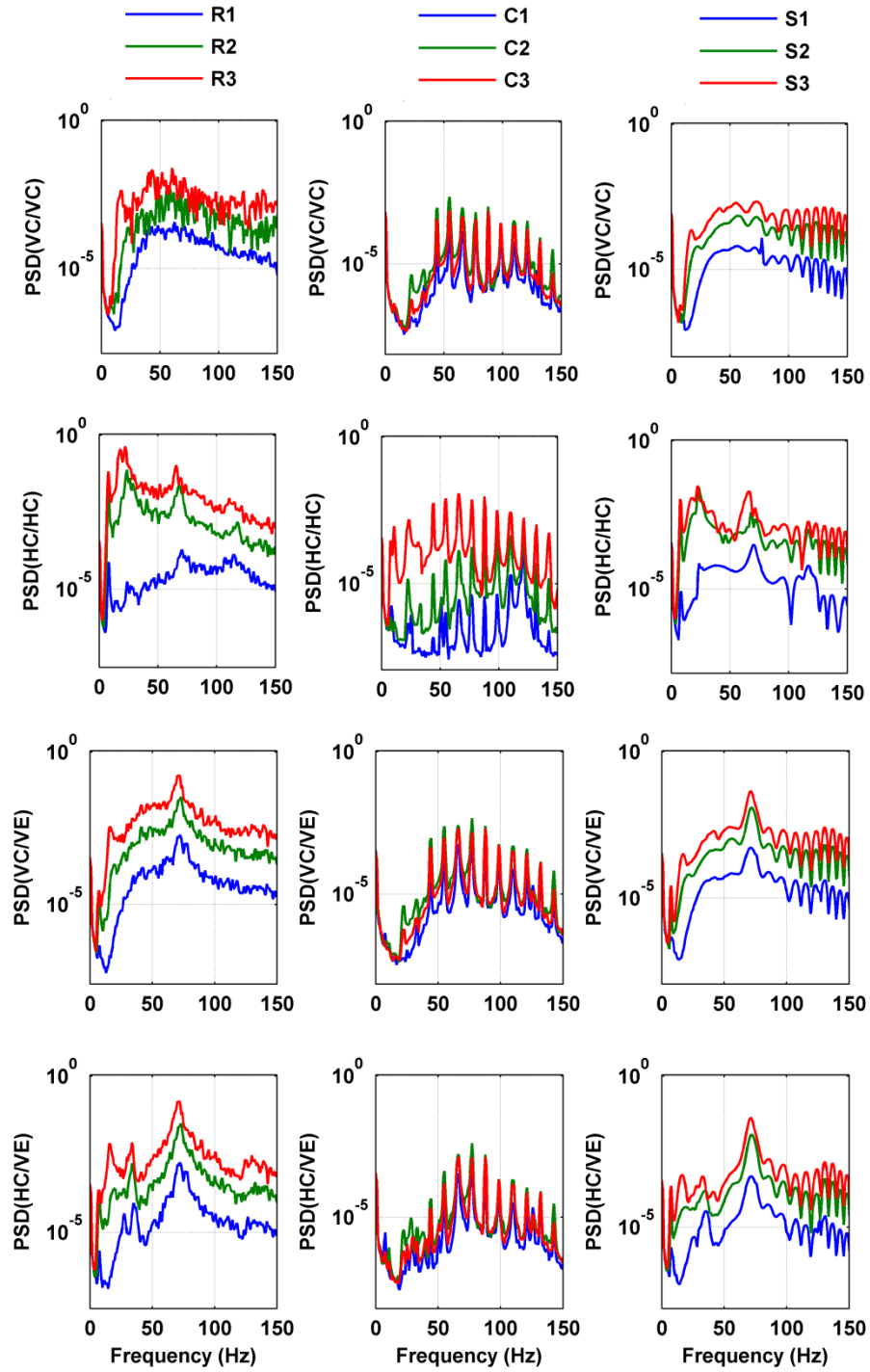


Figure 2-18. PSD $((m/s^2rms)^2/Hz)$ for VC, VE and HC tests with different excitation types (Figure 2-11) and intensities in unimproved soil.

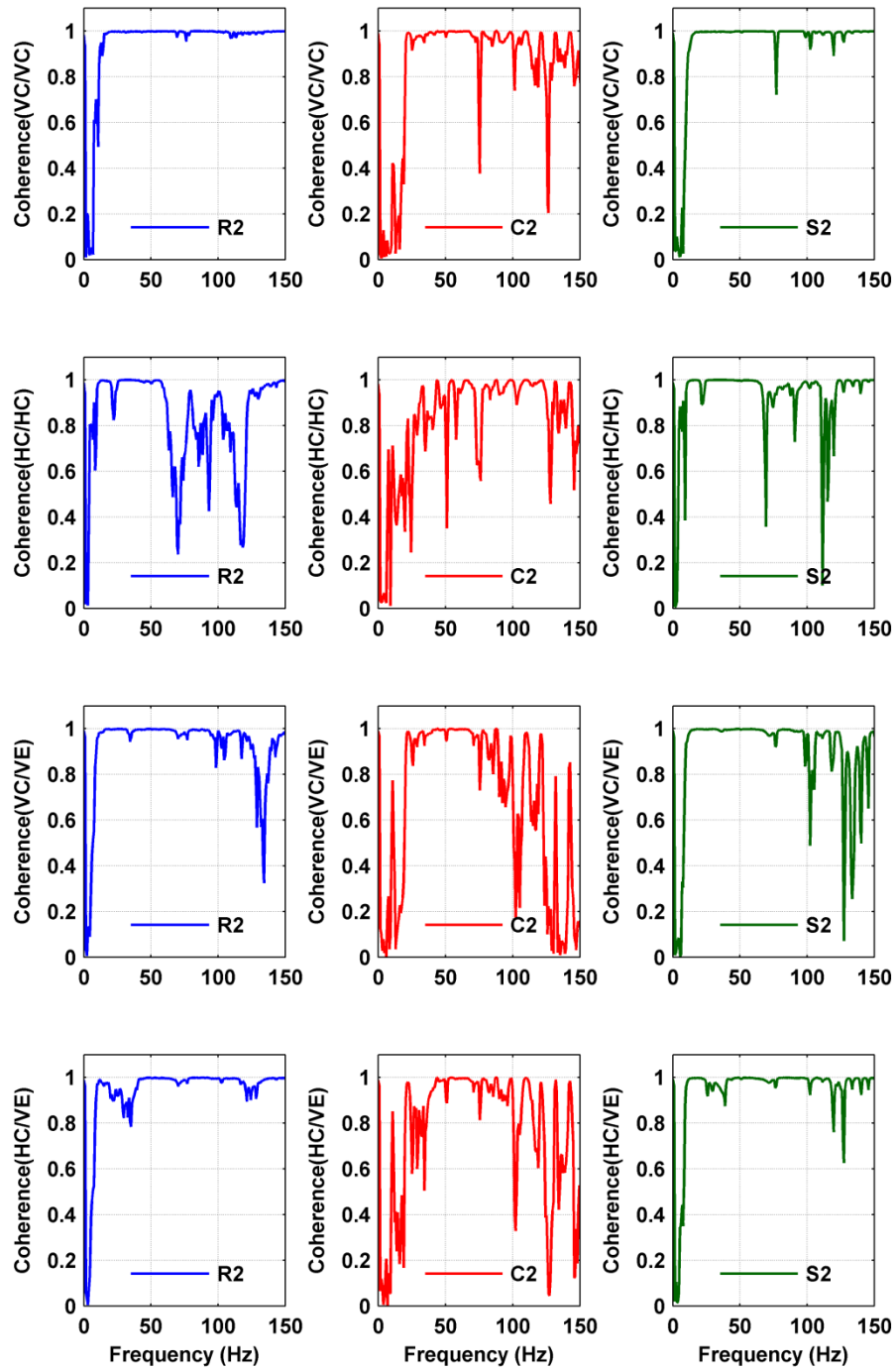


Figure 2-19. Coherence for VC, VE and HC tests with different excitation types (Figure 2-11) at intensity level 2 in unimproved soil.

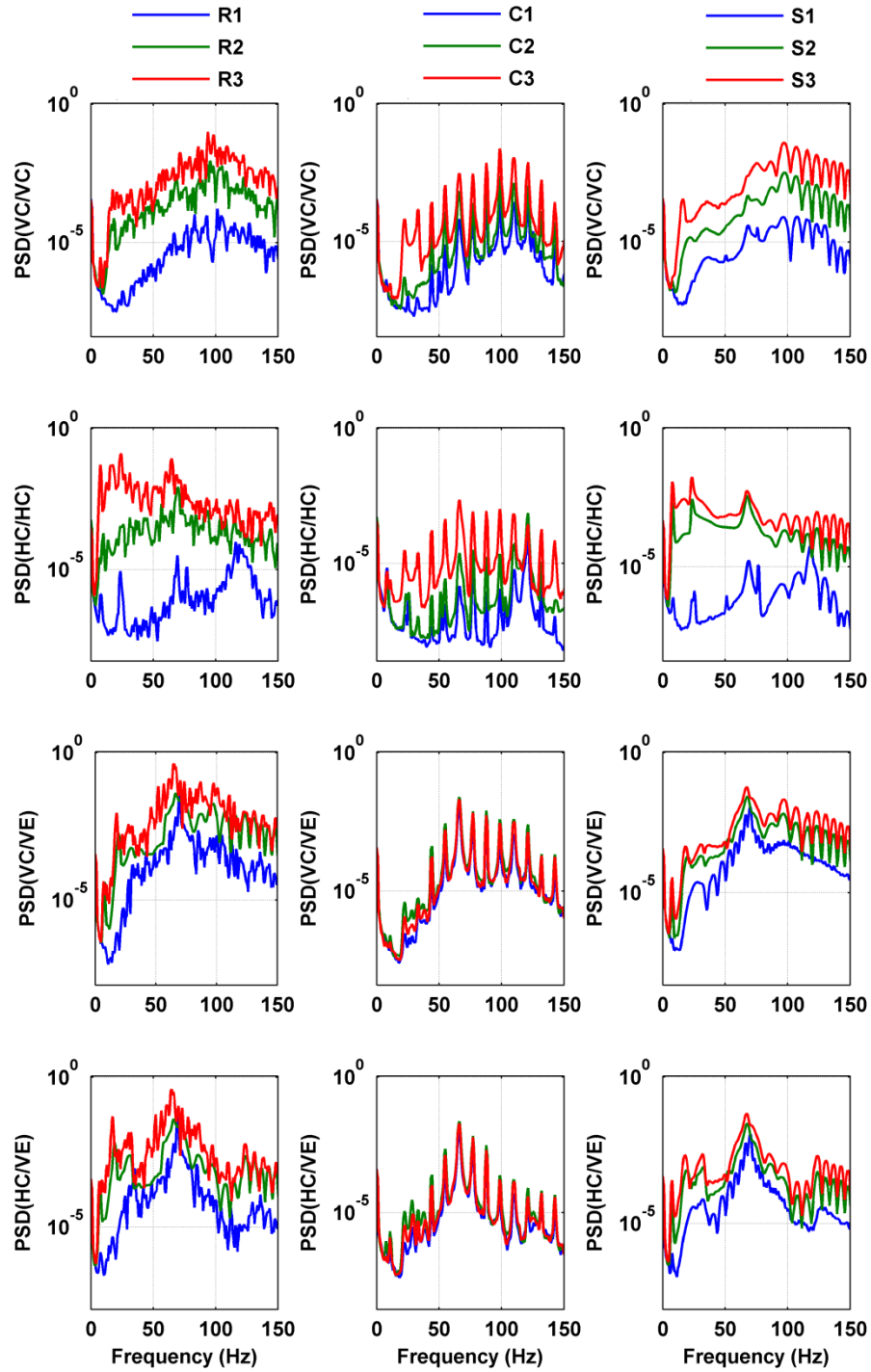


Figure 2-20. PSD $((m/s^2rms)^2/Hz)$ for VC, VE and HC tests with different excitation types (Figure 2-11) and intensities in improved soil.

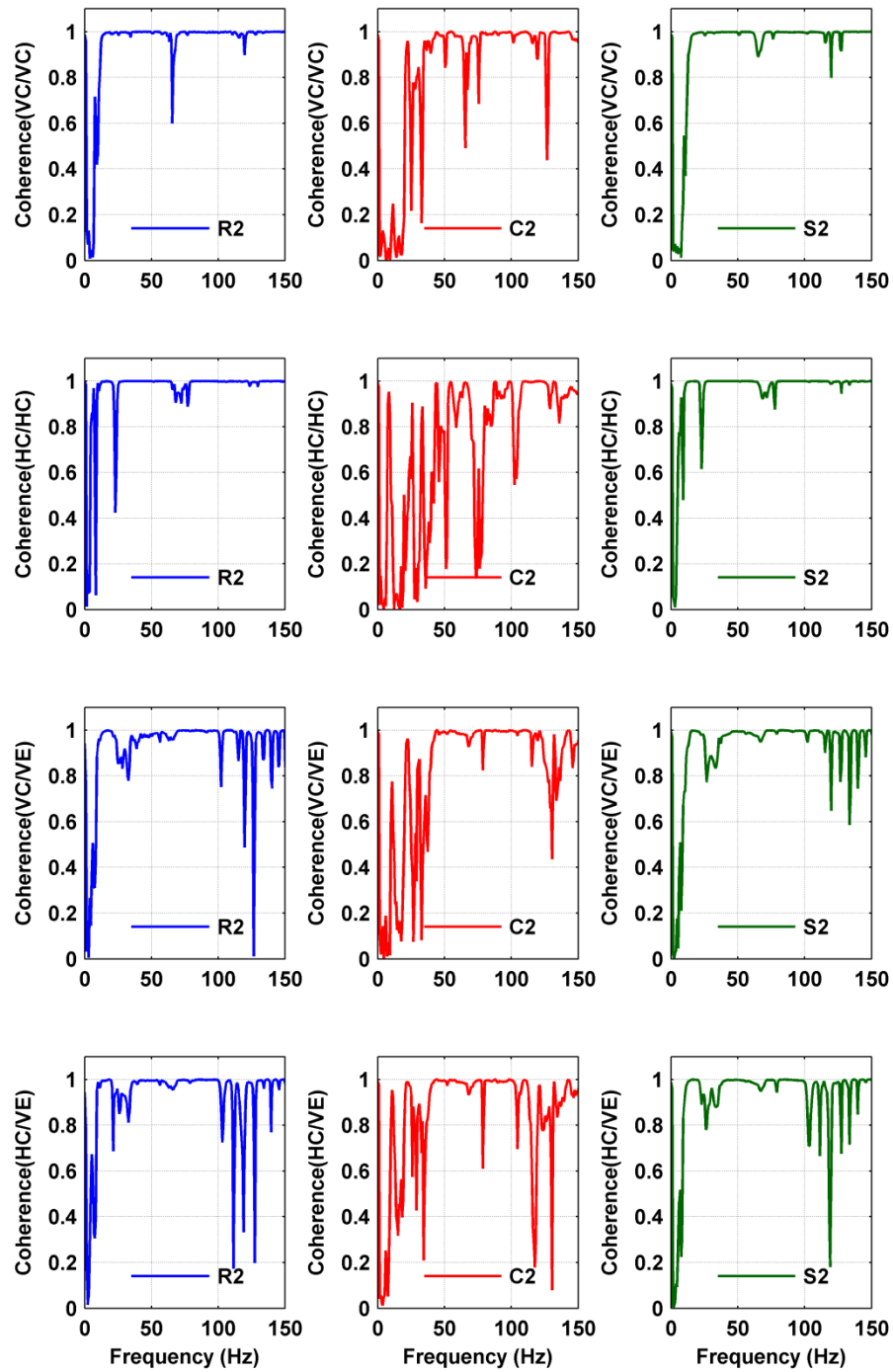


Figure 2-21. Coherence for VC, VE and HC tests with different excitation types (Figure 2-11) at intensity level 2 in improved soil.

The centroidal accelerances, A_{xC} , A_{zC} , and $A_{\theta C}$ are shown in Figure 2-22 to 2-35 for all test types and both soil types. In each figure, the three types and three excitation intensities are compared. The accelerance functions are complex valued, and thus are presented in terms of real and imaginary components. At frequencies less than 3 Hz, the accelerance function is very noisy and doesn't reveal meaningful data due to the physical limitations of the accelerometers and inertial shaker. For VC test the horizontal centroidal accelerance is negligible as expected and hence, has not been shown.

The extracted accelerances generally show the expected trends similar to previous studies. The vertical centroidal accelerance functions for vertical eccentric and vertical centric loading (A_{zC}/VE and A_{zC}/VC , respectively) exhibit the expected trend of a single gentle peak followed by a horizontal asymptote. However in the A_{zC}/VE response in improved soil, a small extra bump near 65 Hz can be seen prior to the major vertical resonance peak at 95 Hz (Figure 2.33). This phenomenon is due to the lack of perfect symmetry of the pile cap, and a similar behavior was observed in the centrifuge pile vibration tests reported in Ashlock (2006).

The chaotic impulse excitation resulted in nearly identical A_{zC}/VE accelerance for all three load intensities studied, owing to the relatively small differences in the three power spectral densities shown in Figure 2-18 and 2-21. This excitation type also resulted in much more noise in the horizontal and rotational accelerances.

For the horizontal response under horizontal and vertical-eccentric loading (A_{xC}/HC and A_{xC}/VE accelerances, respectively), sharp fundamental-mode peaks were measured at low frequencies (around 8-10 Hz), followed by two to three additional minor peaks in the frequency range of interest, with an otherwise fairly constant real response and zero imaginary response.

The minor horizontal peaks occurred near 25 and 70 Hz for HC tests, and near 40, 70, and 130 Hz for VE tests.

For the rotational response, the VC tests resulted in activation of a small rotational accelerance due to the lack of perfect symmetry of the shaker (Figures 2.22 and 2.29). As intended, the HC and VE tests resulted in more significant rotational motion (Figures 2.24, 2.27, 2.31 and 2.34). The strongest peak of the rotational accelerance occurred at a frequency of approximately 70 Hz for all excitation and soil types. For the HC and VE tests, the rotational accelerances exhibited peaks near that of the horizontal mode (at 8 Hz), with additional minor peaks near 25 Hz, 110 Hz, and 125 Hz.

In a linear system with perfect testing conditions and zero noise, all three types of excitation should return similar accelerance functions, which would also be independent of the loading intensity. To examine the first aspect, the accelerances are compared for S2 and R2 excitation in Figure 2-36 and 2-37 for both soil conditions. The figures reveal that random excitation produces smoother response curves than swept-sine, but a good overall agreement exists between the different excitation types, indicating the validity of the results. To examine the linearity as a function of loading intensity, the three different excitation intensities (Levels 1, 2 and 3) were performed for all test configurations. For dynamic pile problems, the frequency and shape of the resonant response peaks has been shown to exhibit a characteristic leftward tilting under increasing levels of nonlinearity (Novak and Grigg 1976, Han and Novak 1988, El-Marsafawi et al. 1992, Han 1997), in which case the system transfer function can be characterized as a function of the forcing level. The results of Figure 2-22 through 2-35 demonstrate that only slight nonlinearities were induced by the increasing excitation levels in this study.

In order to examine the low-frequency behavior in more detail, the bandwidth was decreased from 1,000 to 250 Hz in some tests. This provided a greater frequency resolution in what was ultimately determined to be the bandwidth of interest in this study (0-150 Hz). The 250 Hz bandwidth tests therefore resulted in sharper peaks as shown in Figure 2-38 for the unimproved soil. However, the frequency of a secondary peak near 21 Hz was also increased by a few Hertz due to differences in the power spectra of the high- and low-bandwidth excitation signals. Similar results were observed for the pile in improved soil.

As discussed above, one of the goals of this study was to examine the equivalence of a single VE test to the combination of traditionally separate VC and HC tests, for the real soil conditions and new inertial shaker system. Comparison of the vertical and horizontal responses obtained from separate VC and HC tests and a single VE test (Figure 2-39 and 2-40) demonstrates that the VE test was successful in capturing the vertical mode of vibration. A small extra bump in the vertical response was observed around 70 Hz in the VE tests, which can be shown analytically to result from the slight differences in the inertial symmetry of the pile cap owing to the offset shaker position. While the HC test is seen to produce a stronger fundamental peak around 8 Hz, the VE test is also effective at uncovering this resonant frequency. It should be noted that theoretically, the magnitudes of the HC/VE and HC/HC responses are not equal, owing to the different location and direction of the excitation force in these two tests. The resonant frequencies of the fundamental peak, however, should coincide. Higher forcing levels were also examined in addition to different sweep rates in the swept sine tests, and it was determined that adjusting these parameters could enable one to capture a sharper fundamental peak in the VE test than shown in Figure 2-39 and 2-40. The VE test therefore represents an efficient technique for capturing simultaneously the vertical and

coupled lateral-rocking response of pile-soil systems, while alleviating concerns regarding different soil and contact conditions in separate VC and HC tests.

Finally, the effect of the soil improvement on the dynamic response of the pile can be seen in Figure 2-41. Perhaps as expected, the improved soil results in a stiffer response in the vertical mode, as evidenced by an increase in the A_{zC}/VC resonant frequency from 60 Hz to 100 Hz. Contrary to expectations, however, the fundamental lateral rocking peak frequency around 8 Hz in both HC and VE tests seems to be unaffected by the presence of the stiff CDSM zone, while the second peak exhibits a slight change. This behavior may be related to smaller initial pile-soil contact stresses resulting from inserting the pile into the CDSM mixture before it sets, as opposed to higher lateral stresses caused by forcing the pile into the unimproved but also undisturbed soil. This interesting and unexpected result is discussed in the following chapters. The improved soil is also seen to effectively remove a major resonance peak in the rotational accelerance around 120 Hz.

2.8.1 Representative Test

Owing to the good repeatability and agreement between responses for the different excitation types and intensities (with the exception of chaotic impulse), a single best representative experimental test was first selected for each soil type, and used for comparison against theoretical accelerances for the various computational approaches examined in the remainder of this study. Theoretically, in a perfect linear system with zero noise, all the accelerance functions from different loading types and intensities should be identical. Considering this, the tests with the chaotic impulse loading which contain the most noise in

the response would not be representative. The same reasoning is valid for the loading intensity Level 1, for which the forcing is closer to the ambient noise level. On the other hand, loading Level 3 in both R and S tests generated slight nonlinear effects, as evidenced by peaks moving to lower frequencies. Therefore, the *R2* and *S2* tests will be used in the following to calibrate and validate the theoretical models in parametric studies.

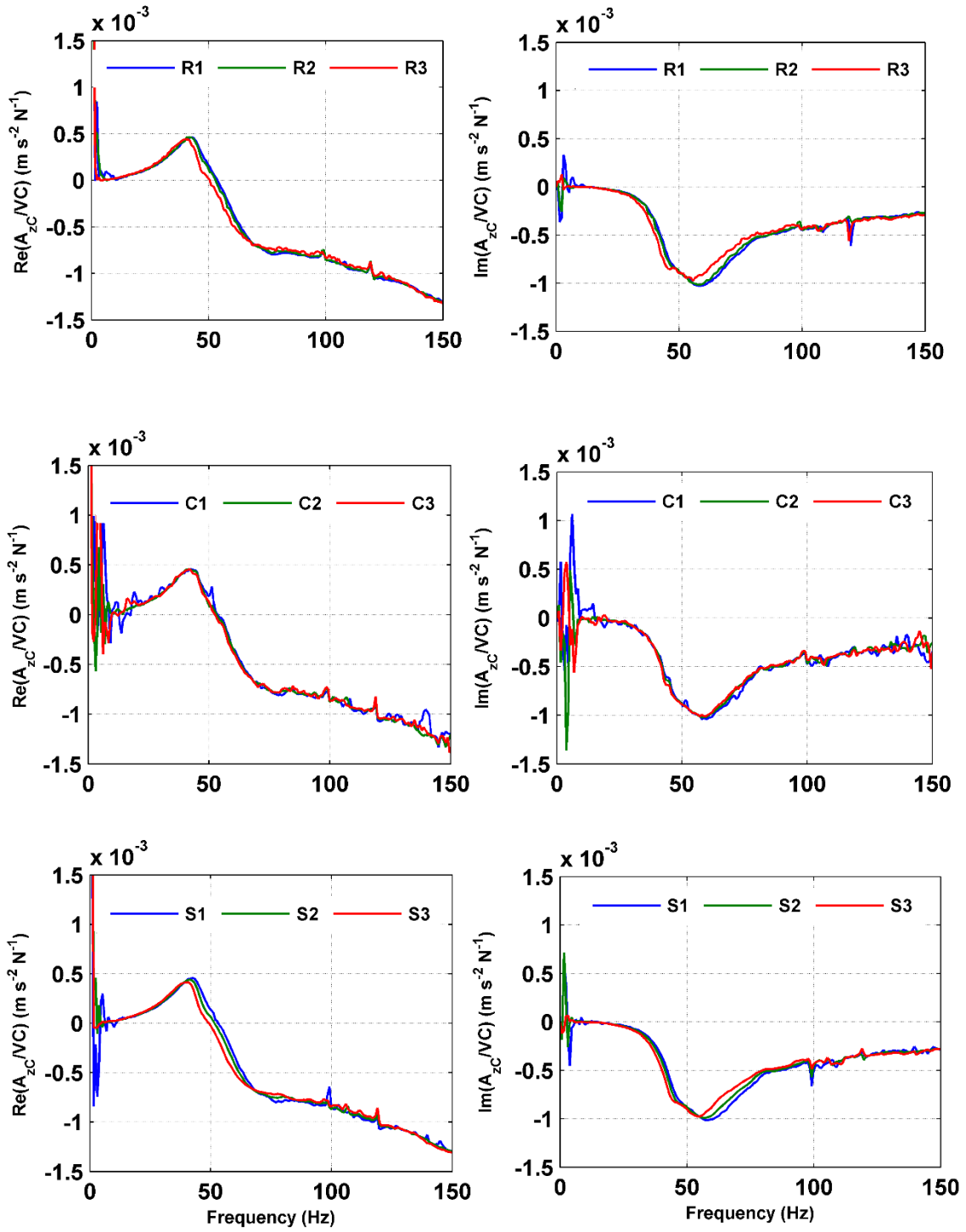


Figure 2-22. A_{zC}/VC accelerance for pile in unimproved soil for different excitation types and intensities.

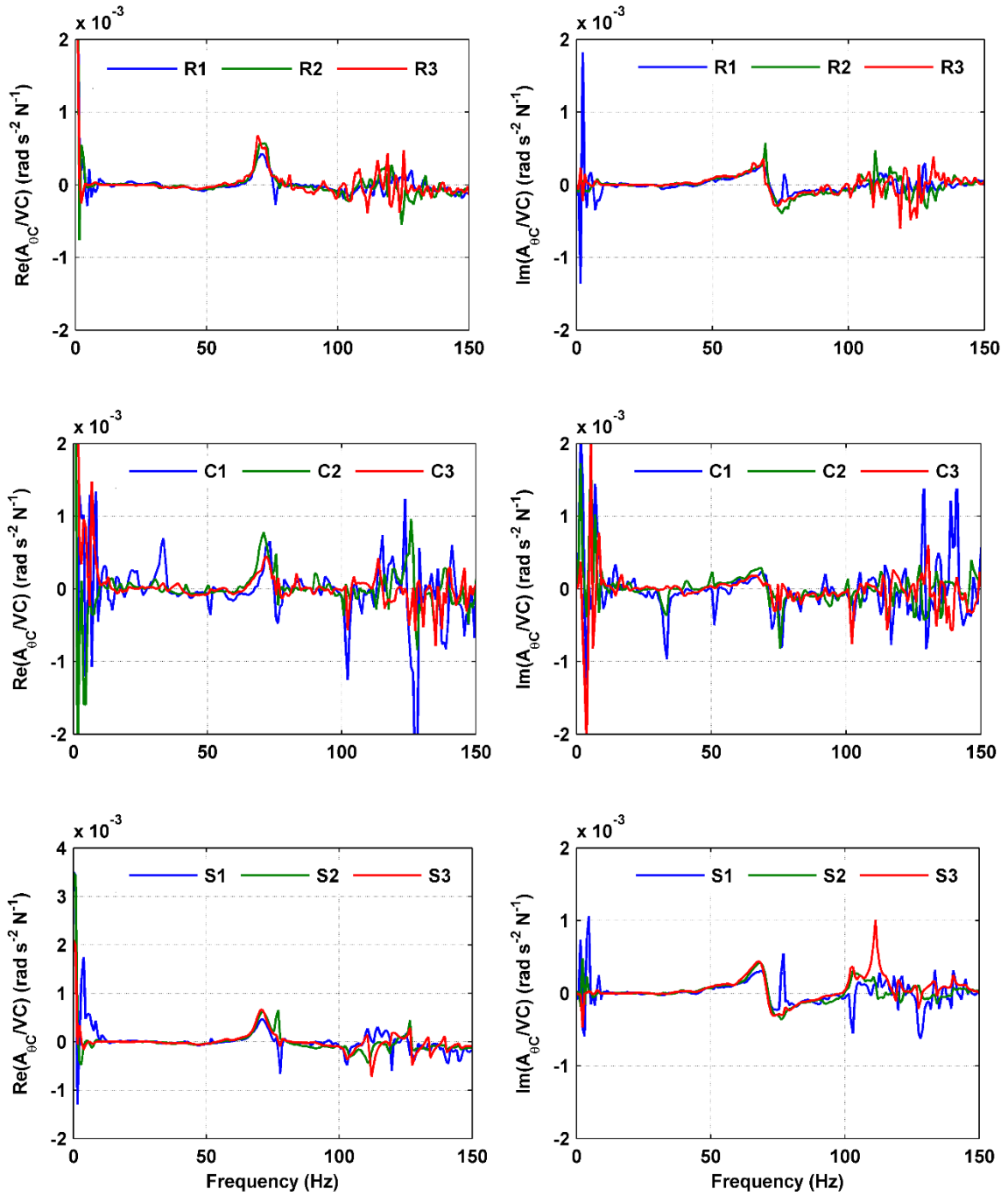


Figure 2-23. $A_{\theta C}/VC$ accelerance for pile in unimproved soil for different excitation types and intensities.

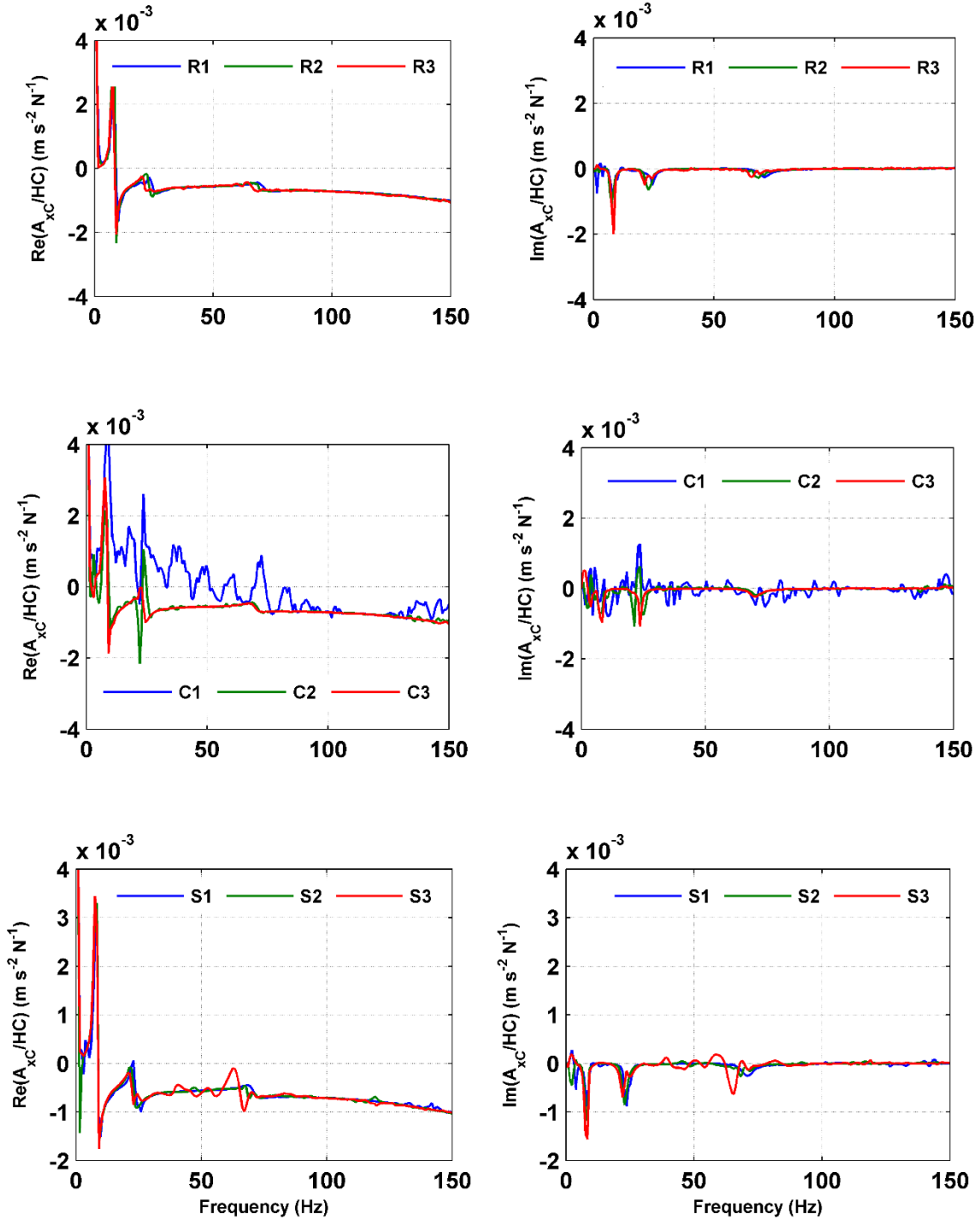


Figure 2-24 A_{xc}/HC accelerance in unimproved soil for different excitation types and intensities.

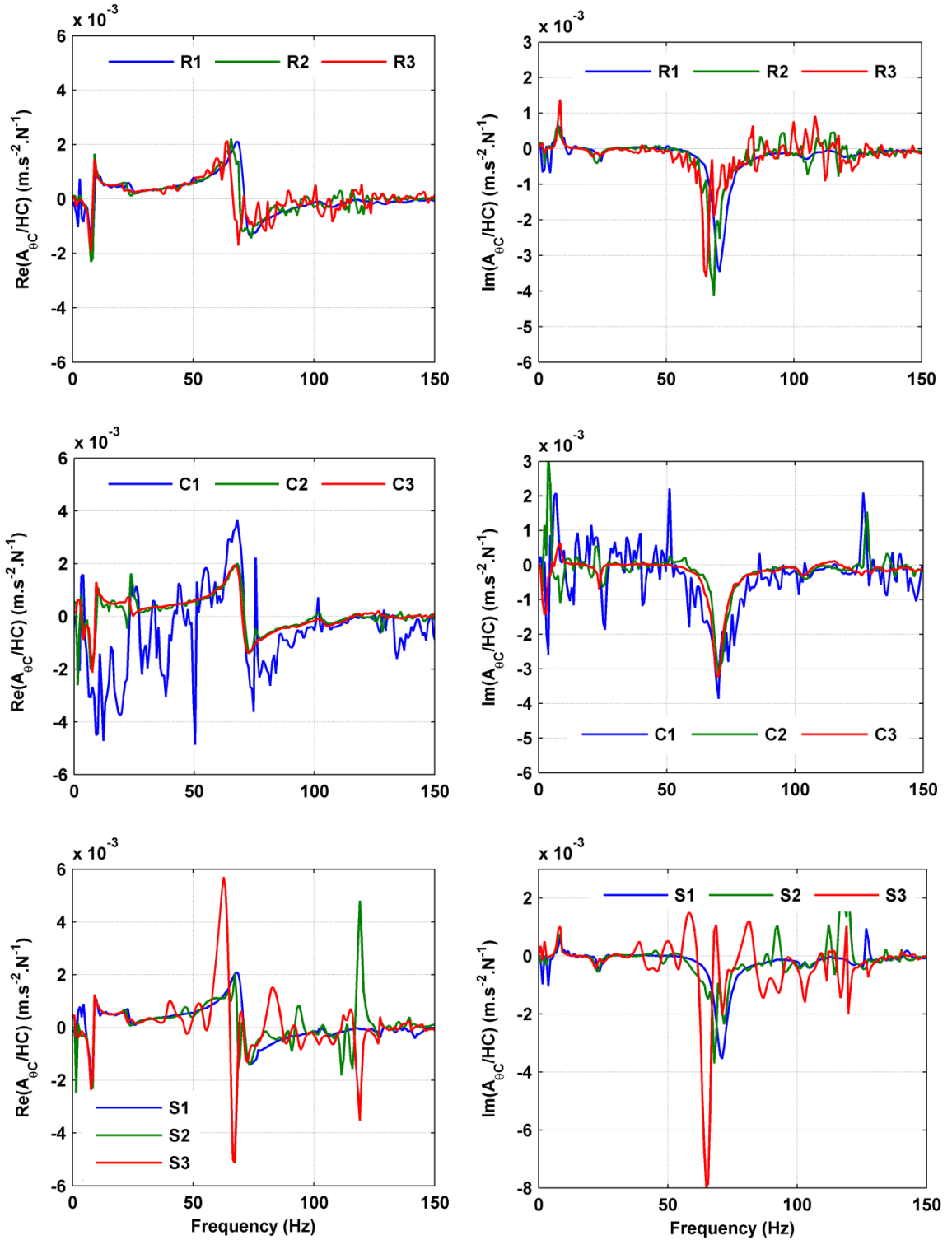


Figure 2-25. A_{0C}/HC accelerance in unimproved soil for different excitation types and intensities.

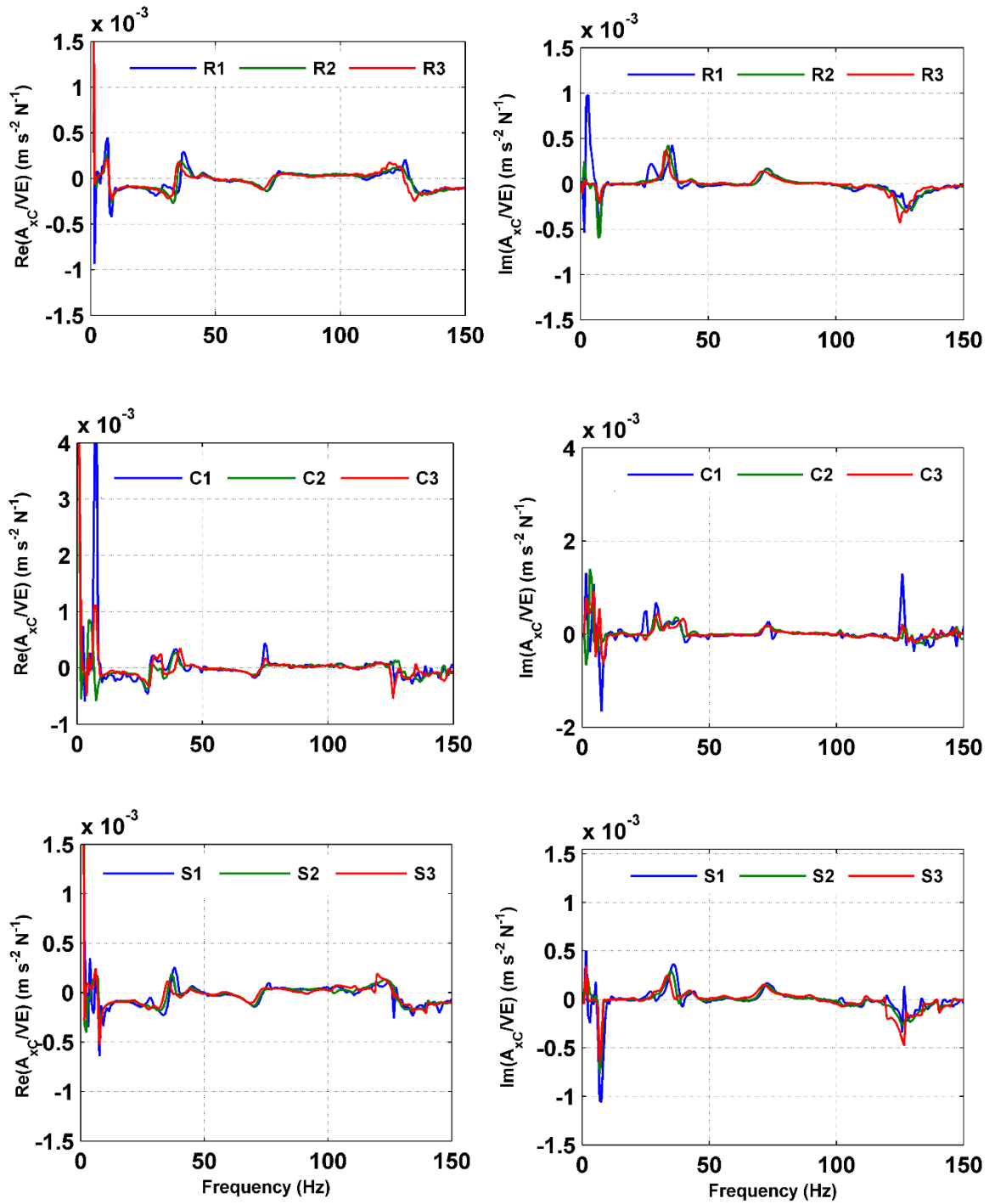


Figure 2-26. A_{xC}/VE accelerance in unimproved soil for different excitation types and intensities.

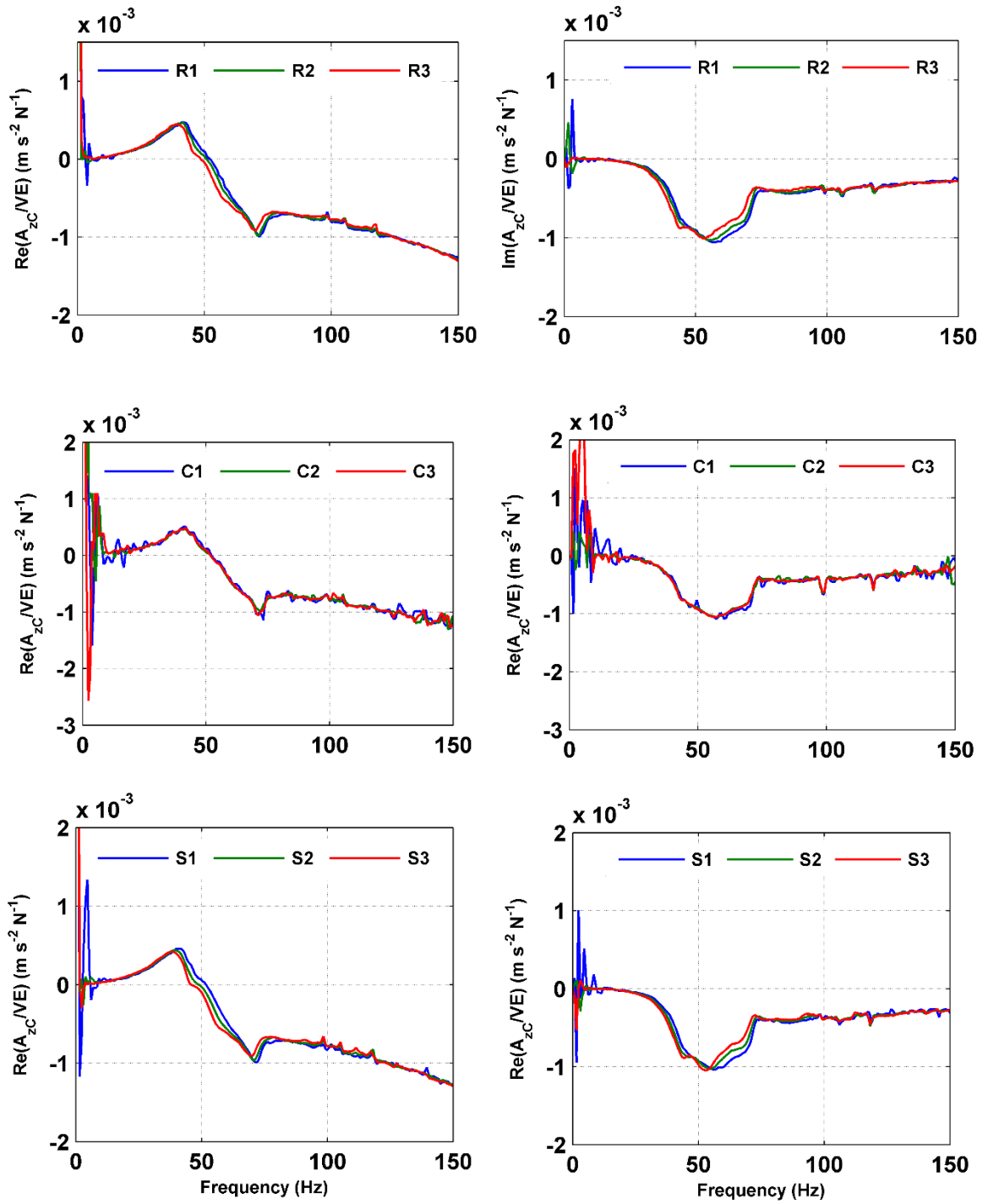


Figure 2-27. A_{zC}/VE accelerance in unimproved soil for different excitation types and intensities.

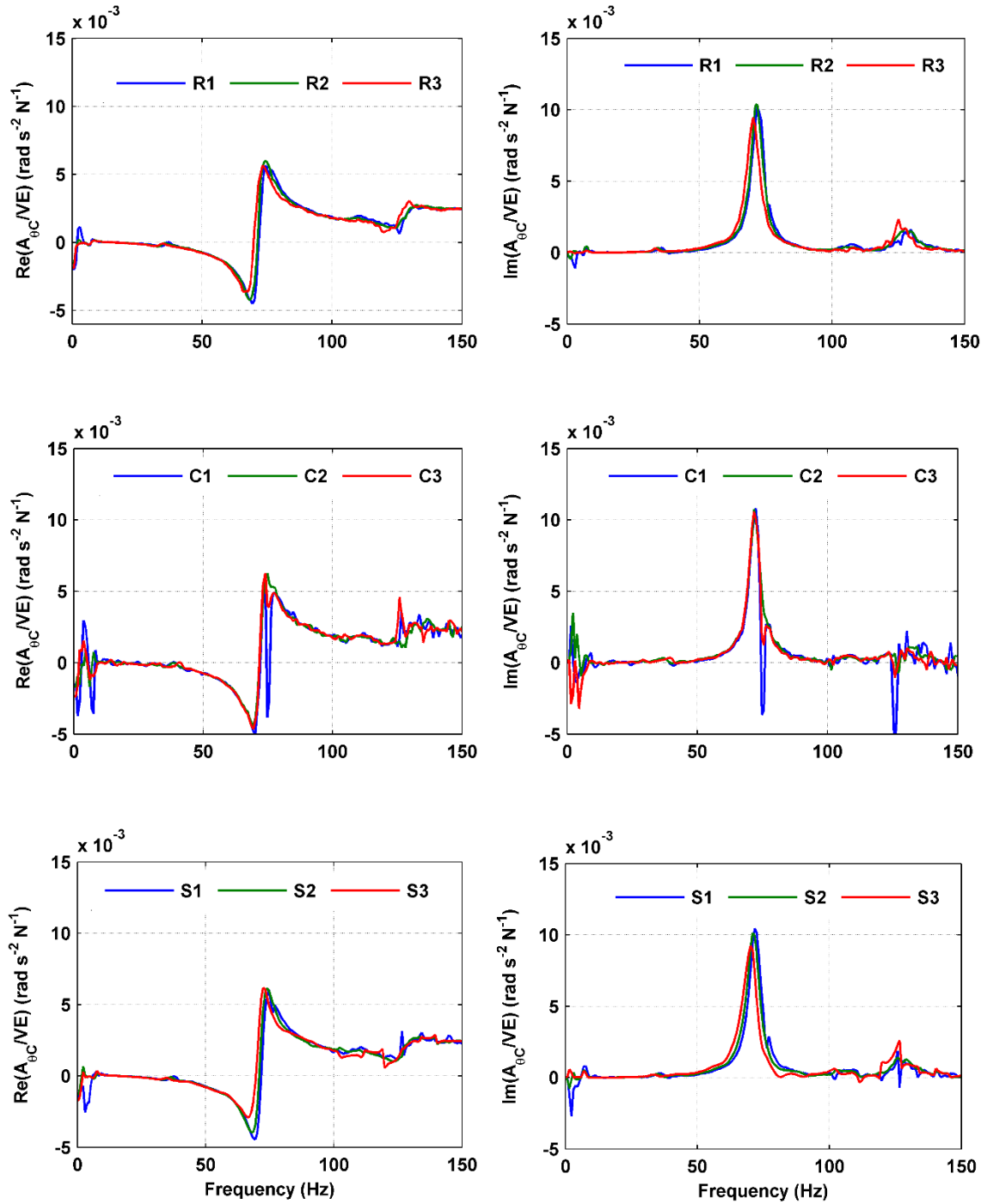


Figure 2-28. $A_{\theta C/VE}$ accelerance in unimproved soil for different excitation types and intensities.

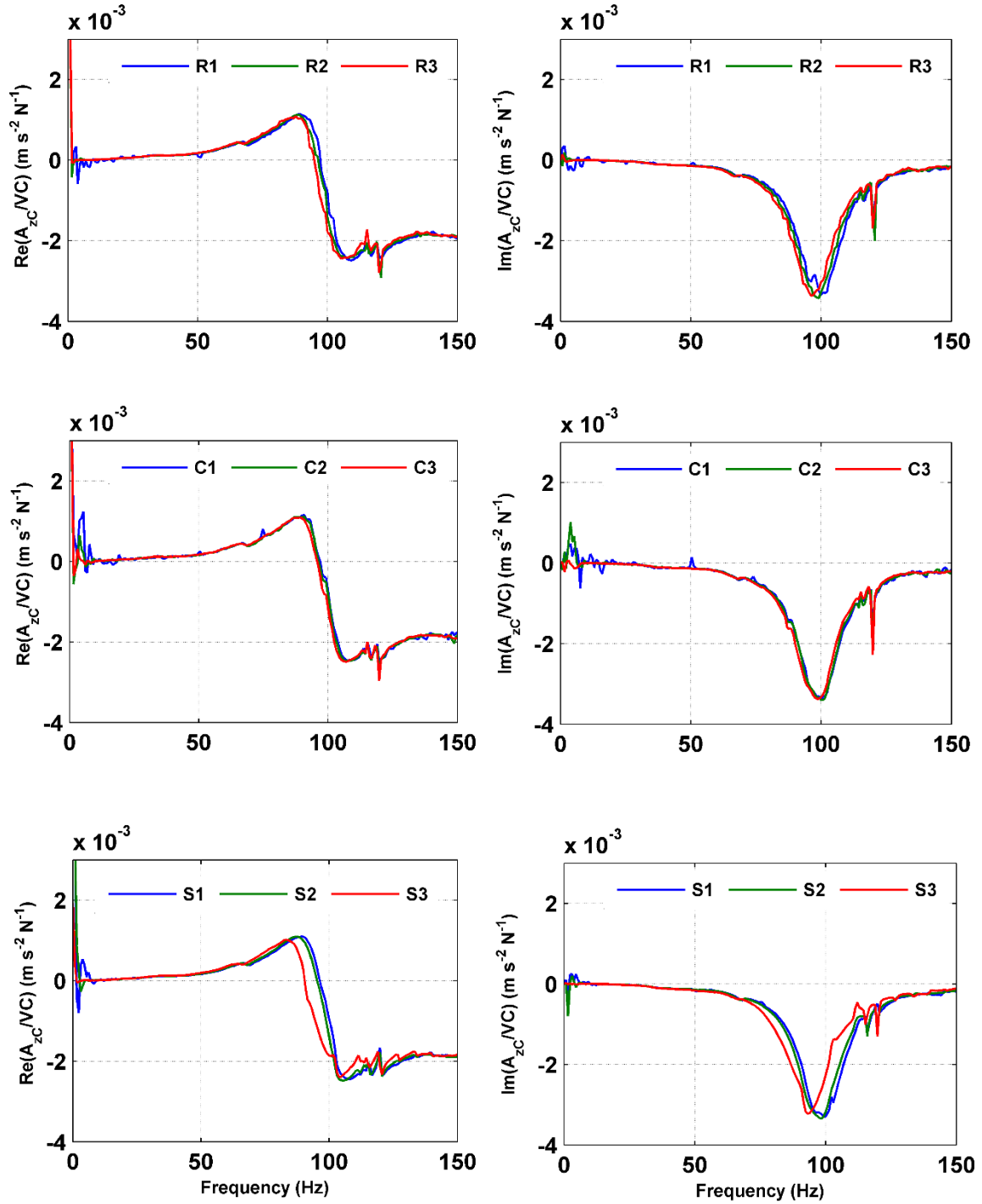


Figure 2-29. A_{zC}/VC accelerance in improved soil for different excitation types and intensities.

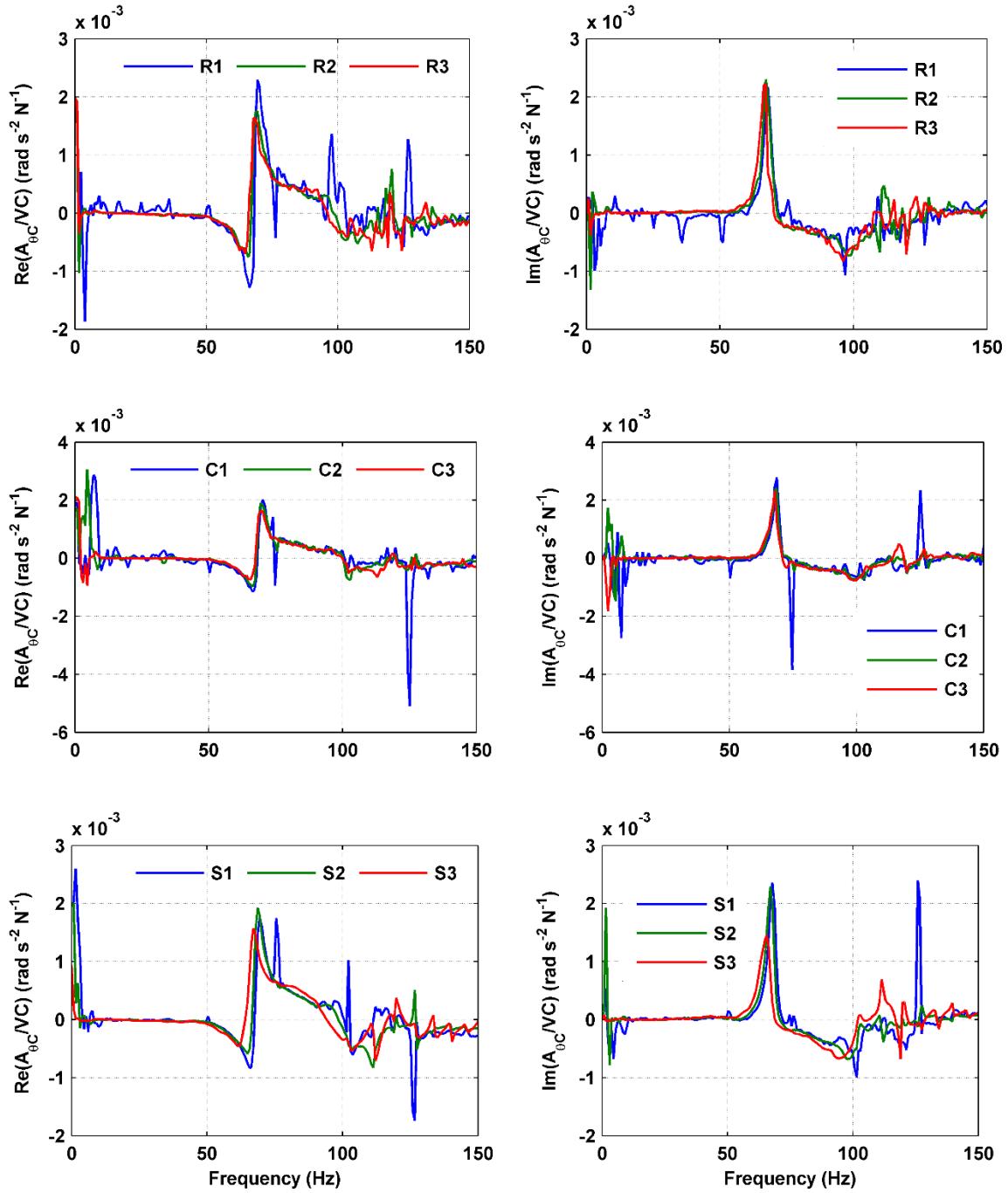


Figure 2-30. $A_{\theta C}/VC$ accelerance in improved soil for different excitation types and intensities.

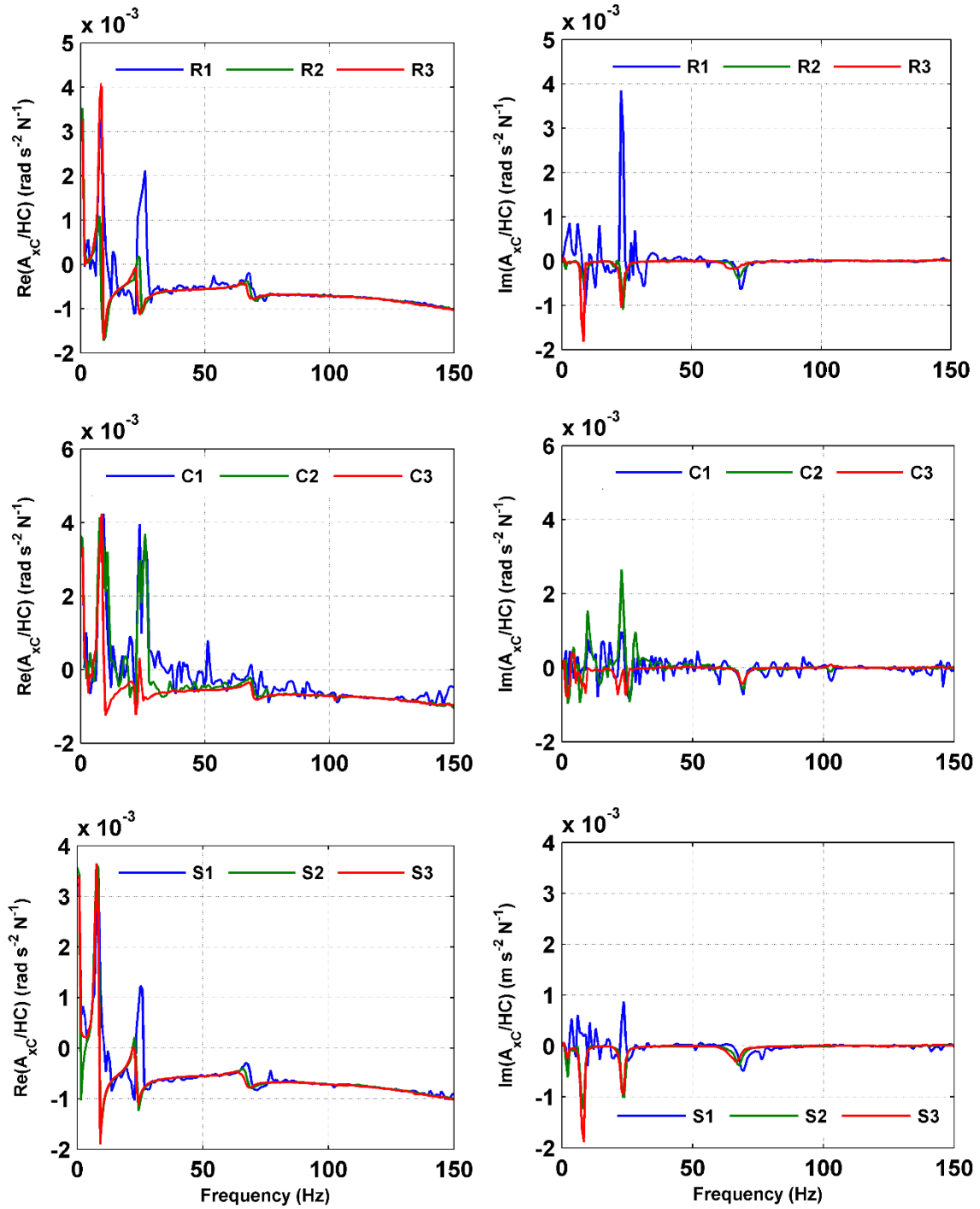


Figure 2-31. A_{x_c}/HC accelerance in improved soil for different excitation types and intensities.

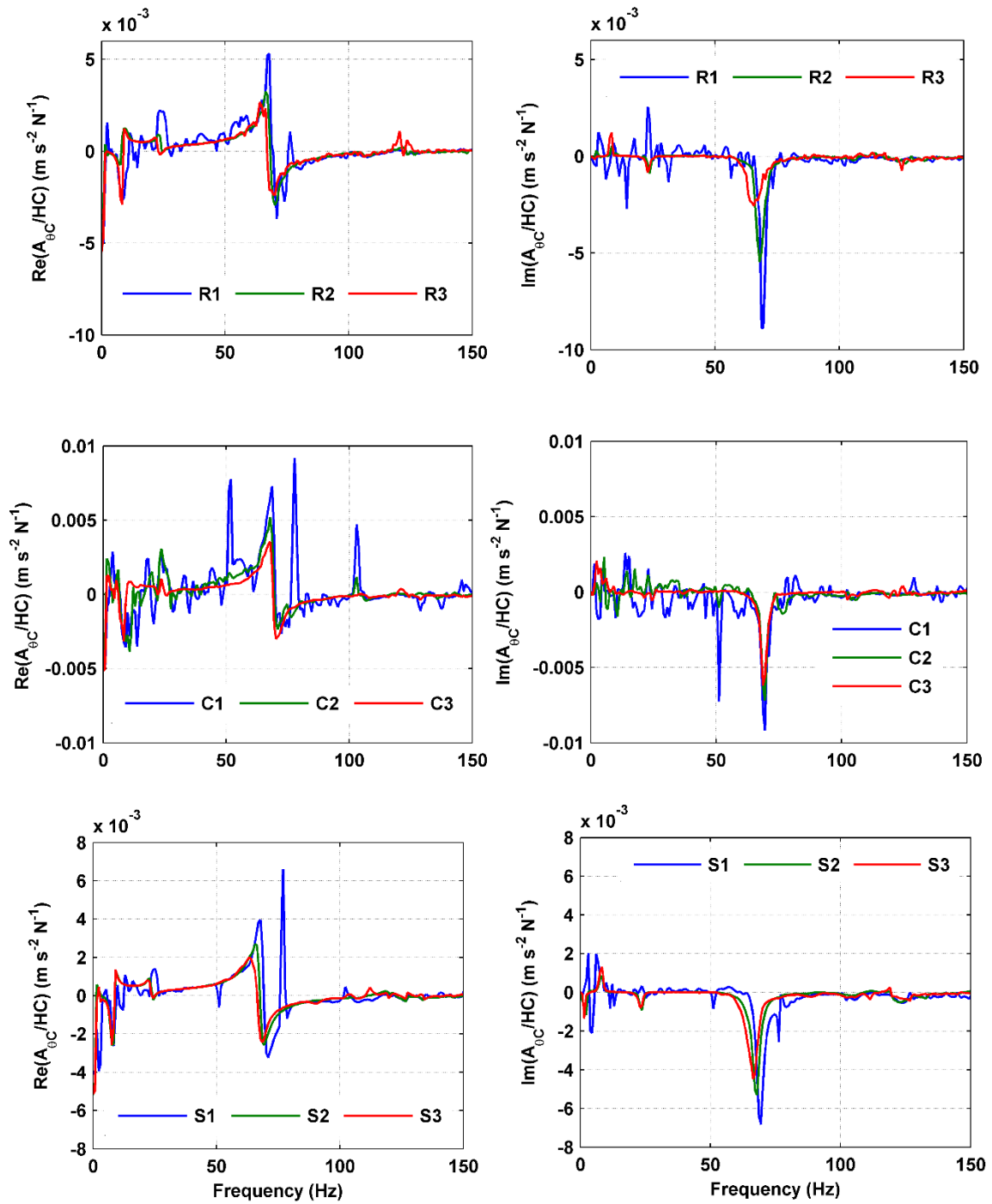


Figure 2-32. A_{0C}/HC accelerance in improved soil for different excitation types and intensities.

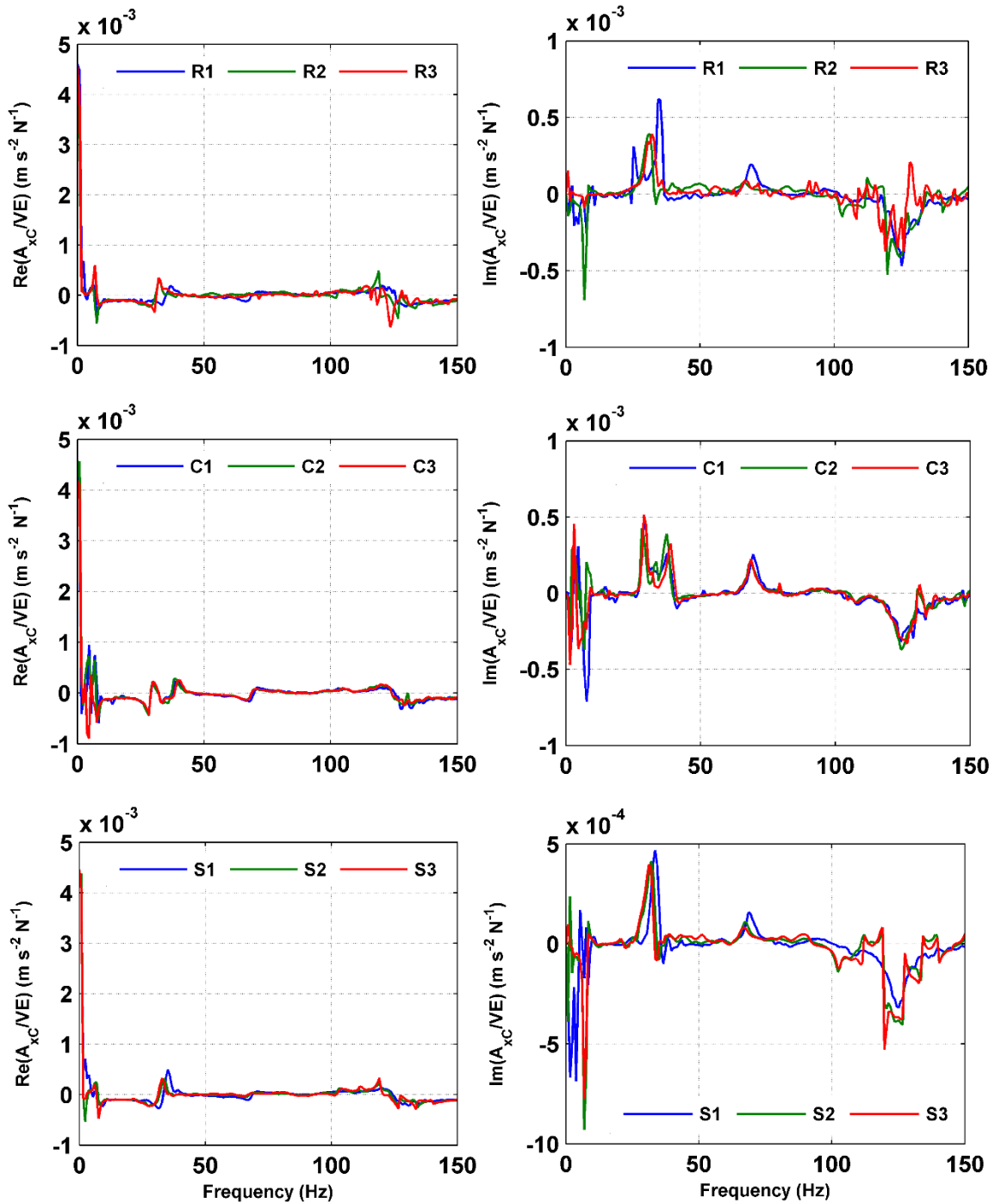


Figure 2-33. $A_{x_C/VE}$ accelerance in improved soil for different excitation types and intensities.

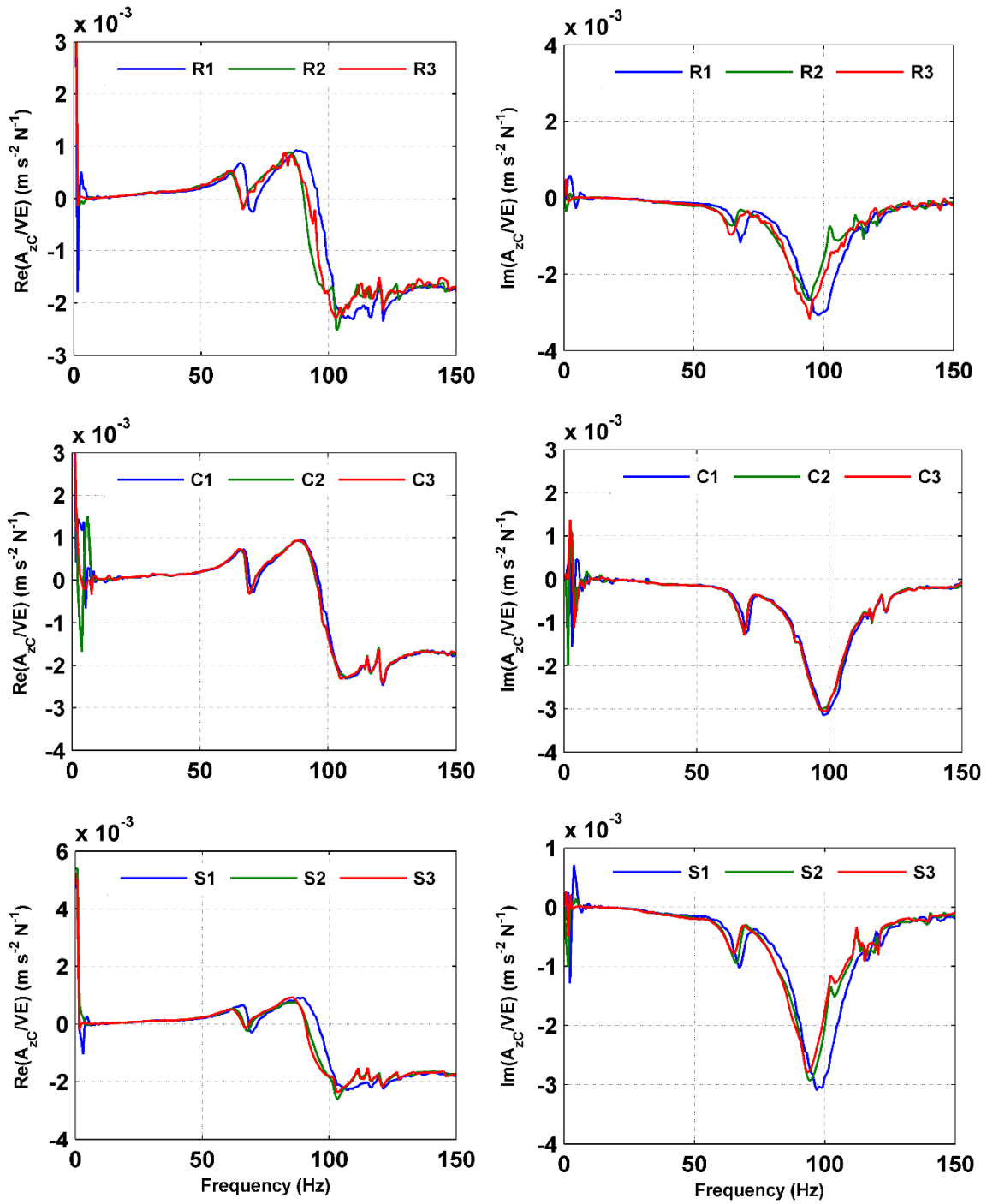


Figure 2-34. A_{zC}/VE acceleration in improved soil for different excitation types and intensities.

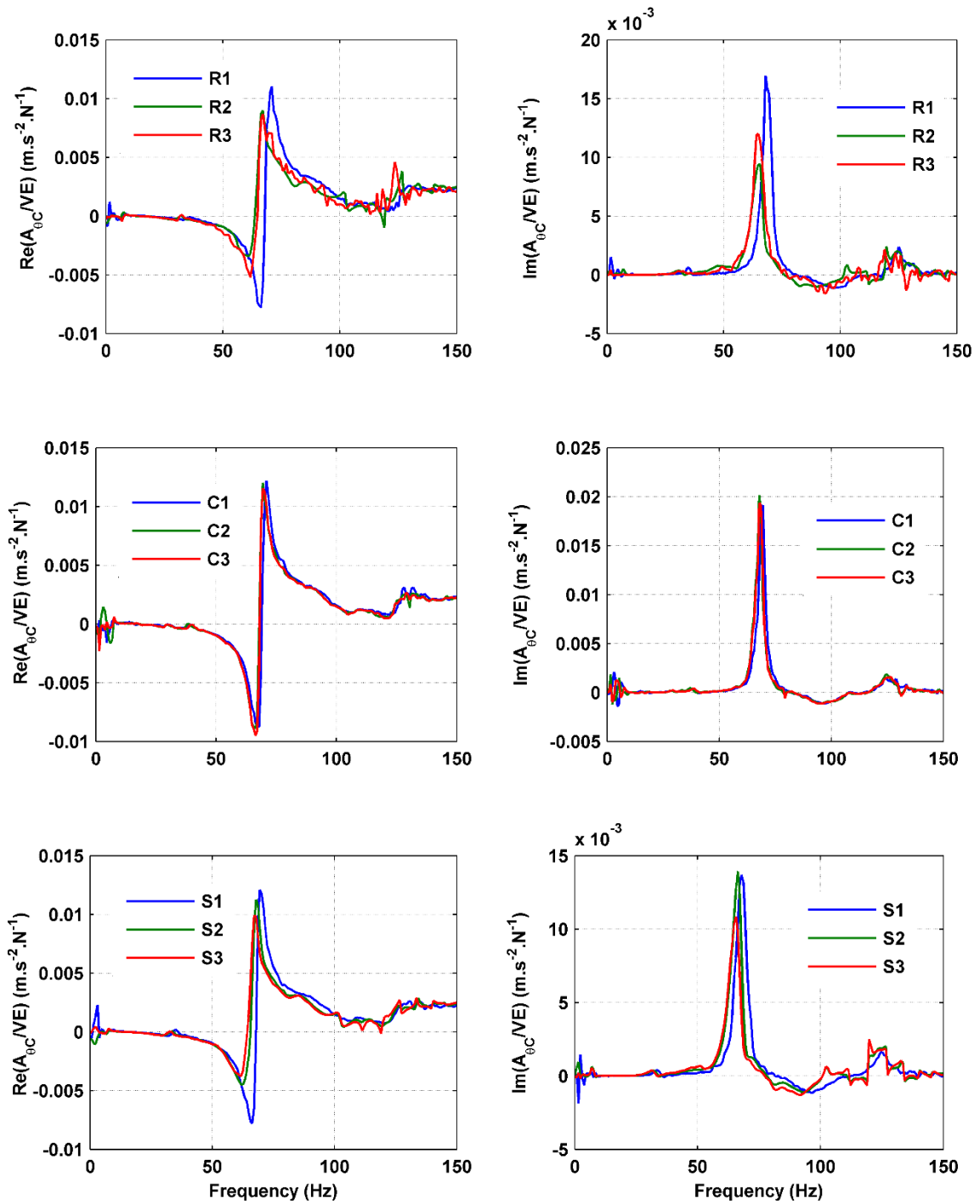


Figure 2-35. A_{0C}/VE accelerance in improved soil for different excitation types and intensities.

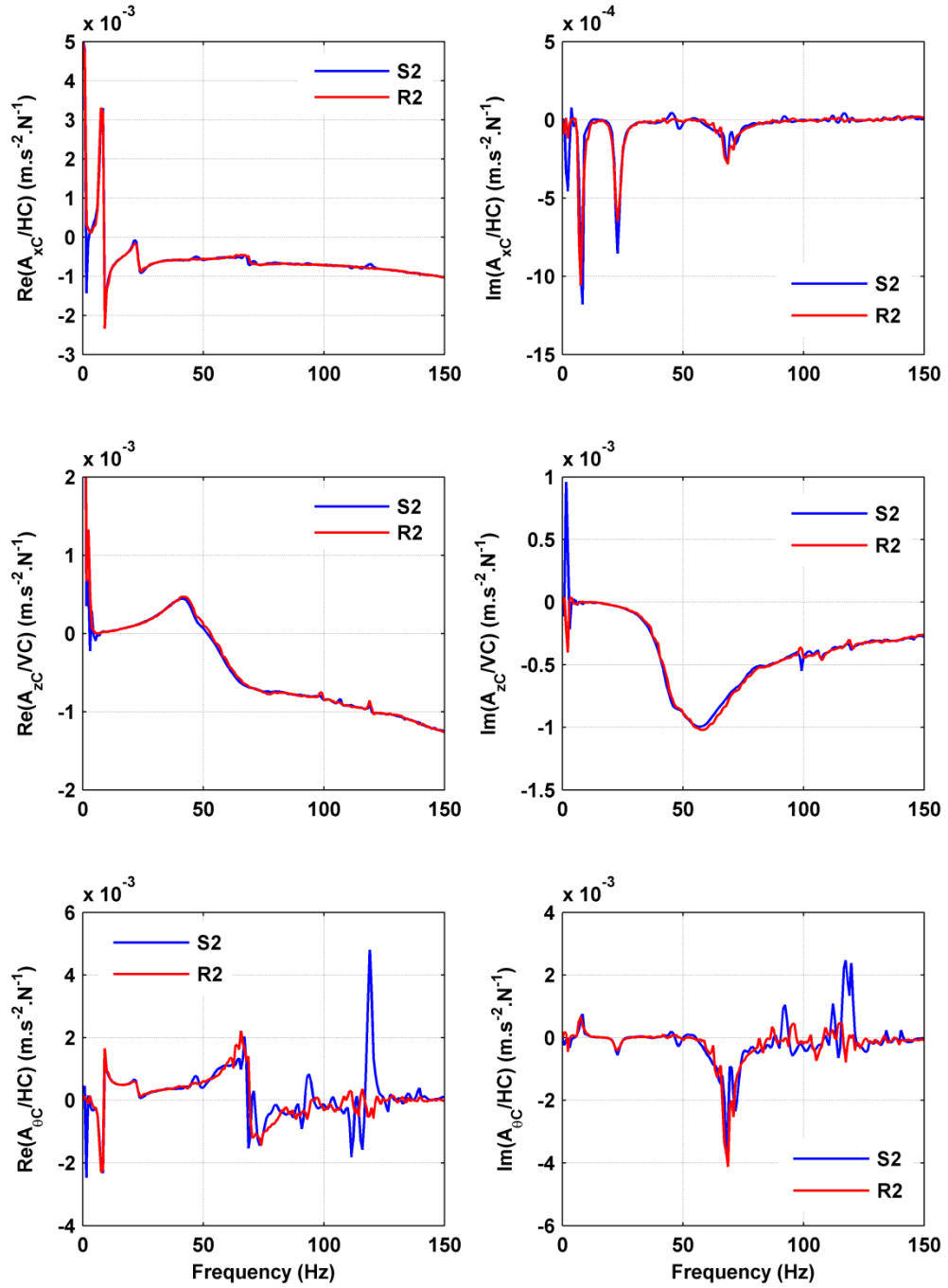


Figure 2-36. Effect of excitation type on centridal accelerance in unimproved soil.

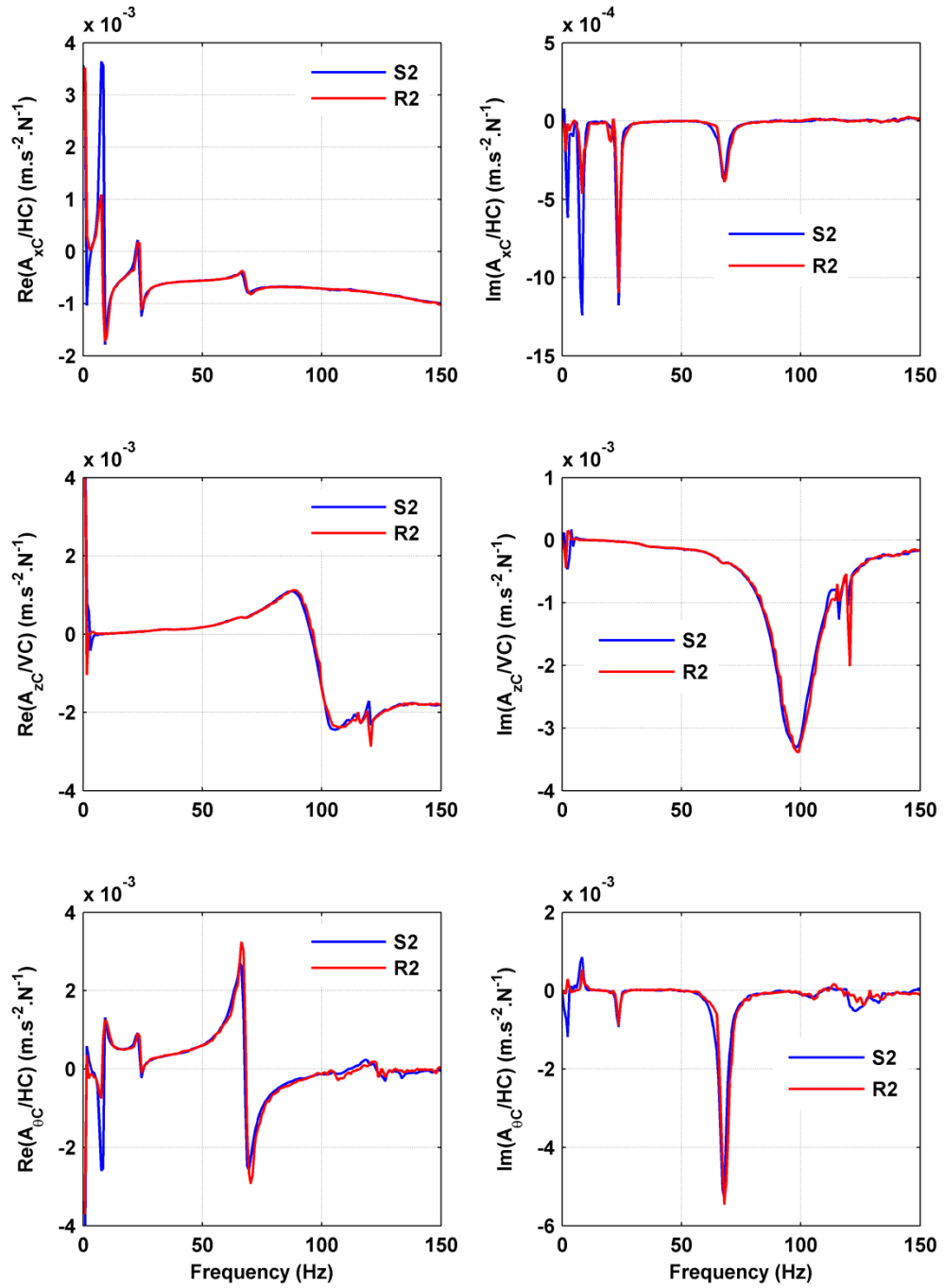


Figure 2-37. Effect of excitation type on centroidal acceleration in improved soil.

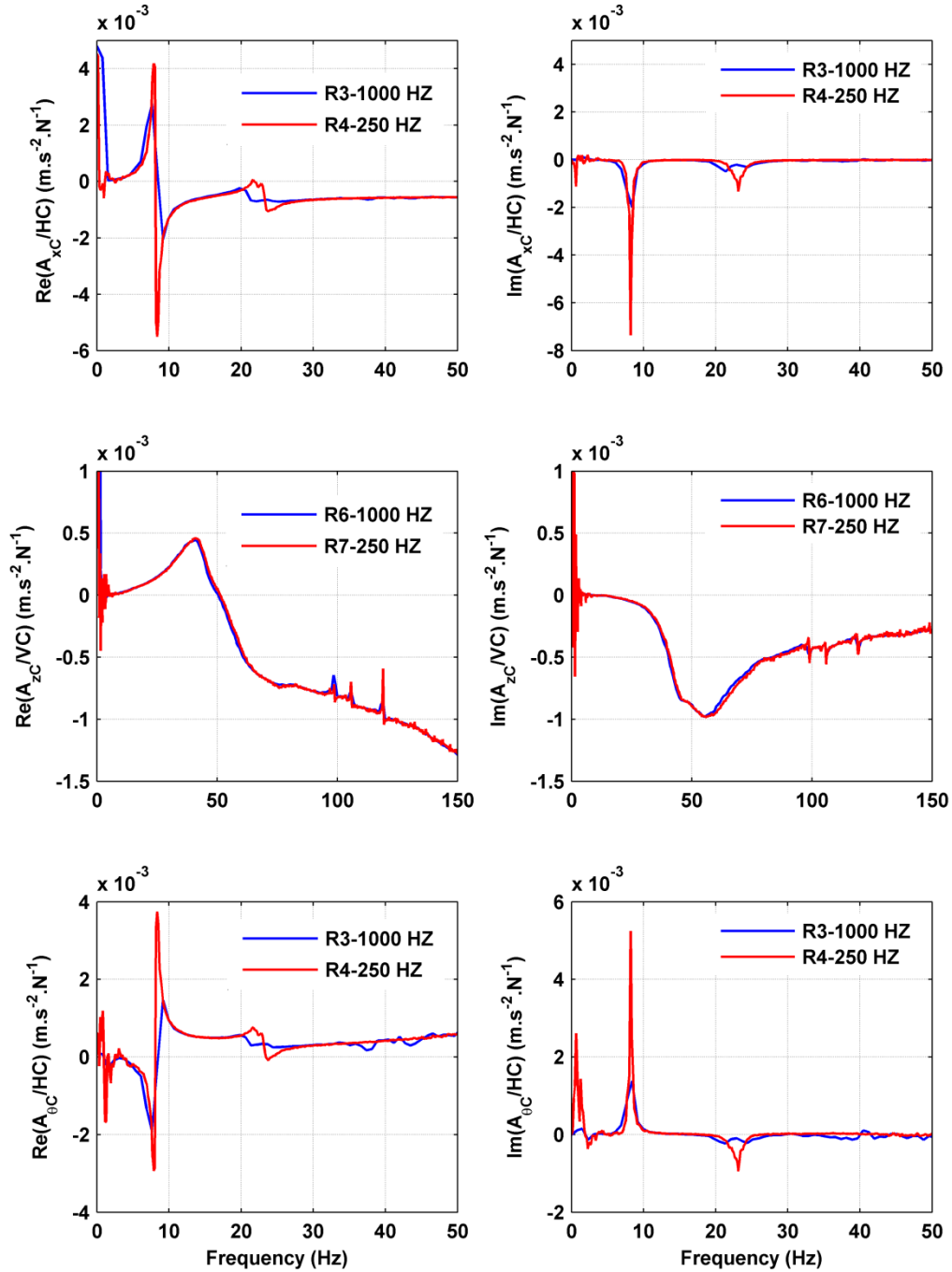


Figure 2-38. Centroidal accelerance for random excitation over 250 Hz and 1,000 Hz frequency bandwidths for pile in unimproved soil.

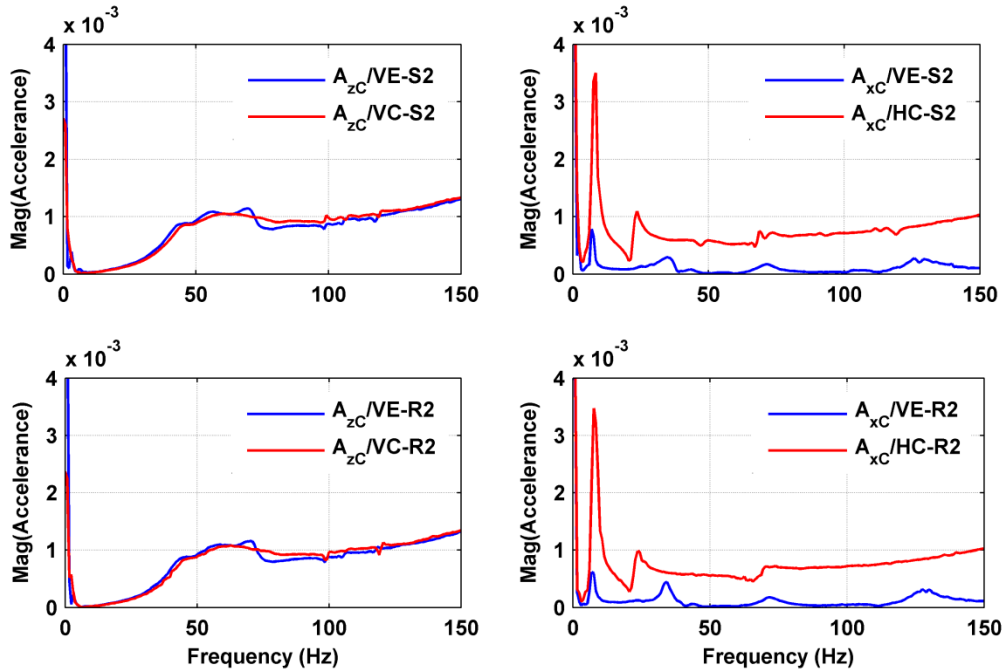


Figure 2-39. Comparison of VE test to combination of VC and HC tests for R2 and S2 excitation in unimproved soil. Left: VC response from VC and VE tests, right: HC response from HC and VE tests.

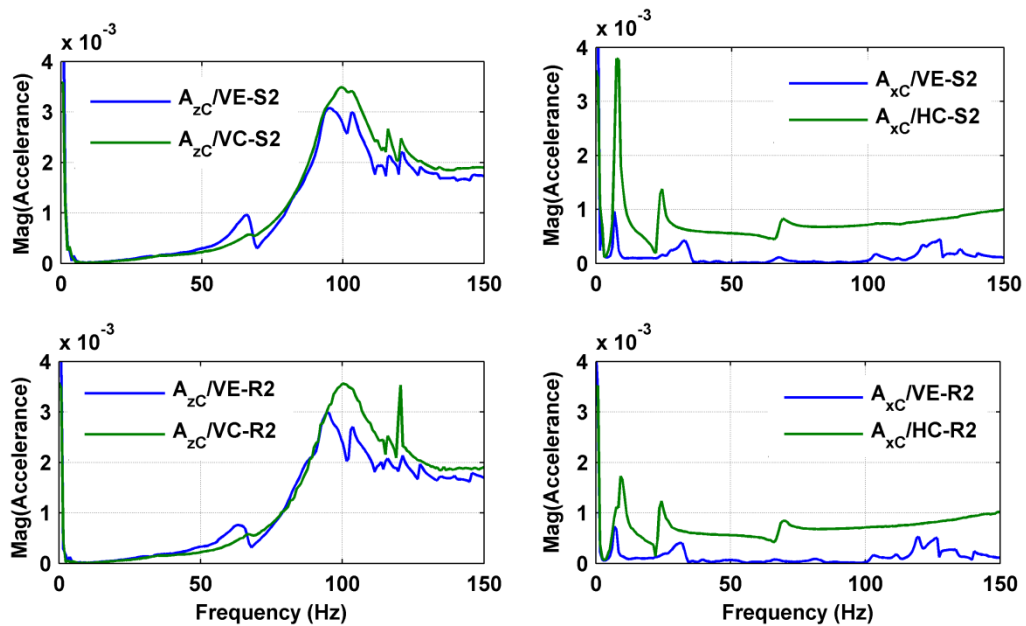


Figure 2-40. Comparison of VE test to combination of VC and HC tests for R2 and S2 excitation in improved soil. Left: VC response from VC and VE tests, right: HC response from HC and VE tests.

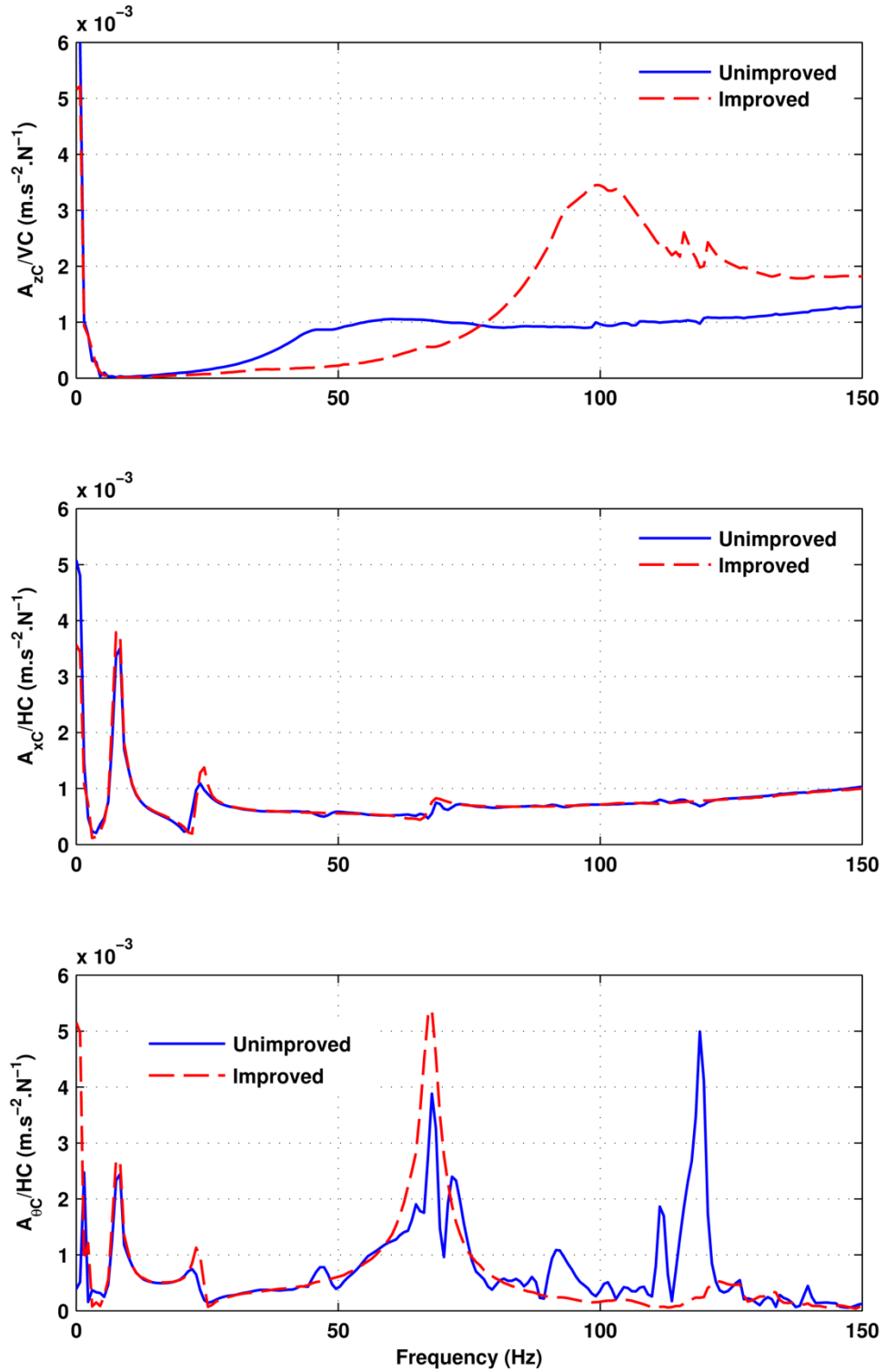


Figure 2-41. Magnitude of A_{zC}/VC , A_{xC}/HC and $A_{\theta C}/HC$ centroidal accelerances for pile in unimproved vs. improved soil (swept-sine excitation at intensity Level 2).

2.9 APPENDIX: Soil Modulus and Damping Profiles

2.9.1 CPT Profile

The soil properties including density, shear modulus, damping, and Poisson's ratio, as well as their variations with depth should be known for elasto-dynamic analysis of the soil-pile system. Soil density was determined from lab tests on intact specimens, and is assumed to be constant in each layer. Borehole soil samples along with CPT test results were used to reveal the soil layering in the field. The correlations in ((TRB), 2007) were then used to classify the soil and estimate material properties based on the CPT data. The layout of the test piles and CPT tests is shown in Figure 2-42, from which it can be seen that boreholes 2a and 5 reflect the properties of the soil near pile U (pile in unimproved soil) and pile I (pile in improved soil), respectively. Both CPT 2a and CPT 5 were performed before any soil improvement or pile driving, as a cone penetrometer would not have been able to penetrate the soil cement. For reference, the estimated soil profiles from the soil report provided by the University of Oklahoma (Amirata Taghavi, 2010) are shown in Figure 2-43 and 2-44.

Considering that the sandy-gravel layer is located over bedrock and overlain by a silty-clay layer of low permeability, the rapid dynamic forced-vibration pile tests can be considered as undrained events. To reflect this undrained condition, the Poisson's ratio is assumed to be 0.40 for all layers in the analyses.

The soil shear modulus profile was estimated using empirical correlations to CPT data (equations 8 for sands and equation 9 for clays in (TRB, 2007)). CPT raw data, cone soil classification index and shear modulus velocity are plotted in Figure 2-45. The resulting shear modulus profile is plotted for both CPT locations 2a and 5 in Figure 2-46. As shown in the

figure, the trend of the data indicates that the profile can be approximated by four different layers for the entire depth of interest. These layers are generally compatible with the unimproved soil profile used in the NEESR-SG project shown in Figure 2-43. The sudden increase in shear modulus at the upper surface of the gravel layer is due to the soil type and density changing from clay to gravel.

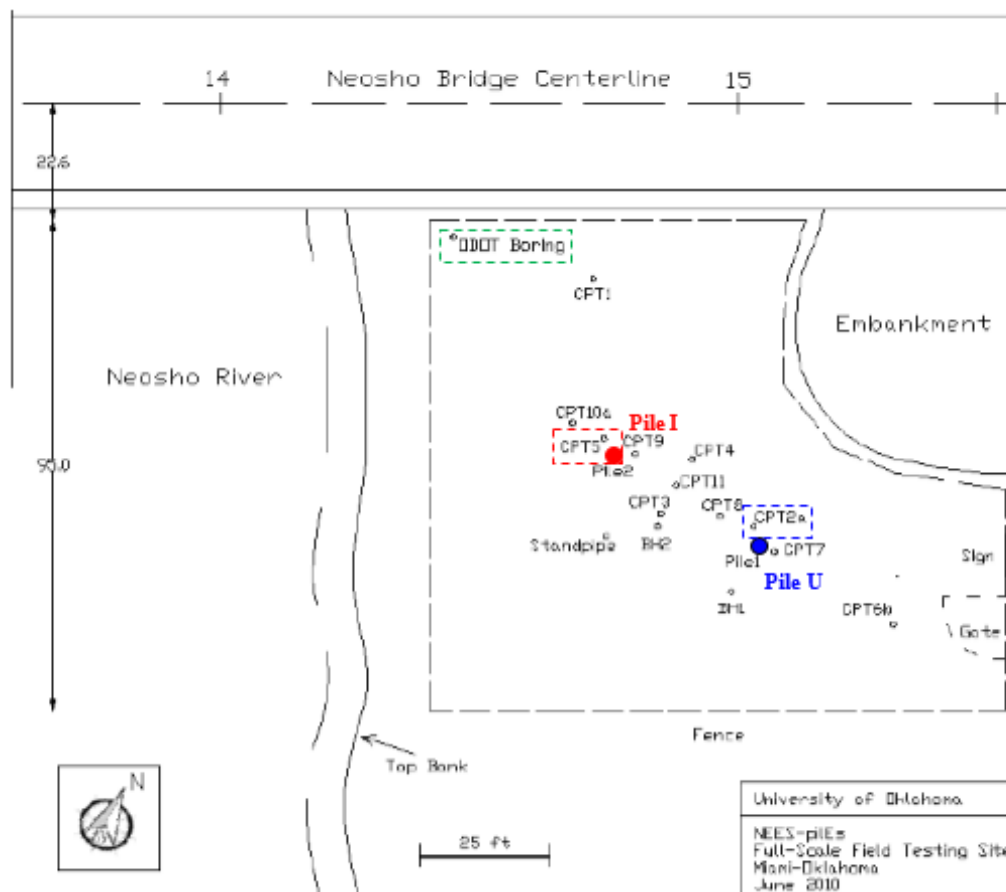


Figure 2-42- Layout of CPT and test pile locations (modified from Amirata Taghavi, 2010).

Soil Profile without Improvement

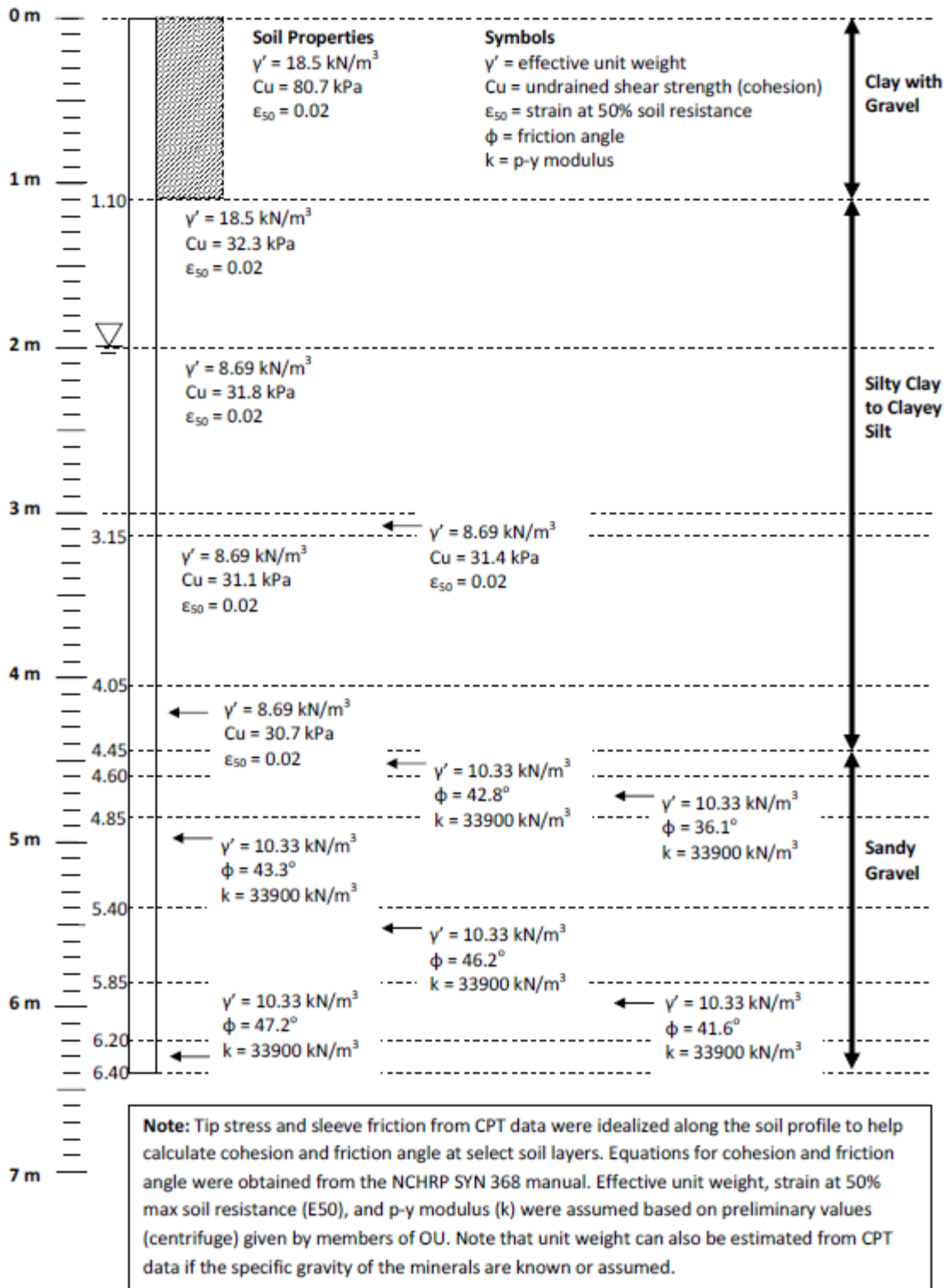


Figure 2-43- Soil profile for unimproved test (Courtesy of Brad Fleming).

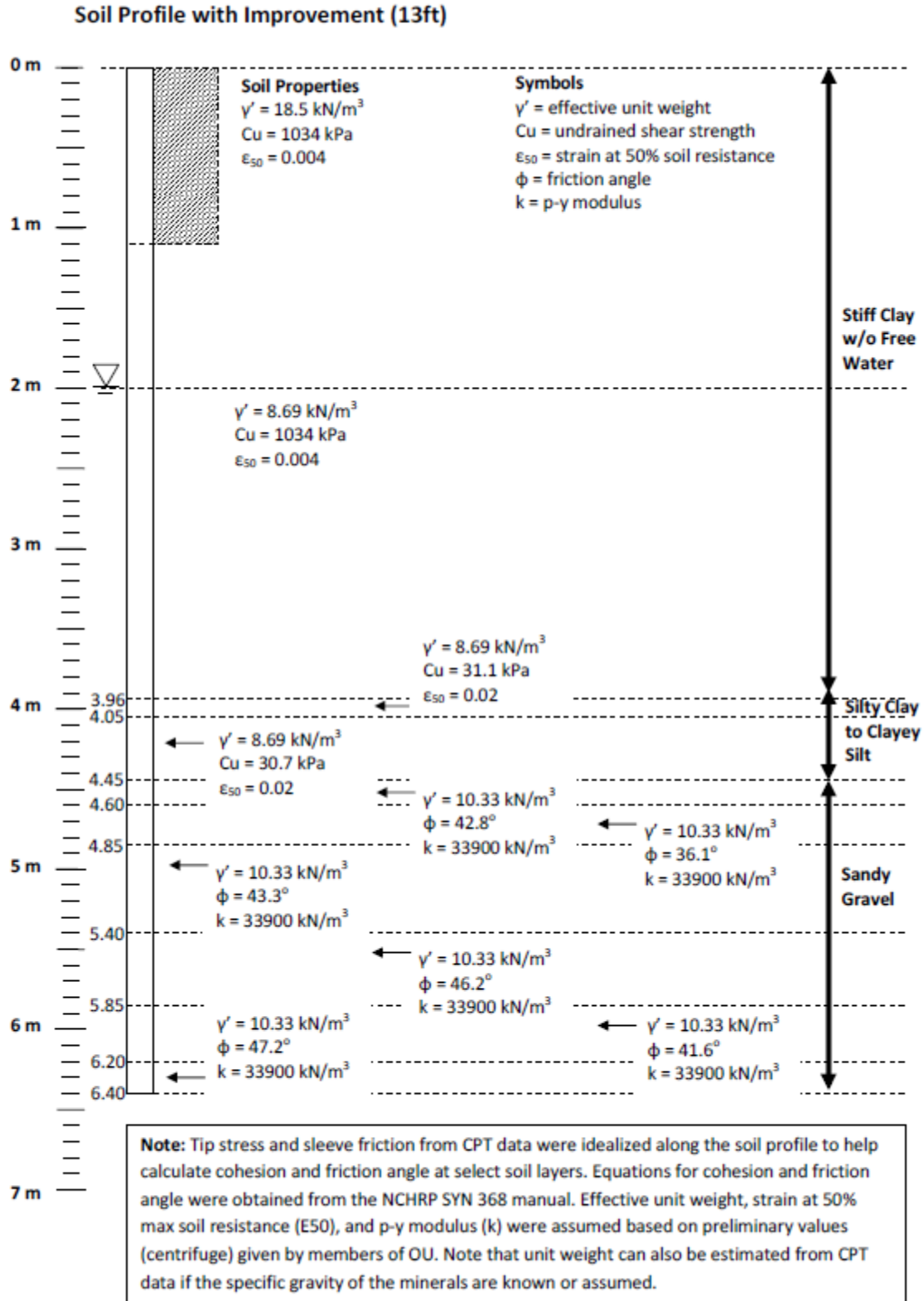


Figure 2-44- Soil profile for improved test (Courtesy of Brad Fleming).

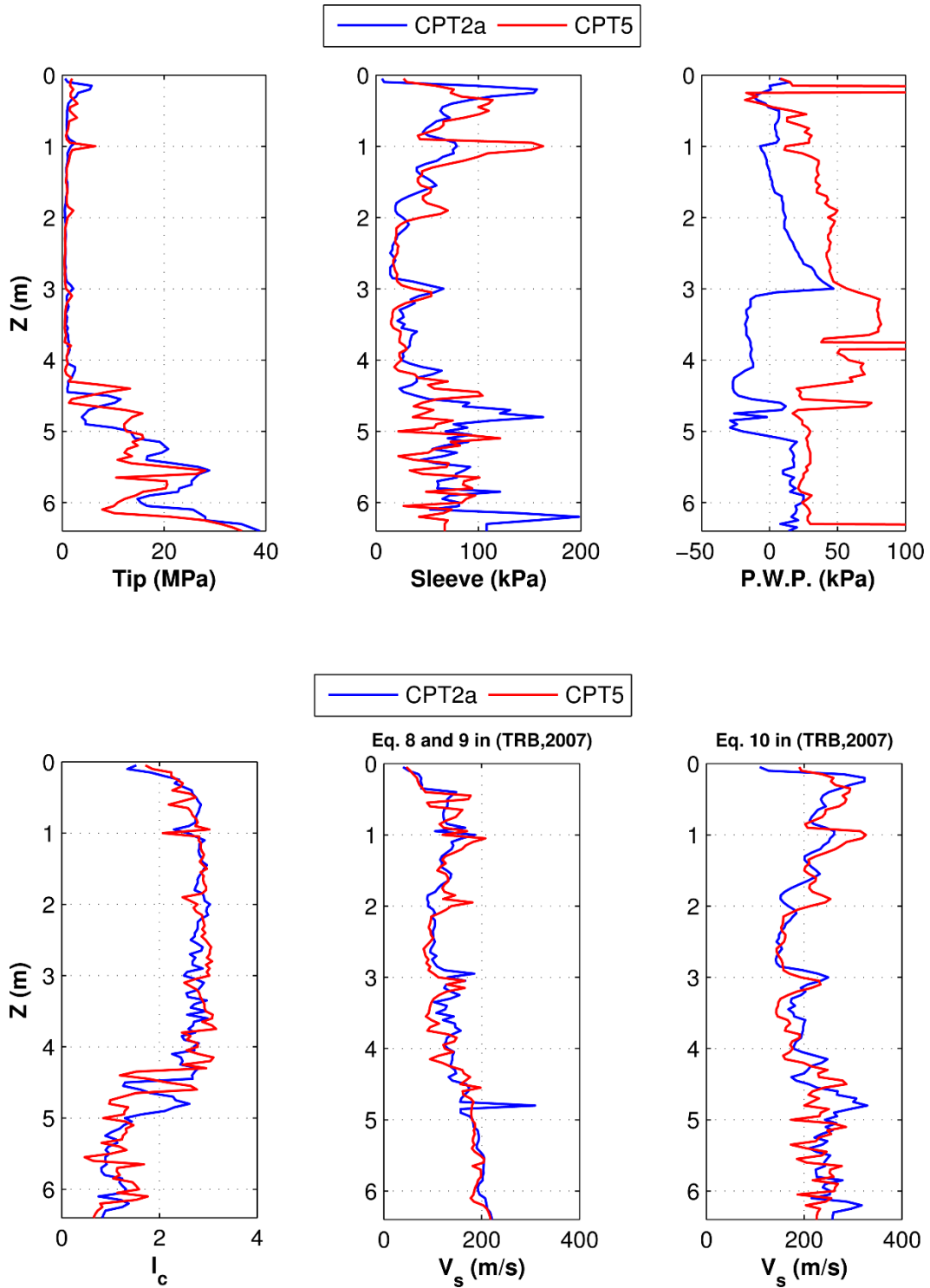


Figure 2-45- CPT raw data, I_c and V_s from correlations in (TRB, 2007)

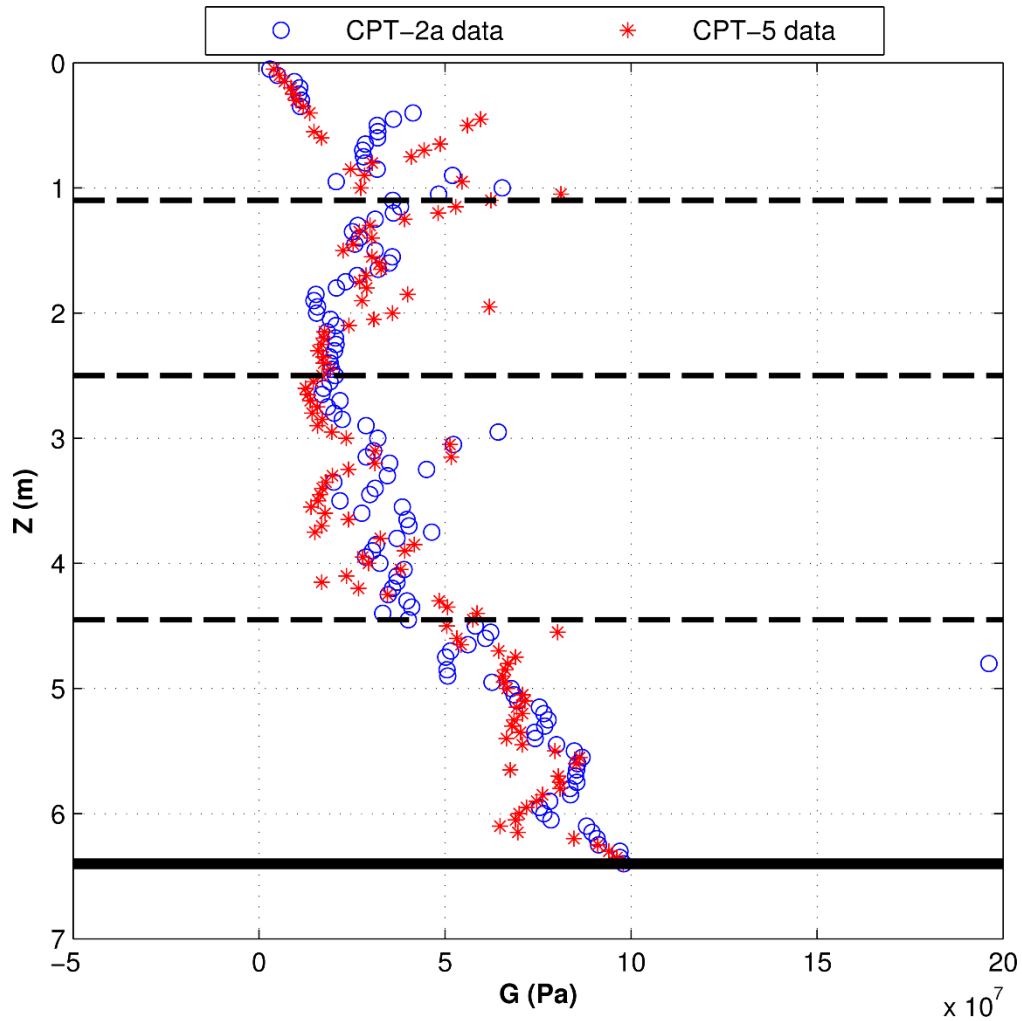


Figure 2-46- Soil shear modulus profiles from CPT Tests 2a and 5.

To enable the soil profile to be more easily discretized in numerical analyses, smooth curves were obtained by fitting quadratic polynomials to the shear modulus data within each layer. The best fit curve and curves delineating $\pm 40\%$ deviation from the best fit are plotted in Figure 2-47 and 2-48 for CPT 2a and CPT 5, respectively. To systematically deal with extreme outliers, the data outside the 40% zone were discarded. New quadratic regressions were then performed on the resulting reduced data sets, giving the modulus profiles shown in Figure 2-49 and 2-50. In order to obtain a continuous profile throughout the top three layers, the quadratic

curves were forced to pass through an average value at layer boundaries as depicted in Figure 2-51. It will be shown that the last step of enforcing continuity at the top two interfaces has a negligible effect on the theoretical impedances and therefore on the pile response. The final smooth profiles and their discretized formats with 55 soil layers down to the bedrock depth of 21 ft are presented in Figure 2-52 and 2-53. These final shear modulus profiles were used in the subsequent pile-soil interaction analyses.

Parametric studies were conducted to investigate the relative influence of the problem parameters on the dynamic pile-soil interaction in terms of the resulting impedance functions. To investigate the effect of shear modulus profile shape on the pile-soil impedances at the soil surface elevation, the profiles of Figure 2-52 and 2-53 were compared with piecewise constant profiles obtained from the averages of the reduced data in each of the four primary geological layers (Figure 2-54 and 2-55). The results of these different levels of precision in representing the in situ soil profiles are shown in terms of the impedance functions in Figure 2-56 and 2-57. Additionally, the impedances from the CPT 2a and CPT 5 soil profiles are compared in Figure 2-58. These figures indicate that the simplified piecewise constant soil profiles can incur errors of 5 to 10% in the real and imaginary components of K_{mm} and K_{hm} , and errors up to 25% in K_{hh} , while the vertical impedances are practically unaffected. Additionally, the impedances for the piecewise quadratic approximations of CPT 2a and CPT 5 are not significantly different, with a maximum difference of only 8% in the imaginary part of K_{hh} at the highest frequency examined.

Material damping is a difficult parameter to measure in situ, and NCHRP Synthesis 368 does not provide any empirical correlations for estimating damping from CPT data. At high frequencies, the contribution of material damping will generally be much smaller than

that of radiation damping. The radiation damping is accounted for rigorously in BEASSI, and is quantified by the imaginary part of the impedances from analyses with zero material damping. As a first approximation, material damping is assumed to be constant within each layer. In some initial analyses, the material damping is assumed to be negligible compared to radiation damping and is thus set to zero.

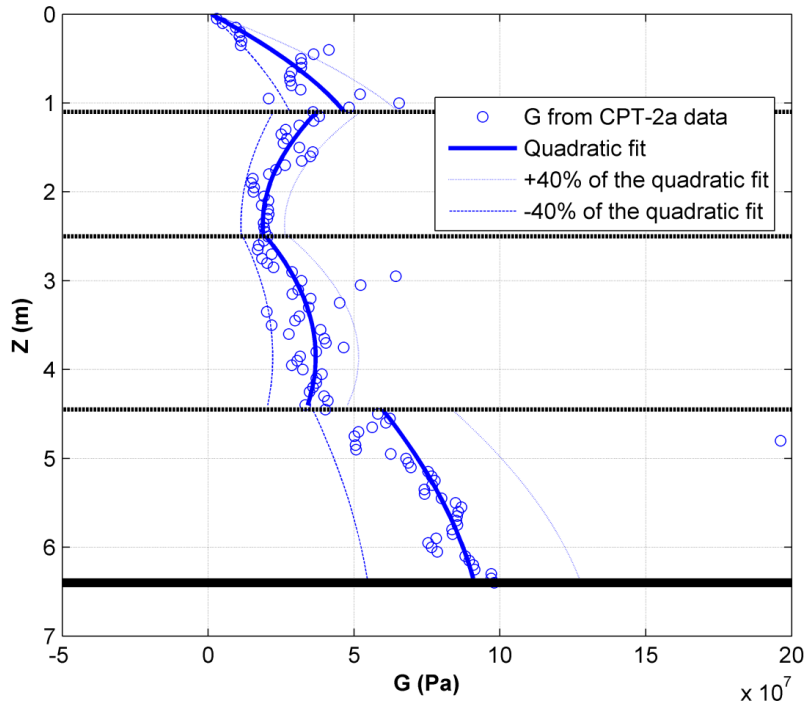


Figure 2-47- Best-fit quadratic polynomial to the raw data within each layer for CPT 2a.

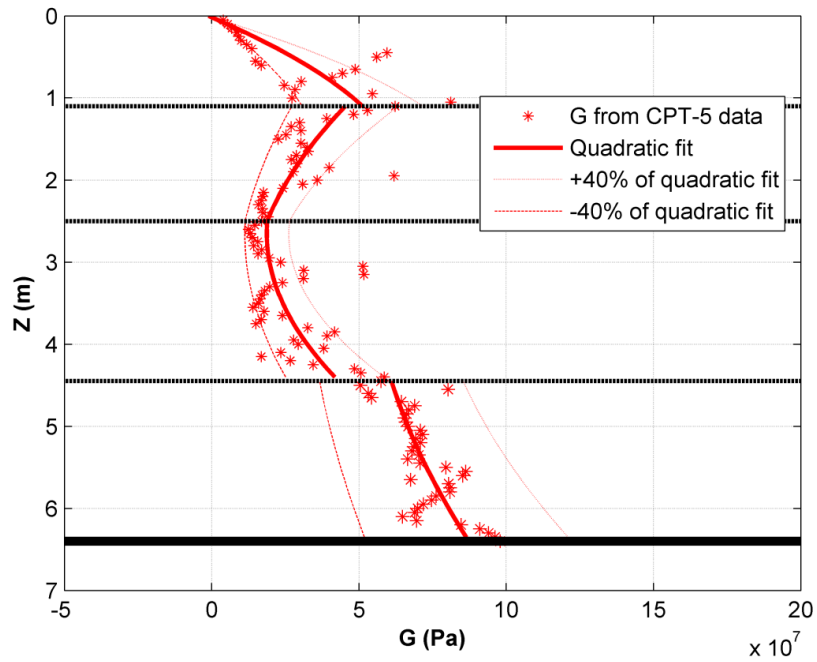


Figure 2-48- Best-fit quadratic polynomial to the raw data within each layer for CPT 5.

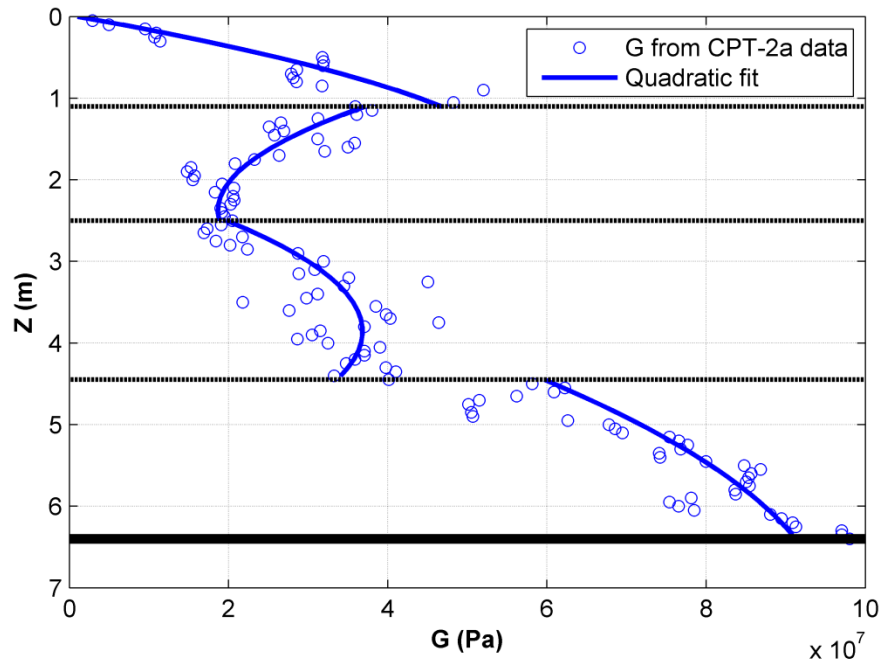


Figure 2-49- Best-fit quadratic polynomial to the reduced data within each layer for CPT 2a.

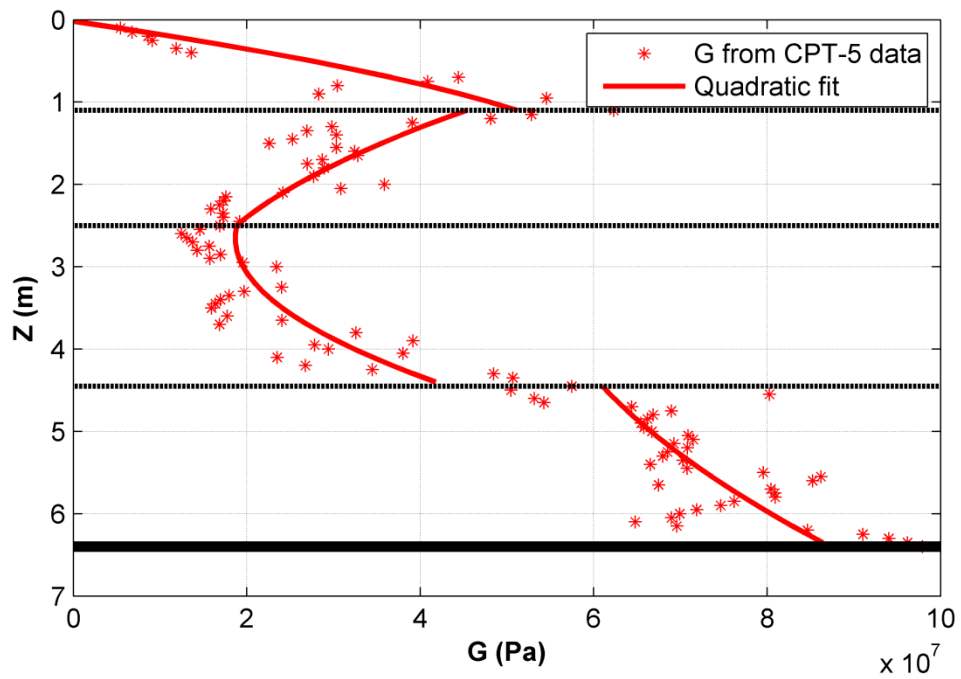


Figure 2-50- Best-fit quadratic polynomial to the reduced data within each layer for CPT 5.

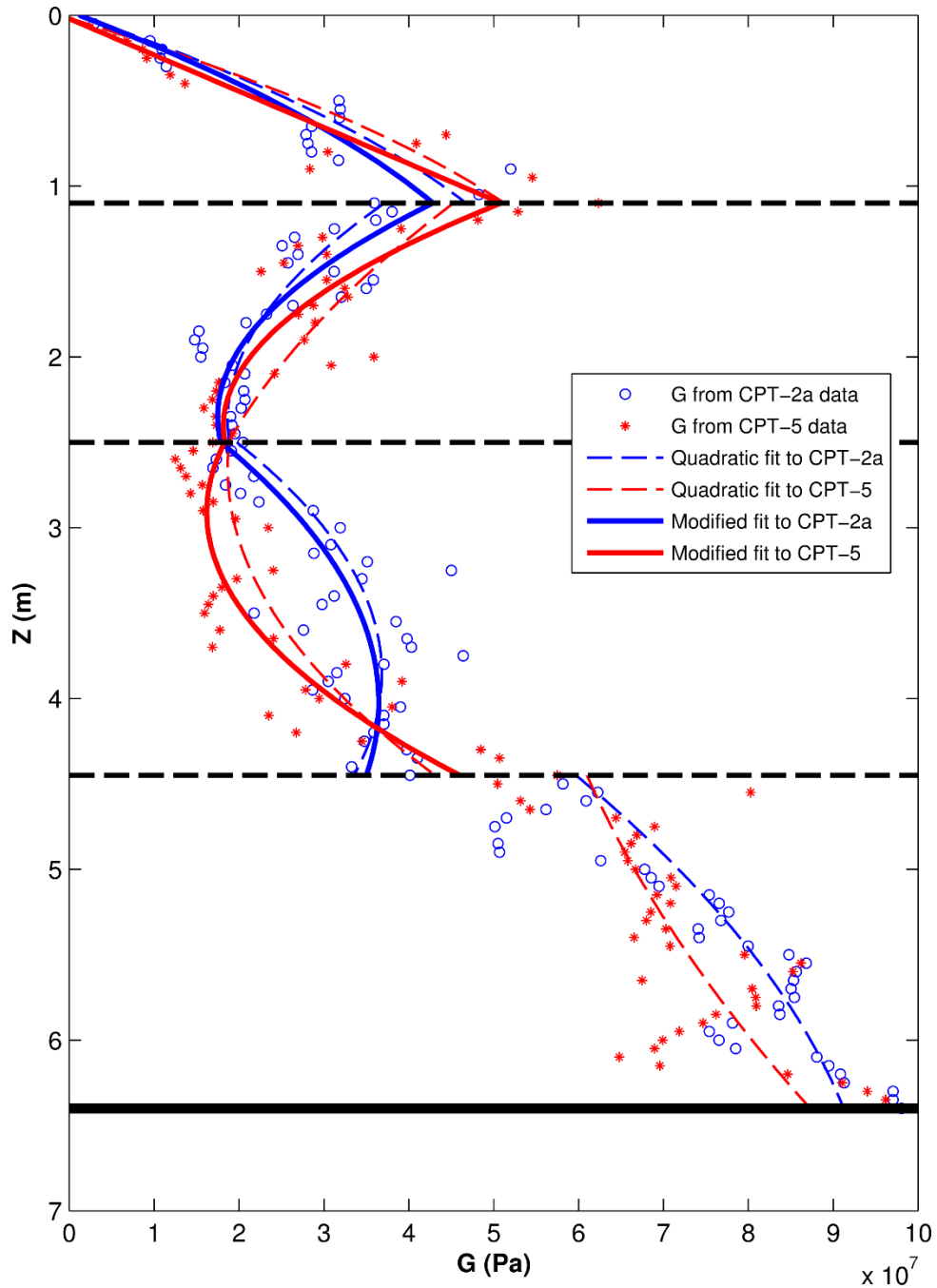


Figure 2-51- Best-fit quadratic polynomial to the reduced data with enforcement of continuity at the top two layer interfaces.

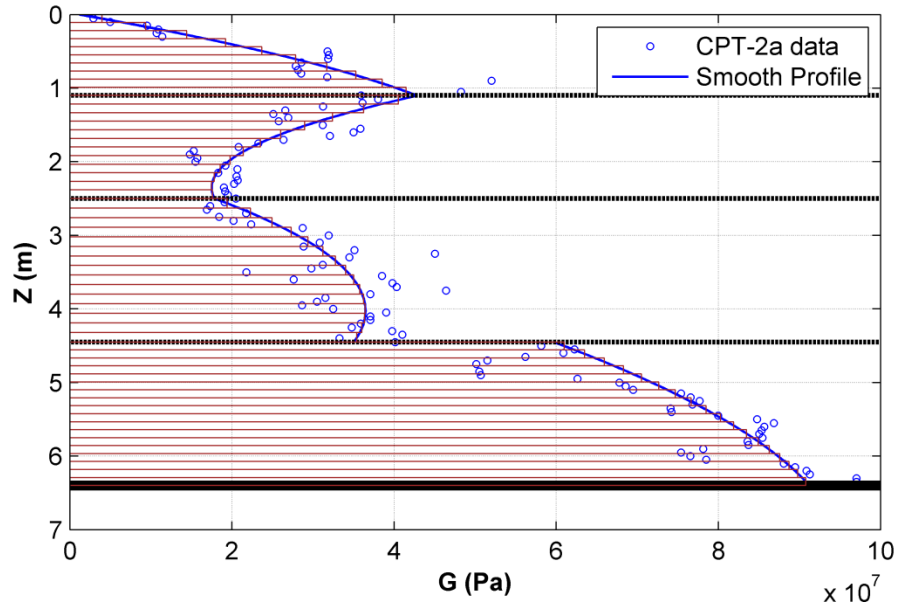


Figure 2-52-Final discretized piecewise quadratic profile for CPT 2a with 55 layers to bedrock (10, 12, 15, and 18 layers).

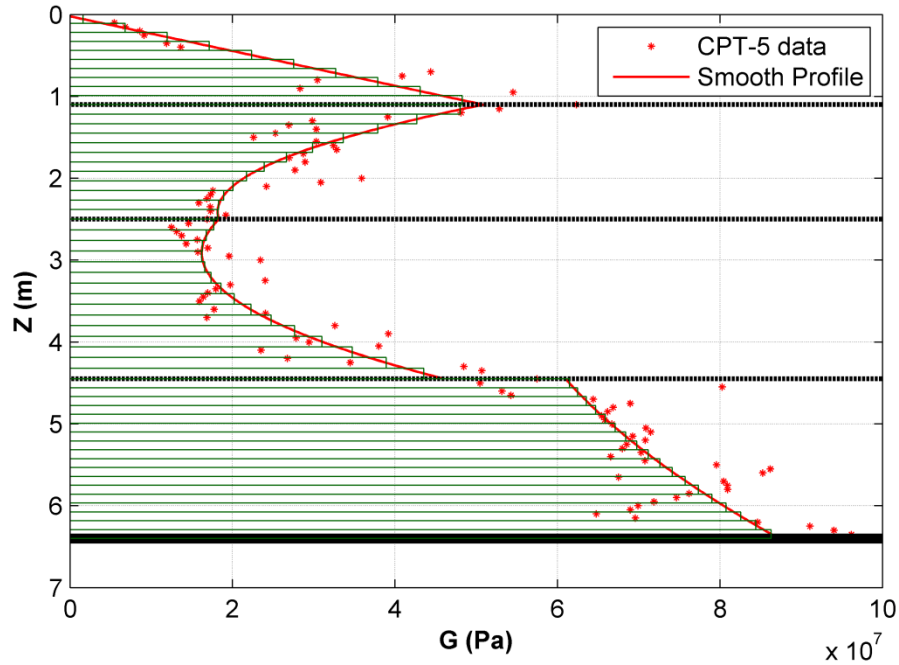


Figure 2-53-Final discretized piecewise quadratic profile for CPT 5 with 55 layers to bedrock (10, 12, 15, and 18 layers).

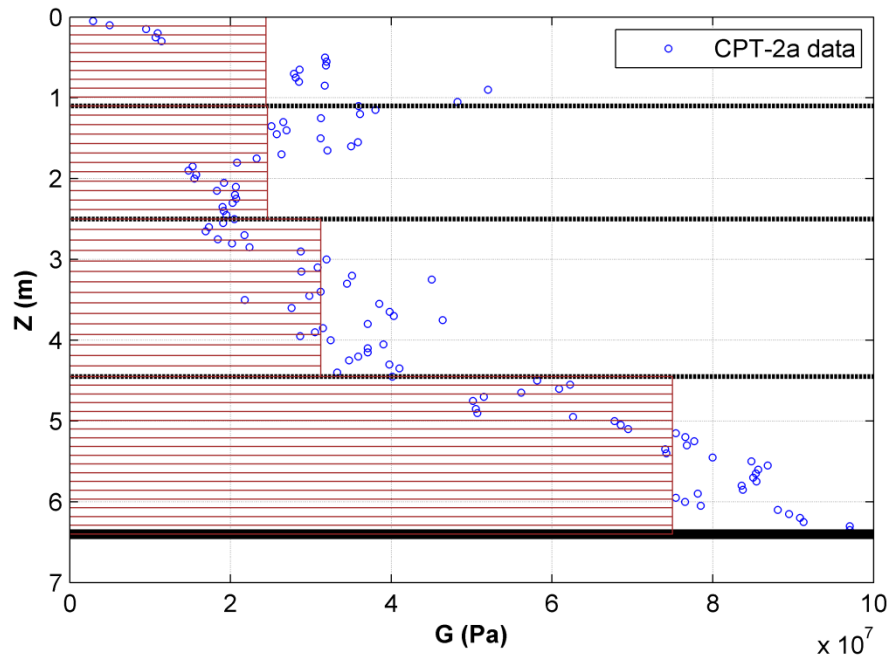


Figure 2-54-Discretized piecewise constant profile for CPT 2a with 55 layers to bedrock (10, 12, 15, and 18 layers).

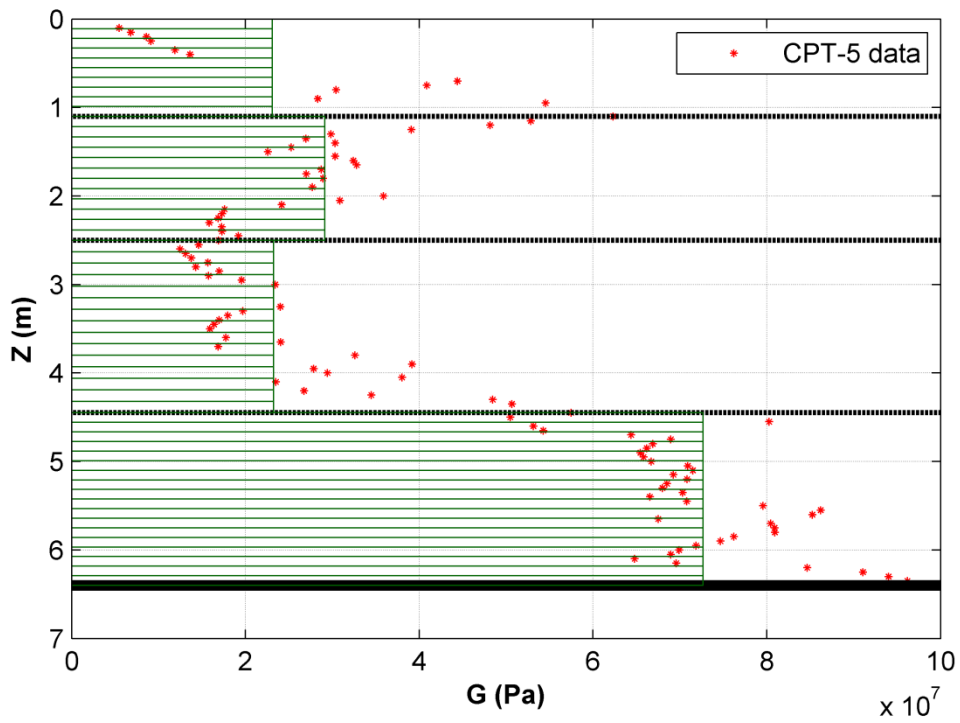


Figure 2-55-Discretized piecewise constant profile for CPT 5 with 55 layers to bedrock (10, 12, 15, and 18 layers).

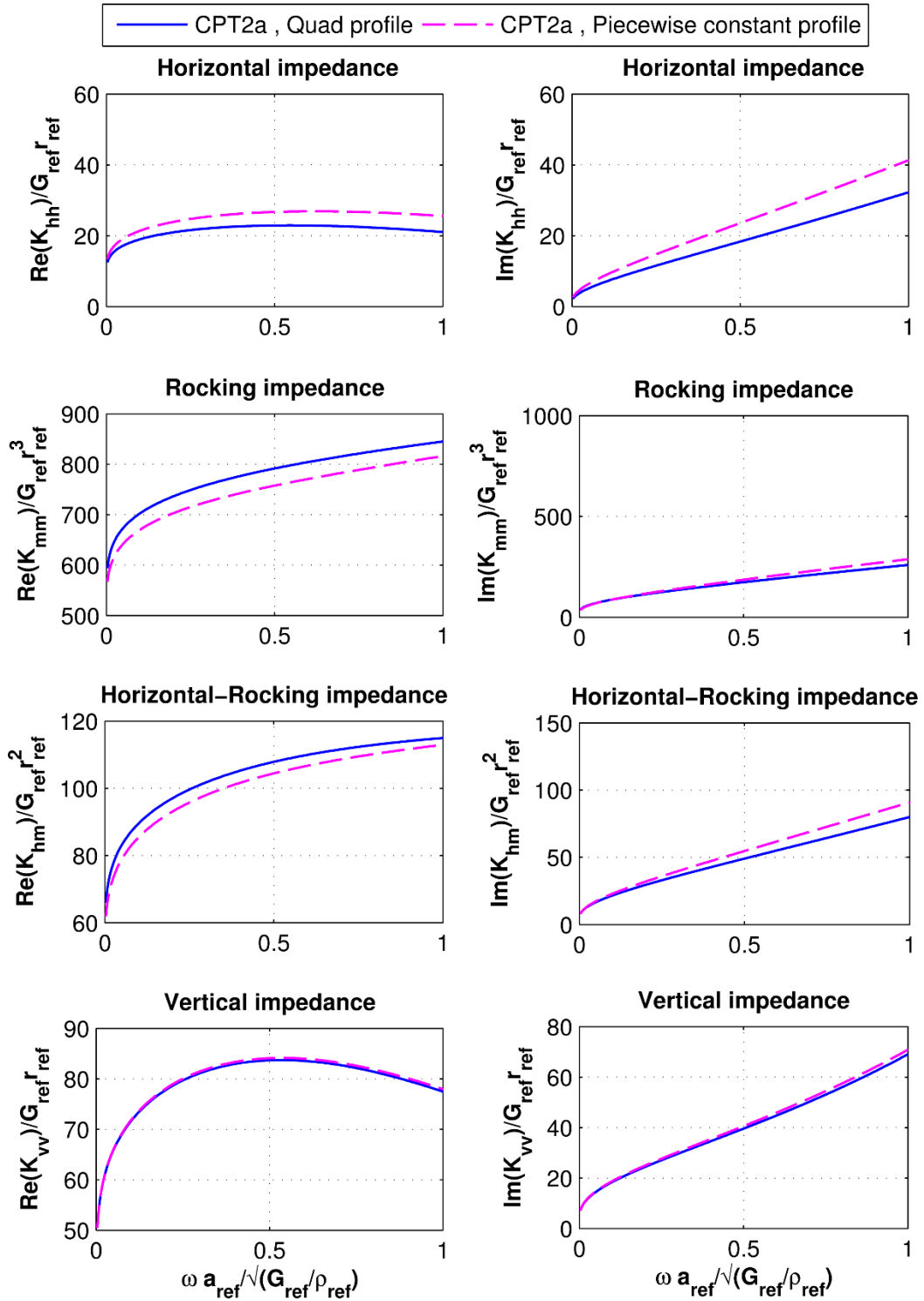


Figure 2-56- Effect of modulus profile shape on soil impedances in the unimproved soil. Material damping is set to zero and other properties reflect the NEES test.

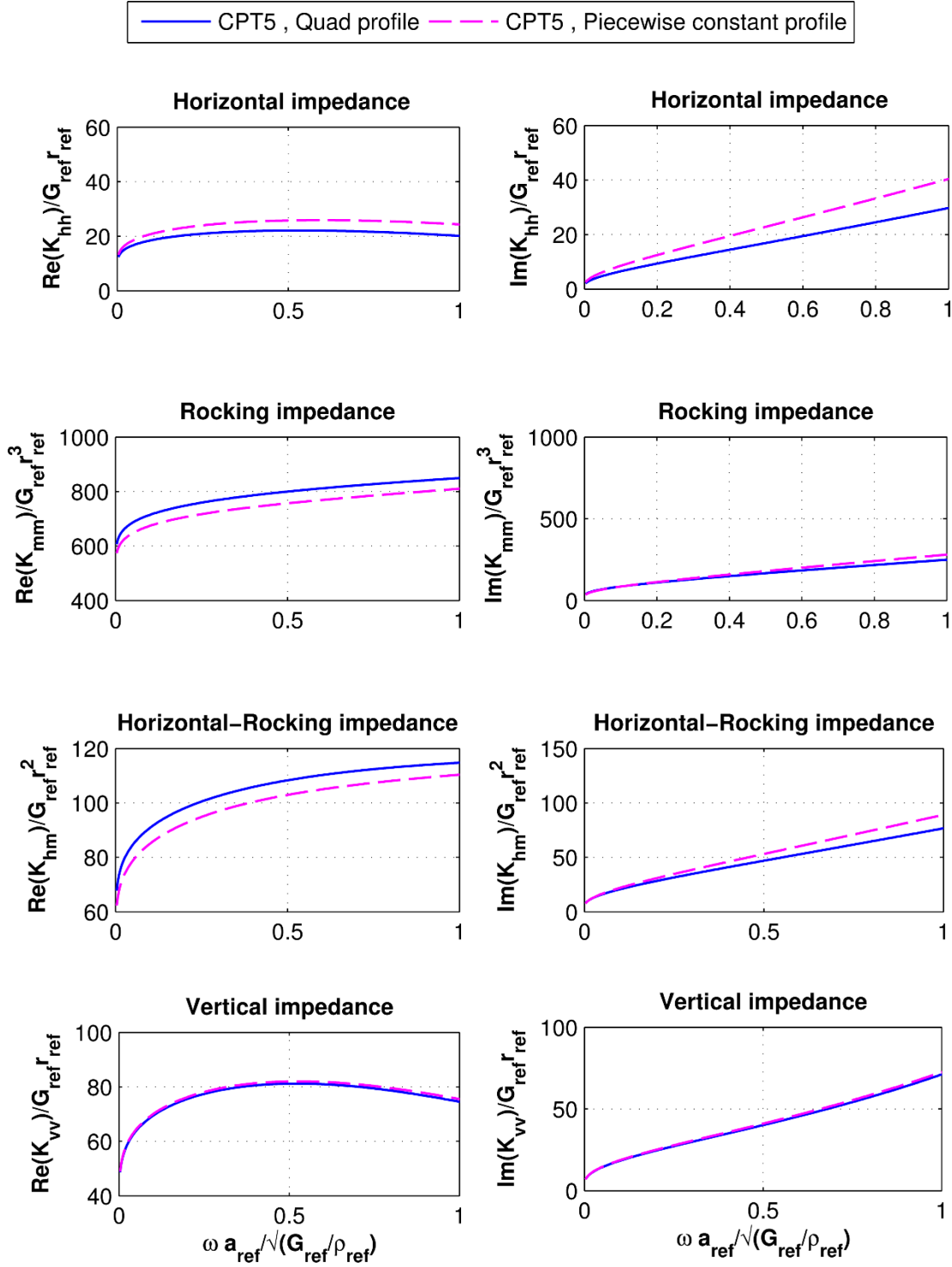


Figure 2-57- Effect of the modulus profile shape on soil impedances in the improved soil. Material damping is set to zero and other properties reflect the NEES test.

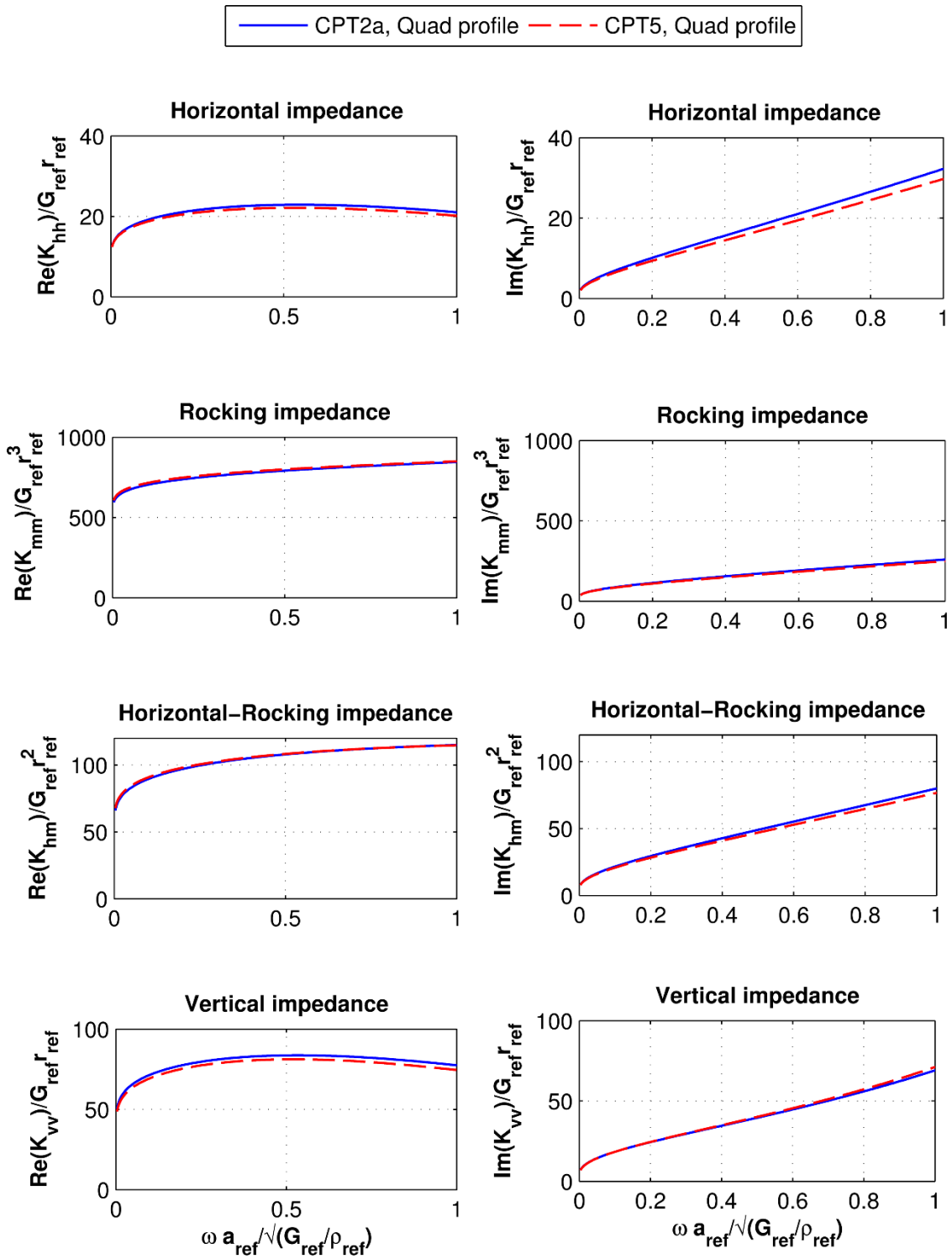


Figure 2-58- Comparison of pile-soil impedances from piecewise quadratic fits of CPT 2a and CPT 5 data in Figures 10 and 11.

2.9.2 Modulus and Damping Profile from Formulas of Hardin & Drnevich

The correlations between CPT resistance and shear-wave velocity used in the previous section are based upon data from a limited range of clean sands (Figure 2-59) and a log-log plot exhibiting measurable scatter for clays and silts (Figure 2-60). These velocity correlations, from which shear modulus is calculated, can therefore incur significant error when applied to the sandy gravels and soft clays existing at the test site. In addition, there is no known method to estimate the material damping profile from CPT data. Although the laboratory testing program of the NEESR-SG project included a few cyclic triaxial tests, the results were not available at the time of writing. Beyond the cyclic triaxial tests, no other dynamic in situ or laboratory tests were performed to measure the modulus and damping properties of the soils used in this study.

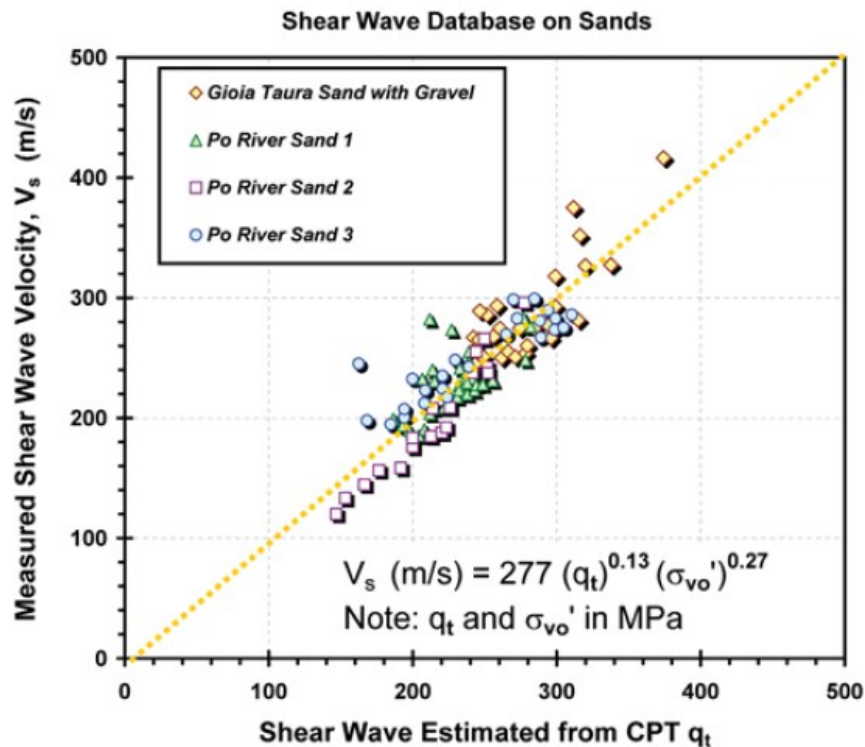


Figure 2-59- CPT data on sand used for shear wave velocity correlation. The figure is borrowed from Figure 28 in (TRB, 2007).

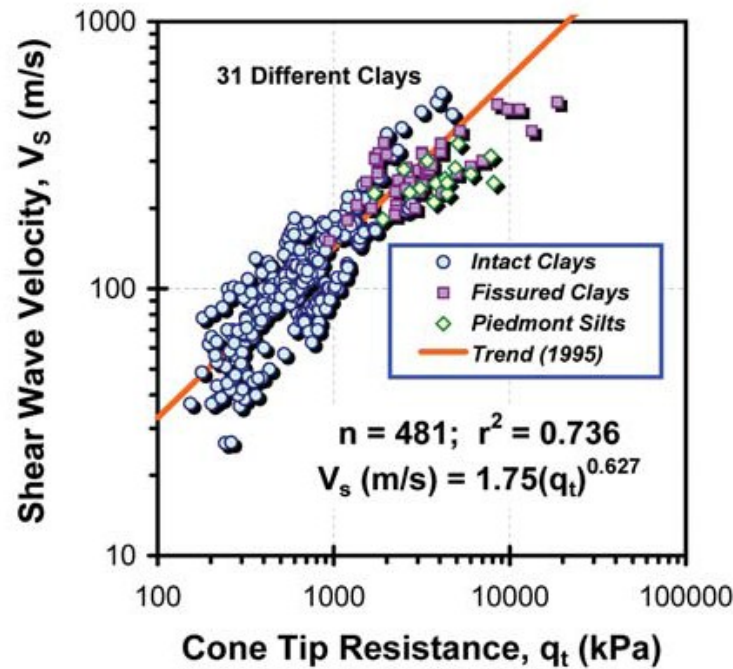


Figure 2-60- CPT data on clay used for shear wave velocity correlation. The figure is borrowed from Figure 28 in (TRB, 2007).

It is therefore useful to estimate the soil modulus and damping profiles using the widely accepted design equations developed in (Hardin & Drnevich, 1972) from extensive laboratory resonant column and low-frequency cyclic torsional shear tests on intact and reconstituted clay and sand specimens covering a wide range of confining stresses, strain levels, void ratios, and number of loading cycles.

In their study, Hardin and Drnevich showed that shear modulus and damping in soils vary significantly with strain amplitude. The shear modulus and damping ratio as nonlinear functions of shear strain were shown to be controlled primarily by the soil's effective mean principal stress and void ratio, and to a lesser extent by the soil type, degree of saturation, stress history, plasticity index, and the frequency and number of cycles of loading. Using their

framework which incorporates the concepts of a hyperbolic backbone curve for the cyclic stress-strain relation, a reference shear strain, a hyperbolic strain, and equations for modulus and damping with laboratory determined soil parameters, one may calculate the modulus and damping profiles with respect to depth. The governing equations for damping ratio (D) and shear modulus (G) are as follows:

$$\frac{G}{G_{\max}} = \frac{1}{1 + \gamma_h} \quad (2.18)$$

$$\frac{D}{D_{\max}} = \frac{\gamma_h}{1 + \gamma_h} \quad (2.19)$$

where

$$G_{\max} = 1230 \text{ psi} \frac{(2.973 - e)^2}{(1 + e)} (OCR)^K \bar{\sigma}_0^{1/2} \quad (2.20)$$

$$\tau_{\max} = \left\{ \left[\frac{(1 + K_0)}{2} \bar{\sigma}_v \sin \bar{\phi} + \bar{c} \cos \bar{\phi} \right]^2 - \left[\frac{(1 - K_0)}{2} \bar{\sigma}_v \right]^2 \right\}^{1/2} \quad (2.21)$$

$$\gamma_h = \frac{\gamma}{\gamma_r} \left\{ 1 + a \exp \left[-b \left(\frac{\gamma}{\gamma_r} \right) \right] \right\} \quad (2.22)$$

$$\gamma_r = \frac{\tau_{\max}}{G_{\max}} \quad (2.23)$$

whereby the constant K is a function of plasticity index and can be interpolated from Table 1 (Hardin & Drnevich, 1972). The maximum damping ratio D_{\max} depends on soil type, number of cycles, and loading frequency, and can be calculated from Table 3 in (Hardin & Drnevich, 1972) (Figure 2-61). In the above, G_{\max} is the small-strain shear modulus which governs elasto-dynamic wave propagation and is accompanied by the minimum damping ratio. As shear strain increases, the shear modulus decreases and the damping increases towards D_{\max} . Table 2 of the same reference (Figure 2-61) provides the values for parameters a and b

in the hyperbolic strain relation. The symbols $\bar{\sigma}_0$ and $\bar{\sigma}_v$ are the mean principal effective stress and vertical effective stress, respectively, and τ_{\max} is the shear stress at failure, all in units of psi. Soil void ratio is denoted by e and K_0 is coefficient of lateral earth pressure at rest. Finally, γ_r is the reference shear strain, and OCR , \bar{c} and $\bar{\phi}$ are the soil's overconsolidation ratio, cohesion, and friction angle, respectively.

TABLE 2.—VALUES OF a AND b^a

Soil type (1)	Modulus or damping (2)	Value of a (3)	Value of b (4)
Clean dry sands	Modulus	$a = -0.5$	$b = 0.16$
	Damping ^b	$a = 0.6(N^{-1/6}) - 1$	$b = 1 - N^{-1/12}$
Clean saturated sands	Modulus ^b	$a = -0.2 \log N$	$b = 0.16$
	Damping ^b	$a = 0.54(N^{-1/6}) - 0.9$	$b = 0.65 - 0.65N^{-1/12}$
Saturated cohesive soils	Modulus	$a = 1 + 0.25 (\log N)$	$b = 1.3$
	Damping	$a = 1 + 0.2(f^{1/2})$	$b = 0.2f \left(e_{xp}^{\frac{-\bar{\sigma}_0}{p_0}} \right) + 2.25\bar{\sigma}_0 + 0.3 (\log N)$

^a f is in cycles per second and $\bar{\sigma}_0$ is in kilograms per square centimeter.

^b These values for modulus and damping of clean sands are for less than 50,000 cycles of loading. Beyond 50,000 cycles the damping begins to increase with number of cycles, possibly due to fatigue effects (2). The behavior of modulus for saturated sands beyond 50,000 cycles is not yet established.

TABLE 3.—VALUES OF D_{\max}^a

Soil type (1)	Value of D_{\max} as a percentage (2)
Clean dry sands	$D_{\max} = 33 - 1.5 (\log N)$
Clean saturated sands	$D_{\max} = 28 - 1.5 (\log N)$
Saturated Lick Creek silt	$D_{\max} = 26 - 4\bar{\sigma}_0^{1/2} + 0.7f^{1/2} - 1.5 (\log N)$
Various saturated cohesive soils including Rhodes Creek Clay	$D_{\max} = 31 - (3 + 0.03f)\bar{\sigma}_0^{1/2} + 1.5f^{1/2} - 1.5 (\log N)$

^a f is in cycles per second and $\bar{\sigma}_0$ is in kilograms per square centimeter.

Figure 2-61- Table 2 and Table 3 from (Hardin & Drnevich, 1972)

For the problem under study, some of the above parameters can be obtained from the soil report (Amirata Taghavi, 2010) and rational assumptions can be made for the remainder. These assumptions are discussed in detail in the following sections, and parametric studies are performed to assess their relative influence on the overall pile-soil system response.

2.9.2.1 Strain range

The vibration tests are conducted using low-amplitude excitation which keeps most of the soil in the quasi-linear small-strain region. From Table 1 in reference (Diaz-Rodriguez & Lopez-Molina, 2008), a shear strain value of 0.001% would be a reasonable value for such problems. This value will be verified later using calculated pile displacements from the soil-pile interaction analysis.

2.9.2.2 Number of cycles

Exact cycle counts for each test are difficult to define due to the use of random and swept-sine forcing excitation waveforms, which contain a wide range of simultaneous or swept frequencies, respectively. However, cycle counts can be estimated from the time domain acceleration data. As a first approximation, every two zero crossings in the acceleration records beyond $t = 0$ could be counted as one cycle, with the caveat that this result could be biased to either higher or lower frequencies, depending on their relative amplitudes. For example, if a large amplitude low-frequency sinusoid is superimposed with a small amplitude high-frequency sinusoid, the number of zero crossings will be biased towards the low frequency component. Conversely, if a large high-frequency sinusoid is superimposed with a small low-

frequency sinusoid, a greater number of zero crossings will result, and the cycle count will be biased towards the high frequency component. In the latter case, however, the higher apparent cycle count may be misleading because the associated high-frequency displacements and strains will generally be smaller than the low-frequency ones and will therefore have a less-significant effect on the soil. A more time-consuming alternative would be to integrate the acceleration records to obtain displacement time-histories, and only count displacement or strain cycles exceeding a minimum threshold. As an example, performing the simpler approach of counting all zero crossings gives the following values for some of unimproved soil tests:

Table 2-3- Number of cycles per test for VC and HC tests of pile in unimproved soil with random and swept-sine excitation types.

Test ID	Number of Cycles
U-VC-R3	1125
U-HC-R3	1022
U-VC-S3	973
U-HC-S3	1063

Similar values result for the improved tests. Due to the high-frequency and low-amplitude excitations used, these values give conservative upper-bounds on the number of cycles. As Table 2-3 suggests, $N=1000$ is a reasonable value to be used in the calculations. However, since the tests are performed in succession, the cumulative effect should also be considered. This can be checked by a parametric study on N , which is discussed further in the following.

2.9.2.3 Plasticity index (PI)

The soil report provides the plasticity index for ODOT borehole soil samples. The average PI value for the top layer is 14 and for the rest of the cohesive soils it is 12, from which Table 1 in (Hardin & Drnevich, 1972) gives $K=0.126$ and 0.108 , respectively.

2.9.2.4 Void ratio (e)

Unfortunately, the void ratio is not provided in the soil report. However, empirical tables such as Table 2-4 can provide reasonable estimates of void ratio based on soil type. Based on the soil types identified in the site investigation phase, $e=0.65$ was assumed for the sandy gravel layer overlying the bedrock and $e=1.0$ was assumed for the remaining layers.

Table 2-4- Void ratio for different soil types (from Das, 2012).

Soil	Void ratio e
Poorly graded sand with loose density	0.8
Well graded dense sand	0.45
Loose density sand with angular particles	0.65
Dense density sand with angular particles	0.4
Stiff clay	0.6
Soft clay	0.9-1.4
Loess	0.9
Soft organic clay	2.5-3.2
Glacial till	0.3

2.9.2.5 Stress history (OCR)

The preconsolidation stress was not evaluated in the soil report and was therefore interpolated from the CPT data. Equations 19 for clays and 24 for sands from reference ((TRB), 2007) were used for the clay and sandy gravel layers, respectively, giving the OCR values shown in Figure 2-62. Considering the low values of K reported above, these OCR values will have a relatively minor effect on Equation (3) compared to the mean principal stress.

2.9.2.6 Effective strength parameters

Friction angle for sand and cohesion for clay are calculated from the CPT data and the correlations presented in reference ((TRB), 2007). Applying this approach to the sandy gravel layer gives $\phi' = 45^\circ$, which is reasonable for gravel with sand (e.g., Das 2010, Table 12.1), while for the top layer c_u is calculated at 70 kPa and for the other cohesive soil layers c_u is calculated to be 40 kPa. A different correlation is used for the friction angle of cohesive soil, as presented in Figure 2-63. One can read $\phi' = 33^\circ$ from the curve for the PI range of the soft clay and silty clay layers. The coefficient of lateral earth pressure at rest (K_0) was calculated from Mayne and Kulhawy's (Mayne, 1982) correlation $K_0 = (1 - \sin \phi') \times OCR^{\sin \phi'}$.

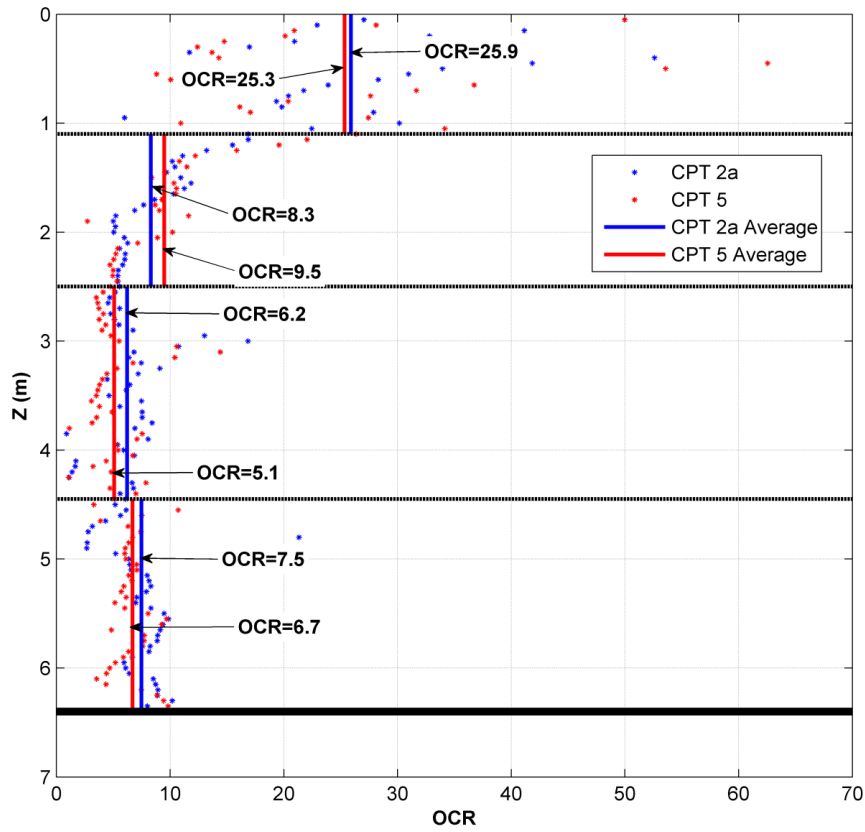


Figure 2-62- OCR profile from CPT data analysis.

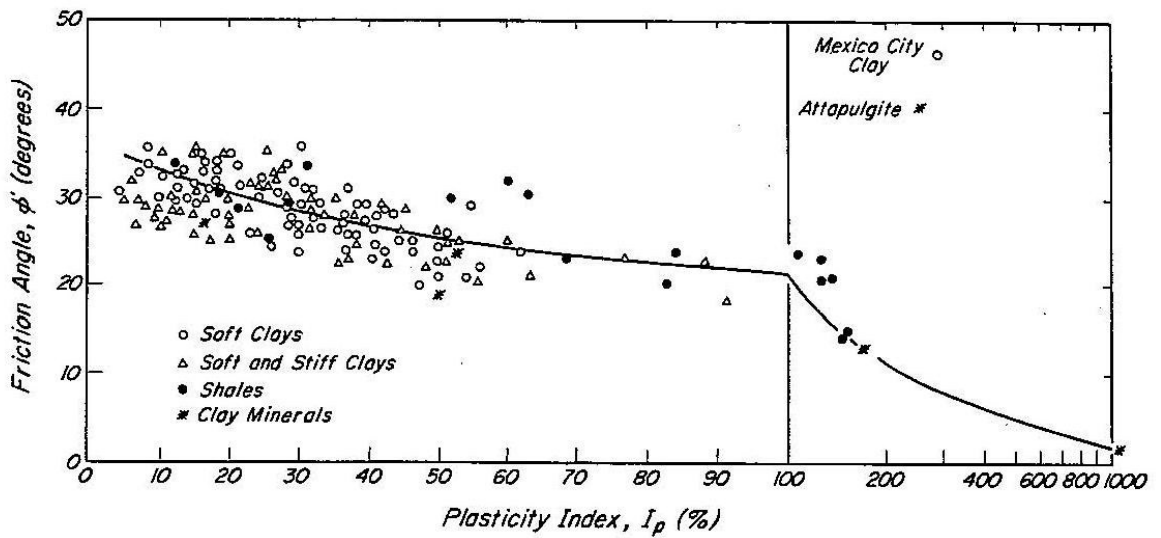


Figure 2-63- Correlation between effective friction angles and plasticity index (Figure 19.7 from Terzaghi, 1996).

2.9.2.7 Summary of soil parameters

The soil parameters needed for elasto-dynamic soil-pile interaction analysis using the modulus and damping relations of Hardin and Drnevich (Hardin & Drnevich, 1972) are summarized in Table 2-5. These values are used in the following sections to construct the profiles of soil shear modulus and damping ratio and also to perform sensitivity analyses on the parameters.

Table 2-5- Summary of parameters for modulus and damping profiles using formulas from (Hardin & Drnevich, 1972).

Soil Layer	Parameters involved
Layer 1 (fill: lean clay with gravel)	$\phi' = 33^\circ$, $\sigma'_{vc} = 14$, $OCR = 25.5$, $e = 1.0$, $\rho_s = 1885 \text{ kg/m}^3$ $c = 70 \text{ kPa}$, $N = 1000$, $f = 75 \text{ HZ}$, $\gamma = 0.001\%$
Layer 2 (soft silty clay to clayey silt)	$\phi' = 33^\circ$, $\sigma'_{vc} = 12$, $OCR = 9$, $e = 1.0$, $\rho_s = 1885 \text{ kg/m}^3$ $c = 40 \text{ kPa}$, $N = 1000$, $f = 75 \text{ HZ}$, $\gamma = 0.001\%$
Layer 3 (soft silty clay to clayey silt)	$\phi' = 33^\circ$, $\sigma'_{vc} = 12$, $OCR = 5.5$, $e = 1.0$, $\rho_s = 1885 \text{ kg/m}^3$ $c = 40 \text{ kPa}$, $N = 1000$, $f = 75 \text{ HZ}$, $\gamma = 0.001\%$
Layer 4 (sandy gravel)	$\phi' = 45^\circ$, $\sigma'_{vc} = 12$, $OCR = 7$, $e = 0.65$, $\rho_s = 2053 \text{ kg/m}^3$ $c = 0 \text{ kPa}$, $N = 1000$, $f = 75 \text{ HZ}$, $\gamma = 0.001\%$

2.9.2.8 Sensitivity analyses

In the relations of Hardin and Drnevich, the most significant parameter affecting modulus and damping at a point is the amplitude of shear strain (γ). The next most significant parameters are the maximum values D_{\max} and G_{\max} , with the latter governing wave propagation in small-strain elasto-dynamic problems. The small-strain shear modulus G_{\max} is most sensitive to the mean principal stress. To assess the relative sensitivity of G_{\max} , D_{\max} , and τ_{\max} to parametric variations of the other problem parameters over reasonable ranges, several analyses were conducted. For the analyses, the modulus, damping, and shear stress at failure were calculated at the middle of each layer using the default values reported in Table 2-5. From the results, shown in Figure 2-64 to 2-71, it can be concluded that void ratio and OCR have the greatest influence (next to shear strain and mean principal stress), while the effect of N is negligible after the first few cycles.

Figure 2-72 depicts the shear modulus and damping ratio profiles using the formulas of Hardin and Drnevich with the default values given in Table 2-5, overlaid with its piecewise constant discretized version using 55 layers to bedrock. The shear modulus profile later is also compared to the CPT profiles in Figure 2-73, from which it can be seen that the average CPT profile values are approximately 50% lower than those of the Hardin and Drnevich relations.

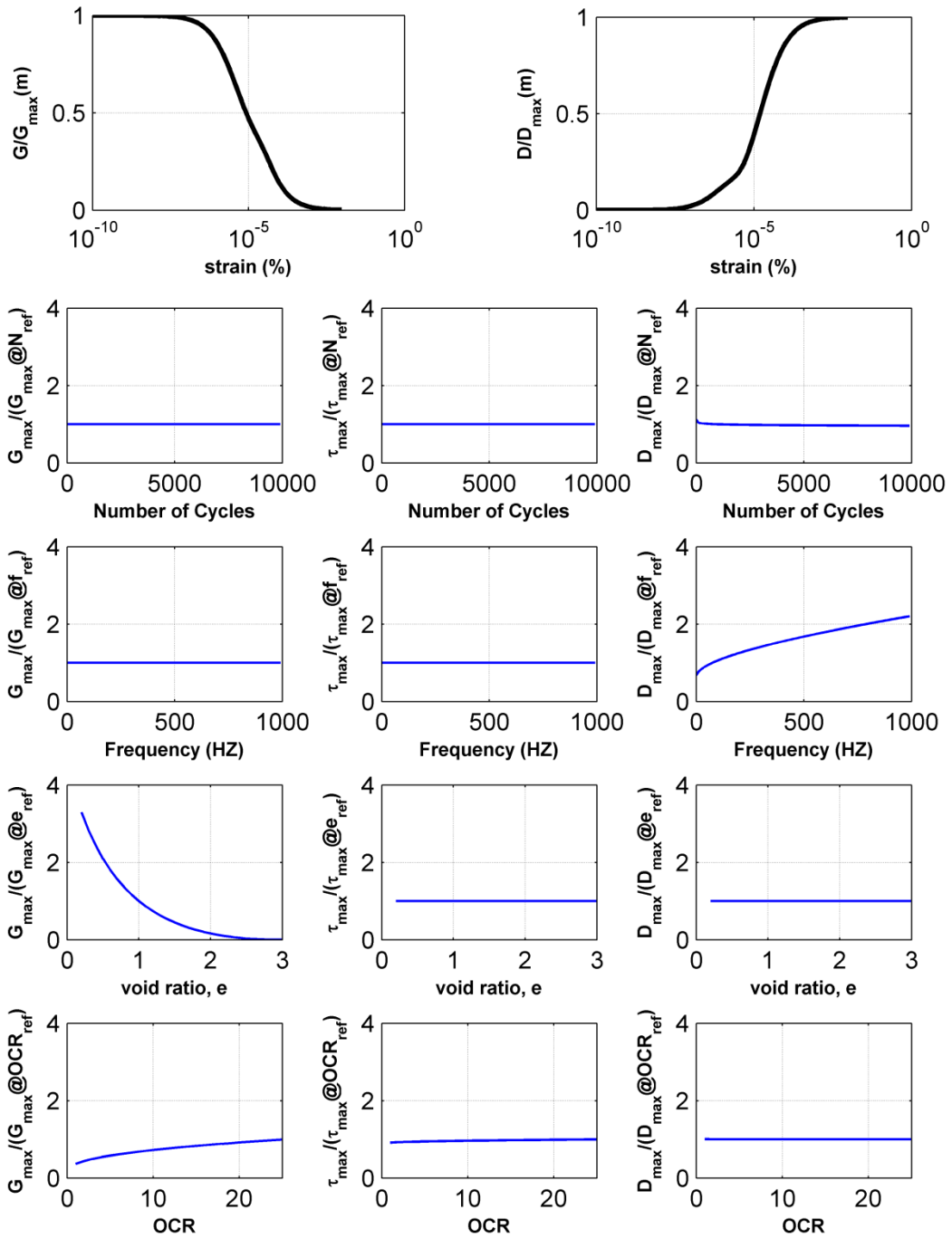


Figure 2-64- Parametric sensitivity analysis of shear modulus, ultimate shear strength, and damping ratio from Hardin and Drnevich formula (Hardin & Drnevich, 1972) at the middle of layer 1 (depth $z=0.55$ m).

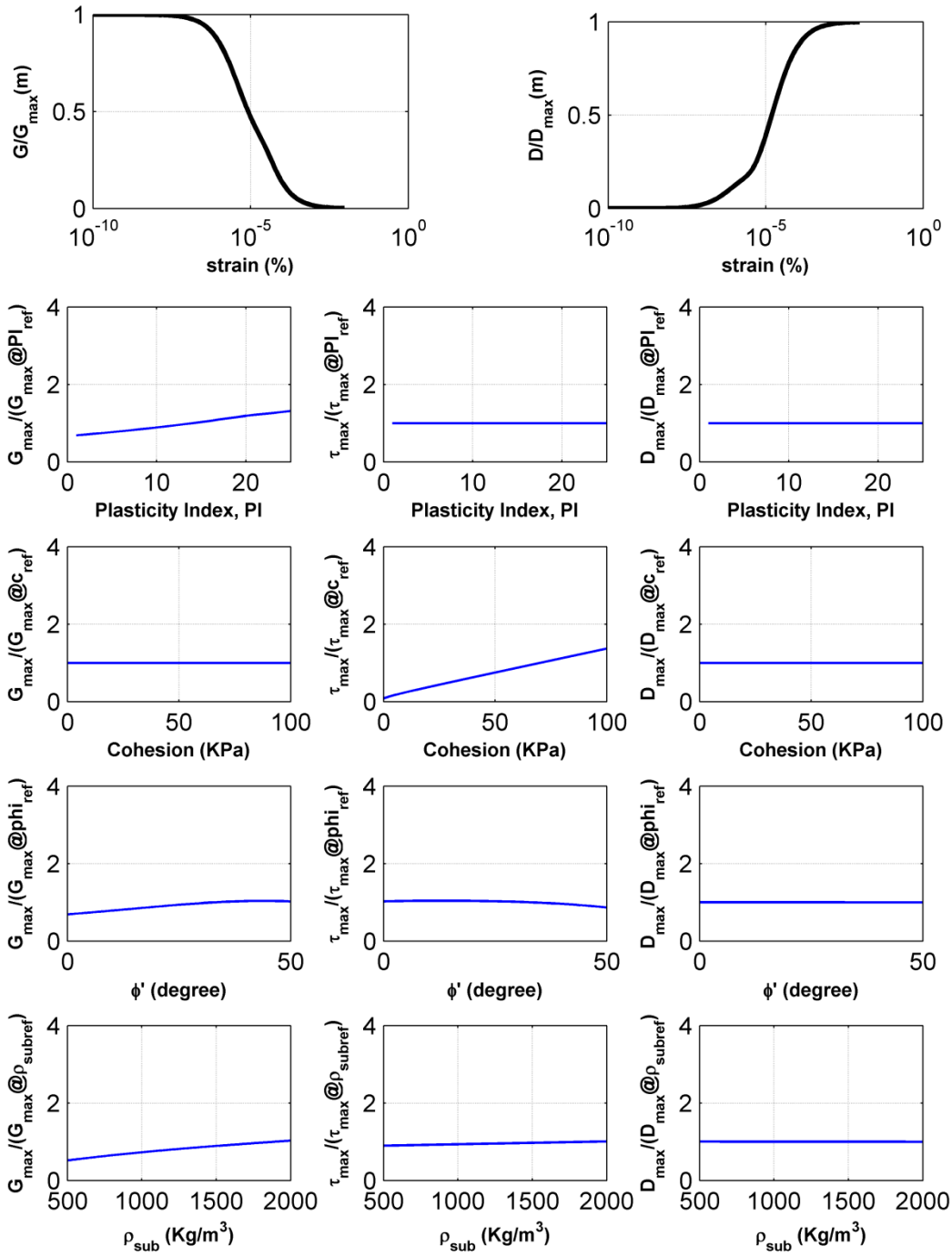


Figure 2-65- Shear modulus and damping ratio from Hardin and Drnevich formula (Hardin & Drnevich, 1972) at the middle of layer 1 ($z=0.55$ m) and the effect of changing the involved parameters on the results.

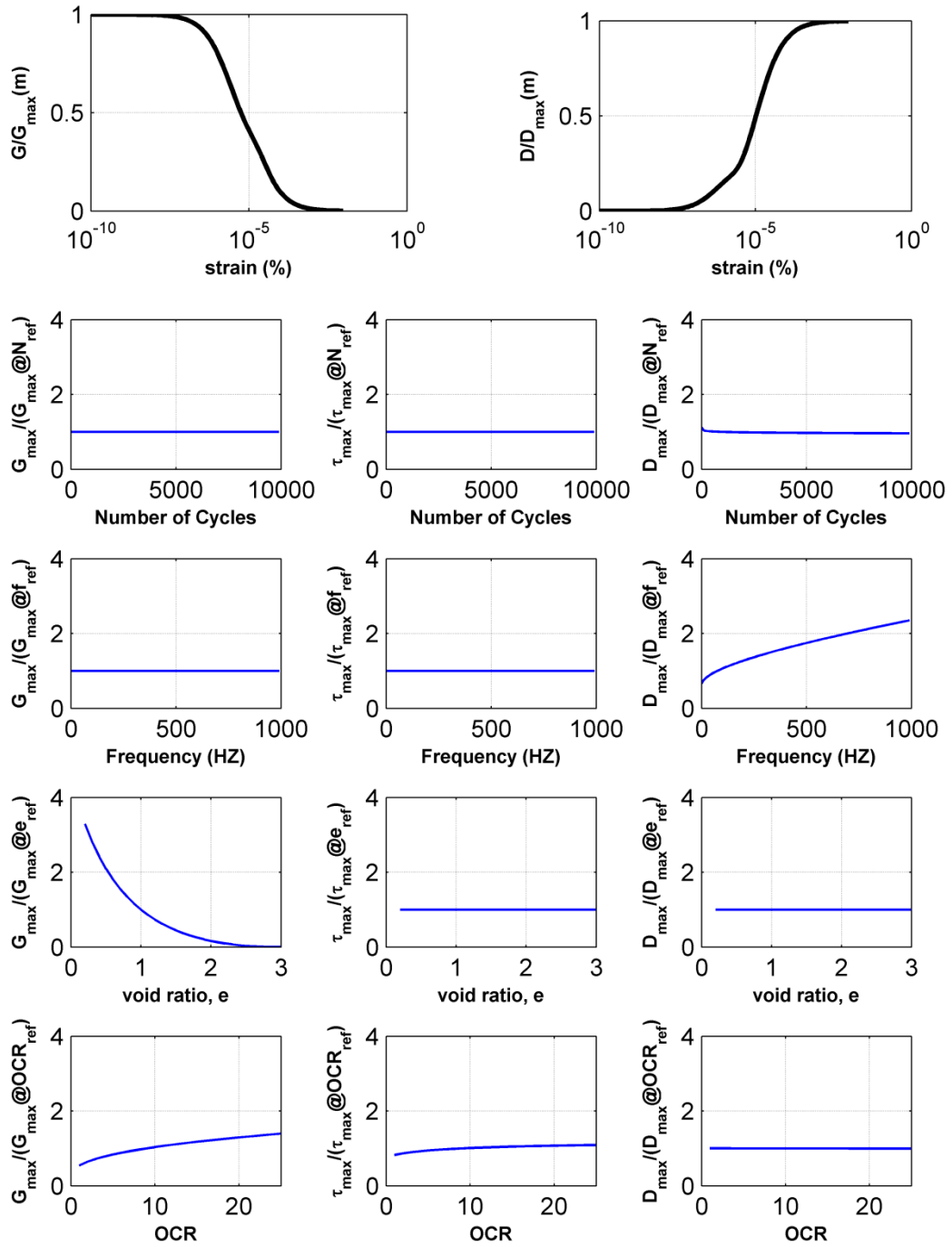


Figure 2-66- Shear modulus and damping ratio from Hardin and Drnevich formula (Hardin & Drnevich, 1972) at the middle of layer 2 (z=1.80 m) and the effect of changing the involved parameters on the results.

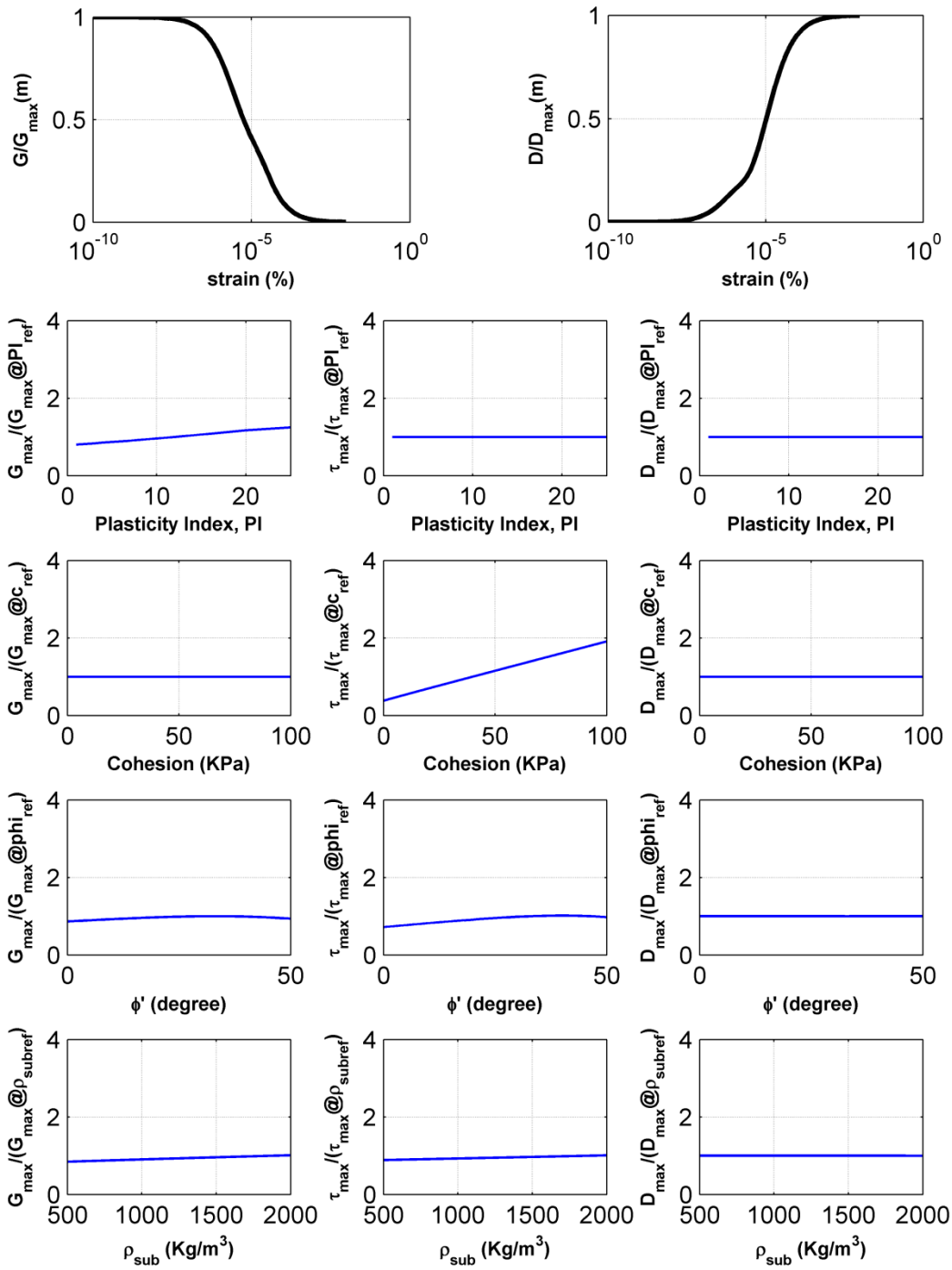


Figure 2-67- Shear modulus and damping ratio from Hardin and Drnevich formula (Hardin & Drnevich, 1972) at the middle of layer 2 (z=1.80 m) and the effect of changing the involved parameters on the results.

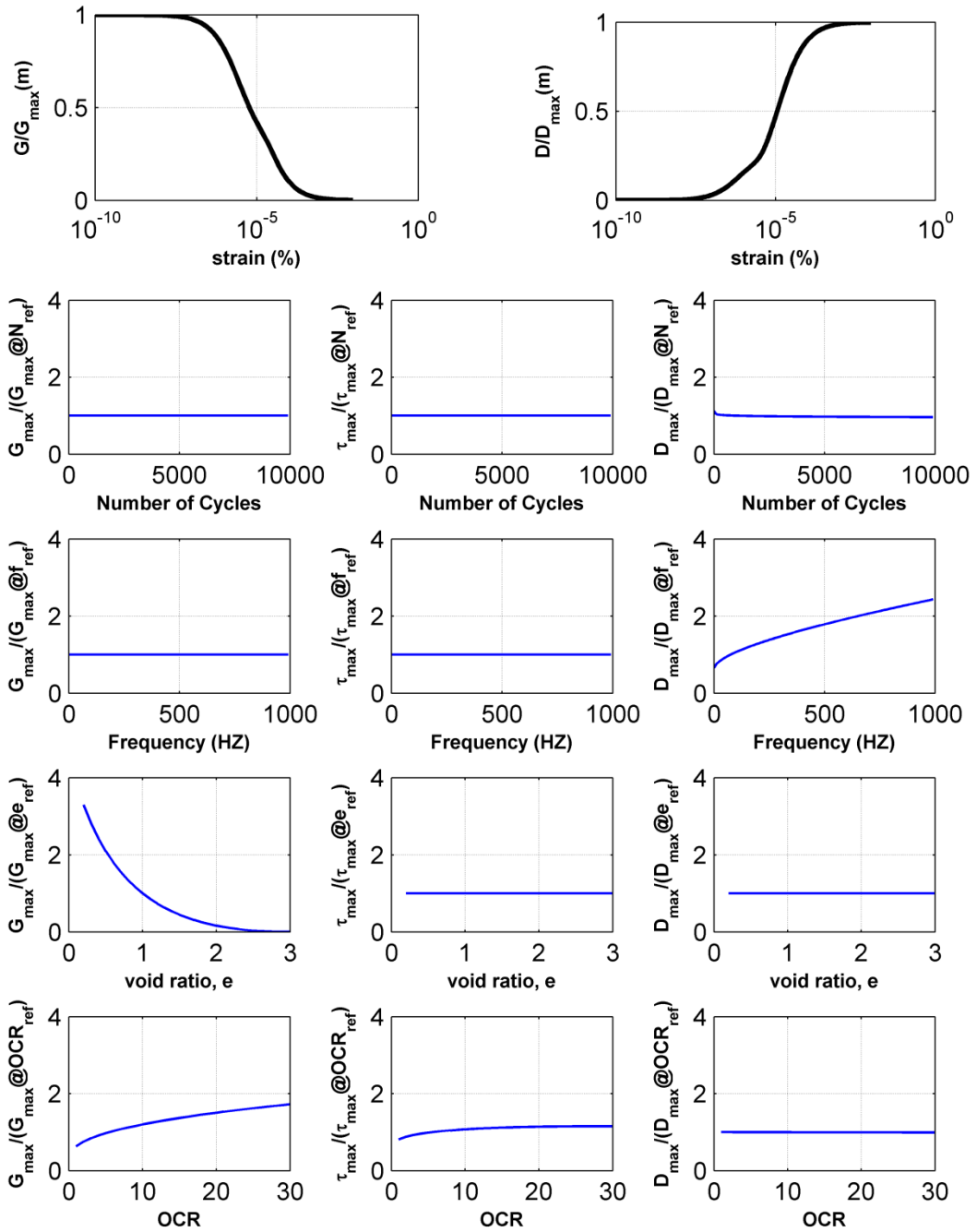


Figure 2-68- Shear modulus and damping ratio from Hardin and Drnevich formula (Hardin & Drnevich, 1972) at the middle of layer 3 ($z=3.475$ m) and the effect of changing the involved parameters on the results.

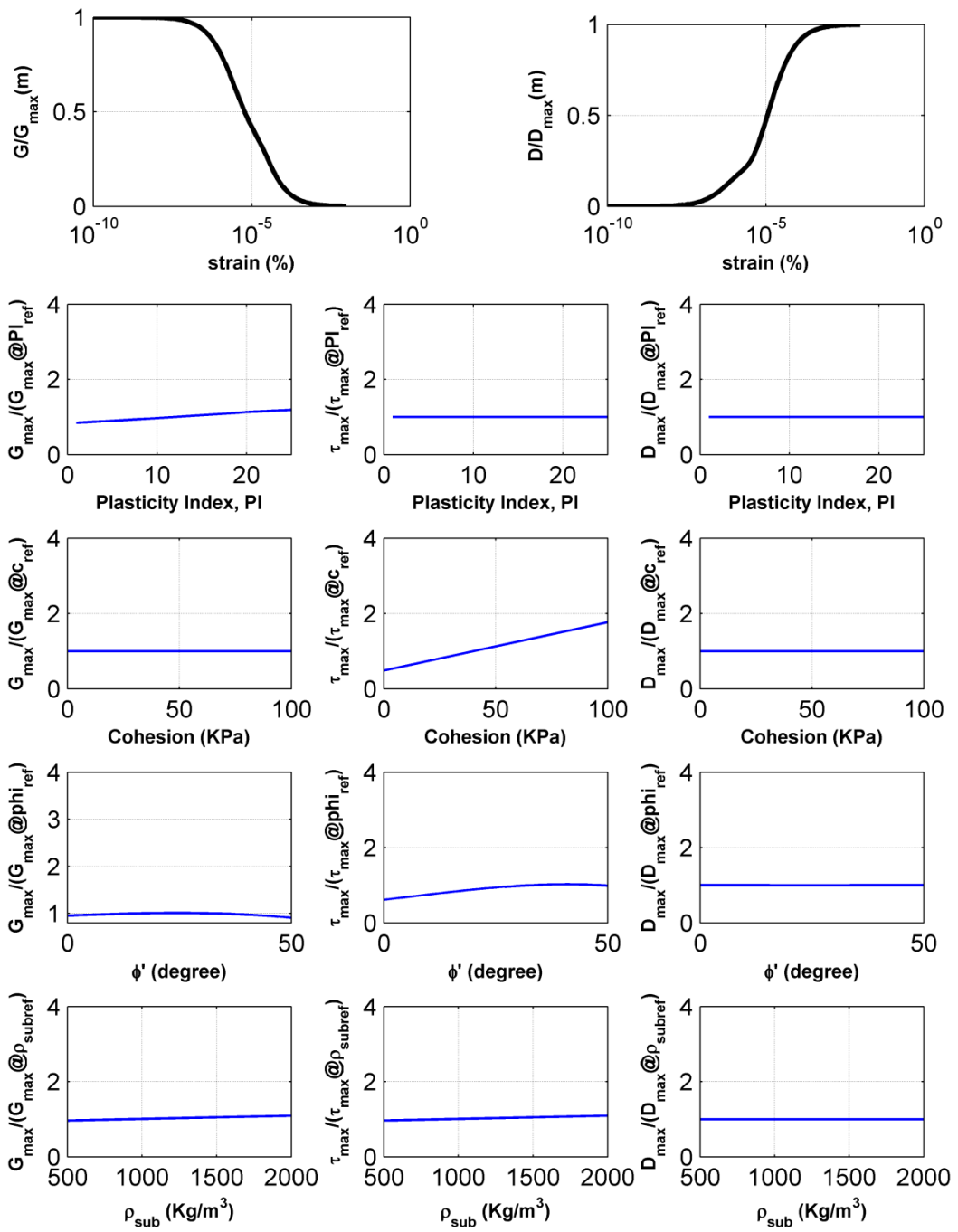


Figure 2-69- Shear modulus and damping ratio from Hardin and Drnevich formula (Hardin & Drnevich, 1972) at the middle of layer 3 ($h=3.475$ m) and the effect of changing the involved parameters on the results.

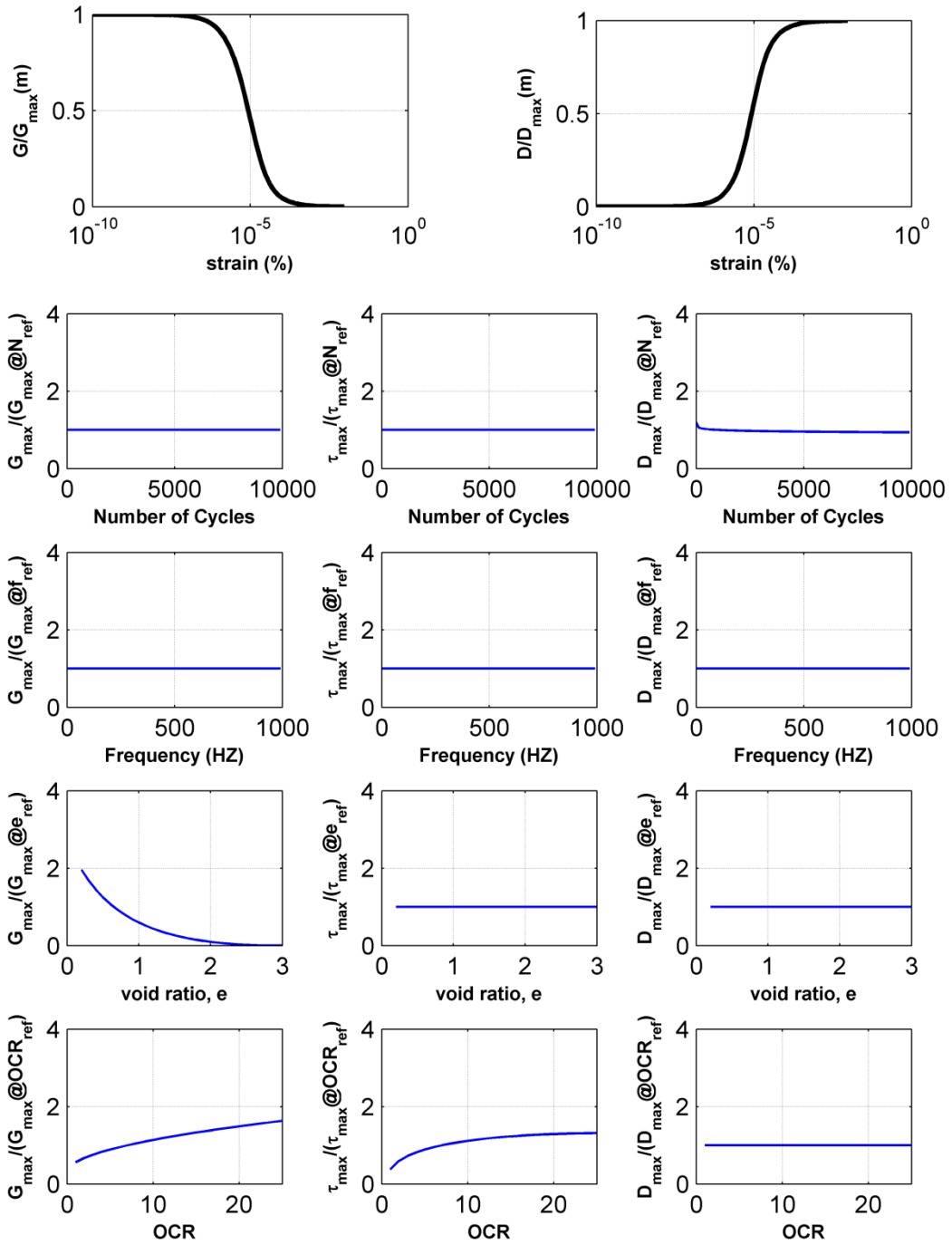


Figure 2-70- Shear modulus and damping ratio from Hardin and Drnevich formula (Hardin & Drnevich, 1972) at the middle of layer 4 ($z=5.425$ m) and the effect of changing the involved parameters on the results.

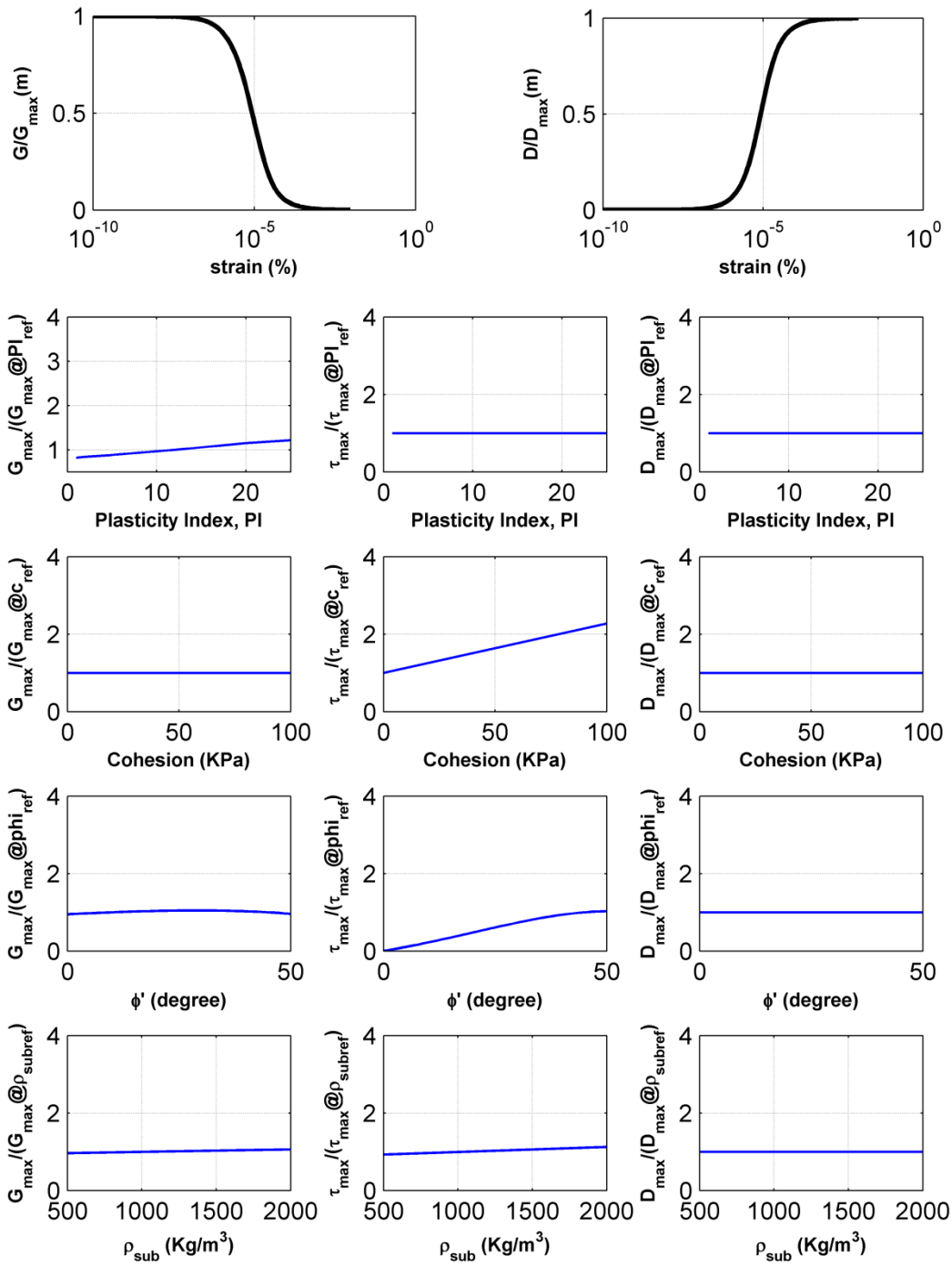


Figure 2-71- Shear modulus and damping ratio from Hardin and Drnevich formula (Hardin & Drnevich, 1972) at the middle of layer 4 ($z=5.425$ m) and the effect of changing the involved parameters on the results.

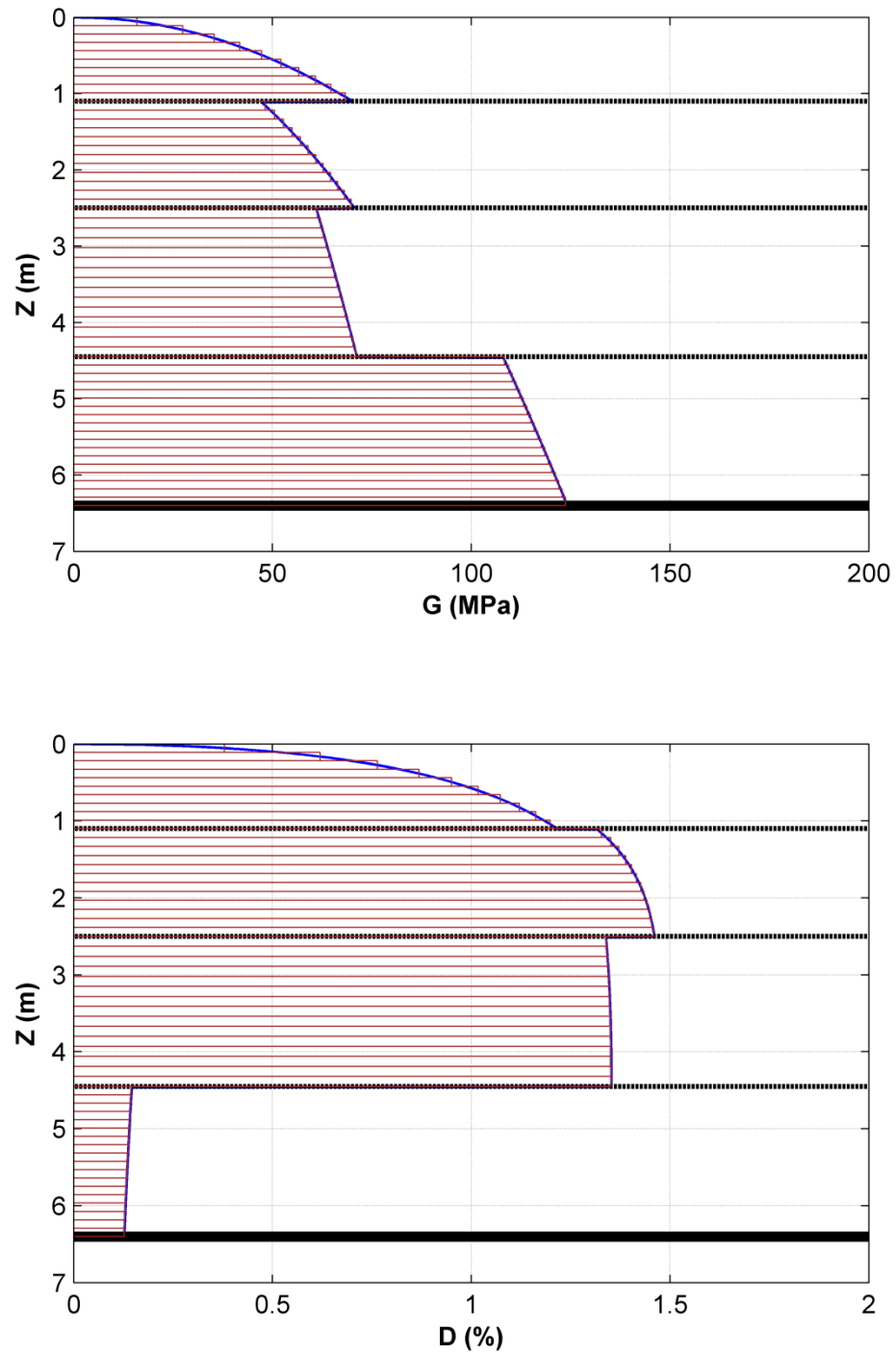


Figure 2-72- Shear modulus and damping ratio profile from Hardin and Drnevich method using the values reported in Table 2-5.

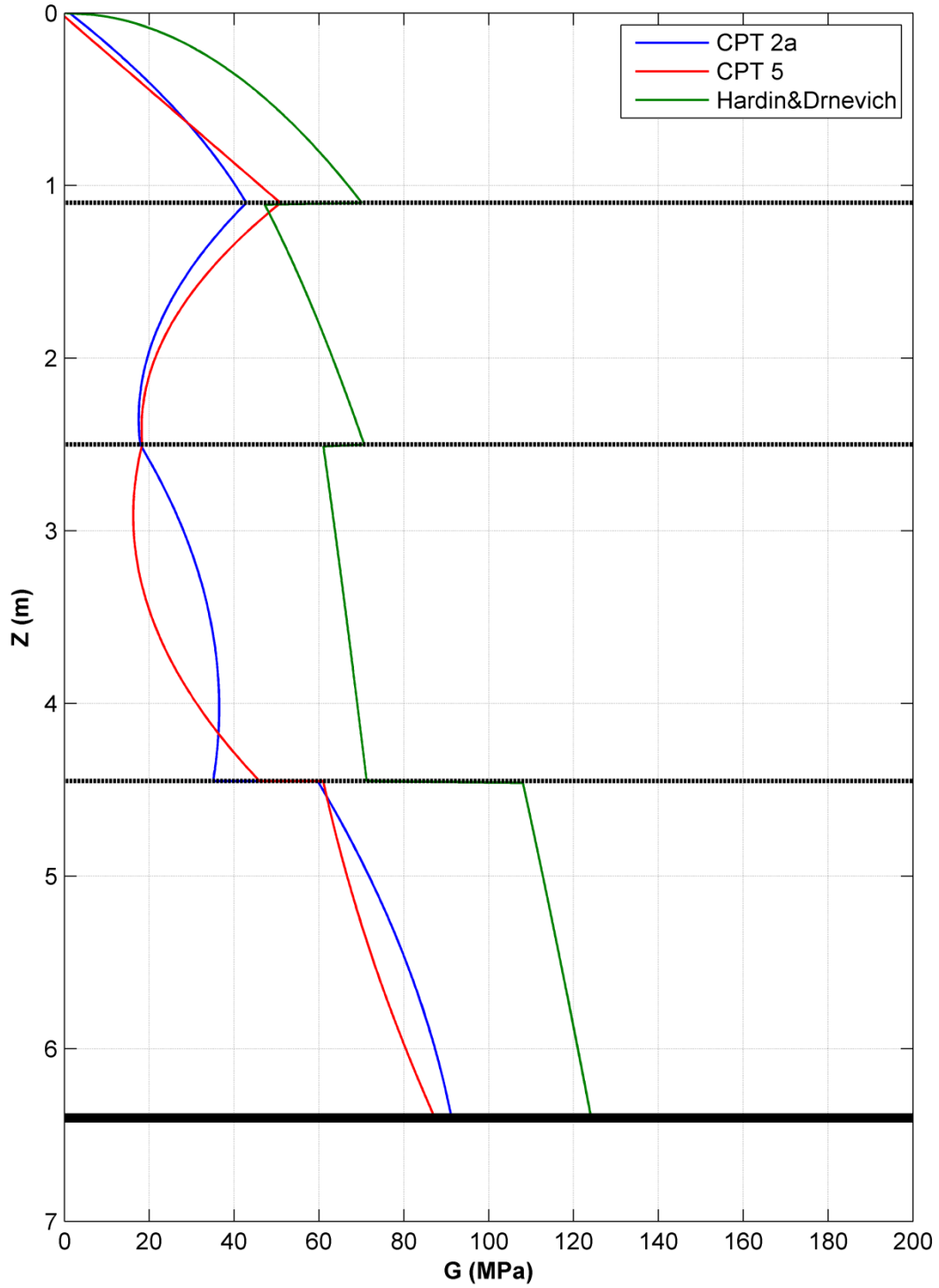


Figure 2-73- The three shear modulus profiles discussed throughout this section.

CHAPTER III: THEORETICAL MODELING AND VERIFICATION

3.1 Overview

Over the years, many different approaches have been used to solve soil-pile interaction problems, ranging from simple approximate solutions to rigorous boundary-integral equation approaches, or numerical finite-element, boundary-element, or finite-difference methods. For quasi-elastic vibration response, a sub-structuring method is commonly employed due to its speed, flexibility, and efficiency. In this method, the system is divided into separate components, allowing different analytical or numerical solution methods to be chosen for each substructure. Approximate methods typically cannot fully capture all the aspects of the problem, such as the influence of inhomogeneous or layered soil profiles, the propagation and scattering of body and surface waves, or the coupled response of the foundation-soil system. However, such methods can be useful for estimating the sensitivity and range of results, and also as initial models preceding more detailed analyses. For more rigorous analyses, crucial aspects of the problem that exhibit a significant influence must be considered, including three-dimensional wave propagation, soil stratification, and modulus and damping profiles.

In pile-vibration problems, especially those involving high frequencies, there are several numerical issues that one must contend with. Kuhlemeyer (Kuhlemeyer & Lysmer, 1973) showed for finite-element models of wave propagation in soils, that the element size should be less than one-tenth of the minimum wave length. For example, an element size smaller than 10 cm by 10 cm would be required to capture a shear wave propagating with a phase velocity of 150 m/s at a frequency of 150 Hz. For such high-frequency problems, this approach could result in a prohibitively large number of elements for discretization of an entire soil-foundation system.

Additionally, many finite-element procedures for the solution of dynamic soil-pile interaction problems must address the problem of reflection of dynamic waves at artificial boundaries. Despite many improvements in transmitting-boundary (Givoli, 2004), (Guddati & Lim, 2006) and infinite-element (Astley, 2000) techniques for FEM analyses of general soil-foundation problems, these techniques do not completely eliminate the problem of reflected seismic waves from the boundaries of the soil domain. On the other hand, global procedures such as the boundary-element method that involve integral equations rather than differential equations can exactly satisfy the radiation condition and thus be free from wave reflection at the boundaries. Additionally, boundary-element methods are generally more rigorous and accurate for linear problems. For realistic treatment of soil stratigraphy by boundary-element methods, fundamental solutions for a viscoelastic multi-layered half-space that satisfy the radiation condition at the infinite boundary (Pak & Guzina, 2002) are available. However, these Green's functions include singular integrals that, even if analytically regularized, can still lead to nearly-singular integrals that can result in solution error if not further transformed and accurately integrated (Ashlock, 2006).

Because pile foundations are used routinely in engineering practice, time-consuming computational methods are not always justified. Thus much research effort in the past has focused on approximate or simplified methods which can capture the essence of a problem, but may be limited to specific conditions. For dynamic soil-foundation problems, such widely-used methods include the work of Blaney et al. (Blaney G. W., 1976), Gazetas (Gazetas, 1991), Novak and Aboul-Ella (Novak & Aboul-Ella, 1978), Novak (Novak, 1974), Dobry and Gazetas (Dobry & Gazetas, 1988), Nogami and Novak (Novak & Nogami, 1977), (Nogami & Novák, 1976), and Kaynia and Kausel (Kaynia & Kausel, 1991). To understand the limitations and capabilities of

these solutions and provide direction for needed improvements, it is essential that they be verified by experiment and/or more rigorous solutions.

In this chapter, the dynamic response will be analyzed by taking into account the dynamic pile-soil interaction and wave propagation within the soil, as well as the dynamics of the shaker, pile-cap, and elastic un-embedded pile segment. This will help to better understand the complex behavior of the soil-pile system, and generate a framework for predicting the response of similar systems. The method of sub-structuring will be used to formulate the theoretical transfer functions of the pile-cap-shaker system. The sub-structure above the soil surface is decomposed into a rigid-body pile-cap and a deformable beam-column pile stem (Figure 3-1), with compatibility conditions enforced at their interface.

The general matrix equations of motion for the entire system in HC and VE test set-ups will first be formulated; it should be noted that VC test can be considered as a special case of a VE test where the eccentricity of forcing is zero. As indicated in Figure 3-1, the complex soil impedances at the ground level are calculated using either the aforementioned approximate or rigorous methods. Throughout this chapter, some commonly used approximate approaches will be discussed and verified for standard problems. A brief description of the BEM program along with program verification analyses are also included. Finally, a parametric study is performed to evaluate the sensitivity of the results to the parameters of the different substructures.

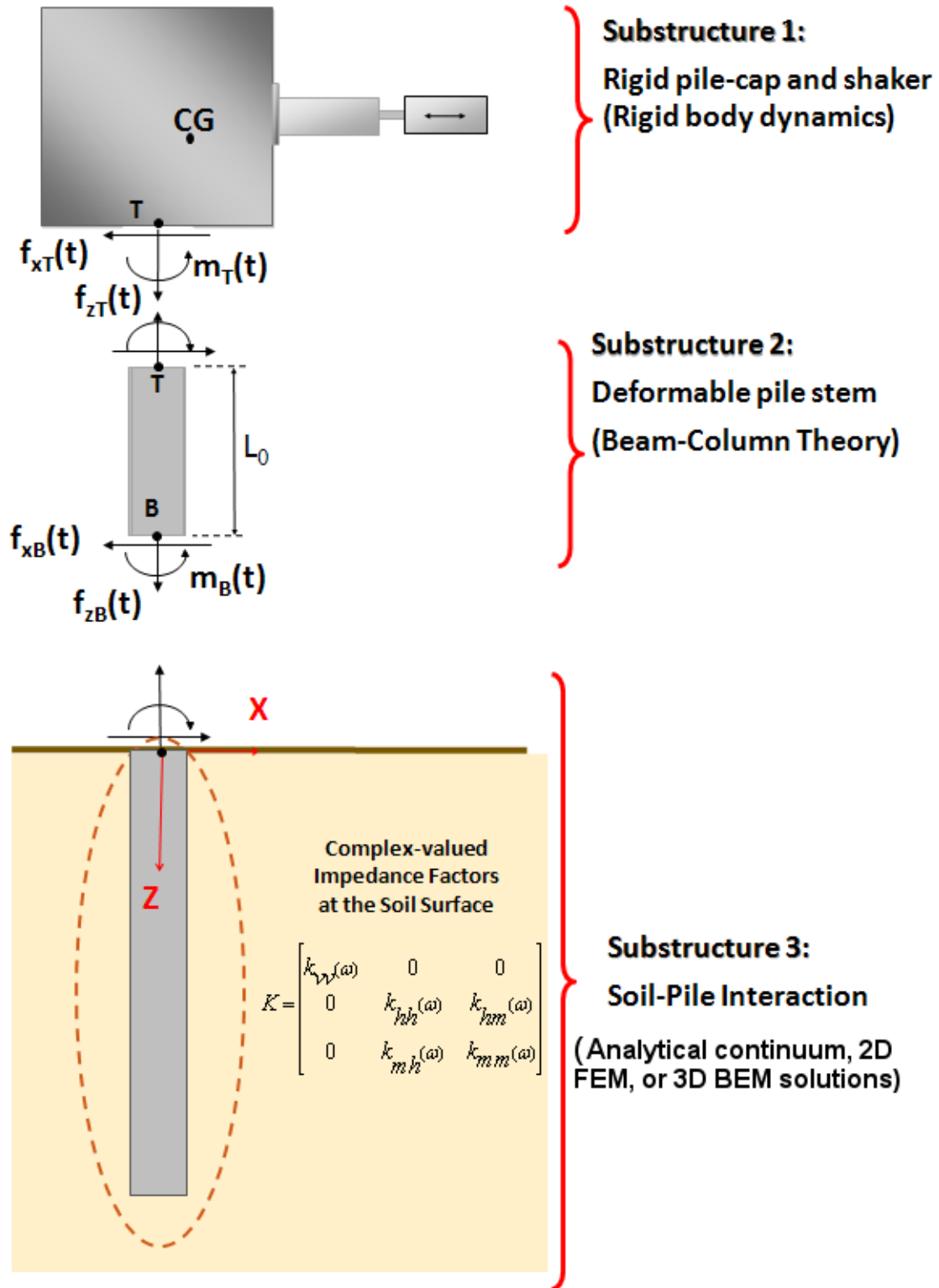


Figure 3-1. Substructures and interfacial stress resultants used in transfer function formulation.

3.2 Theoretical Accelerance Formulation

The free-body diagrams of the substructures described in Figure 3-1 are shown in Figure 3-2 and 3-3 for HC and VE test configurations, respectively. The formulations presented in Sections 3.2.1 and 3.2.2 below will result in a matrix system of equations in the frequency-domain, which provide the centroidal accelerance of the system under HC, VE, and VC forcing conditions.

3.2.1 HC test configuration

By considering harmonic loading, or more formally taking Fourier transforms of the time-dependent quantities, the Frequency-domain rigid-body equations of motion may be written for the moving mass of the shaker and the pile cap using the sign conventions shown in Figure 3-2 as

$$\begin{cases} F_{zmm} - M_{mm}g\delta(\omega) + \omega^2 M_{mm}U_{zmm} = 0 \\ -F_{xmm} + \omega^2 M_{mm}U_{xmm} = 0 \\ B_{mm} + F_{zmm}e_{mm} + \omega^2 J_{mm}\Theta_{mm} = 0 \end{cases} \quad (3.1)$$

$$\begin{cases} -F_{zmm} - F_{zT} - M_Rg\delta(\omega) + \omega^2 M_RU_{zR} = 0 \\ F_{xmm} - F_{xT} + \omega^2 M_RU_{xR} = 0 \\ -B_{mm} - B_T - F_{xmm}h_{p1} - F_{zmm}e_{p1} + F_{xT}h_{p2} - F_{zT}e_{p2} + \omega^2 J_R\Theta_R = 0 \end{cases} \quad (3.2)$$

where $\delta(\omega)$ is the Dirac delta function, M denotes mass, J denotes polar moment of inertia, and $B_{mm}(\omega)$ and $B_T(\omega)$ are the Fourier transforms of $m_{mm}(t)$ and $m_T(t)$, respectively. In the above two equations, the eccentricity and height of a given point (i) relative to a centroidal point of interest in Figure 3-2 are defined as

$$e_i = x_i - x_C, \quad \text{and} \quad h_i = z_i - z_C, \quad (3.3)$$

which are negative-valued for points lying to the left or below the centroidal point (indicated by arrows pointing in the negative x or z directions in the figure). Note for the HC configuration that

$$e_{mm} = (x_{p1} - x_{C2}).$$

Equations (3.1) and (3.2) can be written in matrix form as

$$\mathbf{T}_{mm}\mathbf{F}_{mm} + \omega^2\mathbf{M}_{mm}\mathbf{U}_{mm} - M_{mm}\mathbf{g}\mathbf{W} = 0 \quad (3.4)$$

$$-\mathbf{T}_R\mathbf{F}_{mm} - \mathbf{T}_T\mathbf{F}_T + \omega^2\mathbf{M}_R\mathbf{U}_R - M_R\mathbf{g}\mathbf{W} = 0 \quad (3.5)$$

where

$$\mathbf{F}_{mm} = \begin{Bmatrix} F_{zmm} \\ F_{xmm} \\ B_{mm} \end{Bmatrix}, \quad \mathbf{U}_{mm} = \begin{Bmatrix} U_{zmm} \\ U_{xmm} \\ \Theta_{mm} \end{Bmatrix}, \quad \mathbf{F}_T = \begin{Bmatrix} F_{zT} \\ F_{xT} \\ B_T \end{Bmatrix}, \quad \mathbf{U}_R = \begin{Bmatrix} U_{zR} \\ U_{xR} \\ \Theta_R \end{Bmatrix} \quad (3.6)$$

$$\mathbf{M}_{mm} = \begin{bmatrix} M_{mm} & 0 & 0 \\ 0 & M_{mm} & 0 \\ 0 & 0 & J_{mm} \end{bmatrix}, \quad \mathbf{M}_R = \begin{bmatrix} M_R & 0 & 0 \\ 0 & M_R & 0 \\ 0 & 0 & J_R \end{bmatrix}, \quad \mathbf{W} = \begin{Bmatrix} \delta(\omega) \\ 0 \\ 0 \end{Bmatrix} \quad (3.7)$$

$$\mathbf{T}_{mm} = \begin{bmatrix} 1 & 0 & 0 \\ 0 & -1 & 0 \\ e_{mm} & 0 & 1 \end{bmatrix}, \quad \mathbf{T}_R = \begin{bmatrix} 1 & 0 & 0 \\ 0 & -1 & 0 \\ e_{p1} & h_{p1} & 1 \end{bmatrix} \quad \text{and} \quad \mathbf{T}_T = \begin{bmatrix} 1 & 0 & 0 \\ 0 & 1 & 0 \\ e_{p2} & -h_{p2} & 1 \end{bmatrix} \quad (3.8)$$

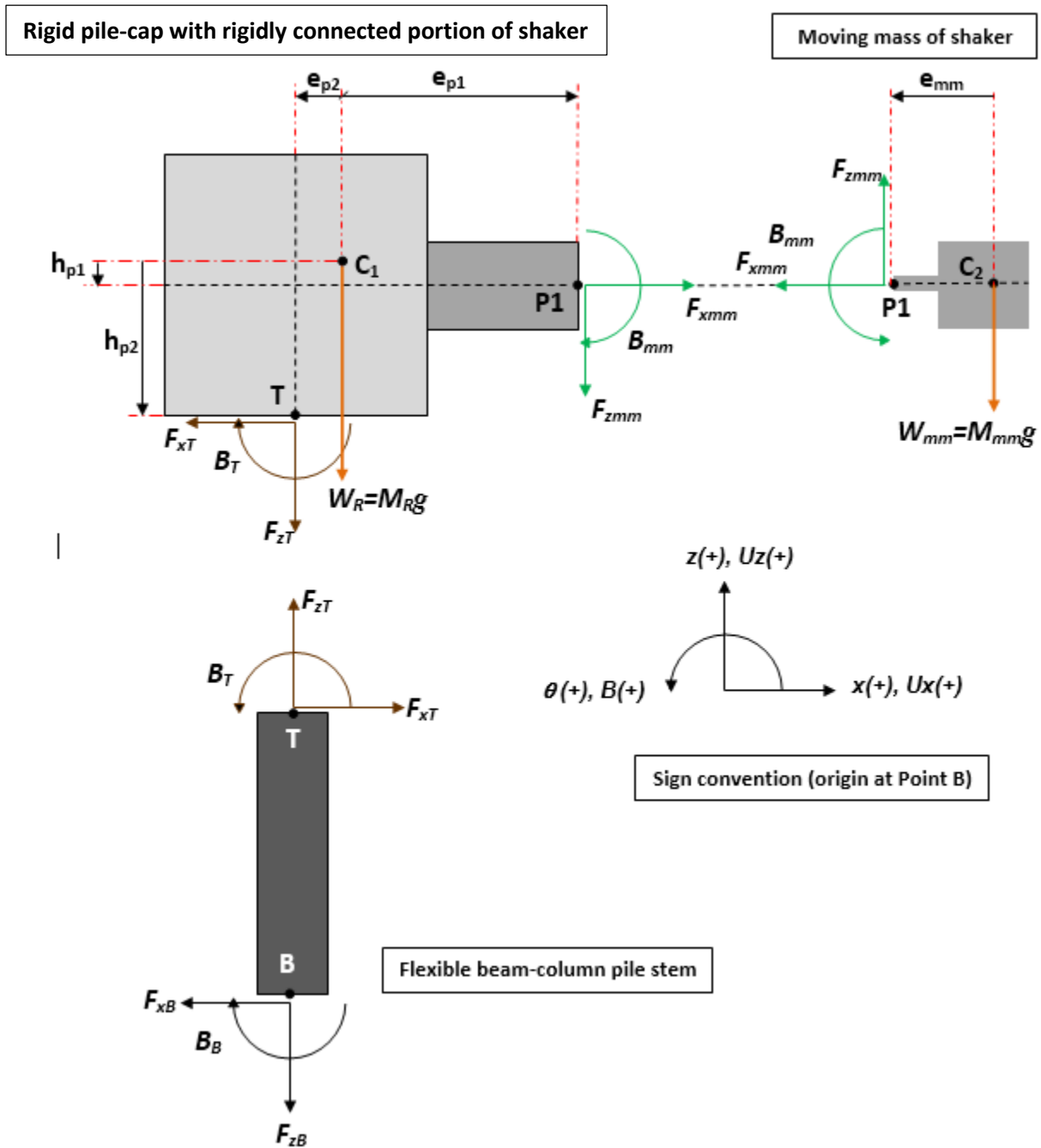


Figure 3-2- Free body diagram of pile-pile cap-shaker system in HC test configuration showing dimensions and sign conventions.

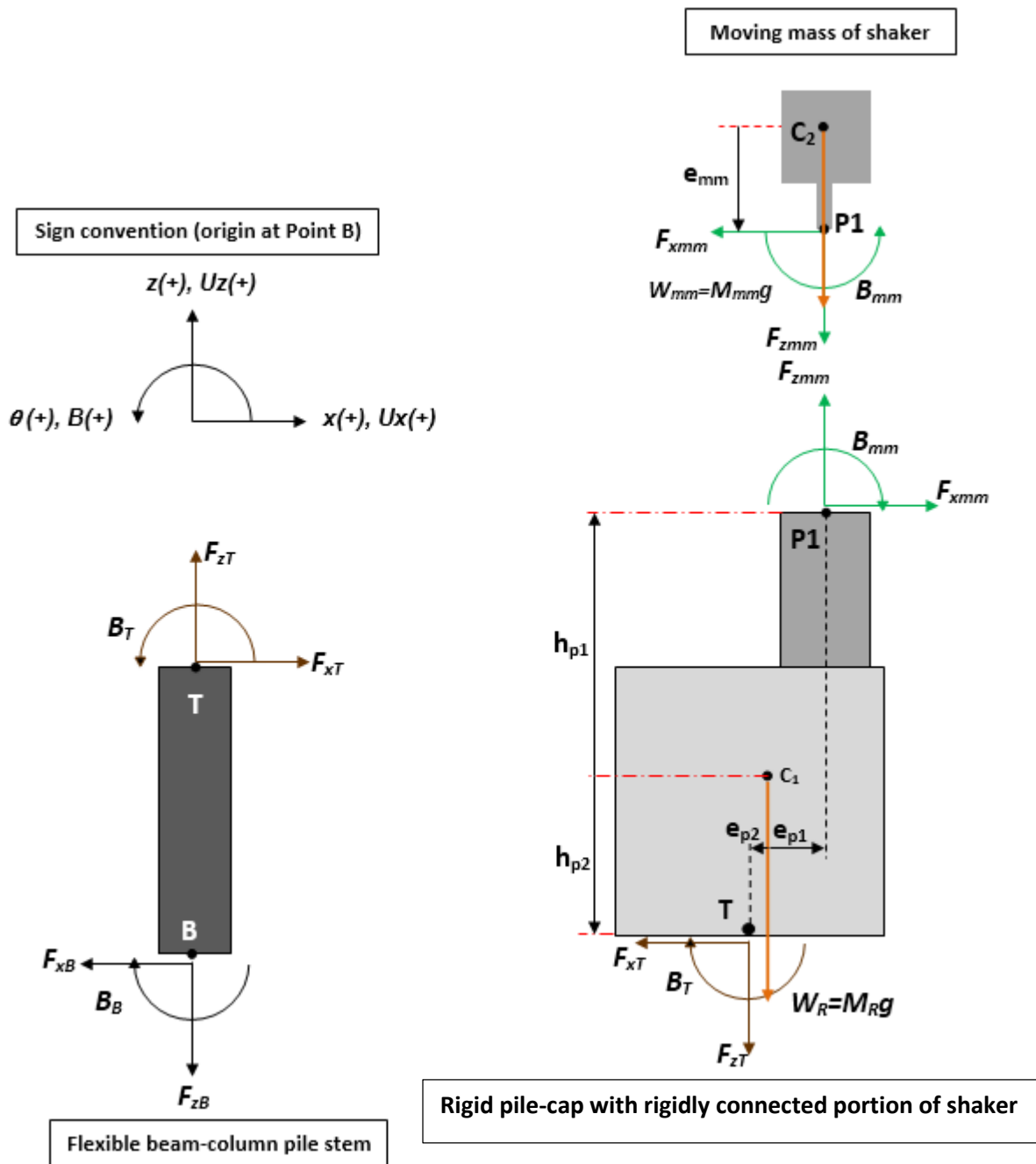


Figure 3-3- Free-body diagram of pile-pile cap-shaker system in VE test configuration showing dimensions and sign conventions.

In the above equations, \mathbf{T}_j are rigid-body motion matrices relating the displacement vectors at different points on the pile cap. They can be calculated knowing the pile-cap centroid coordinates and dimensions of the shaker. Calculations of the centroidal coordinates and inertial properties of the pile cap are detailed in Appendix 1. \mathbf{M}_{mm} and \mathbf{M}_R represent the mass matrices of the shaker's inertial moving mass, and the mass of the rigid pile cap including the stationary portion of the shaker, respectively. \mathbf{U} and \mathbf{F} represent the displacement and force vectors detailed in Figure 3-2, and ω denotes the angular frequency.

It should be noted that for non-zero frequencies the vector \mathbf{W} is zero and hence Eq. (3.4) reduces to

$$\mathbf{F}_{mm} = -\omega^2 \mathbf{T}_{mm}^{-1} \mathbf{M}_{mm} \mathbf{U}_{mm} \quad (3.9)$$

Using Eq. (3.9) in (3.5), the forcing components at the top of the un-embedded pile segment may be related to the properties and motion of the pile-cap and shaker as

$$\mathbf{F}_T = \omega^2 \left(\mathbf{T}_T^{-1} \mathbf{M}_R \mathbf{U}_R + \mathbf{T}_{eq1} \mathbf{M}_{mm} \mathbf{U}_{mm} \right) \quad (3.10)$$

where

$$\mathbf{T}_{eq1} = \mathbf{T}_T^{-1} \mathbf{T}_R \mathbf{T}_{mm}^{-1} \quad (3.11)$$

To relate the centroidal displacement \mathbf{U}_R at point C_1 to the displacement \mathbf{U}_T at point T, for small rotations one can employ the kinematic transformation matrix \mathbf{T}_{TR}

$$\mathbf{T}_{TR} = \begin{bmatrix} 1 & 0 & e_{p2} \\ 0 & 1 & -h_{p2} \\ 0 & 0 & 1 \end{bmatrix} \quad (3.12)$$

so that

$$\mathbf{U}_R = \mathbf{T}_{TR}^{-1} \mathbf{U}_T \quad (3.13)$$

where $e_{p2} = x_T - x_{C1}$ and $h_{p2} = z_T - z_{C1}$.

Substituting this relation into Eq. (3.10) gives

$$\mathbf{F}_T = \omega^2 \left(\mathbf{T}_T^{-1} \mathbf{M}_R \mathbf{T}_{TR}^{-1} \mathbf{U}_T + \mathbf{T}_{eq1} \mathbf{M}_{mm} \mathbf{U}_{mm} \right) \quad (3.14)$$

For the un-embedded pile segment subjected only to end loadings, one may use an Euler-Bernoulli beam-column formulation and solve the differential equations of motion in the frequency domain (Ashlock, 2006). The force and displacement vectors at the top and bottom of the deformable pile-stem (points T and B in Figure 3-2) may then be related through

$$\mathbf{S}_T^{-1} \begin{Bmatrix} \mathbf{U}_T \\ \mathbf{F}_T \end{Bmatrix} = \mathbf{S}_B^{-1} \begin{Bmatrix} \mathbf{U}_B \\ \mathbf{F}_B \end{Bmatrix} \quad (3.15)$$

in which \mathbf{S} is a 6x6 matrix that is a function of frequency and the elastic pile properties and dimensions (Ashlock, 2006). At any arbitrary point P in the un-embedded segment of the pile, this matrix has the form

$$\left[- \begin{bmatrix} \mathbf{I}_{3 \times 3} \\ \omega^2 \mathbf{T}_T^{-1} \mathbf{M}_R \mathbf{T}_{TR}^{-1} \end{bmatrix} \mathbf{S}_T \mathbf{S}_B^{-1} \begin{bmatrix} \mathbf{I}_{3 \times 3} \\ \mathbf{K}_{3 \times 3} \end{bmatrix} \right] \begin{Bmatrix} \mathbf{U}_T \\ \mathbf{U}_B \end{Bmatrix} = \begin{bmatrix} \mathbf{0}_{3 \times 3} \\ \omega^2 \mathbf{T}_{eq1} \mathbf{M}_{mm} \end{bmatrix} \mathbf{U}_{mm} \quad (3.19)$$

Assuming that the rotations of the shaker's moving mass and the pile-cap are equal, i.e., that the moving mass translates only axially along the actuator's shaft, and also neglecting the small dynamic perturbations of e_{mm} as the masses are vibrated, one can relate U_{zmm} and Θ_{mm} to the pile cap's centroidal motion through

$$\mathbf{U}_{mm} = U_{xmm} \times \begin{Bmatrix} \frac{U_{zR}}{U_{xmm}} + (e_{p1} - e_{mm}) \frac{\Theta_R}{U_{xmm}} \\ 1 \\ \frac{\Theta_R}{U_{xmm}} \end{Bmatrix} \quad (3.20)$$

Equation 3.19 can also be written in terms of displacements at point T as

$$\mathbf{U}_{mm} = U_{xmm} \times \begin{Bmatrix} \frac{U_{zT}}{U_{xmm}} + (e_{p1} - e_{mm} - e_{p2}) \frac{\Theta_T}{U_{xmm}} \\ 1 \\ \frac{\Theta_T}{U_{xmm}} \end{Bmatrix} \quad (3.21)$$

As defined previously, the transfer function of a point (i) on the pile cap is the ratio of the acceleration at that point to the acceleration of the moving mass, i.e.,

$$H_i = \frac{\ddot{\iota}}{\ddot{\iota}} \quad \frac{\omega^2 U_i}{\omega^2 U_{mm}} = \frac{U_i}{U_{mm}} \quad (3.22)$$

Thus Eq. (3.21) can be expressed in the compact form

$$\mathbf{U}_{mm} = U_{xmm} \mathbf{T}_{xfer} \begin{Bmatrix} H_{zT} \\ 1 \\ H_{\Theta T} \end{Bmatrix} \quad (3.23)$$

where

$$\mathbf{T}_{xfer} = \begin{bmatrix} 1 & 0 & (e_{p1} - e_{mm} - e_{p2}) \\ 0 & 1 & 0 \\ 0 & 0 & 1 \end{bmatrix} \quad (3.24)$$

Combining equations (3.19) and (3.23) gives a system of 6 equations and 6 unknowns that can be solved at each frequency. This equation can be further simplified by defining $\mathbf{T}_1 = \mathbf{T}_T^{-1} \mathbf{M}_R \mathbf{T}_{TR}^{-1}$ and

$$\mathbf{T}_2 = \mathbf{T}_{eq1} \mathbf{M}_{mm} \mathbf{T}_{xfer}$$
 to

$$\begin{bmatrix} - \begin{bmatrix} \mathbf{I}_{3 \times 3} \\ \omega^2 \mathbf{T}_1 \end{bmatrix} \mathbf{S}_T \mathbf{S}_B^{-1} \begin{bmatrix} \mathbf{I}_{3 \times 3} \\ \mathbf{K}_{3 \times 3} \end{bmatrix} \end{bmatrix} \begin{Bmatrix} H_{zT} \\ H_{xT} \\ H_{\Theta T} \\ H_{zB} \\ H_{xB} \\ H_{\Theta B} \end{Bmatrix} = \begin{bmatrix} \mathbf{0}_{3 \times 3} \\ \omega^2 \mathbf{T}_2 \end{bmatrix} \times \begin{Bmatrix} H_{zT} \\ 1 \\ H_{\Theta T} \end{Bmatrix} \quad (3.25)$$

The unknowns in this system are the transfer functions $\mathbf{H}_T = \{H_{zT}, H_{xT}, H_{\Theta T}\}^T$ and $\mathbf{H}_B = \{H_{zB}, H_{xB}, H_{\Theta B}\}^T$ at the top and bottom of the pile segment, from which the transfer functions at the centroid or at the position of each accelerometer can be found from the rigid body motion of the pile cap. Equation (3.25) has unknown transfer functions on both sides of the equation. To facilitate its solution, it can be reordered into a system of linear equations $\mathbf{A}\mathbf{H}=\mathbf{B}$ with all unknowns on the left-hand side:

$$\underbrace{\left[-\left[\begin{array}{c} \mathbf{I}_{3 \times 3} \\ \omega^2 (\mathbf{T}_T + \mathbf{T}_U) \end{array} \right] \mathbf{S}_T \mathbf{S}_B^{-1} \left[\begin{array}{c} \mathbf{I}_{3 \times 3} \\ \mathbf{V} \end{array} \right] \right]}_{\mathbf{A}} \underbrace{\left\{ \begin{array}{c} H_{zT} \\ H_{xT} \\ H_{\Theta T} \\ H_{x_B} \\ H_{\Theta B} \end{array} \right\}}_{\mathbf{H}} = \underbrace{\left\{ \begin{array}{c} 0 \\ 0 \\ 0 \\ \omega^2 \mathbf{T}_2 \left\{ \begin{array}{c} 0 \\ 1 \end{array} \right\} \end{array} \right\}}_{\mathbf{F}} \quad (3.26)$$

where

$$\mathbf{I}_2 = \begin{bmatrix} 1 & 0 & 0 \\ 0 & 0 & 0 \\ 0 & 0 & 1 \end{bmatrix}$$

Finally, as previously discussed in Chapter 2, the accelerance function A corresponding to each transfer function H in the above equation can be simply calculated as

$$A_i = \frac{H_i}{M_{mm}} \quad (3.27)$$

3.2.2 VE test configuration

A procedure similar to that described for the HC test configuration in the previous section is presented here for the VE forcing configuration. The free-body diagram and sign conventions for this problem are shown in Figure 3-3.

The first step once again is to write the frequency-domain rigid-body equations of motion:

$$\begin{cases} -F_{zmm} - M_{mm} g \delta(\omega) + \omega^2 M_{mm} U_{zmm} = 0 \\ -F_{xmm} + \omega^2 M_{mm} U_{xmm} = 0 \\ B_{mm} - F_{xmm} e_{mm} + \omega^2 J_{mm} \Theta_{mm} = 0 \end{cases} \quad (3.28)$$

$$\begin{cases} F_{zmm} - F_{zT} - M_R g \delta(\omega) + \omega^2 M_R U_{zR} = 0 \\ F_{xmm} - F_{xT} + \omega^2 M_R U_{xR} = 0 \\ -B_{mm} - B_T - F_{xmm} h_{p1} + F_{zmm} e_{p1} + F_{xT} h_{p2} - F_{zT} e_{p2} + \omega^2 J_R \Theta_R = 0 \end{cases} \quad (3.29)$$

or in matrix form as in Equations (3.4) and (3.5), where the following matrices replace those of Equation (3.8) :

$$\mathbf{T}_{mm} = \begin{bmatrix} -1 & 0 & 0 \\ 0 & -1 & 0 \\ 0 & e_{mm} & 1 \end{bmatrix}, \quad \mathbf{T}_R = \begin{bmatrix} -1 & 0 & 0 \\ 0 & -1 & 0 \\ -e_{p1} & h_{p1} & 1 \end{bmatrix} \quad \text{and} \quad \mathbf{T}_T = \begin{bmatrix} 1 & 0 & 0 \\ 0 & 1 & 0 \\ e_{p2} & -h_{p2} & 1 \end{bmatrix} \quad (3.30)$$

and $e_{mm} = (z_{p1} - z_{C2})$.

Equations (3.9) through (3.19) are also valid in this case. For the VE forcing condition, Eq. (3.20) and (3.21) are replaced with

$$\mathbf{U}_{mm} = U_{zmm} \times \left\{ \begin{array}{c} 1 \\ \frac{U_{xR}}{U_{zmm}} - (h_{p1} - e_{mm}) \frac{\Theta_R}{U_{zmm}} \\ \frac{\Theta_R}{U_{zmm}} \end{array} \right\} \quad (3.31)$$

and

$$\mathbf{U}_{mm} = U_{zmm} \times \left\{ \begin{array}{c} 1 \\ \frac{U_{xT}}{U_{zmm}} - (h_{p1} - e_{mm} - h_{p2}) \frac{\Theta_T}{U_{zmm}} \\ \frac{\Theta_T}{U_{zmm}} \end{array} \right\} \quad (3.32)$$

or

$$\mathbf{U}_{mm} = U_{zmm} \mathbf{T}_{xfer} \left\{ \begin{array}{c} 1 \\ H_{xT} \\ H_{\Theta T} \end{array} \right\} \quad (3.33)$$

where

$$\mathbf{T}_{xfer} = \begin{bmatrix} 1 & 0 & 0 \\ 0 & 1 & -(h_{p1} - e_{mm} - h_{p2}) \\ 0 & 0 & 1 \end{bmatrix} \quad (3.34)$$

Applying these changes to the formulations for the HC case gives the following system of linear equations for the VE case, which may be solved for the unknown transfer functions

$\mathbf{H}_T = \{H_{zT}, H_{xT}, H_{\Theta T}\}^T$ and $\mathbf{H}_B = \{H_{zB}, H_{xB}, H_{\Theta B}\}^T$:

$$\underbrace{\left[- \left[\begin{array}{c} \mathbf{I}_{3 \times 3} \\ \dots (\mathbf{T}_T, \mathbf{T}_B) \end{array} \right] \mathbf{S}_T \mathbf{S}_B^{-1} \left[\begin{array}{c} \mathbf{I}_{3 \times 3} \\ \dots \end{array} \right] \right]}_a \left\{ \begin{array}{c} H_{zT} \\ H_{xT} \\ H_{\Theta T} \\ \dots \\ H_{xB} \\ H_{\Theta B} \end{array} \right\} = \underbrace{\left\{ \begin{array}{c} 0 \\ 0 \\ 0 \\ \dots \\ \omega^2 \mathbf{T}_2 \left\{ \begin{array}{c} 1 \\ 0 \\ \dots \end{array} \right\} \end{array} \right\}}_b \quad (3.35)$$

Where

$$\mathbf{I}_2 = \begin{bmatrix} 0 & 0 & 0 \\ 0 & 1 & 0 \\ 0 & 0 & 1 \end{bmatrix}.$$

The desired accelerance functions may subsequently be found using Eq. (3.27).

The formulations presented above for HC and VE tests were programmed in MATLAB to solve Equations (3.26) and (3.35) for the theoretical accelerance functions. The program uses soil impedance functions as input, which will be discussed in Sections 3.3 and 3.4.

The VC case is simply a special case of the VE formulation with $e_{p1}=e_{p2}=0$.

3.3 Soil-Pile Impedance Functions by Approximate Methods

3.3.1 Overview of relevant previous studies

Many analytical and numerical methods have been proposed over the past several decades by researchers studying dynamic soil-pile interaction problems. The topic remains an advancing field of scholarly work as new theories and dramatically expanding computing capabilities have provided increasingly powerful tools for supporting more complex methods. However, sophisticated computational methods can only lead to accurate predictions if all input materials and procedures are defined with equal accuracy. Even if modeling error were minimal, and assuming that all input parameters and values were introduced correctly, there are still many potential sources for programming errors, numerical errors, and instabilities, including insufficient numerical precision, inherent element stiffness, unanticipated behavior due to meshing problems, etc. It is therefore wise to verify numerical results using simple approximate methods that have generally been accepted and verified by the engineering community. Such approximate solutions

for complicated dynamic soil-pile interaction problems are also routinely employed in many research papers to provide engineering insight before applying much more sophisticated, time-consuming, and computationally expensive methods. Moreover, depending on the type of project, approximate methods are useful tools for performing parametric studies and preliminary or in some cases even final designs. To demonstrate the essence of such methods in this area, some of the major proposed methods will first be reviewed. The approximate solution presented by Novak and Aboul-Ella (Novak & Aboul-Ella, 1978), which is the primary one examined in this study, will be discussed in more detail in the next section.

Blaney et al. (Blaney G. W., 1976) presented a discrete model for calculating the approximate dynamic stiffness of a pile-soil system undergoing lateral rocking vibration. This method was based on the previous work of Kausel et al. (Kausel, et al., 1975), and employs finite-element methods for analyzing the soil surrounding the pile, and an absorbing-boundary approach for approximating the radiation condition in the far-field soil. Soil properties in a zone next to the pile can vary with depth as well as horizontally, but in the far-field are constant in the horizontal direction. This method in its general form can simulate the nonlinear behavior of the soil by considering horizontally-variable soil properties for the region surrounding the pile. However, in the study the soil was assumed to be linearly elastic and homogenous, so the intermediate region was not considered. Among the key assumptions of the model were the existence of a relatively rigid layer beneath the soil domain on which the pile tip rests. A rigid cross-section of beam elements for the pile (i.e., uniform horizontal displacements at any depth) and hysteretic internal damping in the soil were also assumed. The hysteretic (frequency independent) damping was implemented through a complex modulus, $G_s(1+2i\xi)$, where ξ is the damping ratio. For the case of zero internal damping in the soil for the approximate analysis, the imaginary part of the soil

stiffness, or radiation damping, was shown to be zero for frequencies less than the fundamental frequency of the stratum, $\omega = \frac{2\pi V_s}{4H}$, where V_s is the shear wave velocity and H is the stratum thickness. Compared to Novak's solution (Novak, 1974), the stiffness functions produced by this method are more accurate in the low-frequency range, which is of importance to earthquake engineering. Finally, the following approximate relationships were suggested for the horizontal and rocking modes of vibration:

$$K = \begin{bmatrix} K_{xx} & K_{x\phi} \\ K_{\phi x} & K_{\phi\phi} \end{bmatrix} \quad (3.36)$$

where

$$K_{ij} = (k_{ij} + ia_0 c_{ij})(1 + 2i\xi)^b \quad (3.37)$$

$a_0 = \frac{\omega R}{\sqrt{G_s/\rho_s}}$ is the dimensionless frequency, and b is equal to 0.75, 0.5 and 0.25 for the horizontal,

horizontal-rocking and rocking stiffness, respectively. The approximate stiffness and damping coefficients obtained by fitting the numerical results in the study were given for the limitations of

$H/R > 25$ and $E_s/E_p < 5 \times 10^{-3}$ as

$$k_{xx} \approx \left(\frac{E_s}{E_p} \right)^{0.75}, \quad c_{xx} = \begin{cases} 2k_{xx} : a_0 > \frac{\pi R}{2H} \\ 0 : a_0 \leq \frac{\pi R}{2H} \end{cases} \quad (3.38)$$

$$k_{x\phi} \approx \left(\frac{E_s}{E_p} \right)^{0.50}, c_{x\phi} = \begin{cases} 1.5k_{x\phi} & : a_0 > \frac{\pi R}{2H} \\ 0 & : a_0 \leq \frac{\pi R}{2H} \end{cases} \quad (3.39)$$

$$k_{\phi\phi} \approx \left(\frac{E_s}{E_p} \right)^{0.25}, c_{\phi\phi} = \begin{cases} 0.5k_{\phi\phi} & \\ : a_0 > \frac{\pi R}{2H} \sqrt{2(1-\nu_s)/(1-2\nu_s)} & \\ 0 & \\ : a_0 \leq \frac{\pi R}{2H} \sqrt{2(1-\nu_s)/(1-2\nu_s)} & \end{cases} \quad (3.40)$$

Dobry and Gazetas (Dobry, 1985) published a collection of approximate stiffness and damping charts and equations for different types of soil-foundation configurations, including the soil-pile problem in which a layered soil media may have different properties within each layer. Their work reduces the tedious job of searching the literature for the best applicable curve or equation for the problem under study. These simple methods have been rather completely verified and calibrated with respect to more complex computational methods and actual experiments. As in Blaney et al. [7], rigid bedrock beneath the soil can affect the mechanism of energy dissipation in the pile-soil system such that no radiation damping occurs for frequencies below the fundamental frequency of the soil layer. The dynamic impedance curve reflects this effect by a dip in the real part at the fundamental frequency and a zero imaginary part below the fundamental frequency. This phenomenon was discussed in the paper and charts were presented for the fundamental frequency of arbitrarily layered soil profiles overlying rigid bedrock. In higher-frequency ranges, the concept of one-dimensional wave propagation has been shown to apply for 3D problems as well, so the simple relationships describing a perfect 1D viscous dashpot was employed for the formulations. The charts and equations of Dobry and Gazetas are applicable to

arbitrary pile cross-sections and both end-bearing and floating piles. However, they are restricted to flexible fixed-head piles (i.e., zero rotation at the pile head), and are limited to horizontal vibration.

The procedure of Dobry and Gazetas involves three main steps. First a *static* horizontal force P_0 is applied to the pile head and the resulting displacement profile $y_s(z)$ and the pile-head stiffness $K_h = P_0 / y_s(0)$ are calculated by any reasonable method such as a beam-on-Winkler-foundation approach with linear or nonlinear springs, static finite element simulations, or full-scale instrumented load tests. Dimensionless dynamic stiffness versus dimensionless frequency curves corresponding to different soil profiles and layer thicknesses are then obtained from the formulas and charts presented. The aforementioned static stiffness value is used to determine the dimensional dynamic stiffness from the normalized curves. The second step is to calculate the distributed-material and radiation damping dashpot coefficients per unit length of pile, c_m and c_r respectively, along the pile. Based on a plane-strain 2-D approximate model for wave propagation, if the soil is underlain by rigid bedrock, Dobry and Gazetas recommend using

$$c_m \approx \quad \quad \quad (3.41)$$

$$\frac{c_r}{4B\rho_s V_s} = \begin{cases} 1.67a_0^{-0.25} & : z < 5B, a_0 > 2a_{0s} \\ 0.83 \left[1 + \left(\frac{3.4}{\pi(1-\nu)} \right)^{1.25} \right] a_0^{-0.25} & : z > 5B, a_0 > 2a_{0s} \\ 0 & : a_0 < a_{0s} \end{cases} \quad (3.42)$$

where β is the soil material damping ratio, k relates to the soil stiffness, a_0 is the corresponding dimensionless frequency, B is the equivalent circular radius of the pile, and a_{0s} is the dimensionless fundamental frequency of the soil layer. For frequencies between a_{0s} and $2a_{0s}$, linear interpolation is suggested. A thorough discussion on approximate methods for estimating the fundamental frequency of arbitrary horizontally-layered soil profiles overlying bedrock is also presented in the paper. The third and final step is to integrate the distributed damping along the pile length to find the damping coefficient C_h at the pile head;

$$C_h(\beta) = \int_0^L (c_r + c_m) Y_s^2(z) dz \quad (3.43)$$

with the normalized displacement Y_s defined as $Y_s(z) = y_s(z)/y_s(0)$. Unfortunately, the study was restricted to horizontal pile vibration, and did not include vertical or rocking stiffness and damping properties.

Gazetas (1984) presented a set of approximate closed-form solutions for dynamic stiffness and damping of end-bearing single piles for three types of soil modulus profiles shown in Figure 3-4. A circular cross-section with linear elastic behavior was assumed for the pile. The pile-soil interaction analysis was divided into kinematic and inertial interaction, and a detailed parametric study of kinematic interaction was presented. The parametric study investigated the effects of pile-soil stiffness ratio, soil modulus profile, and slenderness ratio on kinematic interaction, and presented a set of synthesized kinematic interaction factors for the three soil profiles. The interaction factors vary with frequency and give the ratio of actual pile-top horizontal displacement to the horizontal displacement of the free-field for vertically propagating SH waves.

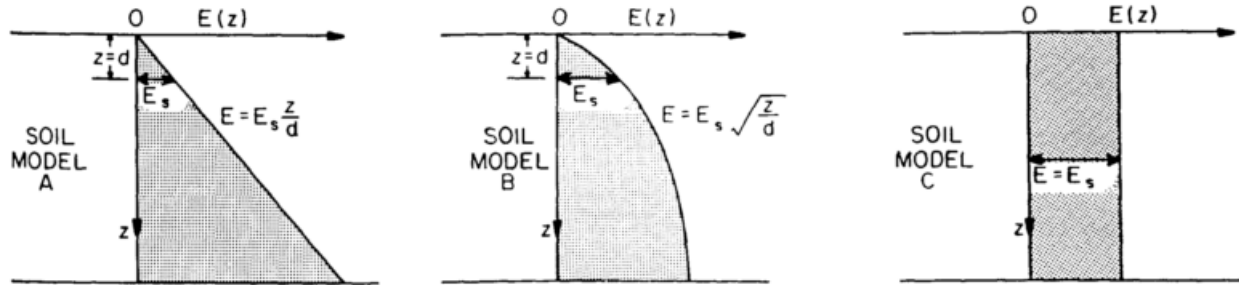


Figure 3-4. Three soil modulus profiles studied by Gazetas. (Gazetas, 1984)

In the study by Gazetas, the approximate pile head swaying, rocking, and coupled swaying-rocking dynamic stiffnesses are presented in the form

$$K = K_{st} (k_d + 2iD) \quad (3.44)$$

where the static stiffness K_{st} is calculated from Table 3-1. A dynamic active length, l_a , is defined as the length contributing to pile deformation, and flexible piles are defined as those for which $L > l_a$. In other words, the lower segment of the pile remains idle and doesn't contribute to the dynamic interaction. The approximate expressions for active length, obtained by curve-fitting of finite-element solutions, are presented in Table 3-2. The FEM analyses were performed for a pile length L equal to $40d$. Although the author claims that the results are applicable for other pile lengths as long as $L \geq l_a$, the L value would also significantly affect radiation damping, which is sensitive to the bedrock depth.

Table 3-1. Suggested static stiffness for the horizontal-rocking modes of vibration for soil profiles in Figure 3-4 (from Gazetas, 1984).

Soil model (Figure 3-4)	$\frac{K_{st-HH}}{dE_{sc}}$	$\frac{K_{st-MM}}{dE_{sc}}$	$\frac{K_{st-HM}}{dE_{sc}}$
A	$0.60 \left(\frac{E_p}{E_s} \right)^{0.35}$	$0.14 \left(\frac{E_p}{E_s} \right)^{0.80}$	$-0.17 \left(\frac{E_p}{E_s} \right)^{0.60}$
B	$0.79 \left(\frac{E_p}{E_s} \right)^{0.28}$	$0.15 \left(\frac{E_p}{E_s} \right)^{0.77}$	$-0.24 \left(\frac{E_p}{E_s} \right)^{0.53}$
C	$1.08 \left(\frac{E_p}{E_s} \right)^{0.21}$	$0.16 \left(\frac{E_p}{E_s} \right)^{0.75}$	$-0.22 \left(\frac{E_p}{E_s} \right)^{0.50}$

Table 3-2-Expression for estimated active length of flexible piles under lateral dynamic loading for soil profiles in Figure 3-4 (from Gazetas, 1984).

Soil model	Active length l_a	
	Expression	Typical range
A	$3.2d \left(\frac{E_p}{E_s} \right)^{1/6}$	$6d - 15d$
B	$3.2d \left(\frac{E_p}{E_s} \right)^{2/11}$	$6d - 17d$
C	$3.3d \left(\frac{E_p}{E_s} \right)^{1/5}$	$8d - 20d$

The dynamic stiffness and damping coefficients in Eq. (3.44), k_d and D , were calculated using finite-element analyses and presented as plots against the dimensionless frequency f/f_1 for the three types of soil profile (Figure 3-4), where f_1 is the fundamental frequency of the free-field soil profile. An estimation of the natural shear frequency of each soil profile (f_1) is taken from (Dobry, 1976) and presented in the paper. These values are shown in Table 3-3.

Table 3-3- Natural shear frequencies of soil profiles in Figure 3-4 having thickness H (from Gazetas, 1984).

Soil model	f_1	f_2/f_1
A	$1.21 V_s / H$	2.33
B	$0.56 V_s / H$	2.66
C	$0.25 V_s / H$	3.00

V_s =shear wave velocity at depth $z=d$.

The study confirms previous findings from relevant studies on the trends of dynamic stiffness and damping of pile-soil systems; the dynamic stiffness does not vary significantly over the frequency range examined, except for at the natural frequency of the soil deposit, where a dip occurs. The damping is constant at frequencies lower than the natural frequency f_1 , for which no radiation damping occurs, while at high frequencies the damping increases with frequency due primarily to radiation damping. However, the numerical values and resulting expressions from the study are limited to a particular case of finite-element simulation ($\beta_s=0.05$, $\nu_s=0.4$, $\rho_p/\rho_s=1.60$, $H=L=40d$), so they are not necessarily applicable to general pile-soil problems.

3.3.2 Novak and Aboul-Ella method

The approximate method of Novak and Aboul-Ella (Novak & Aboul-Ella, 1978) is useful for analyzing dynamic stiffness and damping of piles for vertical and coupled horizontal-rocking modes. Advantages of this approach include capability of modeling variations with depth in soil and pile properties, and employment of a 2D stiffness matrix approach to efficiently model the flexural behavior of the pile in terms of horizontal and lateral displacements, rotations, bending moments, and shear forces. This soil model can take into account various soil modulus profiles

and layering at negligible computational cost, making it a useful tool for parametric studies. However, the method is limited to assumptions of plane strain elastic behavior, circular pile cross-sections, hysteretic soil damping, and horizontally homogeneous soil profiles. Additionally, the reaction beneath the pile tip is approximated as that of a rigid circular footing resting on the surface of a homogeneous viscoelastic half-space (Veletsos & Verbič, 1973). The results are also dependent upon the choice of pile mesh, as the pile and soil properties are considered constant over each pile element. The solution also cannot model pile installation effects or soil-pile separation. By introducing unit displacements or rotations at the pile head or ground surface and solving the global stiffness-matrix equation for displacements, one may determine the desired pile-soil impedances. To analyze non-circular sections such as common H-piles, different circular sections with equivalent axial or bending stiffness must be used.

Novak and Aboul-Ella (Novak & Aboul-Ella, 1978) stated one important caveat for the approximate method with respect to its performance in the low-frequency region; the imaginary parts of the impedances do not approach zero as they should, and the real parts decay rather than converging to the true static stiffness values. To address this issue, Novak and Aboul-Ella proposed a general modification to correct the horizontal impedance by approximating its real part as constant below the dimensionless frequency $\omega r_0 / V_s = 0.3$ and projecting its imaginary part towards zero.

Considering the advantages and disadvantages of this method, it has been selected as an approximate approach for solving the soil-pile interaction problem represented by the matrix $\mathbf{K}_{3 \times 3}$ in Equations (3.26) and (3.35). Unlike the previously-mentioned methods in this chapter, the method of Novak and Aboul-Ella is more general and can handle soil stratification through variation of soil properties with depth. Additionally, the method provides internal pile forces and

displacement in the outputs, and consists of closed-form solutions that can be efficiently programmed and applied to different problems. A MATLAB program was developed for this study to perform the following steps:

1- Find complex soil reactions around the pile perimeter for the plane-strain case (Novak et al., 1978) (Novak, et al., 1978).

2- Find the reaction of the soil acting on the pile tip (Veletsos & Verbic, 1973) (Veletsos & Verbič, 1973).

3- Construct the complex frequency parameters and functions (Novak & Aboul-Ella, 1978) (Novak & Aboul-Ella, 1978).

4- Construct the element stiffness matrices (Novak & Aboul-Ella, 1978) (Novak & Aboul-Ella, 1978).

5- Assemble the global stiffness matrices of the pile (Novak & Aboul-Ella, 1978) (Novak & Aboul-Ella, 1978).

6- Find the pile-head impedances by solving the global matrix equations for unit displacements and rotations at the soil surface (Novak & Aboul-Ella, 1978) (Novak & Aboul-Ella, 1978).

The validity of the method is examined through verification of the program against various benchmark problems and rigorous methods in the following sub-sections.

3.3.2.1 Verification of approximate method of Novak and Aboul-Ella

3.3.2.1.1 Comparison of MATLAB program to previously published work

The validity of the MATLAB program in producing accurate stiffness and damping parameters by Novak and Aboul-Ella's method was first tested through comparison to the published examples in (Novak, et al., 1978), (Veletsos & Verbič, 1973) and (Novak & Aboul-Ella, 1978). This covers the first two steps of soil impedance calculations in the program. Figure 3-5 through 3-7 show that the MATLAB program successfully achieves the desired accuracy.

3.3.2.1.2 Cantilever column benchmark problem

As another check of the method, the approximate solution program was used to calculate the impedances of the soil-pile problem shown in Figure 3-10, in which the pile is fixed at the tip and the soil shear modulus approaches zero. This problem degenerates to the classical case of a cantilever beam-column for which a closed-form solution is easily obtained by setting the base displacement equal zero in the general matrix formulation presented in section 3.2.2. Upon comparing the exact to the approximate solution for the cantilever problem with the soil modulus in the MATLAB program approaching zero numerically ($G_s \approx 0$), it was verified that the program produces a result very close to the exact answer (Figure 3-10). This confirms the accuracy of the element and global-stiffness matrix programming as well as the matrix-equation solution (Steps 3 to 6 in Section 3.3.2)

3.3.2.1.3 Convergence study by varying mesh size

Before using the approximate method of Novak and Aboul-Ella to analyze the pile vibration experiments in this study, the number of pile elements necessary to produce an accurate solution in the model must be determined. For this purpose, the actual soil-pile problem for the unimproved soil profile described in Chapter 2 was modeled using different numbers of elements for the Hardin-Drnevich soil profile described in Chapter 2 and scaled to have a maximum material damping of 5%. The pile was modeled as a floating pile, as the soil properties beneath the pile tip were taken to be the same as the soil above the tip. The impedance functions shown in Figure 3-9 indicate that meshes with greater than 50 elements will produce essentially the same results with good accuracy. Since the program is very fast, meshes with 100 pile elements were used throughout this study whenever approximate solutions were used.

3.3.2.1.4 Comparison to rigorous solutions for nonlinear soil profile

To verify the accuracy of the MATLAB program, the simple problem of a circular pile in a soil with a nonlinear square-root shear modulus profile was solved using both the approximate MATLAB program and the rigorous BEM program BEASSI (Pak & Guzina, 1999). The boundary-element method and BEASSI are discussed in detail in Section 3.4. The results match reasonably well for the horizontal impedance k_{uu} for this problem, provided that one uses the slight modification suggested by Novak and Aboul-Ella for low frequencies, as shown in Figure 3-10. However, the approximate method gives an impedance whose real part is 5% lower than the BEM solution at zero frequency, and the imaginary component is slightly larger than the BEM solution at all frequencies.

One of the limitations of the approximate method described above is its assumption of a circular pile cross-section. For such methods, it is common practice to model a non-circular or hollow pile section using a circular cross-section of equivalent axial or bending stiffness. However, the magnitude and distribution of contact stresses between pile and soil are quite different for square and circular pile-soil interface geometries. To assess the significance of the error introduced by the equivalent-circular-pile approach, BEASSI was used to obtain rigorous solutions for the 3D pile-soil interaction configuration of circular and square piles having equivalent axial and flexural stiffness and embedded in a homogeneous half-space over a stiff bedrock. The impedances were also compared to those from the approximate method of Novak and Aboul-Ella, for which the square-pile solution was obtained using circular sections of equivalent axial and bending stiffness for the vertical and horizontal-rocking modes, respectively. The details of the BEM mesh and the soil-pile model are presented in Table 3-4 and 3-5 and Figure 3-11. As can be seen in Figure 3-12, the BEM and approximate method results are in good agreement for the lateral-rocking impedances except in the low-frequency range where only the BEM solution exhibits the expected phenomena of a dip in the real part at the fundamental frequency of the free-field soil stratum, and zero imaginary part (damping) below this frequency, both of which are discussed above. This low-frequency range where the approximate method exhibits its maximum error is important for seismic problems, and the approximate method should therefore be replaced in this situation with a more rigorous method that can capture the wave reflections and damping phenomena caused by the bedrock. The impedances for the vertical mode of vibration are quite different for the approximate and BEM solutions, with the approximate method giving much higher stiffness and lower damping than BEM. This is likely related to the limitation of the approximate method treating the pile tip as a circular surface footing resting on a homogeneous half-space. As far as

the approximation of the square pile by an equivalent circular one, the impedances of Figure 3-12 reveal that this results in only slight errors in the low-frequency region.

Table 3-4. Properties of two soil-pile models with square and circular cross sections having equivalent pile bending stiffness, used to find k_{hh} , k_{hm} , k_{mm} , c_{hh} , c_{hm} and c_{mm} .

	Actual pile (square)	Pile with equivalent section (circular)
2b (or 2a) (m)	0.254000	0.289931
Area (m ²)	0.064516	0.066021
Moment of inertia (m ⁴)	0.000347	0.000347
Ref. length used in modelling (m)	$a_{ref}=0.127$	$b_{ref}=0.144965$
G_{ref} used in modelling and plots (Pa)	27758262.378066	27758262.378066
ρ_{ref} used in modelling and plots (kg/m ³)	2000.0	2000.0
a_{ref} used in plots (m)	0.127	0.127
Pile length (m)	6.15	6.15
Rigid bedrock depth (m)	6.40	6.40
Uniform soil shear modulus (Pa)	$2G_{ref}$	$2G_{ref}$
Uniform soil material damping ratio	5%	5%
Mesh size (x,y,z or r, θ ,z)	5x5x18	4x20x18

Table 3-5. Properties of two soil-pile models with square and circular cross sections having equivalent axial pile stiffness (used to find k_{vv} and c_{vv}).

	Actual pile (square)	Pile with equivalent section (circular)
2b (or 2a) (m)	0.254000	0.286608
Area (m ²)	0.064516	0.064516
Moment of inertia (m ⁴)	0.000347	0.000331
Ref. length used in modelling (m)	$a_{ref}=0.127$	$b_{ref}=0.143304$
G_{ref} used in modelling and plots (Pa)	27758262.378066	27758262.378066
ρ_{ref} used in modelling and plots (kg/m ³)	2000.0	2000.0
a_{ref} used in plots (m)	0.127	0.127
Pile length (m)	6.15	6.15
Bedrock depth (m)	6.40	6.40
Uniform soil shear modulus (Pa)	$2G_{ref}$	$2G_{ref}$
Uniform soil material damping ratio	5%	5%
Mesh size (x,y,z or r, θ ,z)	5x5x18	4x20x18

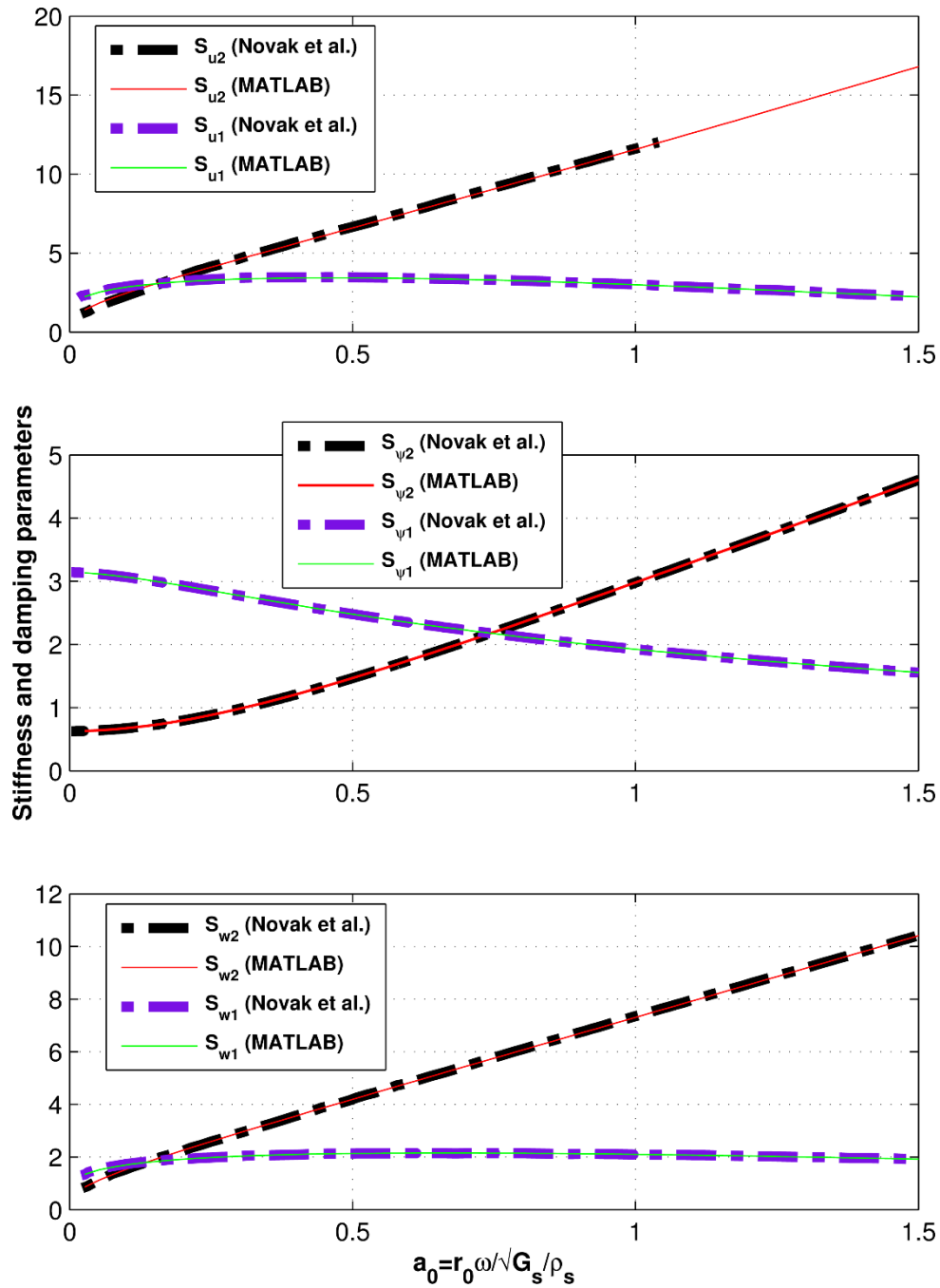


Figure 3-5. Comparison of MATLAB program stiffness and damping parameters with results presented in Figures 2, 4 and 5 of Novak et al. (1978) for $\nu=0.4$ and $D_s=0.2$.

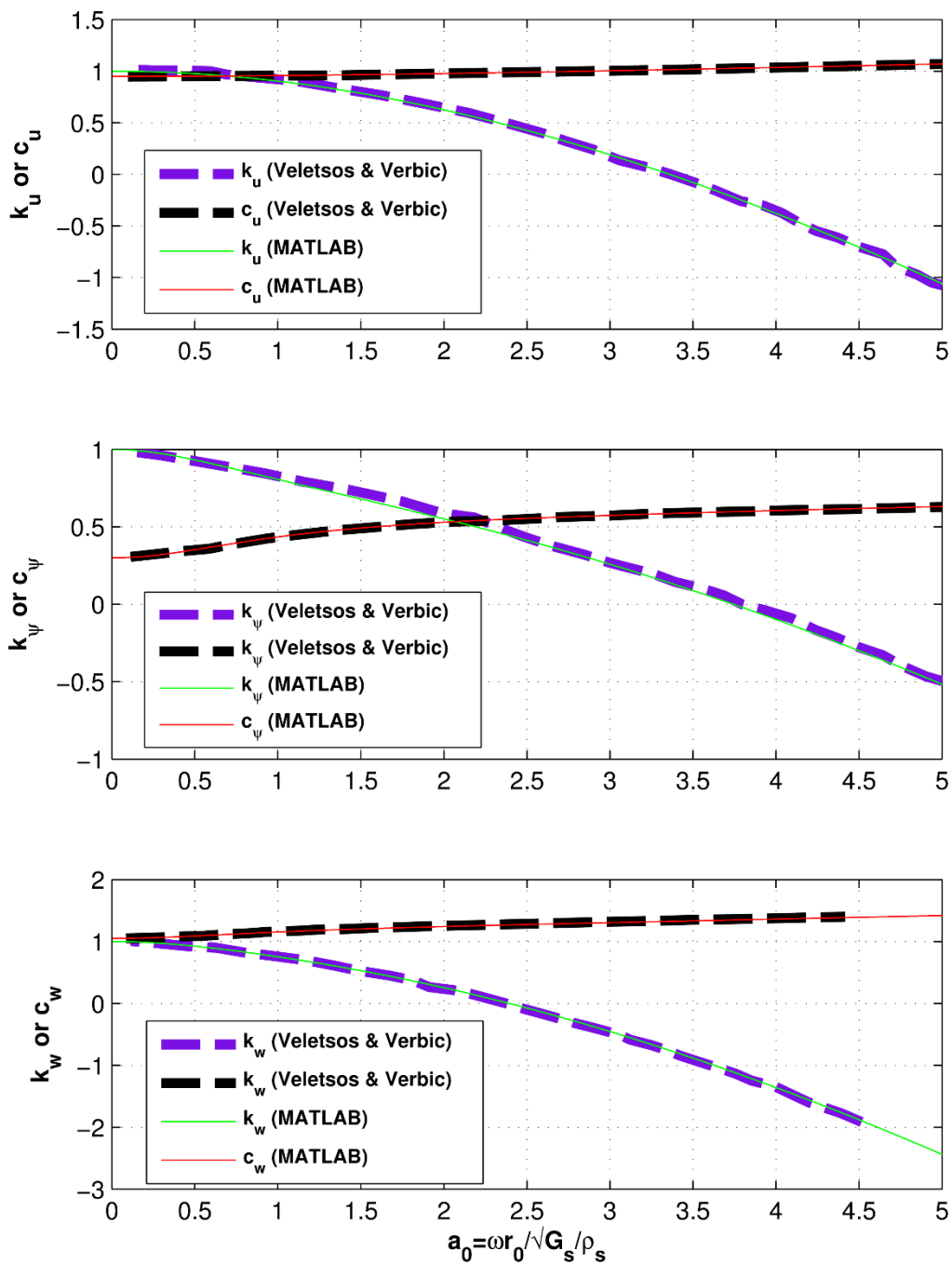


Figure 3-6. Comparison of MATLAB program stiffness and damping parameters at pile tip with results in Figures 3 to 5 of Veletsos and Verbic (1973) for $\nu=1/3$ and $\xi=0.3$.

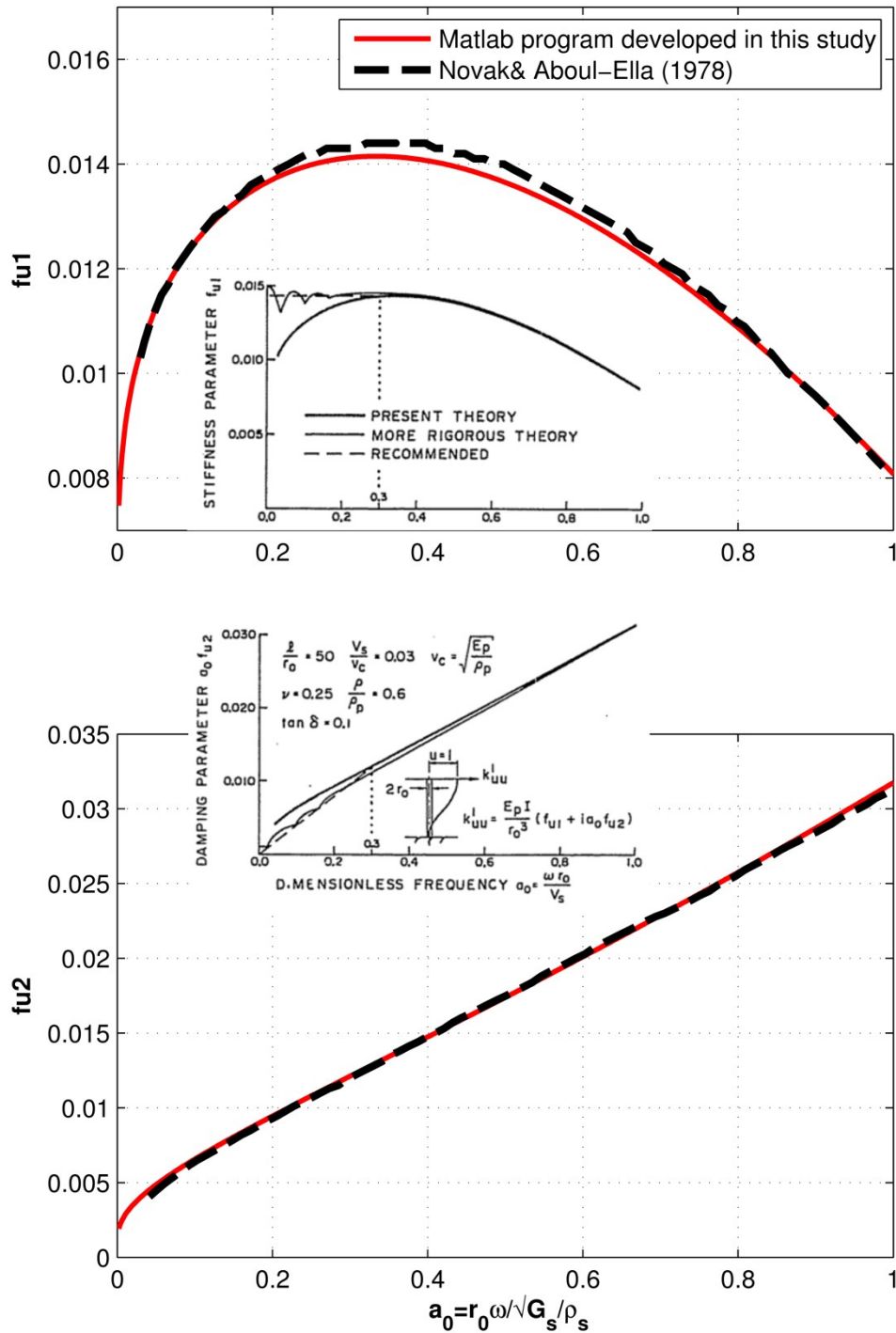


Figure 3-7. Comparison of MATLAB program stiffness and damping parameters at pile tip with results in Figure 1 of Novak and Aboul-Ella (1978) for $\nu_p=0.25$ and fixed tip.

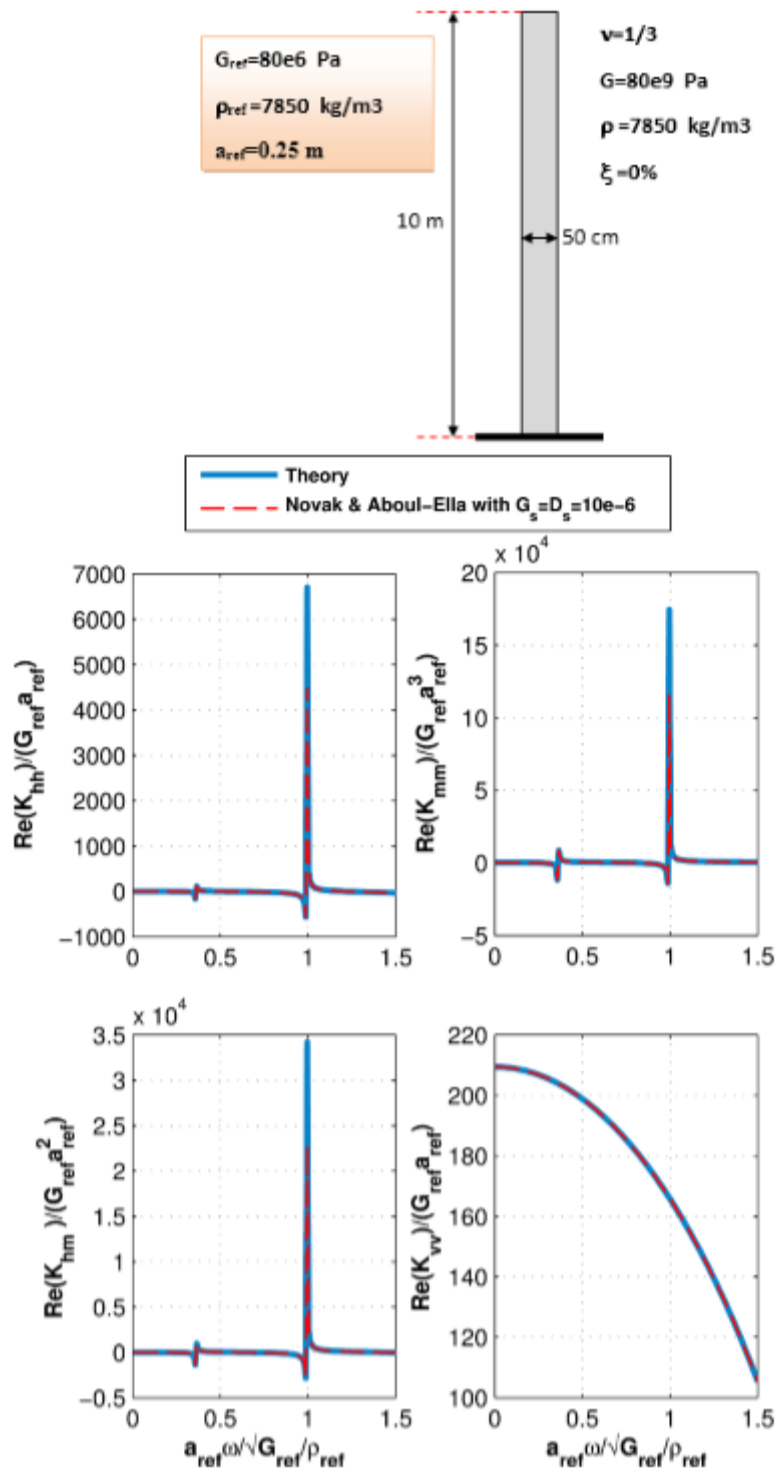


Figure 3-8. Comparison of impedances from MATLAB program for soil-pile problem with $G_s \approx 0$ to exact solution for a cantilever column. The program uses Novak and Aboul-Ella's approximate method.

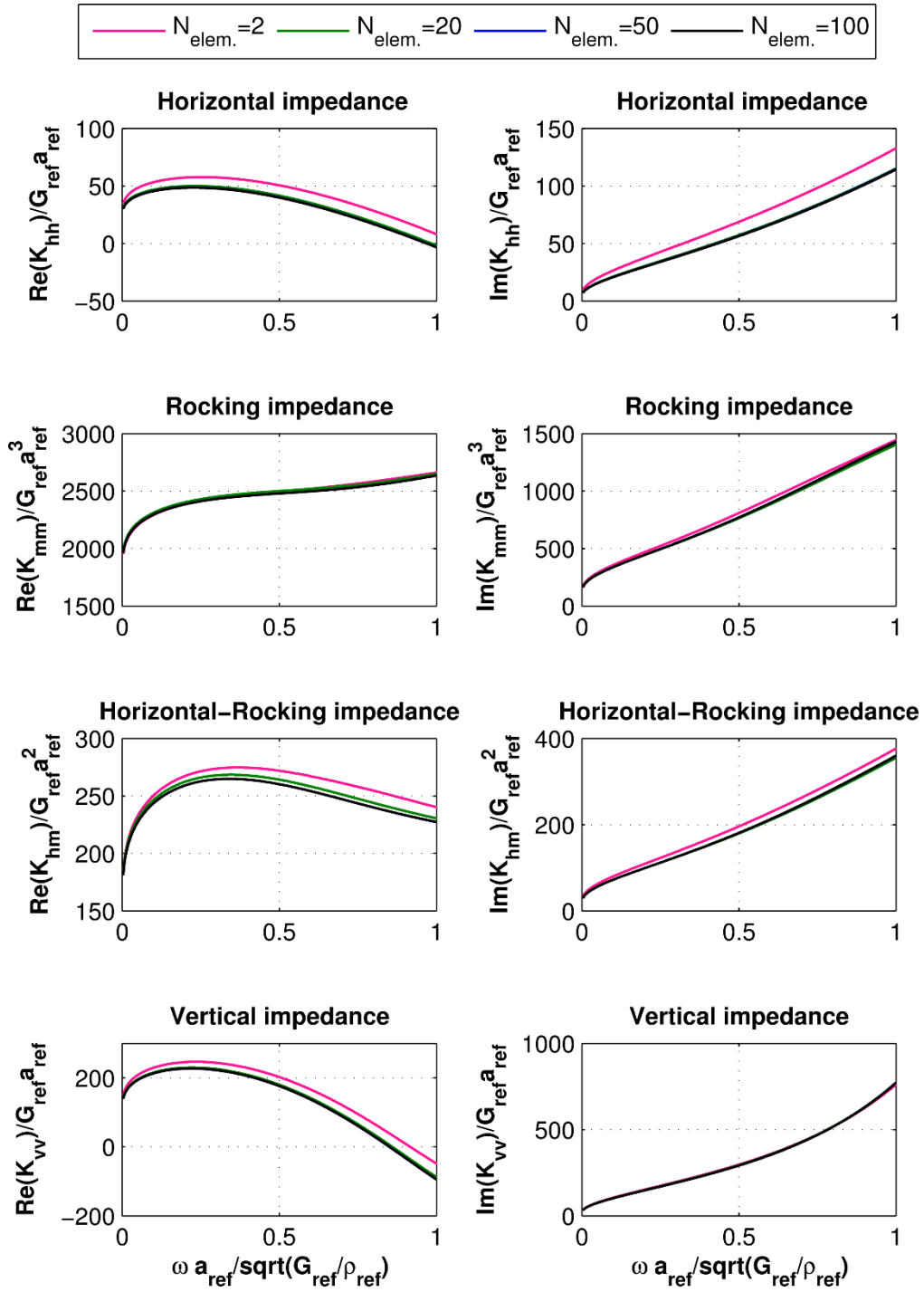


Figure 3-9. Effect of pile mesh size on impedance functions for soil-pile experiment in unimproved soil.

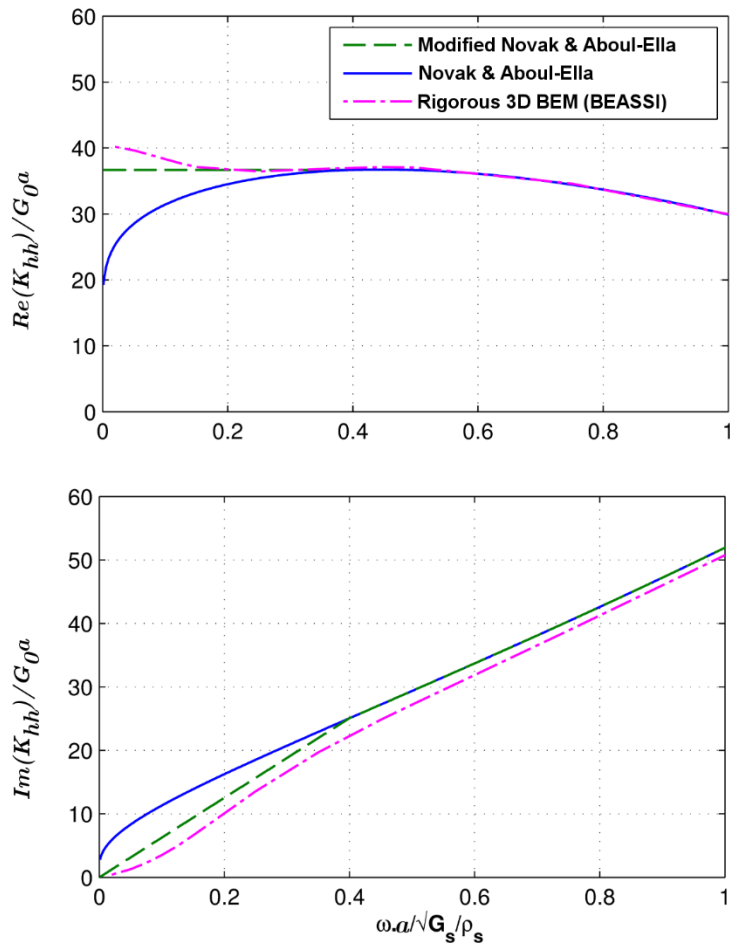
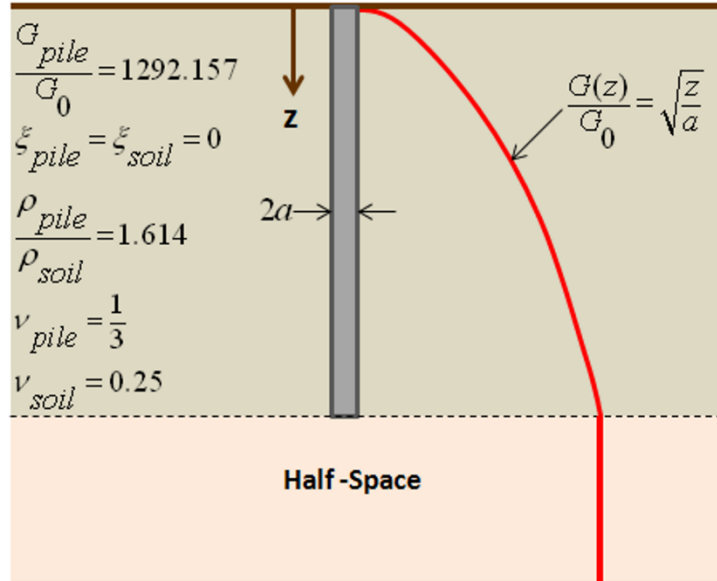


Figure 3-10. Verification of MATLAB program for approximate solution against rigorous 3D boundary element program BEASSI. Horizontal impedance K_{uu} is shown.

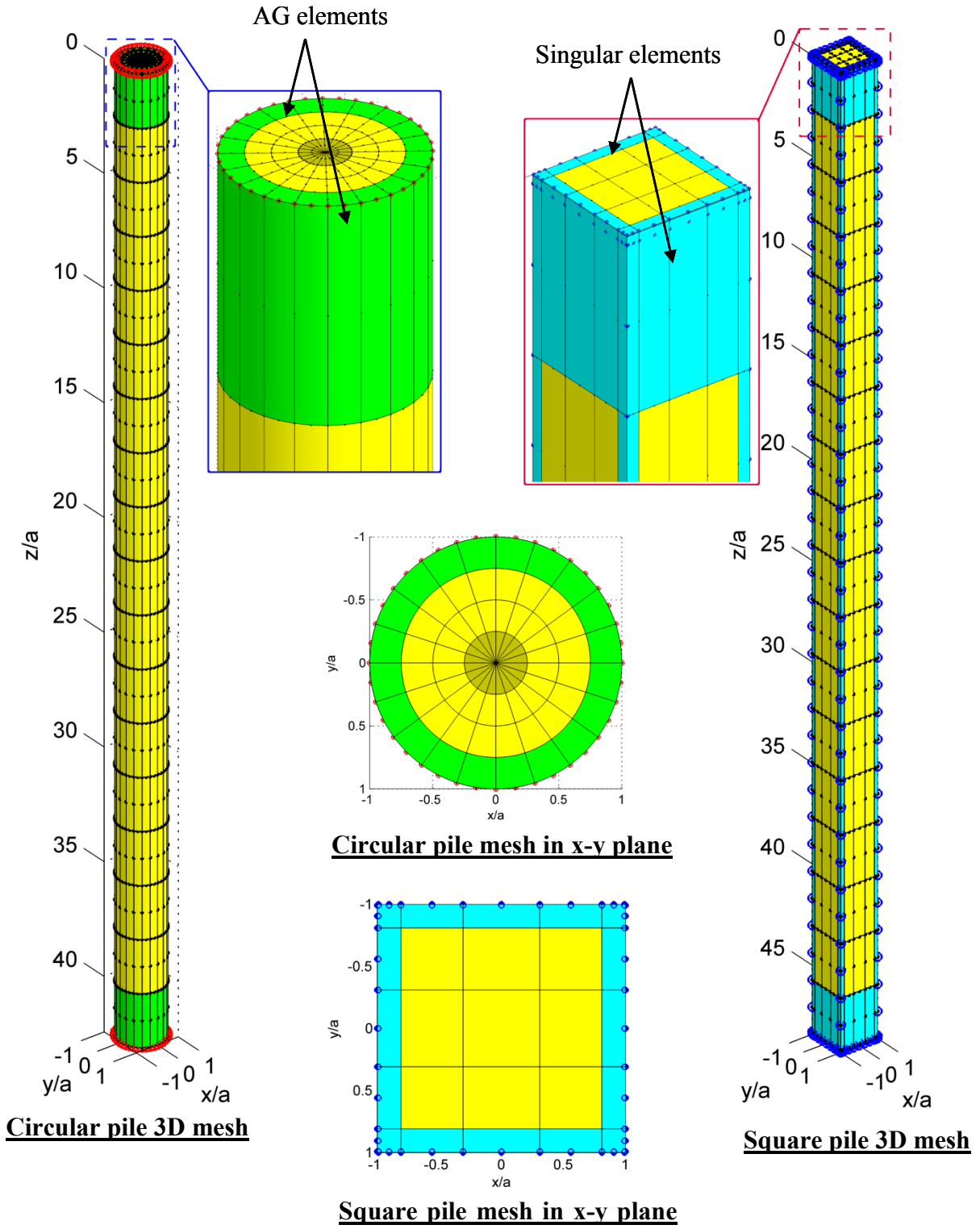


Figure 3-11. BEM meshes for the problems detailed in Table 3-4 and 3-5.

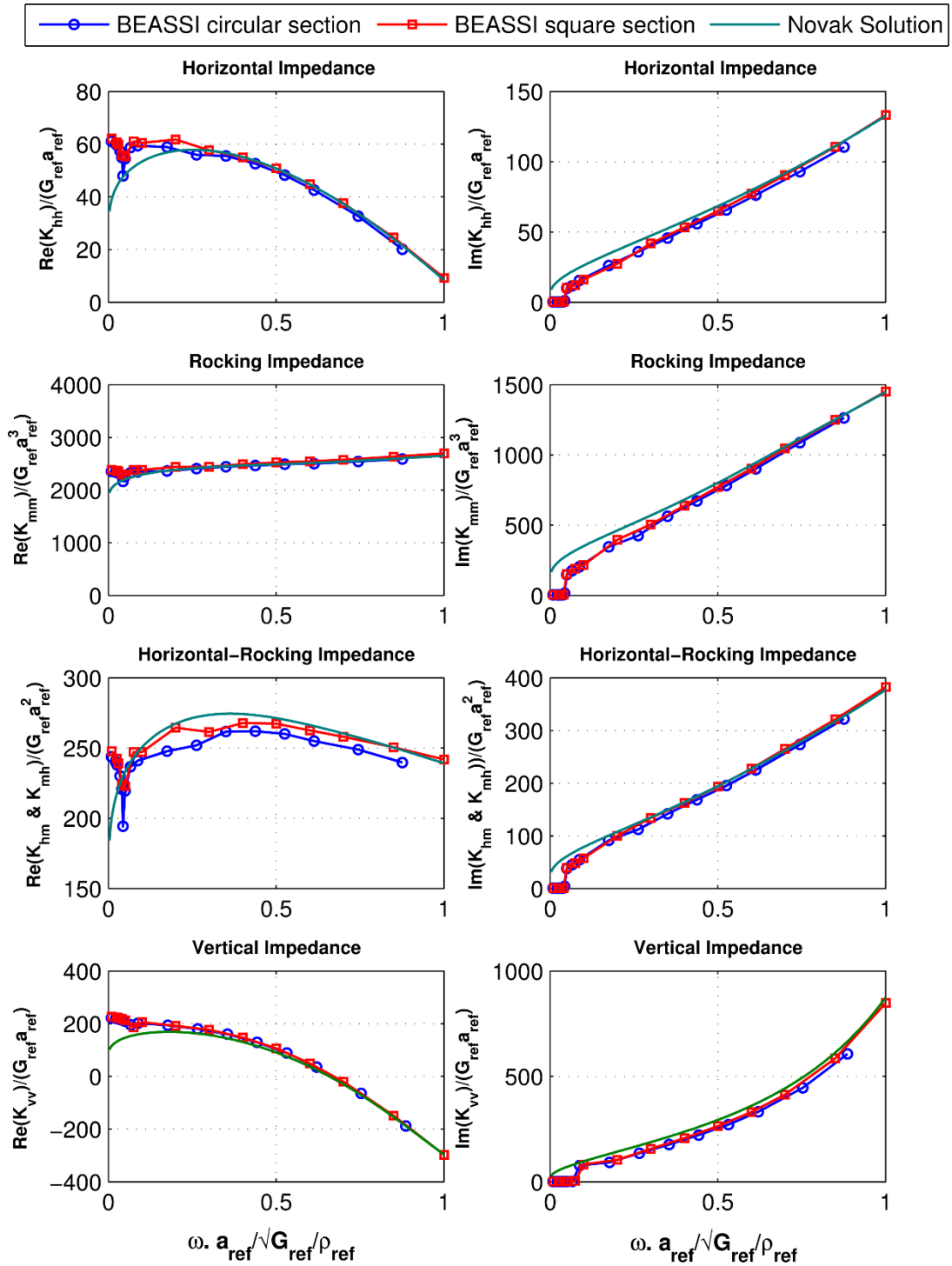


Figure 3-12. Impedance functions for square pile and equivalent circular pile from rigorous 3D BEM analysis compared to approximate solution of Novak and Aboul-Ella.

3.4 Soil-Pile Impedance Functions by Boundary Element Method (BEM)

3.4.1 Overview

The use of integral equation formulations to solve problems in elasto-dynamics dates back to over a century ago (Manolis & Beskos, 1988; Beskos, 1997). Improvements in the numerical techniques required to solve the resulting integral equations, along with advancements in computational power and availability, have refocused attention on integral equation techniques and made this approach useful for many engineering problems, including 3D wave propagation in a half space (Manolis & Beskos, 1988; Beskos, 1997; Bouchon & Sánchez-Sesma, 2007; Hall & Oliveto, 2003; Brebbia & Dominguez, 1996; Brebbia, et al., 1984; Andersen, 2006). One common approach for numerical solution of integral equations is the Boundary Element Method (BEM). In this method, the dimensionality of the original system is reduced by one, such that a 3D problem requires only 2D boundaries of the 3D domains to be discretized. In this section, the basic equations of 3D elasto-dynamics are reviewed and the procedure which leads to the final BEM is summarized.

The following set of basic elasto-dynamic equations govern the 3D wave propagation equation (from Manolis & Beskos, 1988):

$$\begin{array}{l} \text{Equations} \\ \text{of motion:} \end{array} \quad \sigma_{ij,i} + f_j = \rho \ddot{u}_j \quad (3.45)$$

$$\begin{array}{l} \text{Kinematic} \\ \text{relationships:} \end{array} \quad \varepsilon_{ij} = \frac{1}{2} (u_{i,j} + u_{j,i}) \quad (3.46)$$

**Constitutive
law:**

$$\sigma_{ij} = \lambda \varepsilon_{kk} \delta_{ij} + 2\mu \varepsilon_{ij} \quad (3.47)$$

where u , f , σ , ε , and ρ are the displacement, body force, stress tensor, strain tensor and mass density, respectively, and δ_{ij} is the Kronecker delta:

$$\delta_{ij} = \begin{cases} 1, & i = j \\ 0, & i \neq j \end{cases}$$

The Cartesian coordinate system ($i, j=1,2,3$) and the Einstein summation convention for repeated indices are assumed in the formulation, and the Lamé constants are represented by λ and μ .

Combining Equations (3.45) to (3.47) one can write the Navier-Cauchy equations:

$$(\lambda + \mu)u_{i,ij} + \mu u_{j,ii} + f_j = \rho \ddot{u}_i \quad (3.48)$$

with the following boundary and initial conditions:

$$u_i(\mathbf{x}, 0) = u_i^0, \quad \mathbf{x} \in \Omega \quad (3.49)$$

$$\begin{aligned} u_i(\mathbf{x}, t) &= \bar{u}_i, & \mathbf{x} \in \Gamma_u \\ t_i(\mathbf{x}, t) &= \sigma_{ij} n_j = \bar{t}_i, & \mathbf{x} \in \Gamma_t \end{aligned} \quad (3.50)$$

Where \mathbf{x} is the global Cartesian coordinate vector, t_i are traction components, and \mathbf{n} is the unit-outward normal vector. The boundary surface Γ ($\Gamma = \Gamma_u + \Gamma_t$) surrounds domain Ω as shown in

Figure 3-13.

In order to arrive at an integral equation formulation, one can select from among a number of approaches, including the dynamic reciprocal theorem method, variational methods, or weighted residuals. In the weighted residuals method, integration by parts is applied to the basic equations and the fundamental solutions replace the weighting functions which yields the final governing equation.

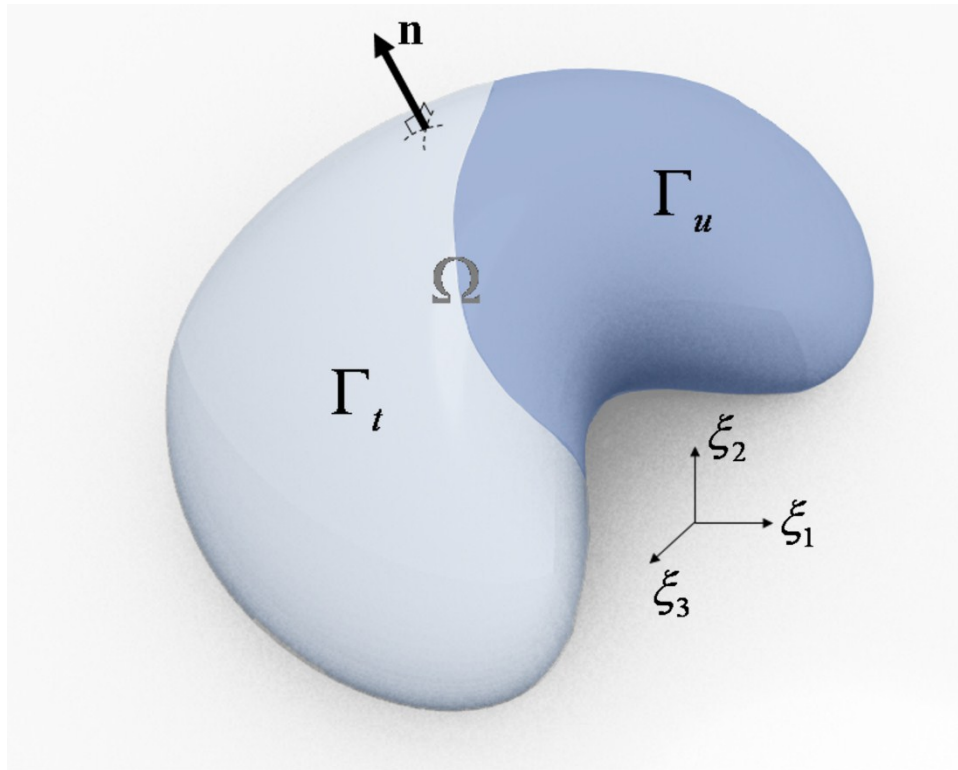


Figure 3-13. Arbitrary 3D solid with finite interior domain Ω bounded by surface $\Gamma = \Gamma_u + \Gamma_t$ (internal problem).

In this study the reciprocal theorem approach is used, which relates two admissible elastodynamic states that satisfy Eq. (3.45). Integrating both sides of the equation of each state over Ω and applying mathematical manipulations that include the divergence theorem leads to the dynamic Betti reciprocal theorem:

$$\begin{aligned}
& \int_{\Gamma} t_i^1 * u_i^2 d\Gamma + \int_{\Omega} f_i^1 * u_i^2 + \rho \left\{ \dot{u}_i^1 \right. \\
& = \int_{\Gamma} t_i^2 * u_i^1 d\Gamma + \int_{\Omega} f_i^2 * u_i^1 + \rho \left\{ \dot{u}_i^2 \right.
\end{aligned} \tag{3.51}$$

where the * operator denotes time convolution, and superscripts refer to the two elasto-dynamic states. The integral equations are most often transformed to the frequency domain to avoid the convolution integrals in the formulation and simplify the analysis. The frequency domain version of Eq. (3.51) can be achieved by taking Fourier transform (\mathcal{F}) of both sides and employing the property that the Fourier transform of a convolution of two functions g and h is the product of the Fourier transforms of the two functions, i.e. $\mathcal{F}[g(t)*h(t)] = G(f)H(f)$, where t and f denote time and frequency, respectively. Taking the Fourier transform of Equation (3.50) thus gives

$$\int_{\Gamma} T_i^1 U_i^2 d\Gamma + \int_{\Omega} F_i^1 U_i^2 d\Omega = \int_{\Gamma} T_i^2 U_i^1 d\Gamma + \int_{\Omega} F_i^2 U_i^1 d\Omega \tag{3.52}$$

This frequency domain formulation simplifies the solution of problems in linear viscoelasticity. Material damping can be easily handled in the frequency domain according to the elastic-viscoelastic correspondence principle (Christensen, 1971) by replacing the elasticity constants with complex values, with the imaginary part proportional to material damping.

The solution for displacement at a point ξ in direction i due to a concentrated pulse at point \mathbf{x} in direction k is known as fundamental solution. In other words, the fundamental solution is the solution to Eq. (3.48) with the body force (or its Fourier transform) taken as

$$f_i^k = \delta_{ik} \delta(\boldsymbol{\xi} - \mathbf{x}) \delta(t - \tau) \quad (F_i^k = \delta_{ik} \delta(\boldsymbol{\xi} - \mathbf{x})) \quad (3.53)$$

Where the Dirac delta function is defined as:

$$\delta(\mathbf{x} - \boldsymbol{\xi}) = \begin{cases} \infty, & \mathbf{x} = \boldsymbol{\xi} \\ \mathbf{0}, & \mathbf{x} \neq \boldsymbol{\xi} \end{cases} \quad \text{and} \quad \int_{\Omega} \delta(\mathbf{x} - \boldsymbol{\xi}) d\Omega = 1 \quad (3.54)$$

Green's functions are the fundamental solutions that are forced to satisfy the boundary conditions. For the problem of wave propagation in a half-space, the fundamental solution is defined as the exact solution to the governing equation of the external-domain problem, where a concentrated unit load is applied inside the domain Ω , and the displacement and traction also satisfy the radiation conditions which specify that they decay to zero at the infinite boundary.

Now if one of the two states in Eq. (3.52) is taken as the fundamental solution, $(\hat{U}_i^k, \hat{T}_i^k, \hat{F}_i^k)$, and the other as the unknown solution to physical problem, Eq. (3.52) reduces to the following governing integral equation for the internal-domain problem:

$$\begin{aligned} D(\mathbf{x})U_k(\mathbf{x}, \omega) &= \int_{\Gamma} \hat{U}_i^k(\mathbf{x}, \boldsymbol{\xi}, \omega) T_i(\boldsymbol{\xi}, \omega) d\Gamma - \int_{\Gamma} \hat{T}_i^k(\mathbf{x}, \boldsymbol{\xi}, \omega) U_i(\boldsymbol{\xi}, \omega) d\Gamma \\ &+ \int_{\Omega} \hat{U}_i^k(\mathbf{x}, \boldsymbol{\xi}, \omega) F_i(\boldsymbol{\xi}, \omega) d\Omega \quad D(\mathbf{x}) = \begin{cases} 1 & \mathbf{x} \in \Omega \\ 0 & \mathbf{x} \notin \Omega \end{cases} \end{aligned} \quad (3.55)$$

since

$$\int_{\Omega} \delta_{ik} \delta(\mathbf{x} - \boldsymbol{\xi}) U_i(\boldsymbol{\xi}, \omega) d\Omega = U_k(\mathbf{x}, \omega) \quad (3.56)$$

by the sifting property of the delta function.

Upon deriving the integral equation formulation for an external-domain problem where Γ is a closed surface surrounded by an infinite domain Ω which also has a boundary Γ_ρ at infinity, one will arrive at the same equation as (3.55) with the only difference that the normal vector \mathbf{n} is in the opposite direction (Brebbia & Dominguez, 1996), (Brebbia, et al., 1984).

The integral equation (3.55) provides the value of $U_i(\mathbf{x}, \omega)$ at any point in Ω , in terms of the boundary values of traction and displacement, and the body force F . For dynamic soil problems in which the only body force is due to gravity, the resulting static components of stress are easily calculated, so F is commonly set to zero and the only unknowns in Eq. (3.55) are the dynamic tractions and displacements on the boundary. Therefore unlike the finite element method, only the boundary surface Γ is discretized rather than the entire domain volume Ω .

The integrals over the surface Γ in Eq. (3.55) are regular and calculable if point \mathbf{x} is not located on the boundary. Otherwise if ($\xi=\mathbf{x}$) the first two integrals will become singular and require special treatment. This fact suggests the investigation of Eq. (3.55) for the limiting case where $\mathbf{x} \rightarrow \mathbf{y} \in \Gamma$. It will be performed by decomposing the surface into Γ_ε and $\Gamma - \Gamma_\varepsilon$ where Γ_ε is a small region with radius ε surrounding point \mathbf{y} (Figure 3-14). Taking the limit, $\varepsilon \rightarrow 0$ the prescribed limiting case is reached.

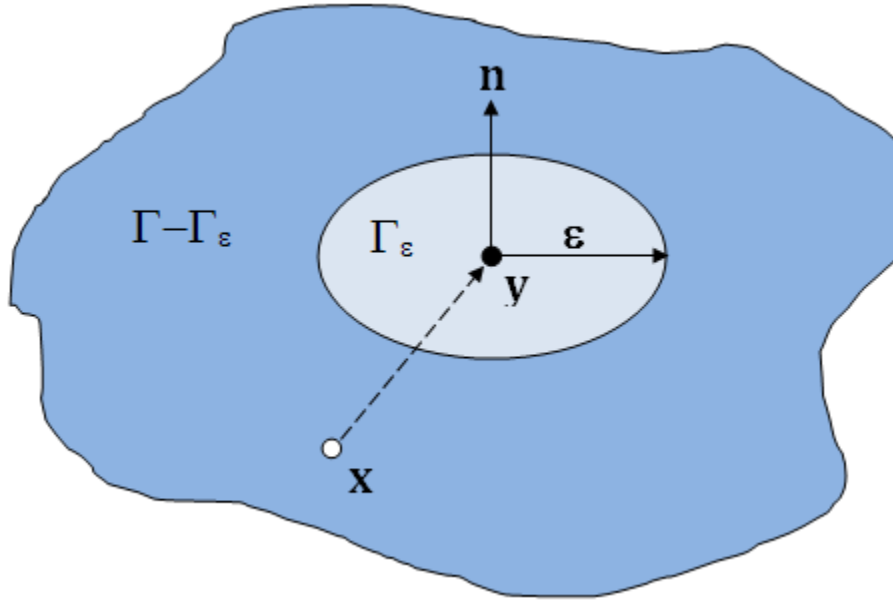


Figure 3-14. Part of the boundary surface that has been decomposed into Γ_ε and $\Gamma - \Gamma_\varepsilon$ where $\mathbf{x} \in \Omega$ and $\mathbf{x} \rightarrow \mathbf{y} \in \Gamma$.

The limiting state can be expressed in the form of the following conventional direct boundary integral equations (one for each direction k of the point load):

$$c_{ik}(\mathbf{y})U_i(\mathbf{y}, \omega) = \int_{\Gamma} \hat{U}_i^k(\mathbf{y}, \boldsymbol{\xi}, \omega) T_i(\boldsymbol{\xi}, \omega) d\Gamma - \int_{\Gamma} \hat{T}_i^k(\mathbf{y}, \boldsymbol{\xi}, \omega) U_i(\boldsymbol{\xi}, \omega) d\Gamma + \int_{\Omega} \hat{U}_i^k(\mathbf{y}, \boldsymbol{\xi}, \omega) F_i(\boldsymbol{\xi}, \omega) d\Omega \quad (3.57)$$

where the second integral is the Cauchy principal value of the surface integral, and

$$c_{ik}(\mathbf{y}) = \delta_{ik} + \lim_{\varepsilon \rightarrow 0} \lim_{\mathbf{x} \rightarrow \mathbf{y}} \int_{\Gamma_\varepsilon} \hat{T}_i^k(\mathbf{x}, \boldsymbol{\xi}, \omega) d\Gamma \quad (3.58)$$

which must first be evaluated analytically for various geometries (i.e., a smooth surface or a 2D or 3D corner). For a smooth surface on a homogenous isotropic solid, one can show that $c_{ik} = \delta_{ik} / 2$.

The boundary integral equations must first be solved numerically for the displacement and traction

on the boundary. Having the boundary values one can then find the displacement of any point in the domain Ω using Eq. (3.55).

The conventional direct BIE formulation above presents challenges in the required evaluation of Cauchy principal values and the coefficients c_{ik} . As an alternative, the regularized direct boundary integral equation approach (Pak & Guzina, 1999, Ashlock, 2006) is free from these difficulties, and will be used in this study. The regularized formulation splits the regular and singular parts of the traction Green's function for zero body-force fields as

$$\int_{\Gamma} \hat{U}_i^k(\mathbf{y}, \boldsymbol{\xi}, \omega) T_i(\boldsymbol{\xi}, \omega) d\Gamma - \int_{\Gamma} [\hat{T}_i^k(\mathbf{y}, \boldsymbol{\xi}, \omega)]_1 [U_i(\boldsymbol{\xi}, \omega) - U_i(\mathbf{y}, \omega)] d\Gamma - \int_{\Gamma} [\hat{T}_i^k(\mathbf{y}, \boldsymbol{\xi}, \omega)]_2 U_i(\boldsymbol{\xi}, \omega) d\Gamma = \begin{cases} 0, & \text{Internal Domain} \\ 1, & \text{External Domain} \end{cases} U_k(\mathbf{y}, \omega) \quad (3.59)$$

where $[\hat{T}_i^k(\mathbf{y}, \boldsymbol{\xi}, \omega)]_1$ and $[\hat{T}_i^k(\mathbf{y}, \boldsymbol{\xi}, \omega)]_2$ are the singular and regular components of the traction Green's function ($\hat{T}_i^k(\mathbf{y}, \boldsymbol{\xi}, \omega) = [\hat{T}_i^k(\mathbf{y}, \boldsymbol{\xi}, \omega)]_1 + [\hat{T}_i^k(\mathbf{y}, \boldsymbol{\xi}, \omega)]_2$). The above regularized BIE contains only regular and weakly singular integrals.

The next step is to divide the boundary of the problem into a finite number of elements incorporating a total of N nodes where, analogous to FEM, the shape functions are used to interpolate the nodal geometry, displacement, and traction values. To obtain the system of equations, the method of collocation (Brebbia, et al., 1984, Pak & Guzina, 1999) is applied, whereby Eq. (3.59) is enforced at the N nodal points on the problem boundary in the three directions (ξ_1, ξ_2, ξ_3). Collocating at each source point in each direction, a system of $3N$ integral equations is generated, with each equation containing $3N$ nodal displacements and $3N$ nodal tractions. The constant nodal values are factored outside the integrals and the remaining terms are

evaluated numerically. Upon evaluating all the integrals for all the collocation nodes, the final global linear system of equations

$$\mathbf{H}\mathbf{U} = \mathbf{G}\mathbf{T} \quad (3.60)$$

results, where \mathbf{T} and \mathbf{U} are the traction and displacement vectors, and the \mathbf{H} and \mathbf{G} matrices contain influence coefficients. Elements of matrix \mathbf{H} contain products of displacement shape functions and traction Green's functions, while matrix \mathbf{G} contains products of traction shape functions and displacement Green's functions. Upon prescribing either displacement or traction at each node (or compatibility conditions for multi-domain problems), Equation (3.59) is rearranged to solve for the remaining unknowns. In contrast to the banded matrices of the finite element method, BEM matrices are full and complex-valued. The main cost of this method is associated with the numerical computation of the Green's functions and integrals, especially for the complicated multi-layered Green's functions used herein, which are not available in closed form.

The boundary element method (BEM) is very attractive for problems with unbounded domains, because fundamental solutions are available which exactly satisfy the radiation conditions. This avoids artificial wave reflections at boundaries, which is a problem for finite element simulations. Although infinite elements and other absorbing boundary techniques have been developed for FEM simulation of wave propagation, they are generally not capable of completely eliminating reflections in 2D or 3D problems.

The boundary element program BEASSI used in this study features Green's functions for a multi-layered viscoelastic half-space (Pak & Guzina, 2002). Despite the many appealing factors in using the BEM, one must address issues of accurate integration of singular Green's functions, as well as integration across their discontinuities at soil layer interfaces. In BEASSI, these issues

are treated by using a regularized multi-domain formulation (Pak & Guzina, 1999), which replaces the conventional direct method and decomposes the formulation into regular and weakly singular parts. The program also employs additional mappings for nearly-singular integrals over elements close to the collocation node, and an adaptive Gauss integration scheme to ensure accuracy of the integrals (Ashlock, 2006). Another issue requiring careful attention is the singularity of tractions near material corners and at locations of mixed boundary conditions. Singular tractions can be handled in BEASSI using special singular elements (Guzina, et al., 2006) or Adaptive-Gradient (AG) elements (Pak & Ashlock, 2007). The singular elements require internal nodes shifted away from the singular edges, while the AG elements are compatible with standard mesh configurations.

3.4.2 BEM program verification

A set of verification scenarios are presented herein to examine BEASSI before using it to analyze the primary problem of interest. A schematic of two approaches discussed in this study to solve pile-soil problems is presented in Figure 3-15. Two-domain problems consist of a pile domain with a semi-infinite far-field soil domain surrounding it, while three-domain problems also include a finite disturbed zone surrounding the pile, sometimes referred to as an “inclusion”. The use of the disturbed zone and its advantages are discussed in detail in Chapter 4. Verifications are presented in this section for both two- and three-domain problems.

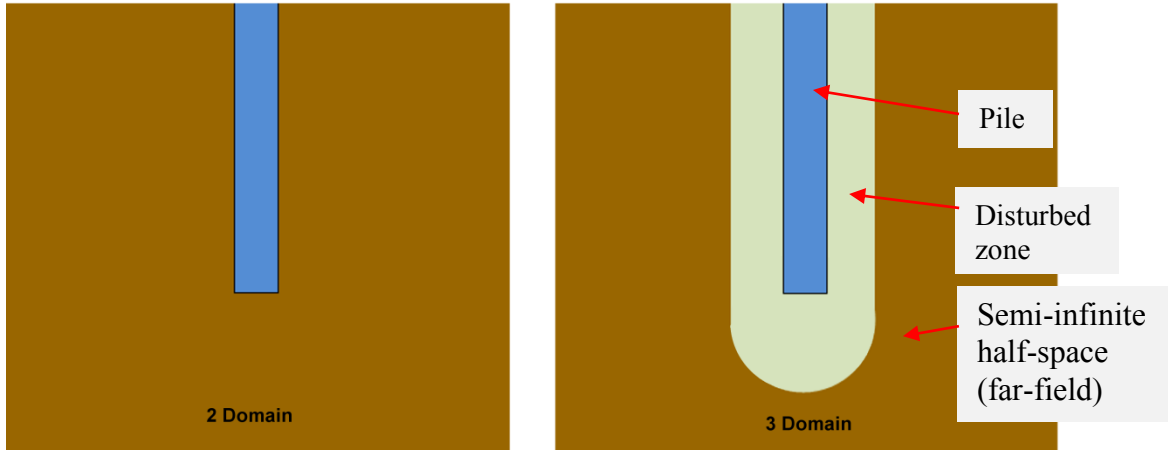


Figure 3-15. Two-domain and three-domain approaches to modelling soil-pile problems.

3.4.2.1 Two-domain model

3.4.2.1.1 Dimensional versus dimensionless input/output

When using the boundary element program BEASSI, the numerical parameters in the text input files (i.e., physical dimensions, moduli, densities, and frequency) can be specified in any consistent set of units, in which case the output values can be interpreted as having the same set of units. Due to the linearity of the program, all input and output can more conveniently be thought of as dimensionless, with all input lengths normalized by a reference length a_{ref} , shear moduli normalized by a reference modulus G_{ref} , and so on. For example, an x -coordinate of 0.5 in the input files would be interpreted as $x/a_{\text{ref}}=0.5$, and a shear modulus of 2 as $G/G_{\text{ref}}=2$.

To verify this behavior, the dimensions of the input parameters and resulting output values were evaluated using BEASSI to solve a two-domain soil-pile problem in a homogenous half-space with three different sets of reference values. The problem inputs for all three cases are given in Table 3-6. The reference values shown in the table were used to normalize the dimensional input parameters and generate corresponding dimensionless input files. For each case, the problem was

run for the four dimensionless angular frequencies $\omega a_{ref} / \sqrt{G_{ref} / \rho_{ref}} = 0.25, 0.5, 1, \text{ and } 2$, and the resulting raw dimensionless output impedances are plotted in Figure 3-16. Since all three cases are modeling the same physical problem, the output impedance functions should be identical regardless of the reference values. This fact is verified in Figure 3-17, where all three cases are shown to result in the same dimensional impedances after scaling the dimensionless values. Figure 3-18 also confirms the same finding for the problem analyzed with the actual dimensional input parameters (i.e., all reference values are set to 1), compared to the dimensionalized results of Case 1.

These test cases verify that the program can be used with dimensionless or dimensional input parameters, and the corresponding raw output values should be interpreted with caution. In particular, users should be careful to convert the dimensionless to corresponding dimensional frequencies.

Table 3-6. Two-domain pile problem defined by three different cases of reference values to check linearity of solution and dimensionality of program input and output.

	Case 1	Case 2	Case 3
a_{pile} (m)	1	1	1
G_{pile} (Pa)	25.099e9	25.099e9	25.099e9
ν_{pile}	0.333	0.333	0.333
ρ_{pile} (kg/m ³)	7850	7850	7850
G_{soil} (Pa)	56e6	56e6	56e6
ν_{soil}	0.25	0.25	0.25
ρ_{soil} (kg/m ³)	2000	2000	2000
L_{pile} (m)	26.6	26.6	26.6
Soil material damping ratio	0%	0%	0%
Mesh size (x,y,z)	6x6x10	6x6x10	6x6x10
a_{ref} (m)	2	1	2
G_{ref} (Pa)	112e6	56e6	14e6
ρ_{ref} (kg/m³)	4000	2000	2000
$\bar{\omega} = \frac{a_{ref}}{\sqrt{\frac{G_{ref}}{\rho_{ref}}}} \omega$	0.01195 ω	0.00598 ω	0.02391 ω
$\bar{k}_{hh} = \frac{k_{hh}}{G_{ref} a_{ref}}$	$\frac{k_{hh}}{224 \times 10^6}$	$\frac{k_{hh}}{56 \times 10^6}$	$\frac{k_{hh}}{28 \times 10^6}$
$\bar{k}_{hm} = \frac{k_{hm}}{G_{ref} a_{ref}^2}$	$\frac{k_{hm}}{448 \times 10^6}$	$\frac{k_{hm}}{56 \times 10^6}$	$\frac{k_{hm}}{56 \times 10^6}$
$\bar{k}_{mm} = \frac{k_{mm}}{G_{ref} a_{ref}^3}$	$\frac{k_{mm}}{896 \times 10^6}$	$\frac{k_{mm}}{56 \times 10^6}$	$\frac{k_{mm}}{112 \times 10^6}$
$\bar{k}_{vv} = \frac{k_{vv}}{G_{ref} a_{ref}}$	$\frac{k_{vv}}{224 \times 10^6}$	$\frac{k_{mm}}{56 \times 10^6}$	$\frac{k_{vv}}{28 \times 10^6}$

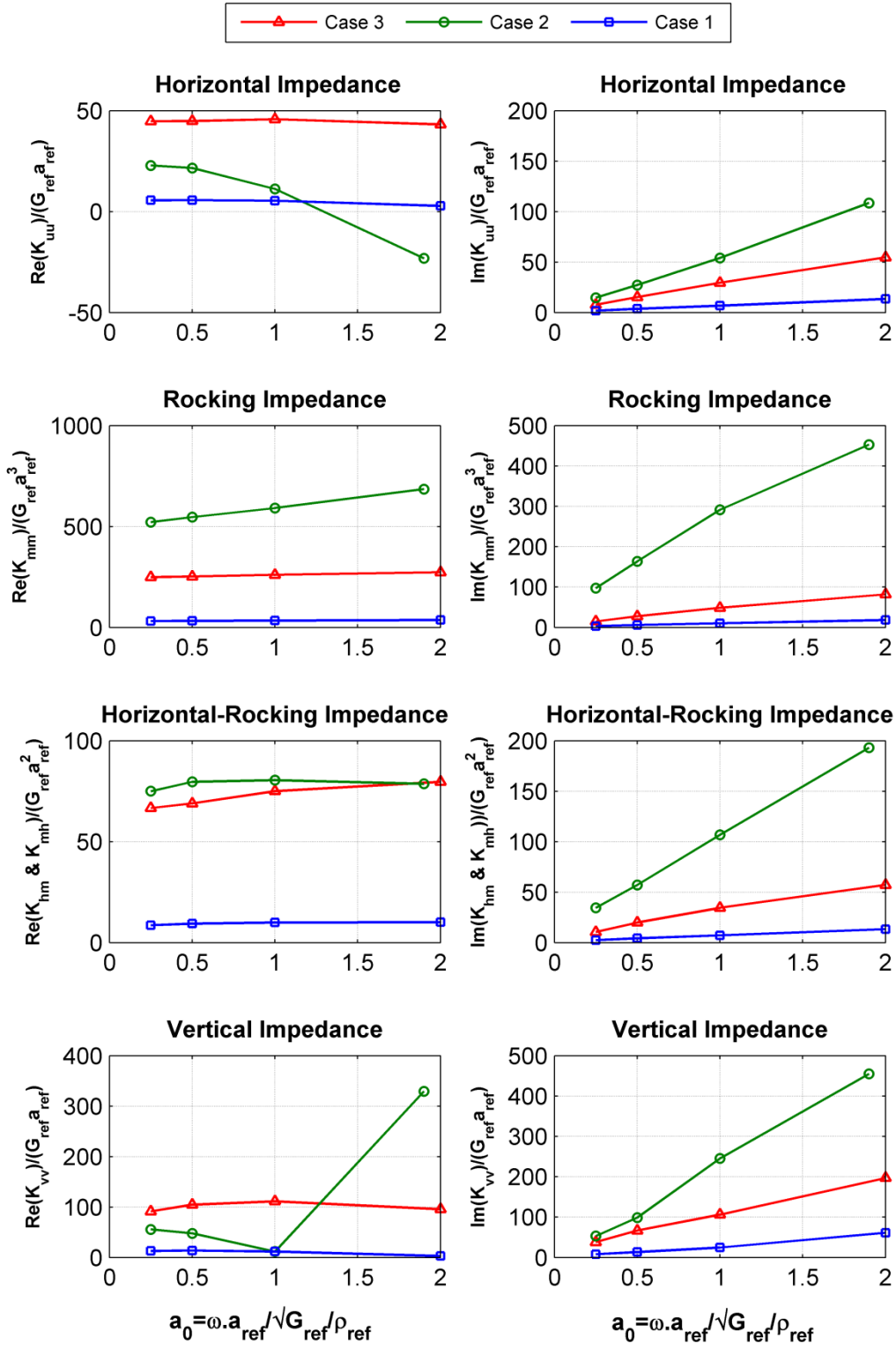


Figure 3-16. Raw non-dimensional impedances output from BEASSI for the three cases under study.

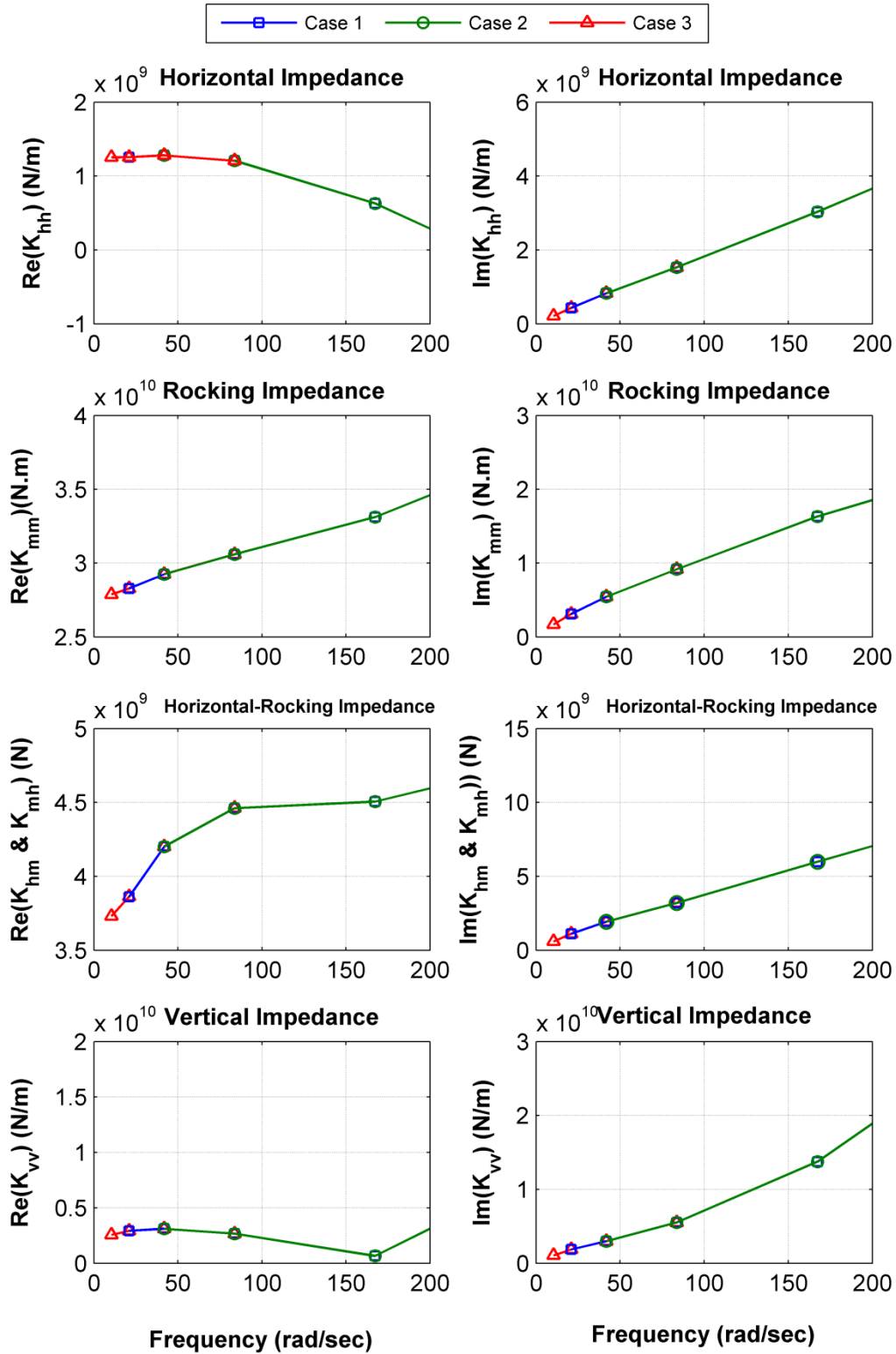


Figure 3-17. Dimensionalized impedances from BEASSI for the three cases under study.

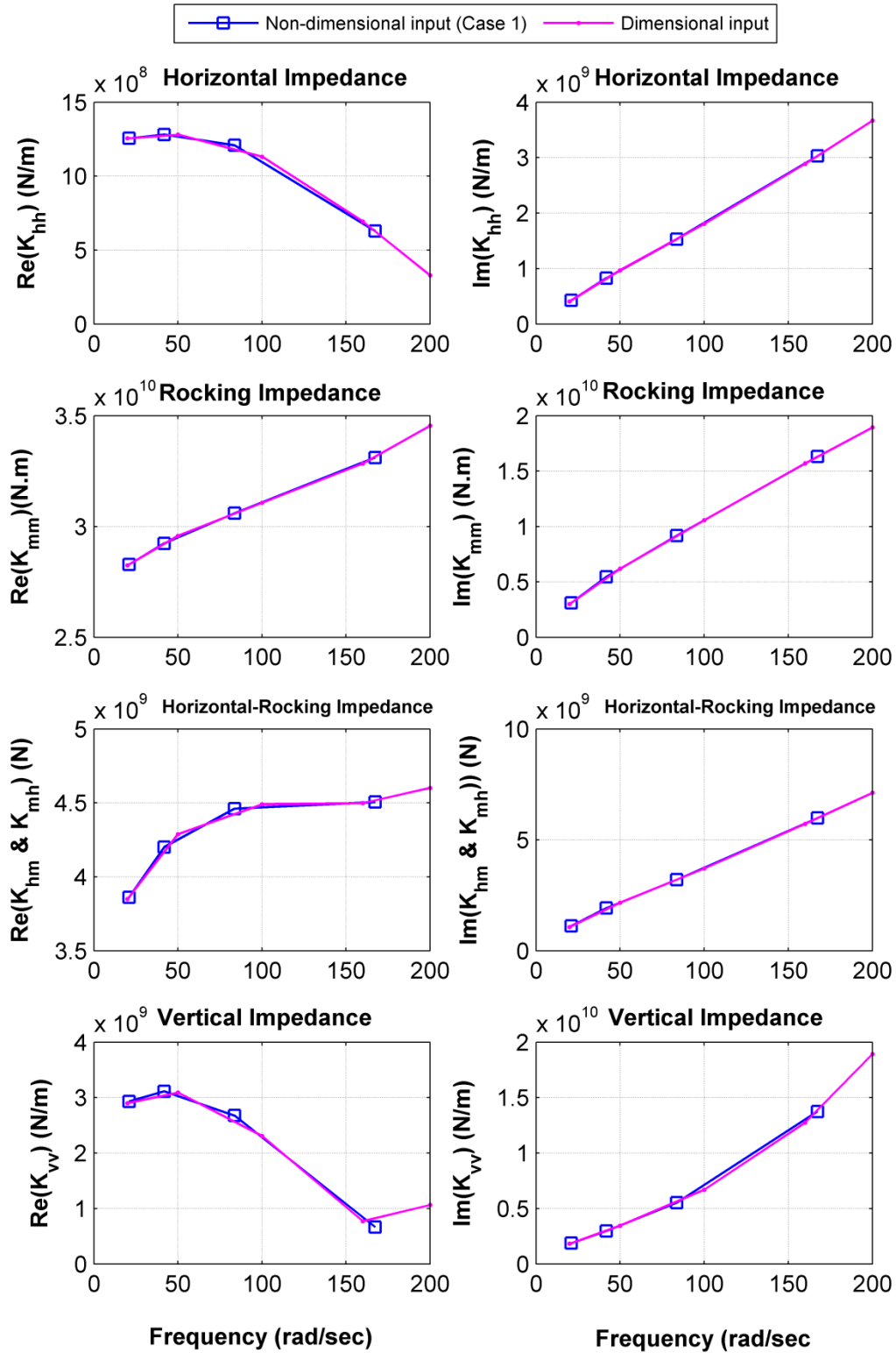


Figure 3-18. Comparison of BEASSI results using dimensional vs. dimensionless input.

3.4.2.1.2 Free-standing cantilever beam-column test problem

The cantilever column problem described in Table 3-7 was used to verify the accuracy of BEASSI for a problem with a known closed-form solution. Unit displacements and rotations were applied at the top of a free-standing beam-column fixed at its bottom end, and the resulting impedance functions were calculated. The comparison of the results with the analytical solution in Figure 3-19 shows that the program accurately follows the exact analytical solution for this problem.

Table 3-7. Properties of free-standing circular cantilever beam-column.

a_{pile} (m)	1
G_{pile} (Pa)	80e9
ν_{pile}	0.333
ρ_{pile} (kg/m ³)	7,850
L_{pile} (m)	26.6
Mesh size (r,θ,z)	4x8x10
a_{ref} (m)	1
G_{ref} (Pa)	40e6
ρ_{ref} (kg/m ³)	7,850

3.4.2.1.3 Adaptive gradient elements vs. singular elements

To assess the performance of the two classes of elements available in BEASSI for handling problems with singularities or high gradients, the problem of a massless, rigid square footing on the surface of a homogeneous half-space was analyzed with a 6x6 mesh of 8-node quadrilateral elements, using singular or AG elements at the edges. The radiation problem type was selected in

BEASSI, for which unit displacements and rotations are prescribed, and the resulting tractions integrated to obtain the dynamic impedance functions. Owing to the efficiency of the AG and singular elements, the impedance functions for both element types are very close, even for this relatively coarse mesh (Figure 3-20).

3.4.2.1.4 One-domain surface footing vs. 2-domain problem with pile mesh

A number of new mesh generators were programmed to analyze the pile-soil problems in this study. To check the validity of the new mesh generators and input files, a high-level verification was performed by comparing the results of a one-domain rigid surface footing analysis to those of a two-domain soil-pile analysis in which the pile properties are set equal to those of the soil. This will test several aspects of the programming and input files at once, including the specification of properties and compatibility conditions for the multiple domains, the element connectivity and singularity parameters, and the shifted node locations for the singular or AG elements at corners and edges. The excellent agreement of impedance functions for the one- and two-domain problems shown in Figure 11 indicate that the new mesh generators are programmed correctly.

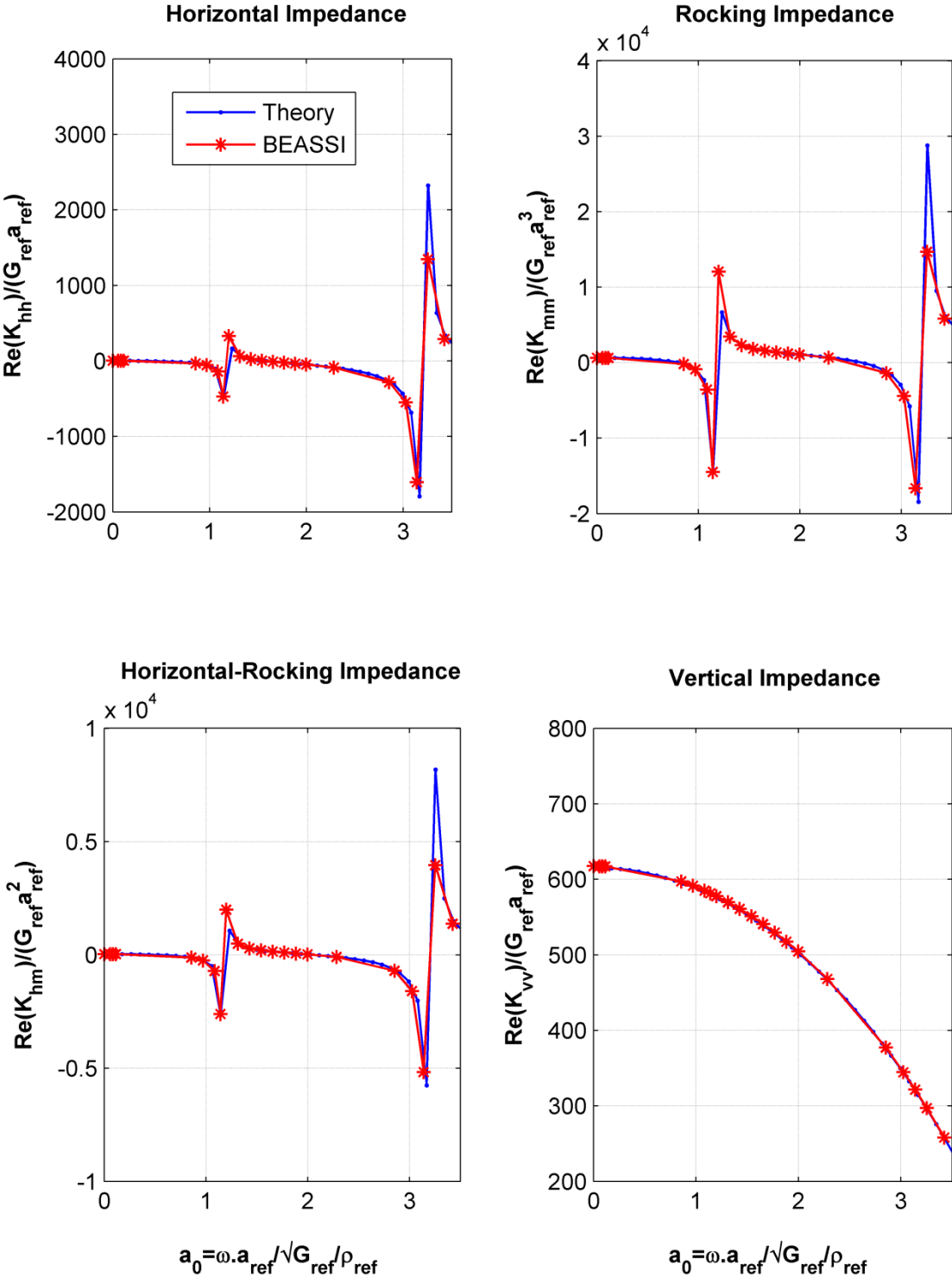


Figure 3-19. BEASSI results vs. theoretical solution for the cantilever beam-column.

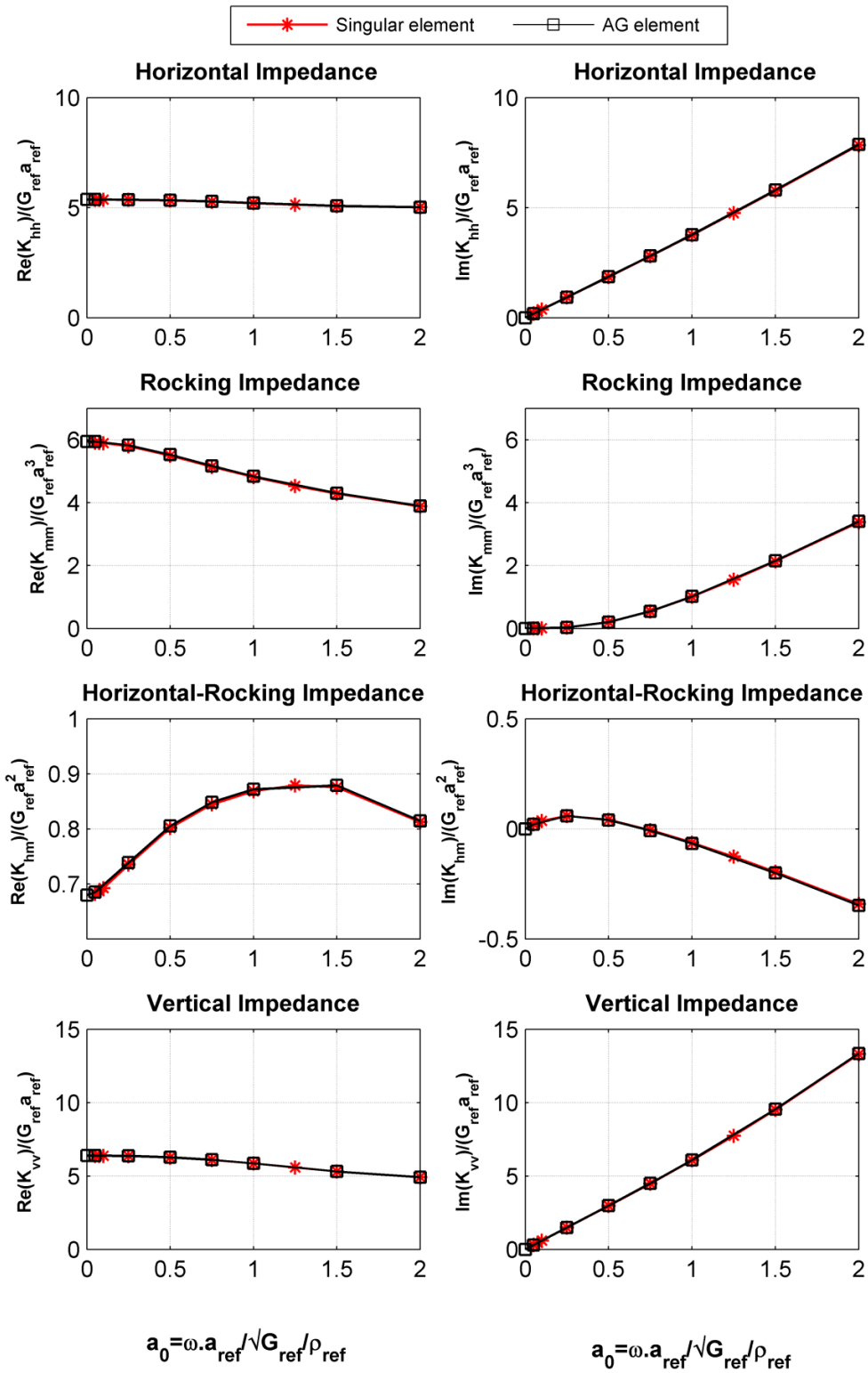


Figure 3-20. Impedance functions for rigid square surface footing on homogeneous half-space, obtained with AG vs. singular elements.

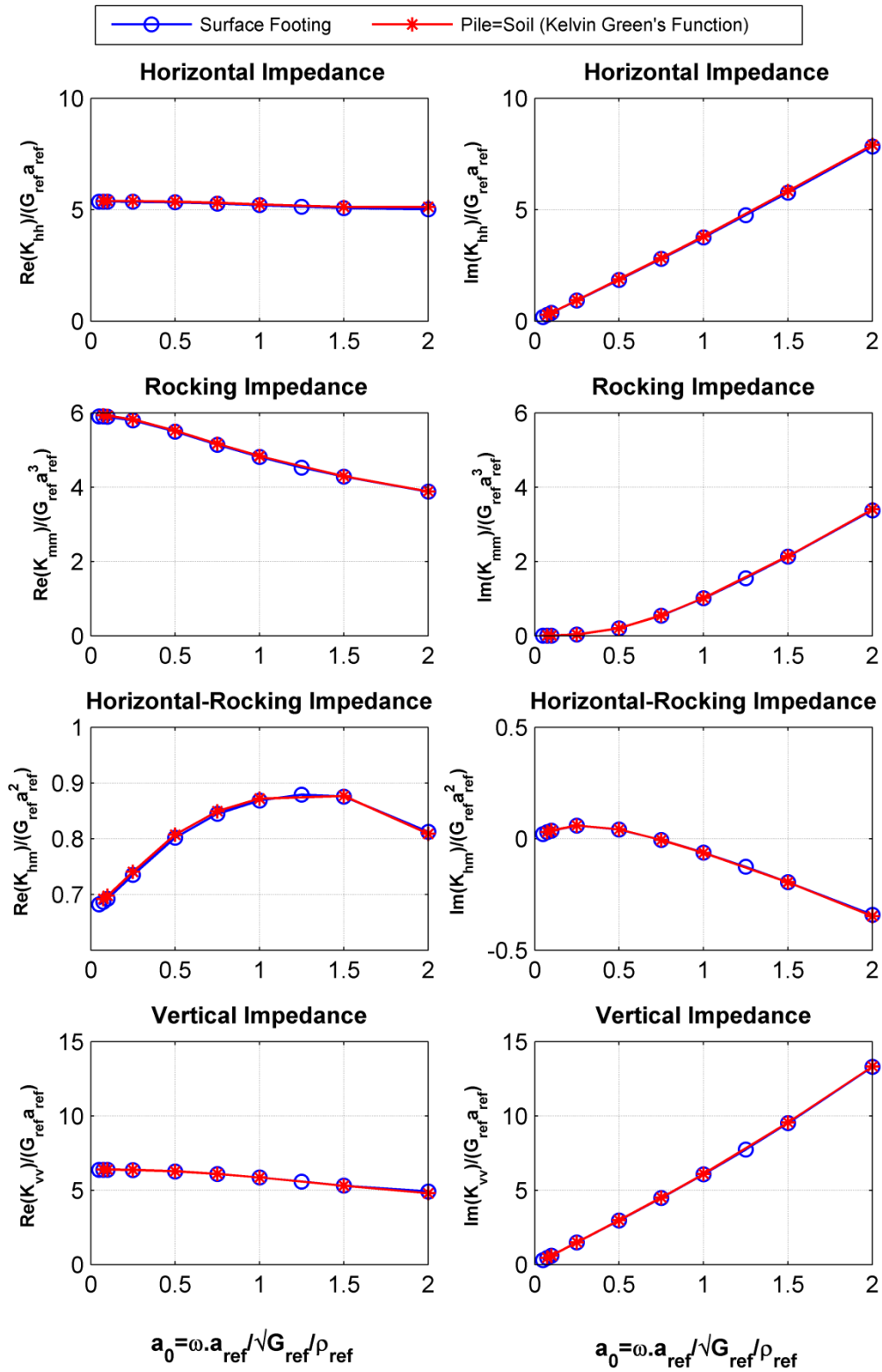


Figure 3-21. Impedances for one-domain surface footing problem and two-domain pile-soil problem where pile has same properties as soil (Kelvin Green's function used for pile domain).

3.4.2.1.5 Integration tolerance for 2-domain problem

As previously demonstrated (Ashlock, 2006), inaccurate integration of singular or weakly-singular integrals for certain BEM mesh and problem configurations can cause significant error in the solution. For this reason, an adaptive integration scheme is used in BEASSI, which ensures that the percent change in each component of the \mathbf{H} and \mathbf{G} matrices remains below a prescribed tolerance when the Gauss integration rule is incremented. It was therefore assumed for the present problem that reducing the integration tolerance would increase the accuracy of the results at a cost of increased analysis time. Although the latter is confirmed in Figure 3-22 for a 2-domain problem of a square pile in a homogenous half-space, Figure 3-23 reveals that using integration tolerances below 1.0 (i.e., 100%) increase the solution time for this problem, without any noticeable increase in accuracy at the impedance level. This finding is likely related to the use of the structural Green's functions for the pile domain and the high pile-to-soil modulus ratio for the present problem, which results in good accuracy with low Gauss rules. Because the modulus profiles examined later will be more complicated, an adaptive integration tolerance of 0.1% was chosen for the remainder of the study for a good balance between speed and accuracy. It should be noted that the effect of integration tolerance using the more demanding metric of traction distributions was not examined.

3.4.2.1.6 Mesh size

Using a finer mesh in BEM or FEM analyses results in a tradeoff between accuracy and cost of analysis. Moreover, using a very fine mesh can lead to memory overflow which can prevent the analysis from completing. This difficulty may be overcome by using computers with large memory, or by parallel computing on clusters. In this study, a parallel version of BEASSI was run on the Stampede supercomputing cluster at the Texas Advanced Computing Center through the

NSF XSEDE computing resource. To assess the adequacy of the mesh size for the present problem, the relative error in impedances resulting from decreasing an 8x8x20 element mesh to a 6x6x10 mesh was investigated for the two domain soil-pile problem described in previous section. The resulting complex-magnitudes of vertical and lateral-rocking impedances changed by less than 0.3% (Figure 3-24). This error is insignificant, indicating the adequacy of the 6x6x10 mesh for the 2 domain soil-pile problems in this study.

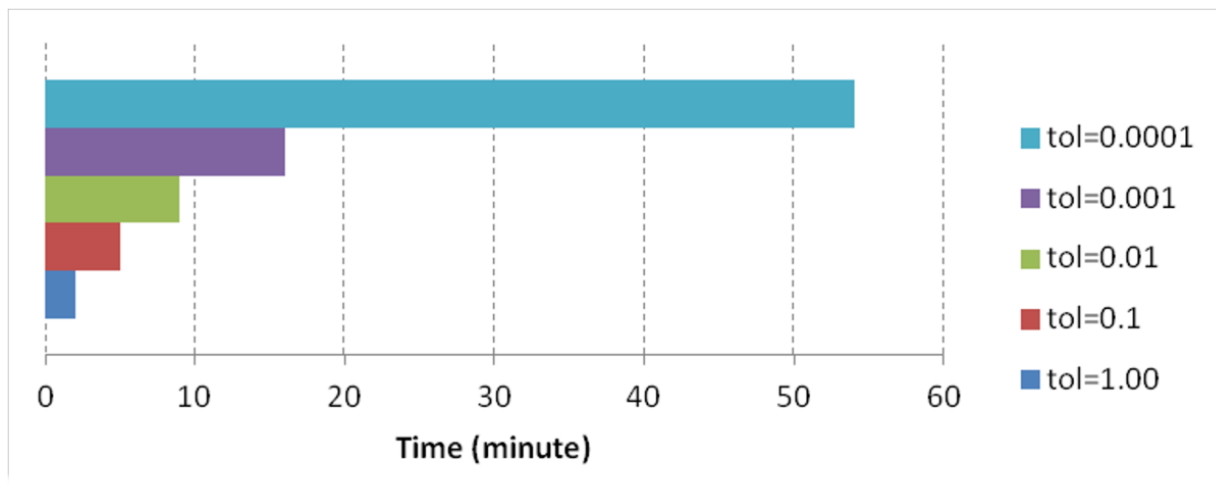


Figure 3-22. Analysis time for a soil-pile problem in homogeneous half-space with $\omega=70$ rad/sec ($a=0.2$ m, $\rho_s=2000$ kg/m³, $\rho_p=7850$ kg/m³, $G_s=40$ MPa, $G_p=80$ GPa, $\nu_s=0.25$, $\nu_p=1/3$).

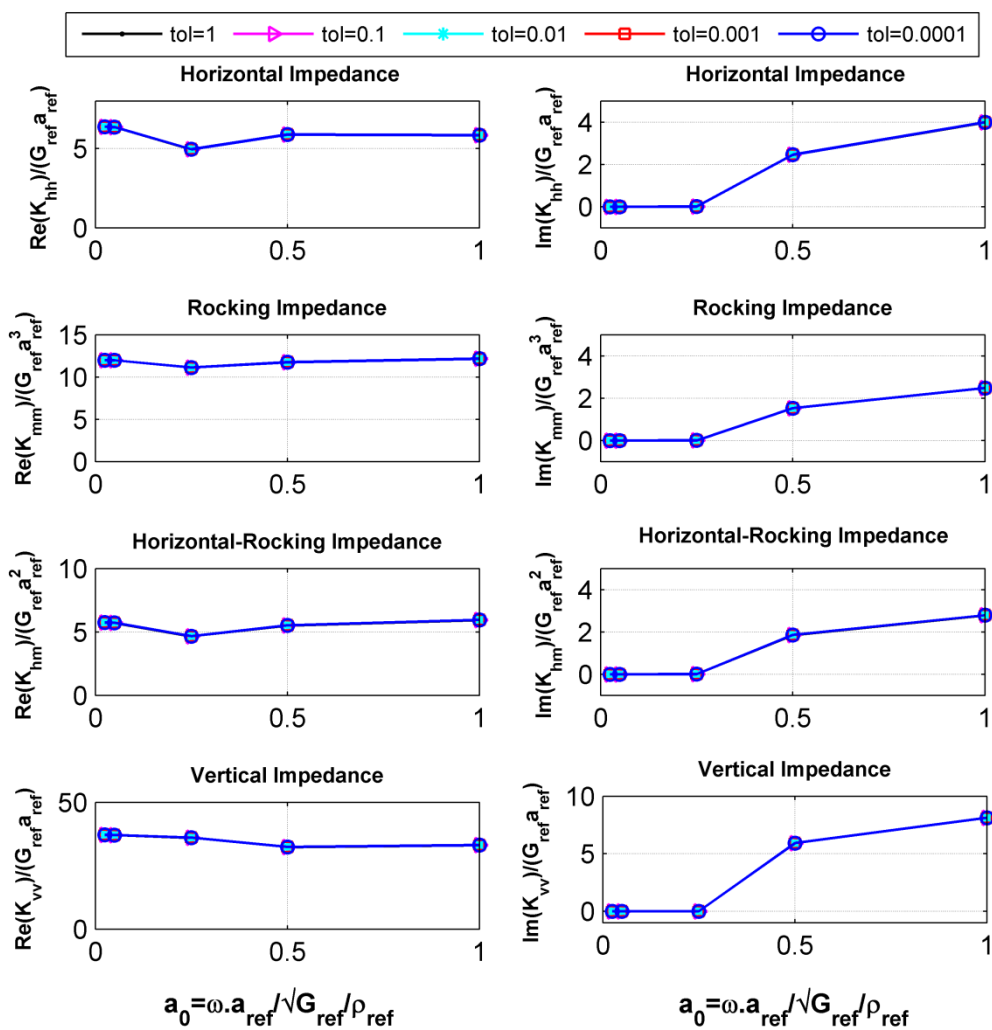


Figure 3-23. Impedances for soil-pile problem analyzed with different integration tolerances. Results appear to be unchanged below a tolerance of 100%.

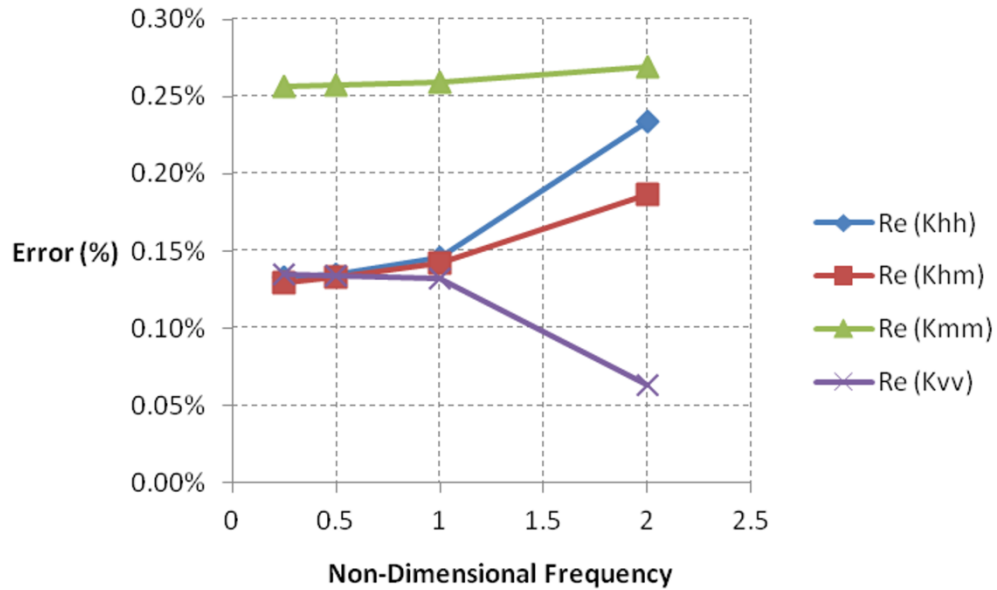


Figure 3-24. Error in impedance magnitude resulting from decreasing mesh size from 8x8x20 to 6x6x10 elements for the problem described in Figure 3-22.

3.4.2.2 Three-domain models

3.4.2.2.1 3-domain vs. 2-domain model for the same problem

To verify the programming of BEASSI and the associated mesh generators for the 3-domain problem, the soil-pile problem described in Table 3-8 was analyzed using both 3-domain and 2-domain approaches, where in the former the soil properties were the same inside and outside the disturbed zone. The details of the mesh are also shown in Figure 3-25. As depicted in the figure, singular elements were used for edge and corner elements of the pile, while AG element were used at edges of the disturbed zone where singularities are possible. These special elements are colored yellow (singular) and orange (AG) in Figure 3-25, while ordinary quadrilateral or triangular elements are colored green. The resulting impedance functions are presented for the problems without and with bedrock in Figure 3-26 and 3-27. The plots clearly show that the three-domain

approach can produce the same results as the two-domain problem when the soil properties are selected to be the same in the disturbed-zone and far-field.

Table 3-8. Details of soil-pile test problems for verifying programming of 3-domain soil-pile models.

	No bedrock	With bedrock
a_{pile} (m)	1	1
G_{pile} (Pa)	80e9	80e9
ν_{pile}	0.333	0.333
ρ_{pile} (kg/m ³)	7850	7850
G_{soil} (Pa)	100e6	100e6
ν_{soil}	0.25	0.25
ρ_{soil} (kg/m ³)	2000	2000
L_{pile} (m)	10	10
Half-space modulus (Pa)	100e6	100e12
Soil material damping ratio	0%	0%
Pile mesh size (x,y,z)	4,4,10	4,4,10
a_{ref} (m)	0.5	0.5
G_{ref} (Pa)	1e6	1e6
ρ_{ref} (kg/m ³)	2000	2000
Bedrock depth (m)	-	15
Disturbed-zone radius (m)	1.5	1.5
Disturbed-zone mesh size (r, θ ,z)	2,16,15	2,16,15
Integration tolerance	0.001	0.001

3.4.2.2.2 Parametric study of rigid bedrock depth

To explore how the rigid bedrock may affect soil-pile impedances, the 2-domain problem of the single pile in a homogenous layer over bedrock described in Section 3.4.2.2.1 was analyzed again with four different bedrock depths. The results are shown and compared in Figure 3-28. As

expected, the impedances converge to the case with no bedrock (infinite depth) as the bedrock depth increases. With increasing bedrock depth, the resonant trough in the real part is also observed to diminish and move to lower frequency, while the cutoff frequency in the imaginary part moves to lower frequency as well. It should be noted that the expected phenomena of a resonant trough and cutoff frequency were also observed for both the 2-domain and 3-domain models in Figure 3-27.

3.4.2.2.3 Mesh size for 3-domain problem

The size of the mesh, and in particular the maximum element size, governs the minimum reliable wavelength that the computational model can capture (Kuhlemeyer & Lysmer, 1973). In order to determine the required number of elements to keep the accuracy of the results in an acceptable range, the 3-domain soil-pile problem described in Table 3-9 was modeled using different mesh configurations. The soil properties of the disturbed zone were selected to be the same as the far-field soil so the results from the 3-domain model could be compared to the corresponding 2-domain analyses. As shown in Figure 3-29, changing the surface mesh doesn't affect the impedances significantly, especially for frequencies less than 100 Hz. However, the 3-domain results diverge from the 2-domain solution at high frequency. As expected, increasing the number of elements in the z-direction solves the divergence issue as shown in Figure 3-30. These analyses suggest that using a pile mesh of 4x4x24 elements and a disturbed-zone mesh of 2x16x15 elements can produce acceptable accuracy for the impedances.

Table 3-9- Model properties used to examine effect of mesh size on 3-domain soil-pile problem.

a_{pile} (m)	0.125
G_{pile} (Pa)	80e9
ν_{pile}	0.333
ρ_{pile} (kg/m ³)	7850
G_{soil} (Pa)	100e6
ν_{soil}	0.25
ρ_{soil} (kg/m ³)	2000
L_{pile} (m)	6
Half-space modulus (Pa)	100e12
Soil material damping ratio	0%
a_{ref} (m)	0.125
G_{ref} (Pa)	2.77583e7
ρ_{ref} (kg/m ³)	2000
Bedrock depth (m)	12
Disturbed zone radius (m)	0.625
Integration tolerance	0.001

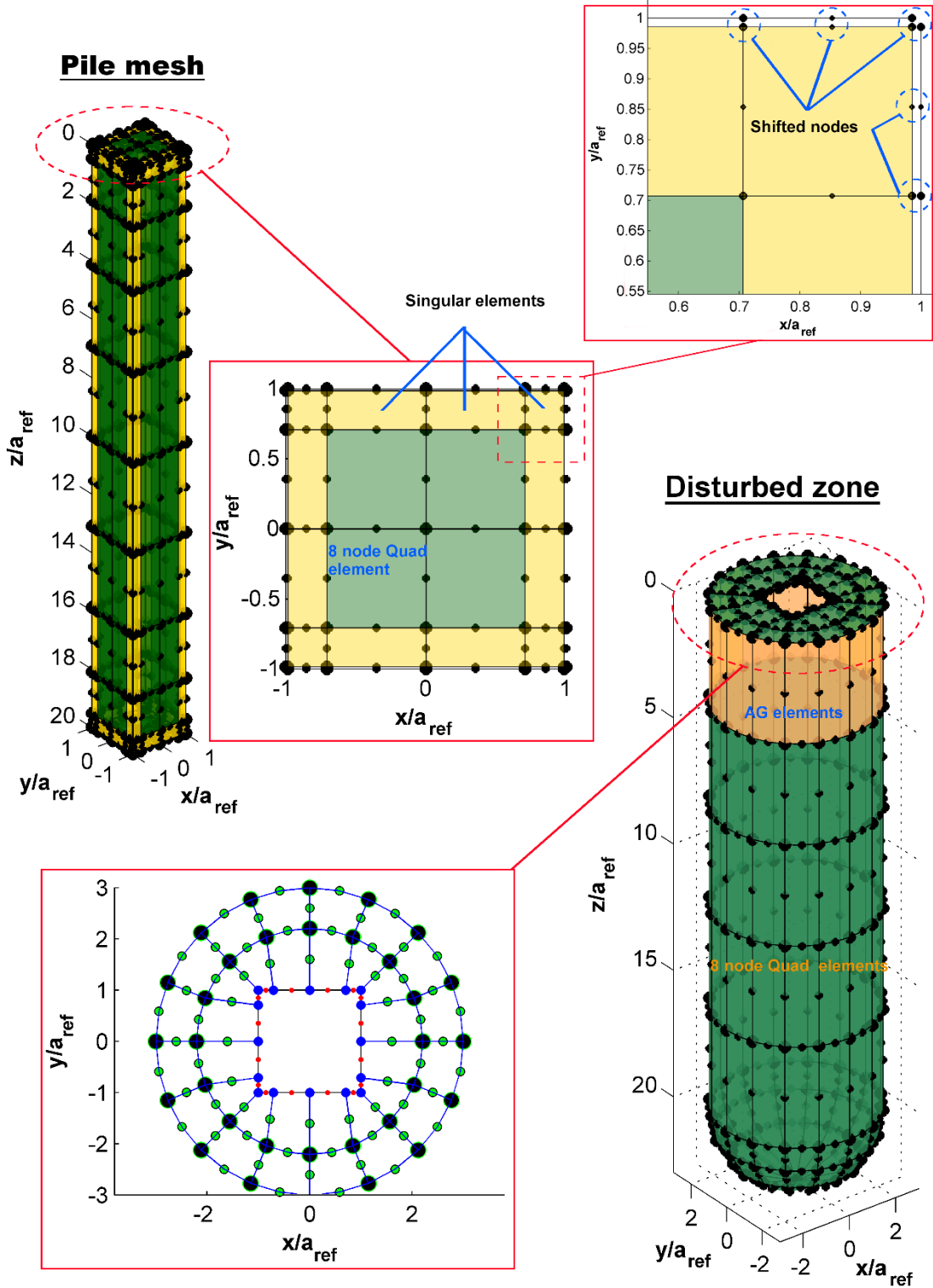


Figure 3-25. Mesh details of the 3-domain soil-pile problem discussed in Section 3.4.2.2.1.

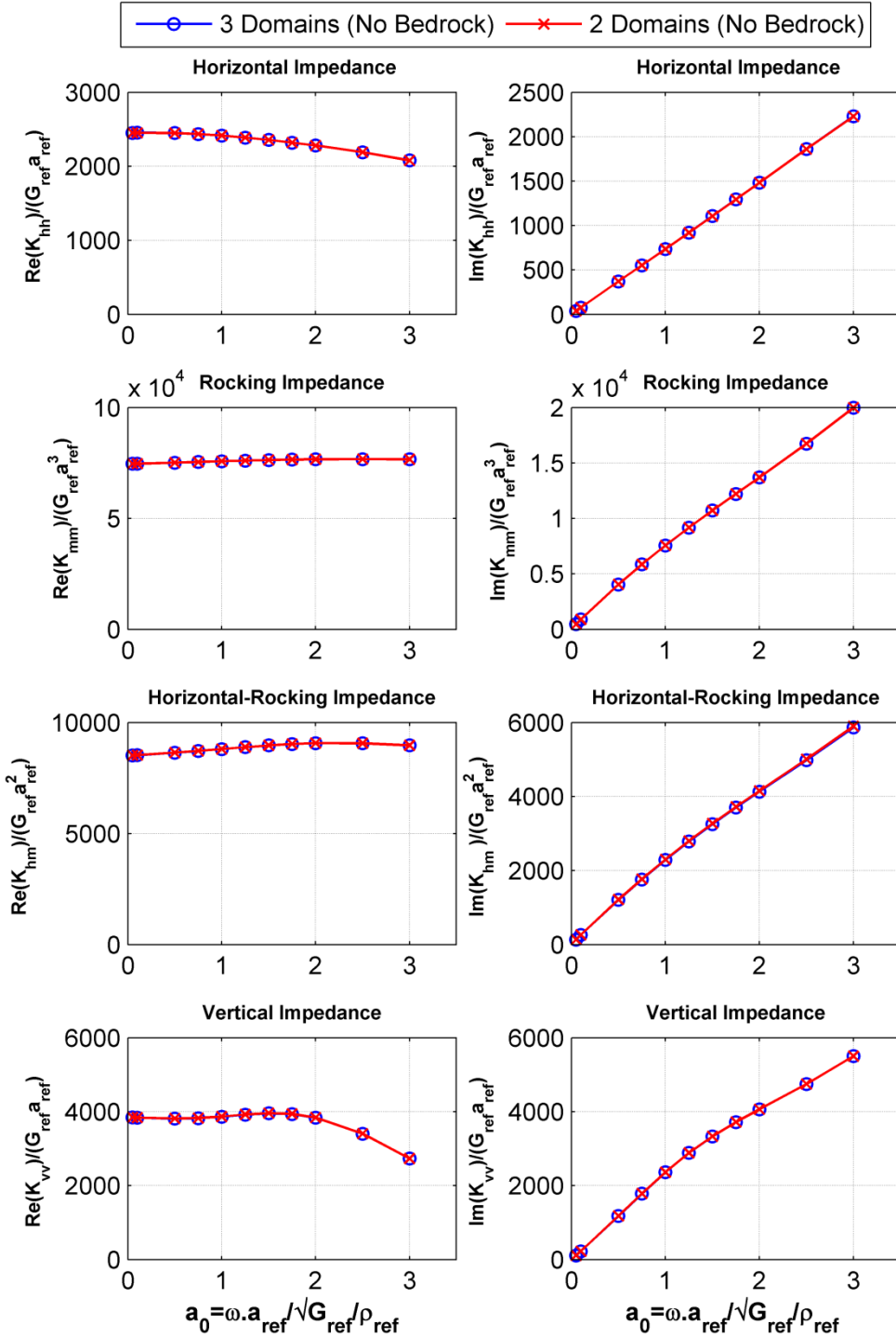


Figure 3-26- Impedances for pile in homogenous half-space analyzed using 2-domains vs. 3-domains with identical soil properties in disturbed zone and far-field.

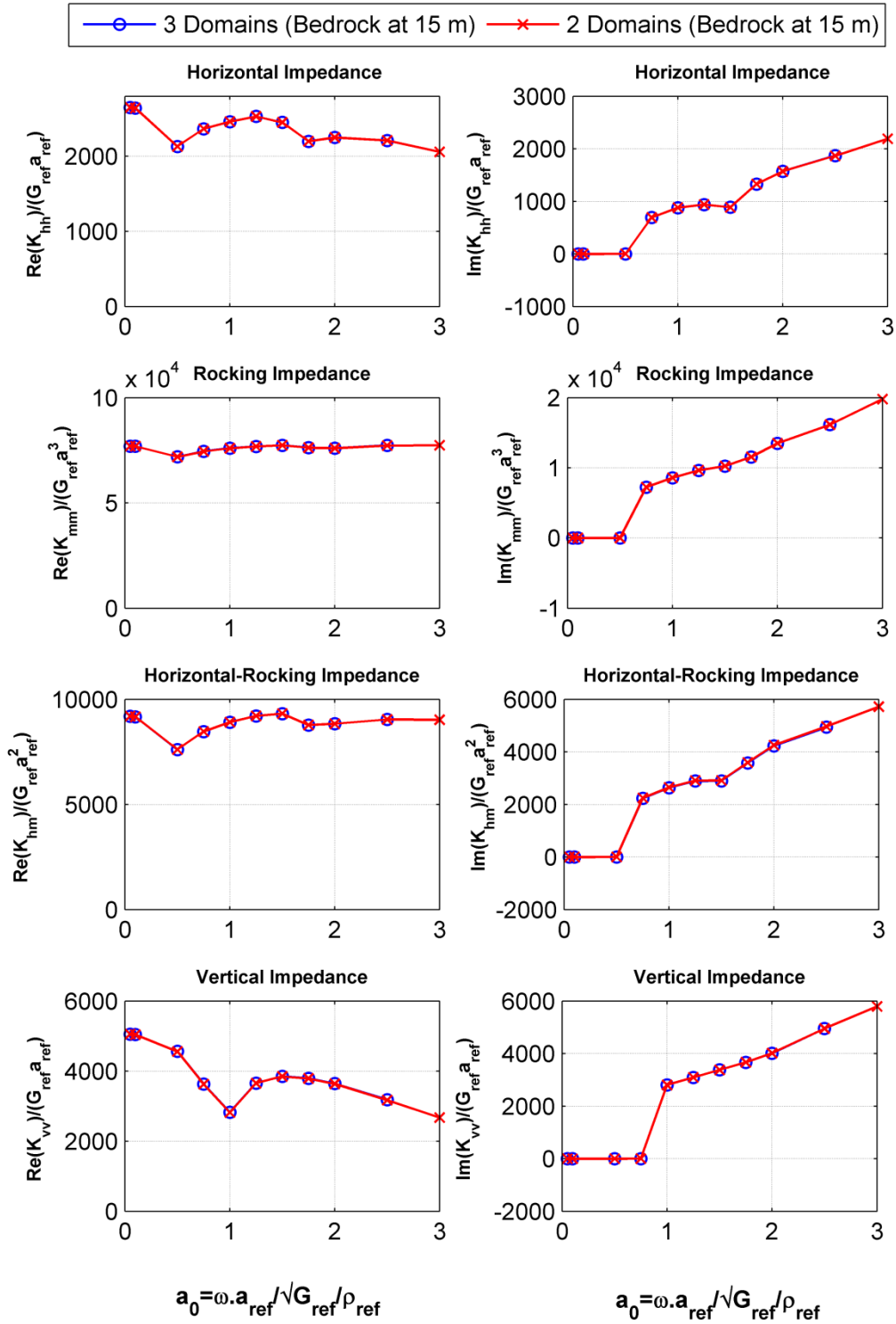


Figure 3-27- Impedances for pile in homogenous soil layer with bedrock at 15 m, analyzed using 2-domains vs. 3-domains with identical soil properties in disturbed zone and far-field.

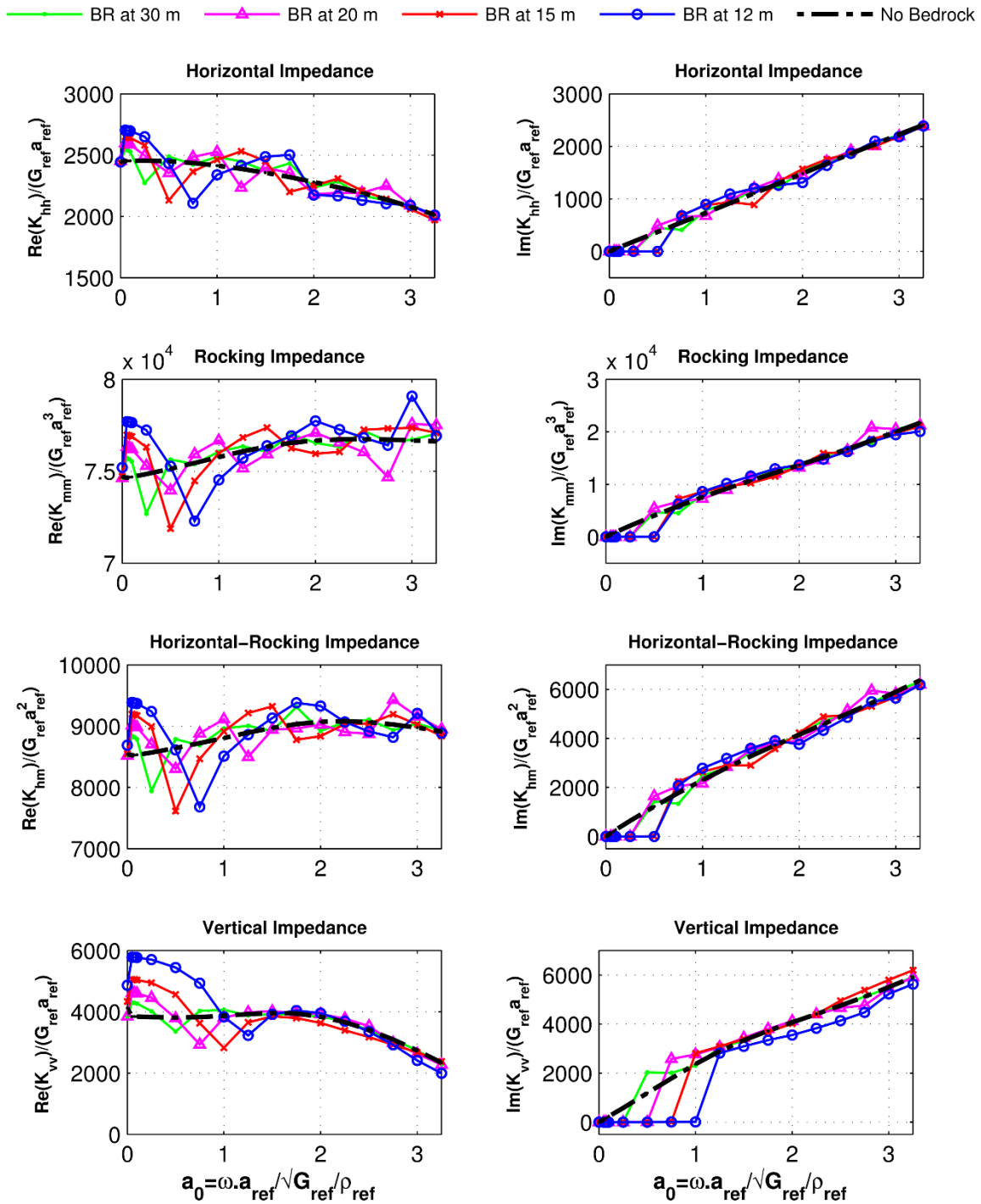


Figure 3-28. Effect of bedrock depth on pile-soil impedances. Resonant trough in real part and cut-off frequency in imaginary part are the expected characteristic traits caused by bedrock.

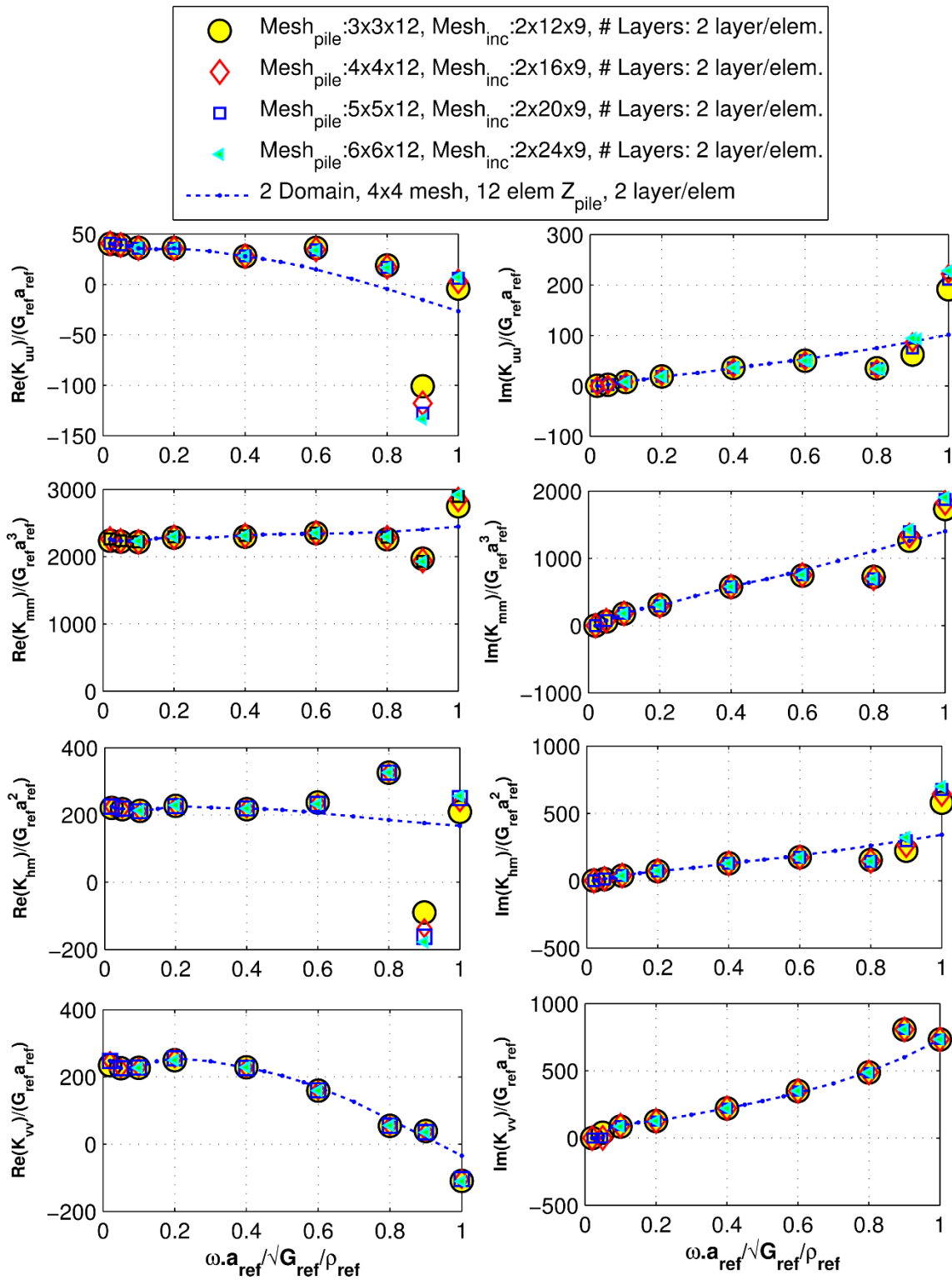


Figure 3-29. Effect of surface mesh size on the soil-pile impedances for the 3-domain problem described in Table 3-9.

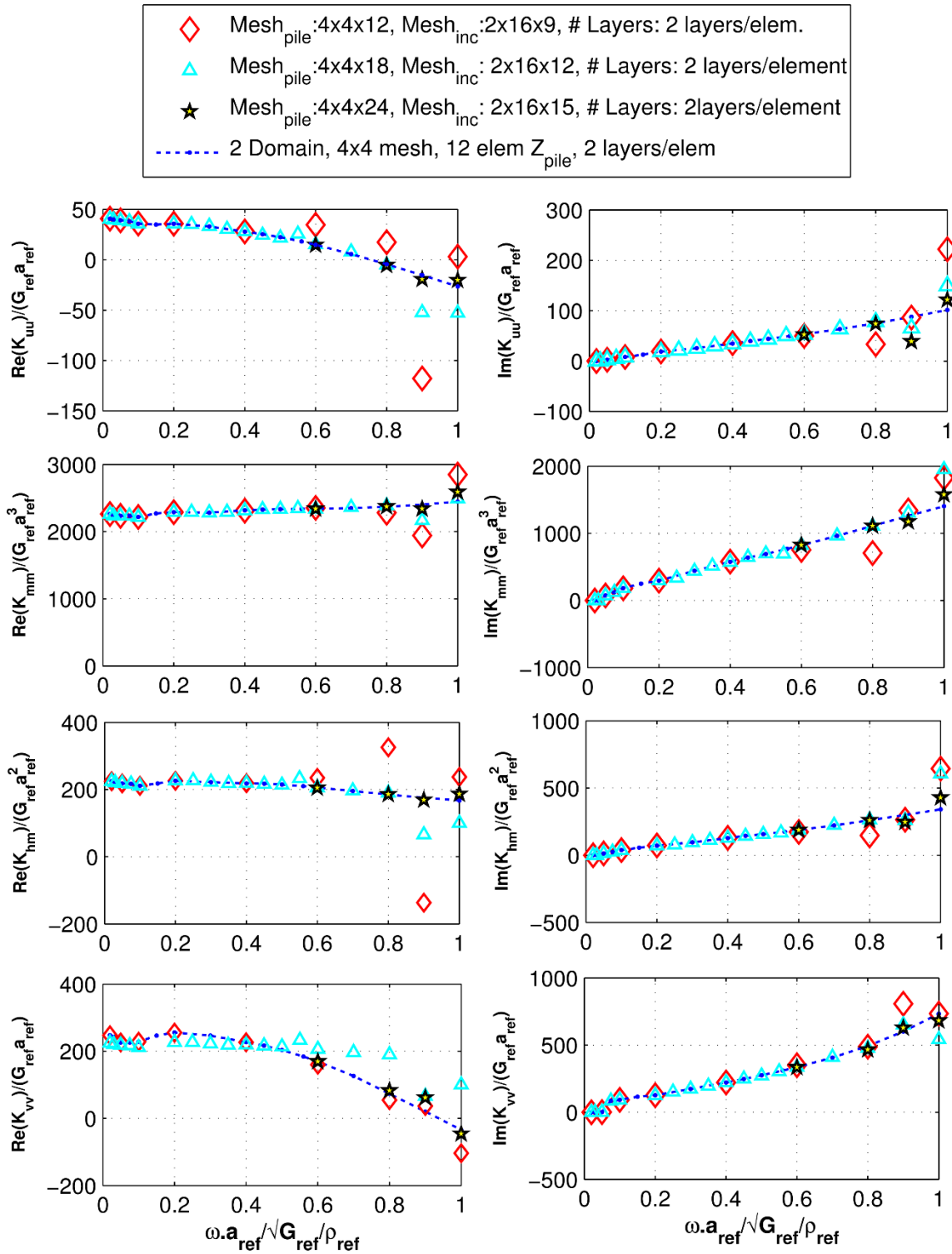


Figure 3-30- Effect of vertical mesh size on soil-pile impedances for the 3-domain problem described in Table 3-9.

3.4.2.2.4 Flat versus hemispherical tip for disturbed zone

For the actual physical pile tests under study, the pile is technically a floating pile with the pile tipped in a gravel layer rather than resting on bedrock. However, the pile tip is very close to the bedrock surface, so its response lies somewhere between the floating-tip and fixed-tip conditions, which creates difficulty for modeling. A disturbed zone with a hemispherical tip has been shown to perform well for floating piles in sands (Ashlock, 2006), and the curved geometry avoids traction singularities at corners. However, for the current situation a hemispherical tip would extend into the rigid bedrock. Since layered half-space Green's functions are used in the disturbed zone, this curved geometry might be acceptable if one sets the layer properties inside the disturbed-zone tip to be the same as those of the bedrock. An alternative method is to use a flat tip on the disturbed zone which may or may not penetrate into bedrock, with singular or AG elements at the edges to handle singularities.

To assess the validity and performance of the hemispherical and flat-tip approaches, a problem with a disturbed-zone was in this part. The soil properties above bedrock in the disturbed-zone and far-field outer-zone were identical and followed a square-root variation with depth. The bedrock depth was selected to be just 0.5 m below the pile tip, and the soil layer properties inside the disturbed zone and below the bedrock surface were assigned those of the bedrock. Figure 3-31 shows the problem assumptions and the soil layer profile. The impedance results shown in Figure 3-32 reveal some numerical difficulties above a dimensionless frequency of 0.75. Considering the results of the mesh convergence study shown in Figure 3-30, it is likely that these difficulties can be solved by increasing the mesh densities in the z -direction.

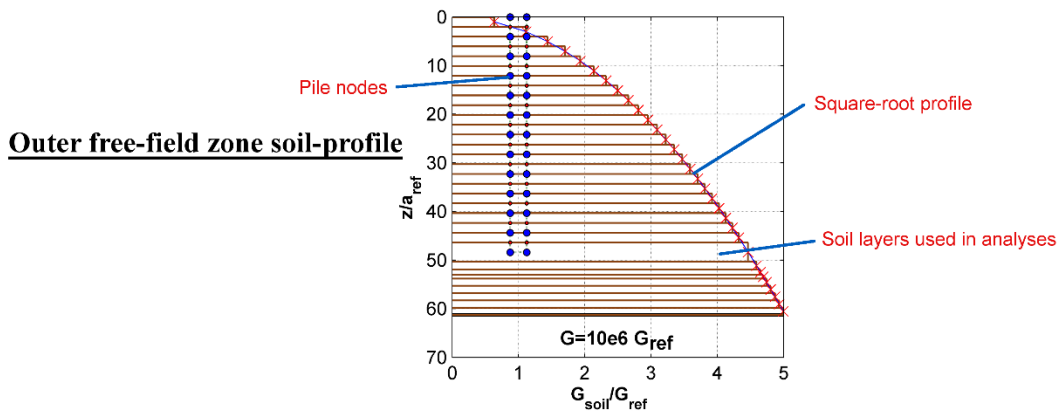
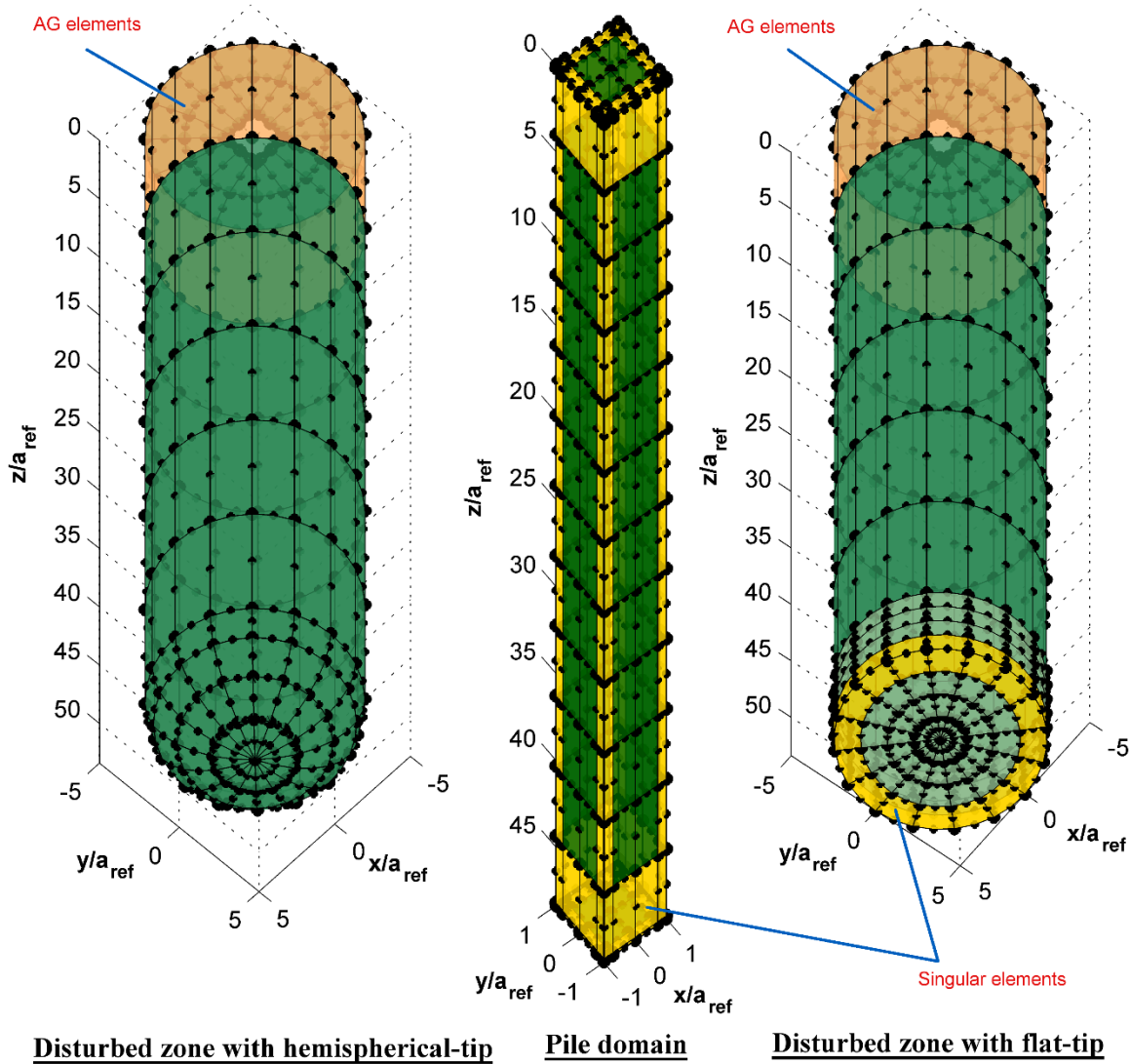


Figure 3-31- Two 3-domain BEM models with hemispherical and flat tips used for the disturbed-zone mesh. A homogenous profile is used in the disturbed zone ($a_{ref}=0.127$ m, $\rho_{ref}=2000$ kg/m³, $G_{ref}=27.7583$ MPa).

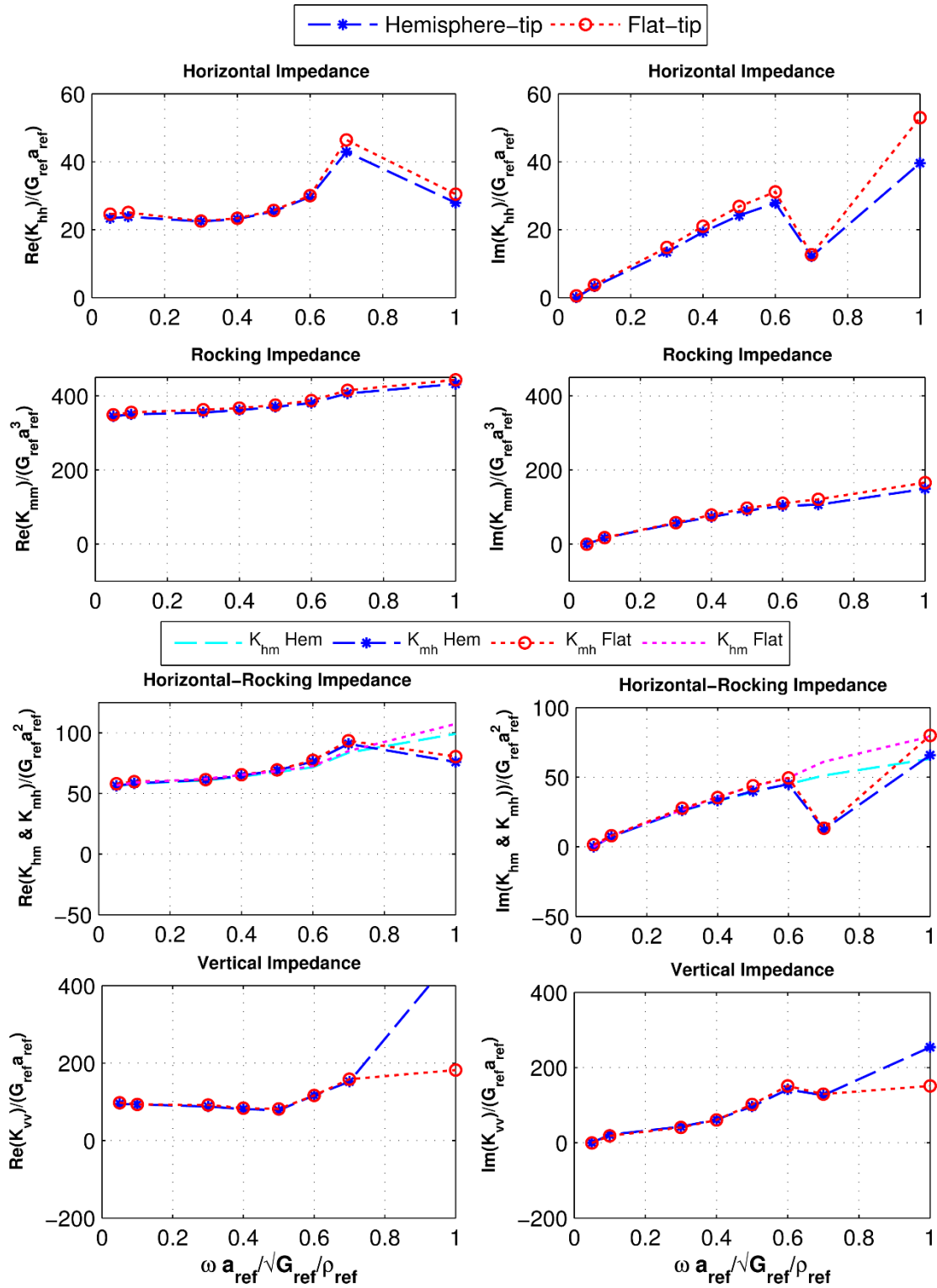


Figure 3-32- Comparison of impedance functions from the two models in Figure 3-31.

3.4.2.2.5 Statistical data from adaptive Gauss integration scheme

BEASSI includes the option to record the final Gauss rule orders for each combination of collocation point and integration element (as well as each integration sub-region for elements with degenerate mappings applied). Different starting Gauss integration rules are specified in the input files for each element type and distance from the active collocation point, with the latter divided into three concentric spherical zones surrounding the active collocation point. The statistical history of the final Gauss rules can help indicate the accuracy of the model and identify areas causing numerical difficulties. For example, if the integration process requires a very high Gauss integration rule or fails to converge after reaching the specified maximum Gauss rule (40x40 for quadrilateral elements and 72 for triangular elements), the validity of the output results should be examined. Despite the regularized formulation used in BEASSI, high element aspect ratios or very close collocation points in the mesh can still lead to folding and skewing of the complicated nearly-singular integrands (Ashlock, 2006), requiring high Gauss rules for accurate integration. As an example, integration histories of a 3-domain model of the physical pile experiments shown in Figure 3-33 are presented in Figure 3-34 and 3-35. As indicated in the figures, except for a few incidences, most of the integrals converge to the specified tolerance of 1% in a reasonable number of Gauss points less than 200 for quad elements and 20 for triangular elements. In general, the closer the collocation point to the element integration region, the higher the converged Gauss rules, with a few of the several thousand combinations not converging after the prescribed maximum Gauss rule. However, these few outliers have a minimal effect on the overall tractions and corresponding impedance functions.

3.4.2.2.6 Agreement between horizontal-rocking coupling impedances as quality measure

For the radiation (impedance) problem, BEASSI calculates the solutions for four different right-hand sides corresponding to imposed rigid-body unit displacements and rotations at the pile-soil interface. The four right-hand sides correspond to a prescribed vertical displacement from which K_{vv} is determined by integrating the interfacial vertical tractions, horizontal displacement from which K_{hh} and K_{mh} are found, unit rotation about the y -axis from which K_{mm} and K_{hm} are found, and torsional rotation about the z -axis from which K_{tt} is found. By the reciprocity theorem of elastodynamics, the coupling impedances K_{hm} and K_{mh} are theoretically equal. For an accurate and perfect computational model, these two values would be exactly the same. However, modeling error, discretization error, numerical issues such as an insufficient number of elements, numerical instabilities, or round-off errors, can all result in different values for these coupling impedances. Thus, the agreement between K_{hm} and K_{mh} is used as a general measure of the modeling accuracy and validity. This check was performed for all problems described in previous sections. In cases where their agreement is deemed acceptable, K_{hm} and K_{mh} are replaced with their average values in subsequent analyses. When their agreement is not acceptable, such as in Figure 3-32, their discrepancy is used to guide and assess the necessary measures to correct the numerical issues. The agreement between K_{hm} and K_{mh} for the 3-domain disturbed-zone model of the actual soil-pile problem in Figure 3-33 is shown in Figure 3-36. As evident in the figure, a good match was obtained between the two horizontal-rocking coupling impedances, thus increasing confidence in the validity of the numerical results.

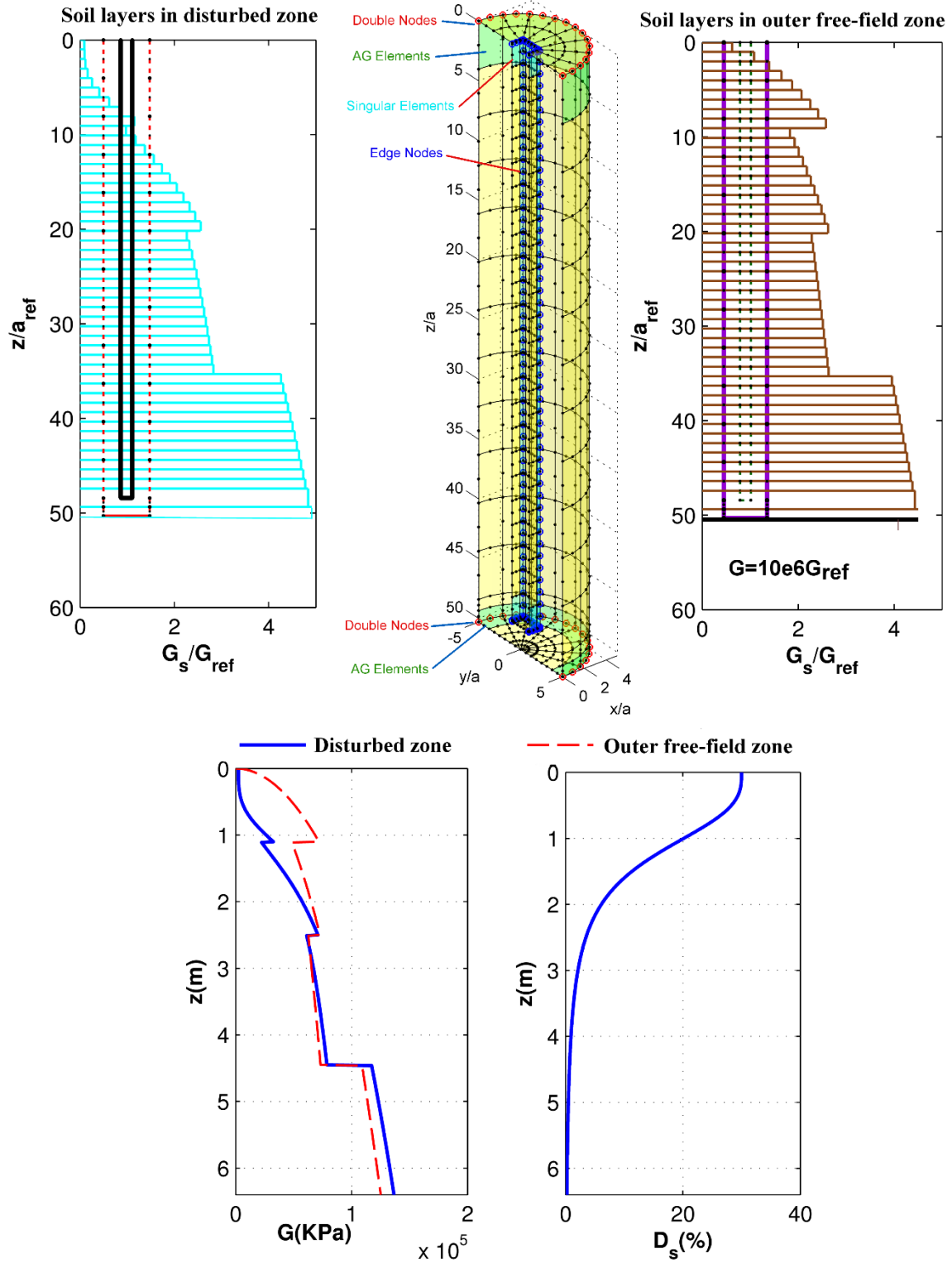


Figure 3-33- Three-domain boundary element model of the actual experiment in unimproved soil discussed in Chapter 2 ($a_{ref}=0.127$ m, $\rho_{ref}=2000$ kg/m³, $G_{ref}=27.7583$ MPa).

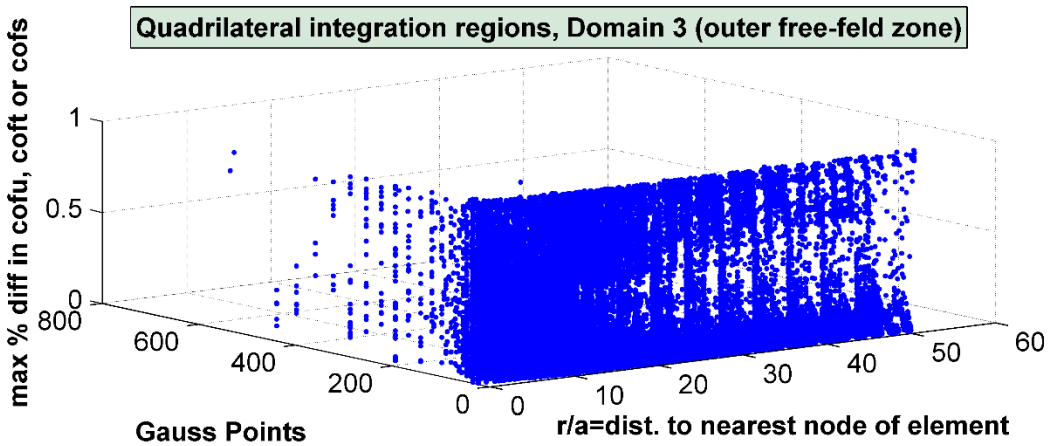
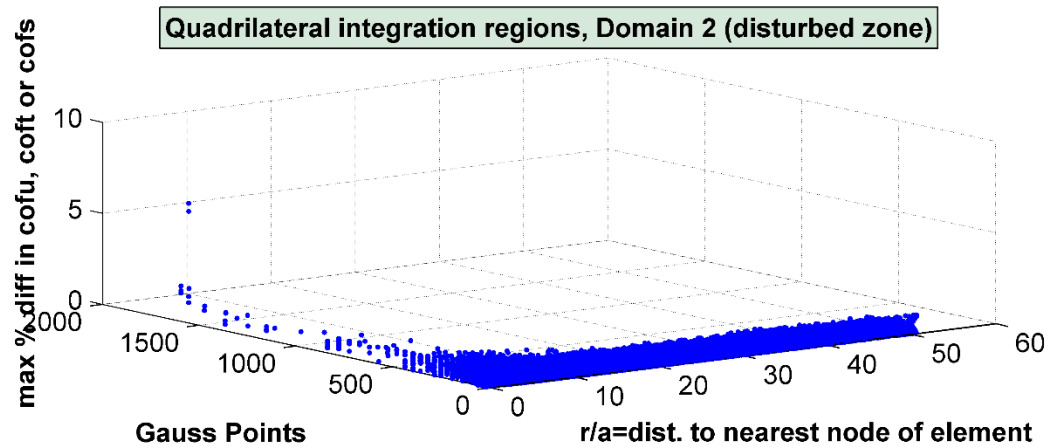
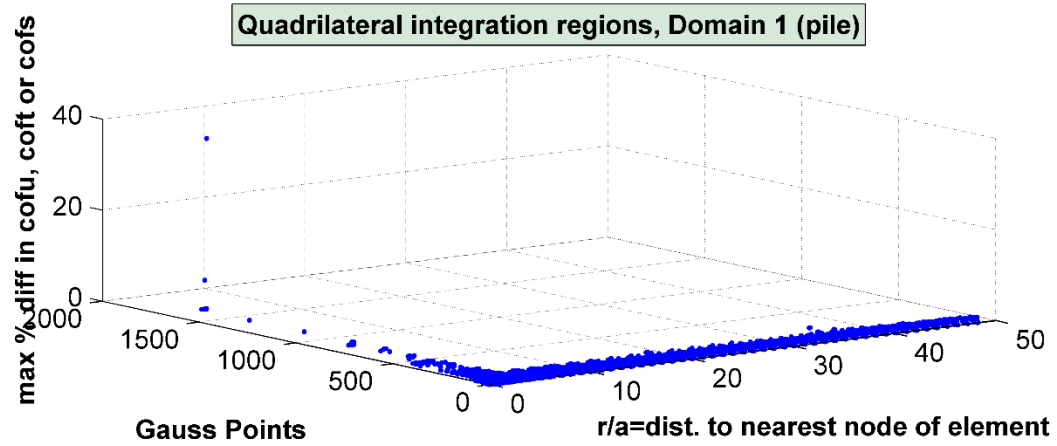


Figure 3-34- Gauss integration history for quadrilateral elements in each domain for the problem shown in Figure 3-33.

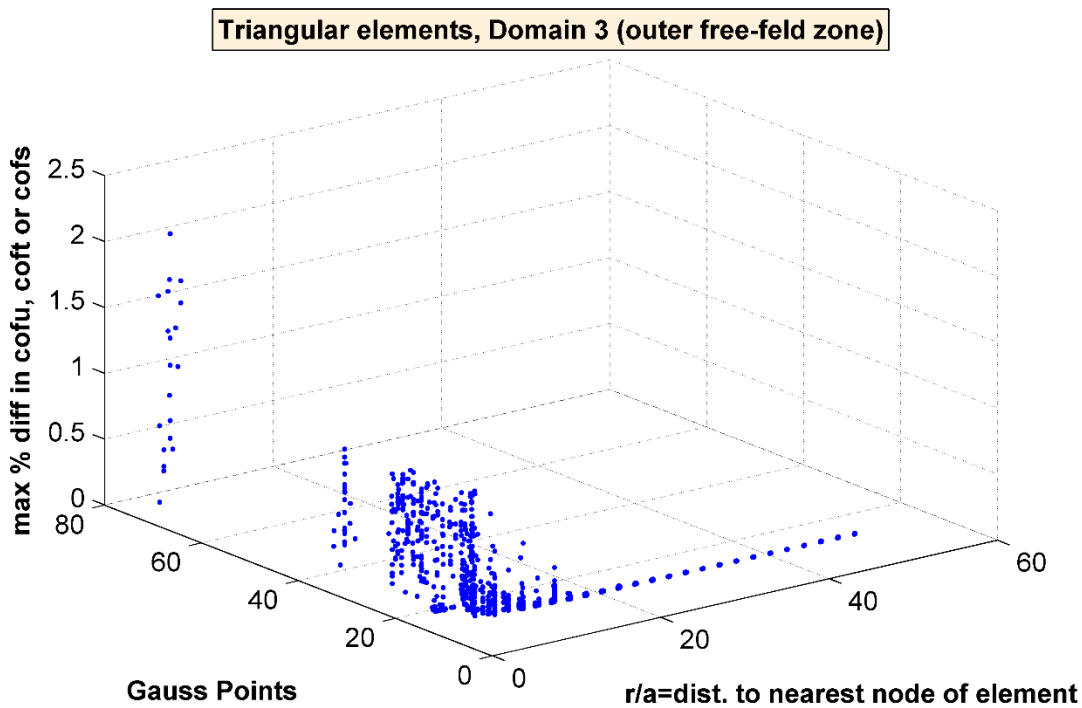
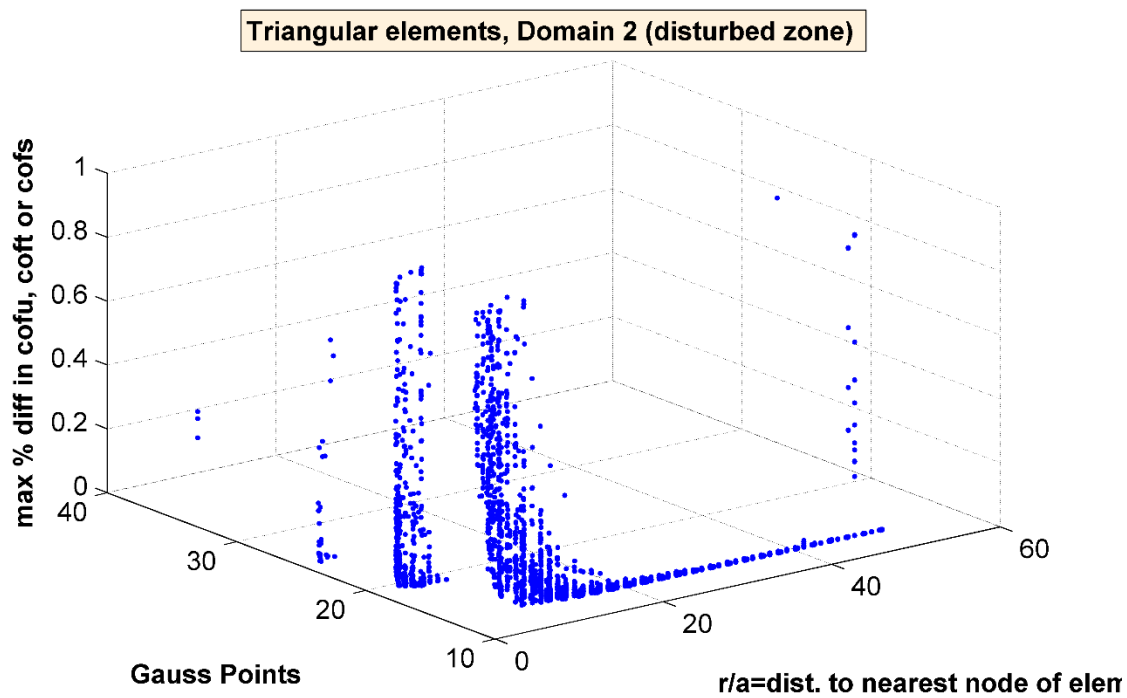


Figure 3-35- Gauss integration history for triangular elements in each domain for the problem shown in Figure 3-33.

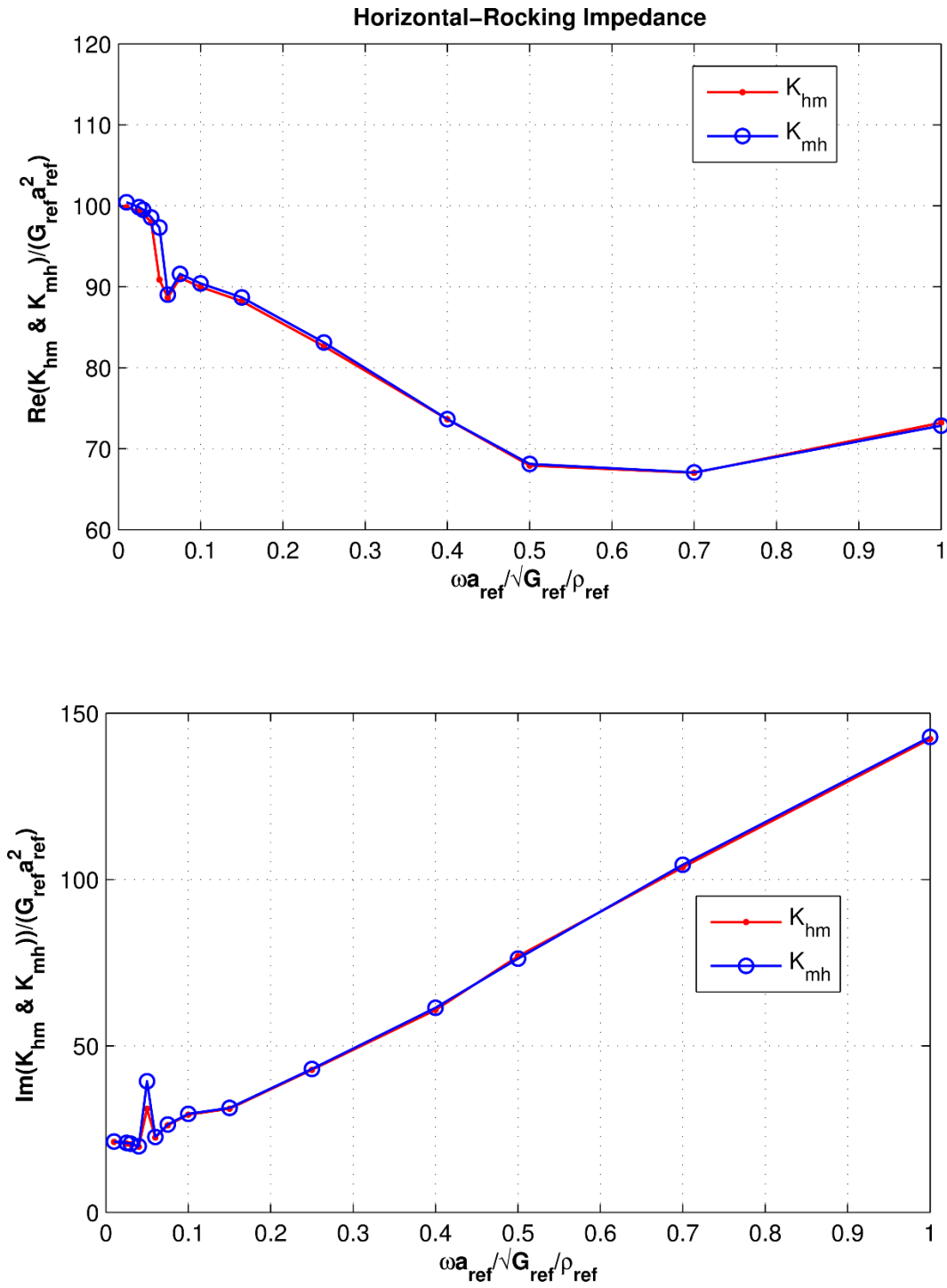


Figure 3-36- Agreement between horizontal-rocking coupling impedances for the problem described in Figure 3-33.

3.5 Parametric Studies and Sensitivity Analyses

In the next chapter, the measured vibration data from full-scale pile tests will be used in an inverse-analysis framework to calibrate the theoretical soil-pile models, and identify the optimum values for each parameter in the solution. A sensitivity analysis will be performed in this section to determine the relative influence of the various parameters and estimate their possible ranges of variation for modeling the experimental observations. These analyses will also help to identify the critical parameters that should be measured or calculated with particular accuracy and caution.

To examine the sensitivity of the theoretical accelerance functions to the model parameters, a parametric study was conducted in which the rigid pile-cap-shaker inertial properties, flexible un-embedded pile-stem properties, soil shear modulus and damping profiles, and depth of a no-contact gapping zone between pile and soil were varied. The model of the pile in unimproved soil described in Chapter 2 was selected as the reference model. Sensitivity analyses for this reference model performed using the small-strain G_{\max} and D_{\max} profiles (Figure 4-6) are shown in Figures 3-37 to 3-39. Similar analyses using strain-dependent Hardin-Drnevich shear modulus and damping profiles iteratively corrected using maximum soil strains estimated from the calculated pile displacement (Figure 4-23) are also shown in Figure 3-40 to 3-42. The latter soil profile will be discussed in more detail in Chapter 4.

The effect of the pile-cap-shaker inertial properties and flexible un-embedded pile stem properties on the amplitude and frequency of the accelerance peaks are presented in Figure 3-37 to 3-39. The accelerance peak values on the y -axes are normalized by those of the reference model. The model parameters on the x -axes are also normalized by those of the reference model, and varied by $\pm 50\%$. The results indicate that the mass of the rigid pile-cap-shaker assembly, M_R , and un-embedded length of the pile stem can significantly affect the accelerance peaks. Great care was

therefore taken to accurately calculate these values. As shown in Appendix, the calculated mass and polar moment of inertia, M_R and J_R respectively, result from adding many complex components which can affect the accuracy of the final estimates. Therefore, small perturbations in the calculated values of M_R and J_R will be examined during the model calibration process in Chapter 4 to assess the possible influence of errors in their calculated values.

To characterize the sensitivity of accelerance to the free length and gapping length, the pile is divided into three segments; L_t is the length of the segment embedded inside the concrete pile-cap but which may not behave rigidly with the pile-cap over some length near its bottom, L_0 is the measured free length of the pile between the bottom of the pile-cap and the ground surface, and L_s is the pile length inside the soil which due to static or dynamic pile-soil separation (gapping) is not a part of the interaction problem. The accelerance formulation of Chapter 2 was modified to include these lengths. Among these three lengths, L_0 could be measured accurately and is not a concern here. Figure 3-39 indicates that even a wide possible range of L_t does not have a major effect on the accelerance functions. Thus, the parameter of primary importance is the gapping separation length, L_s . During the simulation process, this parameter was varied to determine the best match to the experiments. Its effect was examined by increasing the length of the free pile stem L_0 in the theoretical accelerance calculation, while simultaneously decreasing the embedded pile length accordingly in the approximate 3D soil-pile model, essentially translating the coordinate origin downward to the bottom of the gap and removing the non-contacting layers from the model. As rationally expected, increasing L_s makes the system behave softer, moving the peaks to lower frequencies and higher amplitudes. This effect is more severe for horizontal and rotational accelerances than for vertical accelerance.

To examine how uncertainties in the shear modulus and material damping ratio profiles could affect the system response, the modulus profile was varied from 10% to 200% of its reference value, and the damping ratio profile was varied between magnitudes of 5% and 30%. The results are compared for the centroidal accelerances of the HC and VC test configuration in Figure 3-40 and 3-41 . As expected, increasing the modulus makes the system stiffer and moves the peak toward higher frequencies but also higher amplitudes. Also, increasing the material damping decreases the peak amplitudes of the system, with a very minor decrease in the peak frequencies. However, this parameter is not very crucial, especially for the HC test, since the main source of damping in the model arises from geometric damping through wave propagation in the soil.

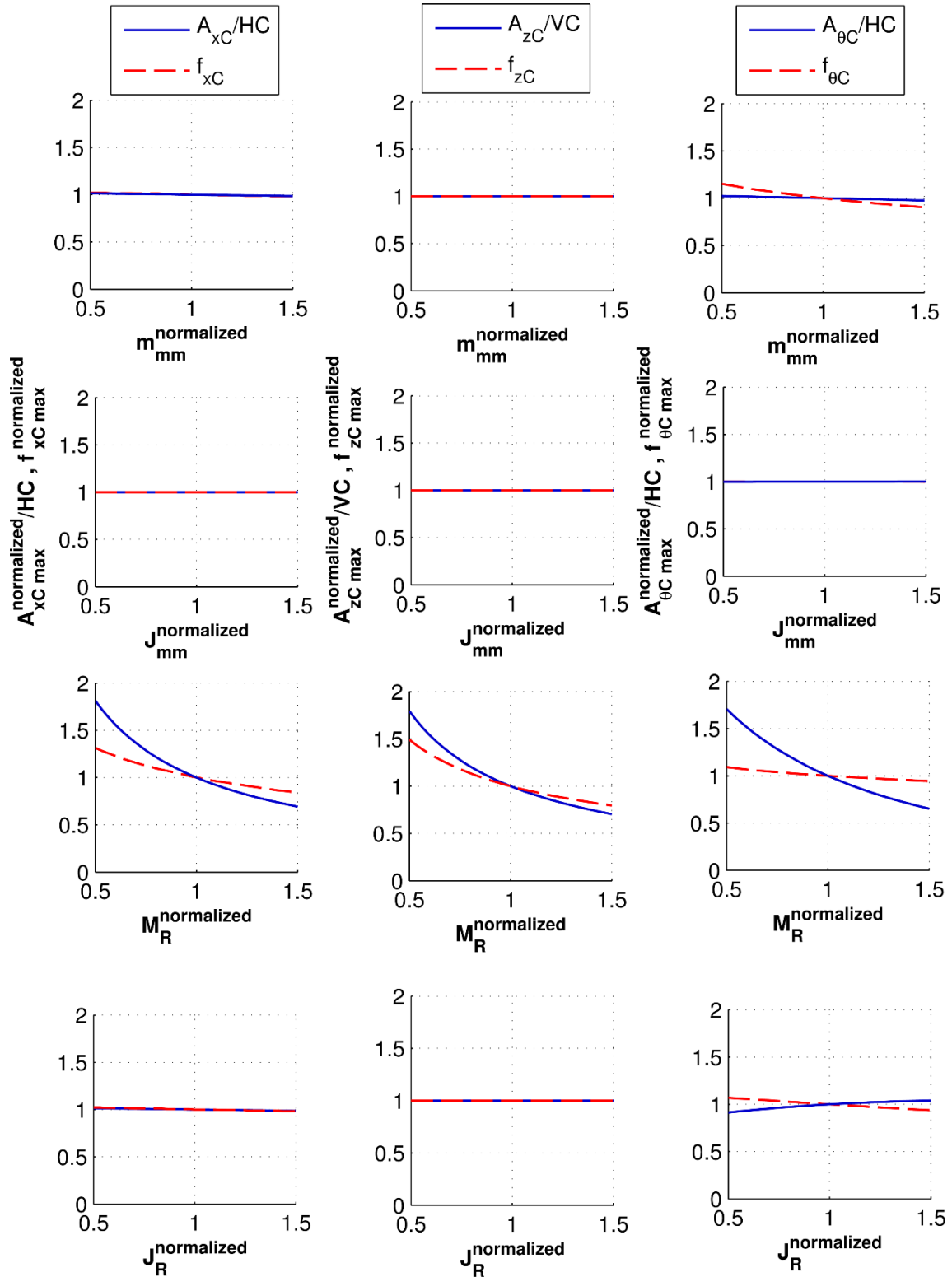


Figure 3-37- Sensitivity of peak frequency and amplitude of centroidal acceleration functions to model parameters (actual values of NEES pile in unimproved soil with G_{max} and D_{max} soil profiles used as reference model).

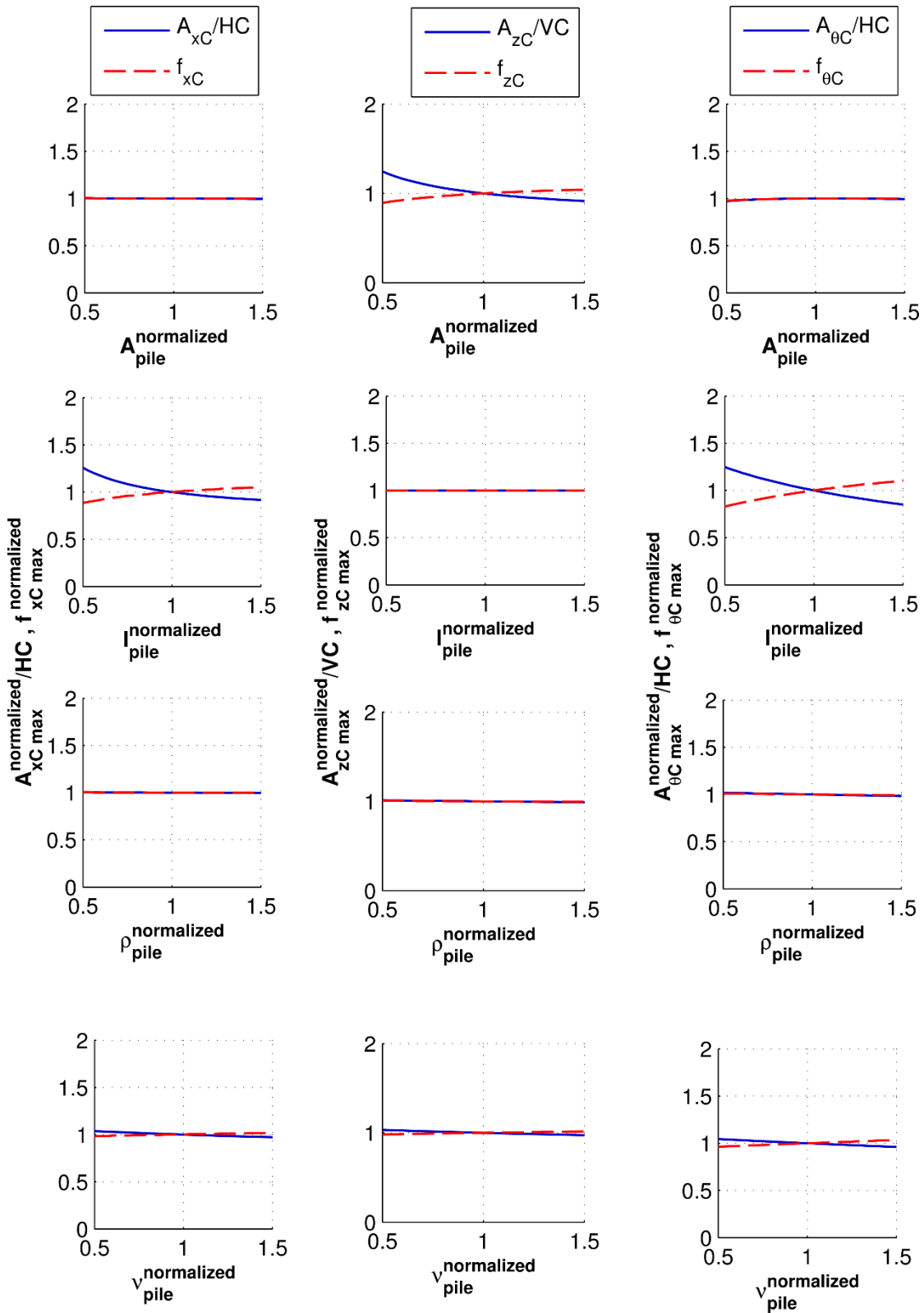


Figure 3-38- Sensitivity of peak frequency and amplitude of centroidal acceleration functions to theoretical model parameters (actual values of NEES pile in unimproved soil with G_{max} and D_{max} soil profiles used as reference model).

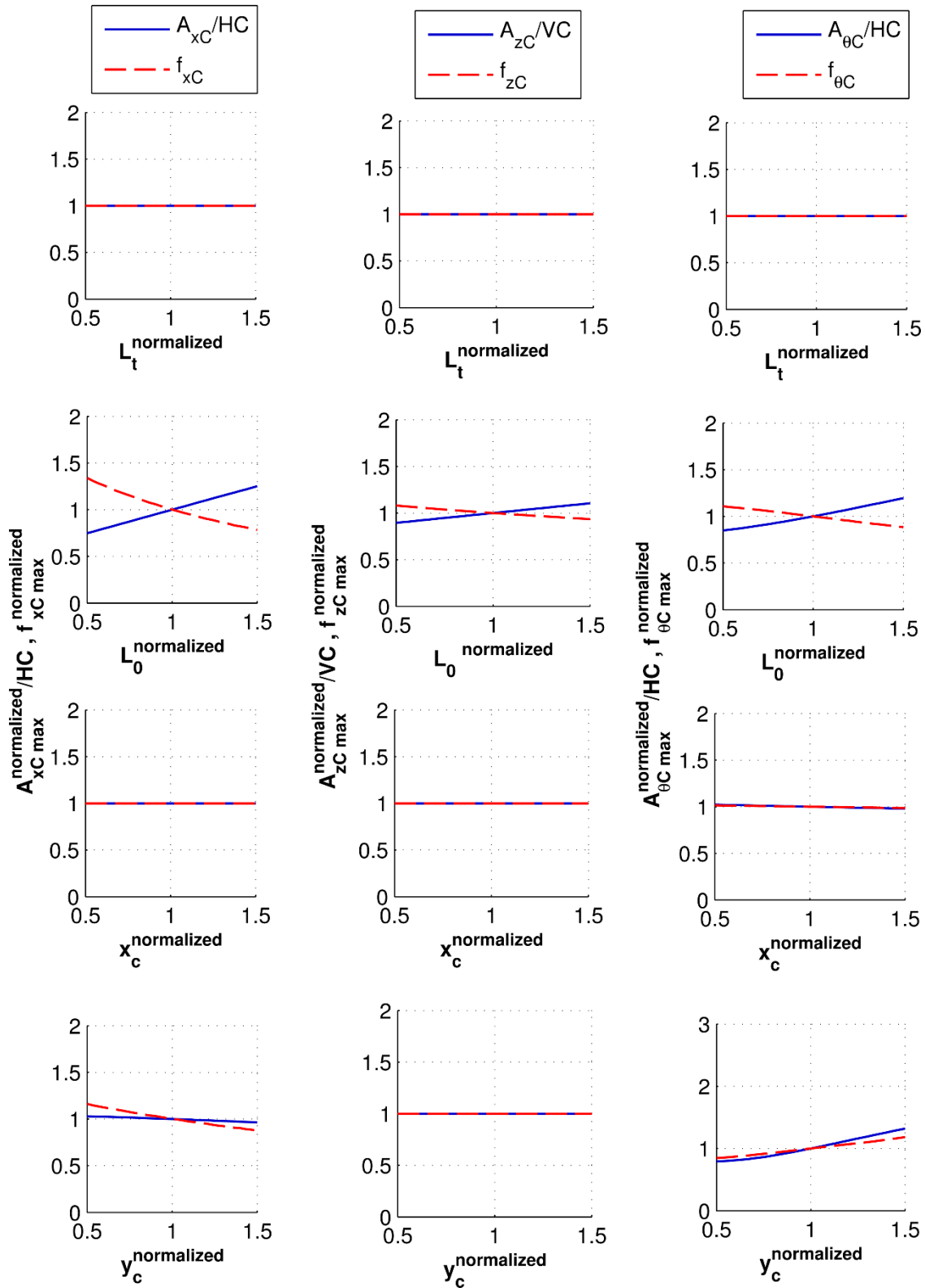


Figure 3-39- Sensitivity of peak frequency and amplitude of centroidal acceleration functions to theoretical model parameters (actual values of NEES pile in unimproved soil with G_{max} and D_{max} soil profiles used as reference model).

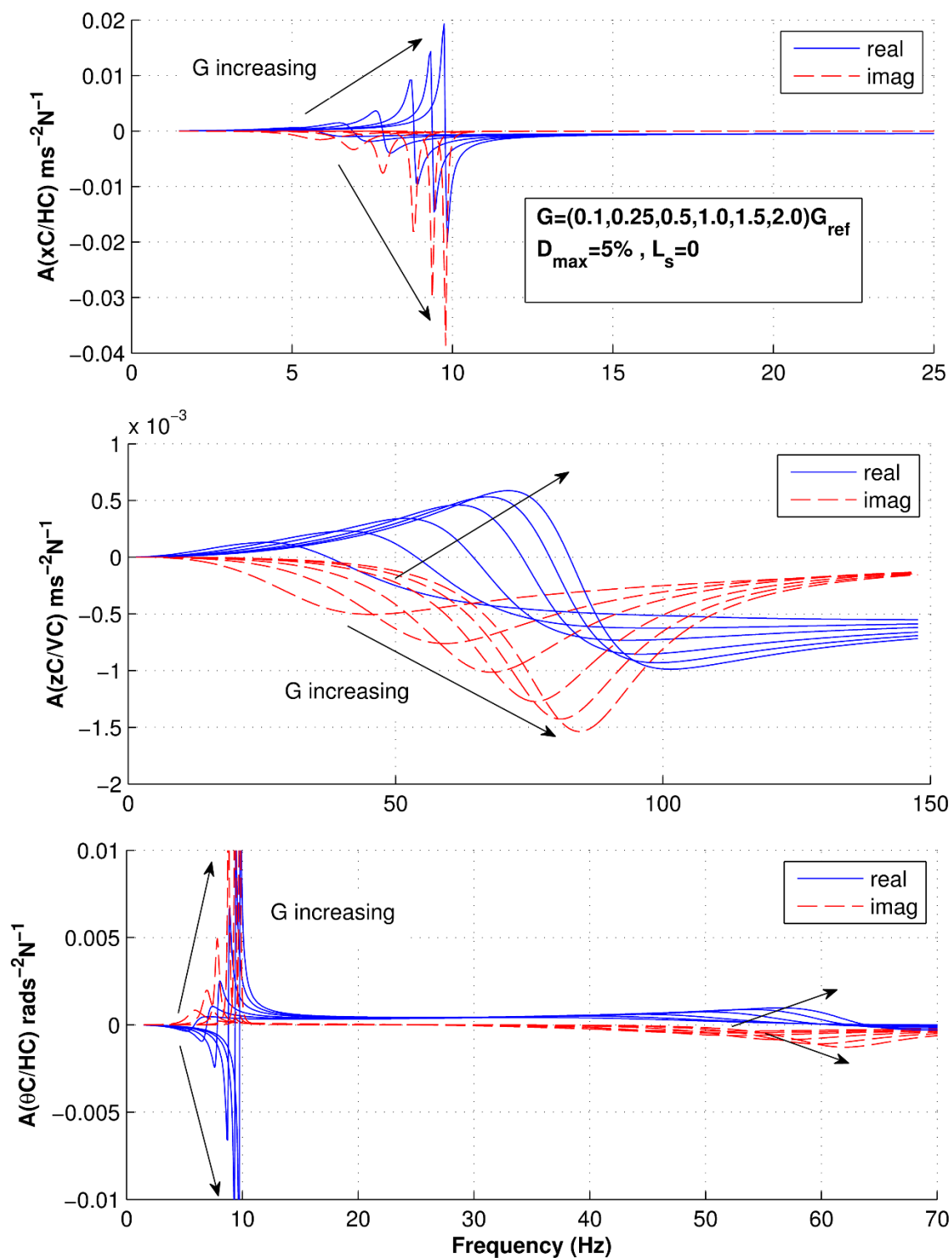


Figure 3-40- Sensitivity of centroidal acceleration functions to magnitude of soil shear modulus profile (reference model uses actual values of NEES pile in unimproved soil with Hardin-Drnevich G and D profiles corrected for the calculated strain profile at the site).

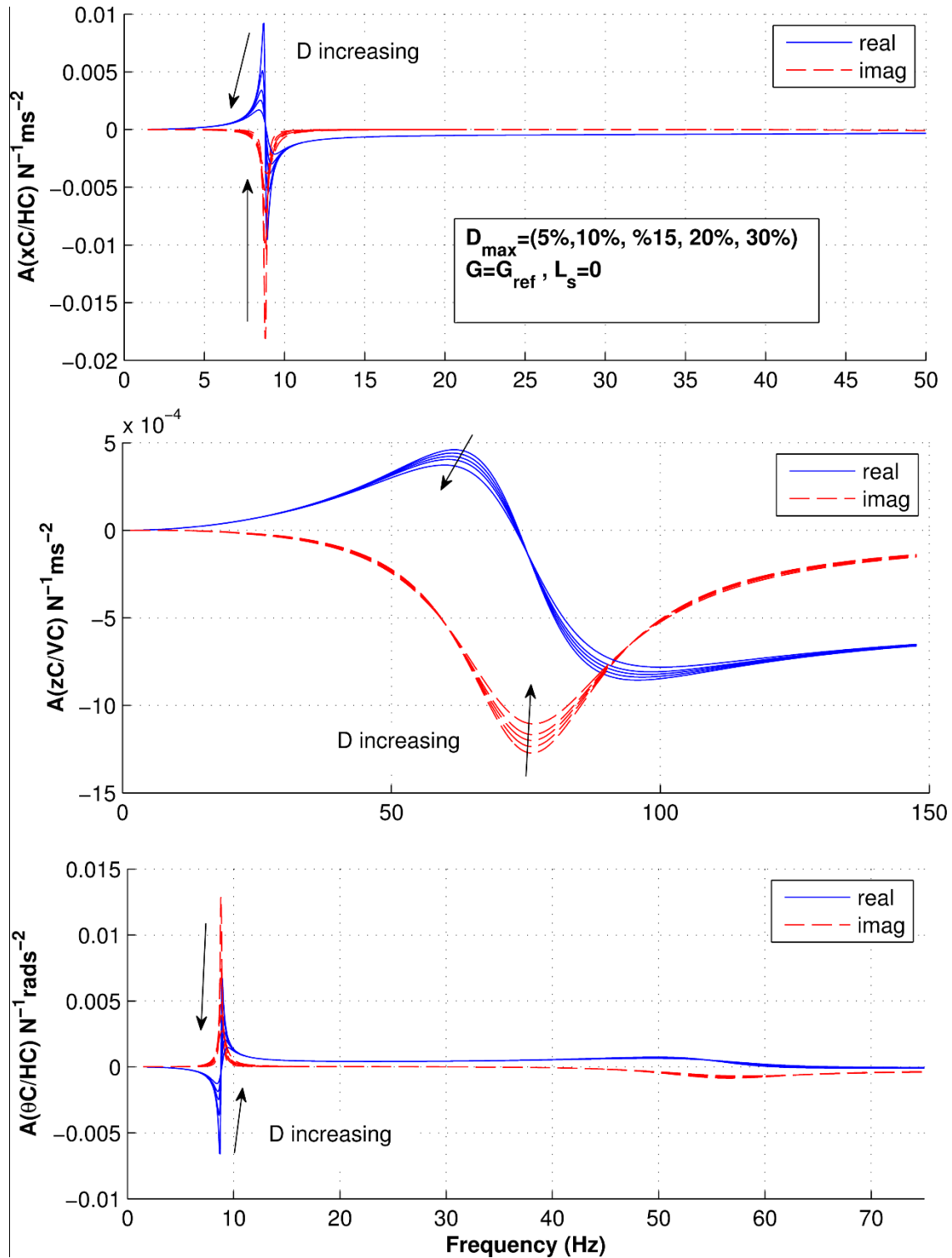


Figure 3-41- Sensitivity of centroidal acceleration functions to magnitude of soil damping profile (reference model uses actual values of NEES pile in unimproved soil with Hardin-Drnevich G and D profiles corrected for the calculated strain profile at the site).

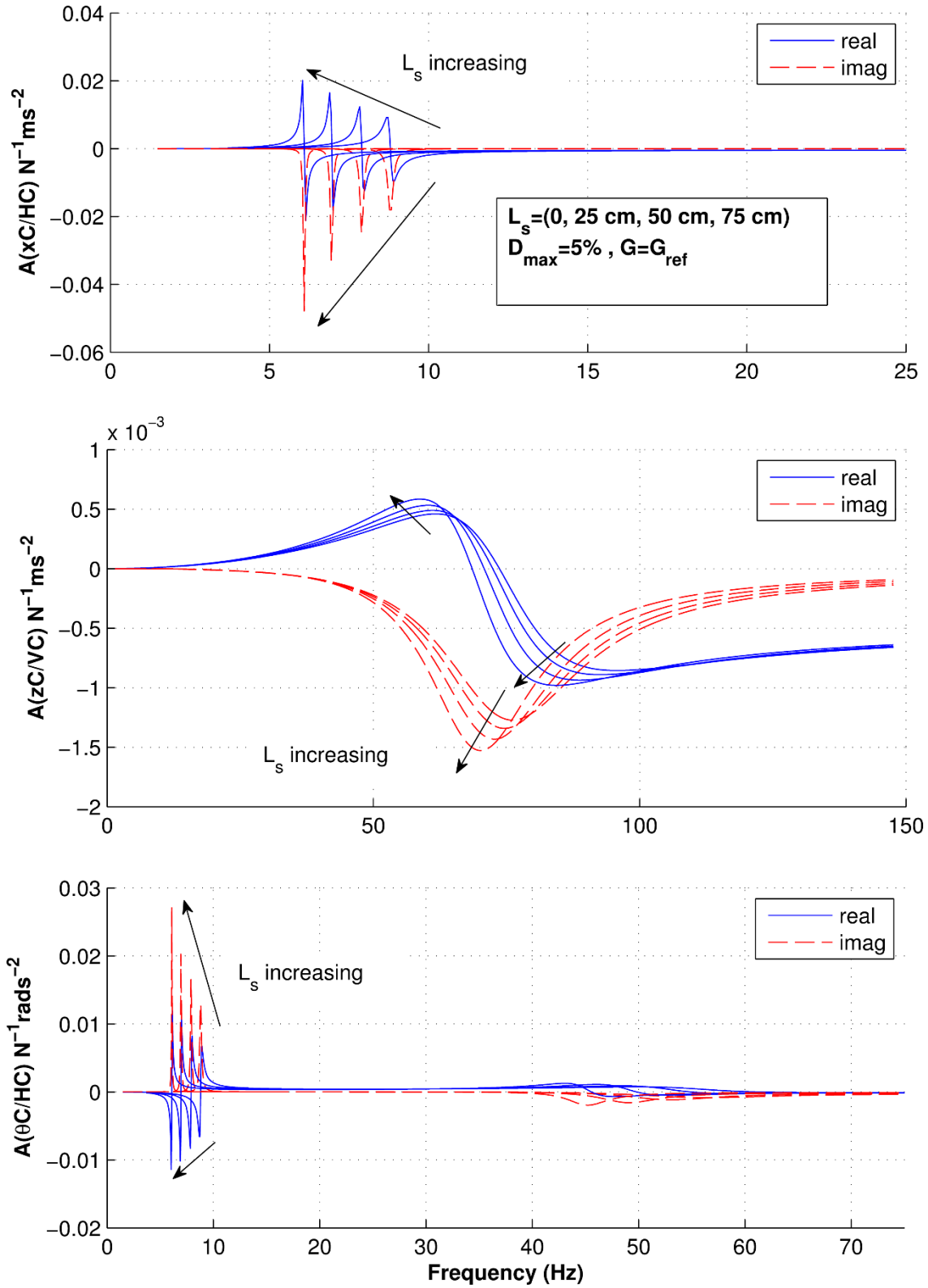


Figure 3-42- Sensitivity of centroidal accelerance functions to gapping depth L_s (reference model uses actual values of NEES pile in unimproved soil with Hardin-Drnevich G and D profiles corrected for the calculated strain profile at the site).

3.6 APPENDIX

This section contains calculations of the inertial properties of the pile-cap, pile, and shaker system for the HC, VC, and VE test configurations.

3.6.1 Inertial properties of system components

3.6.1.1 Rigid pile-cap block with embedded pile segment

The inertial properties of the pile cap and embedded pile segment are calculated based on the volume and centroidal properties obtained from a 3D AutoCAD model generated during design of the pile cap. The AutoCAD output is presented in Figure 3-43. Two different materials that compose the rigid pile-cap, concrete and steel, are considered separately. The composite inertial properties of the pile-cap can be found by combining the results of these two components using the parallel axis theorem. The details of the calculations are presented in Figure 3-44. The resulting combined inertial properties for the concrete block, steel rebar cage and embedded pile segment are summarized in Table 3-10.

Table 3-10- Combined inertial properties of pile-cap and embedded pile segment.

Mass (kg)	X_c (m)	Y_c (m)	Z_c (m)	I_{yc} (kg.m²)
1844.15	0.4572	0.4572	0.461	263.768
Mass (lb)	X_c (in)	Y_c (in)	Z_c (in)	I_{yc} (lb.in²)
4065.42	18.00	18.00	18.13	901340.60

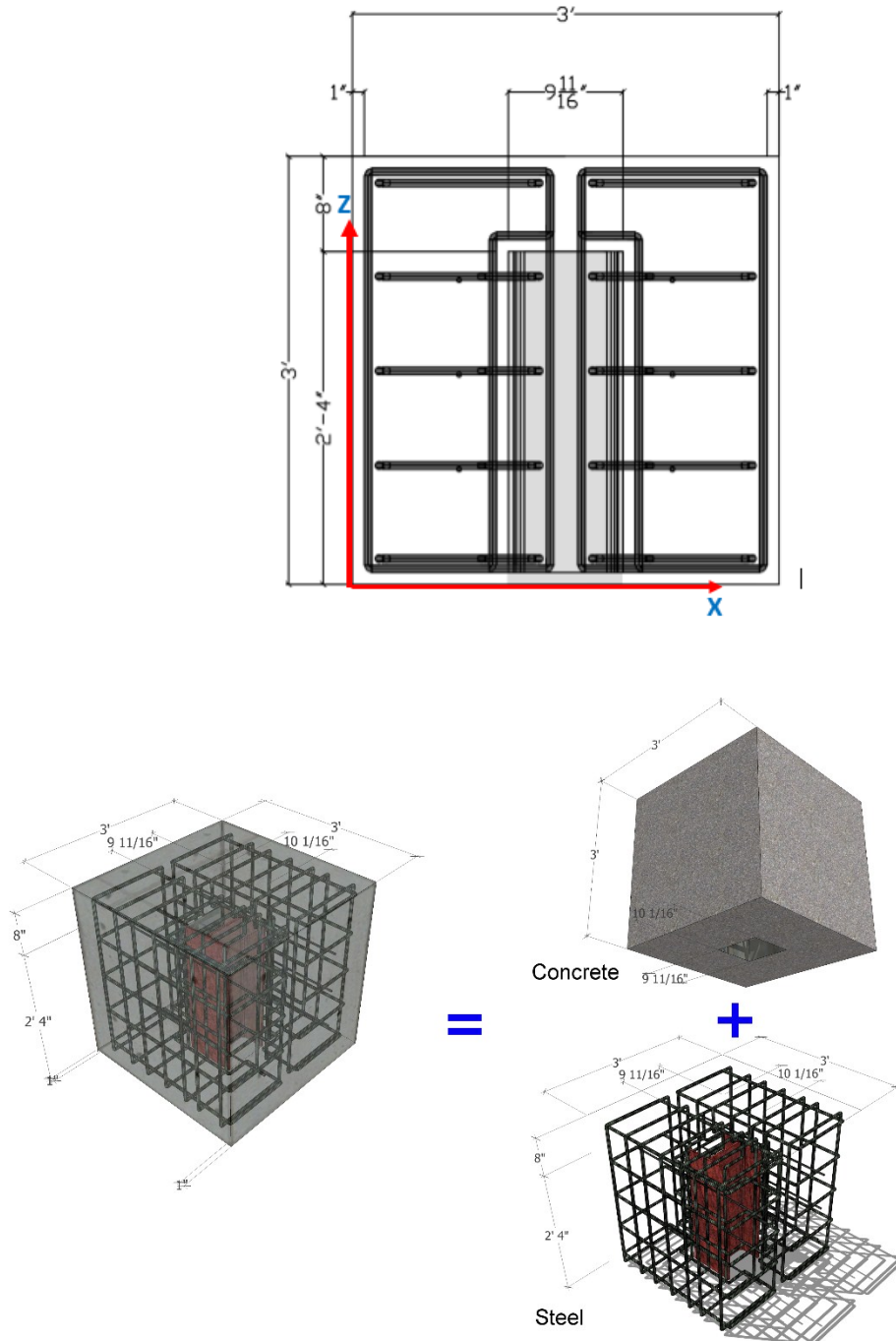
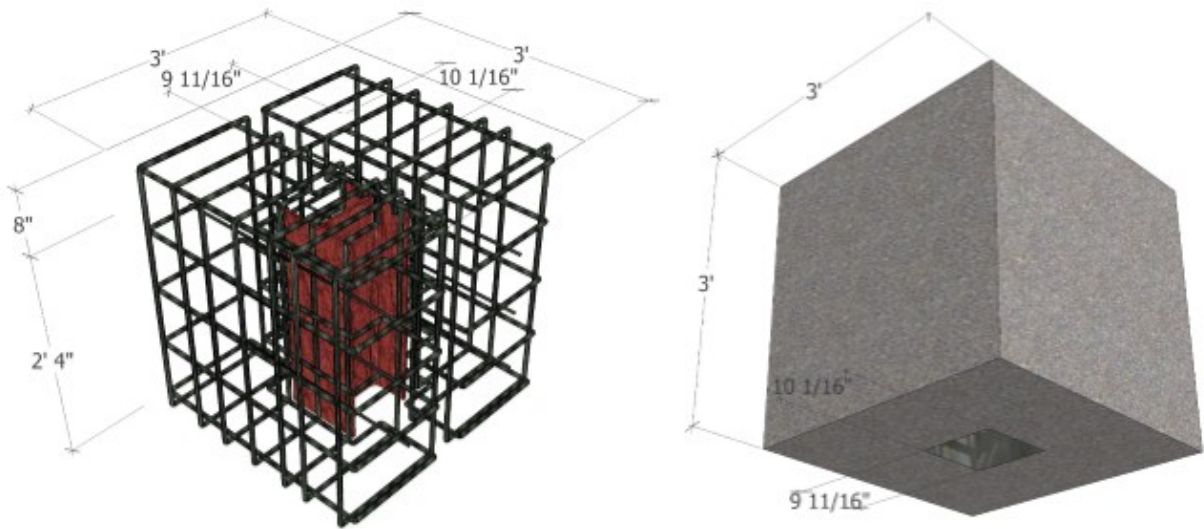


Figure 3-43. 3D CAD model of pile-cap, pile stem, and reinforcing bar.



Concrete	ρ (kg/m ³)	V (m ³)	Mass (kg)	X _c (m)	Y _c (m)	Z _c (m)	I _y (kg.m ²)
	2400	0.707455	1697.89	0.4572	0.4572	0.464	244.535
	ρ (lb/in ³)	V (in ³)	Mass (lb)	X _c (in)	Y _c (in)	Z _c (in)	I _y (lb.in ²)
0.0867	43171.56	3742.97	18.00	18.00	18.25	853741.67	
Steel	ρ (kg/m ³)	V (m ³)	Mass (kg)	X _c (m)	Y _c (m)	Z _c (m)	I _y (kg.m ²)
	7850	0.018632	146.26	0.458066	0.457065	0.425	19.036
	ρ (lb/in ³)	V (in ³)	Mass (lb)	X _c (in)	Y _c (in)	Z _c (in)	I _y (lb.in ²)
0.2836	1136.97	322.44	18.0341	17.9947	16.746	65049.97	

Figure 3-44-Inertial properties of concrete and steel components of pile-cap.

3.6.1.2 Inertial properties of shaker

For the servo hydraulic shaker, the manufacturer provided the inertial properties in Table 3-11. Figure 3-45 shows the rigid and stationary parts of the hydraulic shaker. Since a detailed CAD drawing of the shaker was not available, the following approximate calculations were used to verify the inertial properties provided by the manufacturer before using them in acceleration calculations. Because of the complicated geometry of the stationary part of the shaker, the verification calculations were only performed for the moving part.

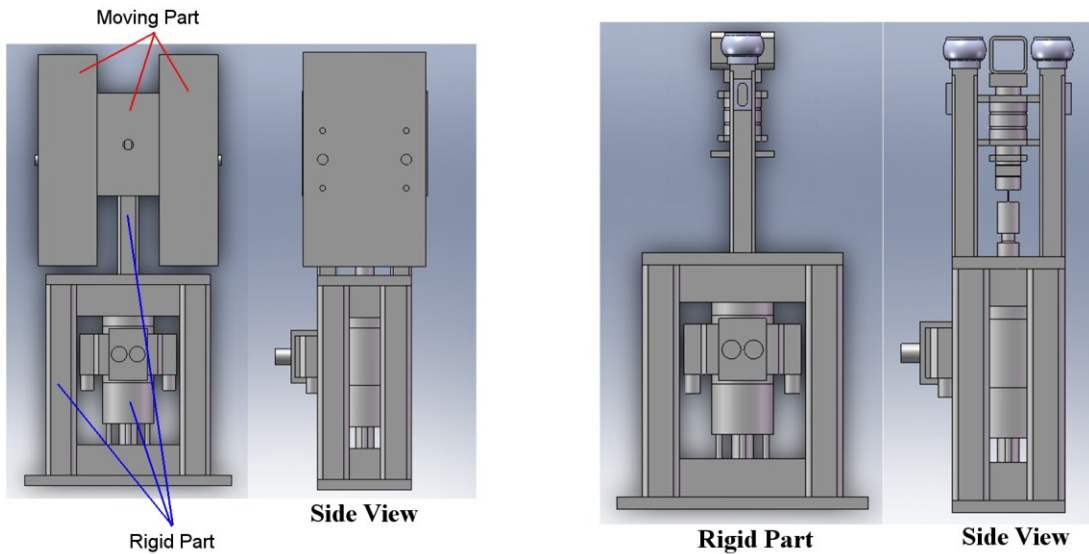


Figure 3-45- Schematic of moving and stationary parts of the hydraulic shaker (courtesy of ANCO Engineers, Inc.).

Table 3-11- Inertial properties of servo-hydraulic shaker provided by Anco Engineers, Inc.

		Mass (lb.)	Axial centroid Distance from mounting surface (in)	centroid location offset from axis (in)	Polar moment of inertia about centroid (lb-in ²)
Stationary Mass	Frame+ actuator- piston	225	12.6	0.18	34691.5
Moving mass+ carriage+pist on	0 weights	0	28.5	0	7838
	2 weights	96	29.68294	0	12560.77
	4 weights	192	30.12606	0	17080.12
	6 weights	288	30.35806	0	21586.53
	8 weights	384	30.5008	0	26095.87
	10 weights	480	30.59748	0	30609.21
	12 weights	576	30.66729	0	35125.85
	14 weights	672	30.72008	0	39645

Figure 3-46 shows a simplified representation of the moving part of the shaker with eight added masses, four on each side.

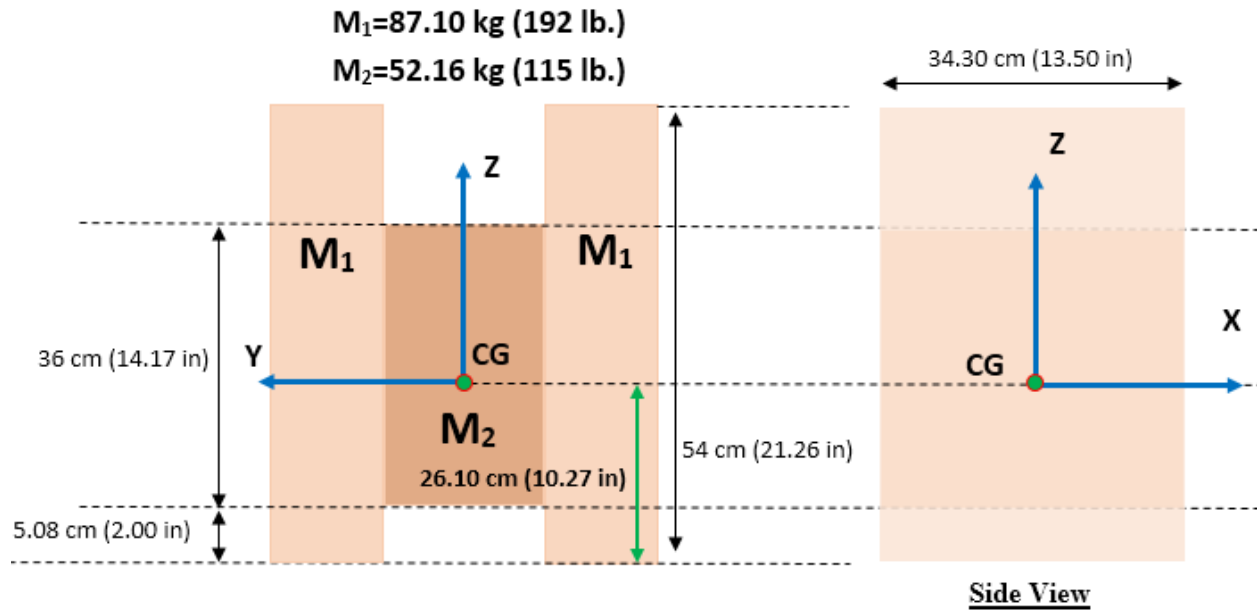


Figure 3-46- Dimensions and inertial properties of the moving part of the hydraulic shaker.

$$J_{yy} = \int_V r^2 dm = \rho \int_V r^2 dV = 2\rho \int_{-y_1}^{+y_2} \int_{-x_1}^{+x_2} \int_{-z_1}^{+z_2} (X^2 + Z^2) dz dx dy + \rho \int_{-y_3}^{+y_4} \int_{-x_1}^{+x_2} \int_{-z_3}^{+z_4} (X^2 + Z^2) dz dx dy \quad (3-61)$$

$$J_{yy} = \frac{2 \times 87.10}{34.3 \times 54} \int_{-34.3/2}^{+34.3/2} \int_{-26.10}^{+27.9} (x^2 + z^2) dz dx + \frac{52.16}{34.3 \times 36} \int_{-34.3/2}^{+34.3/2} \int_{-21.02}^{+14.98} (x^2 + z^2) dz dx$$

$$= 60075.9 + 11321.8 = 71397.7 \text{ Kg.cm}^2 \quad (24397.8214 \text{ lb.in}^2)$$

The estimated inertial properties of the moving mass of the shaker are summarized below. Since they are comparable to the values in Table 3-11, it is assumed that the inertial properties of the stationary portion provided by the manufacturer can be trusted for acceleration calculations.

$$M_{mm}=226.34 \text{ kg (499 lb.)}$$

$$Z_{CG}=75.10 \text{ cm (29.57 in)}$$

$$J_{mm}=7.1398 \text{ kg.m}^2 \text{ (24397.82 lb. in}^2\text{)}$$

Figure 3-47 shows a simplified model of both the rigid stationary and moving parts of the shaker assembled in a global coordinate system. The dimensions and inertial properties from Table 3-11 are also shown on the figure. These values were used for acceleration calculations throughout the thesis.

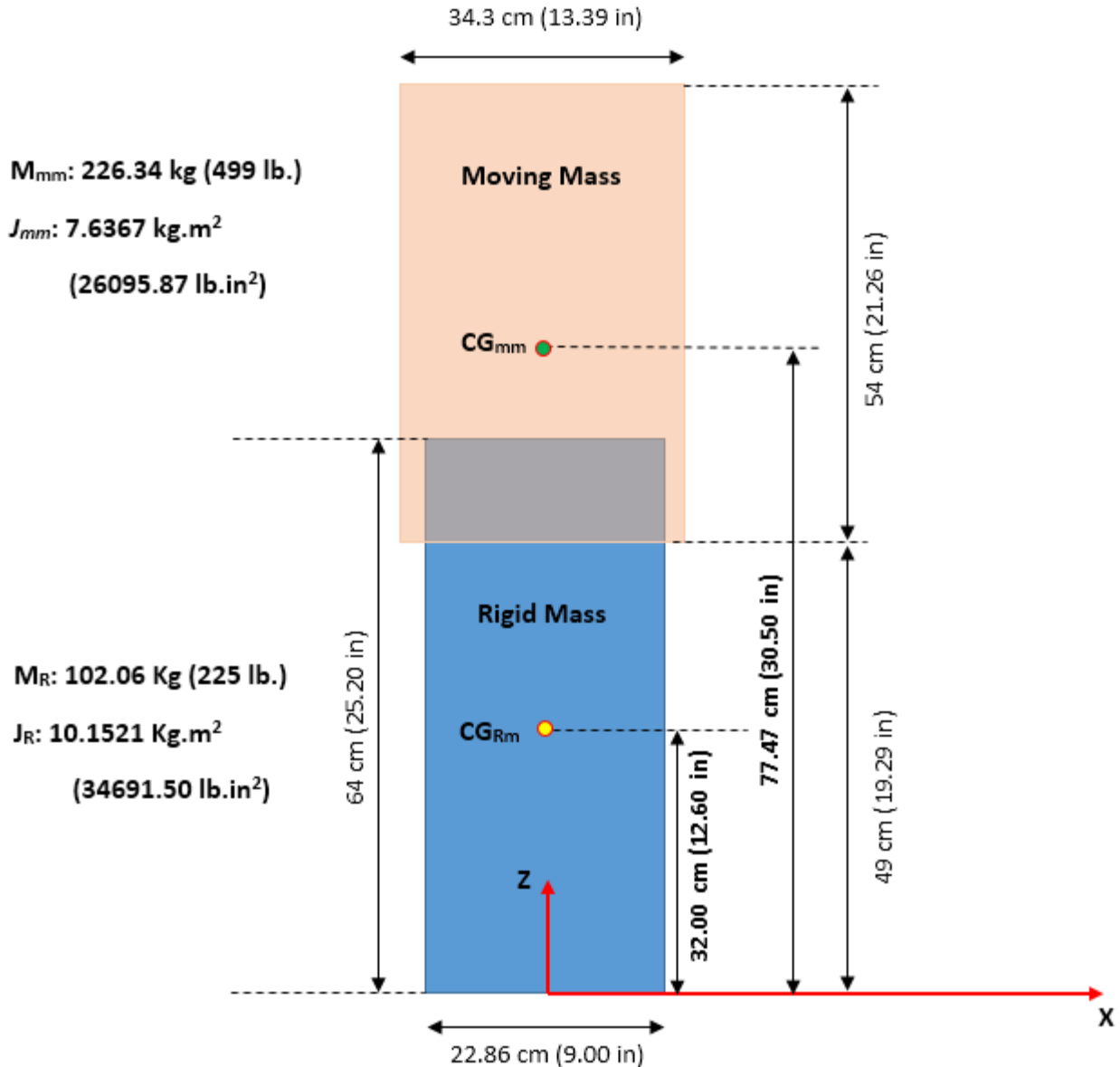


Figure 3-47- Schematic of hydraulic shaker as tested, showing stationary and moving parts and inertial properties provided by Anco Engineers, Inc.

3.6.2 Composite pile-cap-shaker properties for the three test configurations

Based on the location and the orientation of the shaker in each test configuration, one can combine the previous results to calculate the inertial properties of the composite pile-cap-shaker system, which includes only the rigid stationary portion of the shaker. Results of these calculations

are presented for the three test configurations in the sections below. The moving part of the shaker is treated as a separate rigid body in the calculations of Chapter 2.

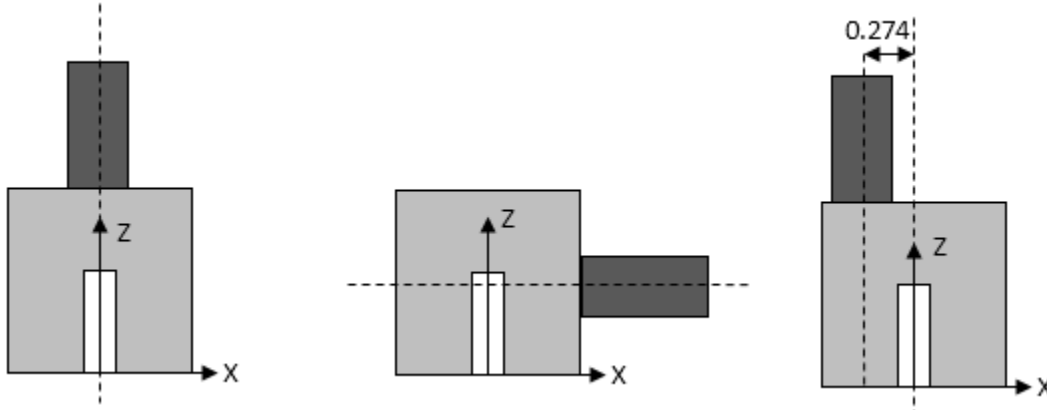


Figure 3-48- Shaker location and orientation in VC, HC, and VE test configurations.

3.6.2.1 VC test configuration

$$M = 1844.15 + 102.06 = 1946.21 \text{ kg } (4290.66 \text{ lb})$$

$$Z_{CM} = \frac{1844.15 \times (0.461) + 102.06 \times (0.32 + 0.9144)}{1946.21} = 0.50 \text{ m } (19.75 \text{ in})$$

$$X_{CM} \approx 0, \quad Y_{CM} = 0$$

$$J_{Y-CM} = 263.768 \text{ kg.m}^2 + 1844.15 \text{ kg} \times (0.502 \text{ m} - 0.461 \text{ m})^2 + 10.152 \text{ kg.m}^2 \\ + 102.06 \text{ kg} \times (0.32 \text{ m} + 0.9144 \text{ m} - 0.49 \text{ m})^2 = 332.13 \text{ kg.m}^2 (1134947.60 \text{ lb.in}^2)$$

3.6.2.2 HC test configuration

$$M = 1844.15 + 102.06 = 1946.21 \text{ kg } (4290.66 \text{ lb})$$

$$Z_{CM} = \frac{1844.15 \times (0.461) + 102.06 \times (0.4572)}{1946.21} = 0.461 \text{ m } (18.15 \text{ in})$$

$$X_{CM} = \frac{102.06 \times (0.4572 + 0.32)}{1946.21} = 0.04 \text{ m } (1.57 \text{ in}), \quad Y_{CM} = 0$$

$$J_{Y-CM} = 263.768 \text{ kg.m}^2 + 1844.15 \text{ kg} \times \left[(0.461 - 0.45)^2 + (0 - 0.04)^2 \right] + 10.1512 \text{ kg.m}^2 \\ + 102.06 \text{ kg} \times \left[(0.4572 - 0.45)^2 + (0.4572 + 0.32 - 0.04)^2 \right] = 332.56 \text{ kg.m}^2 (1136431.31 \text{ lb.in}^2)$$

3.6.2.3 VE test configuration

$$M = 1844.15 + 102.06 = 1946.21 \text{ kg } (4290.66 \text{ lb})$$

$$Z_{CM} = \frac{1844.15 \times (0.461) + 102.06 \times (0.32 + 0.9144)}{1946.21} = 0.49 \text{ m } (19.29 \text{ in})$$

$$X_{CM} = \frac{102.06 \times (-0.274)}{1946.21} = -0.014 \text{ m } (-0.55 \text{ in}), Y_{CM} = 0$$

$$J_{Y-CM} = 263.768 \text{ kg.m}^2 + 1844.15 \text{ kg} \times \left((0.49 - 0.461)^2 + (0.014)^2 \right) + 10.152 \text{ kg.m}^2 \\ + 102.06 \text{ kg} \times \left((0.32 + 0.9144 - 0.49)^2 + (-0.274 + 0.014)^2 \right) = 339.29 \text{ kg.m}^2 (1159401.91 \text{ lb.in}^2)$$

3.6.3 Summary

Table 3-12 summarizes the inertial calculations in this section. These values are used to calculate accelerances functions throughout this study.

Table 3-12- Final inertial properties for three different test configurations.

	VC Test	VE Test	HC Test
M	1946.21 kg (4290.66 lb)	1946.21 kg (4290.66 lb)	1946.21 kg (4290.66 lb)
J _y	332.13 kg.m ² (1134947.60 lb.in ²)	339.29 kg.m ² (1159401.91 lb.in ²)	332.56 kg.m ² (1136431.31 lb.in ²)
X _{CM}	0	-0.014 m (-0.55 in)	0.04 m (1.57 in)
Y _{CM}	0	0	0
Z _{CM}	0.49 m (19.75 in)	0.49 m (19.29 in)	0.46 m (18.15 in)

CHAPTER IV: COMPUTATIONAL MODELING AND OPTIMIZATION

4.1 Overview

The theoretical background and computational methods discussed in Chapter 3 will be employed in this chapter to simulate the experimental results introduced in Chapter 2. The ability and efficiency of the different analysis methods to capture the dynamic impedances of the actual problem are first examined, and the best method is used for the rest of the analyses. In order to find the best theoretical prediction of the experimental data, some adjustments will be applied to the problem's input parameters, including the soil shear modulus and damping profiles and the gapping length of the pile. These modifications to the previously defined parameters are performed to examine the possible effects of additional important physical parameters, such as soil disturbance due to pile installation and a reduced soil-pile contact length due to gapping.

4.2 Approximate Method versus BEM Analysis

As described in detail in Chapter 3, the pile and soil domains can be treated using the rigorous three-dimensional boundary element program BEASSI, or one of the available approximate solutions such as that of Novak and Aboul-Ella (1978). While the rigorous solution can capture significant aspects of the problem such as stress singularities at the boundaries, low-frequency layer resonance, and soil modulus variation below the pile-tip, the approximate solution offers limited options for modeling the soil profile below the pile-tip, and cannot capture the dip in impedance functions in the low-frequency range.

However, it can take 7 to 10 days to analyze the 3-domain soil-pile problem using BEASSI on a modern single CPU system. To speed up the analyses, a parallel version of BEASSI was

modified and compiled in this study to work on the Stampede supercomputing cluster at the Texas Advanced Computing Center (TACC). The Stampede cluster is currently the TACC's most powerful supercomputer, with over one-half million processing cores and a peak performance near 10 petaflops (TACC, 2014). The cluster was accessed through a startup allocation on the Extreme Science and Engineering Discovery Environment (XSEDE), which is supported by National Science Foundation grant number ACI-1053575 (www.xsede.org). After parallelization of the BEASSI code, sequential analyses which required 7-10 days on a single core were performed with the parallelized code in a matter of few hours using between 64 and 96 cores.

Due to the extra computational cost and time required to use the accurate 3D BEM model, it is attractive to use the approximate solution whenever practical. However, to fully understand the limitations of the approximate method, it should be validated against the rigorous BEM solution. The results of such a comparison are presented in Figure 4-1 for the case of the CPT-derived shear modulus profile and zero material damping described in the Appendix of Chapter 2. This figure contains results for both free and fixed pile tip conditions in the Novak-Aboul-Ella solution. Since the pile is flexible (i.e., the active length is less than the total pile length), it can be seen that the pile tip fixity has no effect on the lateral-rocking impedances, but significantly affects the vertical impedance. Additionally, the BEM solution results in impedances having generally greater stiffness and damping than the approximate method, and captures the effects of the soil-layer resonance, which manifests as a dip in the real parts and a cutoff frequency in the imaginary parts of the impedances in the low-frequency range. In contrast, the approximate method does not capture the soil layer resonance effects at low frequencies, and neither the rigid-tip nor the free-tip conditions can provide a close estimation of the vertical mode impedance. This is a consequence

of the approximate method being limited to the fixed or free tip conditions, which makes it incapable of accounting for the soil profile variation beneath the pile tip.

Impedances from the Hardin-Drnevich and CPT soil profiles discussed in Chapter 2 were also examined using both the rigorous BEM and approximate analytical methods (Figure 4-2). For these analyses, the gapping length was set to zero, and the maximum damping ratio for each profile was set to 5%. Similar to the results of Figure 4-1, only the BEM solution captures the soil layer resonance effects at low frequency, and the approximate method cannot capture the vertical response. Additionally, the Hardin-Drnevich profile results in higher impedances than the CPT profile for the entire frequency range. This trend is most significant for the real parts of the impedances.

The effects of these discrepancies in impedance functions on the centroidal pile accelerances are presented in Figures 4-3 to 4-5. The results from the approximate solution in the low frequency range, even if they appear able to capture the experimental accelerance, cannot be fully trusted, as they are known to give erroneous impedances as demonstrated above. Additionally, the CPT-derived shear modulus profile is based upon empirical correlations derived from data with large scatter, and the CPT correlations do not provide a means to estimate a material damping ratio profile. Therefore the results from the CPT profile, if reasonable, can be used as clues to modify the Hardin-Drnevich profile, which has a solid experimental basis relating modulus and damping behavior for a range of several relevant soil parameters.

Among all the analyses shown in Figures 4-3 to 4-5, the model employing the CPT profile and BEASSI solution demonstrates the closest overall agreement with the experimental accelerance results. This agreement is most profound for the vertical mode of motion.

Additionally, the model which uses the Hardin-Drnevich profile and BEASSI solution shows the highest stiffness and lowest damping at low frequencies. This system can be softened to more closely model the observed response by incorporating a gapping depth which is consistent with field observations (the top few feet of soil between the flanges next to the pile web was excavated by others), and also by increasing the material damping ratio to account for the higher strains near the pile top.

A few differences between the theoretical and experimental accelerances in Figures 4-3 to 4-5 should be noted. First, a spurious peak can be seen in the experimental horizontal and rotational accelerances near 23 Hz. This could possibly be from imperfect symmetry of the pile-cap-shaker system beyond that accounted for in the inertial calculations of Chapter 3, or additional excitations that were not accounted for. One possible source of asymmetry and excitation are the hydraulic hoses, which were suspended near the shaker using straps to minimize their influence. Another possible source is torsional motion of the pile cap, which was observed to be easily excitable by hand, but not noticeable during actual tests.

Second, the theoretical vertical accelerance magnitude decreases towards an asymptote equal to the inverse of the pile cap mass at high frequency, but the experimental accelerance increases as it approaches an additional higher-mode peak. This may be due to the simplifying assumption that the fixed portion of the shaker behaves rigidly while its moving mass translates only along the actuator's axis. In reality, dynamic resonance of the shaker base frame or the rod connecting the actuator and moving masses might be influencing the pile cap response at high frequencies.

Third, a large peak exists in the experimental rotational acceleration near 75 Hz, which is not predicted theoretically. None of the presented models are capable of capturing this peak in the rotational mode in Figure 4-5. This extra peak may also be due to the reasons mentioned above, or a result of trends in the actual soil-pile impedances from a phenomenon not yet accounted for in the computational models.

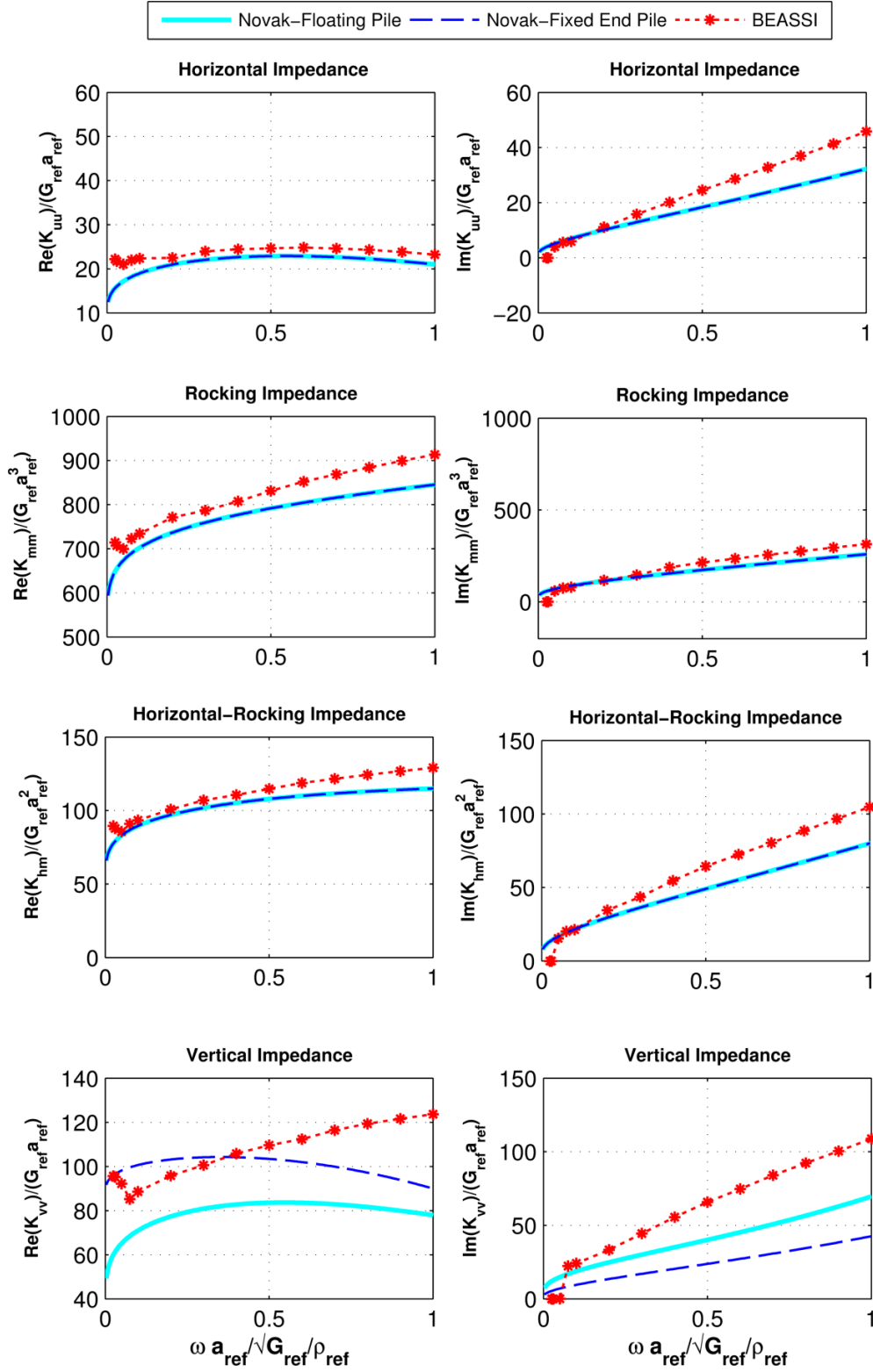


Figure 4-1-Comparison of impedance functions from approximate and rigorous soil-pile interaction analyses. Free and fixed pile-tip conditions are shown for the approximate method.

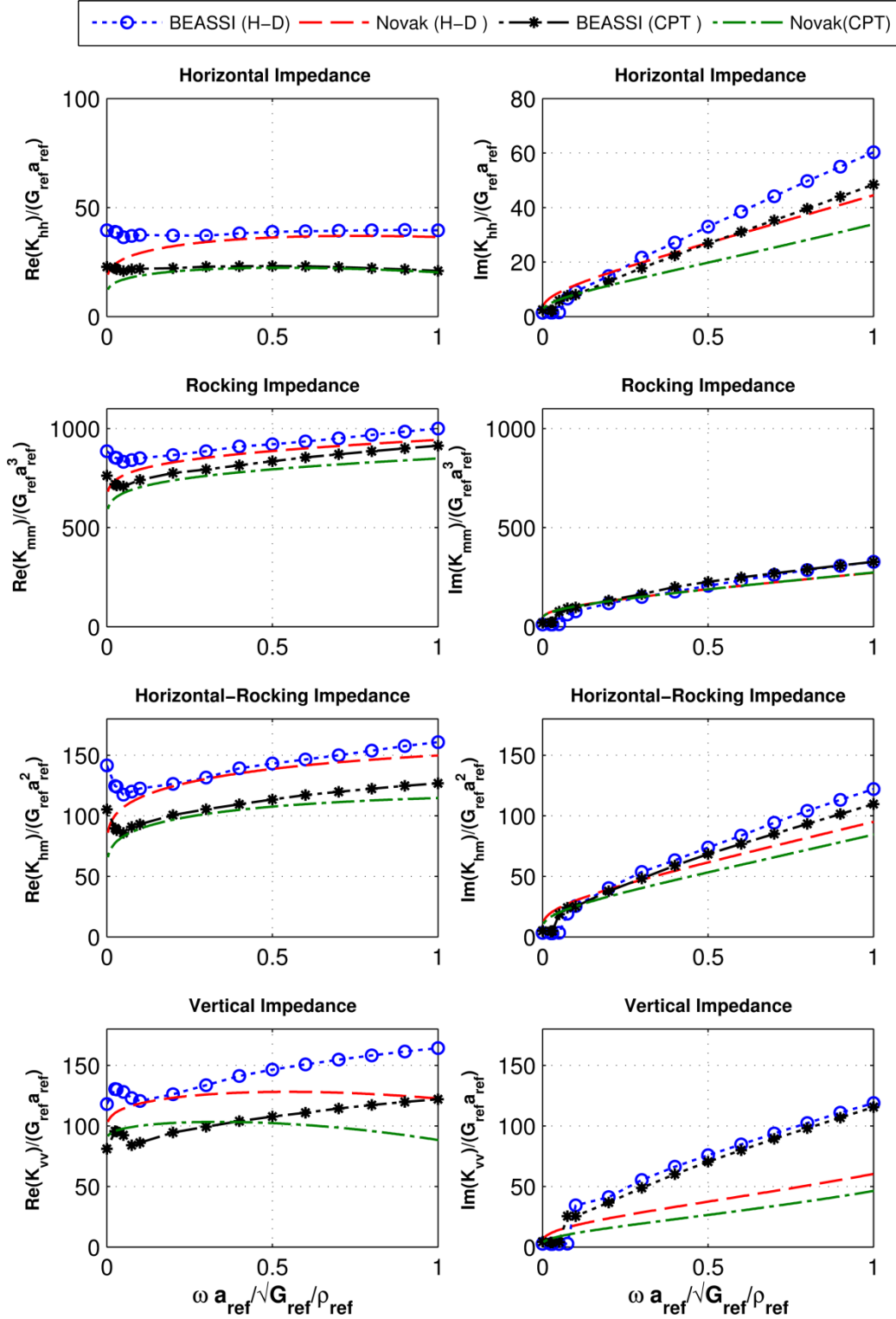


Figure 4-2 Impedance functions from approximate (Novak-Aboul-Ella) and rigorous (BEASSI) soil-pile interaction analyses using CPT and Hardin-Drnevich soil profiles. Zero gapping depth and 5% maximum material damping ratio are assumed.

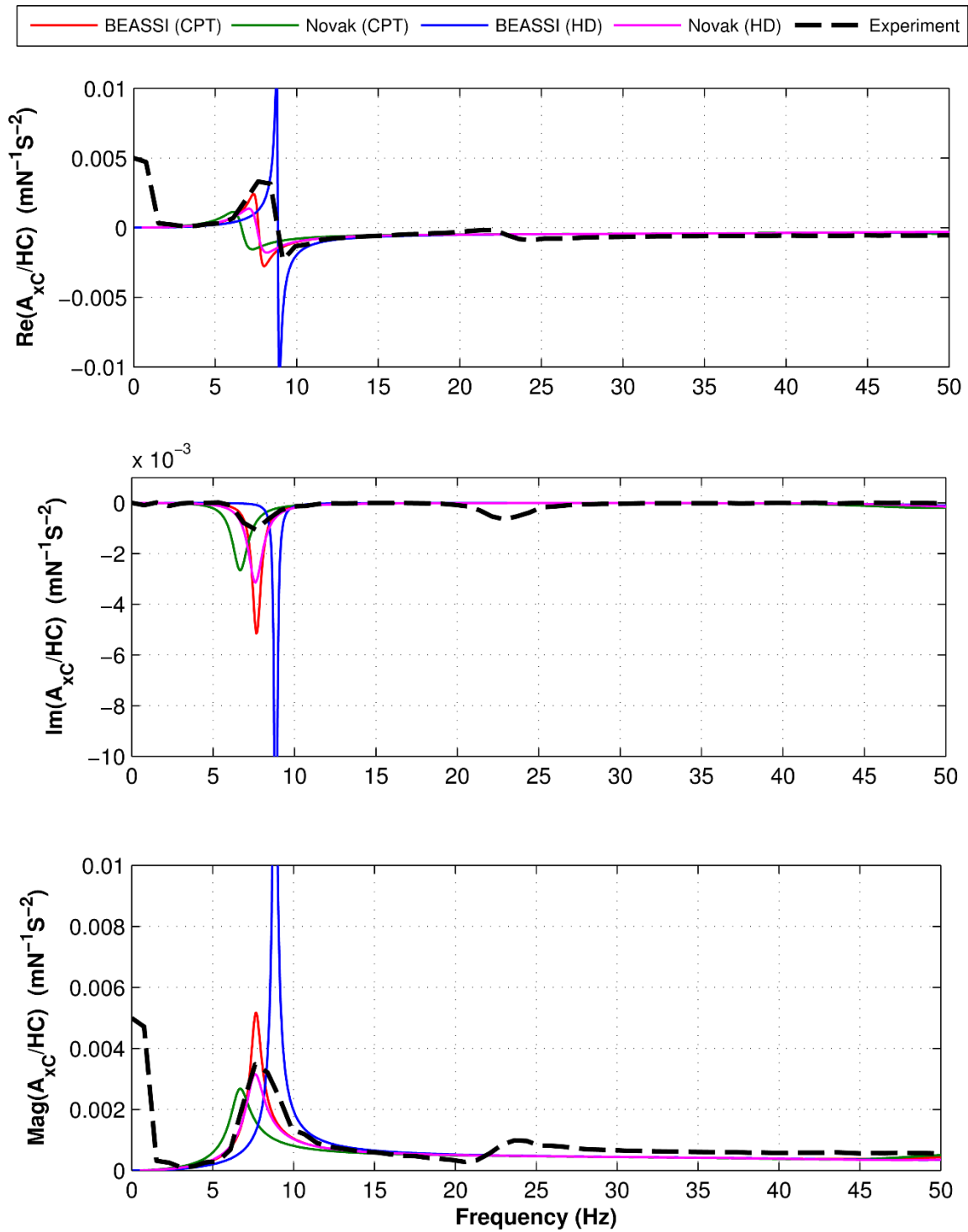


Figure 4-3- A_{x_c}/HC acceleration functions obtained from approximate and rigorous soil-pile interaction analyses using CPT and Hardin-Drnevich soil profiles. Zero gapping depth and 5% maximum material damping ratio are assumed. Experimental data from Test U-HC-R2.

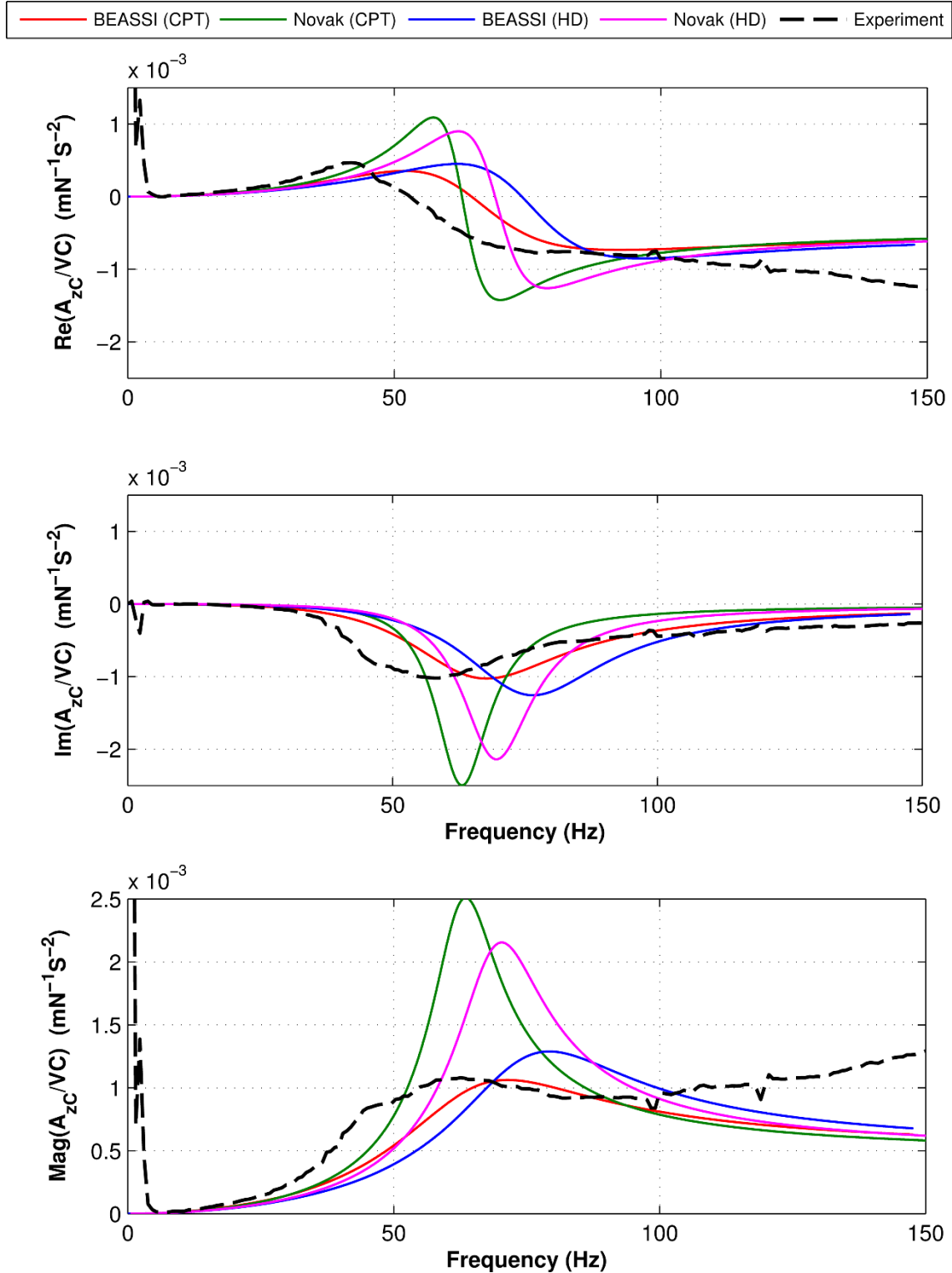


Figure 4-4- A_{zC}/VC acceleration functions obtained from approximate and rigorous soil-pile interaction analyses using CPT and Hardin-Drnevich soil profiles. Zero gapping depth and 5% maximum material damping are assumed. Experimental data from Test U-VC-R2.

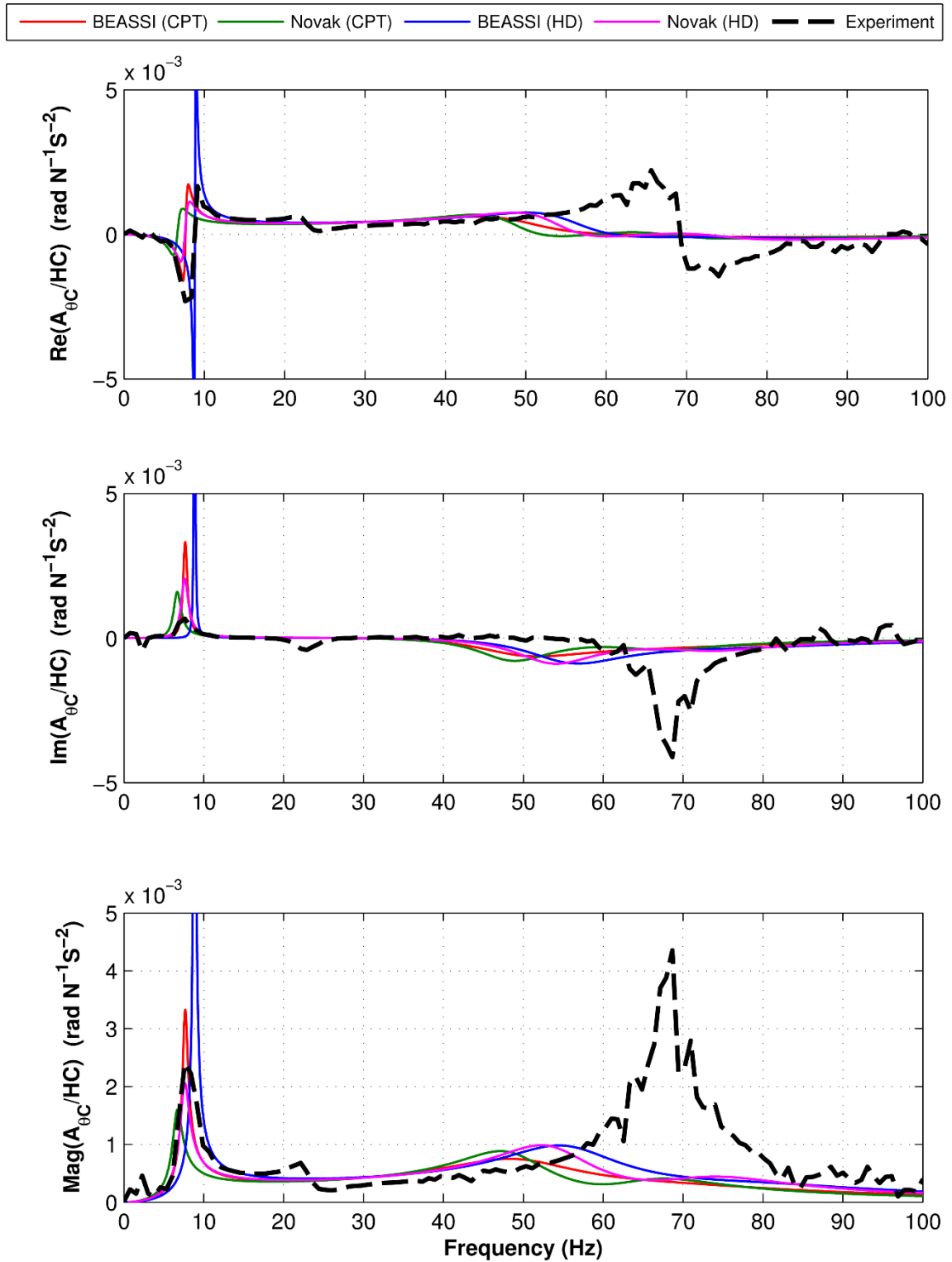


Figure 4-5- $A_{\theta C}/HC$ acceleration functions obtained from approximate and rigorous soil-pile interaction analyses using CPT and Hardin-Drnevich soil profiles. Zero gapping depth and 5% maximum material damping are assumed. Experimental data from Test U-HC-R2.

4.3 Optimization of Soil Profiles

The un-modified shear modulus and damping profiles developed in Chapter 2 using CPT data and the Hardin-Drnevich relations were used in BEASSI to find the theoretical impedances and accelerances shown in the previous section. As discussed above, the main drawback of the CPT method is that it provides only a shear modulus, and an arbitrary damping profile must therefore be assumed for the analyses. Moreover, a number of different correlations available in literature for estimating small-strain shear modulus G_{\max} from CPT data (e.g., TRB, 2007), do not give consistent results and were derived by fitting data sets having significant scatter. Even if the CPT tests were performed carefully, they took place several months before the pile vibration tests and do not subject the soil to the same strain levels experienced in the experiments. The Hardin-Drnevich soil profile, on the other hand, has a solid experimental basis relating both modulus and damping to several soil parameters including soil shear strain as detailed in Chapter 2, which enables parametric sensitivity analyses to be performed. For these reasons, the Hardin-Drnevich soil profile will be used for the remainder of this study.

The Hardin-Drnevich relations incorporate the effect of numerous parameters on the dynamic properties of soil as discussed in Chapter 2. Among these parameters, shear strain has the greatest influence, and its variation with depth can dramatically affect the resulting shear modulus and damping profiles. Therefore, the modulus and damping profiles calculated based on a uniform shear strain profile as presented in Chapter 2 should be iteratively updated for the actual shear strain profile, until a converged set of “strain-compatible” modulus and damping profiles are achieved. Such a procedure will be described in detail in Section 4.3.2. However, other physical aspects of the problem such as the effect of soil disturbance during pile installation, pile-soil gapping near the soil surface, soil heterogeneity, and non-horizontal layering have yet to be

captured simultaneously for a realistic dynamic analysis. The complex theoretical mechanisms for each of the aforementioned effects would require extensive accurate data on pile and soil properties and pile installation processes. However, this information was not available for the present project, nor is such a level of detail available in most practical cases.

As a practical solution, a compound correction factor can be applied to the soil shear modulus and damping profiles to account for those effects mentioned above (as well as others), based on physical reasoning. For example, the larger pile displacements near the soil surface will result in larger soil strains, which will cause a reduction in shear modulus and increase in damping near the soil surface within some zone of influence around the pile. In the far-field, this effect will be negligible and the modulus and damping profiles would therefore be those corresponding to small strains. In other words, the proposed modified soil profile can be expressed as

$$(H - D \text{ Profile})_{\text{modified}} = (H - D \text{ Profile})_{\text{actual strain}} \times MF(z) \quad (4.1)$$

where the modification factor, $MF(z)$, accounts for several factors and should be calculated at each depth. The two terms on the right hand side of Eq. (4.1) are discussed in Sections 4.3.2 and 4.3.3.

4.3.1 G_{\max} and $D_{s \max}$ profiles

As a first attempt, the upper-bound Hardin-Drnevich soil profiles corresponding to the small-strain condition for shear modulus, G_{\max} , and the large-strain condition for damping, $D_{s \max}$, are examined. It should be noted that these profiles are not strain compatible. That is, G_{\max} occurs with D_{\min} at small strain, and G_{\min} occurs with D_{\max} at large strain. However, this simple profile reflects all the soil properties upon which G_{\max} and D_{\max} depend, except for shear strain. The detailed formulations of the profiles shown in Figure 4-6 can be found in the Appendix of

Chapter 2. As described above, the dynamic pile displacements are largest near the soil surface and decrease towards zero with depth. The soil strains will therefore also generally be largest near the surface, leading to reduction of shear modulus from the upper bound G_{\max} in Figure 4-6, and returning towards the G_{\max} profile as strains decrease with depth. Conversely, the larger strains will result in damping that is greatest near the surface (with an upper bound given by the D_{\max} profile in Figure 4-6), and damping will reduce towards zero as strains decrease with depth. For reference, the theoretical acceleration functions resulting from the incompatible G_{\max} and D_{\max} soil profiles of Figure 4-6 are shown in Figures 4-7 to 4-9. It can be seen that this system behaves stiffer than the experiment, especially for the vertical mode of vibration, further pointing to the fact that the shear modulus needs to be reduced over some length of the pile.

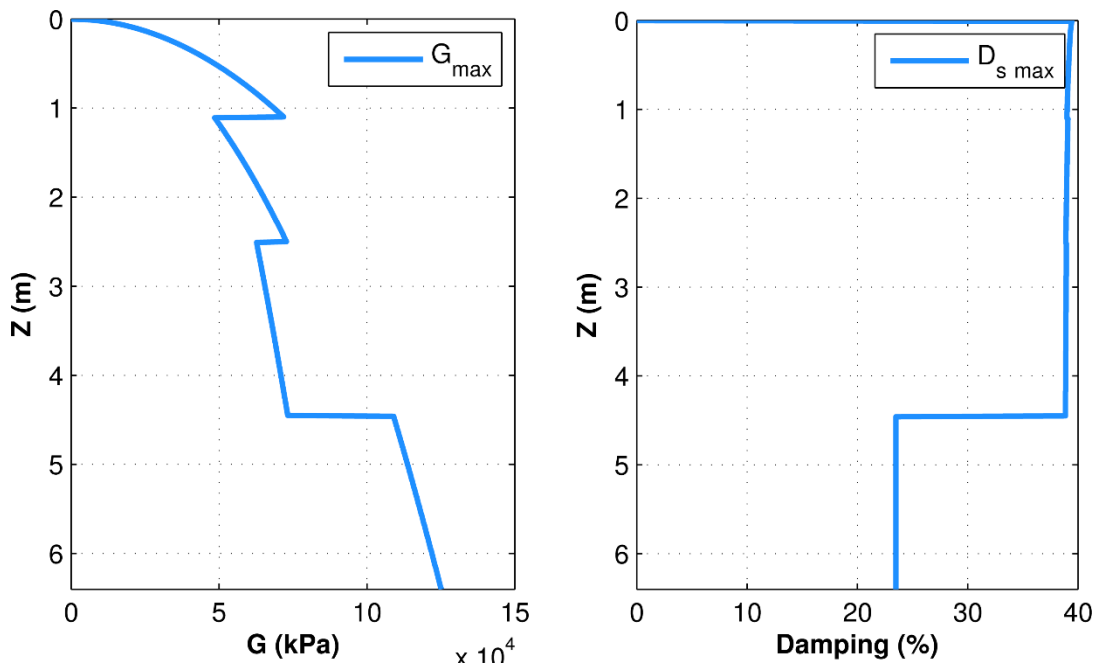


Figure 4-6- G_{\max} and D_{\max} soil profiles obtained from Hardin-Drnevich formulation for the soil properties in the field tests.

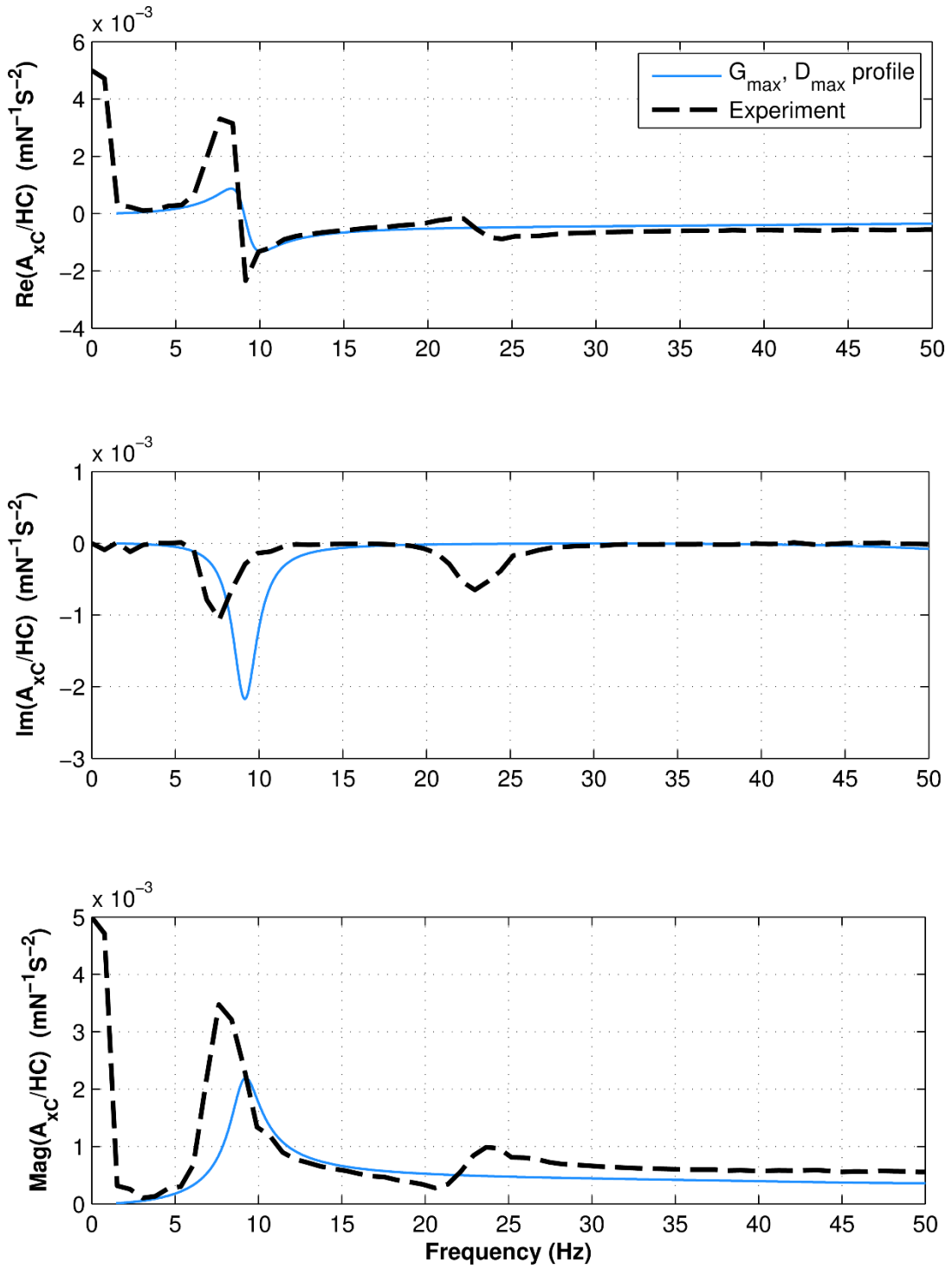


Figure 4-7- A_{x_c}/HC acceleration using G_{max} and D_{max} profiles presented in Figure 4-6. Experimental data from Test U-HC-R2.

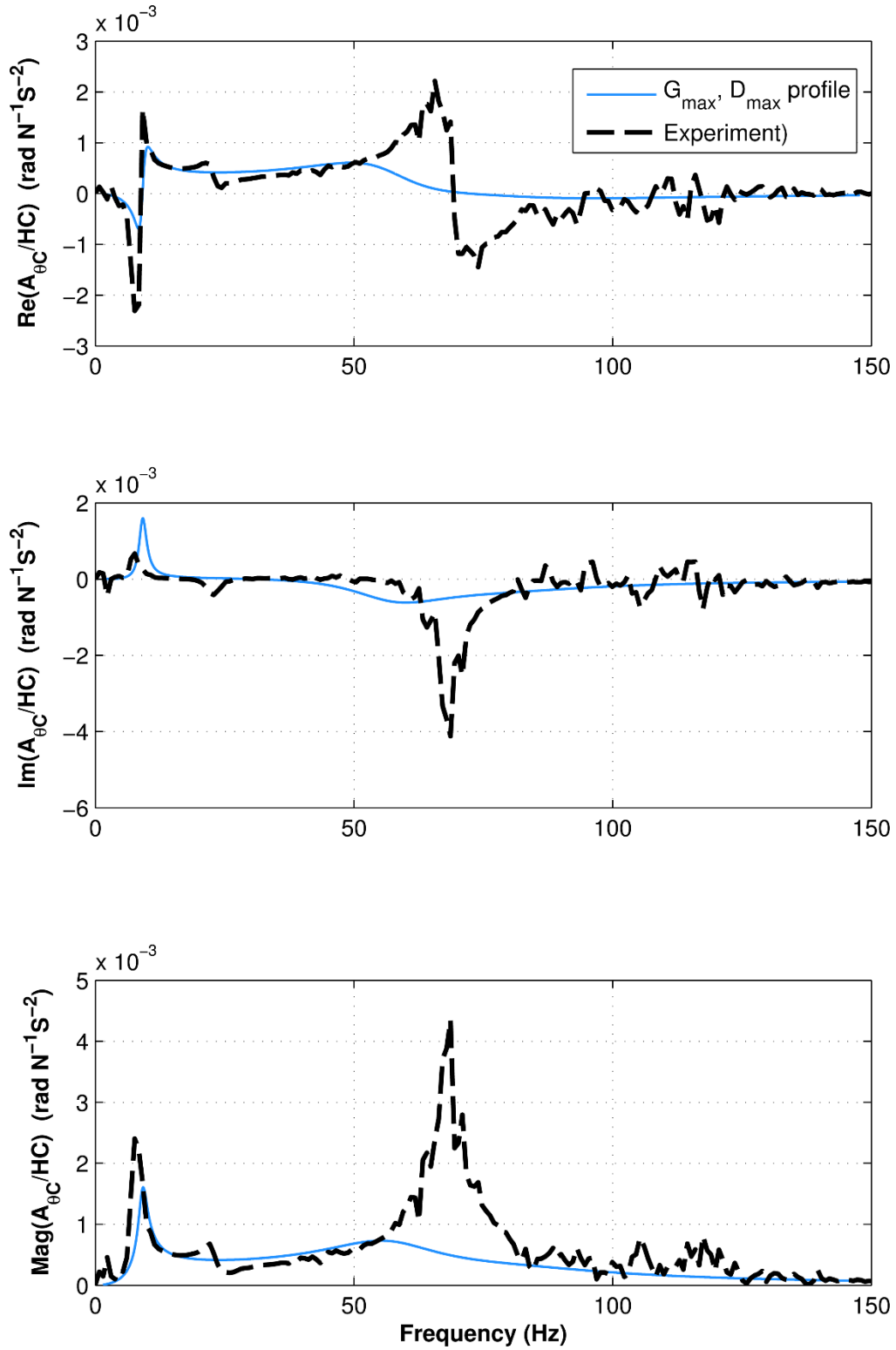


Figure 4-8- $A_{\theta C}/HC$ accelerance using G_{\max} and D_{\max} profiles presented in Figure 4-6. Experimental data from Test U-HC-R3.

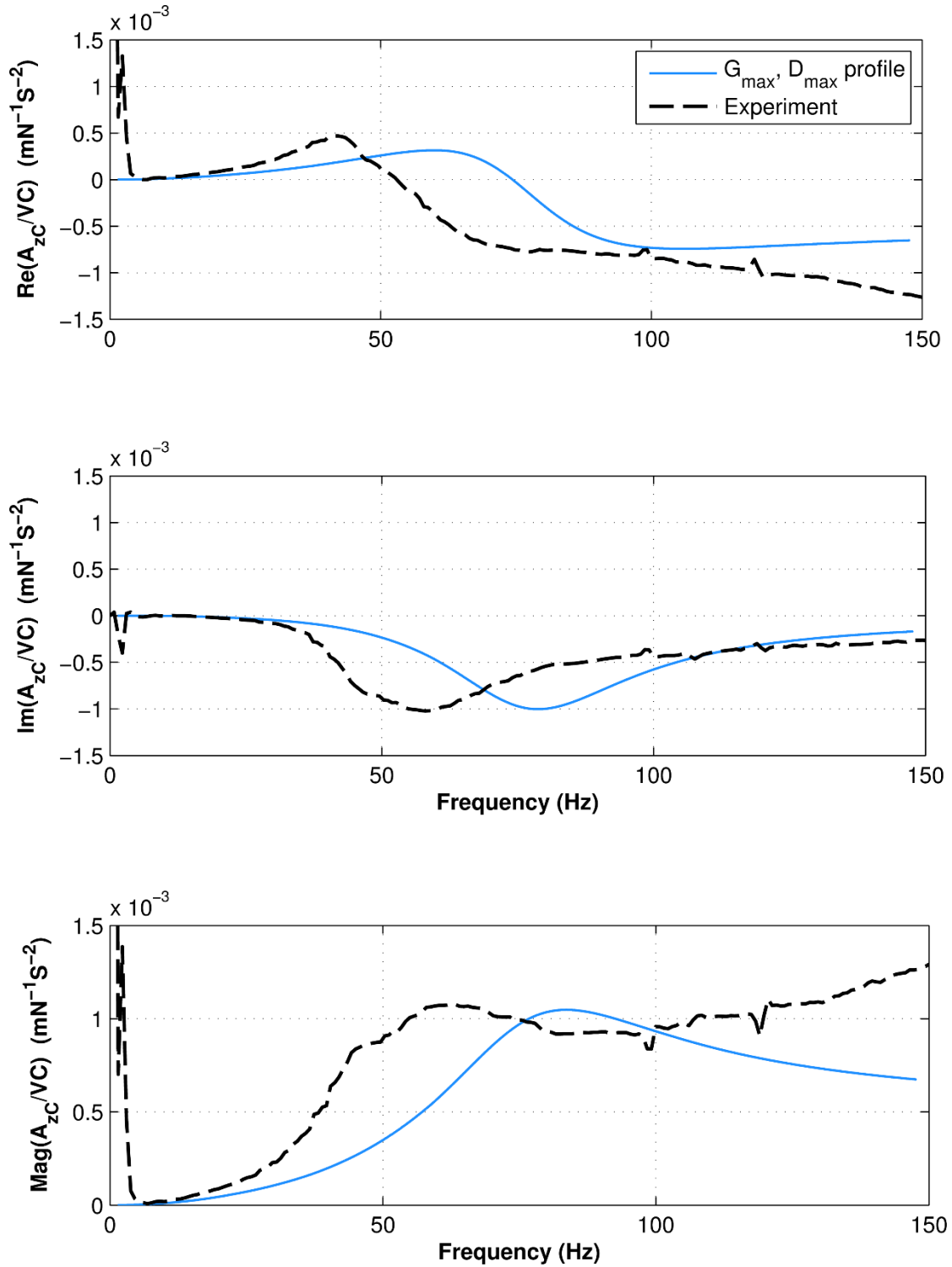


Figure 4-9- A_{zC}/VC accelerance using G_{\max} and D_{\max} profiles presented in Figure 4-6. Experimental data from Test U-HC-R3.

4.3.2 Incorporation of soil shear strain profile

The following procedure is proposed in order to estimate an envelope of the soil shear strain profile based on the calculated pile-soil deflection profile. The procedure is iterative, as the calculated shear strain profile is dependent upon the modulus and damping profiles, which in turn are dependent upon the initial estimated strain profile. The procedure may be said to converge when the final shear strain profile calculated from pile displacements is sufficiently close to the initial strain profile in a given iteration. Unlike the modulus and damping profiles, which may exhibit jumps due to the different soil properties in each layer, it is assumed that the shear strain profile next to the pile is a smooth continuous curve along the depth.

4.3.2.1 Step 1

The frequency at which the strain profile is desired should be first determined. Since they correspond to the maximum strain profiles, the frequencies of the peak vertical and peak horizontal centroidal accelerance are selected as the target frequencies. The centroidal accelerance analyses are then performed using soil impedances from BEASSI with the Hardin-Drnevich modulus and damping profiles. For the initial iteration, a uniform strain profile with $\gamma = 10^{-5}$ (i.e., $\gamma = 10^{-3}\%$) is assumed for all layers in the Hardin-Drnevich calculations. A maximum 5% material damping ratio is assumed for the soil, and no modifications are used for un-embedded pile length due to soil-pile gapping. Based on the resulting impedance and accelerance calculations for this case, Figure 4-10 and 4-11 show that $f=15$ Hz and $f=72$ Hz are the target frequencies corresponding to the horizontal and vertical accelerance peaks.

4.3.2.2 Step 2

The displacement of the nodes along the central axis of the pile due to unit displacements and rotations at the soil surface are calculated from the pile-soil interaction analyses in BEASSI. For ease of notation, Ux_RHS1 is used to refer to the normalized pile displacement profile u_x/a_{ref} corresponding to a unit vertical displacement of the pile cross-section imposed at the ground level (i.e., for right-hand-side 1 in BEASSI). Similarly, Ux_RHS2 and Ux_RH3 are used to refer to the normalized horizontal displacement profiles resulting from a unit horizontal displacement and a unit rotation about the y -axis at the ground level, respectively (right-hand-sides 2 and 3). Similar naming conventions are used for the profiles of the y and z components of displacement. Since the pile is assumed to move only in the x - z plane, the nodes on the line $x/a_{ref}=1, y=0$ can be related to the pile's central axis displacement and rotation. These displacement profiles are shown in Figures 4-12 to 4-17 for the problem under study, at the two target frequencies of 15 and 75 Hz obtained in Step 1.

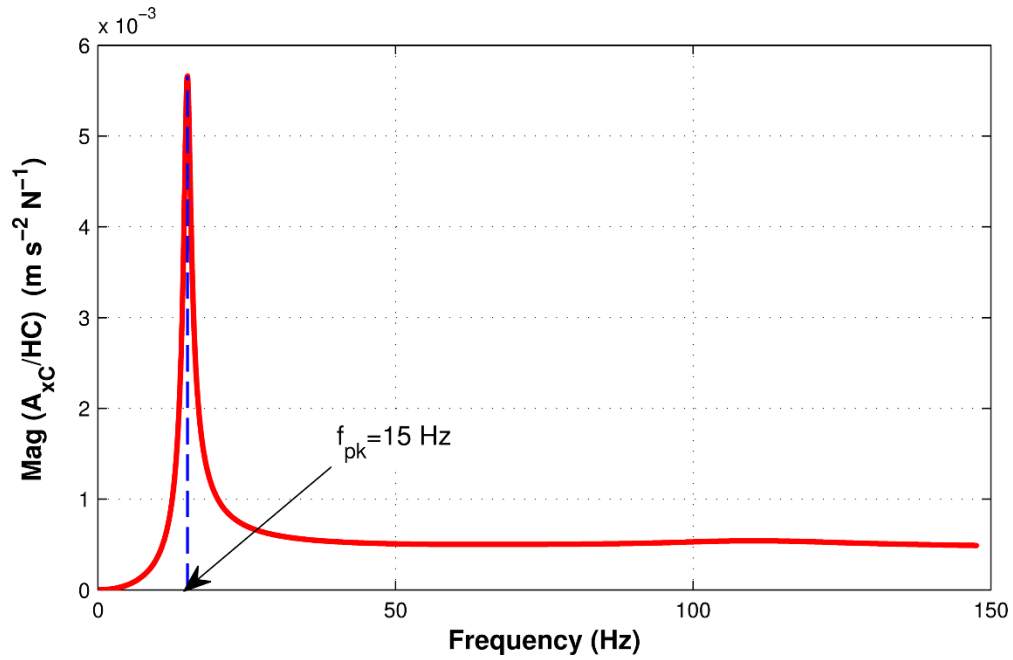


Figure 4-10. Magnitude of pile-cap centroidal HC/HC acceleration using BEASSI impedances for Hardin-Drnevich profile with $D_{s \max} = 5\%$ and $L_s = 0 \text{ m}$.

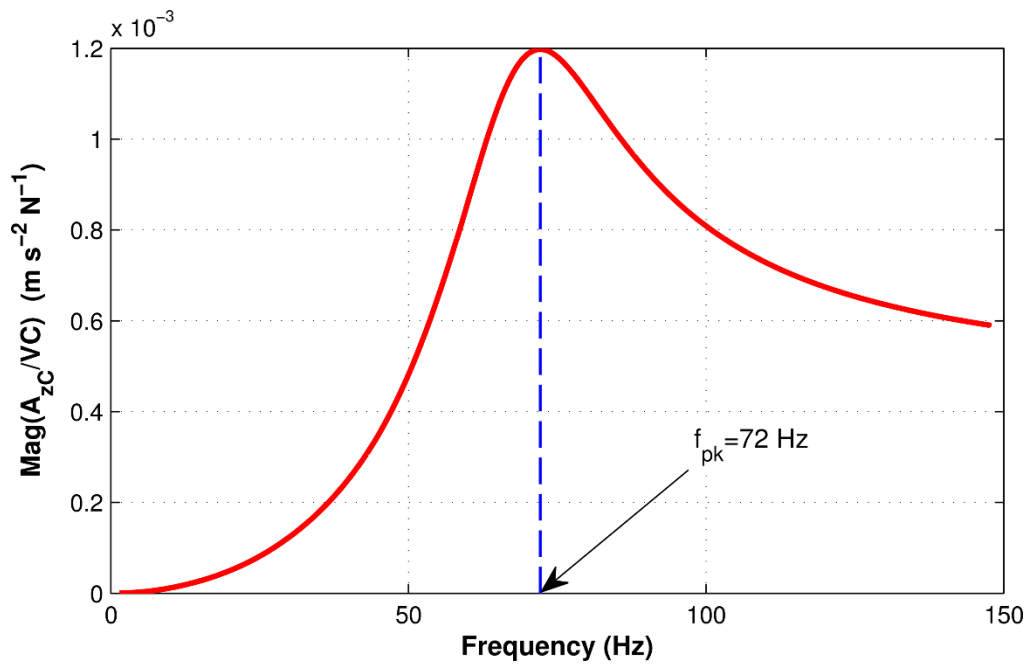


Figure 4-11. Magnitude of pile-cap centroidal VC/VC acceleration using BEASSI impedances for Hardin-Drnevich profile with $D_{s \max} = 5\%$ and $L_s = 0 \text{ m}$.

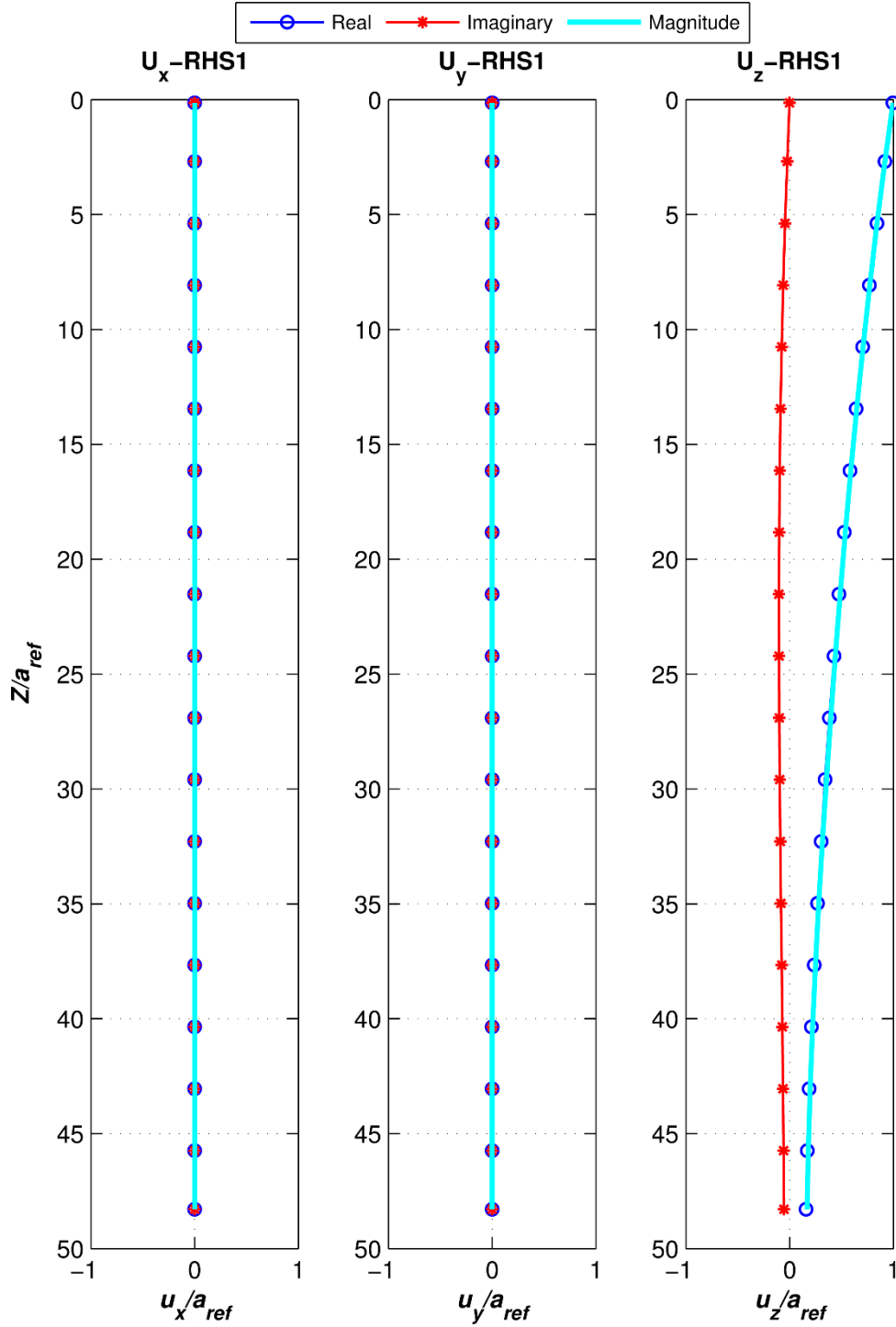


Figure 4-12. u_x/a_{ref} , u_y/a_{ref} and u_z/a_{ref} displacement profiles due to a unit vertical displacement at the ground level in z direction for $f_{pkH}=15$ Hz and Hardin-Drnevich soil profile ($D_{s\max}=5\%$, uniform strain profile $\gamma=10^{-5}$, $a_{ref}=0.127$ m)

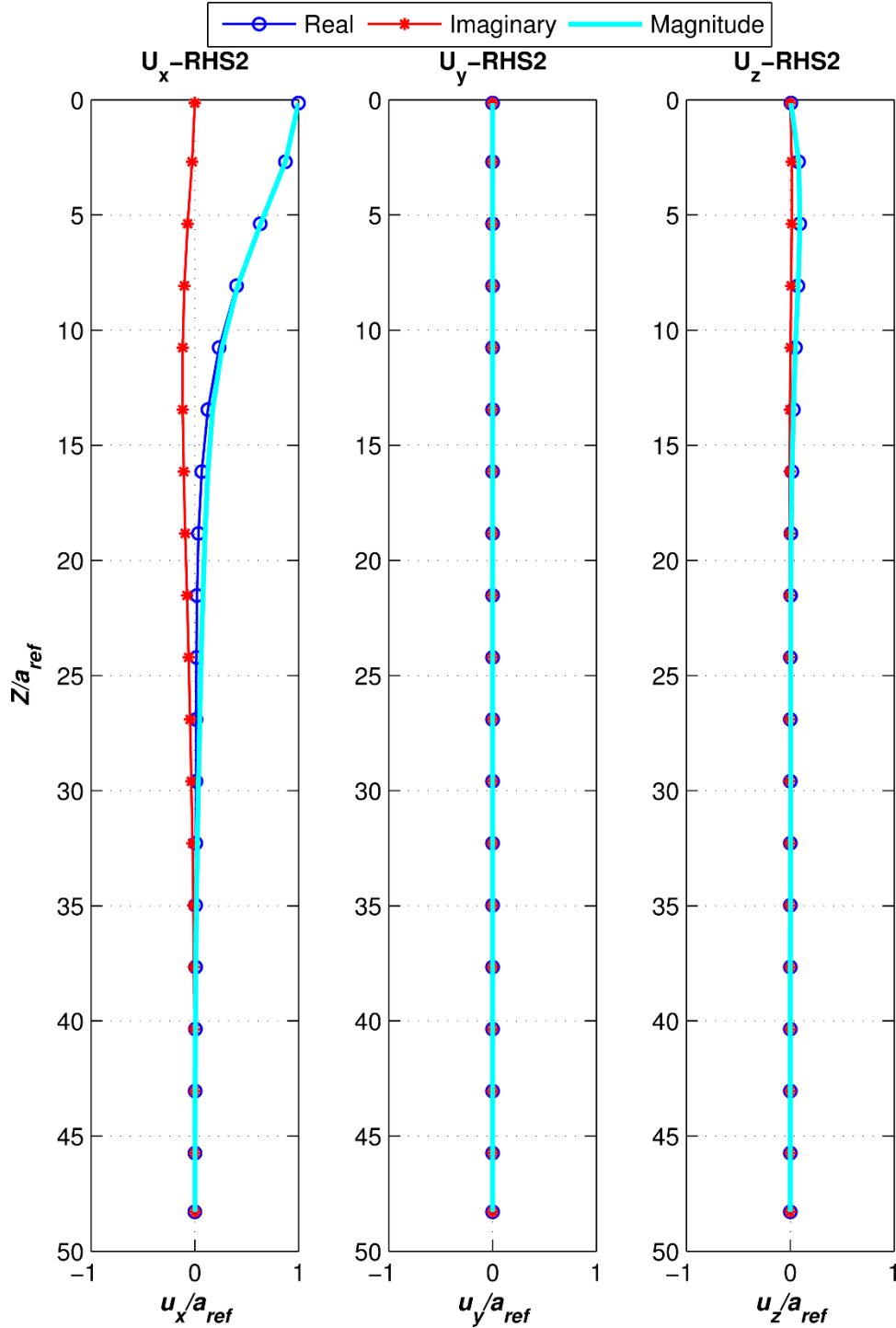


Figure 4-13. u_x/a_{ref} , u_y/a_{ref} and u_z/a_{ref} displacement profiles due to a unit horizontal displacement at the ground level in x direction for $f_{pkH}=15$ Hz and Hardin-Drnevich soil profile ($D_{s\max}=5\%$, uniform strain profile $\gamma=1e-5$, $a_{ref}=0.127$ m)

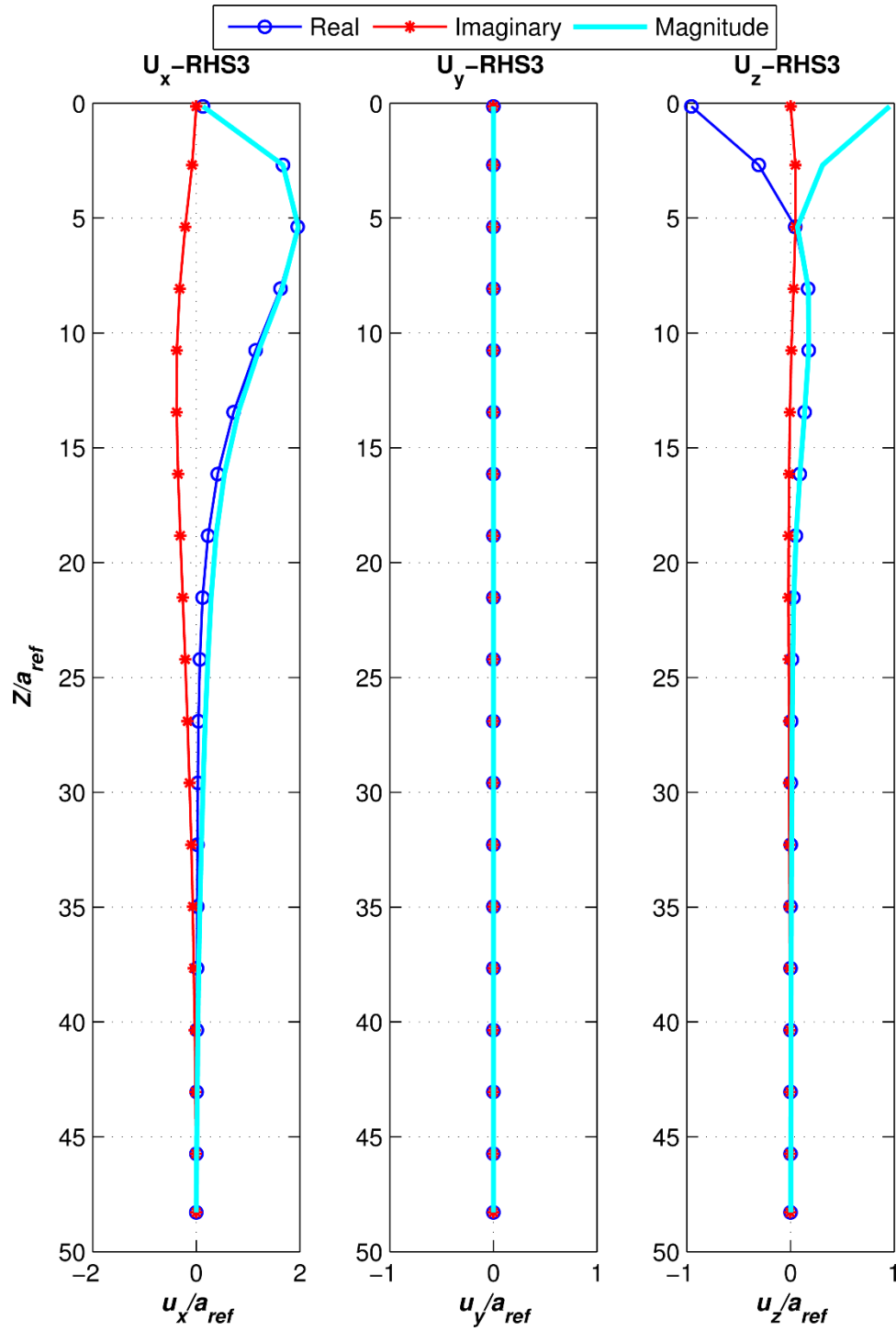


Figure 4-14. u_x/a_{ref} , u_y/a_{ref} and u_z/a_{ref} displacement profiles due to a unit rotation at the ground level around y axis for $f_{pKH}=15$ Hz and Hardin-Drnevich soil profile ($D_{s,max}=5\%$, uniform strain profile $\gamma=1e-5$, $a_{ref}=0.127$ m)

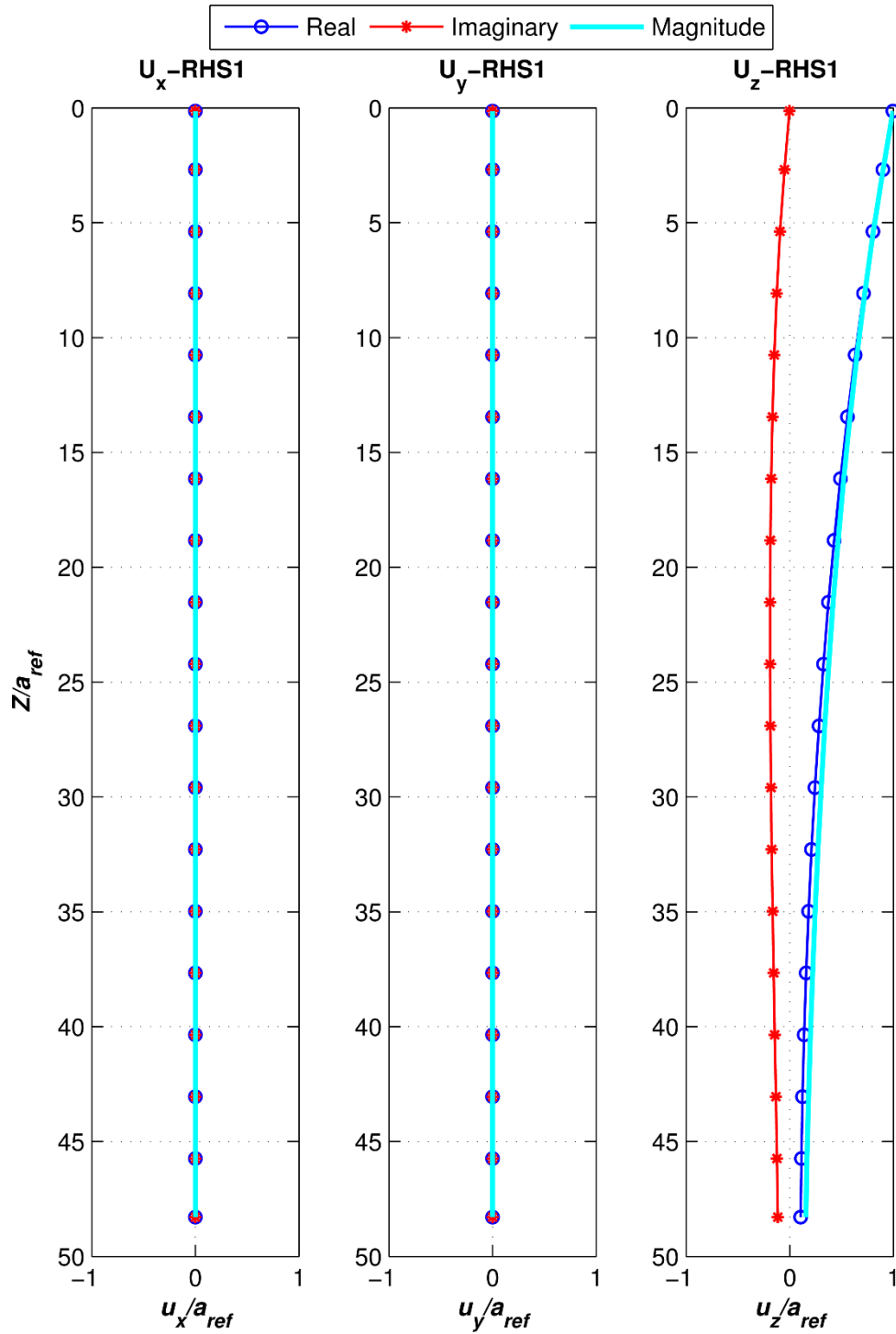


Figure 4-15. u_x/a_{ref} , u_y/a_{ref} and u_z/a_{ref} displacement profiles due to a unit vertical displacement at the ground level in z direction for $f_{pkV}=75$ Hz and Hardin-Drnevich soil profile ($D_{s\max}=5\%$, uniform strain profile $\gamma=1e-5$, $a_{ref}=0.127$ m)

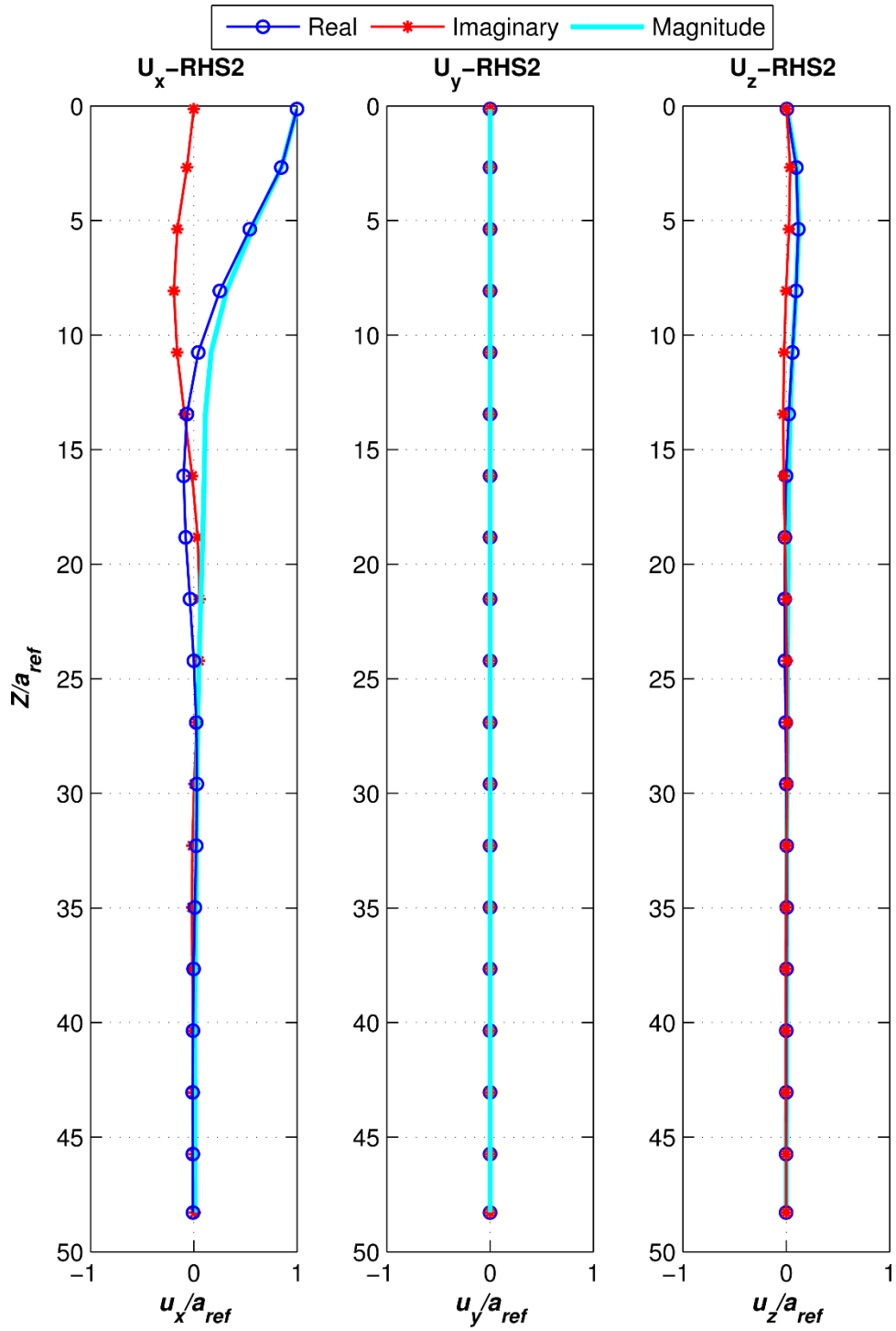


Figure 4-16. u_x/a_{ref} , u_y/a_{ref} and u_z/a_{ref} displacement profiles due to a unit horizontal displacement at the ground level in x direction for $f_{pkV}=75$ Hz and Hardin-Drnevich soil profile ($D_{s,max}=5\%$, uniform strain profile $\gamma=1e-5$, $a_{ref}=0.127$ m)

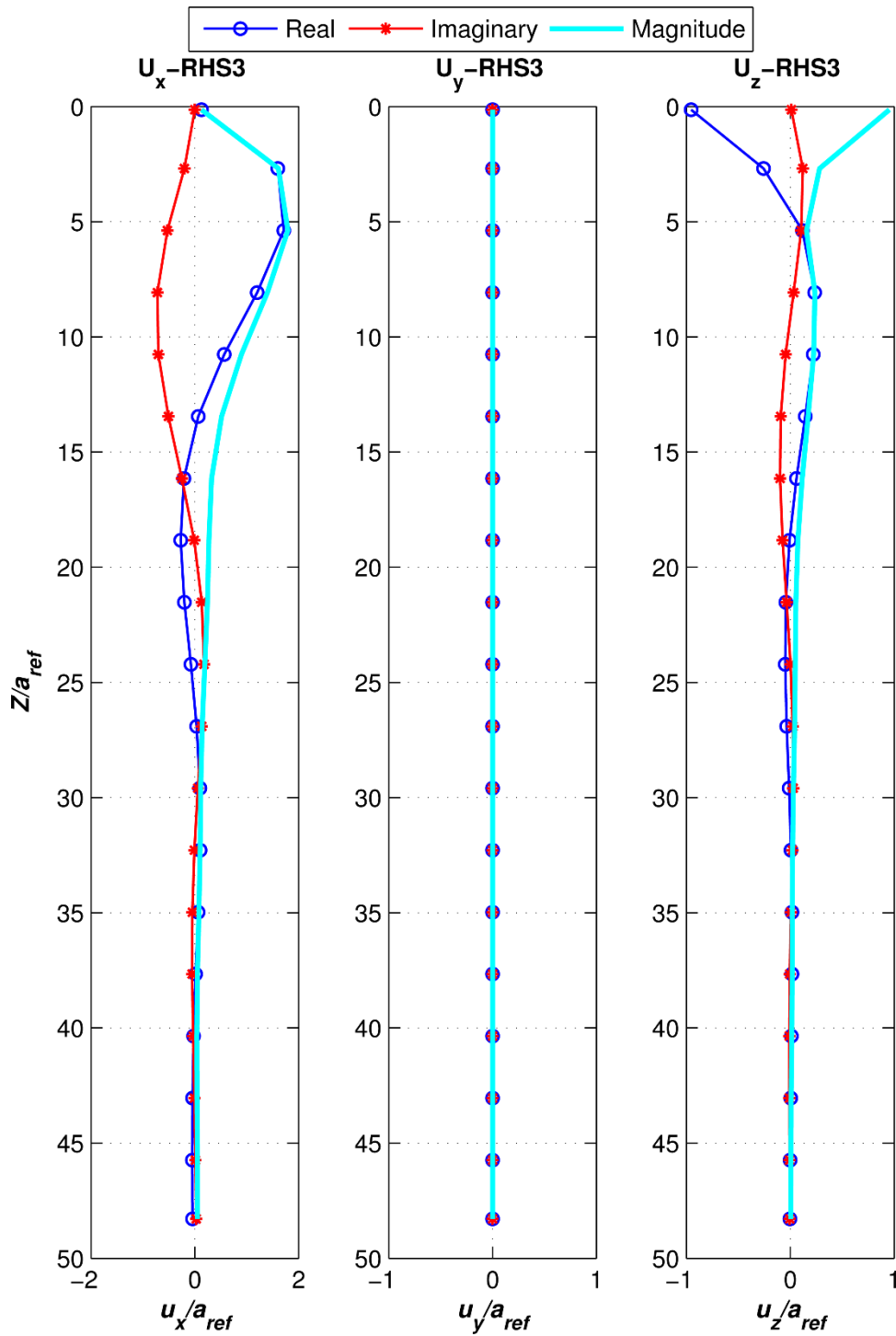


Figure 4-17. u_x/a_{ref} , u_y/a_{ref} and u_z/a_{ref} displacement profiles due to a unit rotation at the ground level around y axis for $f_{pkV}=75$ Hz and Hardin-Drnevich soil profile ($D_{s,max}=5\%$, uniform strain profile $\gamma=1e-5$, $a_{ref}=0.127$ m)

4.3.2.3 Step 3

To obtain the pile displacement profile in the actual soil-pile-cap vibration problem, the x , y and z displacement profiles for RHS1 to RHS 3 obtained in Step 2 should be scaled and combined in proportion to the actual ground-level displacement and rotation values obtained from solution of the theoretical accelerance equations in Sections 3.2.1 or 3.2.2. The following equations describe this process in more detail:

$$\frac{U_{x-actual}(z)}{a_{ref}} = U_{z-actual_ground} \times U_{x_RHS1} + U_{x-actual_ground} \times U_{x_RHS2} + \Theta_{y-actual_ground} \times U_{x_RHS3} \quad (4.2)$$

$$\frac{U_{y-actual}(z)}{a_{ref}} = U_{z-actual_ground} \times U_{y_RHS1} + U_{x-actual_ground} \times U_{y_RHS2} + \Theta_{y-actual_ground} \times U_{y_RHS3} \quad (4.3)$$

$$\frac{U_{z-actual}(z)}{a_{ref}} = U_{z-actual_ground} \times U_{z_RHS1} + U_{x-actual_ground} \times U_{z_RHS2} + \Theta_{y-actual_ground} \times U_{z_RHS3} \quad (4.4)$$

The theoretical ground-level displacements normalized by the moving mass displacement,

$\left(\frac{U_z}{U_{mm}}, \frac{U_x}{U_{mm}}, \frac{\Theta_y}{U_{mm}} \right)$, are found during the solution of the theoretical accelerance equations.

A theoretical displacement U_{mm} is thus required for solution of the displacement profiles in the above three equations. However, the peak frequencies of the experimental transfer functions (see Figure 4-18) are different from the theoretical peak frequencies used above (Figure 4-10 and 4-11). In order to estimate an upper-bound envelope for the strain profile, the maximum experimentally measured U_{mm} from the tests shown in Figure 4-18 are used to scale the theoretical

transfer functions $\left(\frac{U_z}{U_{mm}}, \frac{U_x}{U_{mm}}, \frac{\Theta_y}{U_{mm}} \right)$ to obtain the values of displacements at the ground

surface $(U_{z-actual_ground}, U_{x-actual_ground}, \Theta_{y-actual_ground})$ for solution of Eqs. (4.2) to (4.4) above. For this purpose, the displacement spectrum $U_{mm}(f)$ of the moving mass is calculated from the Fourier transform of its acceleration time history divided by $-(2\pi f)^2$, as shown in Figure 4-19 for the representative experiments. A summary of this procedure is reported in Table 4-1 and Table 4-2.

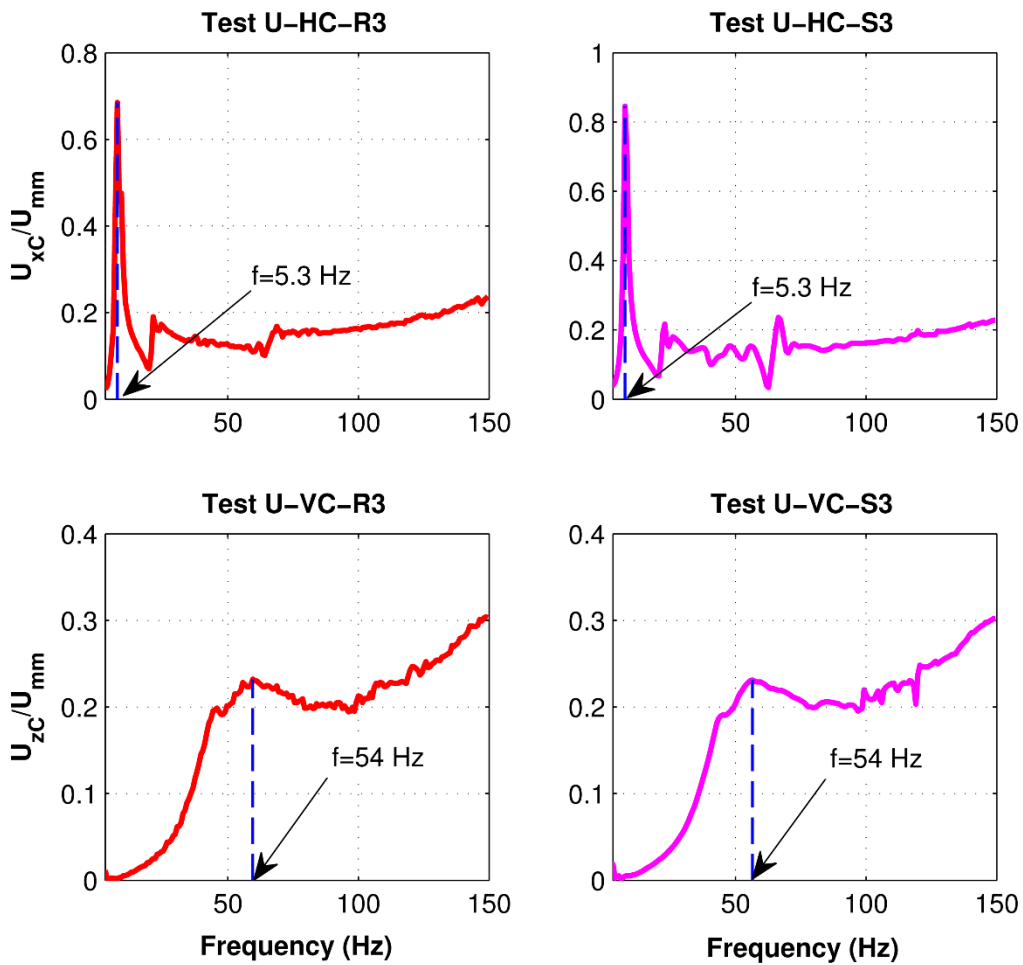


Figure 4-18. Selected experimental transfer functions and peak frequencies for strain profile calculations.

Table 4-1. Theoretical transfer functions at the ground level at peak frequencies shown in Figure 4-10 and 4-11.

	XFER _z (U_z/U_{mm})		XFER _x (U_x/U_{mm})		XFER _ϕ ($ϕ_y/U_{mm}$)		U _{mm max} (m)	
	Re	Im	Re	Im	Re	Im	Re	Im
HC/HC (15 Hz)	0.0011	0.0046	-	-	-0.0355	0.6835	8.20e-4	-1.72e-4
VC/VC (75 Hz)	-	-	0	0	0	0	4.98e-4	4.83e-4

Table 4-2. Calculated displacements and rotation at the ground level due to HC loading in Test U-HC-R3 ($U_{mm}=1.9389e-4$ m at 15 Hz) and VC loading in Test U-VC-R3 ($U_{mm}=7.2385e-7$ m at 75 Hz).

	(U_z) (m)		(U_x) (m)		$(ϕ_y)$ (rad)	
	Re	Im	Re	Im	Re	Im
HC/HC (15 Hz)	1.72e-6	3.54e-6	-9.98e-5	-3.75e-4	8.83e-5	5.67e-4
VC/VC (75 Hz)	5.99e-5	-1.41e-5	0.0	0.0	0.0	0.0

Having the ground level displacements and rotation, the actual displacement profile for the pile-system can then be calculated using Eqs. (4.2) to (4.4). The outcome of this process is depicted in Figure 4-20 and 4-21. From these figures it is confirmed that there is no motion in the y -direction in both HC and VC tests. Moreover, in the VC test, displacement in the x -direction is also very insignificant while displacement in the z -direction exists everywhere along the pile. The displacement profile at $f=15$ Hz has greater values than $f=75$ Hz and will therefore be used for calculating the strain profile in the next step. It can also be concluded from Figure 4-20 that the pile behaves as a flexible pile as discussed in Section 3.3.1, since its active length is smaller than the pile length.

4.3.2.4 Step 4

By having the displacement profile of the pile surface, one can find the engineering strain profile of the adjacent soil using the continuum mechanics definition for shear strain:

$$\gamma_{zx} = \frac{\partial u_z}{\partial x} + \frac{\partial u_x}{\partial z} \quad (1.4)$$

As the vertical displacement in an HC test is not significant compared to the horizontal displacement (see Figure 4-20), the first term in Eq. (1.4) is disregarded and only the second term is used to construct the strain profile. The resulting strain profile is depicted in Figure 4-22, and its mean value is compared to the uniform strain assumption used in the initial step of the calculations. The initial assumed uniform strain value and the calculated mean strain value are fairly close.

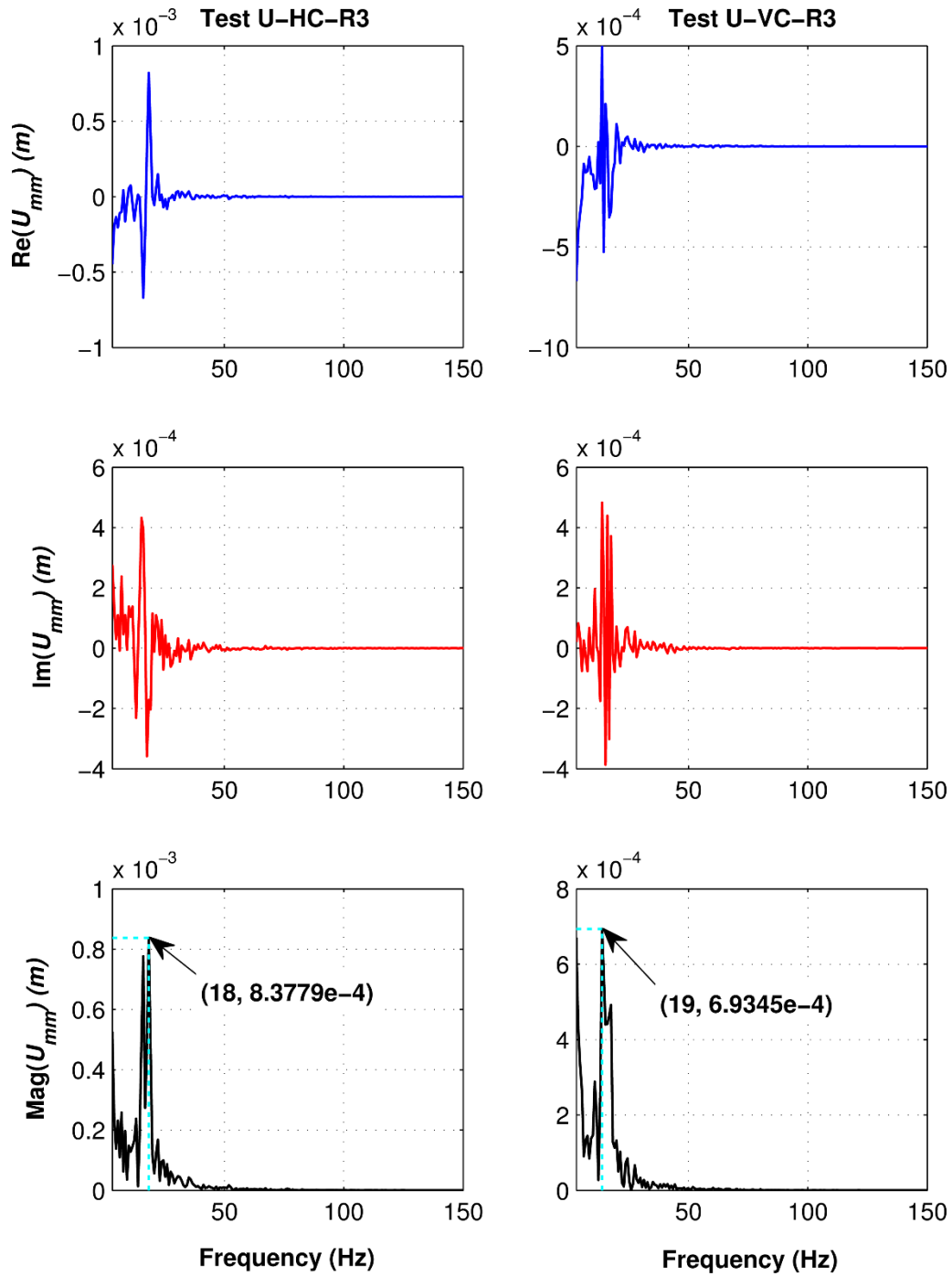


Figure 4-19. Fourier spectrum of moving mass displacement U_{mm} for Tests U-HC-R3 and U-VC-R3. Frequency spectrum is obtained by taking FFT of the acceleration time history then dividing by $-\omega^2$.

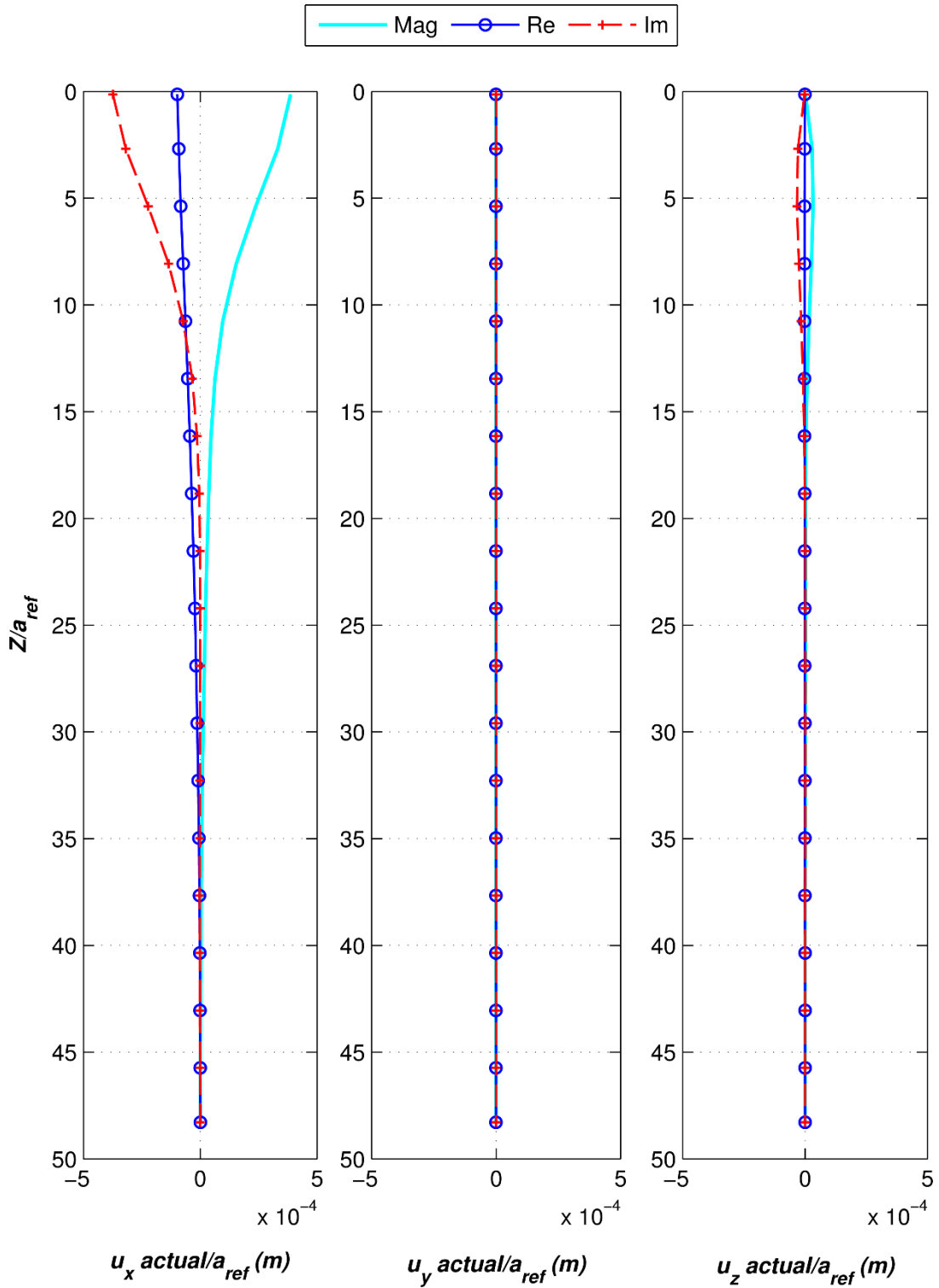


Figure 4-20. Calculated displacement and rotation profiles at $f_{pkH}=15$ Hz using the maximum U_{mm} values from Test U-HC-R3 to scale the theoretical transfer functions at the ground level.

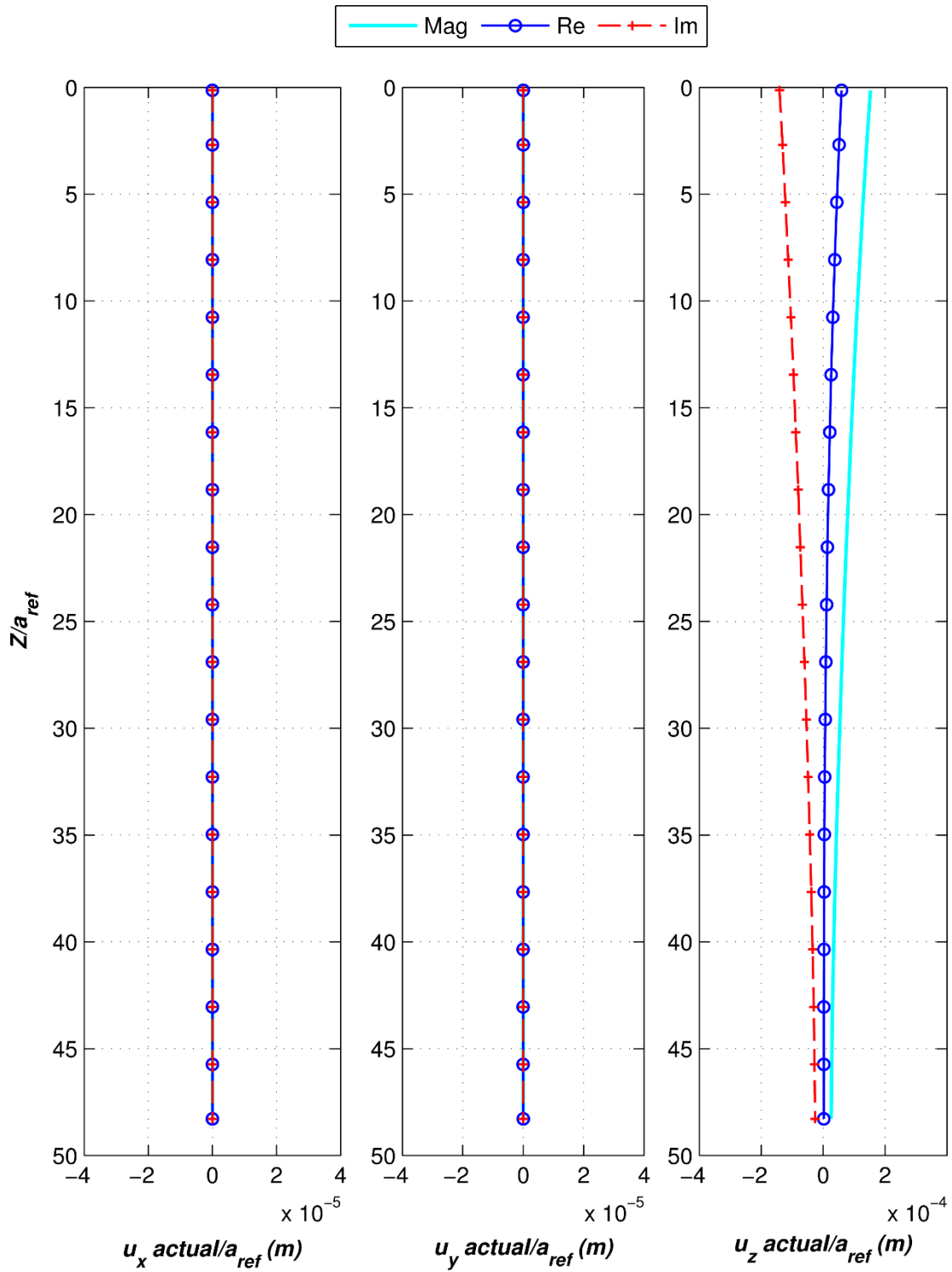


Figure 4-21. Calculated displacement and rotation profiles at $f_{pkv}=75$ Hz using the maximum U_{mm} values from Test U-VC-R3 to scale the theoretical transfer functions at the ground level.

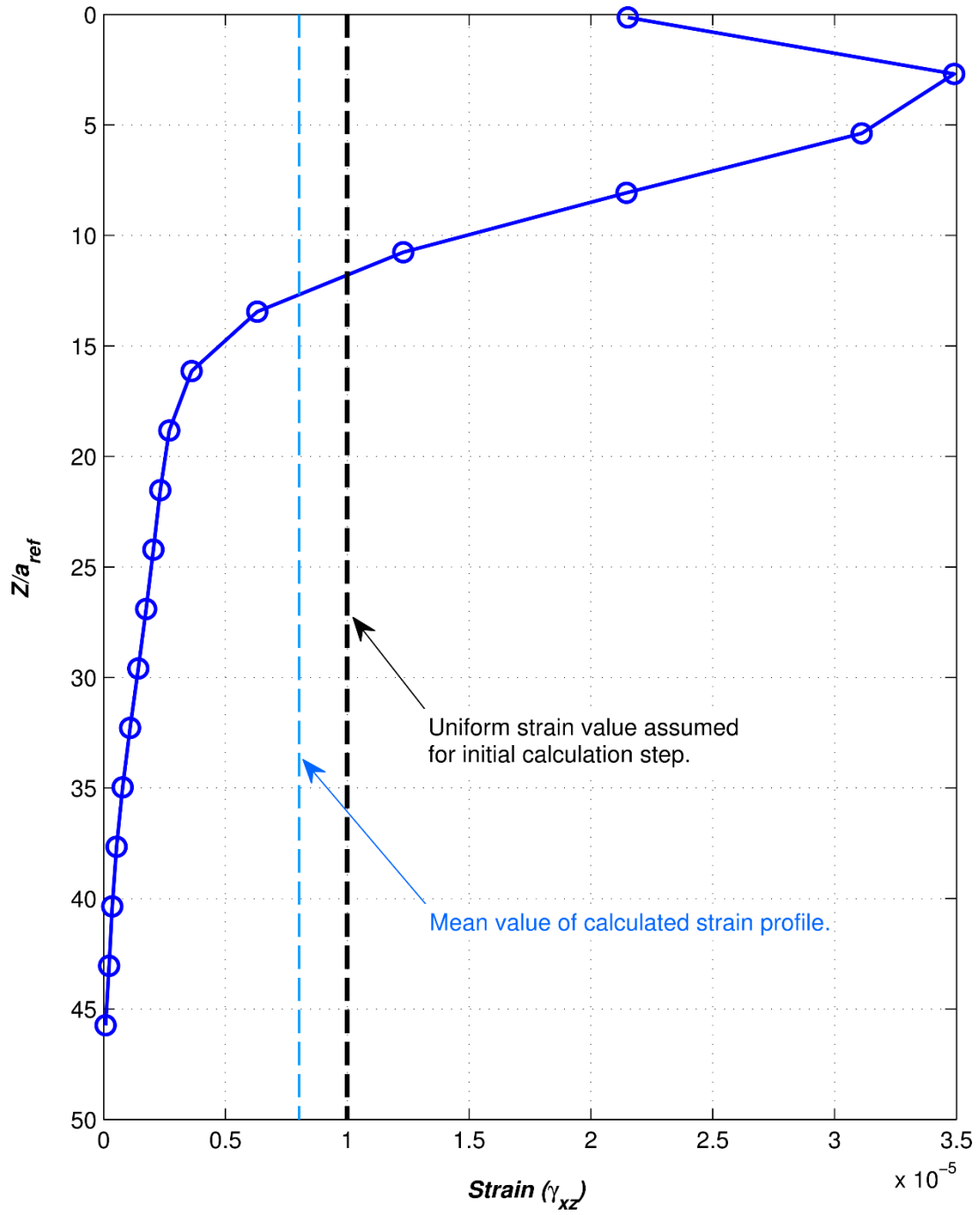


Figure 4-22. Calculated soil shear strain profile after one iteration of using pile displacements from BEM analysis.

4.3.2.5 Step 5

The uniform strain assumption made in the initial step is now replaced by the calculated strain profile of Figure 4-22, which is used in the in Hardin-Drnevich relations to obtain new profiles of stiffness and damping ratio. A second iteration of Steps 2 through 4 is then performed. For the present problem, this results in a drastic change in the material damping ratio profile, while the shear modulus profile remains almost the same, as shown in Figure 4-23. From the formulations, this trend of sensitivity to shear strain, γ , was expected since for small strain values G remains constant and D changes linearly with γ :

$$G = \frac{1}{1 + \gamma} G_{\max} \rightarrow \lim_{\gamma \rightarrow 0} G = G_{\max} \quad (1.5)$$

$$D = \frac{\gamma}{1 + \gamma} D_{\max} \rightarrow \lim_{\gamma \rightarrow 0} D = \gamma D_{\max} \quad (1.6)$$

Therefore any further changes to the strain profile that do not alter its order of magnitude will not significantly affect the modulus profile. However, the damping ratio profile may change dramatically, but the effect of material damping is not significant relative to radiation damping. This implies that continuing the iterations will not result in a considerable improvement of the results of the general dynamic pile-soil interaction problem.

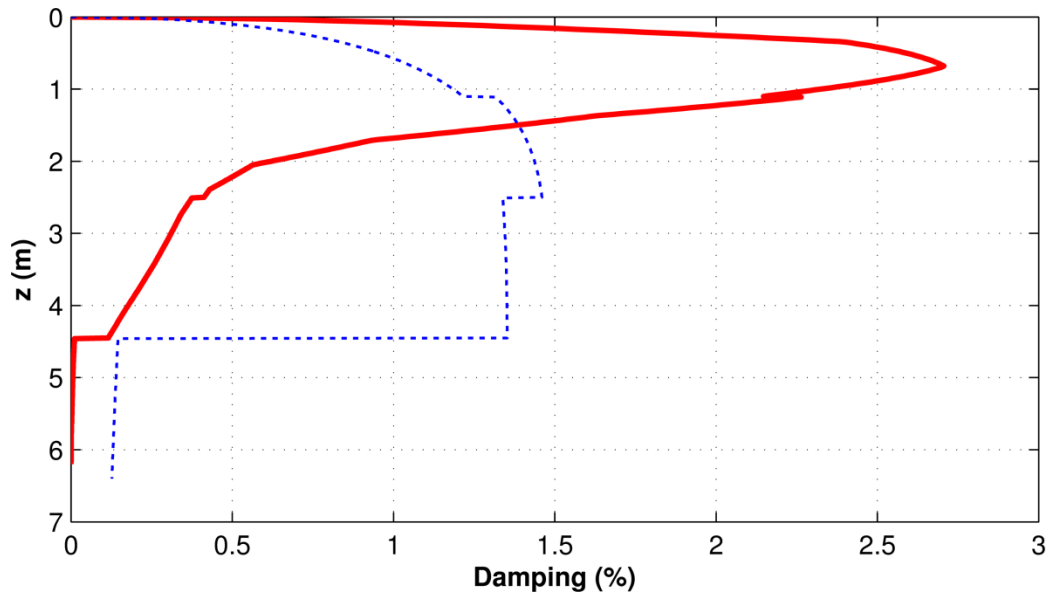
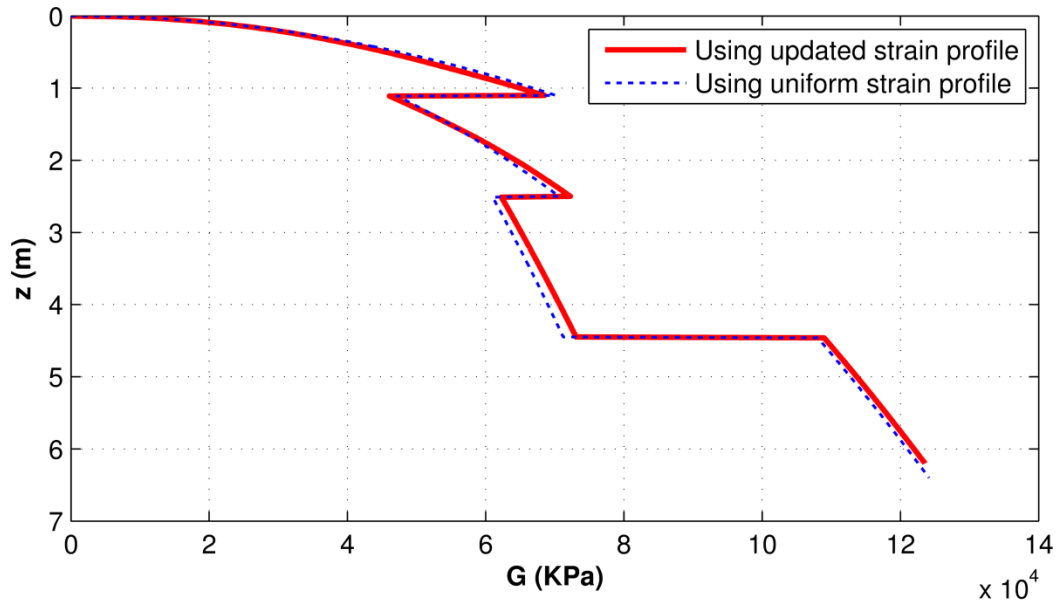


Figure 4-23. Hardin-Drnevich modulus and damping profiles for the calculated strain profile of Figure 4-22.

4.3.3 Modification factor, $MF(z)$

From the physical point of view, the modification factor $MF(z)$ in Eq. (4.1) should decrease the soil shear modulus near the soil surface where the soil may experience the greatest disturbance and yielding during the pile installation, consequently lowering its confining pressure. Additionally, the dynamic strains are largest near the soil surface during experiments. The relations of Hardin and Drnevich indicate that the reduction in confining pressure and increase in the dynamic strain levels both reduce the modulus while increasing damping. Additionally, loss of contact between the soil and pile is a commonly observed phenomenon in lateral piles tests, which could be modeled by a traction-free double elements as in Ashlock (2006), or a severe reduction in the soil shear modulus, or a decrease in the pile embedment depth with equal increase in the unembedded length. The latter two approaches are used in this study.

At greater depths, on the other hand, the installation effects would cause soil compression and corresponding increase in the soil modulus as the pile is forced into the soil (this stiffening effect would be more pronounced for large-displacement piles than for the small-displacement H-piles used in this study). Using the same reasoning, the reverse trend is expected for the material damping modification factor; i.e., a large increase in damping near the surface and a decrease at depth. Such physically motivated modifications to the modulus and damping profiles, along with the use of a 3-domain disturbed-zone model, were previously shown to accurately model results of numerous dynamic scaled-model pile tests (Ashlock, 2006).

A sigmoid function which has an “S” shape can be used as a representative for the depth-wise modification factor, as it can provide the types of modulus reduction and increase described above. A Gompertz sigmoid curve characterized by three constants as

$$MF(z) = ae^{-be^{-c(z-z_d)}} \quad (4.5)$$

can be examined as the modification factor function. In this equation, “ a ” is the deep asymptote, “ b ” sets the depth of the reduced modulus in the no contact zone, “ c ” sets the uniformity of transition in the function, and “ z_d ” is the depth of the inflection point. In theory, these constants could simply be varied to minimize the misfit between the theoretical and experimental accelerances. Due to time constraints, however, this approach was not pursued in this study. Figure 4-24 shows the sensitivity of $MF(z)$ to parameters a , b , and c with respect to a reference Gompertz curve.

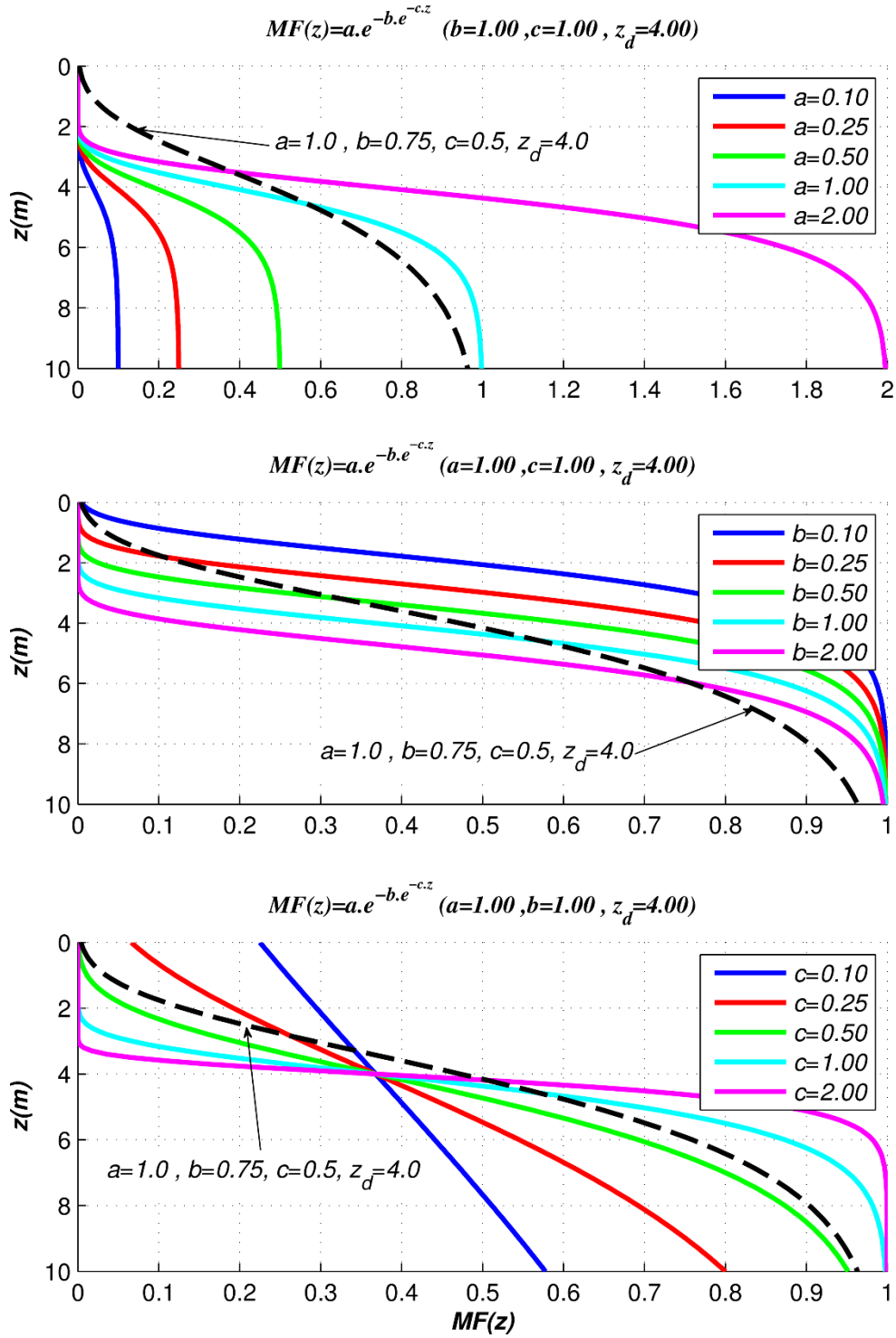


Figure 4-24. Sensitivity of Goempertz curve to parameters a, b, c , and z_d .

4.3.3.1 Special case $b=0$

As a starting point to identify soil parameter profiles that result in an improved match between theoretical and experimental results, the shear modulus and material damping profiles shown in Figure 4-23 were taken as the reference profiles. These profiles were then scaled uniformly at each depth by the constant a in Eq. (4.5) with $b=0$, to create 6 different shear modulus profiles and 5 different damping profiles, as shown in Table 4-3. The 30 resulting combinations were then analyzed in BEASSI to determine the corresponding impedance functions. This procedure was repeated for a total of four gapping separation lengths ($L_s = 0 \text{ cm}$, $L_s = 25 \text{ cm}$, $L_s = 50 \text{ cm}$, and $L_s = 75 \text{ cm}$ in Table 4-3). As discussed in Chapter 3, the effect of the separation length was examined by increasing the length of the free pile stem L_o in the theoretical acceleration calculation, while simultaneously decreasing the embedded pile length accordingly in the BEM model, essentially translating the coordinate origin downward to the bottom of the gap and removing the non-contacting layers from the model (Figure 4-25).

The 120 cases in Table 4-3 were then used to calculate the theoretical centroidal acceleration functions for the pile problem, shown in Figures 4-26 through 4-31. In these figures, the peak amplitudes decrease with increasing damping, and peak frequencies increase with increasing modulus. This creates a multi-dimensional grid of theoretical data that can be interpolated to find the model parameters that best match the experimental results. The validity of using linear interpolation to obtain impedances for a new case with target parameters between those analyzed in Table 4-3 was investigated by comparison to a separate BEM analysis using the target parameters directly. The results are shown in Figure 4-32 and 4-33, demonstrating excellent agreement.

Table 4-3- Parameters of the 120 cases analyzed with different gapping separation lengths (L_s). Soil shear modulus profiles shown in Figure 4-23 are scaled according the left column. Soil material damping profiles in Figure 4-23 are scaled to have the maximum value listed in top row.

$L_s=0$ cm , $L_s=25$ cm , $L_s=50$ cm , $L_s=75$ cm	$D_{sMax}=5\%$	$D_{sMax}=10\%$	$D_{sMax}=15\%$	$D_{sMax}=20\%$	$D_{sMax}=30\%$
$0.1 G_{HD}$	Case 1	Case 2	Case 3	Case 4	Case 5
$0.25 G_{HD}$	Case 6	Case 7	Case 8	Case 9	Case 10
$0.5 G_{HD}$	Case 11	Case 12	Case 13	Case 14	Case 15
G_{HD}	Case 16	Case 17	Case 18	Case 19	Case 20
$1.5 G_{HD}$	Case 21	Case 22	Case 23	Case 24	Case 25
$2G_{HD}$	Case 26	Case 27	Case 28	Case 29	Case 30

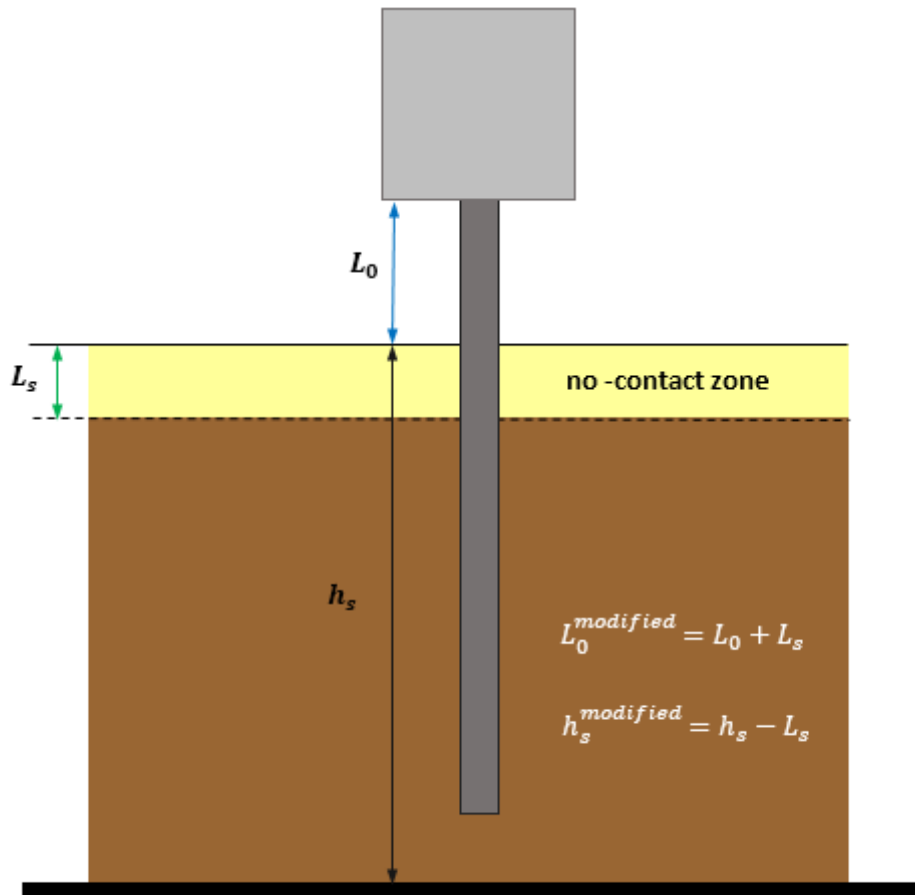


Figure 4-25-Modification of the free un-embedded length L_0 of the pile by decreasing depth of soil layer h_s to account for gapping separation length L_s .

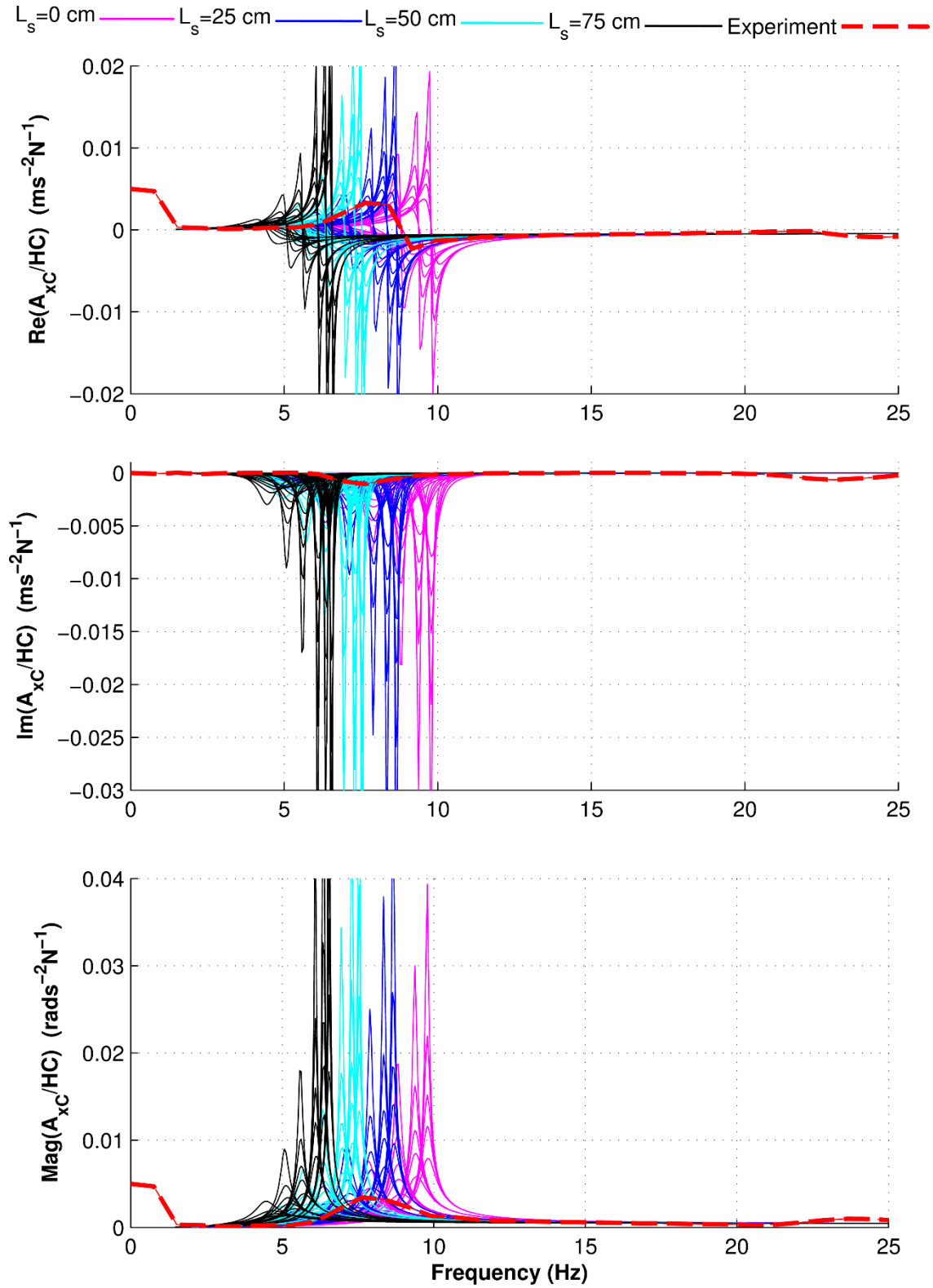


Figure 4-26-Centroidal horizontal acceleration functions for HC loading for the 120 cases described in Table 4-3. Experimental results from Test U-HC-R2.

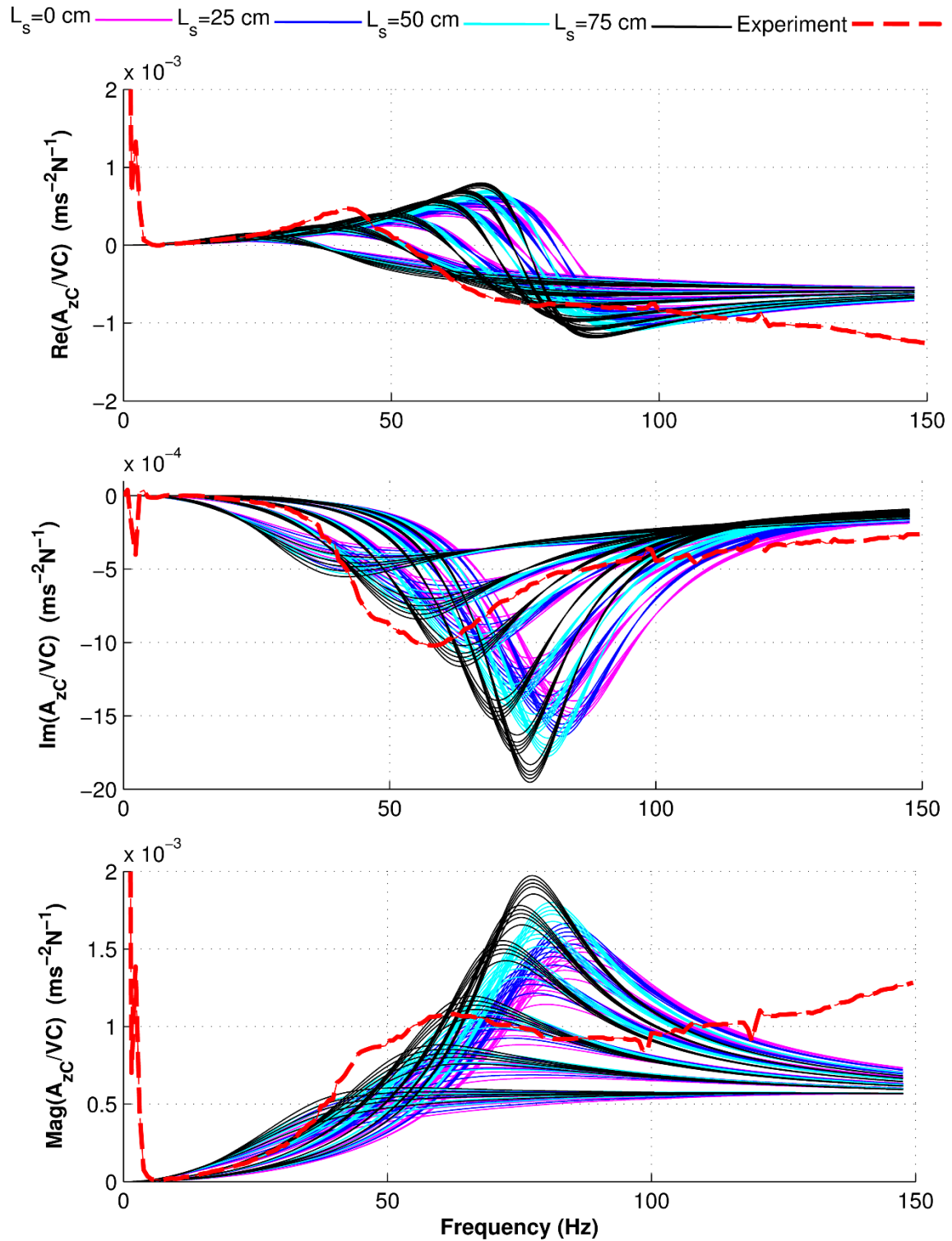


Figure 4-27- Centroidal vertical acceleration functions for VC loading for the 120 cases described in Table 4-3. Experimental results from Test U-VC-R2.

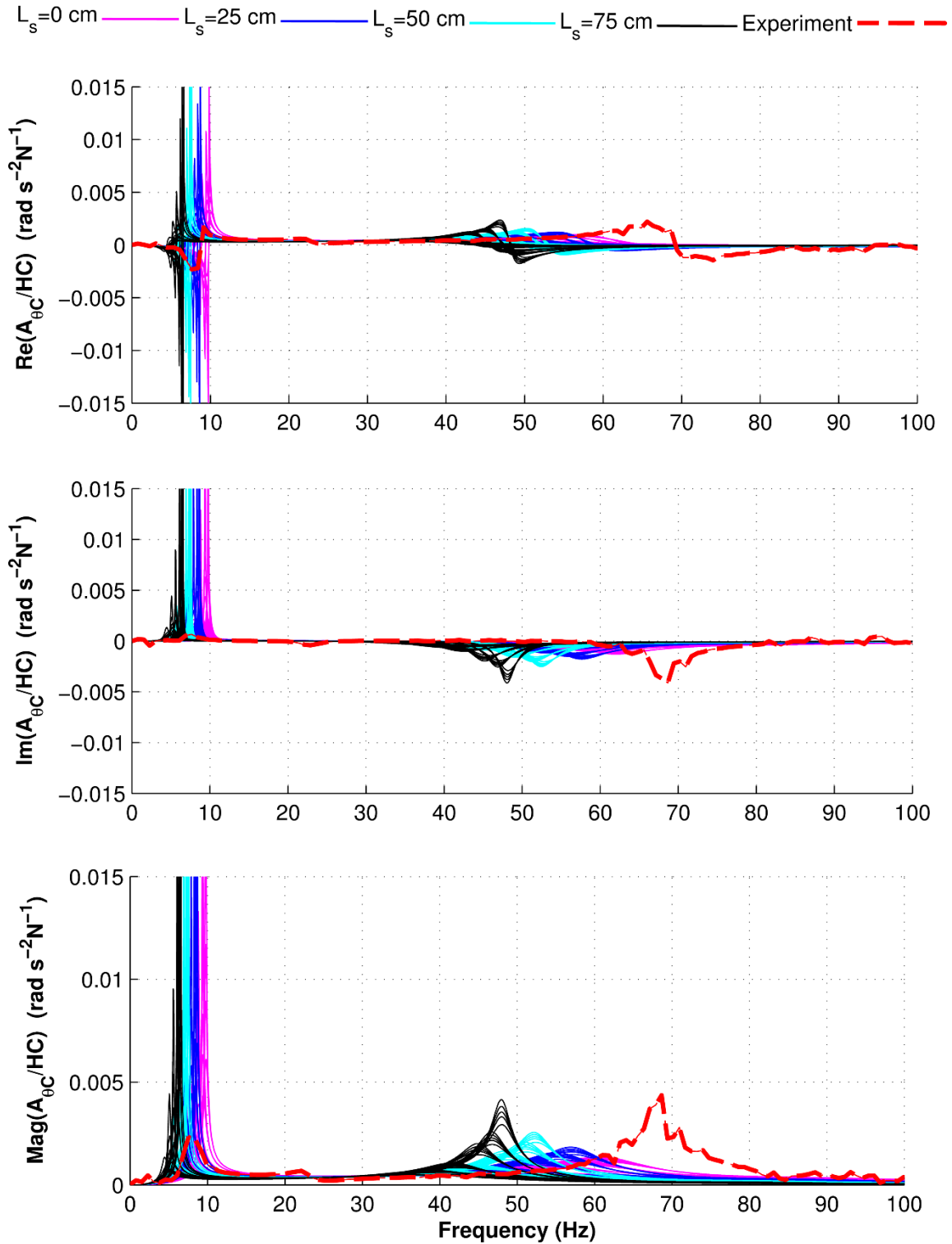


Figure 4-28- Centroidal rotational accelerance functions for HC loading for the 120 cases described in Table 4-3. Experimental results from Test U-HC-R2.

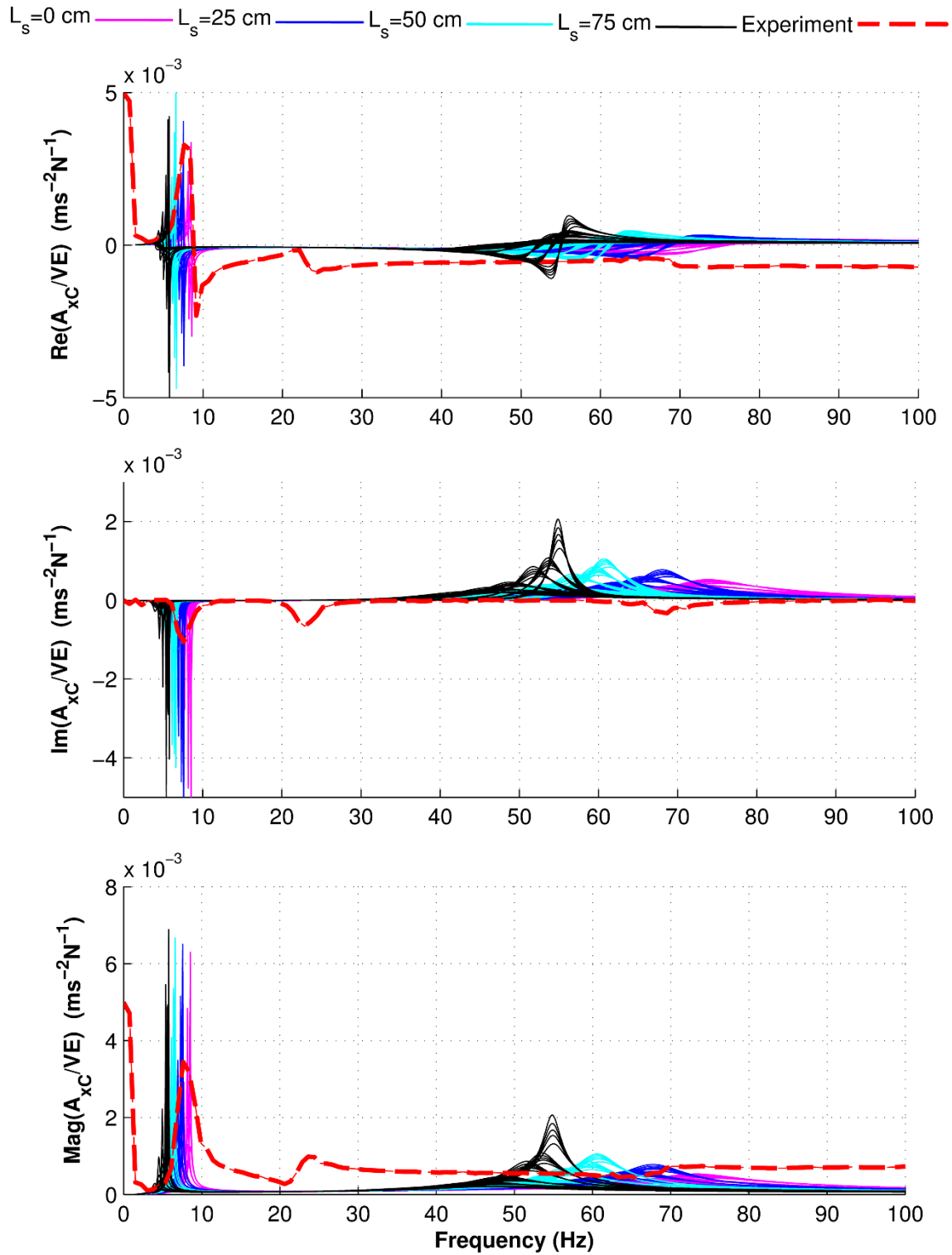


Figure 4-29- Centroidal horizontal acceleration functions for VE loading for the 120 cases described in Table 4-3. Experimental results from Test U-VE-R2.

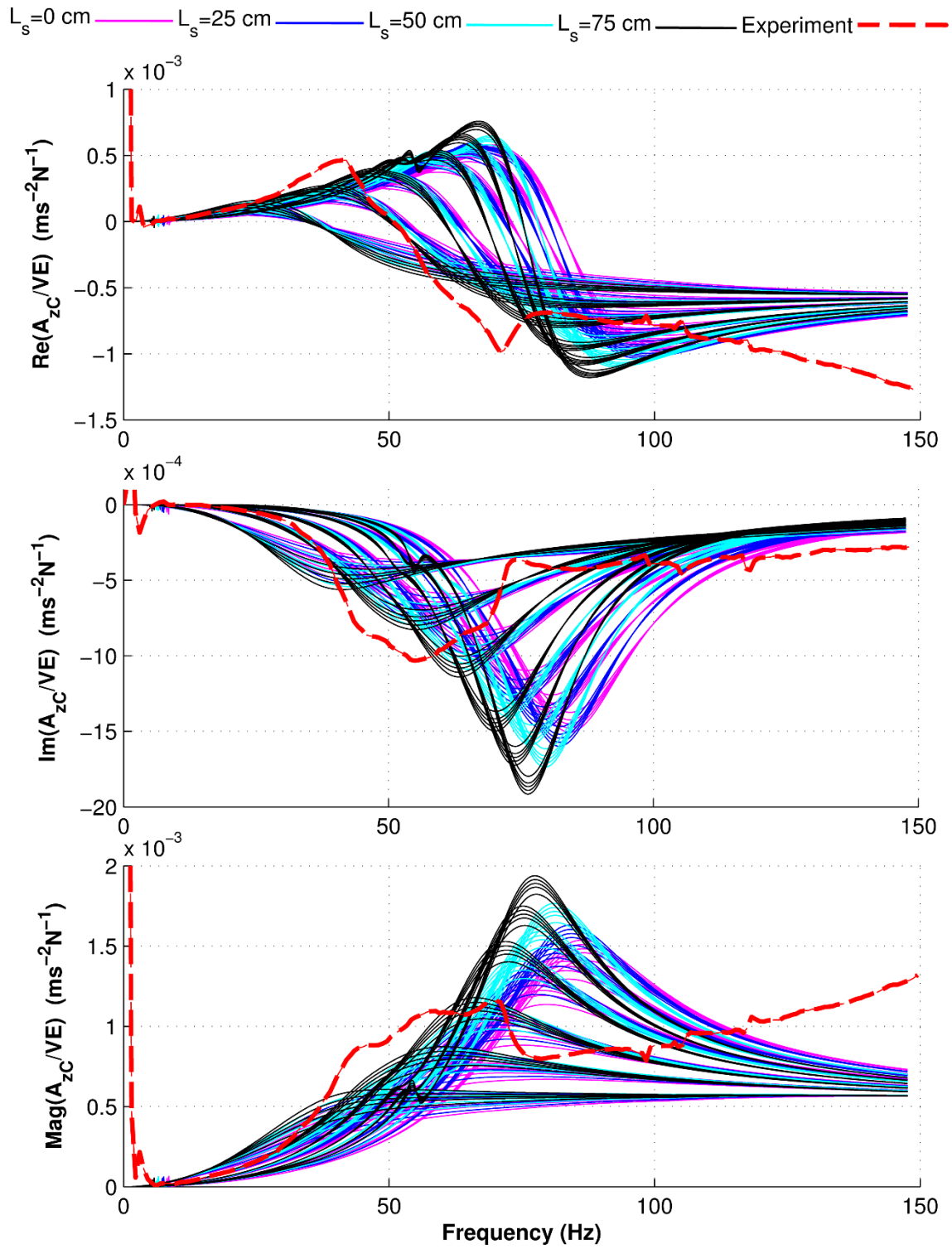


Figure 4-30- Centroidal vertical acceleration functions for VE loading for the 120 cases described in Table 4-3. Experimental results from Test U-VE-R2.

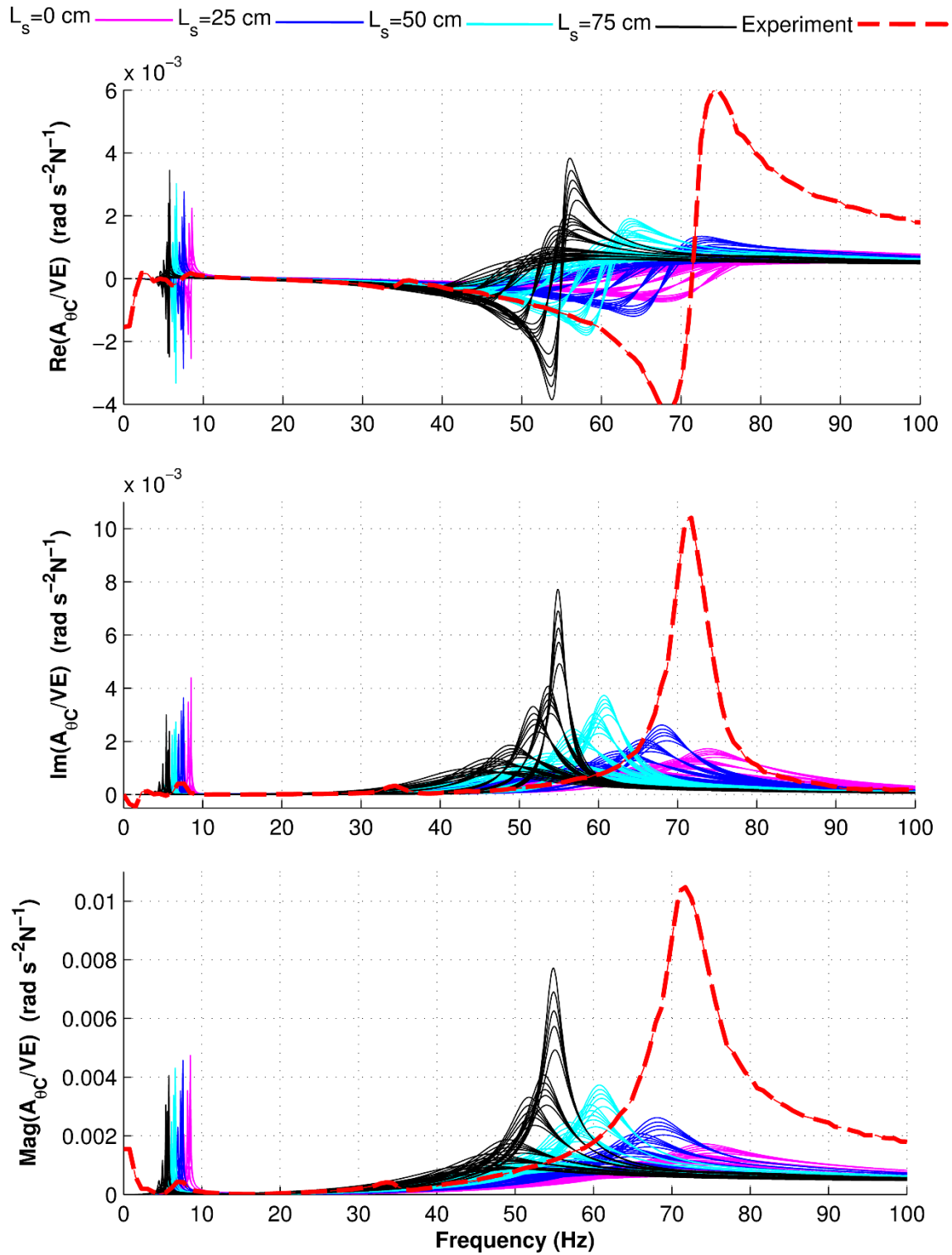


Figure 4-31- Centroidal rotational acceleration functions for VE loading for the 120 cases described in Table 4-3. Experimental results from Test U-VE-R2.

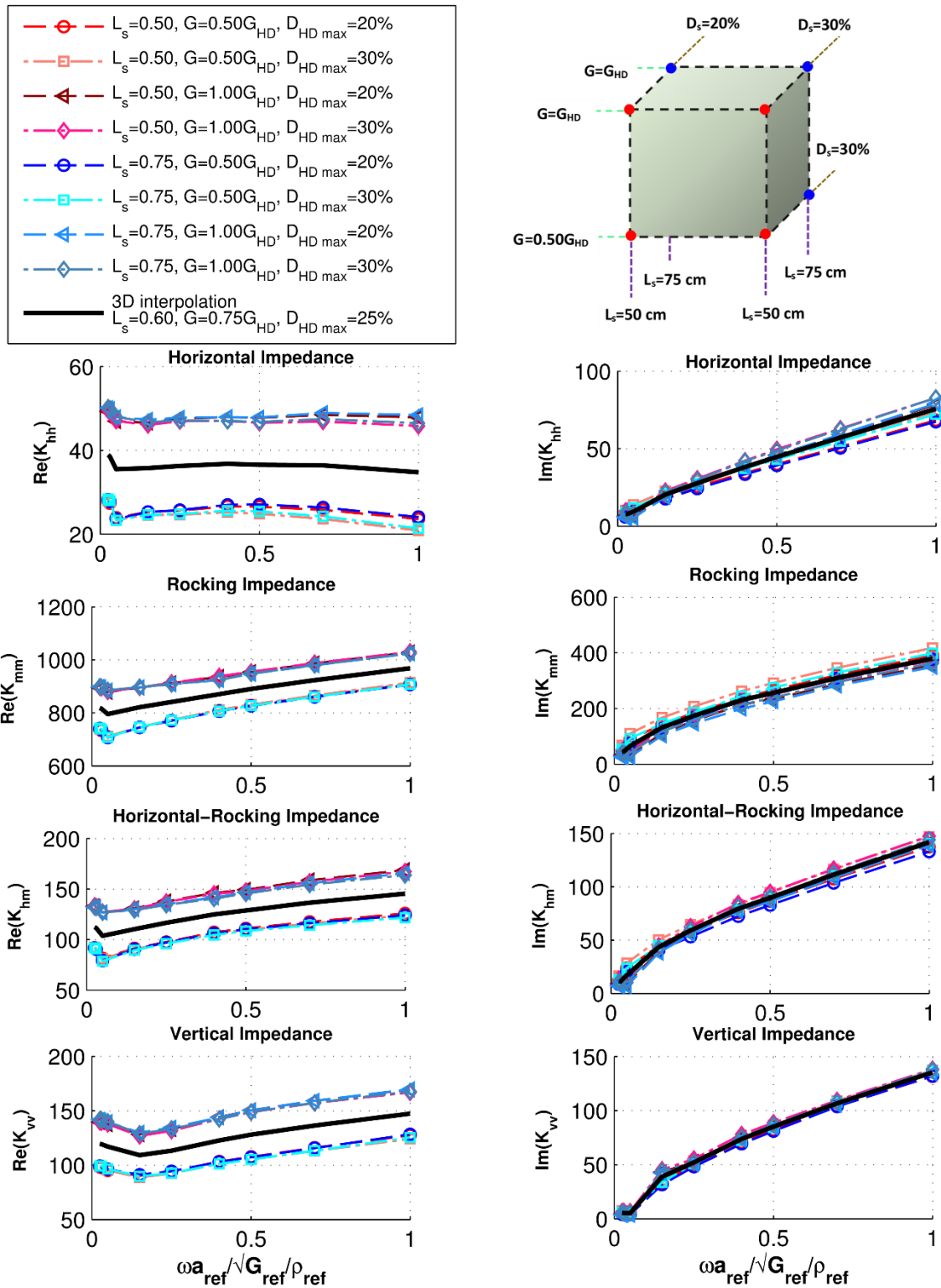


Figure 4-32- Impedance functions by multi-dimensional interpolation for a case with three parameters between the analyzed cases presented in Table 4-3.

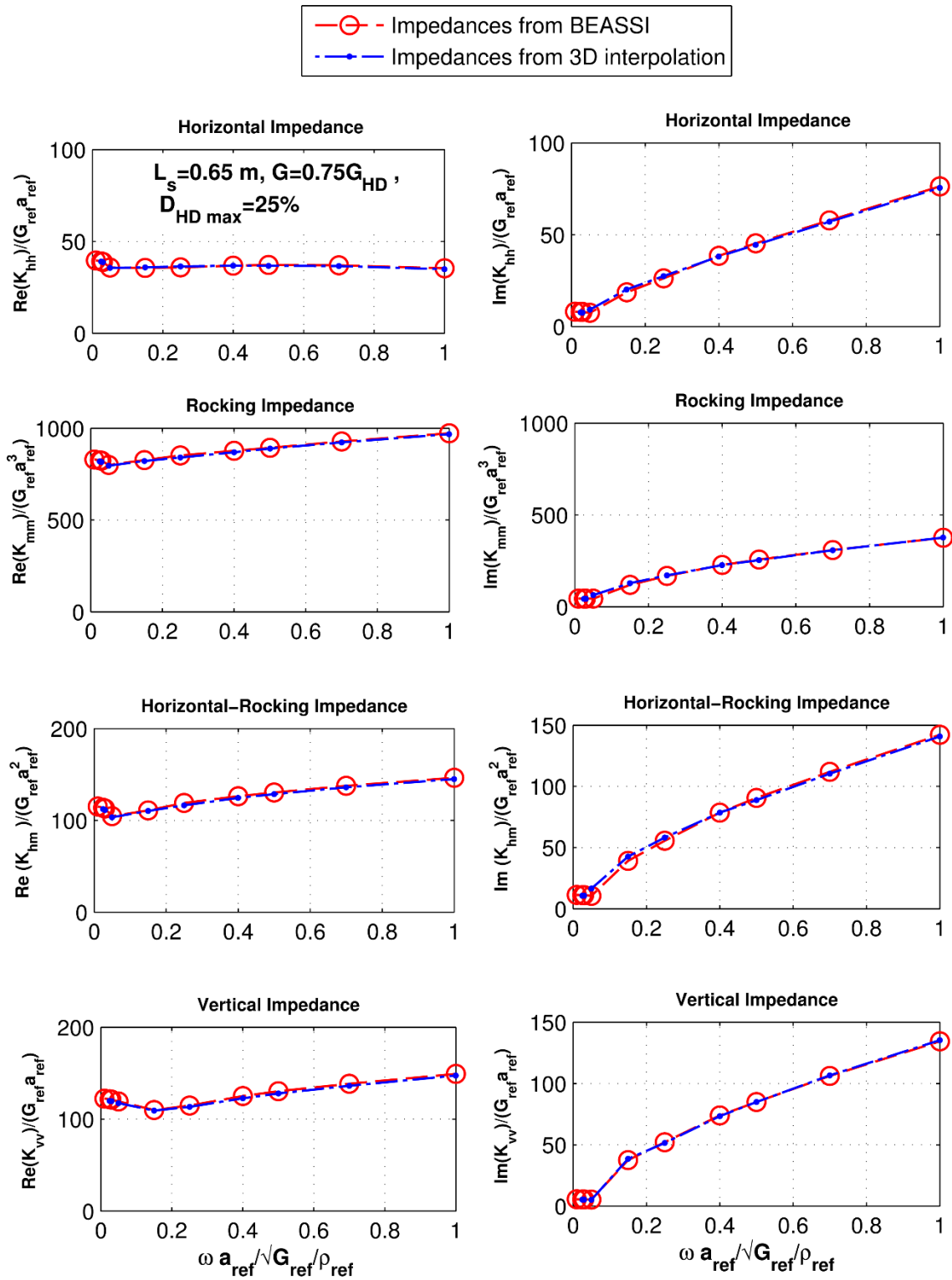


Figure 4-33- Verification of interpolated impedance functions of Figure 4-32 with exact values from BEM analysis using same target parameters.

4.3.3.1.1 Error function

In order to optimize the system parameters including soil modulus profile, damping profile, and separation depth to provide the best match to the experimental results, an appropriate error function must be defined. To this end, the following global error function is defined to quantify the mismatch in the theoretical and experimental accelerances for the vertical, horizontal, and rotational modes:

$$\varepsilon = W_{HC} \frac{\varepsilon_{HC}}{\varepsilon_{HC}^{ref}} + W_{VC} \frac{\varepsilon_{VC}}{\varepsilon_{VC}^{ref}} + W_{RC} \frac{\varepsilon_{RC}}{\varepsilon_{RC}^{ref}} + W_{f_{HC}} \frac{\varepsilon_{Peak-HC}}{\varepsilon_{Peak-HC}^{ref}} + W_{f_{VC}} \frac{\varepsilon_{Peak-VC}}{\varepsilon_{Peak-VC}^{ref}} + W_{f_{RC}} \frac{\varepsilon_{Peak-RC}}{\varepsilon_{Peak-RC}^{ref}} \quad (4.6)$$

where

$$\varepsilon_{Peak-VC} = \left| f_{th-pk}^{VC} - f_{m-pk}^{VC} \right|$$

$$\varepsilon_{Peak-HC} = \left| f_{th-pk}^{HC} - f_{m-pk}^{HC} \right|$$

$$\varepsilon_{Peak-RC} = \left| f_{th-pk}^{RC} - f_{m-pk}^{RC} \right|$$

$$\varepsilon_{Peak-VC}^{ref} = \left| f_{th-pk}^{VCref} - f_{m-pk}^{VC} \right|$$

$$\varepsilon_{Peak-HC}^{ref} = \left| f_{th-pk}^{HCref} - f_{m-pk}^{HC} \right|$$

$$\varepsilon_{Peak-RC}^{ref} = \left| f_{th-pk}^{RCref} - f_{m-pk}^{RC} \right|$$

and

$$\varepsilon_{HC} = \int_{f_1}^{f_2} \sqrt{\left(\operatorname{Re}\left(A_{xC}^{th} / HC\right) - \operatorname{Re}\left(A_{xC}^m / HC\right)\right)^2 + \left(\operatorname{Im}\left(A_{xC}^{th} / HC\right) - \operatorname{Im}\left(A_{xC}^m / HC\right)\right)^2} df$$

$$\varepsilon_{VC} = \int_{f_3}^{f_4} \sqrt{\left(\operatorname{Re}\left(A_{zC}^{th} / VC\right) - \operatorname{Re}\left(A_{zC}^m / VC\right)\right)^2 + \left(\operatorname{Im}\left(A_{zC}^{th} / VC\right) - \operatorname{Im}\left(A_{zC}^m / VC\right)\right)^2} df$$

$$\varepsilon_{RC} = \int_{f_5}^{f_6} \sqrt{\left(\operatorname{Re}\left(A_{\theta C}^{th} / HC\right) - \operatorname{Re}\left(A_{\theta C}^m / HC\right)\right)^2 + \left(\operatorname{Im}\left(A_{\theta C}^{th} / HC\right) - \operatorname{Im}\left(A_{\theta C}^m / HC\right)\right)^2} df$$

$$\varepsilon_{HC}^{ref} = \int_{f_1}^{f_2} \sqrt{\left(\operatorname{Re}\left(A_{xC}^{th\ ref} / HC\right) - \operatorname{Re}\left(A_{xC}^m / HC\right)\right)^2 + \left(\operatorname{Im}\left(A_{xC}^{th\ ref} / HC\right) - \operatorname{Im}\left(A_{xC}^m / HC\right)\right)^2} df$$

$$\varepsilon_{VC}^{ref} = \int_{f_3}^{f_4} \sqrt{\left(\operatorname{Re}\left(A_{zC}^{th\ ref} / VC\right) - \operatorname{Re}\left(A_{zC}^m / VC\right)\right)^2 + \left(\operatorname{Im}\left(A_{zC}^{th\ ref} / VC\right) - \operatorname{Im}\left(A_{zC}^m / VC\right)\right)^2} df$$

$$\varepsilon_{RC}^{ref} = \int_{f_5}^{f_6} \sqrt{\left(\operatorname{Re}\left(A_{\theta C}^{th\ ref} / HC\right) - \operatorname{Re}\left(A_{\theta C}^m / HC\right)\right)^2 + \left(\operatorname{Im}\left(A_{\theta C}^{th\ ref} / HC\right) - \operatorname{Im}\left(A_{\theta C}^m / HC\right)\right)^2} df$$

To obtain a balance between matching peak frequencies and the overall shapes of the curves, the error function contains the difference in peak frequencies as well as an integral of the squared errors between real and imaginary components. To make the relative magnitude of the terms in the error function more consistent when performing parameter sweeps in the theoretical models, each term is normalized by those of a known, fixed reference problem (such as one of the cases in Table 4-3). Additionally, each term has a relative weighting multiplier, W_i , which defines the relative importance placed on matching the peak frequencies versus the overall shapes of the various accelerance curves. Appropriate values must therefore be selected for these weights to inject the engineering judgment of what constitutes a best fit into the matching algorithms. Figure 4-34 depicts graphically the parameters used in the error function for Cases 11 to 15 in Table 4-3 for the case $L_s=0$.

The integration limits for the least-square error components were chosen to fit the frequency ranges exhibiting good-quality experimental accelerances as well as theoretical sensitivity to the parameters. For example, the accelerometers do not give reliable measurements below their minimum frequency, which is typically a few Hertz. Additionally, the experimental accelerances do not perfectly follow the behavior of a rigid-body pile-cap-shaker assembly (possibly due to resonance of the shaker base frame), which causes additional higher modes above 70 to 100 Hz depending on the test and mode. Based on these factors, the integration limits were selected as $f_1=3$ Hz, $f_2=15$ Hz, $f_3=5$ Hz, $f_4=100$ Hz, $f_5=5$ Hz, and $f_6=20$ Hz, as shown in Figure 4-34.

Different weighting factor combinations were also examined in terms of their accelerance matches and resulting calculated error functions, as shown in Figures 4-35 to 4-50. This weighting factor study helps not only to demonstrate the effect of each of the components in the global error measure, but also to find the combination of weights W_i which best captures all aspects of the experiments in the three modes of vibration simultaneously. Based on this study, the weighting values shown in Figure 4-49 ;

$$W_{HC} = 2.0, W_{VC} = 2.0, W_{RC} = 2.0, W_{f_{HC}} = 1.0, W_{f_{VC}} = 1.0, W_{f_{RC}} = 1.0$$

were judged to produce the best overall accelerance matches, and were therefore selected for the rest of the analyses.

Perhaps most importantly, it can be concluded from Figures 4-35 to 4-50 that it is not possible to match the theoretical to experimental accelerances for all the three modes of vibration simultaneously by simply scaling the shear modulus and damping profiles of Figure 4-23.

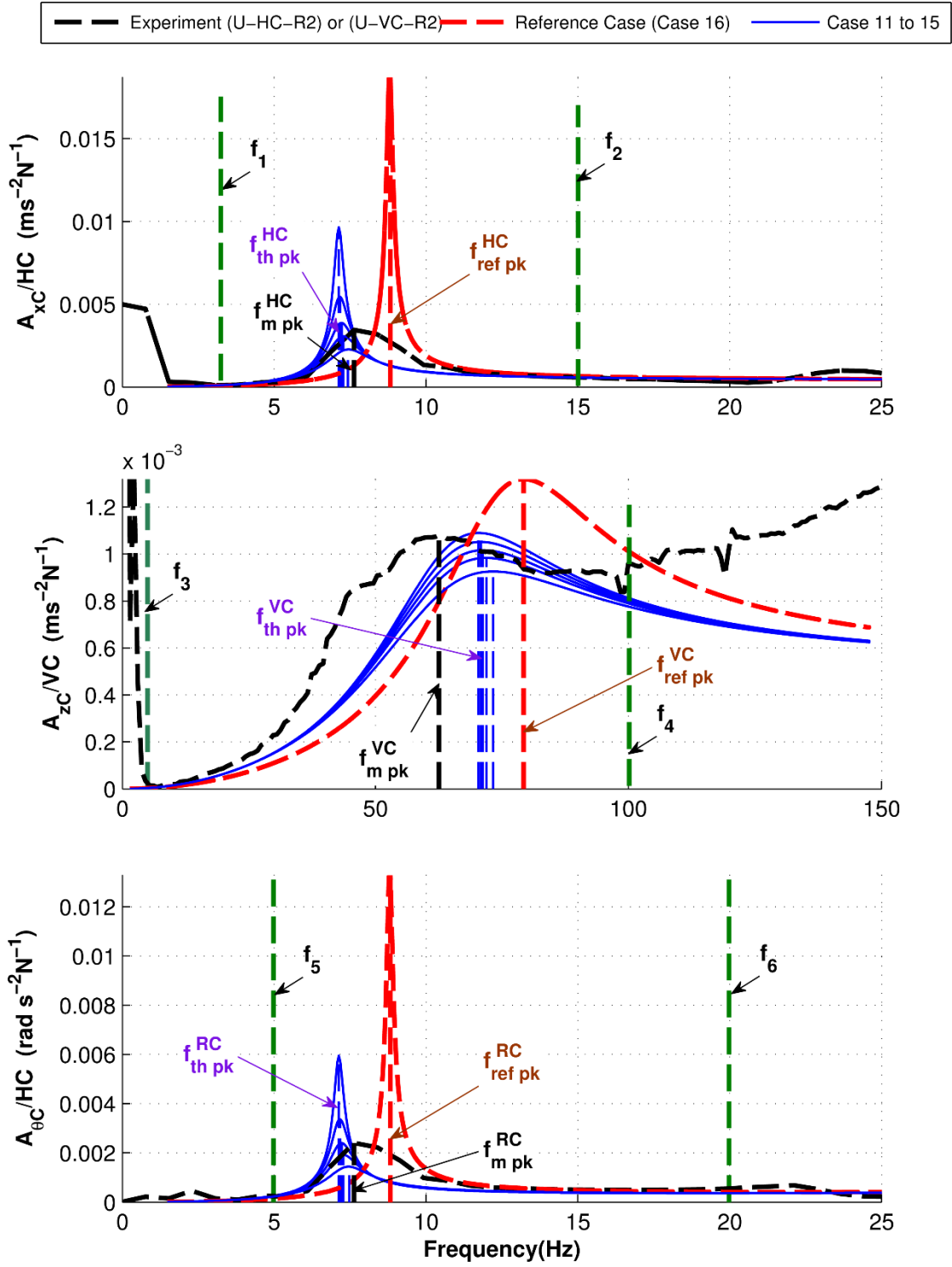


Figure 4-34- Graphical depiction of error function parameters for Cases 11 to 15 with $L_s=0$ cm.

4.3.3.1.2 Case 1: $W_{f_{VC}} = 1$;

$W_{f_{HC}} = 0.00, W_{f_{VC}} = 1.00, W_{f_{RC}} = 0.00, W_{HC} = 0.00, W_{VC} = 0.00, W_{RC} = 0.00 \rightarrow \epsilon_{\min} = 0.0081$
 @ ϵ_{\min} : $G = 0.25G_{HD}, D_{s \max} = 30.0\%, L_s = 0.00 \text{ cm}$
 @ ϵ_{\min} : $\epsilon_{\text{Peak-HC}} = 0.3317, \epsilon_{\text{Peak-VC}} = 0.0081, \epsilon_{\text{Peak-RC}} = 0.3317$
 @ ϵ_{\min} : $\epsilon_{HC} = 1.3346, \epsilon_{VC} = 0.5598, \epsilon_{RC} = 1.4953$

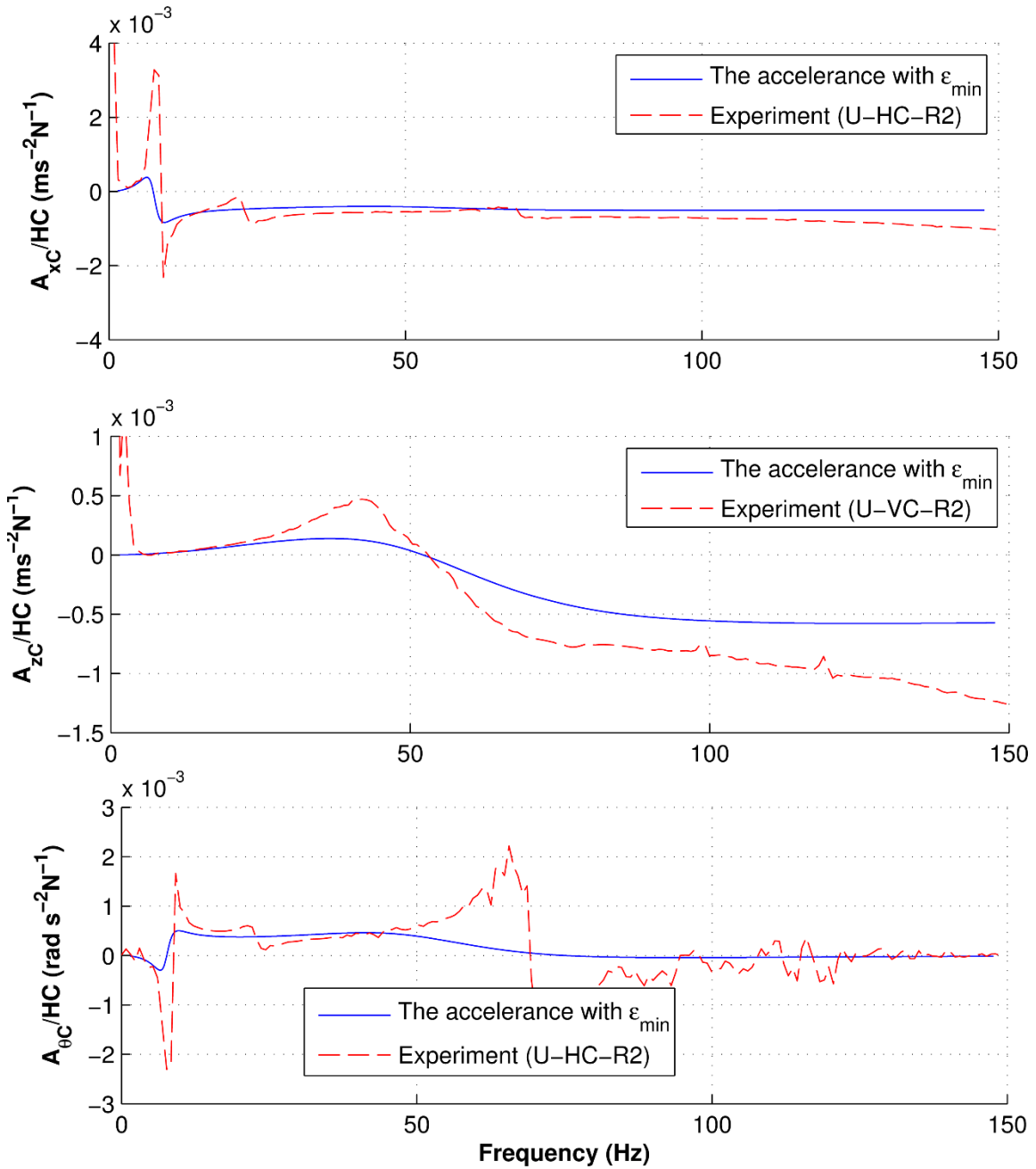


Figure 4-35- Best-fit accelerance function from the G , D , and L_s values that minimize the error function in Equation (4.6). Weighting parameters are indicated in the box.

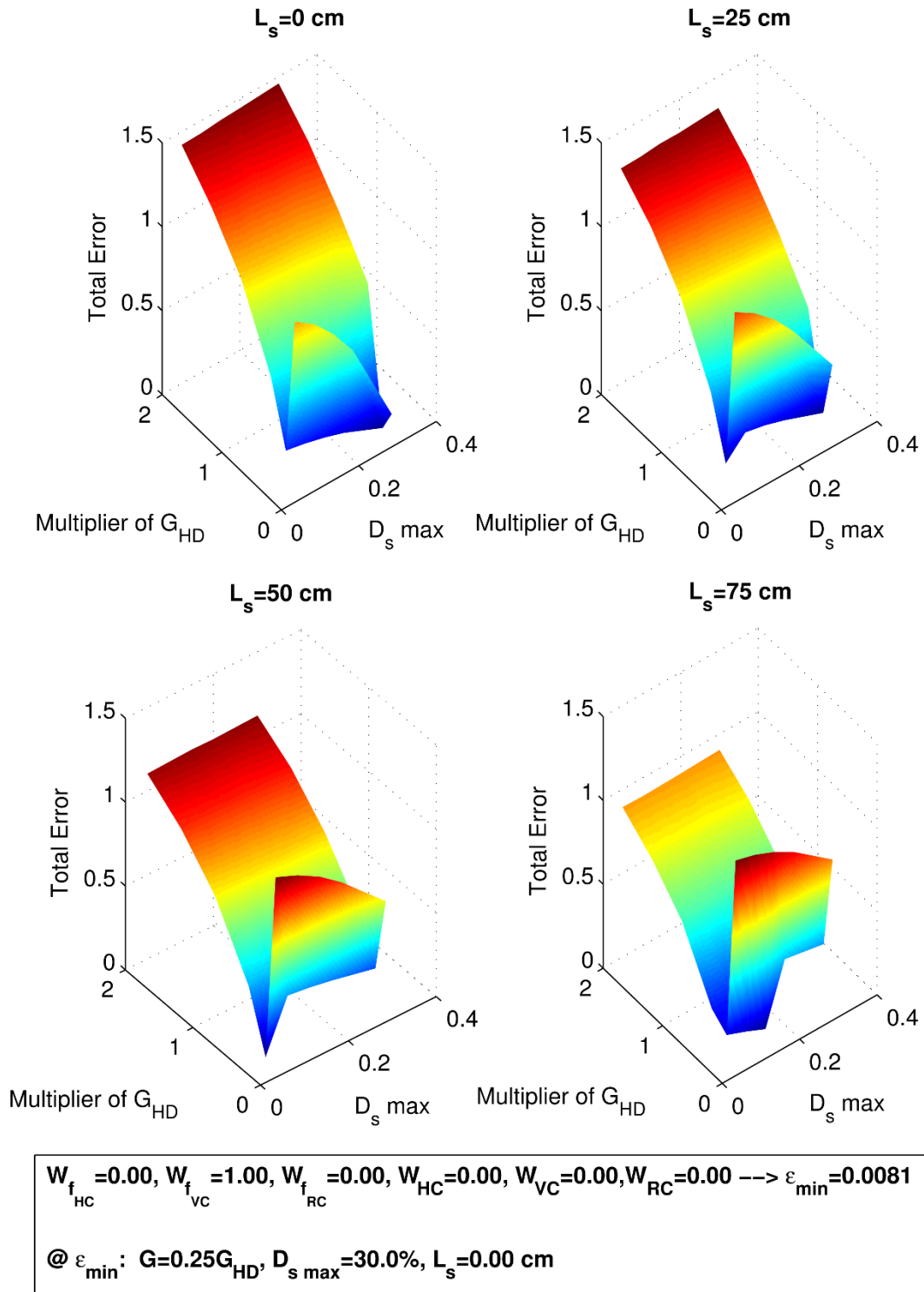


Figure 4-36- Variation of global error function with $G, D,$ and L_s for the given combination of weighting parameters.

4.3.3.1.3 Case 2: $W_{VC} = 1$;

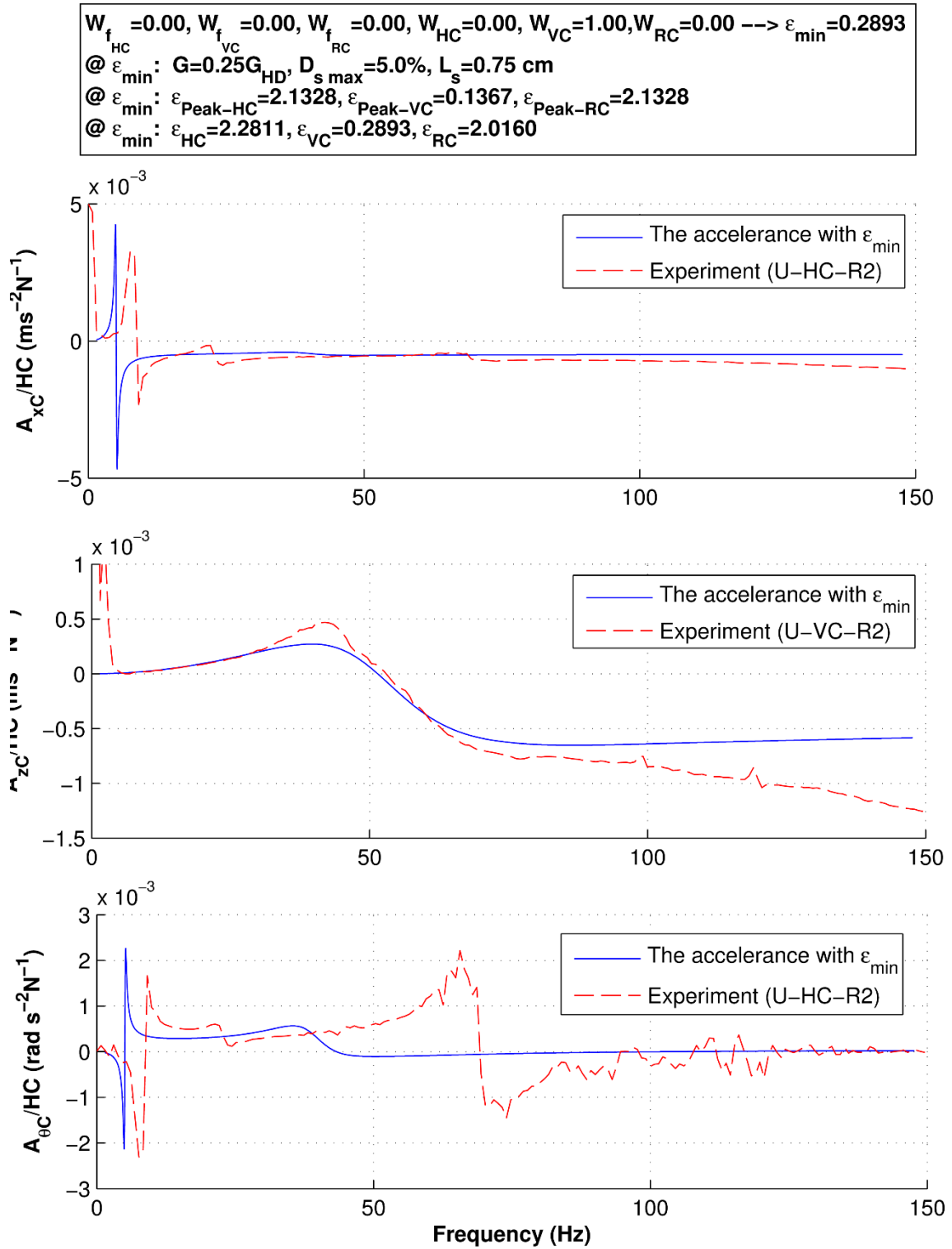


Figure 4-37- Best-fit accelerance function from the G, D, and Ls values that minimize the error function in Equation (4.6). Weighting parameters are indicated in the box.

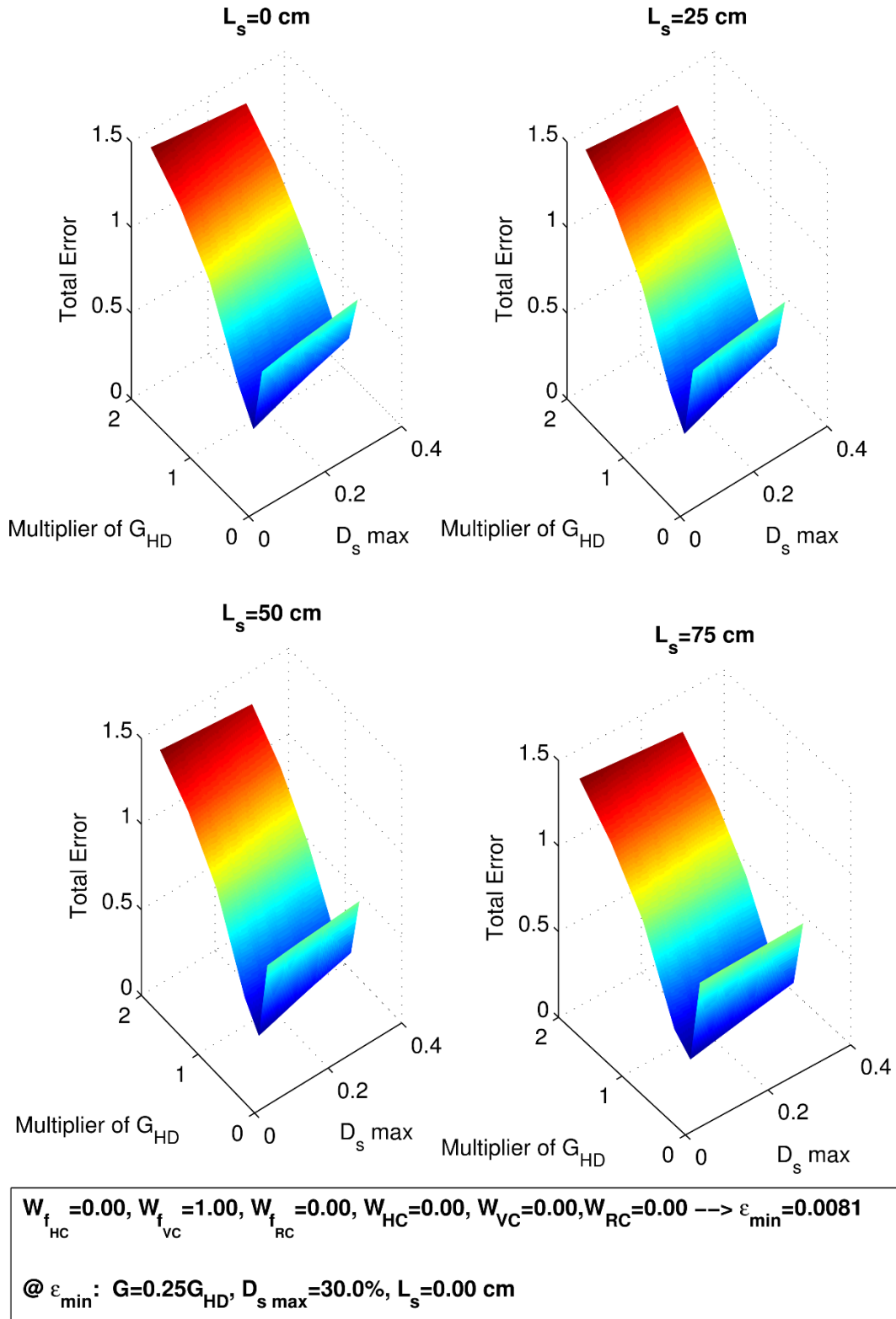


Figure 4-38- Variation of global error function with G, D, and Ls for the given combination of weighting parameters.

4.3.3.1.4 Case 3: $W_{f_{HC}} = 1;$

$W_{f_{HC}} = 1.00, W_{f_{VC}} = 0.00, W_{f_{RC}} = 0.00, W_{HC} = 0.00, W_{VC} = 0.00, W_{RC} = 0.00 \rightarrow \epsilon_{min} = 0.0443$
 @ ϵ_{min} : $G = 0.25G_{HD}, D_{s\ max} = 20.0\%, L_s = 0.00\ cm$
 @ ϵ_{min} : $\epsilon_{Peak-HC} = 0.0443, \epsilon_{Peak-VC} = 0.1098, \epsilon_{Peak-RC} = 0.0443$
 @ ϵ_{min} : $\epsilon_{HC} = 1.3829, \epsilon_{VC} = 0.4879, \epsilon_{RC} = 1.5341$

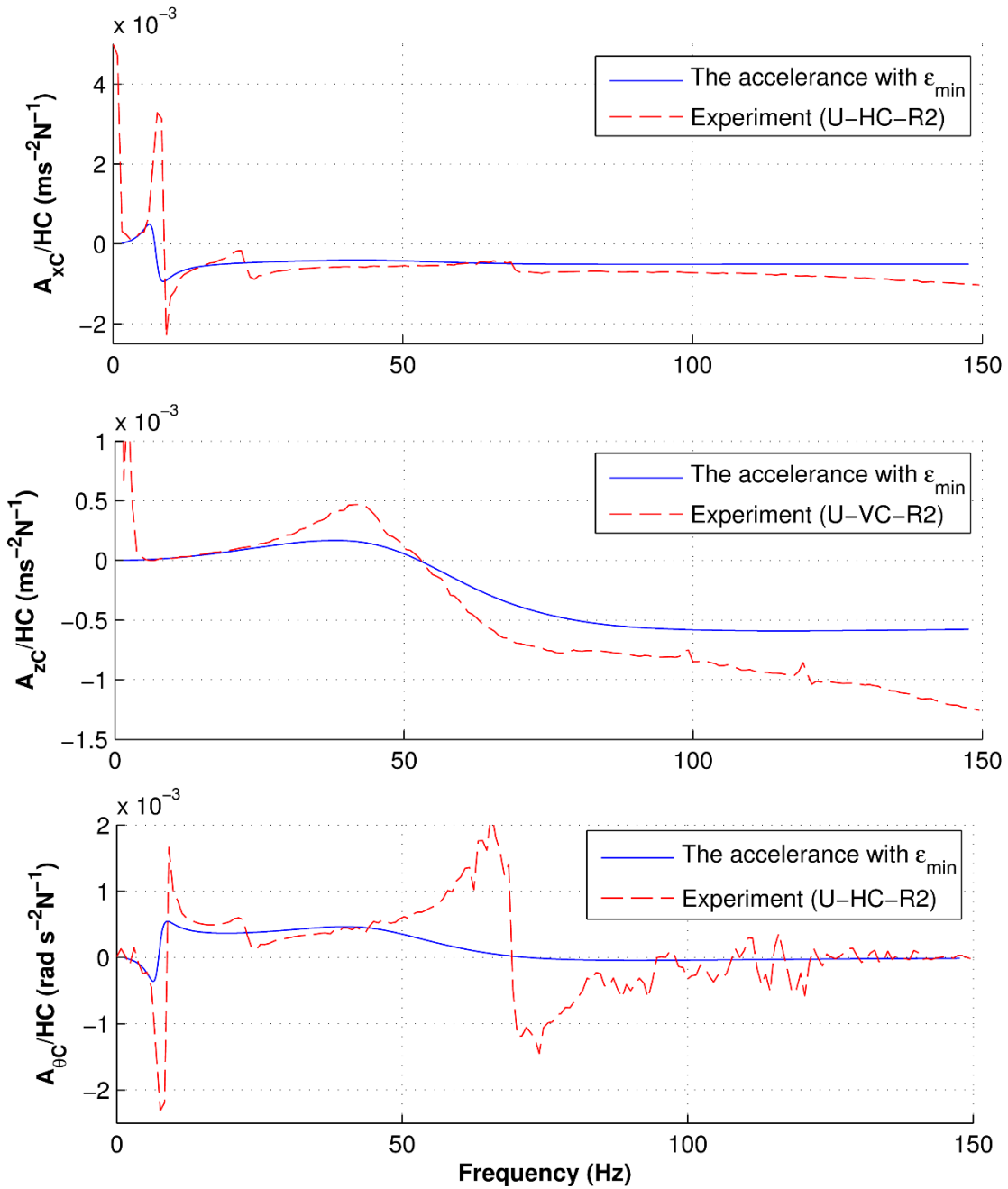


Figure 4-39- Best-fit acceleration function from the $G, D,$ and L_s values that minimize the error function in Equation (4.6). Weighting parameters are indicated in the box.

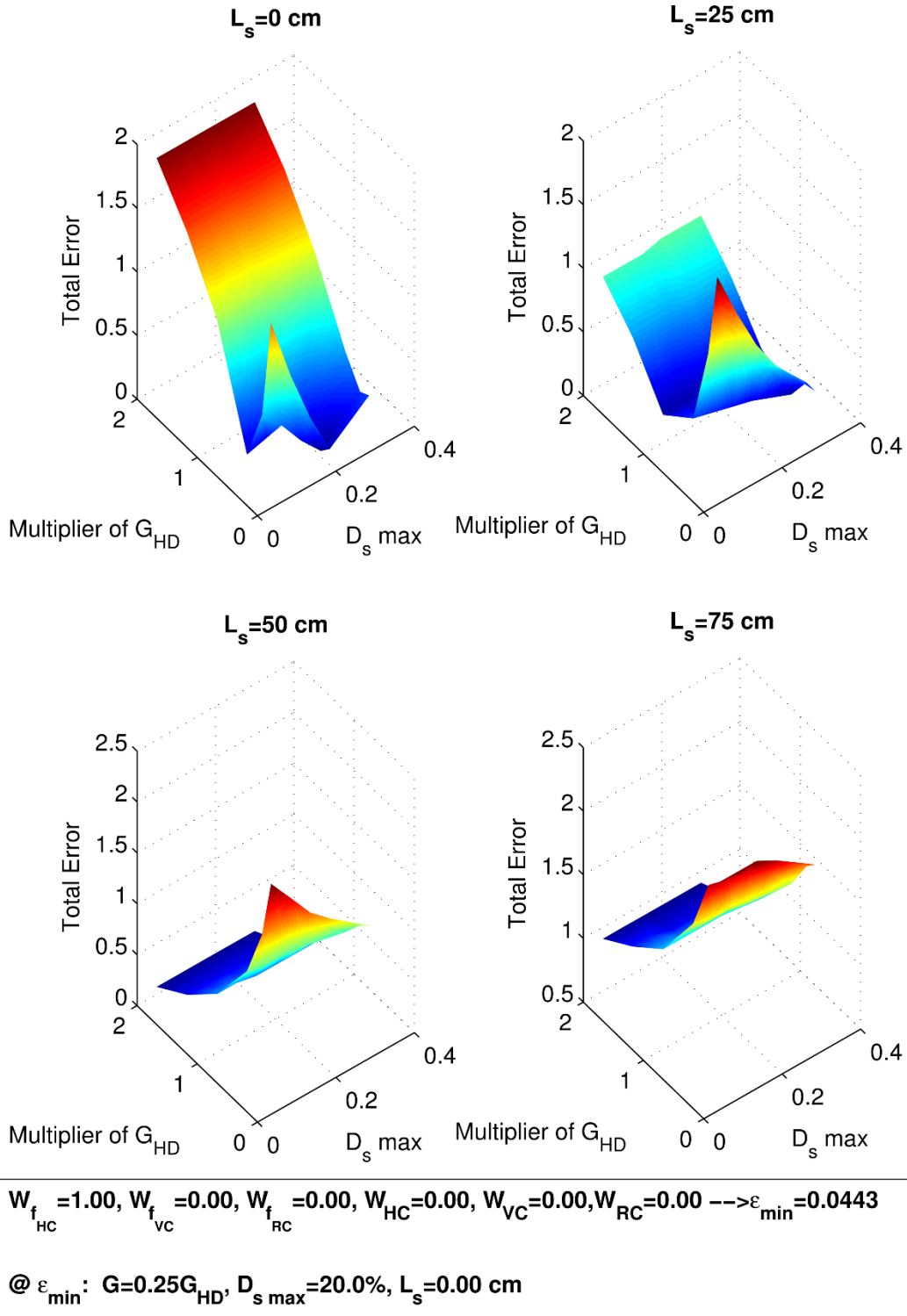


Figure 4-40- Variation of global error function with G, D, and Ls for the given combination of weighting parameters.

4.3.3.1.5 Case 4: $W_{HC} = 1$;

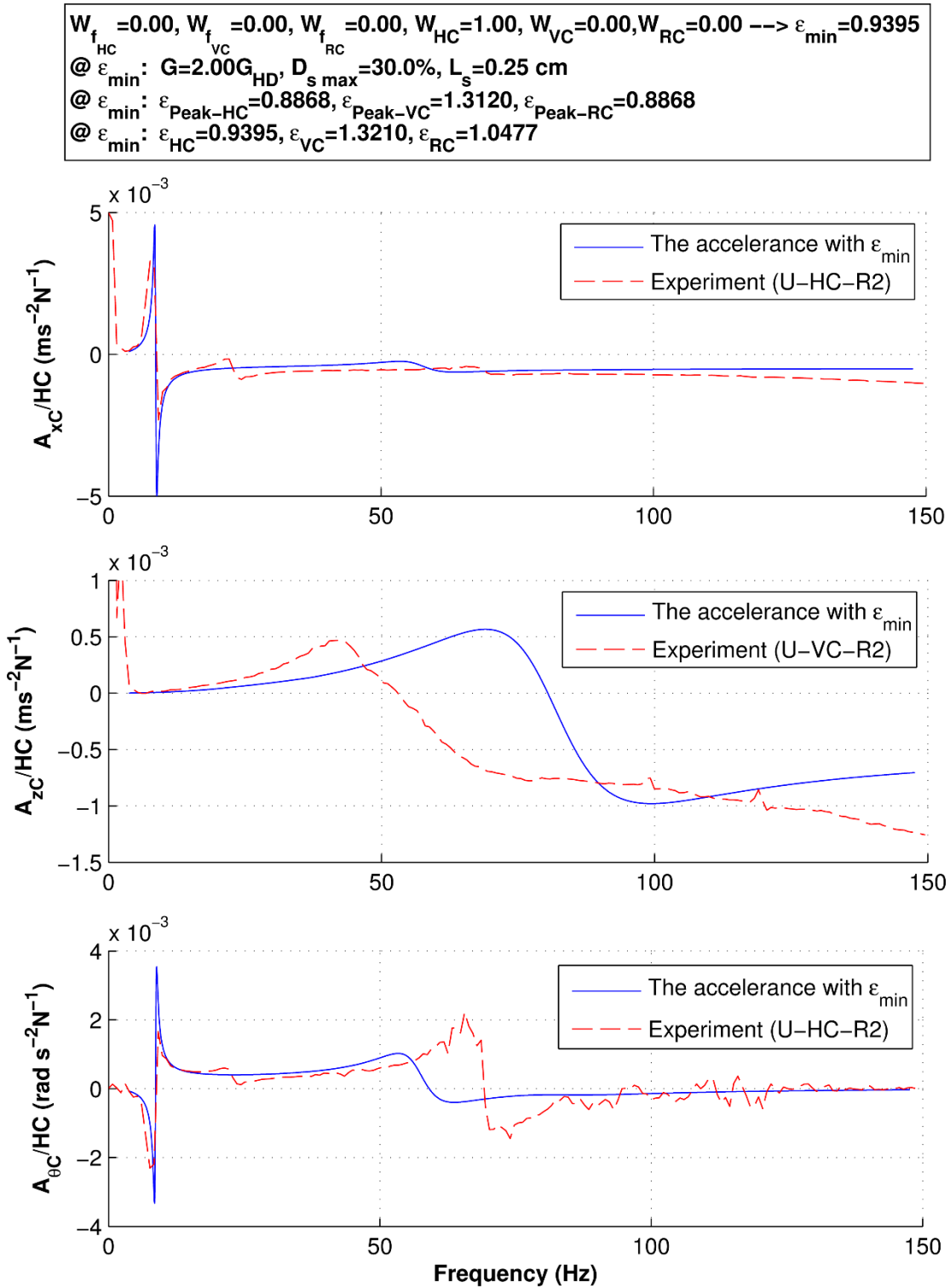


Figure 4-41- Best-fit accelerance function from the G, D, and Ls values that minimize the error function in Equation (4.6). Weighting parameters are indicated in the box.

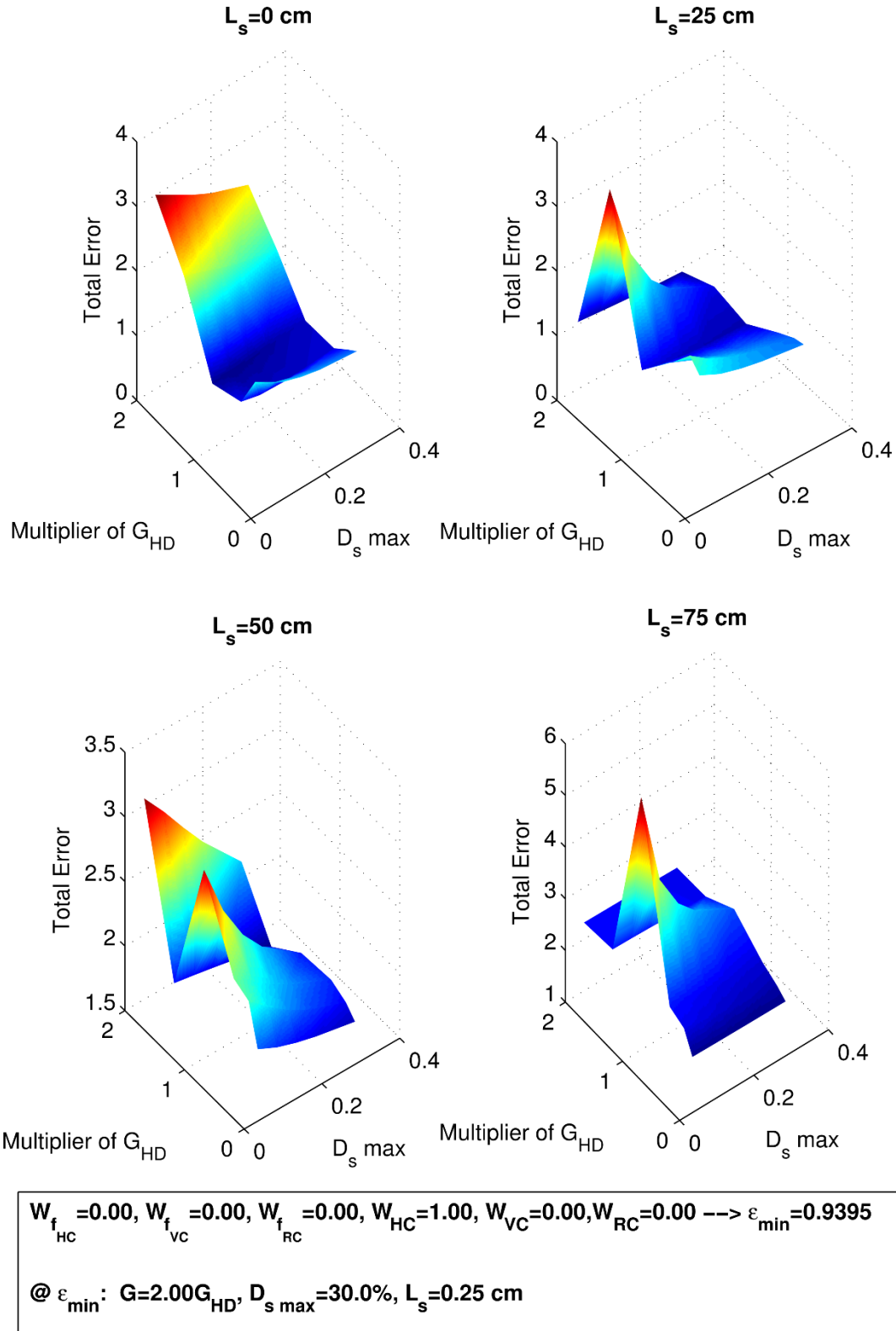


Figure 4-42- Variation of global error function with G, D, and L_s for the given combination of weighting parameters.

4.3.3.1.6 Case 5: $W_{HC} = 0.75, W_{f_{HC}} = 1;$

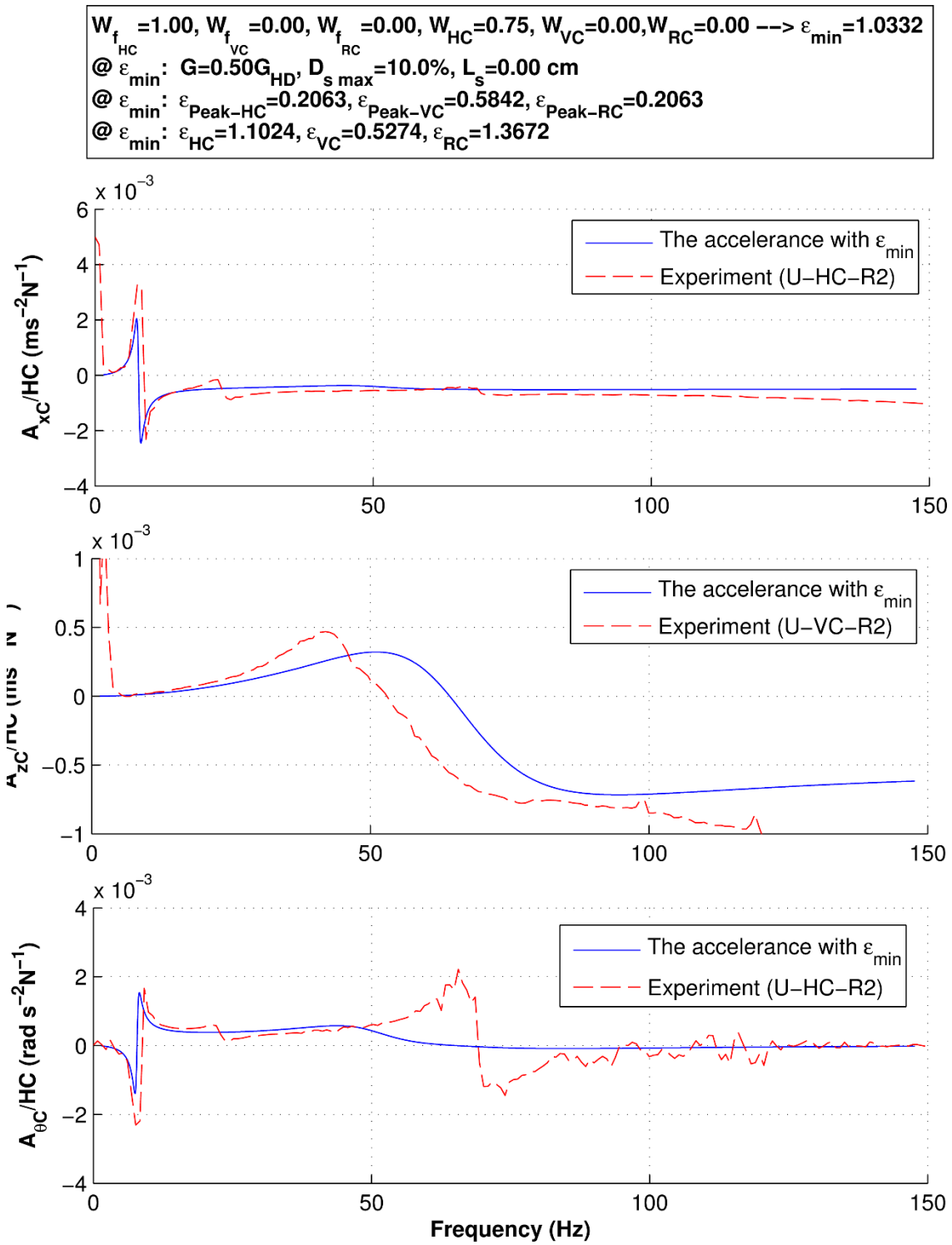


Figure 4-43-Best-fit accelerance function from the G, D, and Ls values that minimize the error function in Equation (4.6). Weighting parameters are indicated in the box.

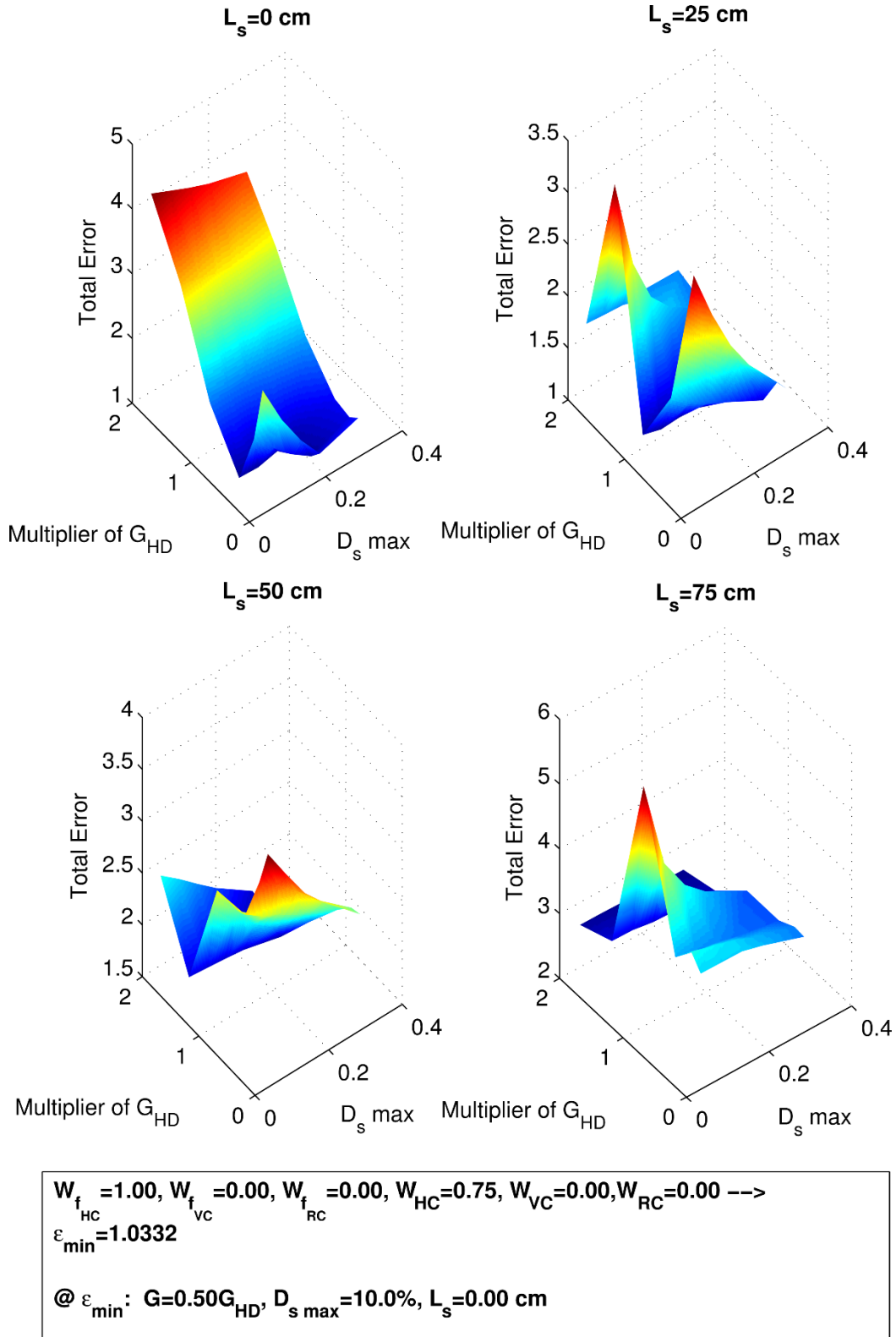


Figure 4-44-Variation of global error function with G, D, and L_s for the given combination of weighting parameters.

4.3.3.1.7 Case 6: $W_{VC} = 0.75, W_{fvc} = 1;$

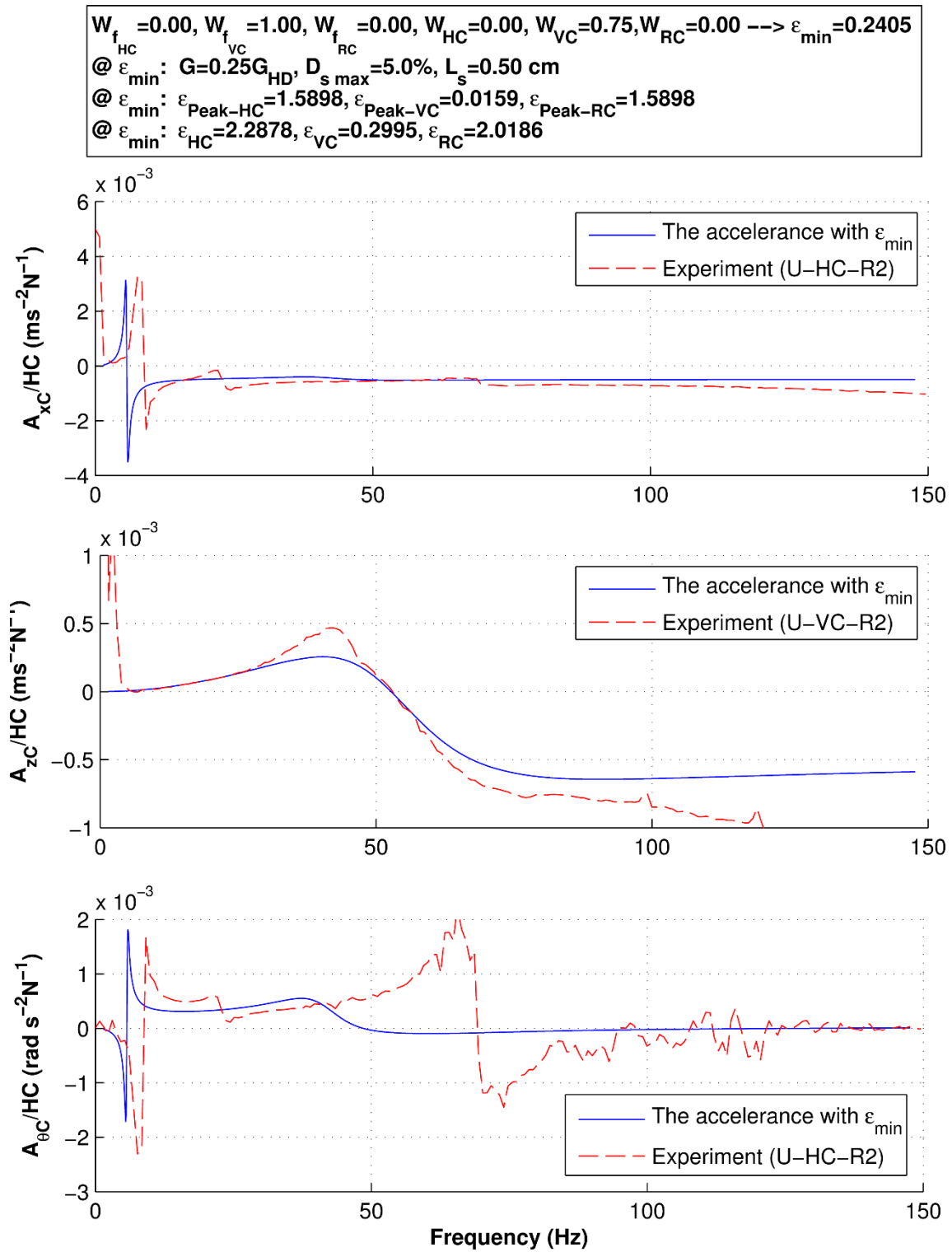


Figure 4-45-Best-fit acceleration ϵ function from the G, D, and L_s values that minimize the error function in Equation (4.6). Weighting parameters are indicated in the box.

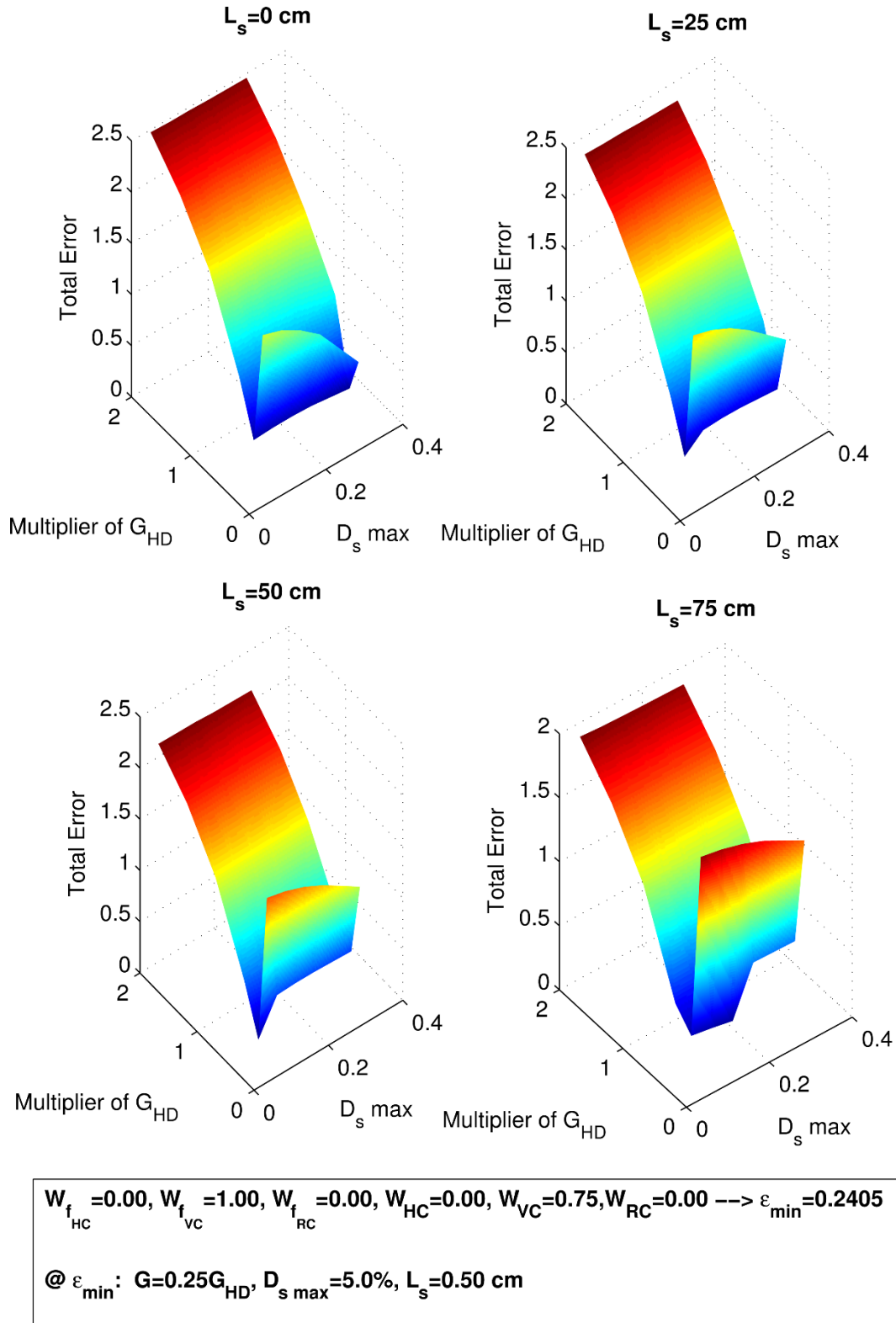


Figure 4-46-Variation of global error function with G, D, and L_s for the given combination of weighting parameters.

4.3.3.1.8 Case 7: $W_{HC} = 0.75, W_{VC} = 0.75, W_{RC} = 0.75, W_{f_{HC}} = 1, W_{f_{VC}} = 1, W_{f_{RC}} = 1;$

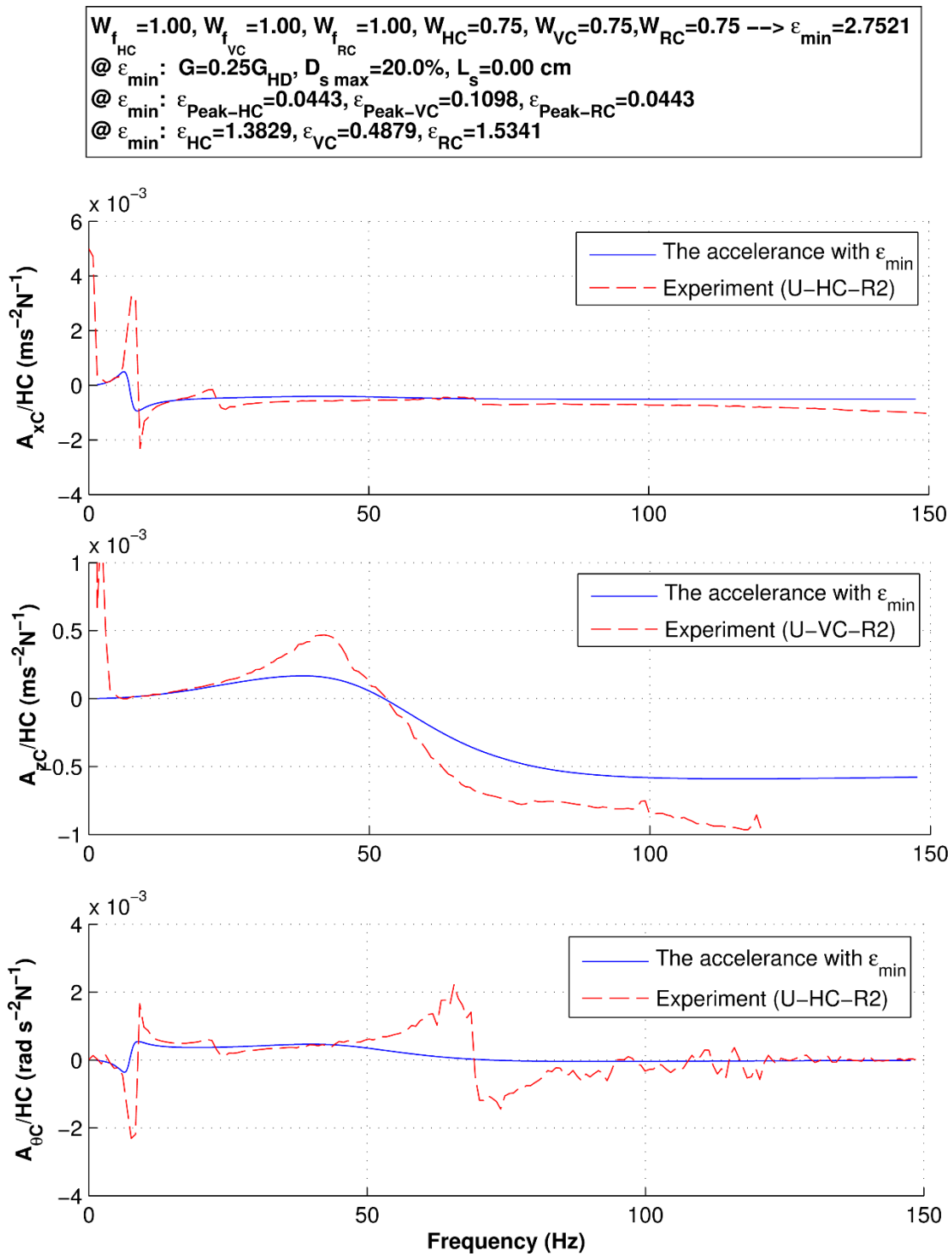


Figure 4-47- Best-fit acceleration function from the G, D, and Ls values that minimize the error function in Equation (4.6). Weighting parameters are indicated in the box.

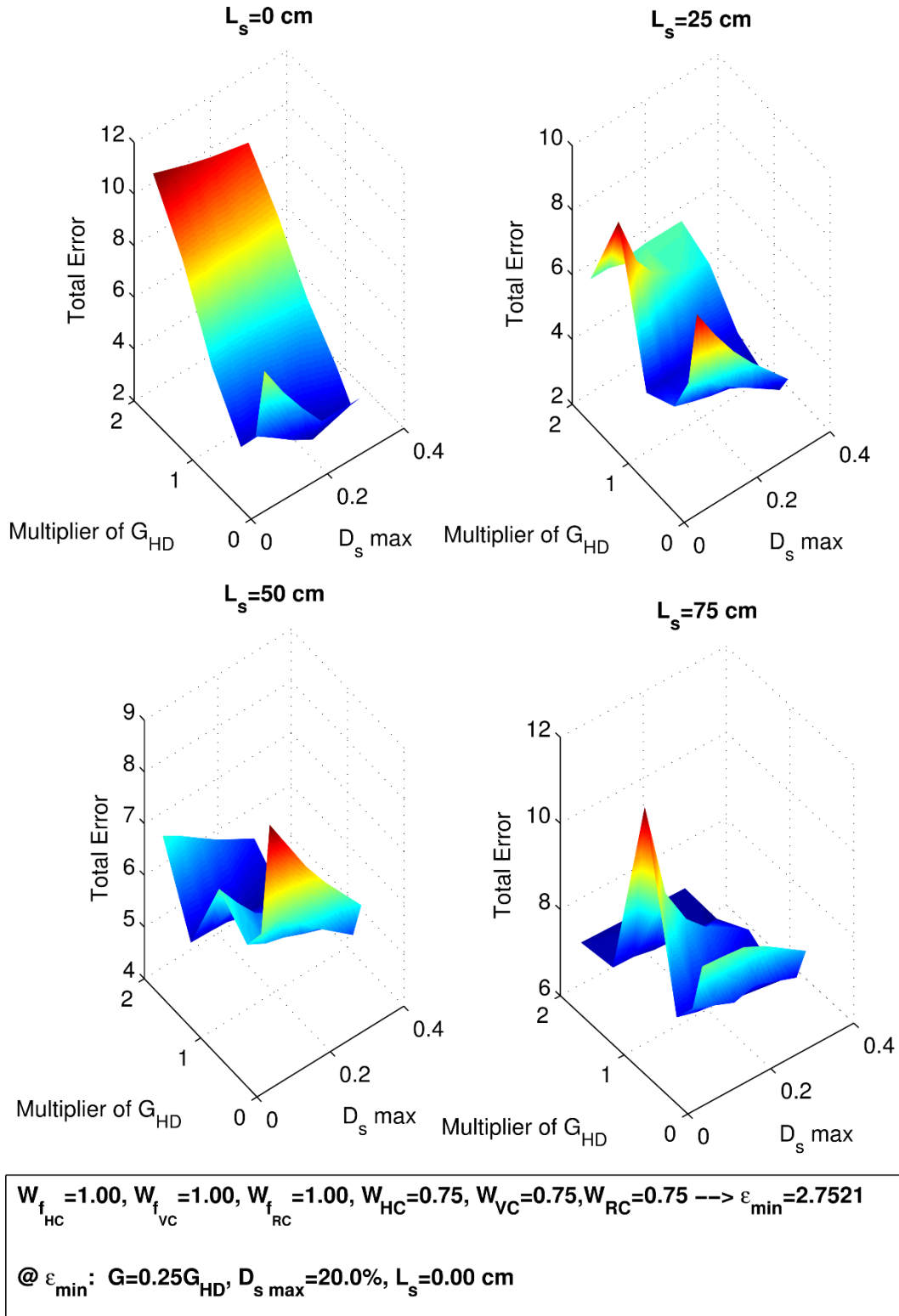


Figure 4-48- Variation of global error function with G, D, and Ls for the given combination of weighting parameters.

4.3.3.1.9 Case 8: $W_{HC} = 2, W_{VC} = 2, W_{RC} = 2, W_{f_{HC}} = 1, W_{f_{VC}} = 1, W_{f_{RC}} = 1;$

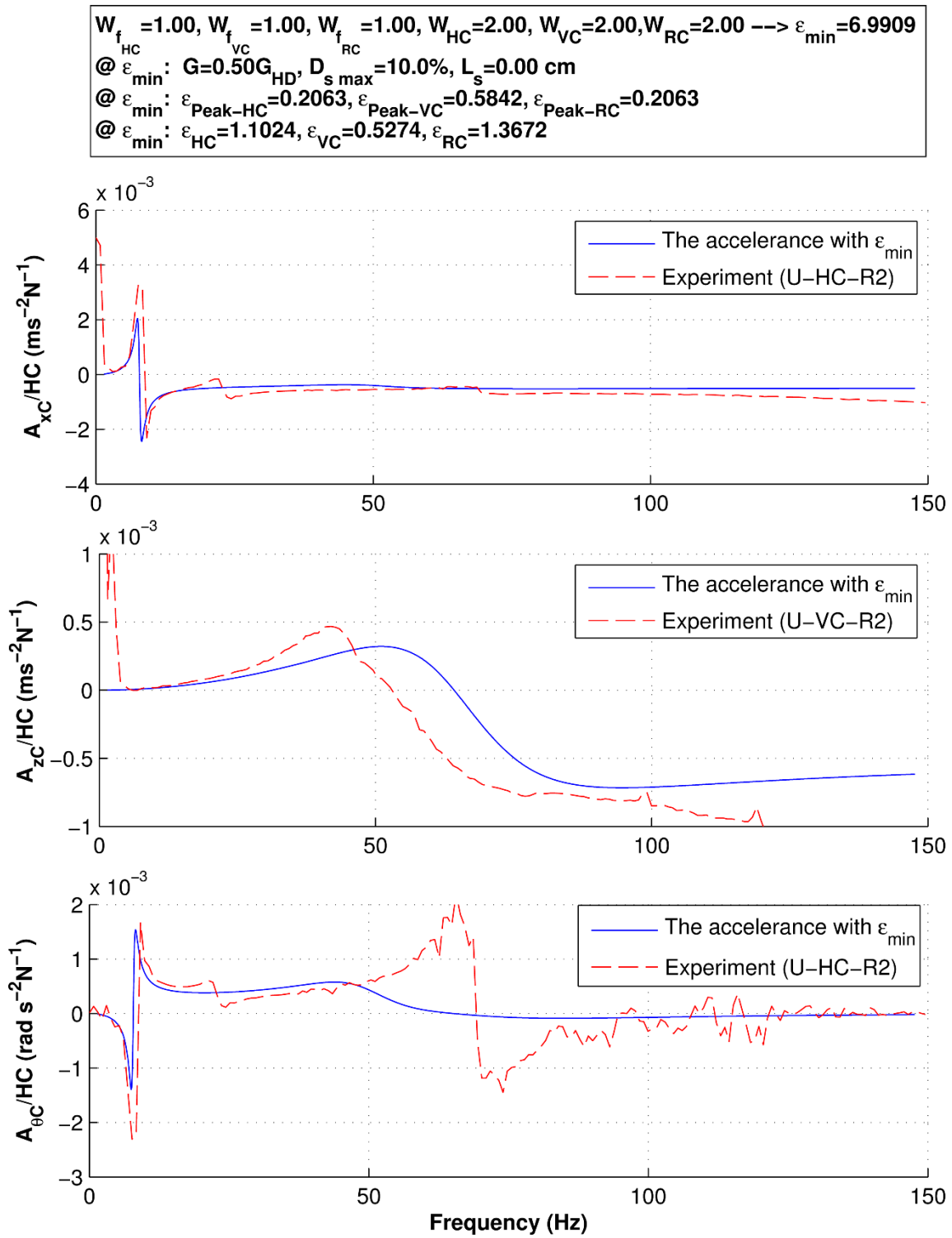


Figure 4-49- Best-fit acceleration function from the G, D, and Ls values that minimize the error function in Equation (4.6). Weighting parameters are indicated in the box.

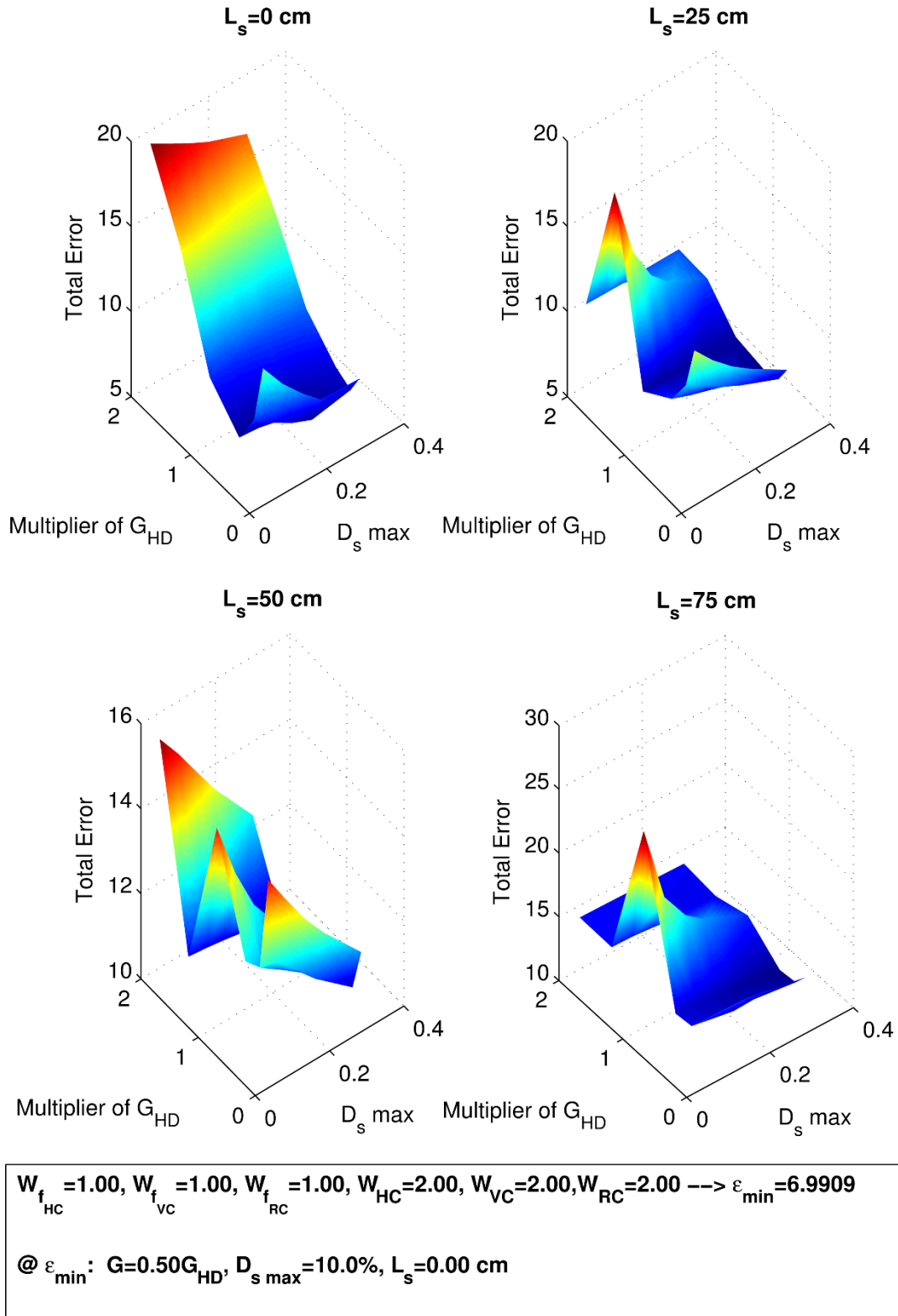


Figure 4-50- Variation of global error function with G, D, and Ls for the given combination of weighting parameters.

4.3.3.2 Modification proposed in previous centrifuge study

In a previous centrifuge and BEM study of solid and hollow circular piles in uniform dry sand, several parametric variations of the form described in Section 4.3.3 were studied to reduce the modulus and increase damping at the surface, while increasing modulus and decreasing damping at depth (Ashlock, 2006). Because the soil in that study was a uniform dry sand, the far-field shear modulus profile had a simple square-root dependence in accord with the Hardin-Drnevich relations, in contrast to the more complex natural soil profile encountered in this study. The resulting best-fit profile from the study (referred to as Case E2), once calibrated to a solid pile with a large prototype diameter and high stiffness, was shown to accurately predict the response for a hollow pile with smaller diameter and much lower stiffness. Therefore, the Case E2 profile was also examined in this study as a first candidate for a nonlinear modification factor with depth.

In the centrifuge study, the outer far-field shear modulus profile had the simple square-root form

$$G^O(z) = G_{0.5}^O \sqrt{z/a_{ref}}$$

and the best fit shear modulus profile for the inner disturbed-zone was defined by

$$G^I(z) = G_{0.5}^O \left[0.1 + 1.1 \left(1 - \frac{1}{1 + \left(\frac{(z/a_{ref})/5}{5} \right)^3} \right) \left((z/a_{ref})^{0.5} - 0.091 \right) \right] \quad (4.7)$$

For this case, one can define the modification function used as $G^I(z) = MF_G^{Case E2}(z) \times G^O(z)$,

where

$$MF_G^{Case\ E2}(z) = \frac{1}{\sqrt{z/a_{ref}}} \left[0.1 + 1.1 \left(1 - \frac{1}{1 + \left(\frac{(z/a_{ref})/5}{5} \right)^3} \right) \left((z/a_{ref})^{0.5} - 0.091 \right) \right] \quad (4.8)$$

The nonlinear damping profile for the Case E2 model was given as

$$\xi(z) = \frac{\xi_0}{1 + \left(\frac{(z/a_{ref})/5}{5} \right)^3} \quad (4.9)$$

The resulting shear modulus modification factor and damping profile for Case E2 are presented in Figure 4-51. Also shown in this figure are the Goempertz model's fit of the $MF_G^{Case\ E2}(z)$ function given above. Figure 4-52 shows the modification factor in Equation (4.8), the resulting shear profile after applying the modification to G_{max} , and the damping profile from Equation (4.9) (Case E2). These profiles were analyzed for the two-domain pile-soil model, but did not result in an improved fit of the measured data. Therefore, the results of this analysis are not shown here. However, the profiles were also used in later three-domain analysis featuring a disturbed-zone around the pile, which is discussed in Section 4.5.

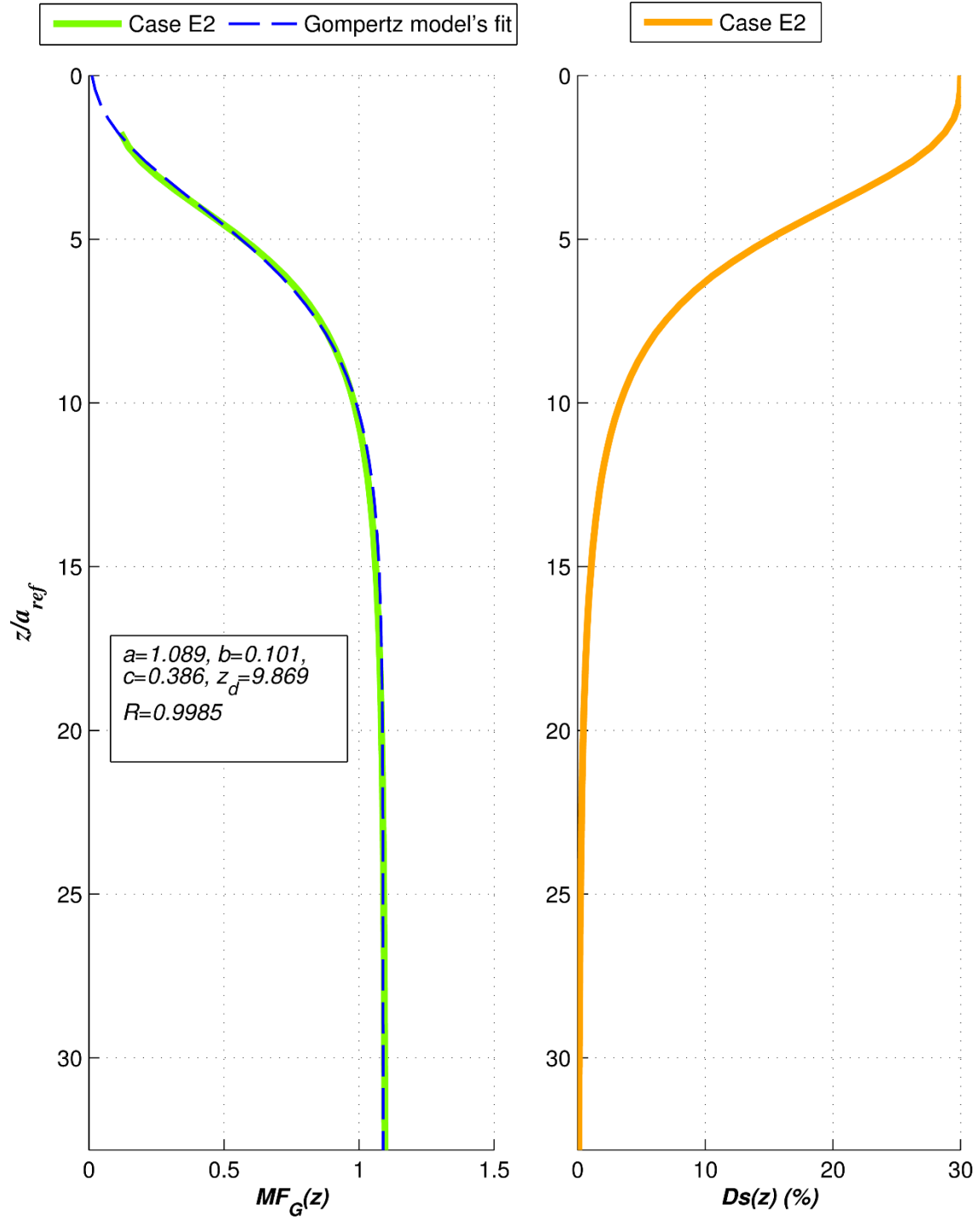


Figure 4-51 Shear modulus modification factor and damping profile for Case E2. The shear modulus is fit by Gompertz model using the shown values for a , b and c .

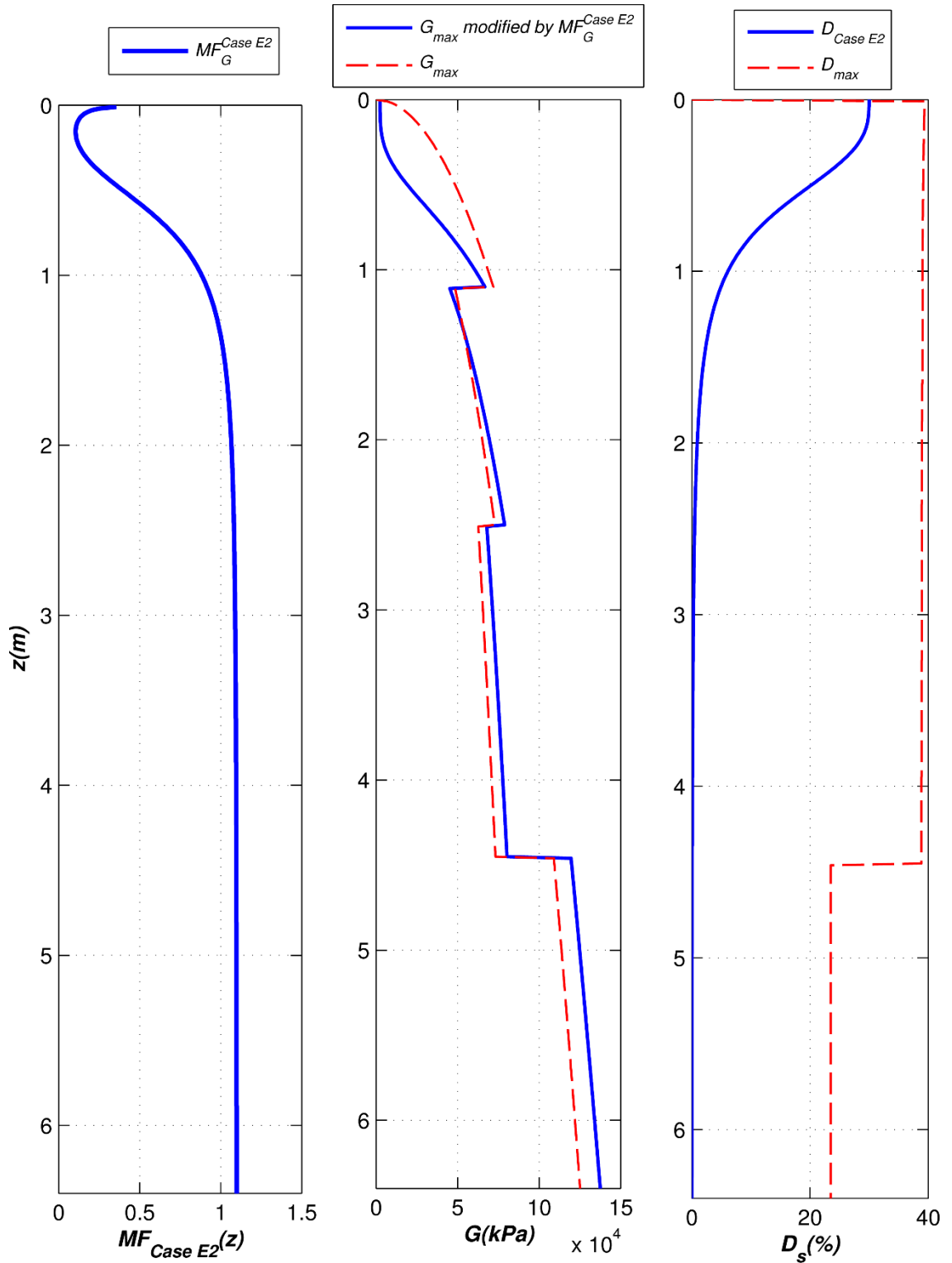


Figure 4-52-Modifications applied to G_{max} profile based on Case E2 (Equation (4.8)) and the corresponding damping profile (Equation (4.9)). G_{max} and D_{max} profiles are shown for comparison.

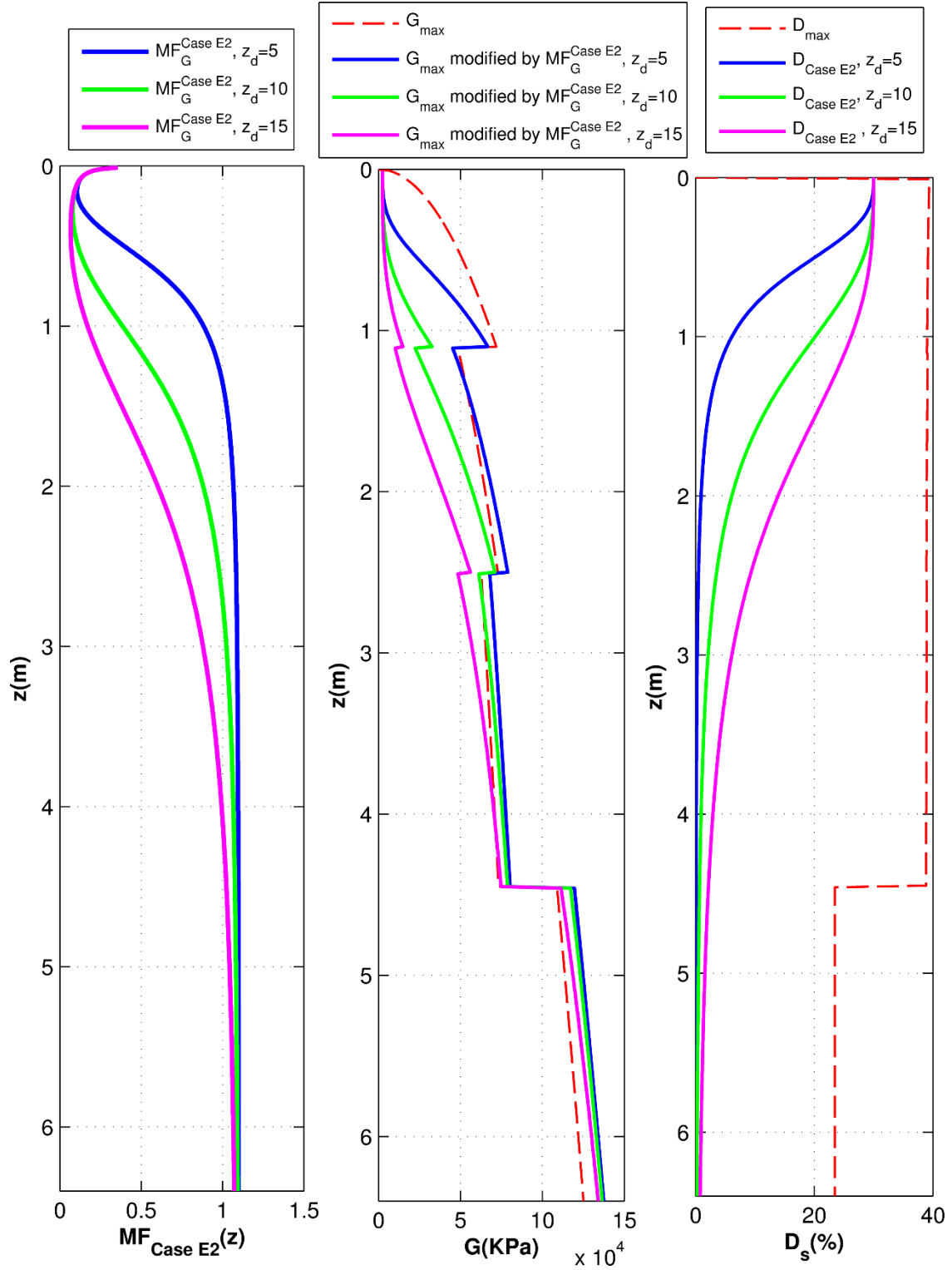


Figure 4-53- Shear modulus and damping profiles of Case E2 (Equation (4.8) and (4.9)) for different values of z_d .

4.4 Impedance Modification Factor (IMF) Approach

4.4.1 Overview

Any solution to the soil-pile interaction problem should consider the applicability of the solution to common engineering practice. Very complicated or time-consuming approaches are not typically practical for daily engineering work. To satisfy the need for simplified practical approaches, the method of Impedance Modification Factors (IMF) is examined in this study. As described in detailed in Pak & Ashlock (2000,2006) and Ashlock (2006), in the IMF method a set of real-valued and frequency-independent factors are defined for a known soil profile. These factors modify the original soil-pile impedances to provide the best possible match between theory and experiment. Using this method, the stiffness matrix in Equation (3.18) is modified to the following form;

$$\mathbf{K} = \begin{bmatrix} \alpha_{vv}k_{vv} & 0 & 0 \\ 0 & \alpha_{hh}k_{hh} & \alpha_{hm}k_{hm} \\ 0 & \alpha_{hm}k_{mh} & \alpha_{mm}k_{mm} \end{bmatrix} \quad (4.10)$$

In this study, the soil profiles of Hardin and Drnevich calculated for the actual strain profile (Case 18 in Table 4-3) with zero gapping length ($L_s=0$) were selected as the reference model for the analyses. It should be noted that the impedances of any other reasonably appropriate theoretical or computational model may be selected as the reference values. Figures 4-54 to 4-57 show a series of sensitivity investigations on how the IMFs affect the centroidal acceleration functions of the three modes of vibration. As expected, α_{vv} mainly changes the vertical mode of vibration and hardly affects the other modes, although there is some slight coupling with the rotational acceleration due to the asymmetry of the pile-cap-shaker assembly. On the other hand, the

remaining modification factors primarily affect the horizontal and rotational modes. While increasing α_{hh} and α_{mm} result in stiffer responses (higher peak frequencies), increasing α_{hm} tends to cause softer behavior.

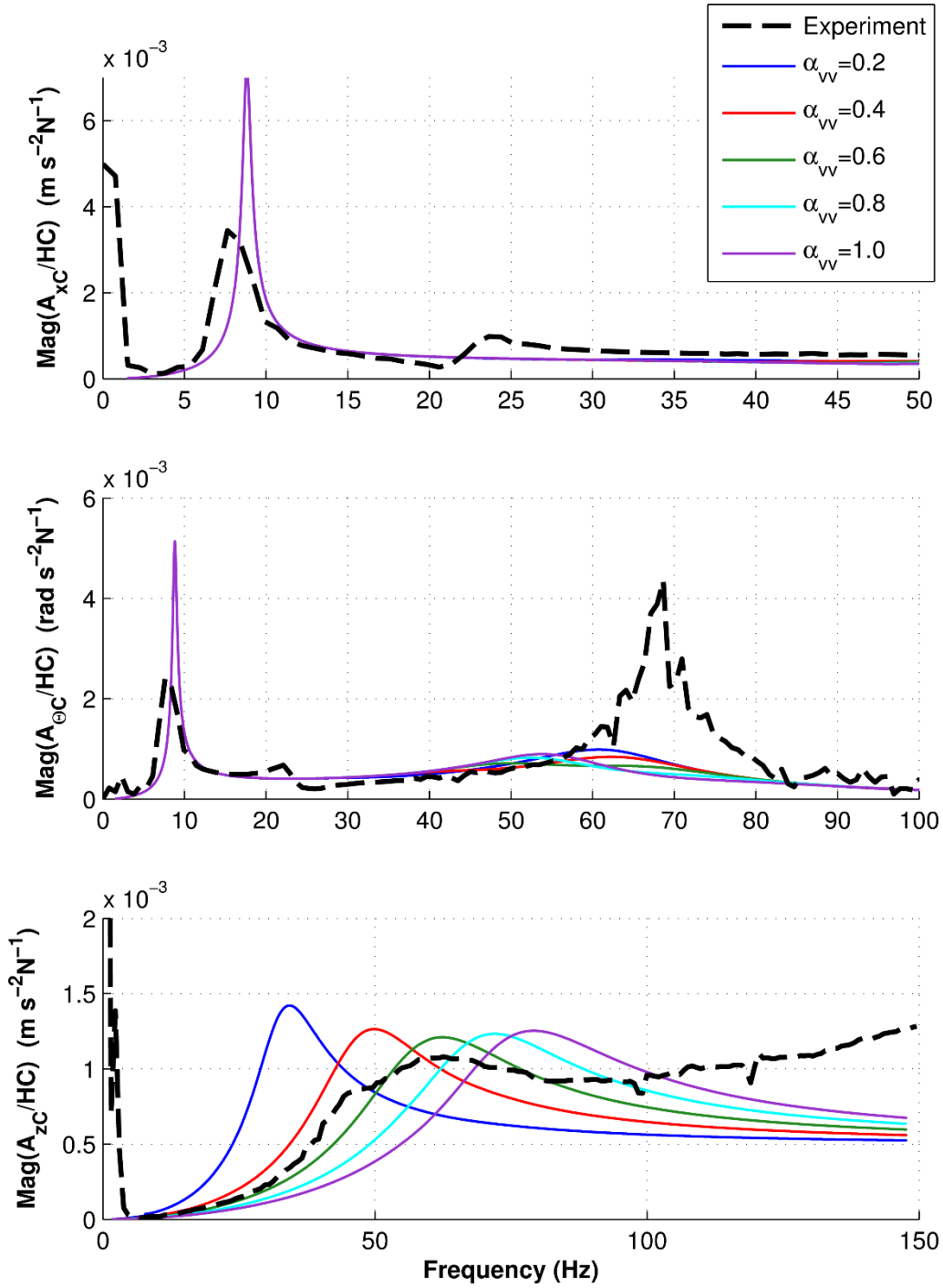


Figure 4-54- Sensitivity of centroidal acceleration functions to α_{vv} . Soil properties of Case 18 in Table 4-3 with $L_s = 0$ are used as the reference model. Experimental acceleration from Tests U-HC-R2 and U-VC-R2.

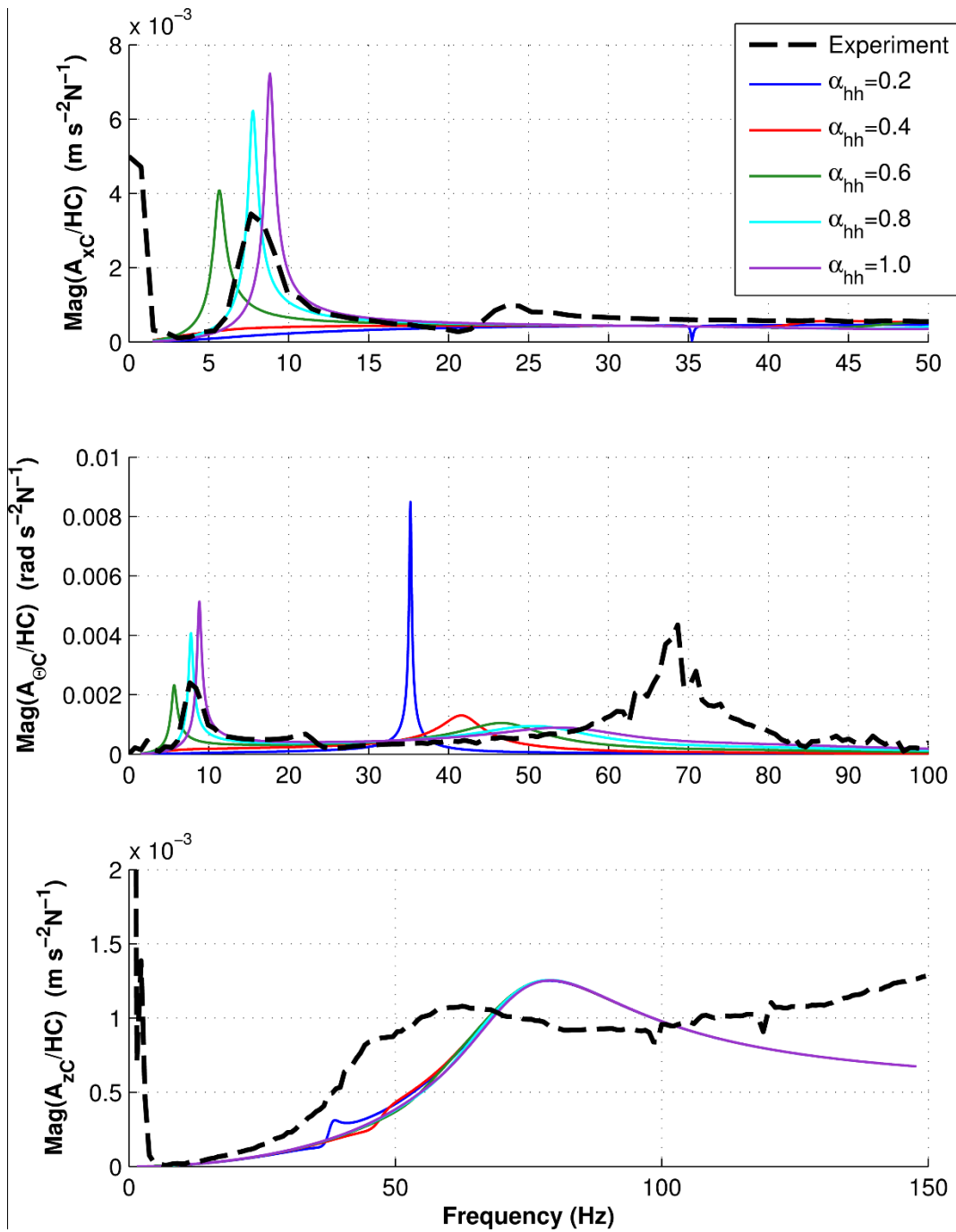


Figure 4-55- Sensitivity of centroidal acceleration functions to α_{hh} . Soil properties of Case 18 in Table 4-3 with $L_s = 0$ are used as the reference model. Experimental accelerances from Tests U-HC-R2 and U-VC-R2.

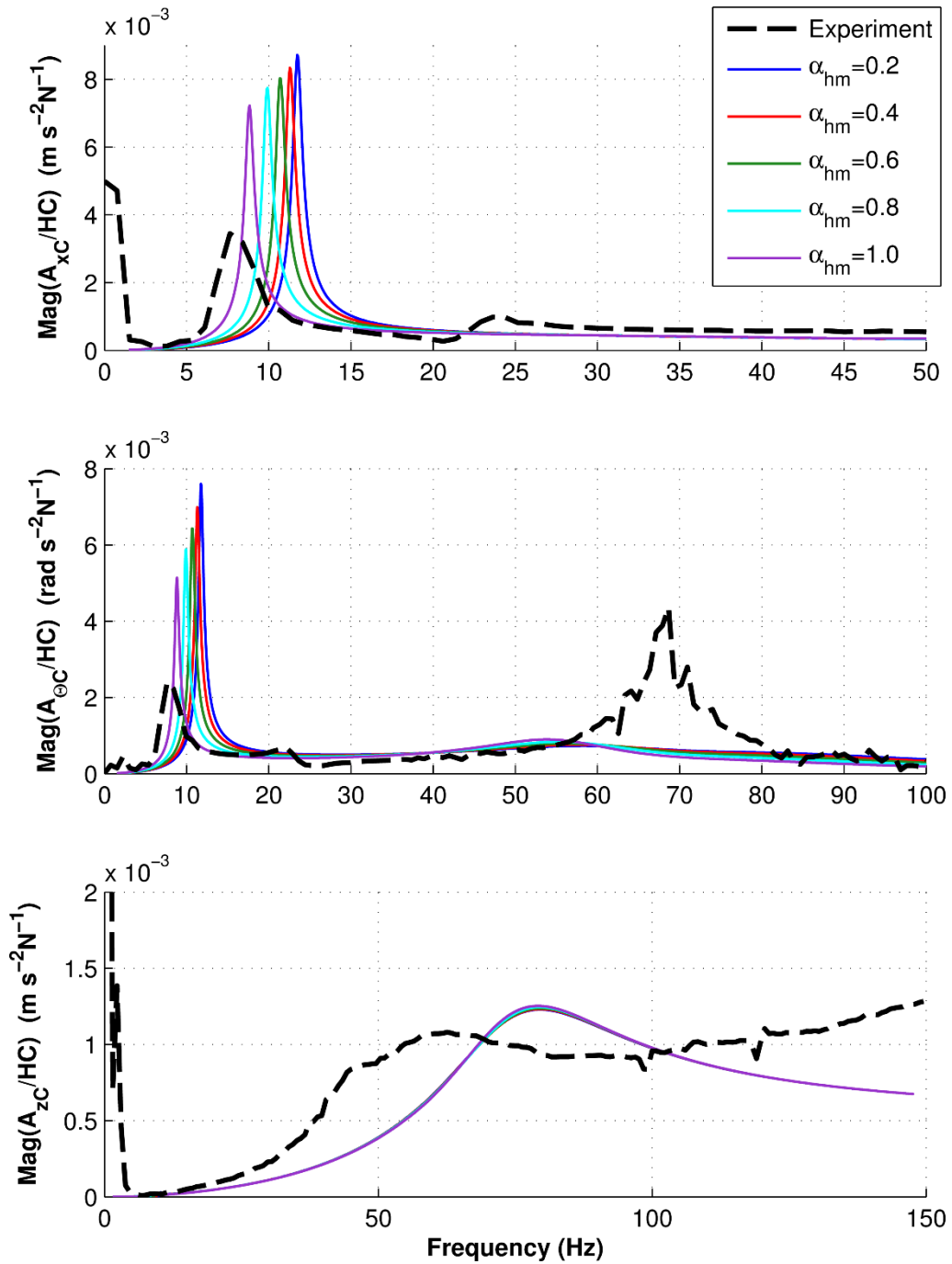


Figure 4-56- Sensitivity of centroidal acceleration functions to α_{hm} . Soil properties of Case 18 in Table 4-3 with $L_s = 0$ are used as the reference model. Experimental accelerances from Tests U-HC-R2 and U-VC-R2.

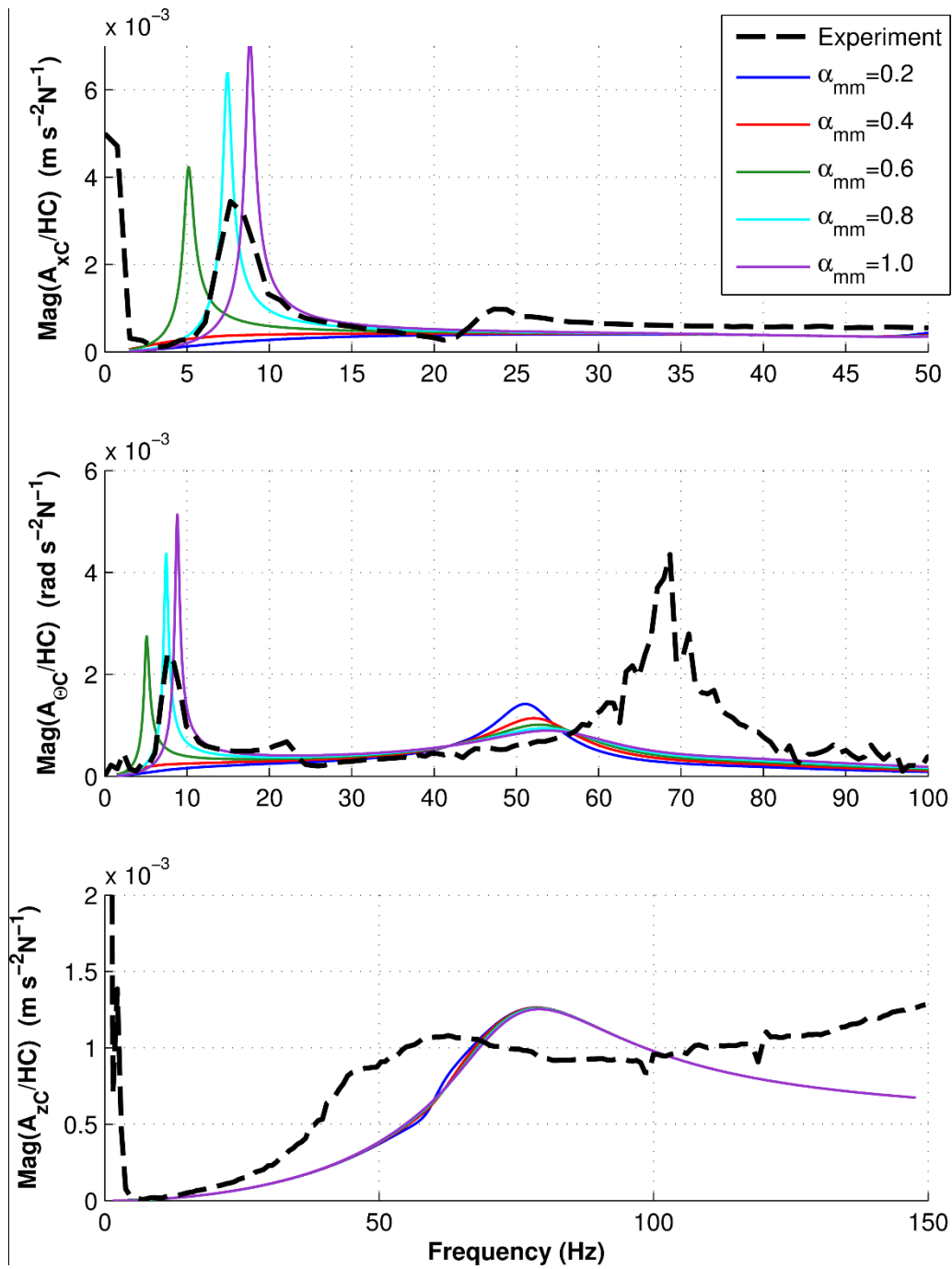


Figure 4-57- Sensitivity of acceleration functions to α_{mm} . Soil properties of Case 18 in Table 4-3 with $L_s = 0$ are used as the reference model. Experimental acceleration from Tests U-HC-R2 and U-VC-R2.

4.4.2 IMF results for tests in unimproved and improved soils

The best-fit accelerance functions obtained from a parametric study in which global error was minimized for a range of the IMFs for the piles in unimproved and improved soils are presented in Figures 4-58 to 4-60. The weighting parameters used in calculating the error function are also shown on the figures.

From the presented results it can be concluded that the experimental results of the pile in unimproved soil profile can be modeled reasonably well by the formulations presented in this study using the soil properties of Case 18 in Table 4-3 and the following set of IMFs:

$$\alpha_{vv} = 0.61, \quad \alpha_{hh} = 0.98, \quad \alpha_{hm} = 0.82, \quad \alpha_{mm} = 0.70 \quad (4.11)$$

These values of IMFs are reasonable and of a similar range to those reported in Pak & Ashlock (2006). They capture the fundamental horizontal and rocking peaks, and do a fair job of capturing the vertical response. However, they do not capture the previously discussed spurious rotational peak near 70 Hz or the high-frequency vertical which diverges from the theory above 70 Hz. These behaviors are believed to be due to resonance of the shaker's base frame as discussed previously. Considering the results of the test with random excitation over the smaller 250 Hz frequency bandwidth (Figure 2-38), which have greater frequency resolution than the 1000 Hz tests presented thus far, one can see an even better match with the IMF results in the low-frequency region in Figures 4-58 to 4-60.

On the other hand, the IMF's ability to capture the experimental behavior for the pile in improved soil is not as good, as shown in Figures 4-61 to 4-63. The IMF method is very dependent on the reference profile used and thus, with the current models this method cannot improve the

prediction any further. As shown in the figures, the best possible match between modified theoretical results and experimental results is obtained with the following IMFs:

$$\alpha_{vv} = 1.77, \quad \alpha_{hh} = 0.33, \quad \alpha_{hm} = 0.26, \quad \alpha_{mm} = 0.72 \quad (4.12)$$

The vertical IMF greater than 1 is consistent with the increased stiffness of the improved soil zone, but a better reference model which is closer to the actual soil conditions is necessary for an improved fit.

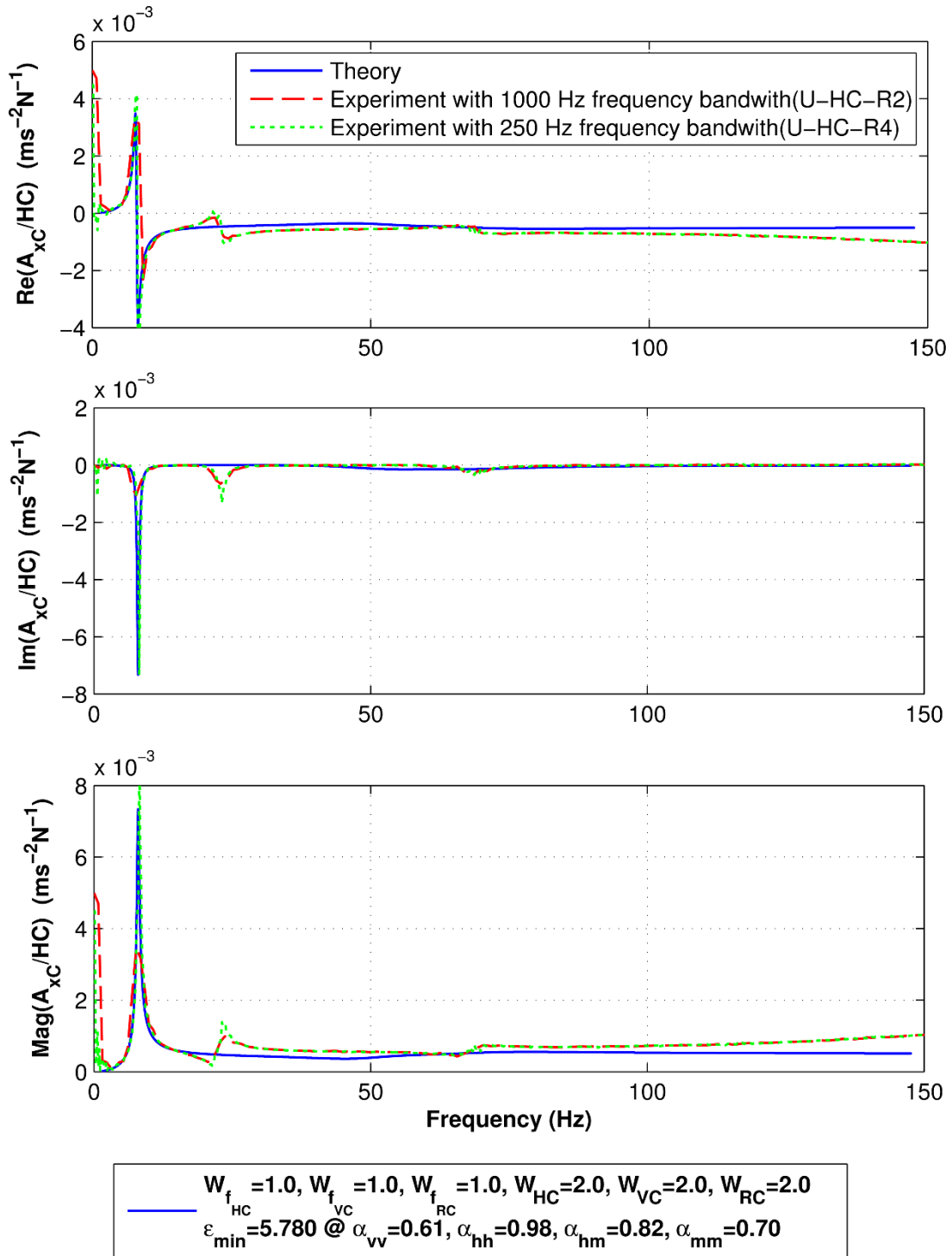


Figure 4-58- Best-fit horizontal centroidal accelerance for IMF approach using the shown weighting parameters. Soil properties of Case 18 in Table 4-3 with $L_s = 0$ are used as the reference model.

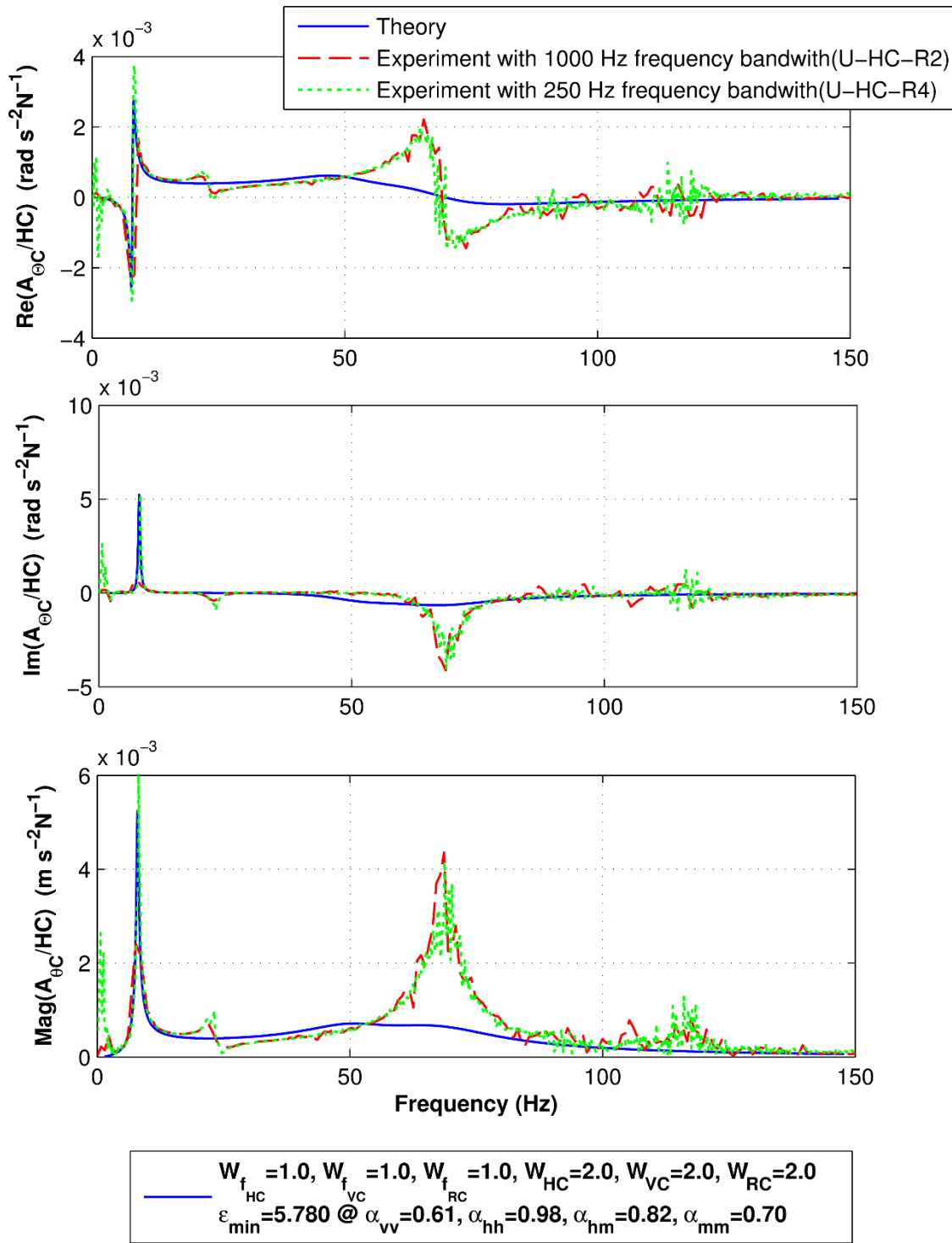


Figure 4-59- Best-fit rotational centroidal acceleration for IMF approach using the shown weighting parameters. Soil properties of Case 18 in Table 4-3 with $L_s = 0$ are used as the reference model.

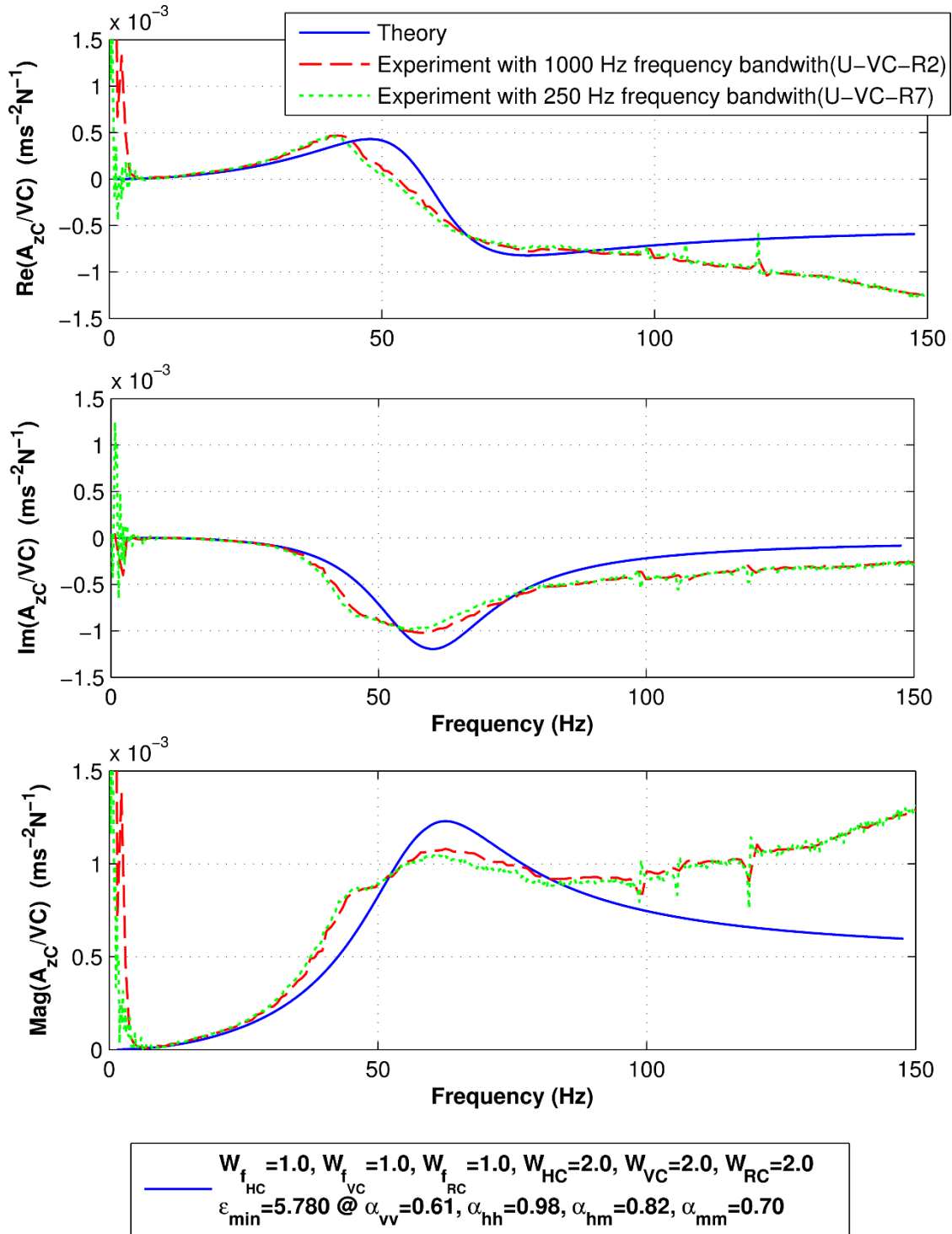


Figure 4-60- Best-fit vertical centroidal acceleration for the IMF approach using the shown weighting parameters. Soil properties of Case 18 in Table 4-3 with $L_s = 0$ are used as the reference model.

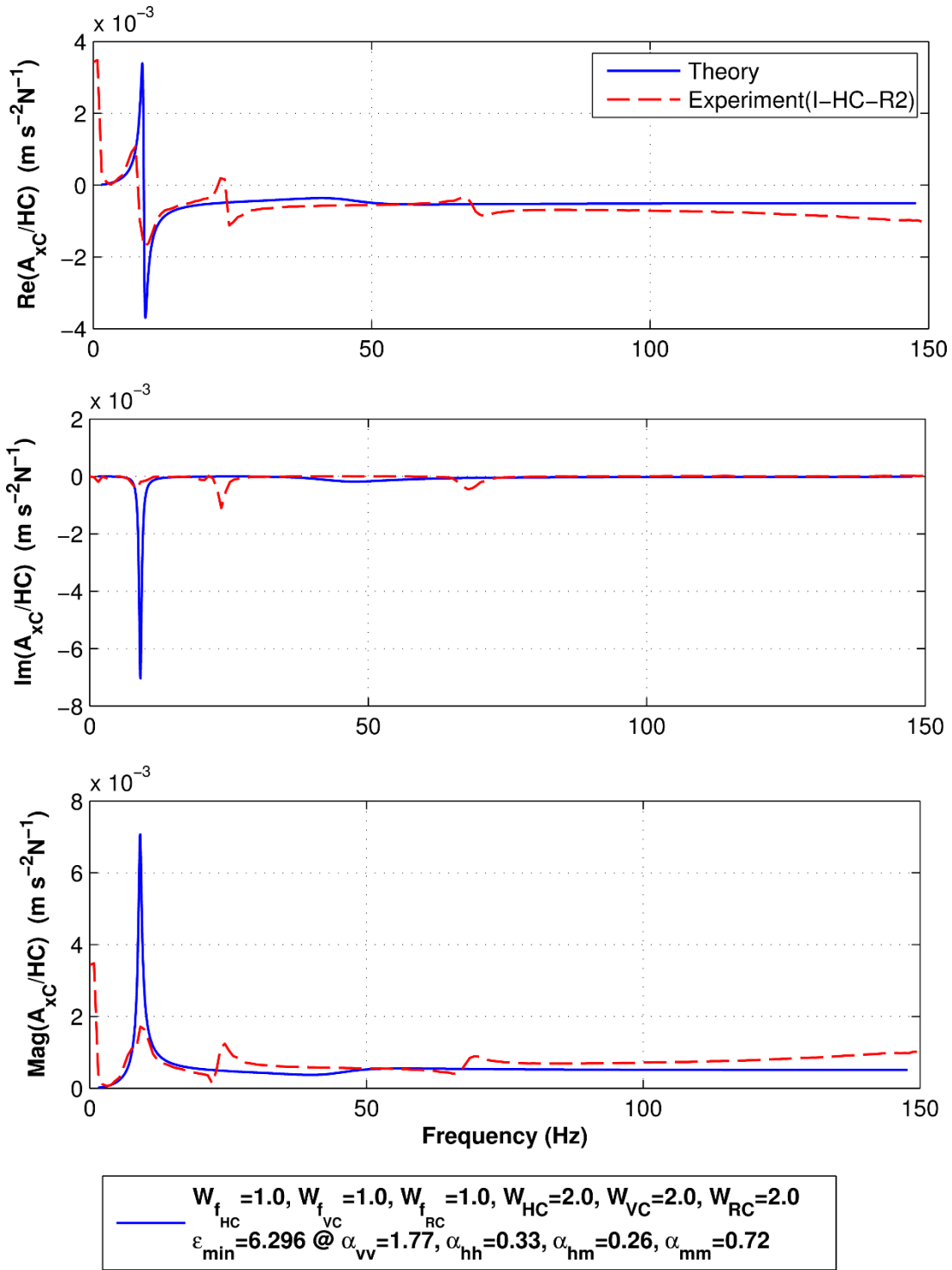


Figure 4-61- Best-fit horizontal centroidal accelerance for the IMF approach using the shown weighting parameters. Soil properties of Case 18 in Table 4-3 with $L_s = 0$ are used as the reference model.

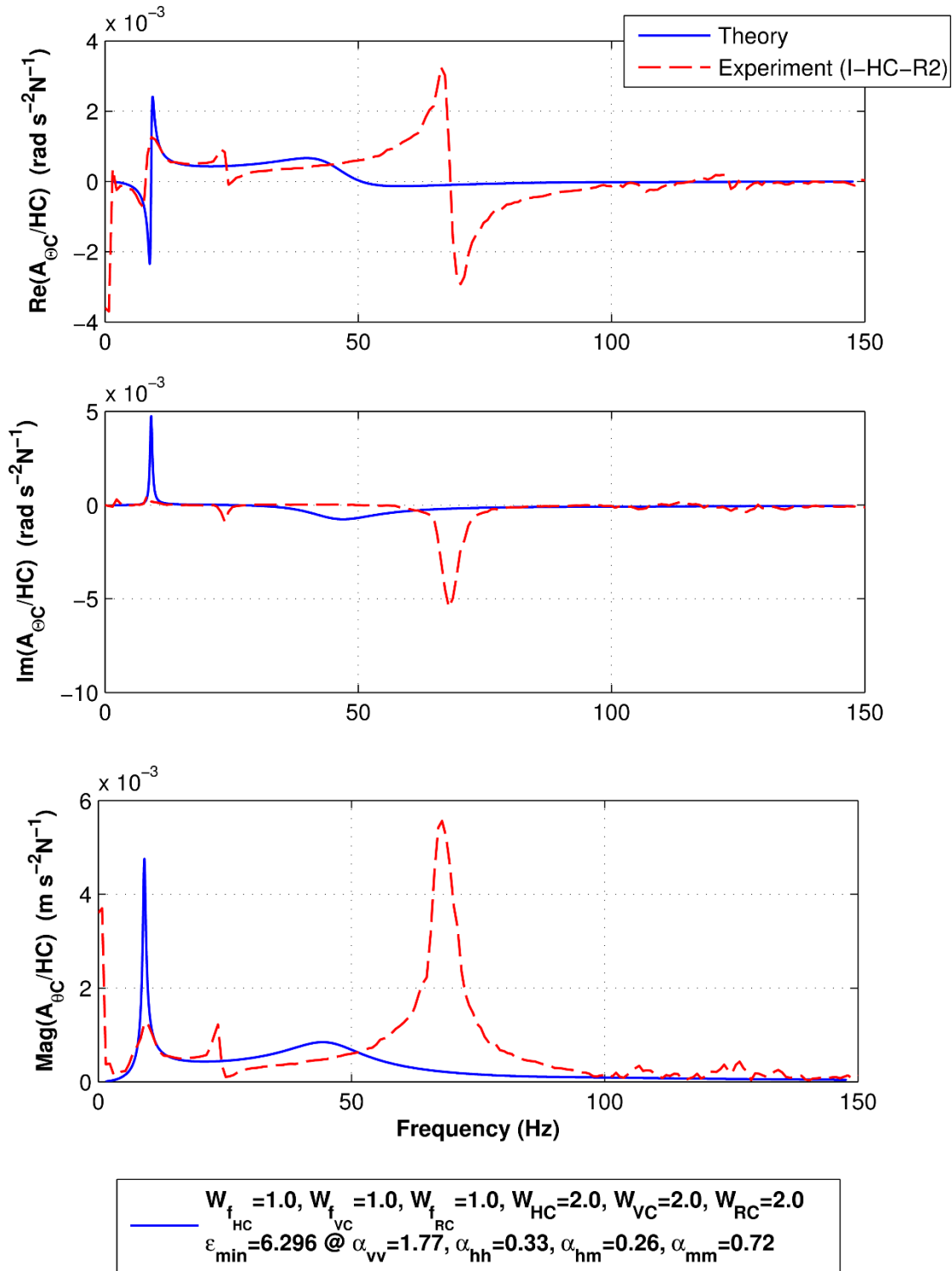
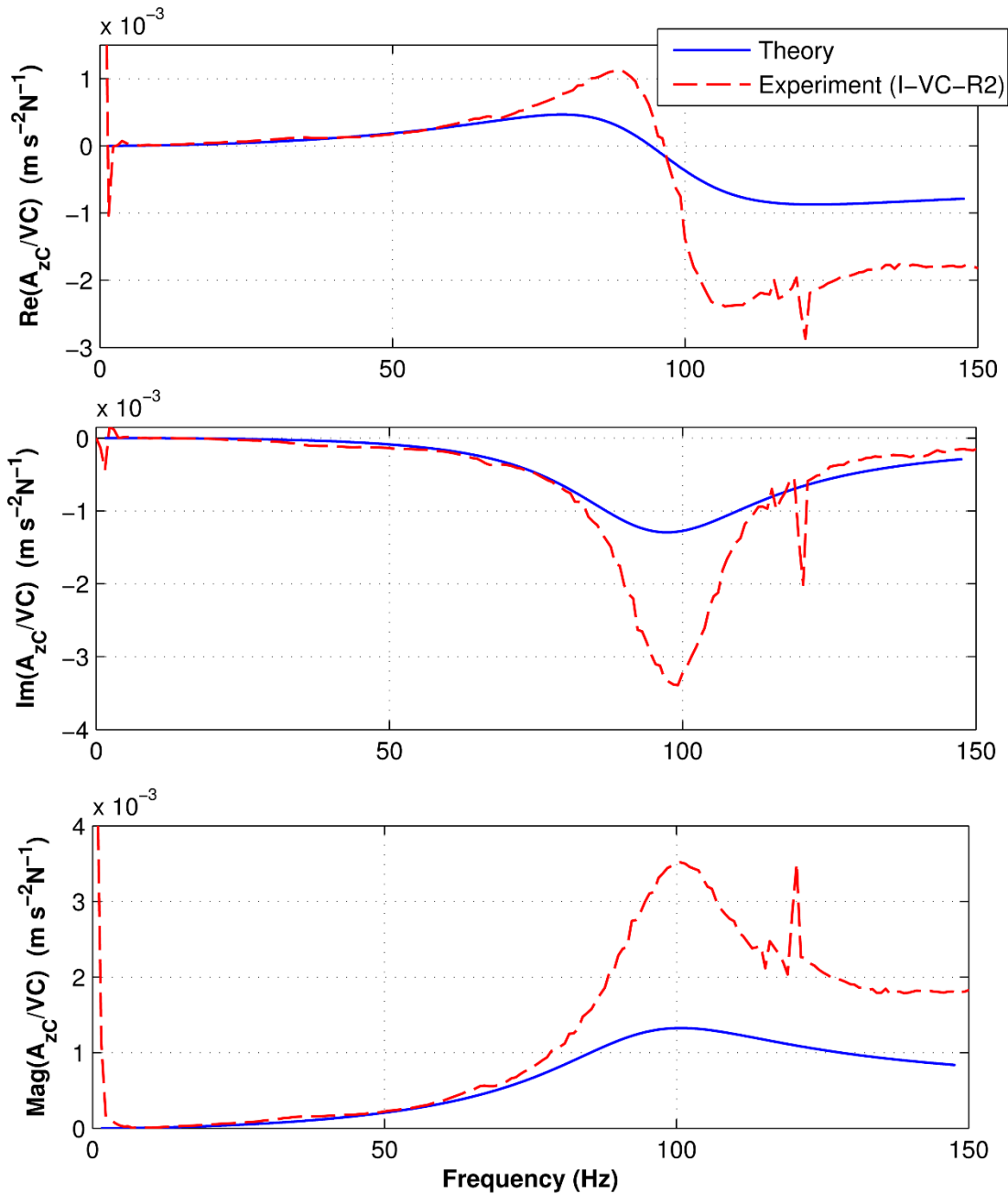


Figure 4-62- Best-fit rotational centroidal accelerance for the IMF approach using the shown weighting parameters. Soil properties of Case 18 in Table 4-3 with $L_s = 0$ are used as the reference model.



$W_{f_{HC}}=1.0, W_{f_{VC}}=1.0, W_{f_{RC}}=1.0, W_{HC}=2.0, W_{VC}=2.0, W_{RC}=2.0$
 $\epsilon_{min}=6.296 @ \alpha_{vv}=1.77, \alpha_{hh}=0.33, \alpha_{hm}=0.26, \alpha_{mm}=0.72$

Figure 4-63- Best-fit vertical centroidal acceleration for the IMF approach using the shown weighting parameters. Soil properties of Case 18 in Table 4-3 with $L_s = 0$ are used as the reference model.

4.4.3 Insights from IMF method

One of the advantages of using the IMF method is the insight that it provides into the behavior of the theoretical model and the effects of its parameters on the impedances. One can apply this knowledge along with the previously presented results on the impedance function variations for the examined shear modulus and damping profiles and gapping depths, to provide guidance towards a rational model that will produce an improved match to the experiments.

For example, Figures 4-64 to 4-67 clearly show that the horizontal accelerance functions are primarily dependent upon the properties of the top soil layers up to a depth of 2.5 m, while the vertical impedance is sensitive to soil properties along the entire depth. Knowing this, and also the values of the IMF-adjusted impedance functions that create the best match, one can modify the soil profile depth-wise to achieve impedances similar to those resulting from the IMF method.

This procedure was examined by scaling the shear modulus and damping profiles of Case 18 in Table 4-3 by different scaling factors for depths greater than 2.5 m (Figure 4-68). As expected, the resulting impedance functions corresponding to these modified soil profiles show negligible changes in horizontal, rocking, and coupling modes, while the vertical impedances change significantly (Figure 4-69). However, the resulting modulus profiles are not physically reasonable, and as the real part of k_{vv} decreases, its imaginary part increases greatly, which introduces a large amount of damping into the system. This unexpected phenomenon prevents the vertical accelerance peak from matching that of the IMF method, despite the horizontal and rotational accelerance functions being relatively unaffected, as shown in Figures 4-70 to 4-72.

For the problem under study, Figure 4-73 indicates that the impedances are not very sensitive to the bedrock modulus even for the vertical mode (with the exception of the very low-

frequency and static stiffness), which means that the pile essentially behaves as a floating pile under dynamic loading. However, it should be noted that if the soil modulus below a certain depth is reduced as described above and shown in Figure 4-68, the floating pile behavior will change towards a fixed-point condition, as load will be redistributed towards the pile tip. In this case, the rigidity of the bedrock is expected to have a significant effect on the vertical impedance, and should be considered in the calibration analyses. Due to the time constraints, however, this scenario was not investigated in this study.

Finally, it should be noted that scaling the entire soil modulus and damping profiles at all depths (including bedrock) by a the same constant will simply change the values of the impedance functions proportionally as confirmed in Figure 4-74, as BEASSI uses a linear elasto-dynamic solution. For such cases, only one BEASSI analysis is needed, and the other solutions can be obtained by interpreting the output using a different value of the reference modulus, G_{ref} .

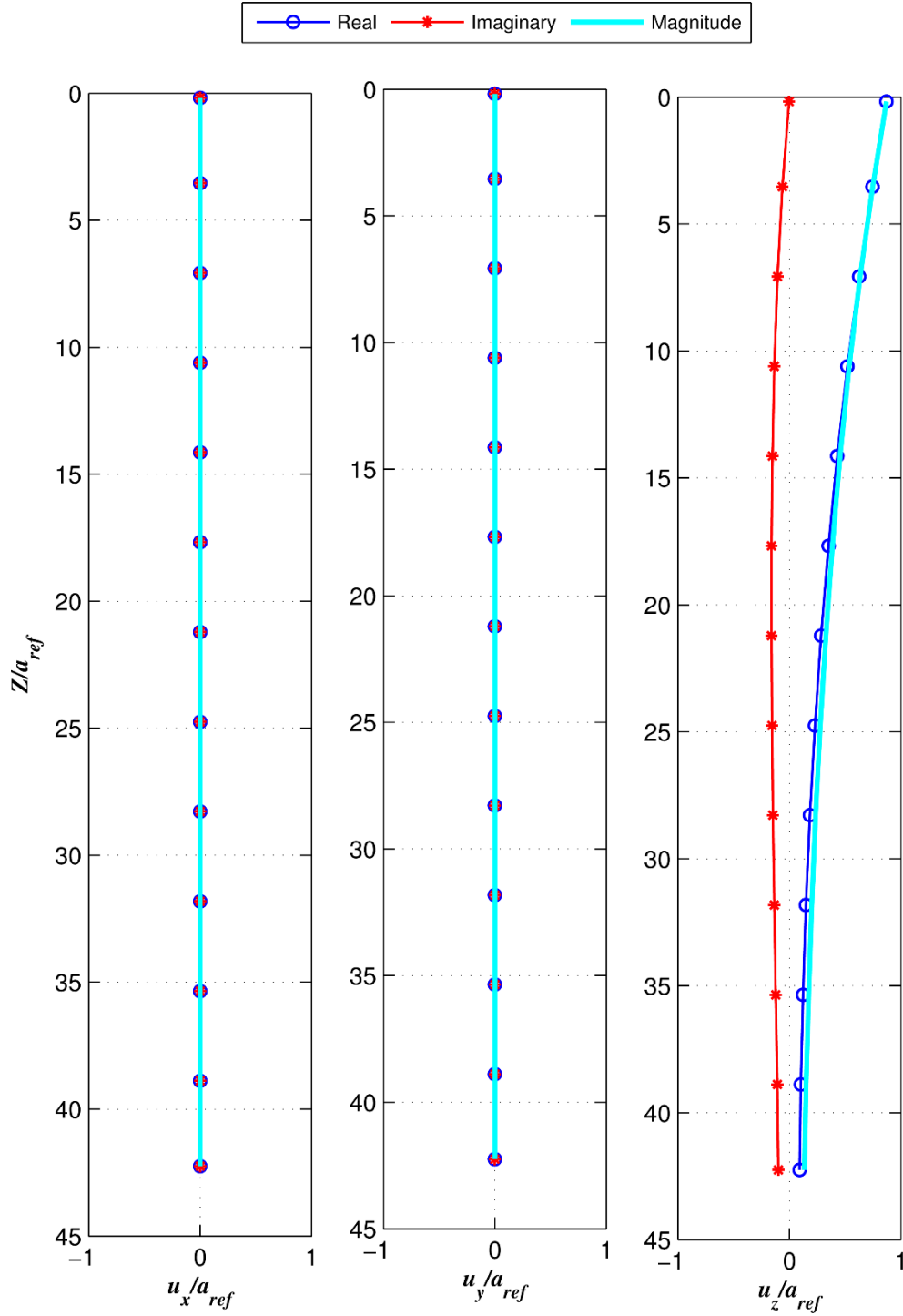


Figure 4-64-. u_x/a_{ref} , u_y/a_{ref} and u_z/a_{ref} displacement profiles due to a unit vertical displacement at the ground level in z -direction for $f=75$ Hz and soil profiles similar to Case 16 in Table 4-3 ($L_s=0$, $a_{ref}=0.127$ m).

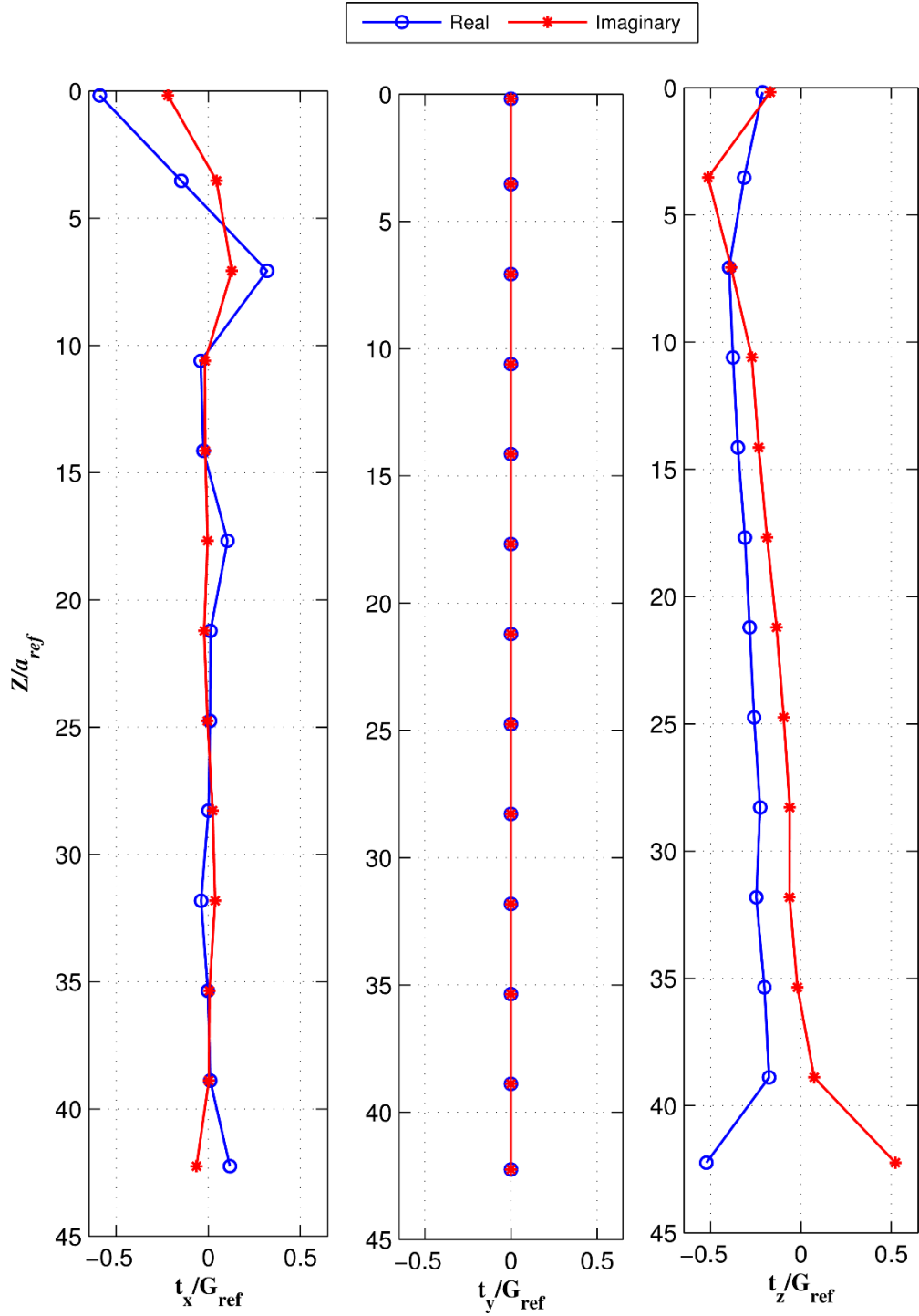


Figure 4-65- t_x/G_{ref} , t_y/G_{ref} and t_z/G_{ref} traction profiles due to a unit vertical displacement at the ground level in z -direction for $f=75$ Hz and soil profiles similar to Case 16 in Table 4-3 ($L_s=0$, $a_{ref}=0.127$ m, $G_{ref}= 27.76$ MPa).

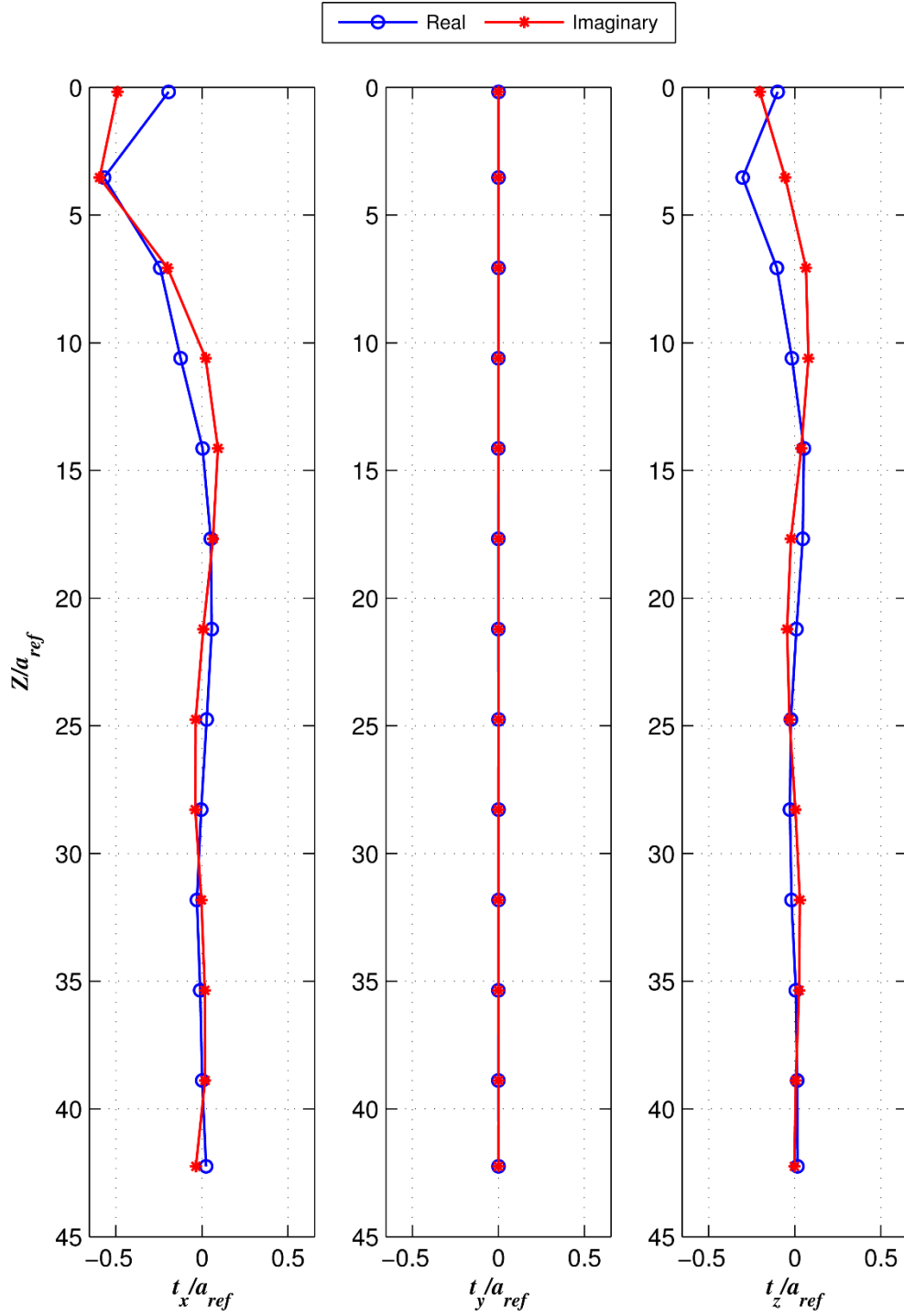


Figure 4-66-- t_x/G_{ref} , t_y/G_{ref} and t_z/G_{ref} traction profiles due to a unit horizontal displacement at the ground level in z -direction for $f=75$ Hz and soil profiles similar to Case 16 in Table 4-3 ($L_s=0$, $a_{ref}=0.127$ m, $G_{ref}= 27.76$ MPa).

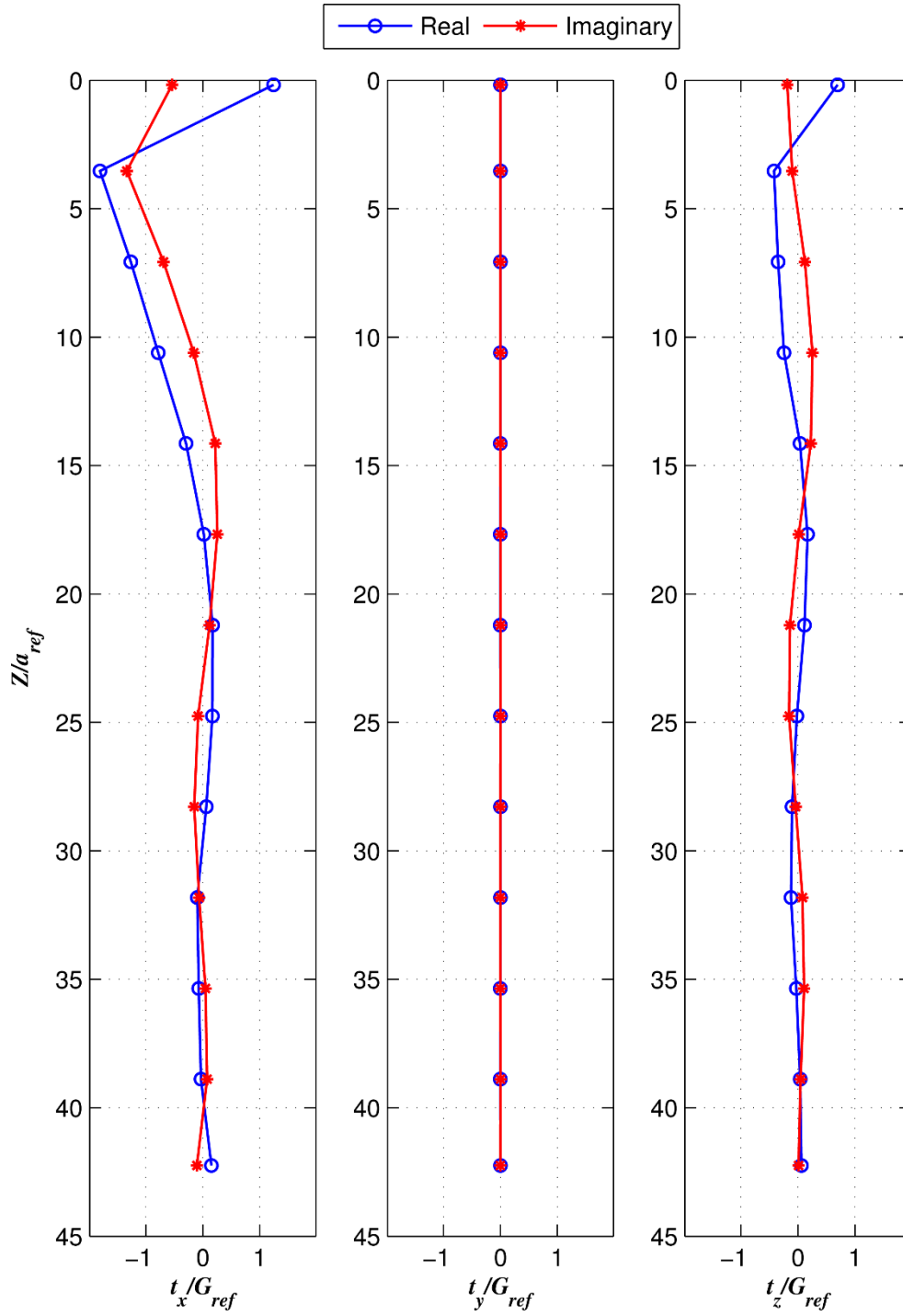


Figure 4-67- t_x/G_{ref} , t_y/G_{ref} and t_z/G_{ref} traction profiles due to a unit rotational displacement at the ground level in z -direction for $f=75$ Hz and soil profiles similar to Case 16 in Table 4-3 ($L_s=0$, $a_{ref}=0.127$ m, $G_{ref}=27.76$ MPa).

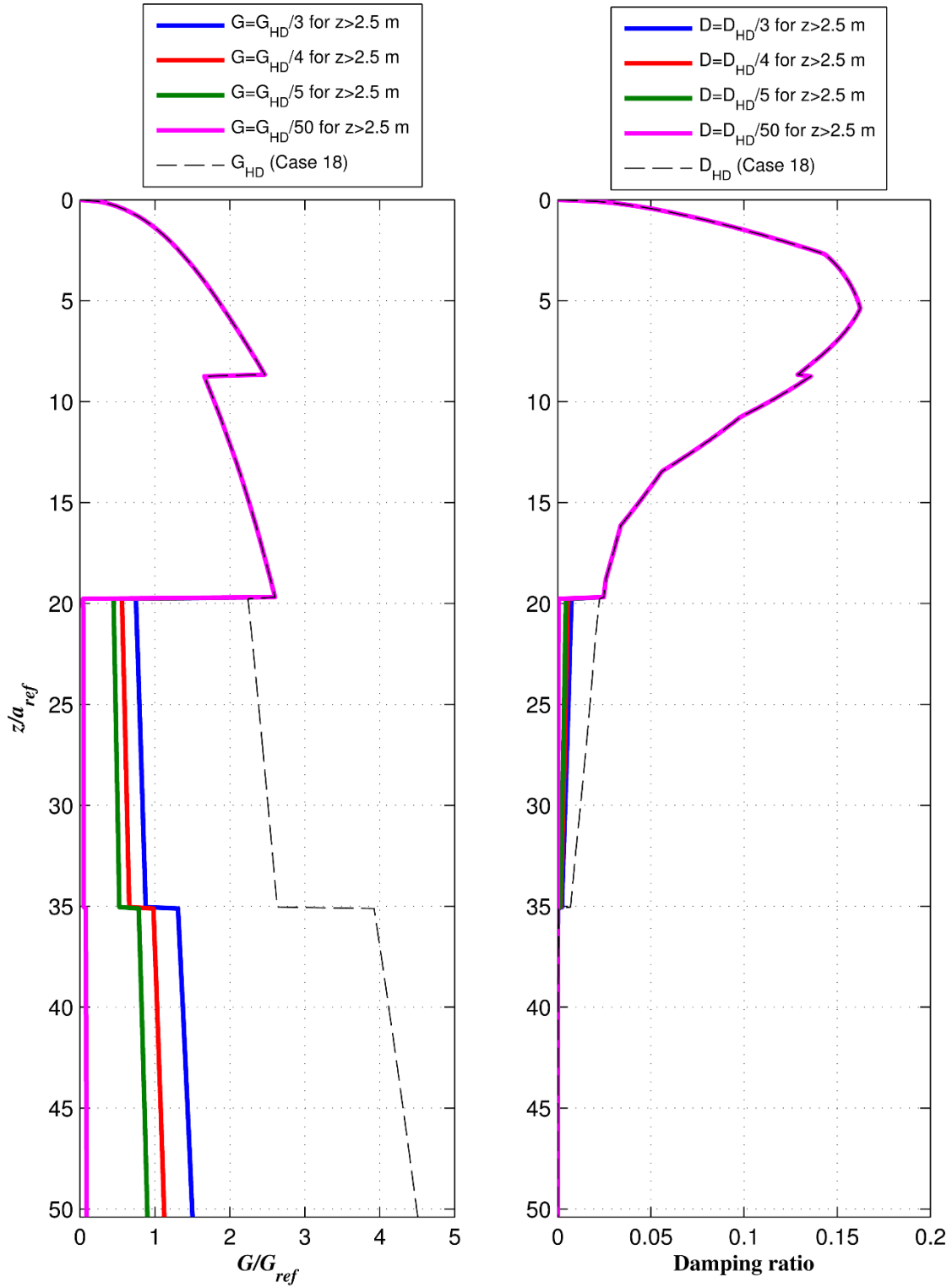


Figure 4-68-Modified shear modulus and damping profiles resulting from scaling the soil profiles of Case 18 in Table 4-3 by different scale factors for depths greater than 2.5 m. Note: the bedrock modulus is unchanged.

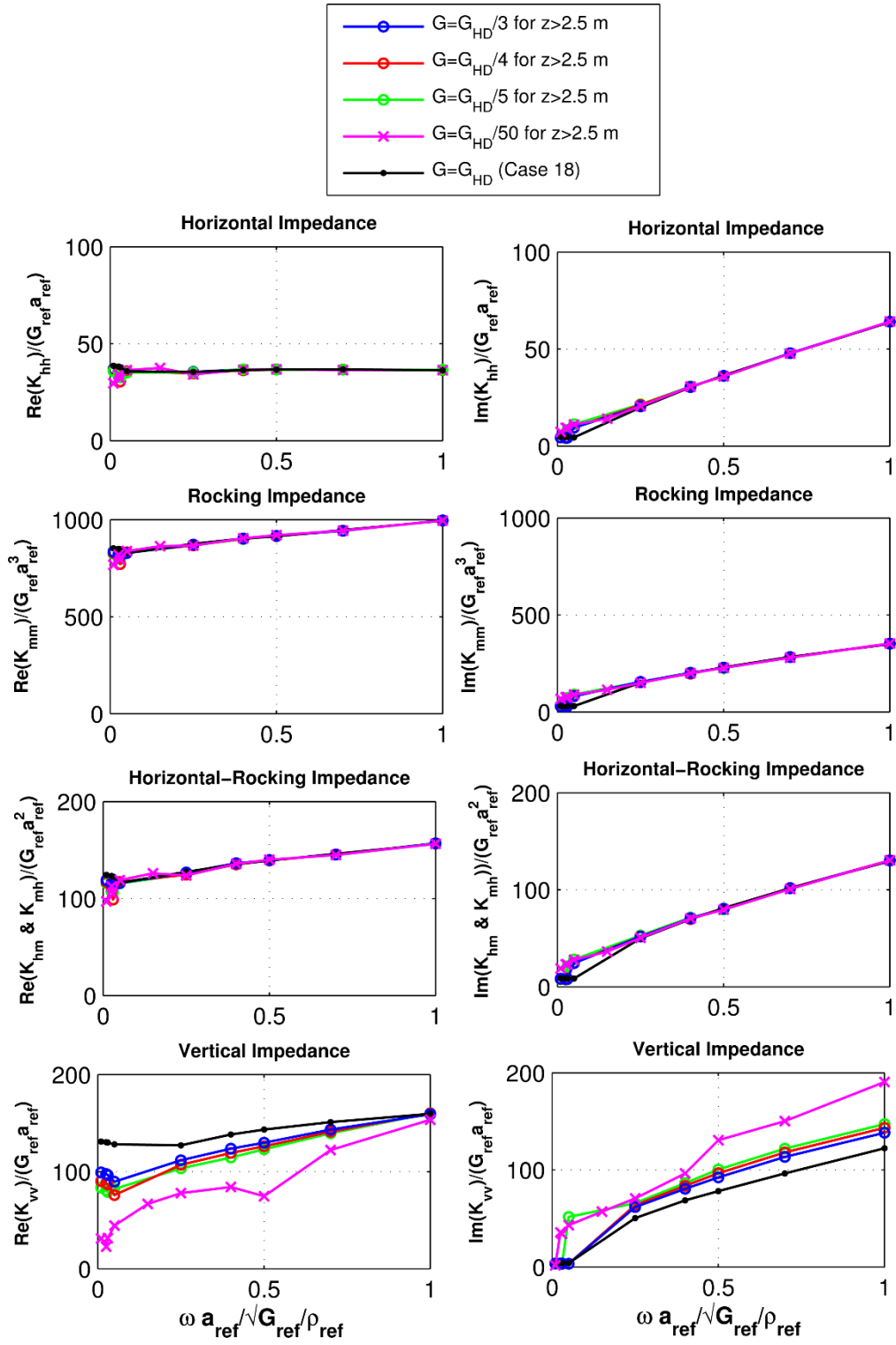


Figure 4-69-Impedance functions corresponding to soil profiles presented in Figure 4-68.

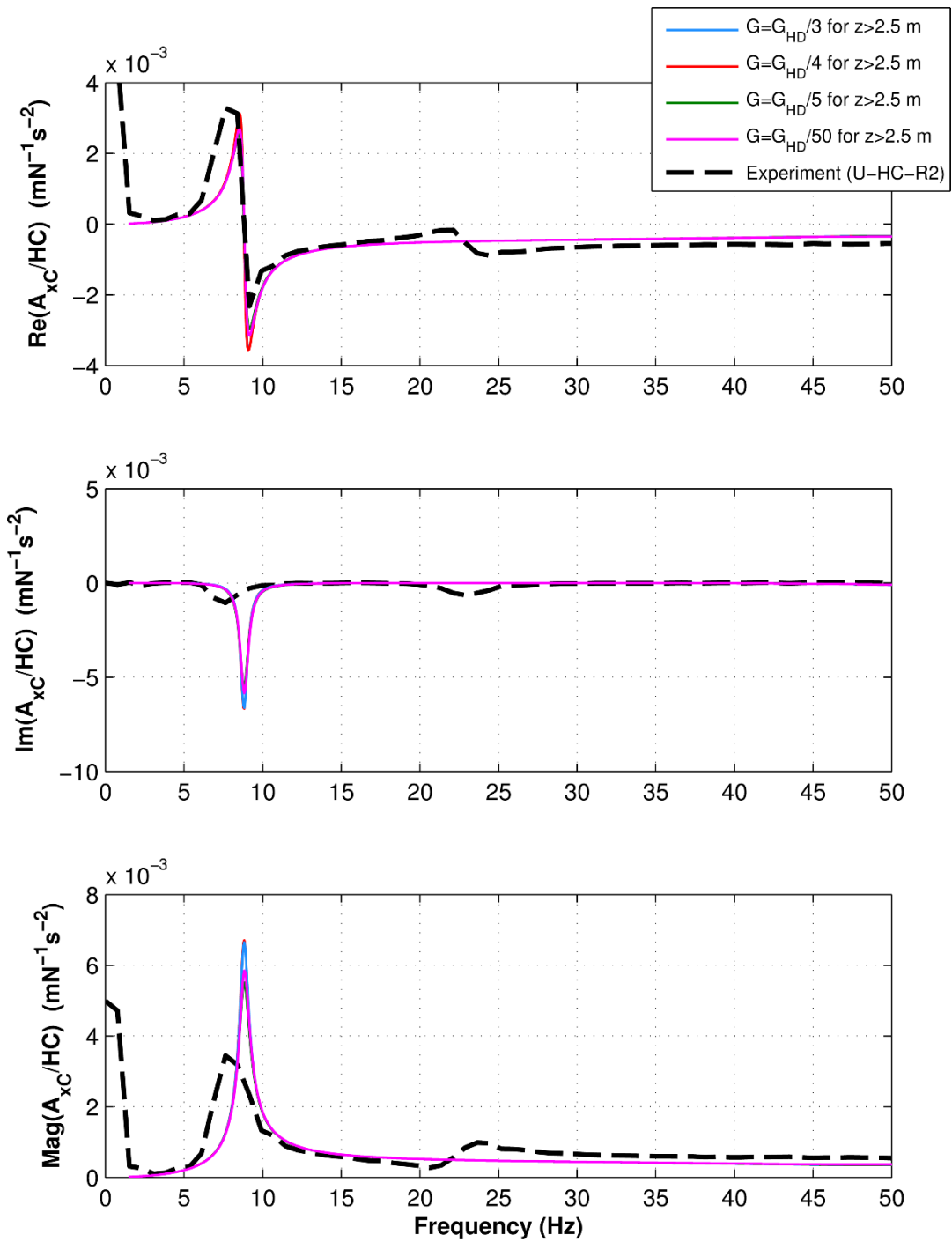


Figure 4-70- Effect of soil profile modifications shown in Figure 4-68 on A_{x_c}/HC acceleration.

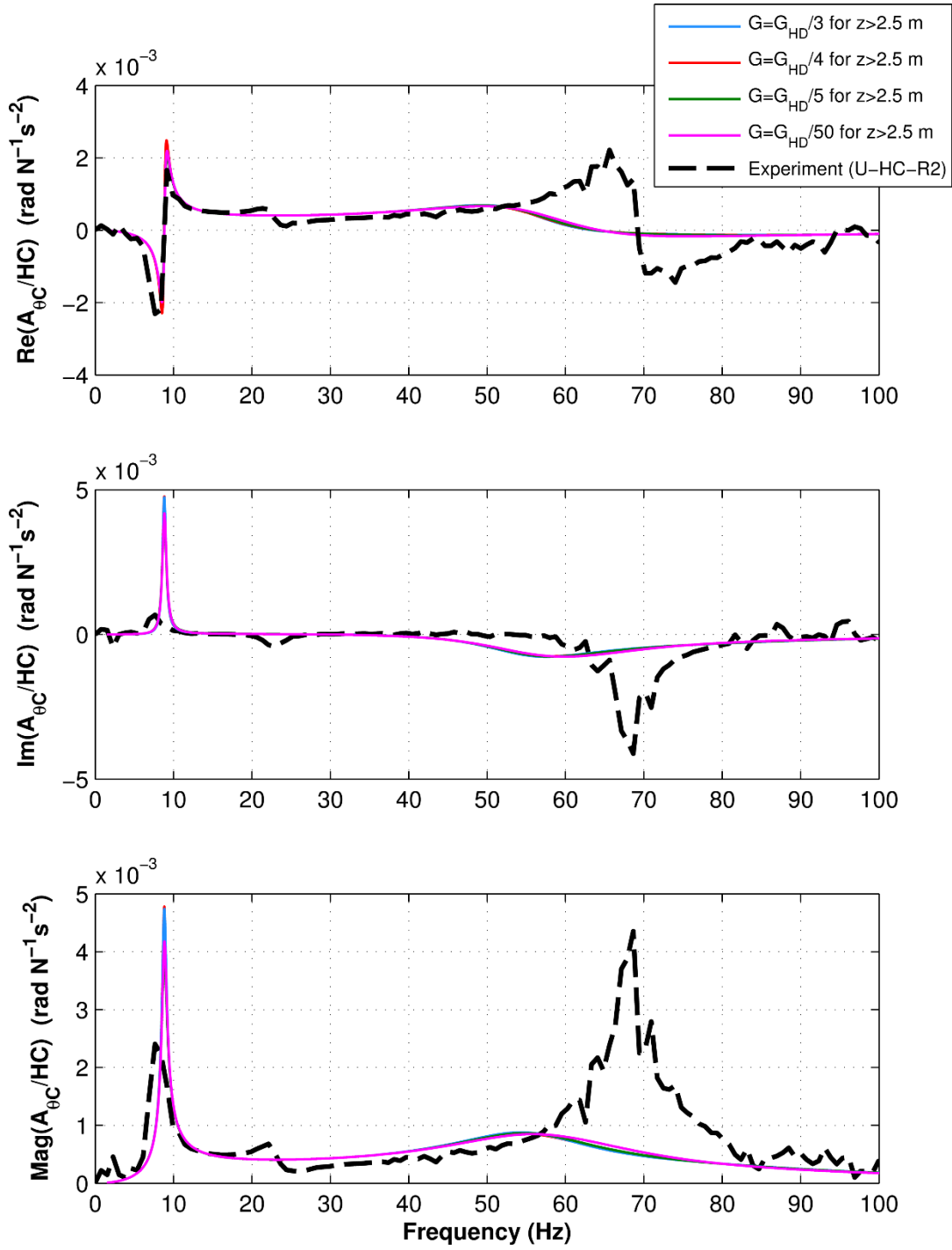


Figure 4-71- Effect of soil profile modifications shown in Figure 4-68 on $A_{\theta C}/HC$ acceleration.

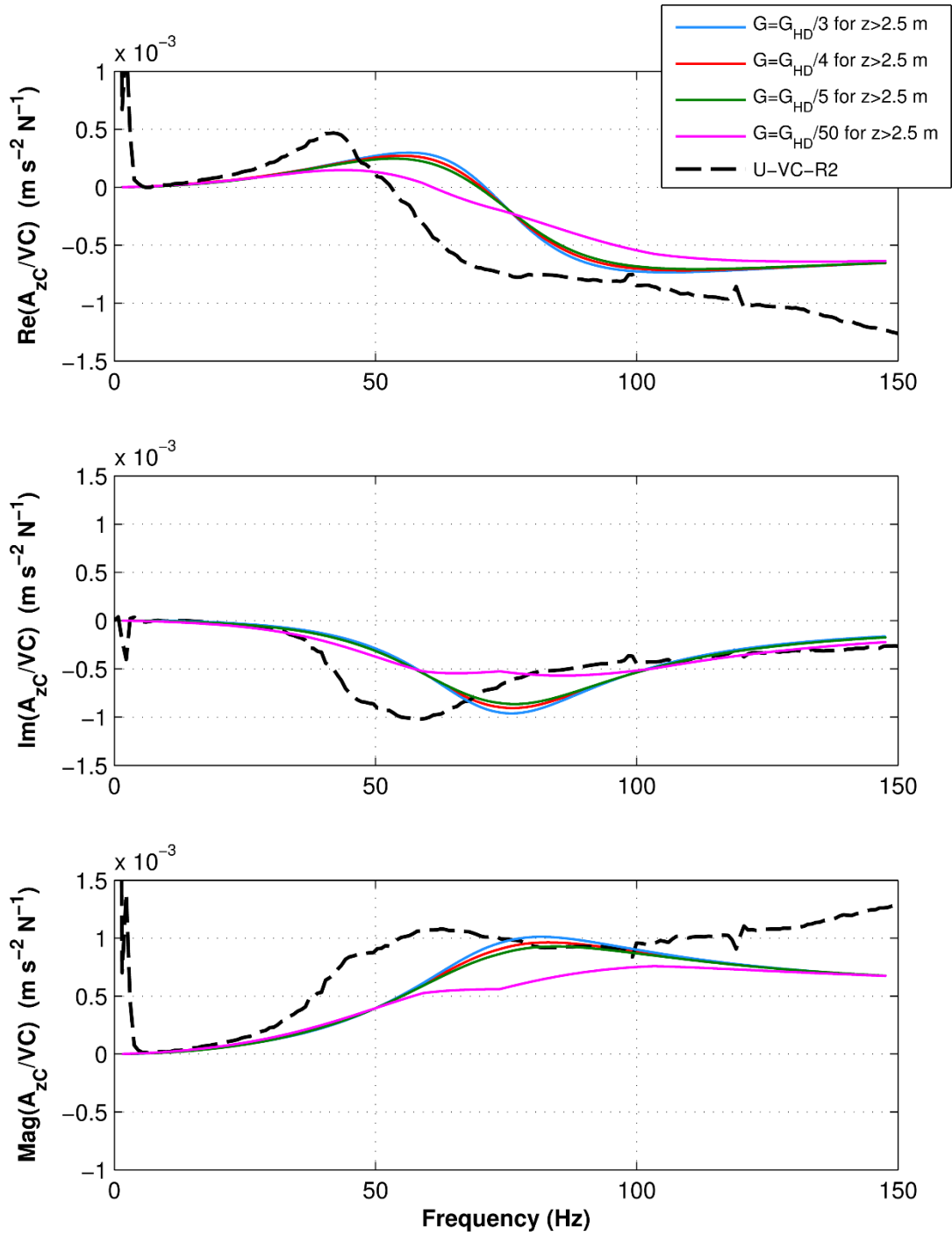


Figure 4-72-Effect of soil profile modifications shown in Figure 4-68 on A_{zC}/VC acceleration.

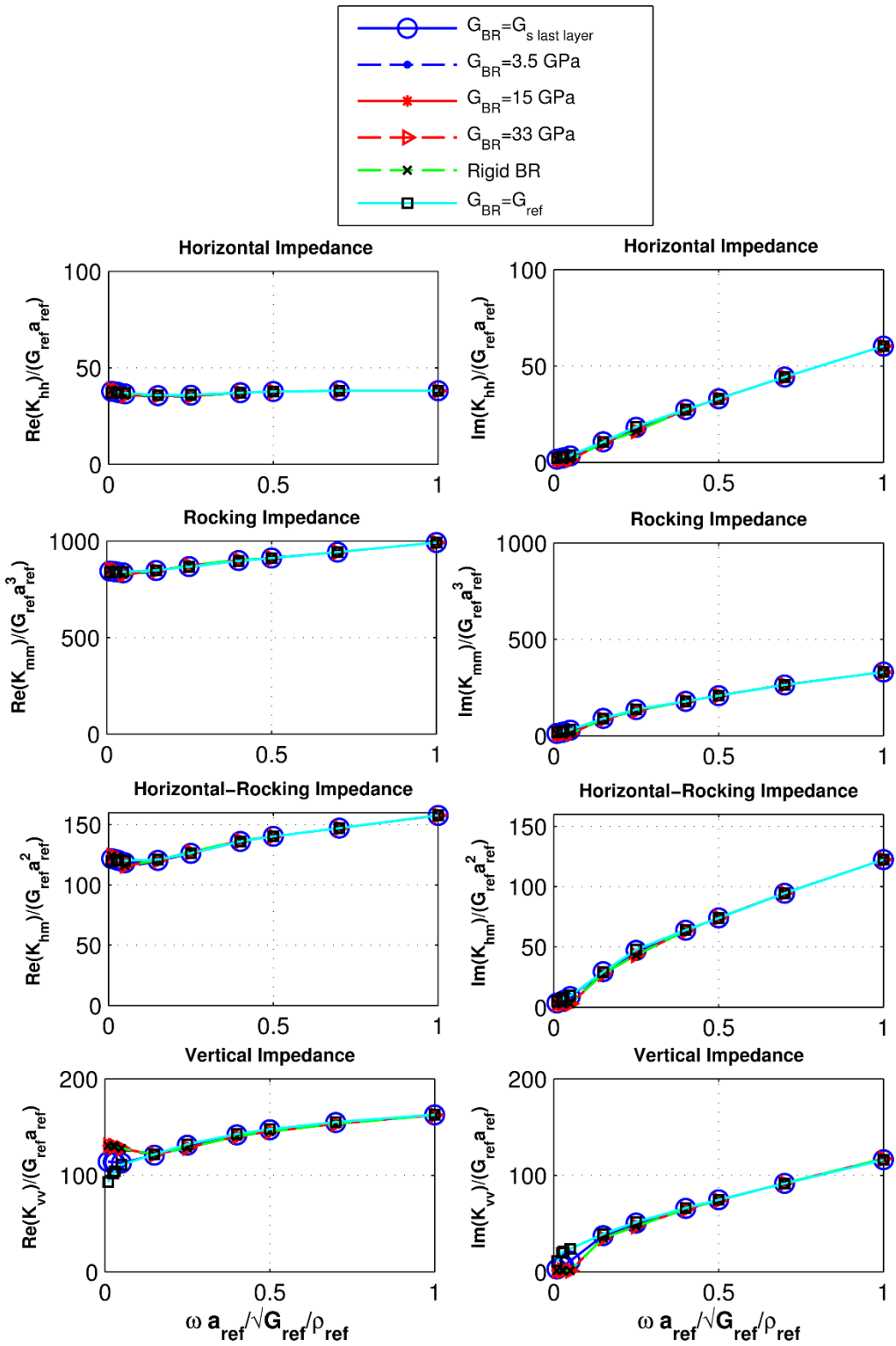


Figure 4-73- Insensitivity of impedances to bedrock modulus for Case 16 with $L_s=0$.

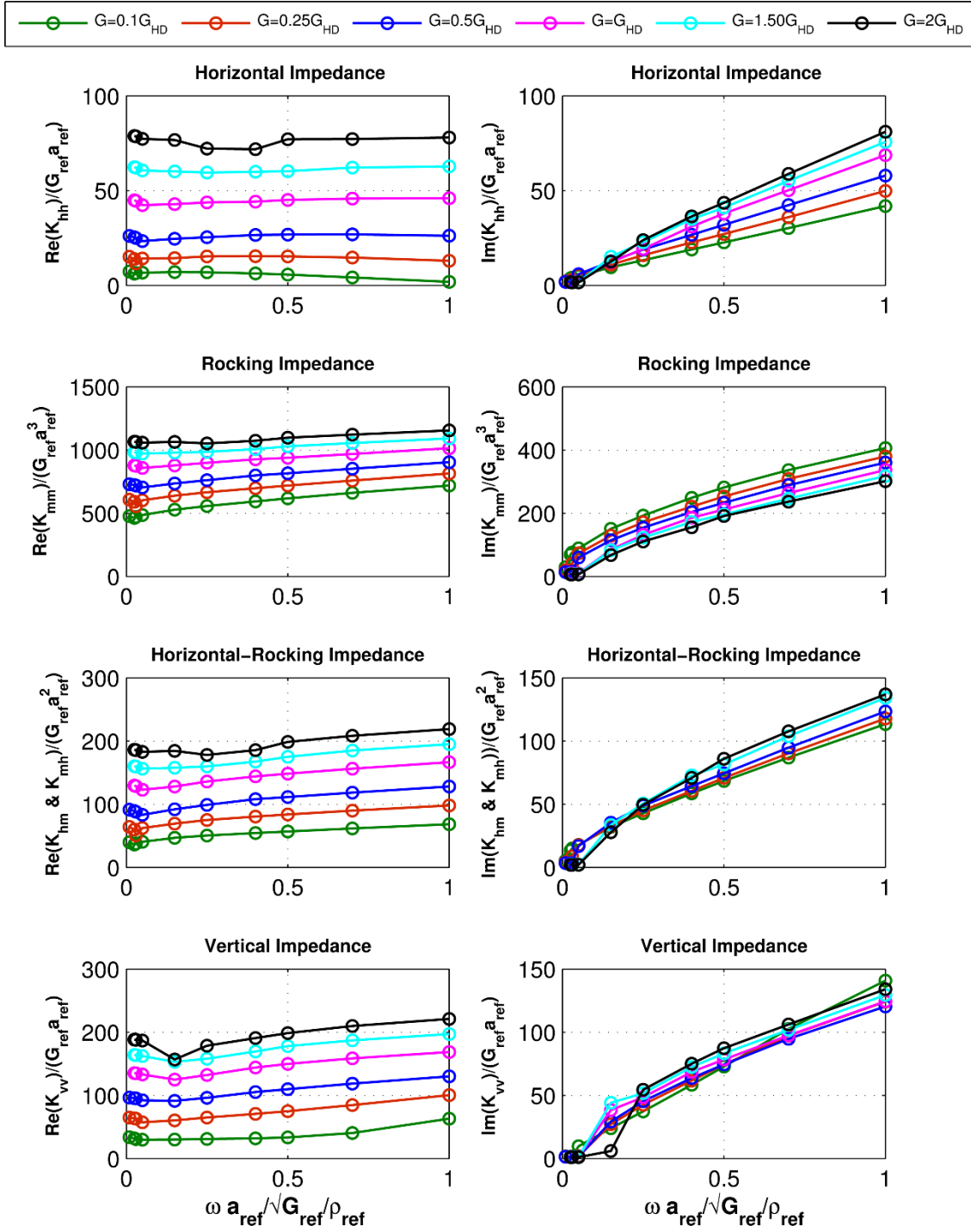


Figure 4-74-Verification of linear change in impedances when soil modulus profile is scaled by a constant for $L_s=25$ cm and $D_s=5\%$.

4.5 Three-Domain Disturbed-Zone Computational Models

In the previous sections, all the soil properties were changing along the depth and all the modification methods were dealing with the soil properties in a depth wise manner, with all soil layers being horizontally homogeneous. However, in reality the soil properties around the pile are not constant horizontally. The assumption of horizontal homogeneity is a very common limitation inherent in numerous existing approximate as well as rigorous methods. This effect is more critical for deep foundations, as the soil around piles and drilled shafts is significantly disturbed due to numerous effects such as pile installation, set-up, vertical and horizontal stress variations due to load-transfer, and three-dimensional variations in strain due to soil-structure interaction.

Thus a disturbed zone around the pile is affected more by dynamic pile-soil interaction and more likely undergoes nonlinear yielding and stress-strain behavior, while the stresses and wave propagation in the far-field are not influenced by these local effects. This logic suggests consideration of an additional domain surrounding the pile, with soil property profiles different from those of the far-field zone. Such a disturbed-zone profile can allow simulation of the many effects on the soil next to the pile discussed above, while also enabling a degree of horizontal inhomogeneity.

Since shear strain will be negligible in the far-field, the small-strain G_{max} modulus profile and zero damping conditions are reasonable assumptions for this region. To account for effects of the 3D strain field around the pile as well as disturbance due to pile installation, the far-field profile can be modified as discussed in Section 4.3.3.2. This concept has been investigated previously for scaled-model centrifuge pile tests using ideal uniform, clean, dry sand specimens (Ashlock, 2006) as previously discussed. The performance of a similar three-domain disturbed-zone continuum

model was also examined for the present study, which features several additional challenges owing to the use of full-scale vibration tests in a complex natural soil profile with soft clays and variable saturation vs. depth, and the new inertial random-vibration excitation method.

Each three-domain BEM analysis of the disturbed-zone model at the time of writing this manuscript required 15 hours of run-time on a supercomputing cluster using 64 high-speed cores (1.5 hours for each of 10 frequencies), and additional time for creating the input and analyzing the results. Due to time constraints, it was therefore not possible in this study to fully explore a large range of soil profiles for the disturbed zone. To investigate whether this approach can be effective in producing more accurate computational simulations of the observed pile response, a few selected three-domain analyses were performed using the previously defined Case E2 profiles (Equation (4.8) and (4.9)) for the disturbed zone. The details of the numerical models examined are shown in Figure 3-33. The following two combinations of shear modulus and damping profile were examined in disturbed zone,

Combination 1: *Case E2* profiles with $z_d = 10$ and $\xi_{\max} = 30\%$

Combination 2: *Case E2* profiles with $z_d = 15$ and $\xi_{\max} = 15\%$

while the G_{\max} and zero damping profiles were used for the far-field soil zone.

The resulting centroidal accelerance functions for the three modes of vibration are presented in Figures 4-75 to 4-77. As shown in these figures, the disturbed-zone model can capture the main peak of the horizontal and rocking accelerance very well. Additionally, the amplitude of the vertical peak accelerance is also acceptably predicted, with more reasonable and physically

motivated modulus and damping profiles that those of the horizontally homogenized two-domain model shown in Figure 4-68. These results show a promising trend towards more accurate modeling of the true multi-modal dynamic response of full-scale pile foundations over a wide range of frequencies. This is the first extension of this type of computational continuum model to full-scale, multi-modal pile vibration tests, and additional analyses are needed to fully explore the parameter space and capabilities of the three-domain disturbed-zone continuum models.

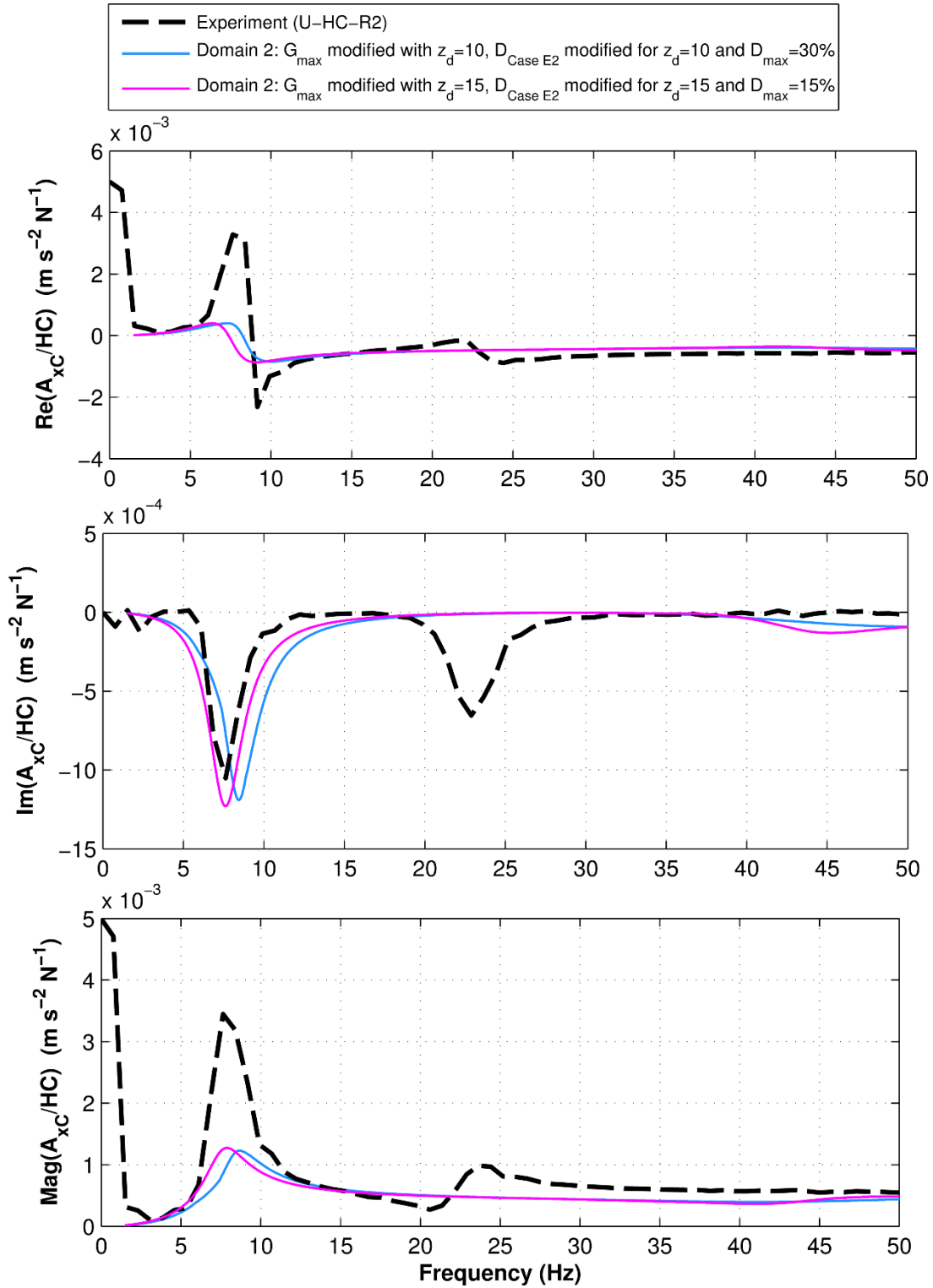


Figure 4-75- A_{x_c}/HC accelerance from three-domain disturbed-zone BEM analysis using the numerical model presented in Figure 3-33 and soil profiles in Figure 4-53.

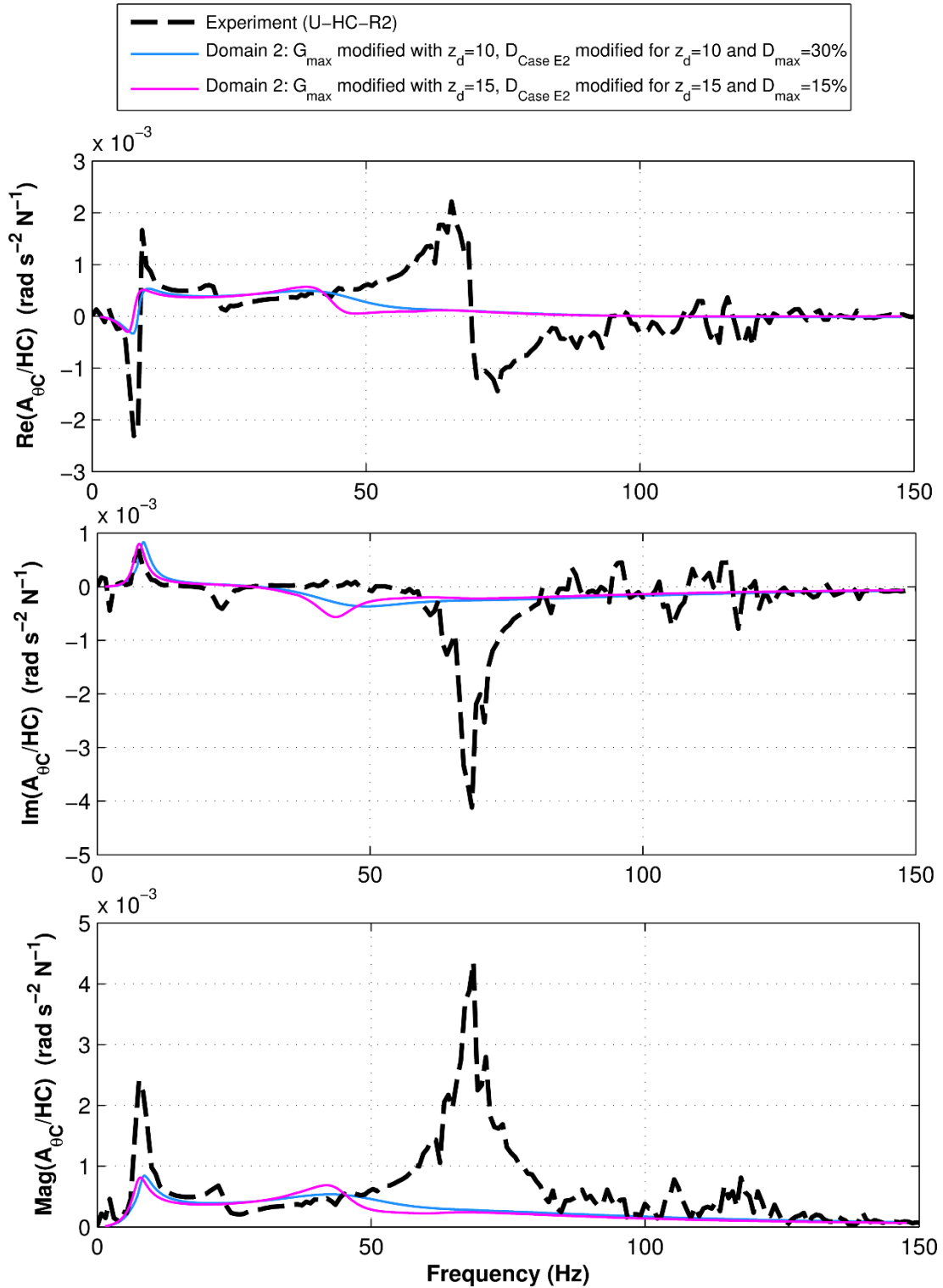


Figure 4-76- $A_{\theta C}/HC$ accelerance from three-domain disturbed-zone BEM analysis using the numerical model presented in Figure 3-33 and soil profiles in Figure 4-53.

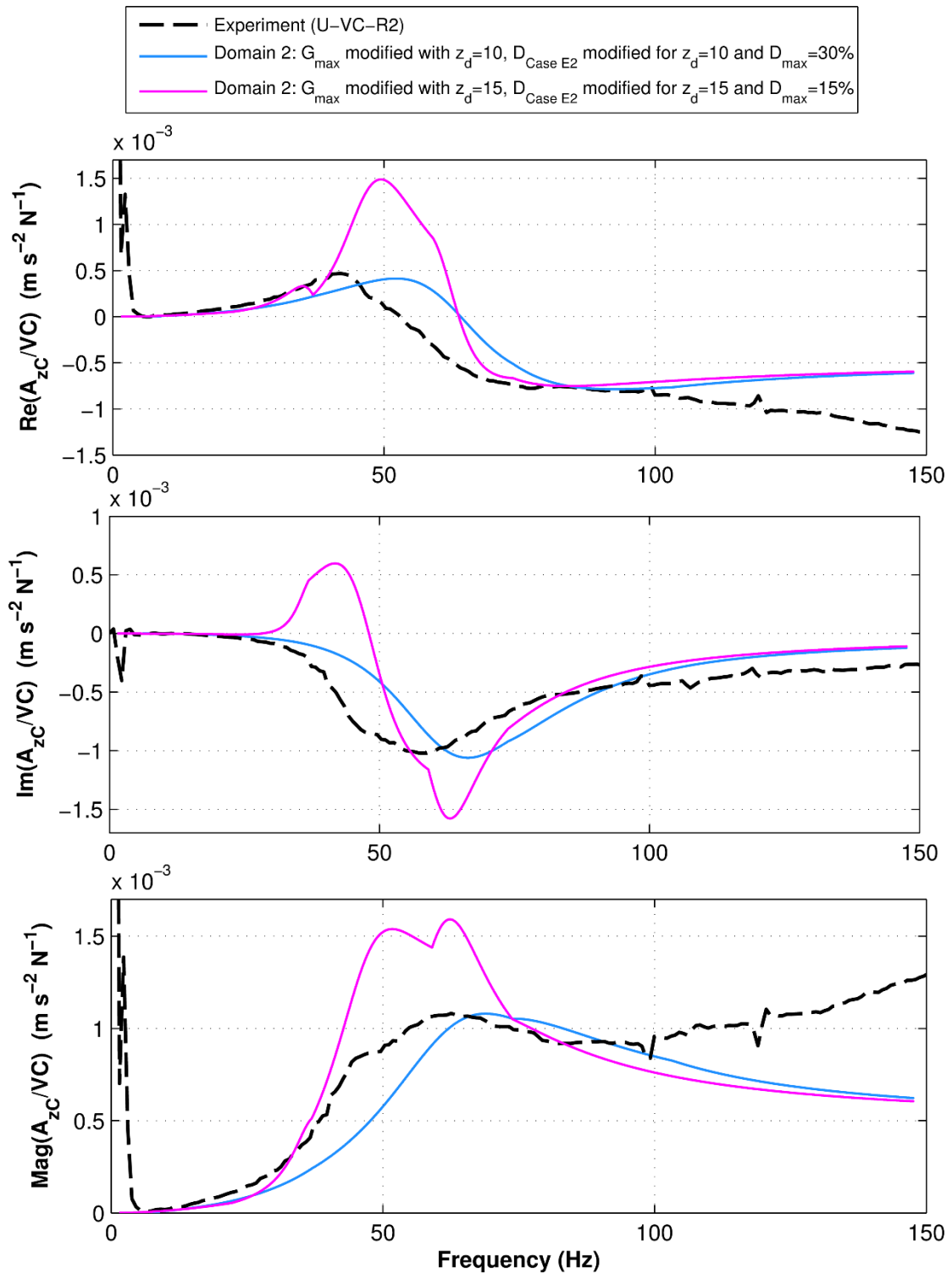


Figure 4-77- A_{zC}/VC accelerance from three-domain disturbed-zone BEM analysis using the numerical model presented in Figure 3-33 and soil profiles in Figure 4-53.

CHAPTER V: SUMMARY AND CONCLUSIONS

This study developed new insights and advancements for the complex problem of dynamic soil-pile interaction through development and validation of new inertial random-vibration testing procedures and equipment, performance of full-scale vibration tests, formulation of new theoretical solutions for analyzing the forced inertial random-vibration problem. The study also provides evaluation and modification of some of the main contemporary approximate and rigorous theoretical solutions, the first extension of the impedance modification factor concept and three-domain disturbed-zone continuum models to the case of full-scale pile tests, and calibrating several other computational continuum models using data from the full-scale pile vibration tests.

In the experimental phase of the study, two H-piles installed to a depth of 6 m in a natural soil profile containing soft clay were tested using different types and levels of random excitations delivered by a newly designed servo-hydraulic inertial shaker system. One of the piles was surrounded by a CDSM zone which made it possible to examine the effect of soil improvement on the dynamic behavior of the pile. Besides the new excitation methods which enable extremely rapid measurement of the system's response across a broad frequency spectrum, the hybrid-mode VE test was performed for the first time in a full-scale pile experiment. It was shown that this test can capture the important aspects of both horizontal and vertical modes of vibration simultaneously, making it a suitable and efficient replacement for traditionally separate tests having vertical and horizontal excitation. In order to characterize the dynamic response of the soil-pile system more consistently, centroidal accelerance functions were introduced as the ratios of the directional acceleration at the pile-cap centroid to the dynamic force delivered by the shaker.

From the experimental data, it was concluded that intermediate levels of random and swept-sine excitation (types R2 and S2) produced the smoothest and most consistent response curves with linear properties, making them the best experimental representatives for calibration of the theoretical model. The soil improvement affected only the vertical mode of vibration, where the experimental results showed a stiffer response for the improved soil condition. The horizontal and rocking responses were relatively unaffected by the soil improvement, which may be related to smaller initial pile-soil contact stresses resulting from inserting the pile into the CDSM mixture before it sets, as opposed to higher lateral stresses caused by forcing the pile into the unimproved but also undisturbed soil.

Using the results of laboratory tests and CPT test data, the formulation presented by Hardin and Drnevich (1972), and the empirical CPT correlations available in (TRB, 2007), two primary soil shear modulus profiles were derived independently, namely, the CPT profile and Hardin-Drnevich profile. The latter provides a means of linking small-strain shear modulus and nonlinear secant shear modulus to shear strain of the soil, and provides estimates of the profiles of maximum damping and nonlinearly strain-dependent damping ratio as well. A parametric study revealed that the void ratio, OCR and cohesion are the critical parameters affecting the centroidal accelerance of the pile-cap. The CPT and Hardin-Drnevich profiles showed reasonable agreement in terms of impedances and theoretical accelerance functions. The strain profile in the soil was calculated and used in an iterative procedure in which the Hardin-Drnevich modulus and damping profiles were updated using soil strains calculated from the pile displacements at resonance. Incorporating the strain was found to not change the shear modulus profile appreciably, while the assumed damping profile decreased dramatically, since it was initially set equal to the maximum damping profile.

Equations of motion of the system were derived for both horizontal and vertical excitation test configurations, and through a parametric study it was shown that (in addition to the soil parameters) the acceleration response was most sensitive to the mass of the rigid pile-cap-shaker system, the stiffness of the pile, and the un-embedded free length of the pile stem. For the soil-pile interaction solution, the 2D approximate solution of Novak and Aboul-Ella was programmed in MATLAB and the validity and accuracy of the method was tested against the experiments and rigorous BEM analyses. It was shown that this approximate method gives good results in the intermediate frequency range, but lacks accuracy in the low-frequency regime. In particular, it cannot capture the fundamental mode of the free-field soil layer at low frequencies, as characterized by a dip in the real impedance and a cutoff frequency in the imaginary impedance component. In addition, it does not allow the effect of soil profiles beneath the pile tip nor the variation of soil properties in the horizontal direction to be accounted for. However, use of the method is recommended for quick verification of the outputs of other methods. The rigorous boundary element method was used for most of the study. Results of the boundary element code BEASSI were successfully verified against known problems. The program was then used to calculate impedance functions corresponding to numerous inhomogeneous and multi-domain soil profiles discussed in the study. These soil profiles were primarily modified versions of the Hardin-Drnevich profile. The goal of these modifications were to find the best profiles that minimized the mismatch between theory and experiment by performing parametric studies. To quantify the mismatch in the three modes of vibration, an error function was developed which can incorporate some degree of engineering judgment into the analysis through the choice of weighting factors for the peak frequencies and shapes of the three acceleration modes. It was shown that a ratio of two between the weighting factors for normalized amplitude to those for normalized peak frequency can give good results. It was shown that it is not possible to match the theoretical to experimental accelerances for

all three modes of vibration simultaneously by simply scaling the updated Hardin-Drnevich shear modulus and damping profiles.

The IMF method which simply scales the impedances in each mode independently was examined for both the unimproved and improved soil problems. This method could provide reasonably good matches of the peak frequencies and amplitudes of the experimental results for the unimproved soil case. However, it was not very effective for the vertical mode in the improved soil case. The results of the IMF method not only help simplify the aspects of the soil-pile interaction problem for engineering applications, but also give insight into the problem and participation of the different modes in the final results. Although the IMF method requires calibration to experimental results before it can be used for prediction, the modification factors resulting from calibration can therefore give clues for further mechanics-based modeling directions.

Finally, the problem was approached by a three-domain computational continuum model in which a disturbed zone was added around the pile. This helps significantly to look at the problem in a more physical way and to incorporate the effects some of the unknown effects around the pile such as gapping, contact mechanisms due to installation, soil nonlinearity, and horizontal heterogeneity. A few representative cases were analyzed for selected soil profiles inside the disturbed zone, and the results showed promise for capturing the horizontal and rocking peak frequencies of the experimental data using reasonable modifications of the far-field modulus and damping profiles.

Since the study employed full-scale field test results, not all of the many parameters and factors affecting the results could be controlled or measured. This makes full-scale dynamic soil-

pile interaction problems very challenging, and requires the use of engineering judgment in daily design and analysis procedures. The results of this study provide several directions for future research to help bridge the gap between theory and observation for dynamic pile design and analysis. In particular, it is recommended that the IMF approach be applied to more existing pile vibration tests to develop a database of modification factors for routine engineering practice. The field tests also featured seven accelerometers in the soil, which were not explored in this study. Theoretical transfer functions can be formulated between any pair of acceleration measurement points on the shaker, pile cap, and soil, and used to further calibrate and refine the theoretical models in the time or frequency domains. Additional soil profiles should be examined inside the disturbed-zone to generate more accurate models and provide further physical insights into the problem. The three-domain disturbed-zone model should also be applied to the improved-soil case by suitably increasing the soil modulus and density in the soil-cement zone to improve the modeling of the experimental results. Finally, the inertial random-vibration experimental approach, IMF concept, and disturbed-zone computational modeling approach should be applied to the more common but more challenging case of pile groups.

REFERENCES

- Alpan, I. (1973). The dynamic response of pile foundations to lateral forces. *In Proc. 5th World Conf. Earthquake Eng., Rome*, Vol. 2, pp. 256-271.
- Andersen, L. (2006). Linear Elastodynamic Analysis. *Aalborg University, Department of Civil Engineering*.
- Ashlock, J. C. (2006). Computational and Experimental Modeling of Dynamic Foundation Interactions With Sand, *Ph.D. Thesis*. University of Colorado at Boulder.
- Ashlock, J. C. & Fotouhi, M. K. (2011). Characterization of Dynamic Soil-Pile Interaction by Random Vibration Methods: Experimental Design and Preliminary Results. *Proceedings of 2011 NSF Engineering Research and Innovation Conference* Atlanta, Georgia.
- Ashlock, J. C. & Pak, R. Y. S. (2009). Experimental Response of Piles in Sand Under Compound Motion. *Journal of Geotechnical and Geoenvironmental Engineering*, 135(6), pp. 799-808.
- Ashlock, J. C. & Phipps, J. N. (2011). Experimental Multi-modal Foundation Vibrations and Comparison with Benchmark Half-space Solutions. *In Geo-Frontiers 2011@ sAdvances in Geotechnical Engineering*, pp. 3118-3127.
- Astley, R. J. (2000). Infinite Elements for Wave Problems: A Review of Current Formulations and An Assessment of Accuracy. *International Journal for Numerical Methods in Engineering*, 49(7), 951-976.
- Ayothiraman, R. , Boominathan, A. & Kumar, S. K. (2014). Lateral Dynamic Response of Full-Scale Single Piles: Case Studies in India. *Full-Scale Testing and Foundation Design: Honoring Bengt H. Fellenius*, 10, pp. 710-721.
- Bendat, J. S. & Piersol, A. G. (1986). *Random Data*. New York: Wiley-Interscience Publications.
- Beskos, D. E. (1997). Boundary Element Methods in Dynamic Analysis: Part II . *Applied Mechanics Reviews*, 50(3), pp. 149-197.
- Beskos, D. E. (1994). Dynamic Soil-Structure Interaction. *Proceedings of The International Symposium on Dynamic Soil-Structure Interaction*. Minneapolis: Taylor & Francis.
- Blaney, G. W., & KauseL, E. Roesset. JM (1976). Dynamic Stiffness of Piles. *The Second International Conference on Numerical Methods in Geomechanics*. Virginia Polytechnic Institute and State University, pp. 1010-1012
- Blaney, G. W. & O'Neill, M. W. (1986). Measured Lateral Response of Mass on Single Pile in Clay. *Journal of Geotechnical Engineering*, 112(4), pp. 443-457.

- Boominathan, A. & Ayothiraman, R. (2005). Dynamic Behaviour of Laterally Loaded Model Piles in Clay. *Proceedings of the ICE-Geotechnical Engineering 158.4*, pp. 207-215.
- Boominathan, A. & Ayothiraman, R. (2006). Dynamic Response of Laterally Loaded Piles in Clay. *Proceedings of the ICE-Geotechnical Engineering, 159*, pp. 233-241.
- Boominathan, A. & Ayothiraman, R. (2007). An Experimental Study on Static and Dynamic Bending Behaviour of Piles in Soft Clay. *Geotechnical and Geological Engineering, 25(2)*, pp. 177-189.
- Bouchon, M. & Sánchez-Sesma, F. J. (2007). Boundary Integral Equations and Boundary Elements Methods in Elastodynamics. *Advances in geophysics, 48*, pp. 157-189.
- Brebbia, C. A. & Dominguez, J. (1996). Boundary Elements: An Introductory Course. *WIT press*.
- Brebbia, C. A. & Telles, J. C. & Wrobel, L. (1984). Boundary Element Techniques. Theory and Applications in Engineering. Berlin, New York.
- Christensen, R. (1971). Theory of Viscoelasticity. New York: Academic Press.
- Clough, R. & Penzien, J. (1993). Dynamics of structures. McGraw Hill.
- Coe, C. J. & Prevost, J. H. & Scanlan, R. H. (1985). Dynamic Stress Wave Reflections/Attenuation: Earthquake Simulation in Centrifuge Soil Models. *Earthquake Engineering & Structural Dynamics, 13(1)*, pp. 109-128.
- Das, B. M. (2012). Principles of Foundation Engineering. CengageBrain.
- Diaz-Rodriguez, J. A. & Lopez-Molina, J. A. (2008). *In the Proceedings of The 14th World Conference on Earthquake Engineering, October 12-17, 2008, Beijing, China*.
- Dobry, R., & Gazetas, G. (1985). Dynamic Stiffness and Damping of Foundations by Simple Methods. *Vibration Problems in Geotechnical Engineering ASCE*, pp. 75-107. Detroit, Michigan.
- Dobry, R., Oweis, I., & Urzua, A. (1976). Simplified Procedures for Estimating the Fundamental Period of a Soil Profile. *Bulletin of the Seismological Society of America, 66(4)*, pp. 1293-1321.
- Dobry, R. & Gazetas, G. (1988). Simple Method for Dynamic Stiffness and Damping of Floating Pile Groups. *Geotechnique, 38(4)*, pp. 557-574.
- Dunnivant, T. W. (1986). Experimental and Analytical Investigation of the Behavior of Single Piles in Over Consolidated Clay Subjected to Cyclic Lateral Loads. *Ph.D. Dissertation, University of Houston*.
- Elgamal, A. & Lu, J. & Yang, Z. & Shantz, T. (2010). A 3D Soil-Structure Interaction Computational Framework. *In 7th International Conference on Urban Earthquake Engineering*, pp. 3-5.

- Finn, W. D. & Gohl, W. B. (1987). *Centrifuge Model Studies of Piles Under Simulated Earthquake Lateral Loading*. In *Dynamic Response of Pile Foundations—Experiment, Analysis and Observation*. pp. 21-38.
- Fotouhi, M. K. & Ashlock, J. C. (2012). Analysis of Experimental Dynamic Soil-Pile Interaction by Approximate Numerical Solutions. *15th WCEE, Lisbon, Portugal*.
- Gazetas, G. (1991). Formulas and Charts for Impedances of Surface and Embedded Foundations. *Journal of Geotechnical Engineering*, 117(9), pp. 1363-1381.
- Gazetas, G. (1984). Seismic Response of End-Bearing Single Piles. *International Journal of Soil Dynamics and Earthquake Engineering*, 3(2), pp. 82-93.
- Givoli, D. (2004). High-Order Local Non-Reflecting Boundary Conditions: A Review. *Wave Motion*, 39(4), pp. 319-326.
- Gle, D. (1981). The Dynamic Lateral Response of Deep Foundations. *Ph.D. Dissertation. University of Michigan, Ann Arbor*.
- Guddati, M. N., & Lim, K. W. (2006). Continued Fraction Absorbing Boundary Conditions for Convex Polygonal Domains. *International Journal for Numerical Methods in Engineering*, 66(6), pp. 949-977.
- Guzina, B. B. & Pak, R. Y. S. & Martínez-Castro, A. E. (2006). Singular Boundary Elements for Three-Dimensional Elasticity Problems. *Engineering Analysis with Boundary Elements*, 30(8), pp. 623-639.
- Hall, W. S. & Oliveto, G. (2003). *Boundary Element Methods for Soil-Structure Interaction. Kluwer Academic Publishers*.
- Hardin, B. O. & Drnevich, V. P. (1972). Shear Modulus and Damping in Soils: Design Equations and Curves. *Journal of Soil Mechanics and Foundations Division*, 98(7), pp. 667-692.
- Hardin, B. O. & Drnevich, V. P. (1972). Shear Modulus and Damping in Soils: Measurement and Parameter Effects. *Journal of the Soil Mechanics and Foundations Division*, 98(6), pp. 603-624.
- Kausel, E. & Waas, G. & Roesset, J. M. (1975). Dynamic Analysis of Footings on Layered Media. *Journal of the Engineering Mechanics Division*, 101(5), pp. 679-693.
- Kaynia, A. M. & Kausel, E. (1991). Dynamics of Piles and Pile Groups in Layered Soil Media. *Soil Dynamics and Earthquake Engineering*, 10(8), pp. 386-401.
- Ko, H. Y. (1988). Summary of the State-Of-The-Art in Centrifuge Model Testing. *Centrifuges in Soil Mechanics*, pp. 11-18.
- Kouroussis, G. & Anastasopoulos, I. & Gazetas, G. & Verlinden, O. (2013). Three-Dimensional Finite Element Modelling of Dynamic Pile-Soil-Pile Interaction in Time

Domain. *Proceedings of the COMPDYN 2013-4th ECCOMAS Thematic Conference on Computational Methods in Structural Dynamics and Earthquake Engineering*.

Kramer, S. (1996). *Geotechnical Earthquake Engineering*. Englewood Cliff, NJ: Prentice-Hall.

Kuhlemeyer, R. L. & Lysmer, J. (1973). Finite Element Method Accuracy for Wave Propagation Problems. *Journal of Soil Mechanics & Foundations Div*, 99(Tech Rpt).

Lenke, L. R., Pak, R. Y., & Ko, H. Y. (1991). Boundary Effects in Modeling of Foundations Subjected to Vertical Excitation. *Centrifuge*, 91, pp. 473-480.

Liu, C. & Soltani, H. & Pinilla, J. D. & Muraleetharan, K. K. & Cerato, A. B. & Miller, G. A. (2011). Centrifuge Investigation of Seismic Behavior of Pile Foundations in Soft Clays. *ASCE Proceedings of the Geo-Frontiers 2011 conference* (pp. 585-594). Dallas, Texas: ASCE.

Maheshwari, B. K. & Truman, K. Z. & El Naggar, M. H. & Gould, P. L. (2004). Three-Dimensional Nonlinear Analysis for Seismic Soil–Pile–Structure Interaction. *Soil Dynamics and Earthquake Engineering*, 24(4), pp. 343-356.

Manna, B. & Baidya, D. K. (2009). Vertical Vibration of Full-scale Pile—Analytical and Experimental Study. *Journal of geotechnical and geoenvironmental engineering*, 135(10), pp. 1452-1461.

Manolis, G. D., & Beskos, D. E. (1988). *Boundary Element Methods in Elastodynamics*. London: Unwin Hyman.

Mason, H. B. & Trombetta, N. W. & Chen, Z. & Bray, J. D. & Hutchinson, T. C. & Kutter, B. L. (2013). Seismic Soil–Foundation–Structure Interaction Observed in Geotechnical Centrifuge Experiments. *Soil Dynamics and Earthquake Engineering*, 48, pp. 162-174.

Meymand, P. J. (1984). Shaking Table Scale Model Tests of Nonlinear Soil-Pile-Superstructure. *Ph.D. Dissertation, University of California, Berkeley*.

Mayne, P. W., & Kulhawy, F. H. (1982). Ko-OCR Relationships in Soil. *Journal of the Geotechnical Engineering Division*, 108(6), pp. 851-872.

Mylonakis, G., & Gazetas, G. (2000). Seismic soil-structure interaction: beneficial or detrimental?. *Journal of Earthquake Engineering*, 4(3), pp. 277-301.

Nogami, T. & Novák, M. (1976). Soil-Pile Interaction in Vertical Vibration. *Earthquake Engineering & Structural Dynamics*, 4(3), pp. 277-293.

Novak, M. (1974). Dynamic Stiffness and Damping of Piles. *Canadian Geotechnical Journal*, 11(4), pp. 574-598.

Novak, M. & Aboul-Ella, F. & Nogami, T. (1978). Dynamic Soil Reactions for Plane Strain Case. *Journal of the Engineering Mechanics Division*, 104(4), pp. 953-959.

Novak, M. & Aboul-Ella, F. (1978). Impedance Functions of Piles in Layered Media. *Journal of the Engineering Mechanics Division*, 104(3), pp. 643-661.

- Novak, M. & Nogami, T. (1977). Soil-Pile Interaction in Horizontal Vibration. *Earthquake Engineering & Structural Dynamics*, 5(3), pp. 263-281.
- Orense, R. P. & Nawawi, C. & Pender, M. J. (Eds). (2010). *Soil-Foundation-Structure Interaction: Selected Papers from the International Workshop on Soil-Structure Interaction (SFSI 09)*. Auckland, New Zealand. CRC Press.
- Pak, R. Y. S. & Ashlock, J. C. (2000). Fundamental Dynamic Behavior of Foundations on Sand. *Denver, CO, USA, ASCE*, pp. 10–19.
- Pak, R. Y. S., & Ashlock, J. C. (2000). Concept of Impedance Modification Factors for Foundations on Cohesionless Soils., *Proc. 14th ASCE Engineering Mechanics Conference*, 4 pages.
- Pak, R. Y. S., & Ashlock, J. C. (2007). Method of Adaptive-Gradient Elements for Computational Mechanics. *Journal of Engineering Mechanics*, 133(1), pp. 87-97.
- Pak, R. Y. & Ashlock, J. C. & Abedzadeh, F. & Turner, N. (2006). Dynamic Hybrid-Mode Test of a Pile on a Centrifuge. *Physical Modeling in Geotechnics, 6th Int. Conf. on Physical Modeling in Geotechnics, Hong Kong*, pp. 1037-1042,
- Pak, R. Y. S. & Guzina, B. B. (2002). Three-Dimensional Green's Functions for a Multilayered Half-Space in Displacement Potentials. *Journal of engineering mechanics*, 128(4), pp. 449-461.
- Pak, R. Y. S. & Guzina, B. B. (1999). Seismic Soil-Structure Interaction Analysis by Direct Boundary Element Methods. *International Journal of Solids and Structures*, 36(31), pp. 4743-4766.
- Scott, R. (1981). Pile Testing in a Centrifuge. *Proc. Int. Conf. on Soil Mech and Found. Eng.* 2, pp. 839-842.
- Taghavi, Amirata, Miller, G. A. & Muraleetharan, K. K. (2010). Soil Report for NEES-Piles Full-Scale Field Testing in Miami, Oklahoma, *The University of Oklahoma*.
- Terzaghi, K. (1996). *Soil Mechanics in Engineering Practice*. Wiley. com.
- Transportation Research Board (TRB) (2007). *National Cooperative Highway Research Program (NCHRP) Synthesis 368, Cone Penetrating Testing*.
- Veletsos, A. S. & Verbič, B. (1973). Vibration of Viscoelastic Foundations. *Earthquake engineering & structural dynamics*, 2(1), pp. 87-102.
- Wilson, D. & Boulanger, R. & Kutter, B. & Abghari, A. (1997). Aspects of Dynamic Centrifuge Testing of Soil-Pile-Superstructure Interaction. *Observations and Modeling in Numerical Analysis and Model Tests in Dynamic Soil-Structure Interaction Problems*. pp. 47-63. ASCE GSP, No. 64.
- Wolf, J. (1985). *Dynamic Soil-Structure Interaction*. Englewood Cliffs, NJ: Prentice-Hall.